Computational Methods in Applied Sciences

Manolis Papadrakakis
Vagelis Plevris
Nikos D. Lagaros *Editors*

Computational Methods in Earthquake Engineering

Volume 3

ECCOMAS
European Community on Computational Methods in Applied Sciences

Springer

Computational Methods in Applied Sciences

Volume 44

Series editor

E. Oñate
CIMNE
Edificio C-1, Campus Norte UPC
Gran Capitán, s/n
08034 Barcelona, Spain
onate@cimne.upc.edu

More information about this series at http://www.springer.com/series/6899

Manolis Papadrakakis · Vagelis Plevris
Nikos D. Lagaros
Editors

Computational Methods in Earthquake Engineering

Volume 3

Springer

Editors
Manolis Papadrakakis
School of Civil Engineering
National Technical University of Athens
Athens
Greece

Nikos D. Lagaros
School of Civil Engineering
National Technical University of Athens
Athens
Greece

Vagelis Plevris
Department of Civil Engineering and Energy Technology
Oslo and Akershus University College of Applied Sciences
Pilestredet 35, Oslo
Norway

ISSN 1871-3033
Computational Methods in Applied Sciences
ISBN 978-3-319-47796-1 ISBN 978-3-319-47798-5 (eBook)
DOI 10.1007/978-3-319-47798-5

Library of Congress Control Number: 2016954584

Printed on acid-free paper

This Springer imprint is published by Springer Nature
The registered company is Springer International Publishing AG
The registered company address is: Gewerbestrasse 11, 6330 Cham, Switzerland

Preface

During the past few decades, advanced methods and computational techniques have been developed for a better description and understanding of the dynamic behaviour of structural systems. Taking advantage of the most recent developments in computers and their technology, the scientific field of computational mechanics has steadily emerged as a discipline initiating revolutionary changes to the theoretical treatment of computers as well as to the engineering practice through innovative design methodologies. These dramatic changes had a profound impact on all fields of structural dynamics such as earthquake engineering, offshore engineering, bridge aerodynamics, vibro-acoustics, soil–structure and fluid–structure interaction, wind-induced vibrations, man-made motions, multi-body dynamics, structural control, etc. The purpose of this volume is to bring together the scientific communities of computational mechanics and structural dynamics with a focus on earthquake engineering. The volume will facilitate the exchange of ideas in topics of mutual interest and can serve as a platform for establishing links between research groups with complementary activities.

The basic idea of this book is to include all the aforementioned research topics into a volume taking advantage of the connecting link between them, which is computational methods and tools. In this direction, the book consists of 15 chapters in total, dealing with the topic of computational methods in Earthquake Engineering. The first of this book chapter addresses the problem of the numerical modelling of buried pipelines subjected to faulting. The advantages and disadvantages of available numerical approaches are highlighted. The impact of fault type on the pipeline mechanical behaviour is investigated, while numerical considerations, such as the geometrical nonlinearity, the ovalization and the internal pressure are evaluated using a simple, well-established and reliable numerical approach. The second chapter presents a recently proposed new method, which allows the explicit determination of the parameters of the pulse contained in pulse-like records. The Mavroeidis and Papageorgiou wavelet is used for the mathematical representation of the pulse but the proposed methodology can be easily modified to cover other types of wavelets as well.

The third chapter deals with the finite element analysis of the sloshing phenomenon occurring in liquid storage tanks under external excitations. The governing equations for the fluid and structure and their solution methodologies are clarified and current nonlinear FE modelling strategies for interactions between liquid, tank and soil are presented in detail. Chapter four presents a procedure based on the analysis of a set of accelerograms recorded in a chosen site to take into account their time and frequency variability. In particular, the generation of artificial fully non-stationary accelerograms is performed using a three-step procedure.

The objective of the fifth chapter is to present the main theoretical features of a recently developed higher-order beam element, accompanied by an illustrative application to members with linear elastic behaviour. The beam performance is assessed by comparison against refined solid finite element analyses, classical beam theory results, and approximate numerical solutions. In the sixth chapter an analytical approach based on small displacement theory is derived using the force analogy method to calculate the plastic rotations of plastic hinges at various locations of moment-resisting frames. Both static and dynamic analyses with nonlinear geometric effects are incorporated in the derivation, together with the element stiffness matrices using a member with plastic hinges in compression, and therefore the coupling of geometric and material nonlinearity effects is included from the beginning of the derivation.

In the seventh chapter a parametric study is conducted on five RC frame structures designed according to Eurocode 8. It is shown that Eurocode formulation for the evaluation of the seismic demand on non-structural components does not fit well the analytical results for a wide range of periods, particularly in the vicinity of the higher mode periods of vibration of the reference structures. A novel formulation is proposed for an easy implementation in future building codes based on the actual Eurocode provisions. In the eighth chapter three methodologies are proposed for the design of Reinforced Concrete Sections with single reinforcement according to EC2-1-1 and the rectangular stress distribution. The purpose of the design is to calculate the necessary tensile steel reinforcement given the forces (bending moment and axial force) acting on the section. Apart from the direct problem, the inverse problem is also addressed, where the steel reinforcement is given and the purpose is to find the maximum bending moment that the section can withstand.

Chapter nine extends the approach of base isolation and investigates the potential effectiveness of multi-storey structures with seismic isolators at different storey-levels. The control concept provides numerous options for the designer in respect to the desired seismic performance of the building. The effectiveness of the proposed control system is investigated in parametric studies. The tenth chapter discusses the role of integration step size in time integration analysis, specifically, from the points of view of accuracy and computational cost. It presents discussions on conventionally accepted comments, codes regulations, and some modern methods for assigning adequate values to the integration step sizes in constant or adaptive time integration.

In the eleventh chapter the seismic vulnerability of smart structures is assessed based on a fragility analysis framework. A three-storey steel frame building employing the nonlinear smart damping system is selected as a case study structure in order to demonstrate the effectiveness of the seismic fragility analysis framework. In chapter twelve the implementation of actuator connections that divide a structure in several substructures is proposed. These connections can be installed on the structure during construction or retrofit; while as it is demonstrated, they can be controlled and excite each substructure separately.

In the thirteenth chapter a fuzzy neural network model is presented capable to compute the structural response of a structural system by training the model for two earthquakes using fuzzified ground motion data. The trained NN is then used to simulate earthquakes by feeding various intensities, exhibiting good predictions for practical purposes. The fourteenth chapter presents a smart fuzzy control algorithm for mitigation of dynamic responses of seismically excited bridge structures equipped with control devices. The smart fuzzy controller is developed through the combination of discrete wavelet transform, backpropagation neural networks and Takagi–Sugeno fuzzy model.

Finally, chapter fifteen presents a methodology for real-time planning of emergency inspections of urban areas. This methodology is based on two nature-inspired algorithms, Harmony Search Algorithm (HS) and Ant Colony Optimization (ACO). HS is used for dividing the area into smaller blocks while ACO is used for defining optimal routes inside each created block.

The aforementioned collection of chapters provides an overview of the present thinking and state-of-the-art developments in the application of advanced computational techniques into the framework of structural dynamics and earthquake engineering. The book is targeted primarily to researchers, postgraduate students and engineers that are active in areas related to earthquake engineering and structural dynamics. We believe that the collection of these chapters in a single volume will be useful to both academics and practicing engineers.

The editors of the book would like to express their deep gratitude to all the contributors for their most valuable support during the preparation of this volume, for their time and effort devoted to the completion of their contributions and for their great expert help in the review process. We are also grateful to all the colleagues who although did not contribute chapters to the book, were kind enough to offer their expert help in reviewing the book chapters. Finally, we would also like to thank the personnel of Springer Publishers, especially Ms. Johanna F.A. (Anneke) Pot (Editorial Assistant in Engineering) and Ms. Natalie Jacobs (Senior Publishing Editor in Engineering) for their most valuable continuous support during the preparation of this book.

Athens, Greece — Manolis Papadrakakis
Oslo, Norway — Vagelis Plevris
Athens, Greece — Nikos D. Lagaros

August 2016

Contents

Numerical Modeling Aspects of Buried Pipeline—Fault Crossing

Vasileios E. Melissianos and Charis J. Gantes

Abstract Onshore buried steel pipelines transporting oil and gas play a major role in the energy supply chain. Hence, when seismic areas are transversed, fault crossing might be inevitable, which may heavily endanger the pipeline integrity. Thus, the design of buried pipelines at fault crossing remains a research topic of great interest both for the industry and the academia. Experimental, analytical and numerical approaches are used for that purpose. In this chapter, the numerical modeling of pipelines subjected to faulting is addressed and the advantages and disadvantages of the available numerical approaches are highlighted. The impact of fault type on the pipeline mechanical behavior is investigated and numerical considerations, such as the geometrical nonlinearity, the ovalization and the internal pressure are evaluated using a simple, well-established and reliable numerical approach. The outcome of this study provides useful information and guidelines to practicing engineers for the analysis and design of buried pipelines at fault crossings.

1 Introduction

Onshore buried steel pipelines with continuous welded joints are nowadays the most efficient way for fuel transportation over long distances and are considered as one of the most valuable links in the energy supply chain. Pipelines are classified as hazardous structures given that any potential failure or leakage may have devastating consequences on the environment, nearby residential areas as well as economic losses. Thus, the design and construction of pipeline systems is undertaken within a strict framework of standards and regulations. However, when seismic areas are transversed, fault crossing might be inevitable due to the numerous limitations that

V.E. Melissianos (✉) · C.J. Gantes
Institute of Steel Structures, School of Civil Engineering, National Technical University of Athens, 9 Iroon Polytechneiou str., Zografou Campus, GR-15780 Athens, Greece
e-mail: melissia@mail.ntua.gr

C.J. Gantes
e-mail: chgantes@central.ntua.gr

M. Papadrakakis et al. (eds.), *Computational Methods in Earthquake Engineering*, Computational Methods in Applied Sciences 44,
DOI 10.1007/978-3-319-47798-5_1

are encountered during the route selection procedure. Fault movement is the result of earth plates' relative movements and imposes large permanent ground displacements on the pipeline, which the latter has to accommodate safely. Faulting has been identified as the main cause of pipeline failure due to earthquake loading among other seismic induced actions, such as liquefaction induced lateral spread and wave propagation [1]. This was the main conclusion after recent major earthquake events, such as the 1971 San Fernando earthquake [2], the 1995 Kobe earthquake [3] and recently the 1999 Kocaeli [4] and the 1999 Chi-Chi earthquakes [5]. Although pipeline steel is a ductile material, high level strain concentration at certain areas of the structure is of great concern. Potential pipeline failure modes in case of faulting are local buckling/wrinkling due to compressive strains, tensile fracture of girth welds between pipeline adjacent parts, cross-section distortion or ovalization and, in case of reverse fault type, upheaval buckling due to compressive forces. These failure modes are directly related to the extensive deformation that pipelines undergo due to faulting, and are not addressed by proper installation of coating and cathodic protection, which aim at protecting the pipeline from non-seismic actions.

The top priority in pipeline earthquake-resistant design is the avoidance of any potential damage that could lead to loss of containment. The financial and environmental importance of pipelines necessitates the implementation of advanced analysis approaches in order to assess the pipe mechanical behavior due to faulting. In such framework, there are two analysis approaches for pipe—fault crossing. The first one is the analytical approach, which is useful in the preliminary design stage and can be also handled as a quick decision making tool for seismic risk assessment. The second is the numerical approach that is realized using advanced finite element software, taking advantage of recent advancements in computational methods and computing power. Pipeline numerical modeling using FEM is a multi-disciplinary research topic, as buried pipeline behavior depends mainly upon the response and the resistance of the surrounding soil. At this point, it should be clarified that the buried pipeline response due to earthquake-induced actions differs from common civil engineering structures. The latter are founded in the soil and in case of an earthquake event, the structure's foundation is forced to follow the ground motion and the superstructure is excited due to its inertial mass. In case of buried pipelines, on the other hand, the soil surrounds the pipeline/structure and thus the pipeline is forced to follow the soil movement by developing excessive deformation. Thus, pipeline—soil interaction stands as the dominant feature in numerical modeling.

2 Pipeline—Fault Crossing Analysis

2.1 Analytical Approach

The analytical approach for buried pipeline—fault crossing analysis has been well investigated during the past decades. The pioneers of such pertinent work were Newmark and Hall [6] who presented an analytical model for assessing the integrity

of a buried pipe crossing a ruptured fault by considering the pipeline as a long cable undergoing small displacements and the fault as a planar surface separating two rigid bodies. Their work was extended by taking into account the lateral soil interaction to evaluate the maximum axial strain [7]. Then, the pipeline—soil friction nonlinearity was incorporated in the model in [8]. Based on the previously established analytical model, the bending stiffness was also added in the calculations in [9]. Later, a more accurate analytical model was proposed [10] by incorporating the deformation of the pipe cross-section and relating the pipe bending angle to the maximum axial strain. Recently, Karamitros et al. [11, 12] improved the previous analytical approaches for both strike-slip and normal faulting by combining the model of beam on elastic foundation and the elastic beam theory to calculate the maximum strains by considering also material and geometrical nonlinearities. Then, Trifonov and Cherniy [13, 14] presented a semi-analytical approach for pipeline stress-strain analysis by considering the contribution of transverse displacements to the axial elongation, while neglecting the symmetry condition about the pipe—fault intersection point.

2.2 *Numerical Approach*

Analytical approaches remain a useful tool during the preliminary design stage of a pipeline project. However, the complexity of the pipeline—soil interaction necessitates the implementation of advanced numerical modeling for the final design. At this point, two alternative numerical approaches are available and are in general accepted by the scientific community. In the first one, the so-called beam-type model, the pipeline is discretized with beam-type finite elements and the surrounding soil is modeled with nonlinear translational springs. In the second approach, which is referred as the continuum model, the pipeline is meshed with shell elements and the surrounding soil either with 3D-solid elements or with nonlinear springs.

The numerical approach was initially adopted to analyze buried pipelines as elastic beams by taking into account both the horizontal and the vertical movement of the fault [15], while the finite element method to evaluate pipeline strain was introduced in [16]. The beam-type model is extensively used by researchers to assess the pipeline integrity due to faulting. For example, the beam-type model was recently employed by Joshi et al. [17] to investigate the pipeline behavior due to reverse fault movement. Special attention was given to numerical parameters, such as the fault motion simulation in steps and the boundary conditions of the springs' "ground nodes". The authors of the present chapter have implemented the beam-type model to investigate the effectiveness of innovative mitigating measures against the consequences of faulting on pipeline [18–20] and also in seismic risk assessment of buried pipelines at fault crossings [21]. Additionally, the beam-type model is proposed nowadays by Standards and Regulations (e.g. ALA [22], Eurocode 8 [23] and ASCE [24]) as a reliable and computationally efficient

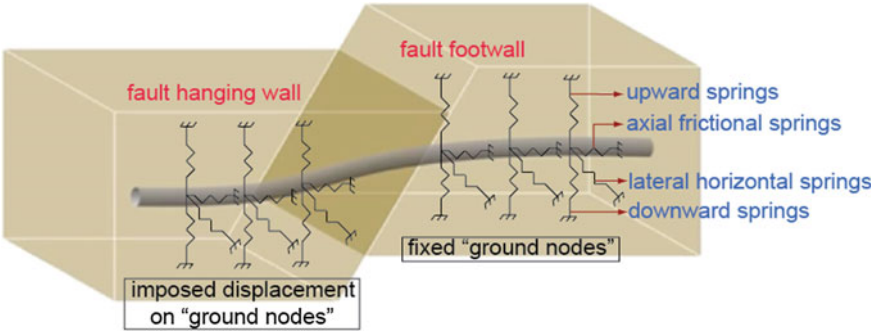

Fig. 1 Schematic representation of beam-type finite element model for buried pipeline—normal fault crossing

numerical approach. Within this modeling technique, the pipeline is meshed with beam-type finite elements that can model its axial, bending and shear deformation and can provide stresses and strains at integration points of cross-sections along the pipeline. The latter allows the engineer to select the desired number of integration points on the cross-section depending on the expected level of accuracy. Moreover, axial and shear forces, as well as bending moments, are nodal forces which are calculated at the beam element's end local nodes. Additionally, using beam elements enables the consideration of pipeline plastic deformations in the vicinity of the fault, as material and geometrical nonlinearities can be taken into account. The soil, then, is represented by a series of mutually independent translational uniaxial elastoplastic springs in three directions, based on the Winkler soil approach, that connect the pipeline to "ground nodes". The beam-type model is illustrated in Fig. 1, where the springs in the axial direction model the pipeline—soil friction, the springs in the horizontal transverse (lateral) direction model the soil response due to the lateral pipeline movement in the trench, while springs in the vertical direction model the soil response due to the pipeline upward and downward movement in the trench. It is noted that beam-type finite elements are not capable of representing neither pipe local buckling, nor cross-section distortion, even though more specialized pipe-type elements are available in commercial software, which can account for the latter. As pipeline integrity is governed by strains, checks on failure modes are then carried out by comparing maximum developing compressive and tensile strains to corresponding strain limit strains provided in pertinent codes. Furthermore, the use of beam-type models raises questions regarding the influence of trench dimensions, acknowledging that spring properties are calculated without proper consideration of them, or of the native soil properties outside the trench.

To overcome the shortcomings of beam-type models, continuum models have recently been employed. Within this numerical technique, the pipeline is meshed with shell elements and the surrounding soil with 3D-solid finite elements or nonlinear translational springs. However, in soil modeling with solid elements special attention is needed regarding the modeling of pipeline—soil interaction by

means of contact elements. Some of the first attempts to employ the continuum model by considering the contact issues between the pipeline and the soil were reported in [25] and [26]. Then, Vazouras et al. [27–29] presented extended numerical simulations of pipe—strike-slip fault crossing by adopting the continuum model. These authors carried out parametric studies on soil parameters, pipe—fault crossing angle and pipeline characteristics and came up with a simplified expression for critical buckling strain. However, the trench was not considered in their analyses. Recently, the effects of trench dimensions, native soil properties and fault motion simulation were employed in the continuum models to evaluate their effects on the pipeline behavior [30, 31]. Furthermore, the continuum model was used by Uckan et al. [32] to introduce a simplified model for calculating the critical pipe length and present the basis of formulating pipeline fragility curves.

Soil representation with springs is an efficient way to model the surrounding medium, as there is no need to consider complex soil material laws nor contact issues between the pipeline and the surrounding soil, while at the same time the computational cost is reduced [33, 34]. However, soil springs in combination with pipe meshing with shell elements may lead to the introduction of local forces on shell elements that, especially in case of coarse mesh, do not represent well the physical problem, as they alter the distribution of stresses and strains on the pipeline wall, hence local buckling considerations are inaccurate. The second alternative for soil modeling in continuum models is to use 3D-solid elements, which highly improves modeling accuracy, while trench dimensions and soil properties can be reliably incorporated into the finite element model. Yet, this technique severely increases modeling complexity and computational effort in terms of the resulting number of degrees of freedom, solution time requirements, convergence difficulties, boundary conditions, fault rupture modeling and especially the introduction of contact elements to model pipe—soil interaction.

Buried pipeline—fault crossing numerical modeling can be carried out by employing, also, a hybrid model that combines the beam-type and the continuum model. In such a case, the pipeline around the fault zone, where higher strains are anticipated, is modeled using the continuum model, while the rest of the pipe length is modeled using the beam-type model [11, 12]. This approach aims at reducing the computational cost and exploiting the advantages of both numerical approaches, even though the above mentioned disadvantages of both models cannot be really avoided.

The fault offset and fault plane simulation are two critical aspects of pipe—fault crossing numerical modeling. Implementing the beam-type model tends to simplify the situation, as “ground nodes” on the fault footwall are considered fixed, while “ground nodes” on the fault hanging wall are subjected to the fault offset. The same conditions are applied in case springs are adopted for soil modeling in the continuum model. On the contrary, soil modeling with 3D-solid elements necessitates the simulation of the fault plane. Then, fault offset is applied on the hanging wall part of the fault. Moreover, appropriate boundary conditions have to be applied to the outer surfaces of the soil “blocks” in order to simulate the natural soil conditions.

3 Finite Element Model Details

As explained above, numerical modeling of buried steel pipeline—fault crossing can be carried out using either the beam-type model, or the continuum model. The advantages and disadvantages of the two models have been discussed in Sect. 2, leading to the conclusion that beam-type models are more appropriate for practical applications, as long as their disadvantages are acknowledged. This is enhanced by the fact that usually pipeline route in seismic areas will be intercepted by several minor or major faults and thus the implementation of continuum models might be expensive in terms of computational cost and time. Thus, the beam-type model is adopted here to investigate some critical numerical aspects, as well as the pipeline mechanical behavior due to normal, strike-slip and reverse faulting.

The pipeline—fault crossing geometry is presented in Fig. 2 both in plan and in section view. The fault displacement is analyzed to its three spatial components, namely Δ_1 horizontal parallel to the fault trace, Δ_2 horizontal perpendicular to the fault trace and Δ_3 vertical to the fault trace. The fault displacement components are defined in the global coordinate system (1, 2, 3), while the pipeline coordinate system (x, y, z) is estimated through the pipe—fault crossing angle β. Moreover, the fault dip angle is defined by ψ.

A straight pipeline segment with length $L = 1000$ m is considered for the analyses, as good engineering practice and the pertinent codes suggest the avoidance of bends in areas prone to large ground displacements, because additional forces may be imposed on the pipeline due to the curves. The fault is assumed to be planar with zero thickness, having dip angle $\psi = 70°$, and intercepts the pipeline at the middle of its modeled length with crossing angle $\beta = 70°$.

The pipeline under consideration is a typical high-pressure natural gas transmission pipeline featuring a cross-section with diameter $D = 914$ mm and thickness $t = 12.7$ mm. Faulting results to imposed large displacements on the pipeline and thus steel yielding is expected to occur around the fault zone, which necessitates the

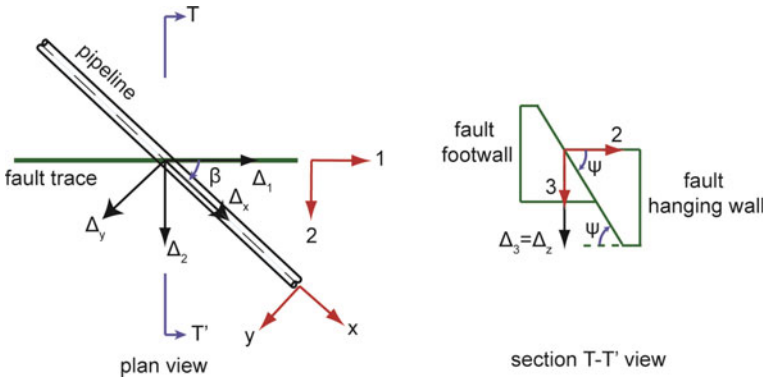

Fig. 2 Pipeline—fault crossing plan and section view

Table 1 API5L-X65 steel properties

Parameter	Value
Poison's ratio	0.3
Young's modulus (GPa)	210
Yield stress (MPa)	448.5
Ultimate stress (MPa)	531.0
Ultimate strain (%)	20

consideration of material nonlinearity in the analyses. Pipeline steel is of type API5L-X65 and is considered as elastic—plastic with isotropic hardening. Steel properties are listed in Table 1.

The numerical modeling is carried out using the commercial FEM software ADINA [35]. The pipeline is meshed with PIPE elements, which are 2-node Hermitian beam-type finite elements with extra degrees of freedom to account for the pipe ovalization. PIPE elements are also capable of being loaded with internal pressure. The pipe mesh typical size is taken equal to 0.25 m, after a mesh density sensitivity analysis was carried out to investigate the optimum length of discretization.

The surrounding soil is modeled using discrete springs, according to ALA [22] provisions. As presented in Fig. 1, every pipeline node is connected to the ground via four different elastic—perfectly plastic translational springs, with "ground nodes" considered fixed on the fault footwall and subjected to imposed displacement on the fault hanging wall. Soil springs are modeled using SPRING elements exhibiting stiffness only in the local axial direction. Then, the pipeline is assumed to be coated with coal-tar having a friction coefficient equal to $f = 0.90$ and to be embedded under 1.30 m of granular loose sand with cohesion $c = 0$, unit weight $\gamma = 18$ kN/m^3 and internal friction angle $\varphi = 36°$.

The pipeline numerical model in this study consists of 4000 beam-type pipe elements, while the surrounding soil comprises 4001 axial frictional springs, 4001 lateral springs, 4001 vertical upward springs and 4001 vertical downward springs. Thus, the finite element model consists of 20,004 nodes and 120,024 degrees of freedom.

Axial soil springs model the pipeline—soil friction and their properties depend on the backfill soil and the pipeline coating material properties. The developing frictional forces are estimated based on geotechnical approaches used to simulate the force transfer on axially loaded interfaces of piles. Especially for sand and for cohesionless soil types in general, frictional forces are estimated through integration of shear stresses along the pipeline—soil interface. The pipe surface roughness is defined by the application of coating and the friction angle δ equals 50 to 100 % of soil internal friction angle φ. The maximum soil resistance is then achieved for relatively small displacement within 2.5 to 5.0 mm for dense to loose sand [36].

Transverse horizontal (lateral) springs model the soil resistance to any pipeline horizontal transverse movement in the trench. Thus, the triggered mechanisms are similar to those of vertical anchor plates or horizontal moving foundation by

Table 2 Soil spring properties according to ALA [22]

Spring type	Force (kN/m)	Yield displacement (mm)
Axial (frictional)	40.69	5.0
Transverse horizontal	320.00	8.9
Upward	45.46	35.0
Downward	1493.70	91.4

activating passive earth pressure. Especially for cohesionless soil type, the transverse force is expressed through a hyperbolic equation [37]. However, for numerical modeling reasons, the nonlinear force—deformation relationship is bilinearized to elastic—perfectly plastic by multiplying the relative soil displacement with a factor of 0.26 to extract the yield displacement.

Vertical upward and downward movement of the pipeline in the trench triggers soil resistance to any movement. However, upward and downward soil spring properties differ significantly as backfill soil above the pipeline has very low stiffness, while the native soil below the pipeline has much higher stiffness. It is noted, also, that the avoidance of significant compaction of the backfill soil is good engineering practice in order to reduce the developing pipe—soil friction. Then, upward movement perpendicular to the pipe axis results to vertical forces at the pipeline—soil interface, whose maximum corresponds to the weight of an inverted prism of soil above the pipe top line. On the other hand, downward movement perpendicular to the pipeline axis results to vertical forces at the pipe—soil interface, which correspond to the vertical bearing capacity of a footing [1]. However, for numerical modeling reasons, the nonlinear force—deformation relationship is bilinearized to elastic—perfectly plastic by multiplying the relative soil displacement with a factor of 0.13 to extract the yield displacement. Finally, the soil spring properties considered in the analyses are listed in Table 2, while force—displacement relationship for every spring type is shown in Fig. 3.

The pipeline is subjected to a fault offset that equals two times its diameter, i.e. $\Delta f = 1.83$ m. Considering, then, the fault dip angle ψ and the pipe—fault crossing angle β, the imposed displacements on the pipeline are listed in Table 3 with reference to Fig. 2 for strike-slip, normal and reverse faulting.

Earthquakes are a characteristic example of natural dynamic phenomena caused by the relative movement of tectonic plates of the earth's crust. However, fault movement is usually considered in the analyses as a quasi-static process. Thus, fault displacement is applied in the numerical analyses as imposed displacement on the "ground nodes" of soil springs at a sufficiently slow rate capable of neglecting the dynamic effects of the natural phenomenon. The nonlinearity of the problem, due to the nonlinear properties of the soil and the pipeline steel, as well as geometrical nonlinearities, is handled by implementing the nonlinear solution algorithm Full Newton—Raphson [38]. The algorithm solves the nonlinear problem by separating it to numerous linear problems and by imposing displacement in load-steps through a linear time function. The displacement division in steps allows the algorithm to

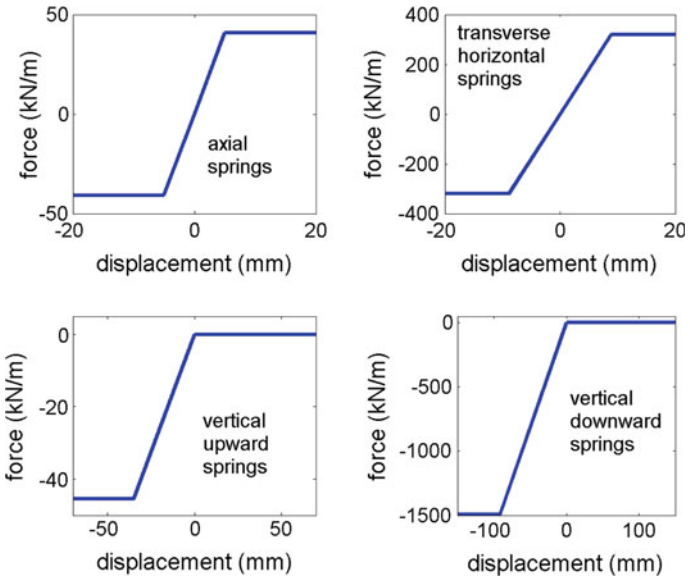

Fig. 3 Axial, transverse horizontal, vertical upward and downward soil springs force—displacement curves

Table 3 Pipeline imposed displacements

Fault type	Δ_x (m)	Δ_y (m)	Δ_z (m)
Strike-slip	0.63	1.72	0
Normal	0.59	0.21	1.72
Reverse	−0.59	0.21	−1.72

solve the linear equilibrium equations and invert the stiffness matrix in every step. Moreover, the selected number of steps has to be sufficiently high in order to achieve convergence and to apply displacement smoothly aiming at following closely the evolution of the response.

4 Numerical Considerations

Adopting the beam-type finite element model for the pipeline—fault crossing raises some numerical considerations. Such considerations are the effects of geometrical nonlinearity in the reliability of the results, the effects of the internal pressure and finally, whether the ovalization degree-of-freedom (DOF) should be considered in the analysis, provided that some finite element software, such as ADINA, include the ovalization DOF to take into account the cross-section ovalization. To investigate these numerical aspects, a strike-slip fault is considered, without vertical

movement, in order to take advantage of the pipeline symmetrical response around the fault zone. The latter is based on the identical soil resistance in the lateral direction according to Fig. 3.

4.1 *Effect of Geometrical Nonlinearity*

Acknowledging that pipeline undergoes large deformations when subjected to fault rupture, it is essential to investigate the effect of geometrical nonlinearity, in terms of comparing results from materially only nonlinear analysis (MNA) and geometrically and materially nonlinear analysis (GMNA). The pipeline is meshed with PIPE elements without taking into account the additional stresses caused by ovalization. The internal pressure is also neglected. The pipeline displacements are presented in Fig. 4 and indicate that considering geometrical nonlinearity leads to smoother pipe deformation with lower curvature in the vicinity of fault.

The axial force and bending moment distributions along the pipeline are shown in Fig. 5, indicating that when geometrical nonlinearity is neglected the axial force

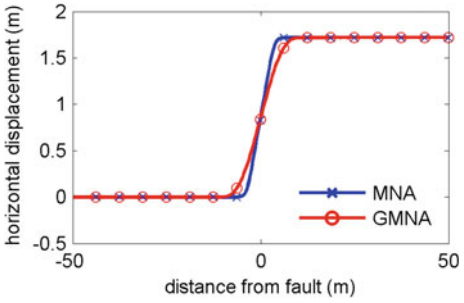

Fig. 4 Pipeline displacements from MNA and GMNA

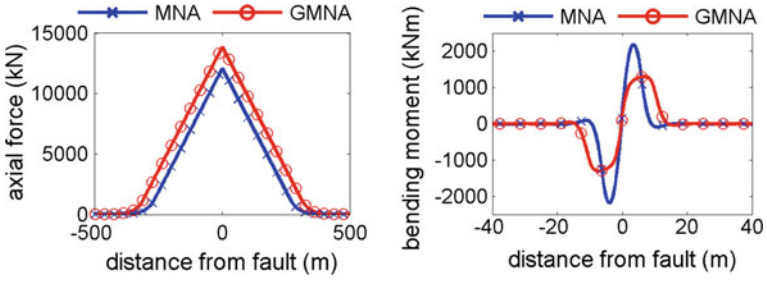

Fig. 5 Axial force and bending moment distributions along the pipeline from MNA and GMNA

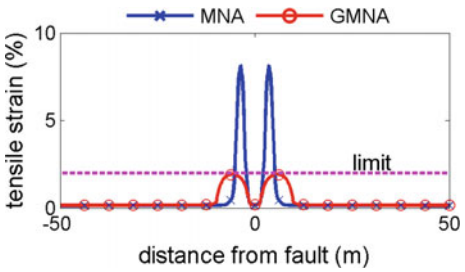

Fig. 6 Tensile strain distributions along the pipeline from MNA and GMNA

is underestimated, the bending moment is overestimated and the difference in the distribution shape is not negligible.

In terms of the developing tensile longitudinal strain along the pipeline, as illustrated in Fig. 6 along with the code-based limit for tensile failure (2 % strain) [22], it is concluded that MNA leads to a significant overestimation of strains, while in the case of GMNA the tensile strains marginally reach the failure criterion. Moreover, in GMNA the strain distribution extends over a longer distance along the pipeline, than in MNA.

The results extracted from the two examined cases, namely by considering (GMNA) or not (MNA) the geometrical nonlinearity indicate that neglecting the geometrical nonlinearity is not on the safe side, not only regarding the peak values of the developing strains but also regarding their distribution along the structure. Thus, the proper analysis approach is to consider always second order effects.

4.2 Effect of Internal Pressure

Pipelines are usually buried a few meters below the ground surface to be protected against external environmental or human factors, such as corrosion and third party damage. Oil and gas pipeline are operating under high pressure that tends to "inflate" the cross-section, while the external earth pressure due to the backfill soil acts inwards. Thus, internal pressure and external pressure often counteract each other. However, pipelines undergo periodical maintenance during which the internal fuel flow is cut off for inspection and repairs. Thus, assuming a less favorable situation, the internal pressure is often neglected in pipeline structural analysis and design against seismic actions, such as fault movement. However, the beam-type model cannot fully assess the balance between the external earth pressure and the internal pressure, as the soil is represented by springs. The latter are adopted to model the soil resistance against the pipeline movement in the trench and are not suitable to model the soil resistance against the developing hoop stresses and strains on the pipeline wall due to the internal pressure. To achieve this balance, the continuum models are the proper numerical approach. Nevertheless, for comparison reasons, in the present study, the effect of internal pressure is examined and assessed.

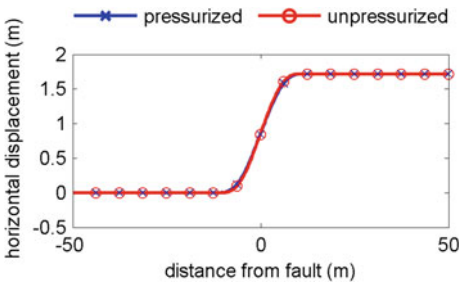

Fig. 7 Unpressurized and pressurized pipeline displacements

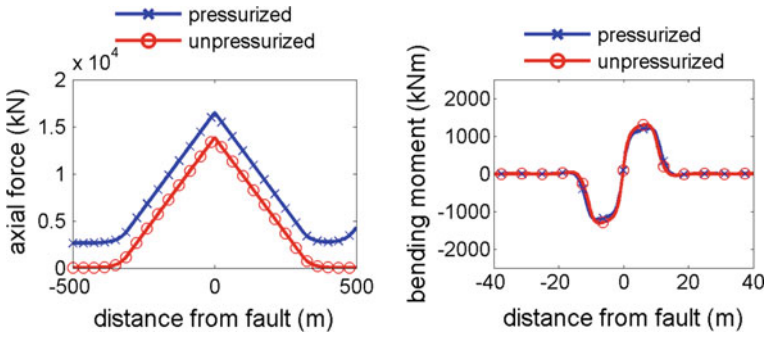

Fig. 8 Unpressurized and pressurized pipeline axial force and bending moment distributions

An unpressurized pipeline and a 70 bar pressurized pipeline are investigated in order to evaluate the effects of internal pressure on the structural response due to fault movement. The pipeline is meshed with PIPE elements and the effect of ovalization is taken into account. The pipeline displacements are shown in Fig. 7, revealing that the internal pressure does not play an important role.

Then, the axial force and bending moment distributions along the pipeline are presented in Fig. 8. The internal pressure tends to increase the developing axial force, while the bending moment is not significantly affected.

In terms of developing strains, the longitudinal tensile strain distributions in Fig. 9 show that in the pressurized case the developing strains are slightly lower than in the unpressurized case, where the strains reach the code-based tensile limit of 2 % [22]. With the exception of this difference that confirms the favorable effect of the internal pressure, in general the strain distributions in both cases are similar.

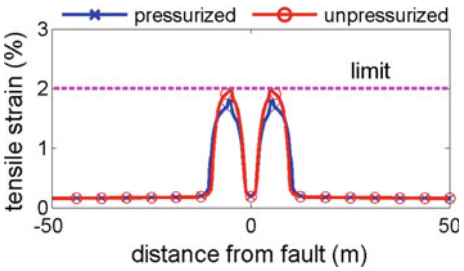

Fig. 9 Unpressurized and pressurized pipeline longitudinal tensile strain distributions

4.3 Effect of Ovalization

Cross-section ovalization is usually considered as a pipeline limit state. Codes and standards provide recommendations on cross-section ovalization limits in order to prevent excessive distortion that may have negative consequences on the pipeline integrity. Even though ovalization may not lead to failure, it may heavily affect pipeline serviceability by obstructing the flow. The latter is crucial for pipeline operators and can lead to costly repairs. Thus, considering ovalization in the analysis is crucial. However, beam-type numerical model does not allow the direct assessment of cross-section deformation, unlike the pipeline modeling with shell elements. Yet, advanced finite element software, such as ADINA, allow the engineer to select whether the ovalization DOF will be considered in the analysis to account for ovalization.

The evaluation of ovalization effects is achieved by analyzing two identical pipeline models. In the first one, ovalization is considered in the analysis using PIPE elements, while in the second typical BEAM elements are used, neglecting ovalization. In both cases, the internal pressure is not considered and GMNA is carried out. The pipeline displacements presented in Fig. 10 unveil no differences in pipe deformation.

The developing axial force and bending moment are presented in Fig. 11, indicating that ovalization does not modify the axial force distribution, while a minor increase in the bending moment is observed.

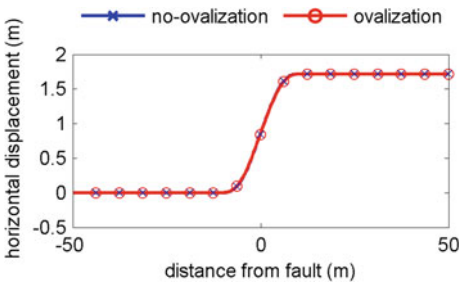

Fig. 10 Pipeline displacements by considering or not cross-section ovalization

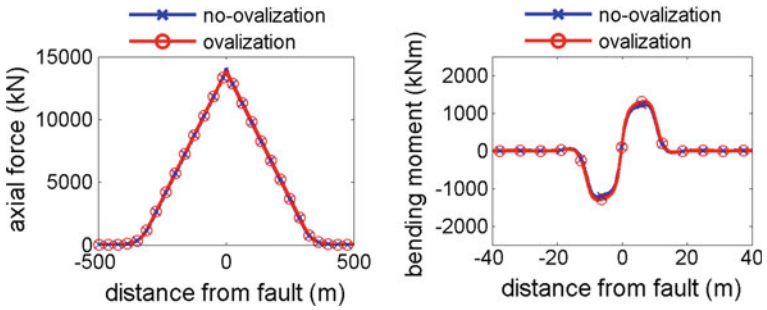

Fig. 11 Pipeline axial force and bending moment distributions by considering or not cross-section ovalization

Fig. 12 Longitudinal tensile strain distributions along the pipeline by considering or not cross-section ovalization

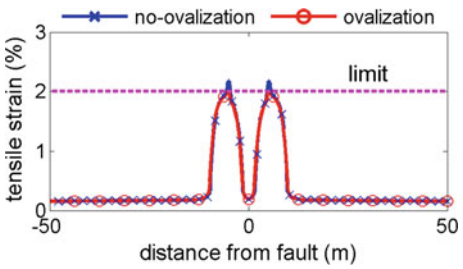

Additionally, in Fig. 12 no remarkable difference is presented regarding the developing longitudinal tensile strains, except for the peak values that exceed the tensile limit in case ovalization is neglected.

4.4 Numerical Considerations

The numerical results presented in Sects. 4.1 through 4.3 aim at demonstrating the effect of alternative parameters considered in the analysis of buried pipe subjected to strike-slip fault rupture, namely geometrical nonlinearity, internal pressure and ovalization. On the basis of these results and in light of maximizing the accuracy of the implemented beam-type model, the following aspects should be considered in the analysis:

1. Pipe modeling with PIPE elements in order to take into account the additional stresses caused by cross-section ovalization.
2. Geometrically and materially nonlinear analysis (GMNA) to account for second order effects and material yielding.
3. Negligence of internal pressure as a less favorable situation.

Table 4 Ratios of solution time for each numerical approach

Numerical element	Analysis parameters	Ratio of solution time
GMNA/MNA	Unpressurized pipe with pipe elements	1.48
Pressurized/unpressurized	GMNA with pipe elements	1.62
Ovalization/no-ovalization	GMNA for unpressurized pipe	1.03

It is also noted that the interaction between the above issues has been found to be negligible, given the simplicity of the beam-type model.

Furthermore, regarding the cost in terms of computing time for each examined numerical aspect, the corresponding ratios of solution time is listed in Table 4. It is observed that considering geometrical nonlinearity and internal pressure increase solution time by 48 and 62 %, respectively. On the other hand, incorporating ovalization does not have an effect on solution time.

5 Effects of Faulting Type

Pipeline mechanical behavior due to faulting is directly related to fault type with reference to fault dip angle (ψ) and pipeline—fault crossing angle (β), as shown in Fig. 2. The effects of strike-slip, normal and reverse faulting are examined in terms of developing nodal forces and strains along the pipeline, as well as soil response due to the pipe movement in the trench.

5.1 Strike-Slip Fault Movement

The pipe deformation due to strike-slip fault offset is schematically illustrated in Fig. 13 for two successive stages of fault movement. When the pipeline crosses the

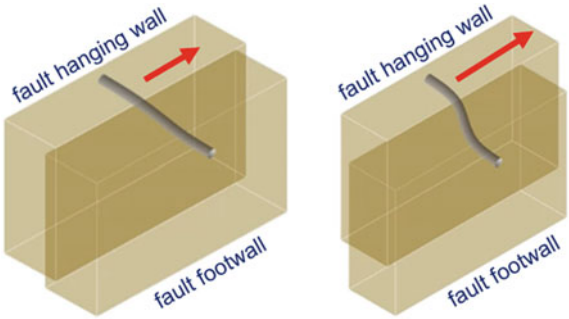

Fig. 13 Schematic illustration of two successive stages of pipeline deformation due to strike-slip faulting

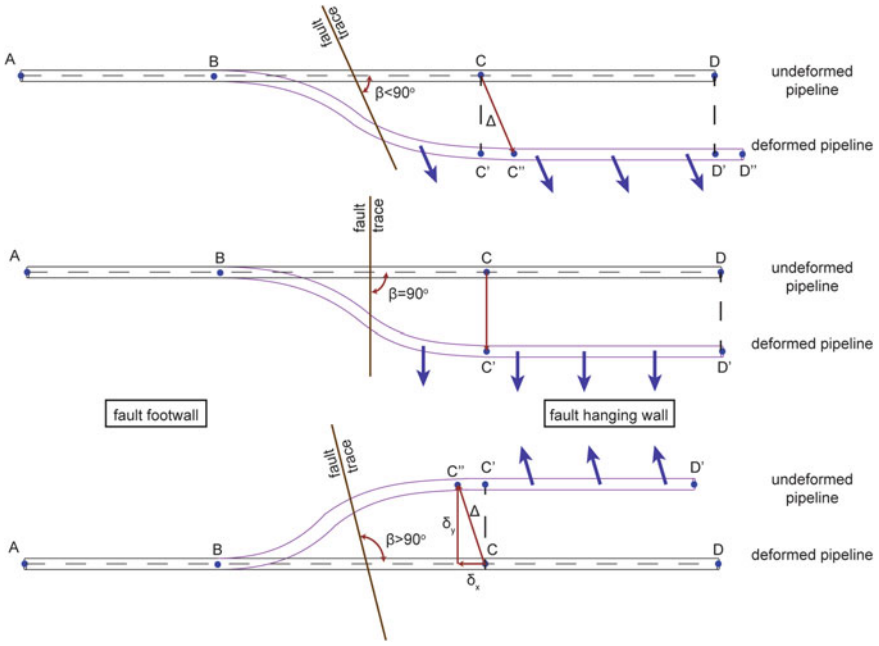

Fig. 14 Effect of pipeline—fault crossing angle on the pipe deformation due to strike-slip fault rupture

fault plane perpendicularly ($\beta = 90°$), it is subjected to axial force and bending, while for $\beta < 90°$ bending and tension develop, and finally for $\beta > 90°$ bending and compression are encountered. Specifically, as the angle β approaches 90°, bending dominates the structural response, while as angle β deviates from 90°, axial force becomes more substantial [39]. To make the effect of crossing angle more perceptible, the pipe deformation due to strike-slip faulting is depicted in Fig. 14 for angles $\beta < 90°$, $\beta = 90°$ and $\beta > 90°$, where it is observed that angle β determines whether the pipe will be elongated ($\beta < 90°$) or shortened ($\beta > 90°$).

Finally, the pipeline—fault crossing is usually designed in such a way that the pipeline intercepts the fault in angles close to 90° in order to prevent excessive tension or compression that would endanger girth welds or cause local buckling of the pipe wall, respectively. Pertinent suggestions are provided by codes (e.g. [22, 23]).

In the case under investigation the crossing angle is $\beta = 70°$ and the pipeline displacement is depicted in Fig. 15.

Axial force and bending moment distributions in Fig. 16 demonstrate the pipeline symmetric response around the fault zone, as the lateral soil response due to the pipeline horizontal transverse movement in the trench is symmetrical. The pipeline is subjected to large imposed displacement due to fault movement and thus the pipe is subjected to tension and bending. The longitudinal tensile strain

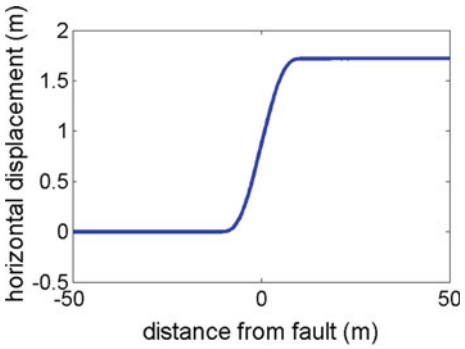

Fig. 15 Pipeline displacement due to strike-slip fault movement

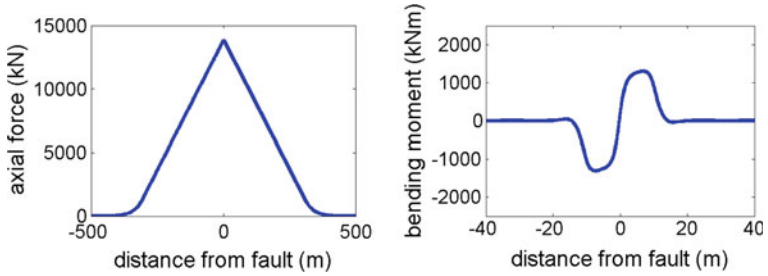

Fig. 16 Pipeline axial force and bending moment distributions due to strike-slip faulting

distribution is presented in Fig. 17, revealing that the pipe will marginally exhibit tensile fracture.

In case of strike-slip faulting the pipeline deforms in the trench within a horizontal plane and thus the axial and lateral soil resistance are "activated". The frictional and horizontal transverse (lateral) soil force distributions are shown in Fig. 18, indicating soil yielding due to frictional forces along 300 m on each side of the fault. On the other hand, soil yielding due to the lateral pipeline movement takes

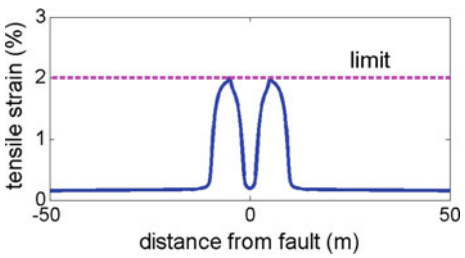

Fig. 17 Longitudinal tensile strain distribution along the pipeline due to strike-slip faulting

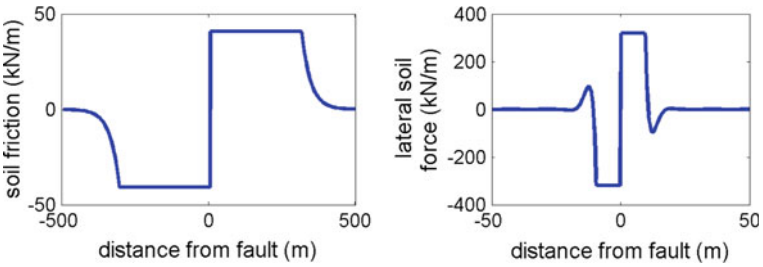

Fig. 18 Soil friction and lateral soil force distributions along the pipeline due to strike-slip faulting

place within a relatively small length, while the force sign alternation is related to the varying pipeline curvature.

5.2 *Normal Fault Movement*

Two successive stages of normal fault movement and the corresponding pipe deformation are schematically illustrated in Fig. 19, resulting mainly to pipeline axial force and bending. The fault dip angle ψ is the main factor affecting the relative importance of bending versus stretching in the pipeline mechanical

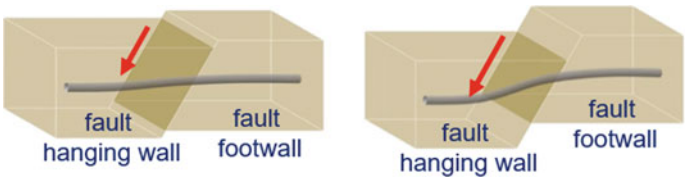

Fig. 19 Schematic illustration of two successive stages of pipeline deformation due to normal fault rupture

Fig. 20 Pipeline displacement due to normal faulting

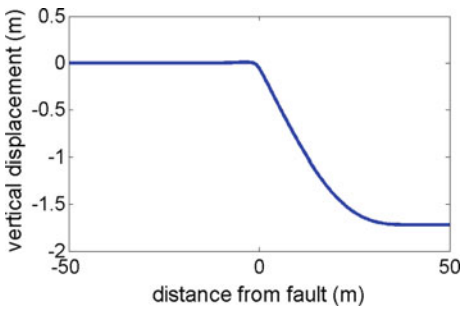

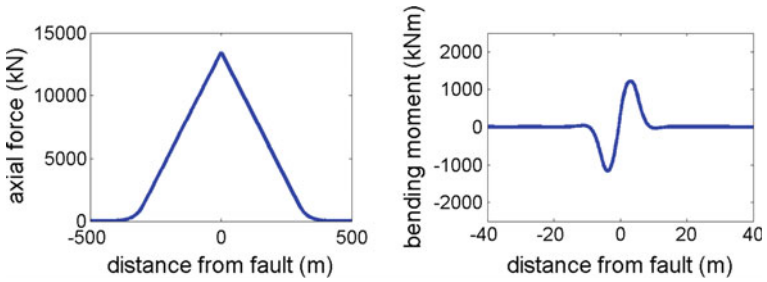

Fig. 21 Pipeline axial force and bending moment distributions due to normal faulting

behavior. As angle ψ tends to 90°, the pipeline is subjected to more bending than axial deformation. In nature, a normal fault dip angle of 70° is common. The pipe—fault angle β also plays a minor role in determining the relationship between pipeline bending and stretching.

In the case under investigation the crossing angle is $\beta = 70°$ and the fault angle is $\psi = 70°$. The pipeline displacement is depicted in Fig. 20.

Axial force and bending moment distributions in Fig. 21 demonstrate that the pipeline mechanical behavior due to the normal fault movement in terms of bending is asymmetric given that the stiffness of upward and downward soil spring is very different.

Fault movement imposes large permanent displacements on the pipeline, which generally leads to pipeline bending, tension or compression and shear, and thus the combined effect of all pertinent actions must be considered for pipeline strength verification. For that purpose, the pipeline design against offset is carried

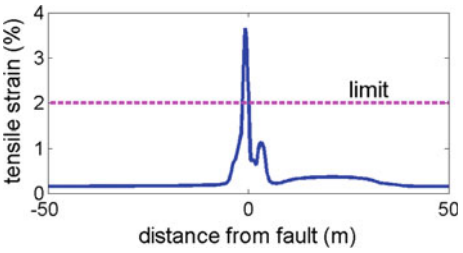

Fig. 22 Longitudinal tensile strains along the pipeline due to normal faulting

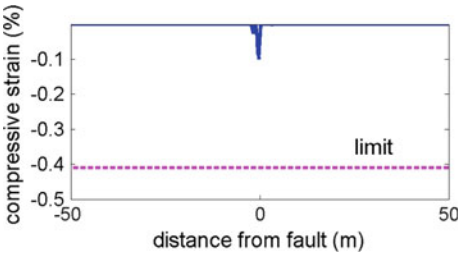

Fig. 23 Longitudinal compressive strains along the pipeline due to normal faulting

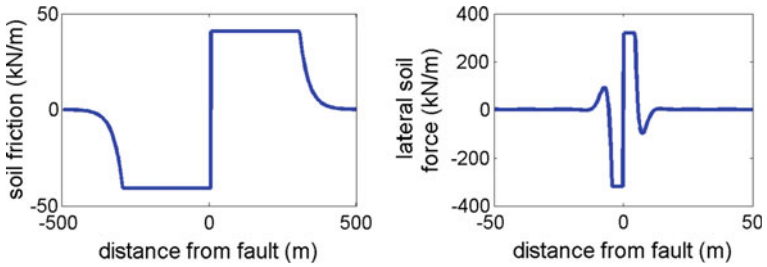

Fig. 24 Soil friction and lateral soil force distributions along the pipeline due to normal faulting

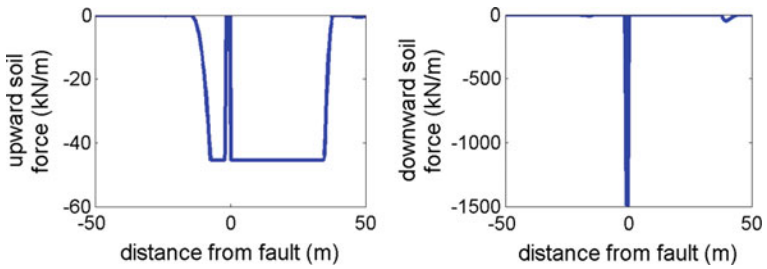

Fig. 25 Upward and downward soil force distributions along the pipeline due to normal faulting

out in strain terms. Then, developing strains are checked against code-based strain limits [22]. The longitudinal tensile strains are presented in Fig. 22, which highlights the likelihood of tensile fracture due to significant strains that exceed the 2 % limit by around 90 %. Meanwhile, the developing compressive strains depicted in Fig. 23 are sufficiently below the 0.39 % limit, thus indicating no damage due to buckling phenomena.

In case of normal faulting, the pipeline deforms simultaneously within a horizontal and a vertical plane. As normal fault movement is three-dimensional, it is sometimes also referred as oblique fault. The frictional and horizontal transverse soil force distributions are shown in Fig. 24 and indicate soil response similar to that of the strike-slip case. Then, the upward and downward soil forces are depicted in Fig. 25 denoting limited soil yielding in the upward direction. At the same time, downward soil resistance is activated within a very small pipeline length due to the pipeline downward movement, which is related to the pipeline curvature change.

5.3 Reverse Fault Movement

The pipeline deformation due to reverse fault offset is schematically illustrated in Fig. 26, resulting mainly to pipeline compression and bending. As in normal fault type, the fault dip angle ψ is the main factor affecting the relative importance of

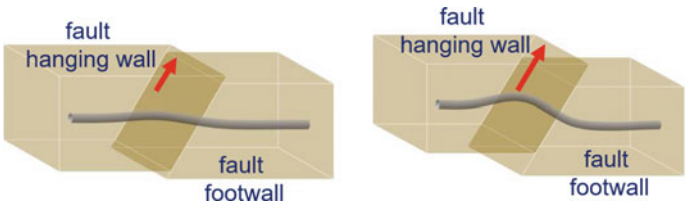

Fig. 26 Schematic illustration of two successive stages of pipeline deformation due to reverse faulting

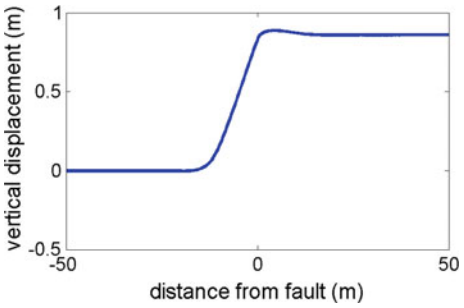

Fig. 27 Pipeline displacement due to reverse faulting

bending versus stretching in the pipeline mechanical behavior. As angle ψ tends to 90°, the pipeline is subjected to more bending than axial deformation. The pipe—fault angle β plays also a minor role in determining the relationship between pipeline bending and stretching.

In the case under investigation the crossing angle is $\beta = 70°$ and the fault angle is $\psi = 70°$. The pipeline displacement is depicted in Fig. 27.

Axial force and bending moment distributions in Fig. 28 demonstrate that the pipe mechanical behavior due to reverse fault movement in terms of bending is

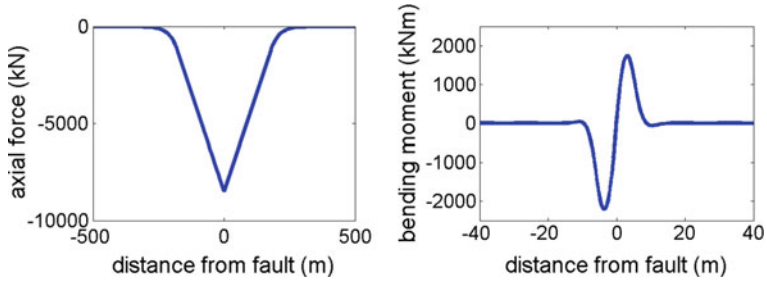

Fig. 28 Pipeline axial force and bending moment distribution due to reverse faulting

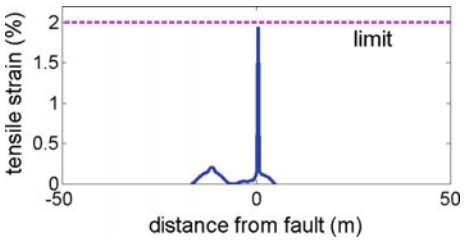

Fig. 29 Pipeline longitudinal tensile strain distribution due to reverse faulting

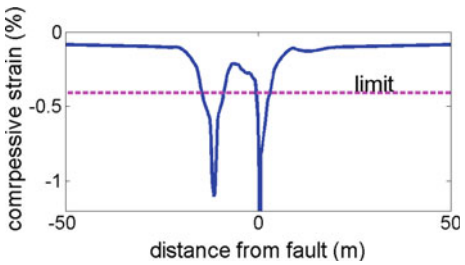

Fig. 30 Pipeline longitudinal compressive strain distribution due to reverse faulting

asymmetric mainly in terms of peak values given that the stiffness of upward and downward soil spring is very different.

The longitudinal tensile and compressive strains are illustrated in Figs. 29 and 30, respectively. The developing tensile strains marginally reach the 2 % code-based limit [22] that is of concern for the integrity of girth welds between pipeline adjacent parts. On the contrary, the developing compressive strains are tens of times larger than the code-based limit [22], which means that the pipeline sustains heavy damage due to local buckling. Thus, even though pipeline steel is a highly ductile material and allows the development of excessive strains, high levels of strains may heavily endanger the pipeline integrity. The use of the beam-type model necessitates thorough checks of the developing strains on integration points against the code-based strain limits.

In case of reverse faulting the pipeline deforms simultaneously within a horizontal and a vertical plane, thus activating soil resistance in all directions, namely, axial/frictional, lateral and vertical. The frictional and horizontal transverse soil

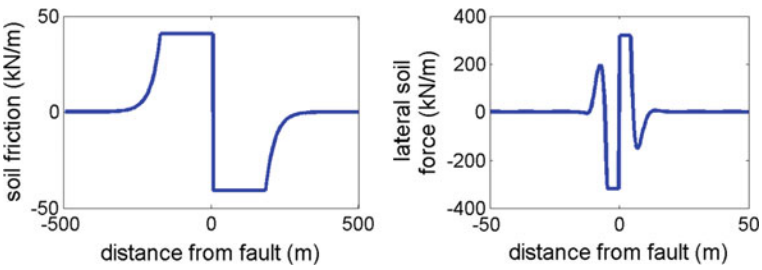

Fig. 31 Soil friction and lateral soil force distributions along the pipeline due to reverse faulting

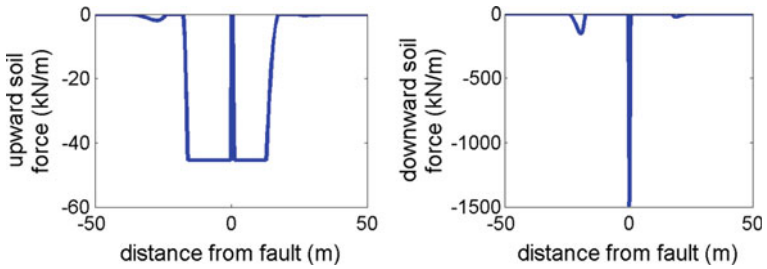

Fig. 32 Upward and downward soil force distributions along the pipeline due to normal faulting

force distributions are shown in Fig. 31 and indicate soil response similar to that of the strike-slip case. Then, the upward and downward soil forces are depicted in Fig. 32 indicating limited soil yielding in the upward direction. At the same time, downward soil resistance is activated within a very small pipeline length due to the pipeline downward movement, which is related to the pipeline curvature change.

5.4 Parameters Affecting Pipeline Behavior

Pipeline—fault crossing is a multi-parameter problem as various natural, constructional and material-related features determine the pipeline mechanical behavior due to fault movement. In brief, the most important parameters are:

- Fault type predefines the potential pipeline failure modes. In case of strike-slip faulting, tensile failure and local buckling are most likely to occur, while in the case of normal faulting, tensile failure is the dominant failure mode, but also local buckling may occur. Finally, in case of reverse faulting, pipe buckling is the most probable failure mode. For shallowly buried pipelines with small diameter to thickness ratio, global upheaval buckling is also possible, while for deeply buried pipelines with large diameter to thickness ratios, shell mode buckling or local buckling is most likely to occur [40].
- Fault dip angle, in case of normal or reverse fault type, is associated with the relation between the developing pipe bending and axial force, given that the steeper the fault plane is, the more bending dominates pipeline behavior and vice versa.
- Pipeline—fault crossing angle is critical for the pipeline mechanical behavior. For crossing angles close to perpendicular, the pipeline behavior is dominated by bending regardless of the fault type. For more acute or obtuse crossing angles, axial force dominates the pipeline response.
- Second order effects cannot be neglected in case of pipeline—fault crossing due to the large imposed displacements and thus geometrical nonlinearity has to be incorporated in the analysis.

- Cross-section distortion due to faulting tends to increase the developing strains and has to be appropriately considered in the analysis.

6 Concluding Remarks

In this chapter an overview of buried pipeline—fault crossing numerical modeling has been presented. The available modeling approaches using the finite element method were examined and the beam-type finite element model was selected as the appropriate approach, not only for preliminary pipeline design, but also for final design, as long as its limitations are acknowledged. The pipeline was meshed with beam-type finite elements with extra degrees of freedom to account for the cross-section ovalization, while the surrounding soil was modeled with nonlinear translational springs. Details on the pipeline and soil modeling were provided, along with aspects of the solution algorithm with reference to the applied fault displacement. Then, the effects of geometrical nonlinearity were evaluated. The internal pressure was also examined, to investigate whether the additional stresses it induces modified the results. Moreover, the pipeline response was assessed by using beam versus pipe finite elements, which account for the cross-section ovalization. The indirect inclusion of cross-section ovalization led to more reliable results and thus it is suggested to be considered in the analysis. Furthermore, the parameters affecting the pipeline mechanical behavior due to fault movement were briefly addressed and examples of pipeline—strike-slip, normal and reverse fault crossing were presented. In each case, the pipe forces, strain-state and the soil reaction were assessed to highlight the special features of response due to each fault type.

Acknowledgments This research has been co-financed by the European Union (European Social Fund—ESF) and Hellenic National Funds through the Operational Program "Education and Lifelong Learning" (NSRF 2007–2013)—Research Funding Program "Aristeia II", project "ENSSTRAM—Novel Design Concepts for Energy Related Steel Structures using Advanced Materials", grant number 4916.

References

1. O'Rourke MJ, Liu X (2012) Seismic design of buried and offshore pipelines. Monograph No. 4. Multidisciplinary Center for Earthquake Engineering Research, Buffalo
2. Jennings PC (1971) Engineering features of the San Fernando earthquake February 7, 1971. California Institute of Technology Report, EERI 71-02, Pasadena
3. Nakata T, Hasuda K (1995) Active fault I 1995 Hyogoken Nanbu earthquake. Kagaku 65:127–142
4. Earthquake Engineering Research Institute (1999) Kocaeli, Turkey Earthquake of August 17. EERI Special Earthquake Report, Pasadena
5. Takada S, Nakayama M, Ueno J, Tajima C (1999) Report on Taiwan Earthquake. RCUSS, Earthquake Laboratory of Kobe University, Kobe

6. Newmark NM, Hall WJ (1975) Pipeline design to resist large fault displacement. In: Proceedings of U.S. National conference on earthquake engineering, 18–20 June 1975, Michigan
7. Kennedy RP, Chow AW, Williamson RA (1977) Fault movement effects of buried oil pipeline. ASCE J Transp Eng 103:617–633
8. Kennedy RP, Kincaid RH (1983) Fault crossing design for buried gas oil pipeline. In: ASME, Proceeding of the PVP conference 1983, vol 77. ASME, New York, pp 1–9
9. Wang LRL, Yeh YA (1985) A refined seismic analysis and design of buried pipelines subjected to vertical fault movement. Earthq Eng Struct Dyn 13:75–96
10. Takada S, Hassani N, Fukuda K (2001) A new proposal for simplified design of buried steel pipes crossing active faults. Earthq Eng Struct Dyn 30:1243–1257
11. Karamitros DK, Bouckovalas GD, Kouretzis GD (2007) Stress analysis of buried steel pipelines at strike-slip fault crossings. Soil Dyn Earthq Eng 27:200–211
12. Karamitros DK, Bouckovalas GD, Kouretzis GD, Gkesouli V (2011) An analytical method for strength verification of buried steel pipelines at normal fault crossings. Soil Dyn Earthq Eng 31:1452–1464
13. Trifonov OV, Cherniy VP (2010) A semi-analytical approach to a nonlinear stress-strain analysis of buried steel pipelines crossing active faults. Soil Dyn Earthq Eng 30:1298–1308
14. Trifonov OV, Cherniy VP (2012) Elastoplastic stress-strain analysis of buried steel pipelines subjected to fault displacement with account for service loads. Soil Dyn Earthq Eng 33(1):54–62
15. Vougioukas EA, Theodossis C, Carydis PG (1979) Seismic analysis of buried pipelines subjected to vertical fault movement. ASCE J Tech Councils 105(TCI): 432–441
16. Ariman T, Lee BJ (1991) Tension/bending behavior of buried pipelines under large ground deformation in active faults. In: U.S. conference on lifeline earthquake engineering, technical council on lifeline earthquake engineering, vol 4. ASCE, New York, pp 226–233
17. Joshi S, Prashant A, Deb A, Jain SK (2011) Analysis of buried pipelines subjected to reverse fault motion. Soil Dyn Earthq Eng 31:930–940
18. Gantes CJ, Melissianos VE (2012) Numerical analysis of buried steel pipelines. In: Proceedings of the 2nd International Balkans conference on challenges of civil engineering. BCCCE, Tirana
19. Melissianos VE, Gantes CJ (2014) On the efficiency of flexible joints in mitigating the consequences of seismic fault activation on buried pipelines. In: Proceedings of the Qatar foundation annual research conference 2014, ARC '14, Doha
20. Melissianos VE, Gantes CJ, Kalfantis PP (2014) Upheaval buckling risk assessment of buried steel pipelines due to reverse seismic fault activation. In: Proceedings of the 8th National conference on steel structures, Tripoli
21. Melissianos VE, Vamvatsikos D, Gantes CJ (2015) Probabilistic assessment of innovative mitigating measures for buried steel pipeline—fault crossing. In: Proceedings of the ASME 2015 pressure vessels & piping conference, Boston
22. ALA American Lifelines Alliance (2001) Guideline for the design of buried steel pipe—July 2001 (with addenda through February 2005). American Society of Civil Engineers, New York
23. Eurocode 8: EN 1998-4 (2006) Design of structures for earthquake resistance—Part 4: Silos, tanks and pipelines, Brussels
24. ASCE (1984) Guidelines for the seismic design of oil and gas pipeline systems. Committee on gas and liquid fuel life-lines, technical council on lifeline earthquake engineering. ASCE, New York
25. Kokavessis NK, Anagnostidis GS (2006) Finite element modeling of buried pipelines subjected to seismic loads: soil structure interaction using contact elements. In: Proceedings of the ASME PVP conference, Vancouver
26. Odina L, Tan R (2009) Seismic fault displacement of buried pipelines using continuum finite element methods. In: Proceedings of the ASME 2009 28th international conference on ocean, offshore and arctic engineering, Honolulu

27. Vazouras P, Karamanos SA, Dakoulas P (2010) Finite element analysis of buried steel pipelines under strike-slip fault displacements. Soil Dyn Earthq Eng 30(11):1361–1376
28. Vazouras P, Karamanos SA, Dakoulas P (2012) Mechanical behavior of buried steel pipes crossing active strike-slip faults. Soil Dyn Earthq Eng 41:164–180
29. Vazouras P, Karamanos SA, Dakoulas P (2015) Pipe-soil interaction and pipeline performance under strike-slip fault movements. Soil Dyn Earthq Eng 72:48–65
30. Zhang J, Liang Z, Han CJ (2014) Buckling behavior analysis of buried gas pipeline under strike-slip fault displacement. J Natural Gas Sci Eng 21:901–928
31. Trifonov OV (2015) Numerical stress-strain analysis of buried steel pipelines crossing active strike-slip faults with an emphasis on fault modeling aspects. ASCE J Pipeline Syst Eng Pract 6(1):04014008
32. Uckan E, Akbas B, Shen J, Rou W, Paolacci F, O'Rourke M (2015) A simplified analysis model for determining the seismic response of buried steel pipes at strike-slip fault crossings. Soil Dyn Earthq Eng 75:55–65
33. Takada S, Liang JW, Tengyan L (1998) Shell-mode response of buried pipelines to large fault movements. J Struct Eng 44A:1637–1646
34. Gantes CJ, Bouckovalas G (2013) Seismic verification of the high pressure natural gas pipeline Komotini-Alexandroupolis-Kipi in areas of active fault crossing. Struct Eng Int 2:204–208
35. ADINA R & D Inc. (2006) Theory and modeling guide. Volume I: ADINA, Report ARD 08-7. ADINA R & D Inc., Watertown—Boston
36. Sanghal AC (1980) Strength characteristics of buried jointed pipelines. American Society of Civil Engineers and Engineering Foundation, Arizona State University, Final Report #R80027, Arizona
37. Trautmann CH, O'Rourke TD (1983) Behavior of pipe in dry sand under lateral and uplift loading. Geotechnical Engineering Report 83-7, Cornell University
38. Bathe KJ (1995) Finite element procedures. Prentice-Hall, New Jersey
39. Ha D, Abdoun TH, O'Rourke MJ, Symans MD, O'Rourke TD, Palmer MC, Stewart HE (2010) Earthquake faulting effects on buried pipelines—case history and centrifuge study. J Earthq Eng 14(5):646–669
40. Yun HD, Kyriakides S (1990) On the beam and shell modes of buckling of buried pipelines. Soil Dyn Earthq Eng 9(4):179–193

Determination of the Parameters of the Directivity Pulse Embedded in Near-Fault Ground Motions and Its Effect on Structural Response

Petros Mimoglou, Ioannis N. Psycharis and Ioannis M. Taflampas

Abstract Near-fault ground motions are affected by directivity phenomena, which produce important velocity pulses, mostly associated with the normal to the fault direction. Directivity pulses amplify the long period coherent component of the ground motions and are explicitly apparent in the velocity and the displacement time histories and the related response spectra. A number of methods are commonly used for the identification of the parameters of the velocity pulses, mainly their period and amplitude. Also, several mathematical expressions have been proposed for their mathematical representation, which vary from simple functions to more complicated wavelets. A very efficient wavelet is the one proposed by Mavroeidis and Papageorgiou (M&P), which, beyond the period and the amplitude, uses additional parameters related to the total duration and the phase shift of the pulse. In this chapter, a recently proposed new method is presented, which allows the explicit determination of the parameters of the pulse contained in pulse-like records. The M&P wavelet is used for the mathematical representation of the pulse but the proposed methodology can be easily modified to cover other types of wavelets as well. First, the period of the pulse is determined from the peak of the $S_d \times S_v$ *product spectrum*, a new concept defined as the product of the velocity and the displacement response spectra. The remaining parameters of the M&P wavelet are derived from the targeted response spectrum of the ground motion applying a relationship that is established between the Cumulative Absolute Displacement (*CAD*) of a wavelet and its peak spectral amplitude. The method follows a well-defined procedure that can be easily implemented in a computer code for the automatic determination of the pulse parameters of a given ground motion. In the last part of the chapter, the identified pulses, inherent in a wide set of ground motions, are used to study the effect of directivity pulses on the nonlinear response of SDOF structures. It is shown that, in a wide range of periods, the seismic behavior is dominated by the presence of the pulse, since the corresponding M&P wavelet alone can capture quite satisfactorily the nonlinear response.

P. Mimoglou · I.N. Psycharis (✉) · I.M. Taflampas
School of Civil Engineering, Laboratory for Earthquake Engineering,
National Technical University of Athens, Zografou, Greece
e-mail: ipsych@central.ntua.gr

M. Papadrakakis et al. (eds.), *Computational Methods in Earthquake Engineering*,
Computational Methods in Applied Sciences 44,
DOI 10.1007/978-3-319-47798-5_2

1 Introduction

The number of recorded near-fault ground motions has increased tremendously in the last decades as a result of denser seismograph stations installed. The plethora of the available records in combination with the use of newer digital instruments, much more capable than the old analog ones, has permitted the identification of important velocity pulses inherent in near-fault ground motions, related to directivity phenomena. These pulses are mostly associated with the normal to the fault direction, and amplify the long period coherent component of the ground motions, explicitly apparent in the velocity and the displacement time histories and the related response spectra.

The identification of the near-fault velocity pulses has instigated further research for the definition of their characteristic parameters, mainly their period and amplitude. Thus, many researchers have presented relations associating the pulse period with the moment magnitude of the event ([1–4] among others).

It should be noted that not all near source ground motions contain directivity pulses, not even all those satisfying the theoretical geometric prerequisites with respect to the rupture geometry. Moreover, although many, if not most, such pulses can be attributed to near-fault effects, it should be pointed out that significant pulses may be produced by other reasons as well, such as basin effects, soil conditions, deep rupture, fling step etc. As noted in the literature [5, 6], long-period record processing can make static displacement due to fling step appear like a directivity pulse.

In this chapter, a new procedure is presented for the determination of the parameters of the velocity pulse inherent in pulse-like ground motions. The proposed methodology can be applied to any record that is a priori known to be impulsive, independently of whether it is near-fault or not. The classification of a record as pulse-like or non-pulse-like is an ongoing research field and several researchers have proposed different techniques for this classification (e.g. [7–9]). This issue is beyond the scope of this chapter and is not further discussed in the following; any of the available techniques can be used for this purpose.

The identification of the directivity pulse that is inherent in near-fault ground motions is important in Earthquake Engineering. First, it allows for the generation of artificial time histories compatible with the specific seismic characteristics of each record. Such generation of artificial ground motions with well-defined properties that are consistent with both the physical condition and the characteristics of the actual recorded ground motions is very important in seismic design. Non-linear dynamic structural analyses generally require the use of large numbers of input ground motions in order to determine the performance of structures, while the number of available recorded ground motions is limited and scaling of existing records is not appropriate in most cases. In general, according to the usual practice for the generation of synthetic ground motions with forward directivity effects, the frequency content of the eventual time histories can be divided in two components: (a) the high-frequency incoherent component of the ground motion, which is

typically generated using stochastic procedures accounting for the distribution of the seismic moment on the fault plane, as the ones proposed in [10–12]; and (b) the low-frequency coherent component, which is associated with the pulse inherent in the ground motion. Mavroeidis and Papageorgiou [13] proposed a method to combine the two components, which requires the selection of a proper scenario based on the statistical characteristics of a dataset for both components. This method has been applied in [14–16] for the analysis of different engineering problems.

Second, it allows for a better selection and scaling of records to be used for linear and nonlinear analyses. It is known that pulse-like ground motions account for large spectral values at periods close to the pulse period [17], while the $R_y - \mu$ relation diverts from unity for periods smaller than half the pulse period [18].

Due to the importance of the velocity pulses for the linear and the nonlinear response of the structures, several mathematical expressions have been proposed for their representation. These models vary from simple functions to more complicated wavelets like the Daubechies wavelet [10] used in [5, 7, 17, 19]. A very efficient wavelet was proposed by Mavroeidis and Papageorgiou [13], who introduced additional parameters regarding the total duration and the phase shift of the pulse.

In the new method presented herein, the efficient Mavroeidis and Papageorgiou wavelet, referred as M&P wavelet hereafter, is used for the pulse representation. Up to now, the properties of the M&P wavelet were determined either with a trial and error procedure, as in the original paper [13], or through a wavelet analysis, as the one proposed in [20]. The new procedure is based on the displacement—velocity product spectrum ($S_d \times S_v$), which is used for the identification of the period of the pulse, and a relation between the ground motion parameter *CAD* (Cumulative Absolute Displacement [21]) and the peak of the displacement response spectrum, which is used for the determination of the remaining parameters of the wavelet.

2 Determination of the Parameters of the Directivity Pulse

2.1 Determination of the Period, $\mathbf{T_p}$

The period T_p of the directivity pulse embedded in near-fault ground motions is the most important parameter and has attracted the attention of several researchers who have presented regression relationships associating its value with the moment magnitude of the event ([1–4] among others). As a common practice, it is usually determined from the peak of the pseudo-velocity response spectrum for 5 % damping. However, the accuracy of this definition has been questioned [7, 22].

An example in which this definition leads to false results is shown in Fig. 1 for the normal to the fault component of the Petrolia record of the Cape Mendocino, 1992 earthquake. In Fig. 1a, the time history of the ground velocity is shown; the motion is characterized by a pulse of period 2.74 s, as evident from the red line

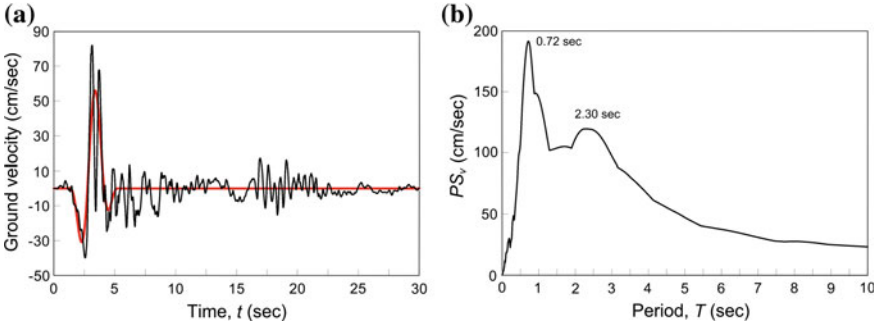

Fig. 1 Normal to the fault component of the Petrolia record of the Cape Mendocino, 1992 earthquake: **a** time history of ground velocity; **b** pseudo-velocity response spectrum for 5 % damping. *Red line* shows the directivity pulse determined with the methodology presented herein

which corresponds to the wavelet identified with the procedure presented in the following. This value is similar to the pulse period T_p = 3.0 s calculated by Baker [7]. However, the period that corresponds to the largest peak of the pseudo-velocity response spectrum for 5 % damping is equal to 0.72 s (Fig. 1b), while a peak of significantly smaller amplitude appears at T = 2.3 s.

An alternative to the calculation of T_p from the pseudo-velocity response spectrum would be to use the displacement response spectrum instead. This consideration comes from the fact that the displacement response spectrum is an adequate envelope curve of the Fourier amplitude spectrum of the ground velocity, similarly with the undamped velocity response spectrum which is an envelope of the Fourier amplitude spectrum of the ground acceleration. Indeed, as proven by Hudson [23]:

$$\tilde{a}_g(\omega) \leq S_{v,0}(\omega) \tag{1}$$

where $\tilde{a}_g(\omega)$ is the Fourier spectrum amplitude of the ground acceleration a_g (t), defined by

$$\tilde{a}_g(\omega) = \sqrt{\left[\int_0^{t_{tot}} a_g(t) \cdot \cos(\omega t) dt\right]^2 + \left[\int_0^{t_{tot}} a_g(t) \cdot \sin(\omega t) dt\right]^2} \tag{2}$$

t_{tot} being the duration of the ground motion, and $S_{v,0}$ (ω) is the velocity response spectrum for zero damping.

Similarly, it can be proven that the undamped displacement response spectrum is an adequate envelope of the Fourier spectrum of the ground velocity. Indeed, for undamped oscillators (ξ = 0) one can assume that the velocity response spectrum, $S_{v,0}$ (ω), coincides with the pseudo-velocity one, $PS_{v,0}$ (ω), except in the long period range. Thus, in a wide range of periods, it can be assumed that $S_{v,0}$ $(\omega) \approx$

$\omega \cdot S_{d,0}(\omega)$, where $S_{d,0}(\omega)$ is the displacement response spectrum for zero damping. Then, dividing both sides of relation (1) by ω and taking under consideration that $\tilde{a}_g(\omega)/\omega = \tilde{v}_g(\omega)$, where $\tilde{v}_g(\omega)$ is the Fourier amplitude spectrum of the ground velocity, $v_g(t)$, determined by

$$\tilde{v}_g(\omega) = \sqrt{\left[\int_0^{t_{tot}} v_g(t) \cdot \cos(\omega t) dt\right]^2 + \left[\int_0^{t_{tot}} v_g(t) \cdot \sin(\omega t) dt\right]^2} \tag{3}$$

one gets:

$$\tilde{v}_g(\omega) \leq S_{d,0}(\omega) \tag{4}$$

which shows that the displacement response spectrum is an adequate envelope curve of the Fourier amplitude spectrum of the ground velocity. An example is shown in Fig. 2a for the normal to the fault component of the Petrolia record of the Cape Mendocino, 1992 earthquake.

Based on the above observation, and taking under consideration that the directivity pulse is prominent in the time history of the ground velocity, it would be reasonable to determine its period, T_p, from the predominant period of the displacement response spectrum. For the Petrolia record, this definition leads to T_p = 2.67 s (Fig. 2b), which is close to the period of the pulse (2.74 s) that can be identified in the ground velocity record using the methodology presented herein (Fig. 1a).

This alternative definition of the pulse period, T_p, however, through the predominant period of the displacement response spectrum, might be problematic, as the peak of the displacement response spectrum can be affected by the presence of

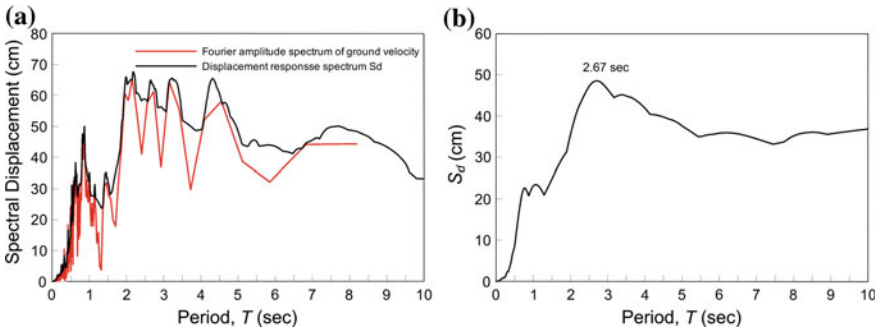

Fig. 2 Normal to the fault component of the Petrolia record of the Cape Mendocino, 1992 earthquake: **a** Comparison of the Fourier amplitude spectrum of the ground velocity with the displacement response spectrum for zero damping; **b** displacement response spectrum for 5 % damping

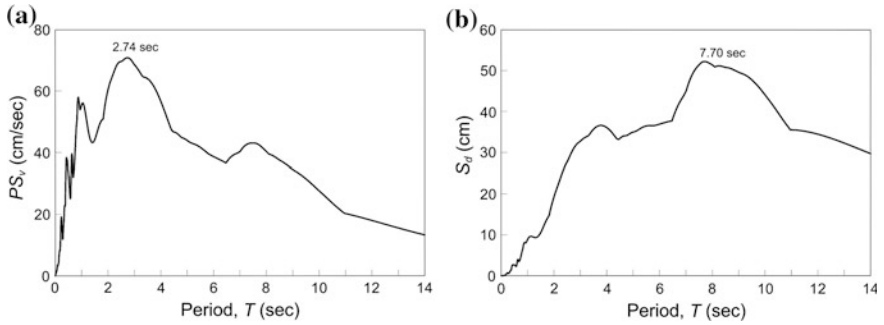

Fig. 3 Normal to the fault component of the Parachute Test Site record of the Westmorland, 1981 earthquake: **a** pseudo-velocity response spectrum for 5 % damping; **b** displacement response spectrum for 5 % damping

long period errors in the ground acceleration record. Furthermore, the peak of the displacement response spectrum may correspond to a velocity pulse with large area but small amplitude, which might not be the prevailing pulse. In addition, it cannot be generalized either, as there are cases in which it is not valid. An example is given in Fig. 3 for the normal to the fault component of the ground motion recorded at Parachute Test Site during the Westmorland, 1981 earthquake. In this case, the period of the directivity pulse, T_p, is equal to 3.6 s according to Baker [7] and to 3.0 s according to the method presented herewith, values which are close to the predominant period of the pseudo-velocity response spectrum (Fig. 3a) and not to the predominant period of the displacement response spectrum which is quite larger, equal to 7.70 s (Fig. 3b).

As evident from the above discussion, neither the pseudo-velocity nor the displacement response spectra can be generally used for the determination of the period of the directivity pulse, since there are cases in which the two approaches lead to significantly different results. This happens because many near-fault ground motions are affected by more than one pulses of different period. Herein, a new methodology is proposed which allows the identification of the predominant pulse that is related to directivity phenomena of near-fault ground motions through a combination of the velocity and the displacement response spectra.

Specifically, since the pulse-like components of near-fault ground motions affect both the ground acceleration and the ground velocity, although to a different degree, the pulse period, T_p, should prevail in the convolution integral of these two time histories. Furthermore, extreme high or low frequency components inherent in the ground acceleration and the ground velocity are attenuated. Consequently, the peak of the acceleration—velocity convolution should correspond to the period of the predominant pulse contained in the ground motion.

It is known that the Fourier spectrum of the convolution integral is equal to the product of the Fourier spectra of the convolved signals. On the other hand, as mentioned above, the undamped velocity spectrum, $S_{v,0}$, is an envelope of the

Fourier amplitude spectrum of the ground acceleration and the undamped displacement spectrum, $S_{d,0}$, is an envelope of the Fourier spectrum of the ground velocity. Using these properties, the Fourier spectrum of the convolution integral can be approximated by the product $S_{v,0} \times S_{d,0}$, which in the following will be referred as the *product spectrum for zero damping*. Accordingly, the period of the directivity pulse can be determined from the peak of the product spectrum.

As mentioned above, this conclusion is justified for the product spectrum for zero damping. However, it can be extended to the product spectrum for 5 % damping, which is defined as the product $S_{v,5} \times S_{d,5}$, where $S_{v,5}$ and $S_{d,5}$ are the velocity and displacement response spectra for 5 % damping, respectively, since the period at which the $S_{v,5} \times S_{d,5}$ product spectrum peaks is expected to be close to the one at which the $S_{v,0} \times S_{d,0}$ product spectrum peaks. Although these periods do not necessarily coincide, it is suggested here to use the spectra for 5 % damping for the calculation of the pulse period for the following reasons:

- Because the results match better the periods derived by Baker [7], which are used here as benchmark data.
- Because the response spectra of the ground motion for 5 % damping, which are more important than the ones for zero damping for typical earthquake engineering applications, are matched better by the corresponding spectra of the extracted velocity pulses. The procedure presented herein for the determination of the parameters of the directivity pulse is based on the best fitting of the response spectrum for 5 % damping.
- Because it is consistent with the above-mentioned current practice of calculating the pulse period from the pseudo-velocity response spectrum for 5 % damping; however, this cannot serve as an argument in favor of using spectra for 5 % damping, due to the above-mentioned shortcomings of this method.

In the following, only the spectra for 5 % damping will be used, denoted as S_d and S_v without further reference to the damping value. Thus, the $S_d \times S_v$ product spectrum will denote the $S_{v,5} \times S_{d,5}$ product.

The application of the new method for the calculation of the pulse period, T_p, is presented in Fig. 4 for the above-mentioned records, namely the normal to the fault components of the Petrolia record and the Parachute Test Site record. As mentioned above, in the former case, the pulse period was calculated to $T_p = 3.0$ s by Baker [7] and is associated with the predominant period of the displacement response spectrum (Fig. 2); in the latter, it was calculated to $T_p = 3.6$ s by Baker and is associated with the predominant period of the pseudo-velocity response spectrum (Fig. 3). The use of the $S_d \times S_v$ product spectrum allows for the correct calculation of the pulse period in both cases, namely, $T_p = 2.74$ s and 3.00 s, respectively.

In Fig. 4, the corresponding product spectra for zero damping are also presented for comparison. It is noted that the selection of the appropriate peaks in this case is somehow uncertain and might lead to different results.

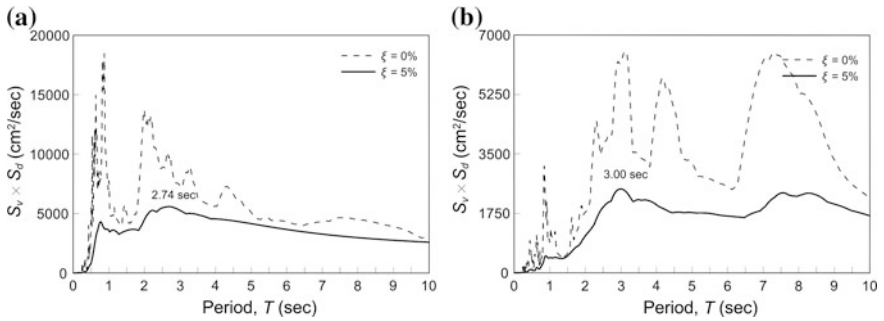

Fig. 4 Determination of the velocity pulse period, T_p, from the peak of the $S_d \times S_v$ product spectrum for 5 % damping (the corresponding curves for zero damping are also shown for comparison): **a** normal to the fault component of the Petrolia record of the Cape Mendocino, 1992 earthquake; **b** normal to the fault component of the Parachute Test Site record of the Westmorland, 1981 earthquake

2.2 *Pulse Determination*

2.2.1 Mathematical Representation of the Pulse

The proposed methodology is based on a wavelet representation of the directivity pulse, the period of which is identified from the peak of the convolution spectrum for 5 % damping, as explained in the previous section. For the mathematical representation of the pulse, the wavelet proposed by Mavroeidis and Papageorgiou [13] (M&P wavelet) is adopted. However, one could modify the proposed methodology appropriately to consider other well-known wavelets proposed in the literature.

The M&P wavelet is derived by the coupling of a harmonic oscillation signal and a bell-shaped envelope. Four parameters are used to define the pulse:

- The period T_p of the harmonic oscillation of the wavelet.
- The amplitude A of the bell-shaped envelope, which is associated with the amplitude of the time history of the velocity.
- The duration γ of the wavelet, which measures the number of the oscillations and is defined as $\gamma = t_{tot}/T_p$ with $\gamma > 1$, t_{tot} being the time duration of the wavelet.
- The phase shift ν.

The duration of the ground motion affects the response of the structures and especially the response spectrum amplification. The phase angle controls the shape of the wavelet, which, thus, can best fit the velocity time history. The importance of the number of cycles and the phase modulation of the wavelets on their capability to match pulse-like ground motions was reported by Vassiliou and Makris [20].

The use of the above-mentioned four parameters gives the M&P wavelet additional flexibility compared to simpler models, enabling it to better approximate more complex velocity pulses. Additionally, it has a closed form solution, which makes it easier to use and study. The ability of the M&P wavelet to capture satisfactorily the effects of the base excitation characteristics on the response has made it popular for the representation of pulse-like ground motions for engineering purposes and several researchers have used it for linear and nonlinear analyses ([14–16] among others). Due to these advantages, and since the proposed methodology is spectrum oriented, the M&P wavelet was selected among other widely used wavelets, the parameters of which are not directly related to the structural response, as for example the Daubechies wavelet [24] used by Baker [7] for the identification of the predominant pulse.

Using the above-mentioned parameters, the acceleration $a_p(t)$ and the velocity $v_p(t)$ of the wavelet can be defined by the following equations [13]:

$$a_p(t) = \begin{cases} -\frac{A\pi}{\gamma T_p}\left[\begin{array}{l}\sin\left(\frac{2\pi}{\gamma T_p}(t-t_0)\right)\cdot\cos\left(\frac{2\pi}{T_p}(t-t_0)+v\right)\\ +\gamma\cdot\sin\left(\frac{2\pi}{T_p}(t-t_0)+v\right)\cdot\left[1+\cos\left(\frac{2\pi}{\gamma T_p}(t-t_0)\right)\right]\end{array}\right], & t_0-\frac{\gamma}{2}T_p\le t\le t_0+\frac{\gamma}{2}T_p \\ 0, & \text{otherwise}\end{cases} \tag{5}$$

$$v_p(t) = \begin{cases} \frac{A}{2}\left[1+\cos\left(\frac{2\pi}{\gamma T_p}(t-t_0)\right)\right]\cdot\cos\left(\frac{2\pi}{T_p}(t-t_0)+v\right), & t_0-\frac{\gamma}{2}T_p\le t\le t_0+\frac{\gamma}{2}T_p \\ 0, & \text{otherwise}\end{cases} \tag{6}$$

where t_0 is *the time defining the epoch of* the envelope's peak.

In the methodology presented herewith, the parameters of the wavelet are determined by best fitting the displacement response spectrum. However, since the pseudo-velocity response spectrum is directly related to the displacement spectrum through the relation $PS_v = \omega \cdot S_d$, the derived wavelet will also fit the pseudo-velocity response spectrum.

Having determined the period, T_p, of the pulse from the peak of the $S_d \times S_v$ product spectrum as described in the previous section, the determination of the three remaining parameters of the wavelet, A, γ and v, is achieved with the use of the recently proposed ground motion index *CAD* (Cumulative Absolute Displacement [21]) and a cross correlation operation between the proposed wavelet and the record time history. *CAD* is defined by the time integral of the absolute ground velocity, in analogy with the *CAV* index (Cumulative Absolute Velocity [25]), i.e.

$$CAD = \int_0^{t_{tot}} |v_g(t)|dt \tag{7}$$

It is noticed that Baker [7] and Zamora and Riddell [26] have also used similar indices, specifically the time integral of the squared acceleration [27] and the time integral of the squared velocity [22], as intensity measures of the pulse-like content of the ground motion.

2.2.2 Determination of the Amplitude, *A*

Let us consider a harmonic ground motion of amplitude $d_{g,\max}$, which is applied as base excitation to an undamped SDOF oscillator. At resonance, the amplitude of the response of the oscillator builds up almost linearly with the number of cycles and for an excitation of γ cycles the maximum response is [28]:

$$S_{d,0}(T_{res}) = \pi\,\gamma\,d_{g,\max} \tag{8}$$

in which $S_{d,0}(T_{res})$ denotes the spectral displacement at resonance for zero damping. On the other hand, the value of *CAD* at the end of the γth cycle of a harmonic excitation is:

$$CAD = 4\,\gamma\,d_{g,\max} \tag{9}$$

Therefore, for a harmonic excitation of γ cycles there is a constant relation between the spectral displacement for zero damping at resonance and *CAD*, which can be expressed as

$$\frac{S_{d,0}(T_{res})}{CAD} = \frac{\pi}{4} \tag{10}$$

If an M&P wavelet is used instead of the purely harmonic excitation, Eqs. (8) and (10) continue to hold approximately, with satisfactory accuracy, despite the fact that the bell-shaped envelope has been applied to the amplitude of the excitation. This is shown in Fig. 5a, in which the ratio of the maximum spectral displacement

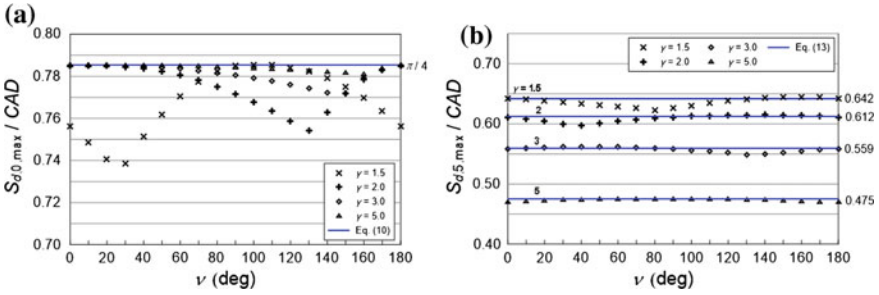

Fig. 5 Relation between the peak spectral displacement $S_{d,\max}$ and *CAD* for M&P wavelets with various values of γ and ν: **a** zero damping; **b** 5 % damping

for zero damping over the cumulative absolute displacement, $S_{d,0,\max}/CAD$, is plotted versus the phase index v for γ = 1.5, 2.0, 3.0 and 5.0. The results are independent of the period T_p and the amplitude A. It is evident that the ratio $S_{d,0,\max}/CAD$ is close to the value $\pi/4$, which holds for harmonic excitations according to Eq. (10), especially for pulses of long duration (large values of γ). The largest discrepancy occurs for γ = 1.5 and v = 30°, but even in that case the error is less than 6 % (lowest value is about 0.74 compared to $\pi/4$ = 0.785).

A similar relation between the peak spectral displacement and *CAD* can also be established for other values of damping, apart from zero. For a SDOF oscillator of damping equal to ξ and for purely harmonic excitation, the displacement at resonance is [28]:

$$S_{d,\xi}(T_{res}) = \frac{1 - e^{-2\pi\gamma\xi}}{2\xi} \cdot d_{g,\max} \tag{11}$$

Using again Eq. (9), the following relation can be established:

$$\frac{S_{d,\xi}(T_{res})}{CAD} = \frac{1 - e^{-2\pi\gamma\xi}}{8\gamma\xi} \tag{12}$$

If the excitation is not purely harmonic but an M&P wavelet, Eq. (12) produces an error for large values of γ. A parametric investigation that was performed showed that a correction factor must be applied in this case, equal to $1 + (\gamma - 1)\xi$. Thus, for M&P wavelets, the following relation applies:

$$\frac{S_{d,\xi,\max}}{CAD} = \frac{1 - e^{-2\pi\gamma\xi}}{8\gamma\xi}[1 + (\gamma - 1)\xi] \tag{13}$$

Comparison of the values produced by Eq. (13) with the actual values of the ratio $S_{d,\xi,\max}/CAD$, obtained for various values of v and γ, is shown in Fig. 5b for ξ = 5 %. It is evident that the accuracy obtained with Eq. (13) is very satisfactory in all cases.

Using Eqs. (10) and (12) and the well-known relation between spectral displacement and pseudo-spectral velocity: $PS_v = (2\pi/T)\cdot S_d$, the following relations can be established between *CAD* and PS_v for M&P wavelets:

$$\frac{PS_{v,0,\max}}{CAD} = \frac{\pi^2}{2T_p} \quad \text{for zero damping} \tag{14}$$

$$\frac{PS_{v,\xi,\max}}{CAD} = \frac{\pi\left(1 - e^{-2\pi\gamma\xi}\right)[1 + (\gamma - 1)\xi]}{4\,\gamma\,\xi\,T_p} \quad \text{for damping } \xi \neq 0 \tag{15}$$

in which $PS_{v,0}$ and $PS_{v,\xi}$ denote the pseudo-spectral velocity for zero damping and damping equal to ξ, respectively.

For M&P wavelets, the value of *CAD* is directly associated with the amplitude A and the duration index γ, since the following relation holds:

$$CAD = \gamma A \, T_p/\pi \tag{16}$$

As already mentioned, the new method is spectrum oriented and the directivity pulse is defined to best fit the response spectrum of the original record. In this sense, substituting *CAD* in Eqs. (14) and (15) using (16) one gets:

$$A = \frac{2PS_{v,0}(T_p)}{\pi \gamma} \quad \text{for zero damping} \tag{17}$$

$$A = \frac{4 \xi PS_{v,\xi}(T_p)}{(1 - e^{-2\pi\gamma\xi}) \cdot [1 + (\gamma - 1)\xi]} \quad \text{for damping } \xi \neq 0 \tag{18}$$

in which $PS_{v,0}$ (T_p) and $PS_{v,\xi}$ (T_p) are the values of the pseudo-velocity response spectrum of the ground motion for zero damping and damping equal to ξ, respectively, calculated for period T_p. As mentioned above, the displacement response spectrum can be used instead of the pseudo-velocity one, since PS_v $(T_p) = (2\pi/T_p) \cdot S_d$ (T_p).

Among Eqs. (17) and (18), Eq. (18) is preferred for the determination of the amplitude A because the produced wavelet matches better the spectra for the desired value of damping. Typically, the pseudo-velocity spectrum for 5 % damping is used, thus Eq. (15) is usually applied for $\xi = 0.05$. However, Eq. (17) should be used in case that one wants to calibrate the wavelets with the response spectrum for zero damping.

2.2.3 Determination of the Duration, γ, and Phase Shift, v

For the determination of the wavelet's amplitude, A, from Eq. (18), the value of the duration, γ, must be known. Since this is an unknown parameter, all the values in a selected range of variation of γ are examined.

From this set of pairs (A, γ), the ones that lead to amplitudes of the wavelet's acceleration, velocity or displacement larger than the corresponding peak values of the ground motion, namely the peak ground acceleration, *pga*, the peak ground velocity, *pgv* and the peak ground displacement, *pgd*, respectively, are rejected.

For the remaining acceptable pairs (A,γ), and for all values of the phase, v, between 0° and 360°, the corresponding wavelets are calculated. For each of these wavelets, several values of time delay, t_d, for the initiation of the pulse are examined. Thus, a set of candidate wavelets is determined, each one corresponding to a different set of parameters A, γ, v and t_d.

From the corresponding pulse time histories, v_p (A, γ, v, t_d, t), the wavelet that correlates best with the time history of the ground velocity, $v_g(t)$, is selected. To this

end, the cross correlation factor, r, is calculated for each pair of time histories (v_p, v_g) and the pulse with the largest r is selected.

It is reminded that the cross-correlation operation between two functions f and g with a time delay t_d is defined by

$$(f * g)(t_d) = \int_{-\infty}^{\infty} f^*(t) \cdot g(t + t_d)dt \tag{19}$$

where f^* is the complex conjugate of f. The cross-correlation factor r is defined by

$$r = \frac{\sum_i \left(f(t_i) - \tilde{f}\right) \cdot (g(t_i - t_d) - \tilde{g})}{\sqrt{\left[\sum_i \left(f(t_i) - \tilde{f}\right)^2\right] \cdot \left[\sum_i \left(g(t_i - t_d) - \tilde{g}\right)^2\right]}} \tag{20}$$

where $\tilde{f}$ and $\tilde{g}$ are the mean values of the functions f and g respectively.

In this way, the cross correlation operation is used to identify not only the pulse which best fits the velocity time history of the ground motion, but also its starting time, t_d. It is mentioned that the time delay, t_d, is related to t_0 defining the epoch of the envelope's peak of the wavelet [see Eqs. (5) and (6)] through the equation:

$$t_d = t_0 - \gamma T_p/2. \tag{21}$$

2.3 The Method in Steps

Based on the aforementioned theoretical background, a straightforward procedure can be established for the determination of the significant pulse and its parameters in terms of the corresponding M&P wavelet. The method, which can be implemented easily in a computer code, consists of the following steps:

Step 1 For the ground motion under consideration produce the $S_d \times S_v$ product spectrum by multiplying the displacement and the pseudo-velocity response spectra for 5 % damping.

Step 2 Identify the period that corresponds to the largest peak of the $S_d \times S_v$ product spectrum and set T_p equal to this value. Calculate the value of $PS_{v,5}(T_p)$ from the corresponding value of the pseudo-velocity response spectrum for ξ = 5 %.

Step 3 Set a maximum value, γ_{max}, for the duration of the M&P wavelet. As the duration of the wavelet is not known a priori, a sweep of all possible values of γ between 1 and γ_{max} is needed for the determination of the most suitable wavelet for the specific ground motion. For directivity pulses of near fault ground motions, γ_{max} = 5 is usually adequate. In some cases, however, larger values of γ_{max} are required, up to γ_{max} = 10

or even larger. A step of $\Delta\gamma = 0.1$ is suggested to be used for the determination of the values of γ during the sweep process.
For each γ_i in the range $1 \leq \gamma_i \leq \gamma_{\max}$ with step $\Delta\gamma$ and for the value of $PS_{v,5}(T_p)$ that was determined in step 2 define the corresponding value of the wavelet amplitude, A_i, using Eq. (18) for $\xi = 0.05$.

Step 4 For each pair (A_i, γ_i) that was determined in step 3 and for values of the phase v ranging from 0° to 360° produce the corresponding M&P wavelet using Eqs. (5) and (6) leaving t_0 as a parameter. A step of $\Delta v = 5°$ is suggested to be used for the sweep of the phase shift.
Reject all the wavelets for which the peak acceleration or the peak velocity or the peak displacement is larger than the corresponding values of the ground motion, *pga*, *pgv* and *pgd*, respectively.

Step 5 For the remaining wavelets, each one corresponding to an acceptable value of γ, and for all values of t_0 ranging from $t_0 = \gamma_i \cdot T_p/2$ to $t_0 = t_{\max} - \gamma_i \cdot T_p/2$, with $t_{\max}$ being the total duration of the record, calculate the corresponding correlation factor r_i between the velocity time history of each wavelet, $v_{p,i}(t)$, and the time history of the original ground velocity, $v_g(t)$, and the time delay $t_{d,i}$ using Eqs. (20) and (21).
Choose the wavelet with the largest cross correlation factor r and define A, γ, v and t_0 from the parameters of this wavelet. Calculate the start time of the pulse from Eq. (21). It must be noted that, if the correlation factors for the selected wavelets are quite low, it is questionable whether the ground motion under consideration can be considered as a pulse-like one.

2.4 Example

As an example, the new method is applied to the Gebze record of the Kocaeli, Turkey, 1999 earthquake. The normal to the fault component of this record, as provided in [29], is used.

Step 1 First, the $S_d \times S_v$ product spectrum of the record is derived as the product of the velocity and the displacement response spectra for 5 % damping (Fig. 6c, solid line).

Step 2 The peak of the $S_d \times S_v$ spectrum corresponds to $T_p = 4.88$ s. It is noted that the corresponding spectrum for zero damping (Fig. 6a, dashed line) peaks at a much larger period, specifically $T = 9.06$ s. However, according to the proposed procedure, the pulse period is assigned to the peak of the $S_d \times S_v$ product spectrum for 5 % damping, thus the pulse period is set to: $T_p = 4.88$ s. The corresponding pseudo-velocity spectral value is $PS_{v,5}(T_p) = 95.19$ cm/s (Fig. 6d). Note that this value does not correspond to a peak of the pseudo-velocity spectrum; in general, however, it is close to a local peak if not to the largest peak.

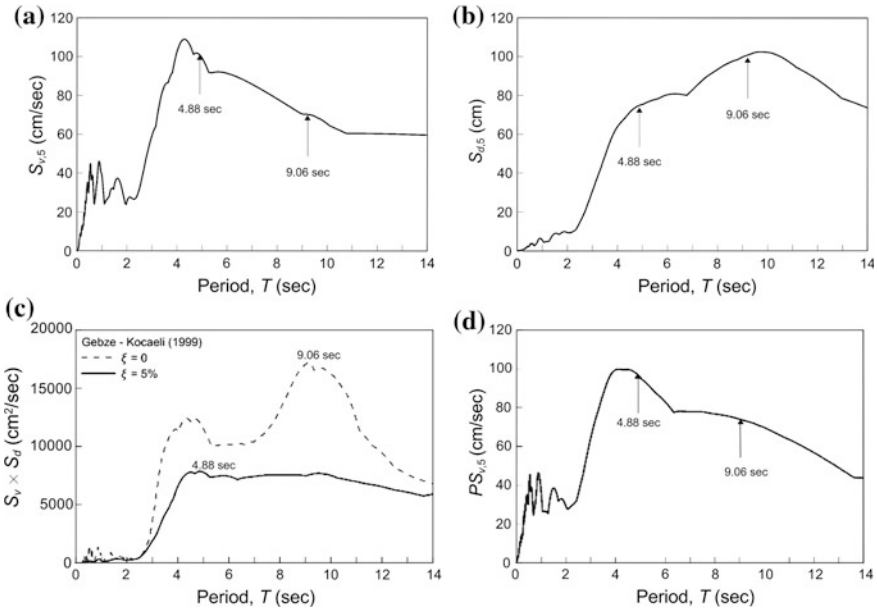

Fig. 6 Normal to the fault component of the Gebze record of the Kocaeli, Turkey, 1999 earthquake: **a** S_v for 5 % damping; **b** S_d for 5 % damping; **c** $S_d \times S_v$ product spectra for 5 % damping (*solid line*) and zero damping (*dashed line*); **d** pseudo-velocity response spectrum for 5 % damping

Step 3 In this example, $\gamma_{\max}$ is set to 5 and the amplitude, A, is derived for each γ in the range $1 \leq \gamma \leq 5$ with step $\Delta\gamma = 0.1$ using Eq. (18).

Step 4 For each pair (A, γ), and for values of the phase, ν, ranging from 0° to 360° with step $\Delta\nu = 5°$, the corresponding M&P wavelet is determined for $T_p = 4.88$ s and leaving t_0 as a parameter. Since for the record under consideration $pga = 233.73$ cm/s^2, $pgv = 51.97$ cm/s and $pgd = 44.09$ cm, all wavelets with peak acceleration larger than 233.73 cm/s^2 or peak velocity larger than 51.97 cm/s or peak displacement larger than 44.09 cm are rejected.

Step 5 For the remaining wavelets and for all values of t_0 ranging from $t_0 = \gamma_i \cdot T_p/2$ to $t_0 = t_{\max} - \gamma_i \cdot T_p/2$, with $t_{\max} = 28$ s being the total duration of the record, the cross correlation factor, r, is calculated between the velocity time history of each wavelet and the time history of the original ground velocity. The wavelet with the largest cross correlation factor is chosen to represent the velocity pulse. In this example, the characteristics of the chosen wavelet are: $A = 42.18$ cm/s, $\gamma = 1.8$, $\nu = 190°$ and $t_0 = 7.76$ s. The start time of the velocity pulse is: $t_d = 7.76 - 1.8 \times 4.88/2 = 3.37$ s.

Comparison of the time histories (acceleration and velocity) of the extracted pulse with those of the original record is shown in Fig. 7a,

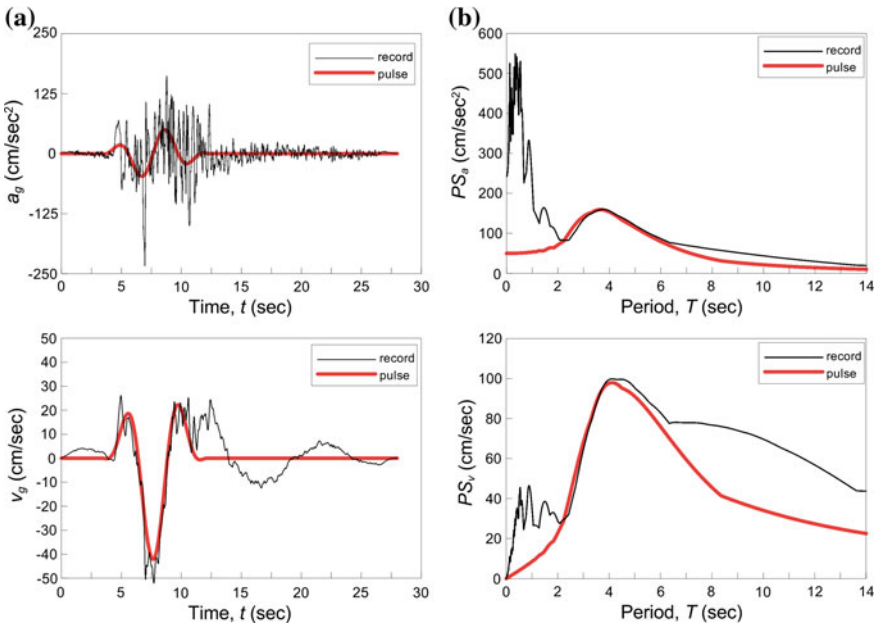

Fig. 7 Normal to the fault component of the Gebze record of the Kocaeli, Turkey, 1999 earthquake: **a** Comparison of the acceleration and velocity time histories of the chosen M&P wavelet (*red line*) with the ones of the original record (*black line*); *b* comparison of the corresponding response spectra for 5 % damping

while the comparison of the corresponding response spectra for 5 % damping is depicted in Fig. 7b. It is seen that the selected pulse can capture very well both the time histories of the velocity pulse inherent in the ground motion and the response spectra of the original record in the period regime around the pulse period.

3 Calculation of Additional Important Pulses

In many near-fault records there are additional significant pulses inherent in the ground motion. In fact, as Mavroeides and Papageorgiou [13] and others have noted, there are cases in which more than one pulses are required to capture the nature of the phenomenon. In order to identify the additional pulses, apart from the predominant one, the proposed methodology can also be used, if applied to the *residual ground motion* instead of the original record. The residual ground motion is derived by subtracting the wavelet that was defined in step 5 of the above-mentioned procedure from the original record. The resulting record is considered as a *new ground motion* to which the methodology for the identification of the significant pulse can be applied. This procedure can be repeated until all the

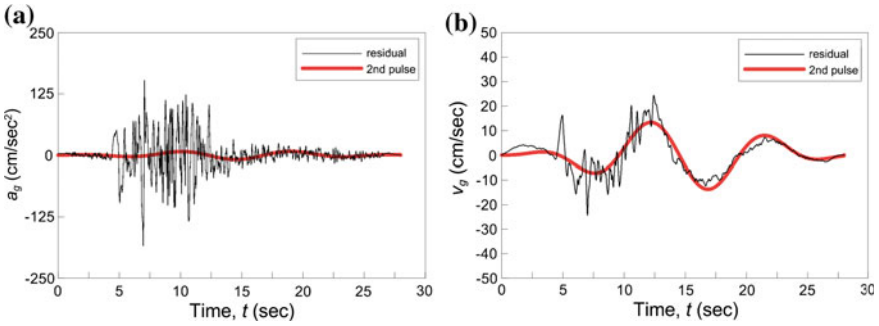

Fig. 8 Significant pulse embedded in the *residual* ground motion of the Gebze record after subtraction of the pulse of Fig. 7a: Comparison of **a** the acceleration and **b** the velocity time histories of the pulse and the residual record

significant pulses are identified. Note that other researchers (e.g. Shahi [19]) have used their own methods to extract multiple pulses.

It should be mentioned that, although this process will identify additional pulses, it lacks a criterion to judge if the detected pulses are, in fact, primary characteristics of the ground motion. Several criteria have been proposed for the characterization of pulses as significant and the interested reader may refer to the bibliography. This issue exceeds the scope of this chapter and is not further discussed in the ensuing.

As an example, the proposed method is applied to the normal to the fault component of the Gebze record of the Kocaeli, Turkey, 1999 earthquake, for which the first significant pulse was determined previously (Sect. 2.4). This pulse is subtracted from the original ground motion and the *residual motion* is calculated, which is used for the identification of the second pulse. Application of steps 1–5 to the residual record ends up with the second pulse which is shown in Fig. 8.

Adding the two pulses, a *combined* pulse is derived, which provides a better approximation to the original record. This is shown in Fig. 9 (top row), where the time histories of the original record are compared with the time histories of the combined pulse. The corresponding response spectra are compared in the bottom row of Fig. 9.

4 Effect of the Directivity Pulse on the Inelastic Response

The existence of the directivity pulse in the ground motion has an important effect on the response of the structures. In what regards the elastic response, it is known that it produces a bell shaped amplification to the acceleration response spectrum, centered around the pulse period (Shahi and Baker [17]). This spectral amplification, if measured as the ratio of the spectral acceleration corresponding to the time history containing the pulse over the spectral acceleration corresponding to the time history of the residual ground motion after the extraction of the pulse, attains values

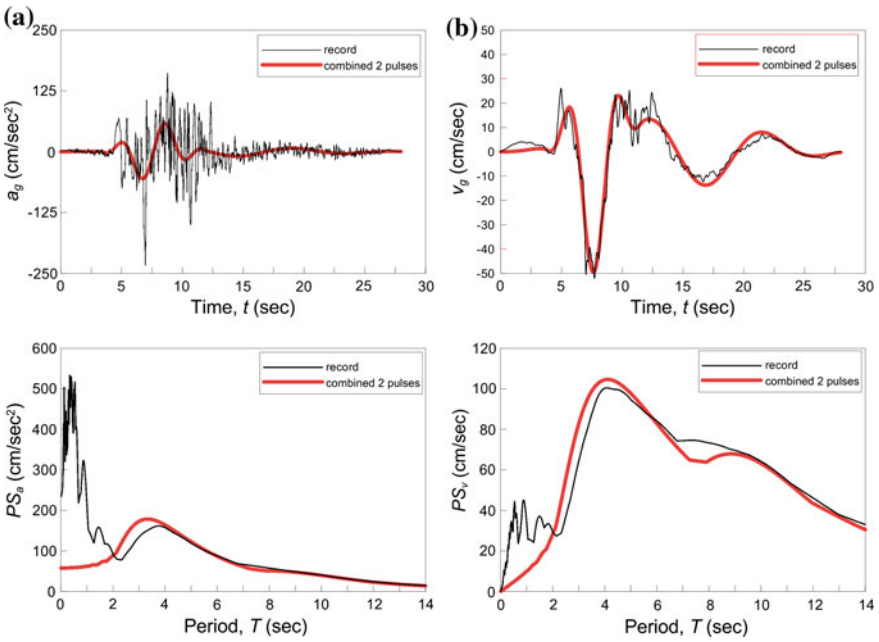

Fig. 9 Normal to the fault component of the Gebze record of the Kocaeli, Turkey, 1999 earthquake: comparison of **a** the acceleration and **b** the velocity time histories (*top row*) and corresponding response spectra (*bottom row*) of the *combined* pulse, composed of the superposition of the two first detected significant pulses, and the original record

of about 3 in the average, while its maximum value can be as large as 5–6. This means that, if directivity phenomena are ignored, the design spectral accelerations, as given by modern design codes, can be significantly underestimated for structures with fundamental period around the pulse period.

The effect of the directivity pulse embedded in the ground motion on the inelastic response of the structures might also be very significant. For example, Iervolino and Cornell [18] reported that, for periods about half the period of the pulse, the inelastic displacements can be five times larger than the elastic ones; this means that the equal displacement rule does not hold in this range of periods. It appears that, if directivity phenomena are present, the equal displacement rule holds for periods larger than the pulse period [30]. It is noted that the inelastic behavior of structures to various pulses has been the object of interest of several researchers [13, 31]. A common observation is that the inelastic behavior can be very sensitive to multiple parameters, such as the viscous damping and the inelastic model used.

In this section, the effect of the most significant (first detected) directivity pulse inherent in near-fault ground motions on the inelastic response of SDOF structures is investigated. To this end, the predominant pulse embedded in the normal to the fault component of 91 records from the NGA strong motion data base, which were characterized as pulse-like by Baker [7], was identified first, using the

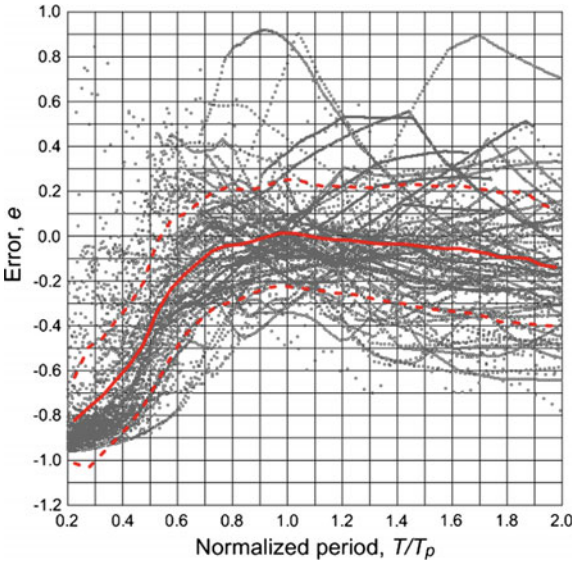

Fig. 10 Error produced in the maximum inelastic displacement of SDOF structures with $R_y = 4$ if only the predominant pulse is considered as the base excitation. *Solid red line* shows the mean error for ninety one records, *dashed red lines* show the curves corresponding to the mean error plus/minus one standard deviation

above-mentioned procedure. The corresponding values of the pulse parameters can be found in [32]. For each record, the inelastic response of SDOF structures with varying period is calculated, assuming that the base excitation consists of: (a) the original record; and (b) only the corresponding directivity pulse. This comparison can be extended to additional pulses embedded in the ground motion, but this investigation exceeds the purpose of this chapter.

Indicative results are presented in Fig. 10 for oscillators with periods up to 20 s and strength corresponding to $R_y = 4$. It is reminded that the *strength reduction factor*, R_y, (equivalent to the term *yield behavior factor*, q_y, used in Eurocode 8 [33]) is defined as

$$R_y = F_e/F_y \tag{22}$$

where $F_e = ma_e$ is the maximum force for elastic response and $F_y = ma_y$ is the yielding force of the nonlinear system, m being the mass of the oscillator and a_e and a_y being the corresponding elastic acceleration and yield acceleration, respectively. Note that many typical RC structures are designed for values of R_y around 4. In the results presented here, a_e was calculated first for each record and each SDOF oscillator assuming elastic response. Then the inelastic response was calculated assuming that yielding was occurring at acceleration $a_y = a_e/4$ and that the system possesses a horizontal post-yield branch (elastic − perfectly plastic response without hardening). It is noted that a_y was calculated only for the original record and this value was used in the calculation of the inelastic response under both the original record and the pulse excitation.

In Fig. 10, the error e for all records, that is produced in the maximum inelastic displacement if only the predominant pulse excitation is used, is plotted versus the normalized (with respect to the pulse period T_p) period of the oscillators, T/T_p. For each record and each oscillator of period T, the error was calculated from the relation:

$$e(T) = \left[d_p(T) - d_{or}(T)\right]/d_{or}(T) \tag{23}$$

in which $d_{or}(T)$ is the maximum displacement of the oscillator of period T under the original record and $d_p(T)$ the displacement under the corresponding pulse excitation. In Fig. 10, the solid red line shows the mean curve and the dashed red lines show the mean plus/minus one standard deviation curves.

These results show that, on average, the error is less than 20 % for structures with period $T > 0.6\ T_p$. The minimum error occurs for oscillators with period T close to T_p while the mean error is less than 5 % and the mean error plus/minus one standard deviation is no more than 30 % for structures with periods in the range from about $0.8\ T_p$ to about $1.5\ T_p$. This behavior implies that the directivity pulse governs the inelastic response of structures with period $T > 0.6\ T_p$ since the pulse alone can capture quite well the overall response. On the contrary, the effect of the directivity pulse seems not to be important for structures with period T less than $0.5\ T_p$, where the pulse alone underestimates the nonlinear response significantly.

As shown in Fig. 10, the error produced by the first pulse alone is quite large in some cases, even for $T > 0.6\ T_p$. This happens because the second pulse is important in such cases. It is noted that the first identified pulse is not necessarily the most important one (e.g. in terms of the corresponding energy flux) and there are few cases in which the second pulse is equally or even more important. Additional analyses (not presented here) show that the addition of the second pulse improves the results significantly, reducing the error to acceptable limits for all records and for a larger range of periods.

5 Conclusions

A new method for the identification of the directivity pulse embedded in near-fault ground motions is presented. The pulse is mathematically represented by the Mavroeidis and Papageorgiou (M&P) wavelet [13], the parameters of which are determined through a well-defined procedure that is based on several new concepts, specifically:

- The period of the pulse is determined from the peak of the $S_d \times S_v$ product spectrum for 5 % damping, which is defined as the product of the velocity and the displacement response spectra. It is proven that the $S_d \times S_v$ product spectrum for zero damping is an adequate envelope of the Fourier amplitude spectrum of the convolution integral of the ground velocity and the ground acceleration.

- The remaining parameters of the wavelet (amplitude, duration and phase shift) are determined from the matching of the targeted spectral amplitudes of the ground motion using a new relationship which is established between the cumulative absolute displacement (*CAD*) of the M&P wavelet and its spectral amplitude.

The proposed method can be extended to the determination of additional pulses inherent in the ground motion. To this end, the detected significant pulse is subtracted from the original record to derive the *residual record*, to which the method is applied for the derivation of the second pulse. This procedure can be repeated several times until all significant pulses are derived. The summation of all significant pulses produces a mathematical representation of the original record.

The new method is applied to ninety-one pulse-like records from the NGA strong motion database in order to investigate the effect of the directivity pulse on the inelastic response of SDOF structures. The investigation is restricted to the effect of the most significant pulse only. Comparison of the inelastic responses produced by the pulse alone with the corresponding one produced by the original record shows that the directivity pulse governs the inelastic response of structures with period $T > 0.6\ T_p$ while its effect seems not to be important for structures with period T less than $0.5\ T_p$.

References

1. Somerville PG (1998) Development of an improved representation of near-fault ground motions. In: Proceedings of SMIP98 seminar on utilization of strong motion data California strong motion instrumentation program Sacramento CA, 1–20
2. Alavi B, Krawinkler H (2000) Consideration of near-fault ground motion effects in seismic design. In: Proceedings of 12th world conference on earthquake engineering, New Zealand
3. Sasani M, Bertero VV (2000) Importance of severe pulse-type ground motion in performance-based engineering: historical and critical review. In: Proceeding of 12th world conference on earthquake engineering, New Zealand
4. Rupakhety R, Sigurdsson SU, Papageorgiou AS, Sigbjornsson R (2011) Quantification of ground motion parameters and response spectra in the near field region. Bull Earthq Eng 9:893–930
5. Baker JW (2008) Identification of near-fault velocity pulses and prediction of resulting response spectra. In: Proceeding of geotechnical earthquake engineering and structural dynamics IV, Sacramento CA, 18–22 May 2008
6. Burks LS and Baker JW (2014) Fling in near-fault ground motions and its effect on structural collapse capacity. In: Proceedings of 10th U.S. national conference on earthquake engineering, frontiers of earthquake engineering, Anchorage, Alaska, 21–25 July 2014
7. Baker JW (2007) Quantitative classification of near-fault ground motions using wavelet analysis. Bull Seismol Soc Am 97:1486–1501
8. Zhai C, Chang Z, Li S, Chen Z, Xie L (2013) Quantitative identification of near-fault pulse-like ground motions based on energy. Bull Seismol Soc Am 103:2591–2603
9. Kardoutsou V, Taflampas I, Psycharis I (2014) A new method for the classification of ground motions as pulse-like or non pulse-like. In: Proceedings of 2nd European conference on earthquake engineering and seismology, Istanbul, Turkey, 25–29 August 2014

10. Beresnev IA, Atkinson GM (1998) Stochastic finite-fault modeling of ground motions from the 1994 Northridge California earthquake. I Validation on rock sites. Bull Seismol Soc Am 88:1392–1401
11. Boore DM (2003) Simulation of ground motion using the stochastic method. Pure appl Geophys 160:635–675
12. Motazedian D, Atkinson G (2005) Stochastic finite-fault modeling based on a dynamic corner frequency. Bull Seismol Soc Am 95:995–1010
13. Mavroeidis GP, Papageorgiou AS (2003) A mathematical representation of near-fault ground motions. Bull Seismol Soc Am 93(3):1099–1131
14. Motazedian D, Moinfar A (2006) Hybrid stochastic finite fault modeling of 2003 M6.5 Bam earthquake (Iran). J Seismolog 10:91–103
15. Taflanidis AA, Scruggs JT, Beck JL (2008) Probabilistically robust nonlinear design of control systems for base-isolated structures. J Struct Control Health Monit 15:697–719
16. Psycharis IN, Fragiadakis M, Stefanou I (2013) Seismic reliability assessment of classical columns subjected to near-fault ground motions. Earthquake Eng Struct Dynam 42:2061–2079
17. Shahi S, Baker JW (2011) An empirically calibrated framework for including the effects of near-fault directivity in probabilistic seismic hazard analysis. Bull Seismol Soc Am 101 (2):742–755
18. Iervolino I, Cornell CA (2008) Probability of occurrence of velocity pulses in near-source ground motions. Bull Seismol Soc Am 98(5):2262–2277
19. Shahi SK (2013) A probabilistic framework to include the effects of near-fault directivity in seismic hazard assessment, Ph.D. Dissertation, Stanford University
20. Vassiliou MF, Makris N (2011) Estimating time scales and length scales in pulse-like earthquake acceleration records with wavelet analysis. Bull Seismol Soc Am 101(2):596–618
21. Taflampas IM, Spyrakos CC, Koutromanos LA (2009) A new definition of strong motion duration and related parameters affecting the response of medium-long period structures. Soil Dyn Earthquake Eng 29(4):752–763
22. Rodriguez-Marek A (2000) Near-fault seismic site response. Ph.D. Dissertation, Department of Civil Engineering, University of California, Berkeley
23. Hudson DE (1979) Reading and interpreting strong motion accelerograms. EERI engineering monographs on earthquake criteria, structural design and strong motion records
24. Daubechies I (1992) Ten lectures on wavelets CMBS-NSF Regional Conference Series in Applied Mathematics. SIAM, Philadelphia (Ch. 3)
25. EPRI (1991) Standardization of the cumulative absolute velocity. EPRI Report RP3096-1, Electric Power Research Institute, Palo Alto, California
26. Zamora M, Riddell R (2011) Elastic and inelastic response spectra considering near-fault effects. J Earthquake Eng 15:775–808
27. Arias A (1970) A measure of earthquake intensity. In: Hansen RJ (ed) Seismic design for nuclear power plants, MIT Press, Cambridge, MA, pp 438–483
28. Clough RW, Penzien J (1997) Dynamics of Structures. McGraw-Hill
29. Baker JW (2014) http://www.stanfordedu/∼bakerjw/pulse-classification_old.html. (Last visited May 2014)
30. Taflampas I, Psycharis IN (2008) Investigation of the effect of the ground motion characteristics on the R_y−μ relation for the inelastic response of SDOF structures. In: 14th world conference on earthquake engineering, Beijing, China, 12–17 October 2008
31. Panagiotou M (2008) Seismic design, testing and analysis of reinforced concrete wall buildings. Ph.D. Dissertation, University of California, San Diego
32. Mimoglou P, Psycharis IN, Taflampas IM (2014) Explicit determination of the pulse inherent in pulse-like ground motions. Earthquake Eng Struct Dynam 43:2261–2281
33. European Committee for Standardization (CEN) (2004) Eurocode 8: design of structures for earthquake resistance. EN 1998, Brussels

Numerical Simulation of Liquid Sloshing in Tanks

Zuhal Ozdemir, Yasin M. Fahjan and Mhamed Souli

Abstract Sloshing waves induced by long-period components of earthquake ground motions may generate high magnitude hydrodynamic forces on liquid storage tanks. Past earthquake experience has shown that the forces generated by the sloshing waves may affect the overall safety of tanks by causing extensive damage on the tank wall and roof. Therefore, the accurate description of these forces is vital for reducing the potential risk of tank failure during an earthquake. Appropriate numerical simulation methods can be used to predict response of liquid storage tanks, as they offer a concise way of accurate consideration of all nonlinearities associated with fluid, tank and soil response in the same model. This chapter is, therefore, devoted to the Finite Element (FE) analysis of the sloshing phenomenon occurring in liquid storage tanks under external excitations. The governing equations for the fluid and structure and their solution methodologies are clarified. Current nonlinear FE modelling strategies for interactions between liquid, tank and soil are presented in great detail. The presented numerical modelling schemes are applied to analyze sloshing response of rectangular and cylindrical tanks when subjected to external excitations. Strong correlation between experimental and numerical results is obtained in terms of sloshing wave height for a rectangular tank model under resonant harmonic motion. Numerical simulations on cylindrical tanks have indicated that tank material, boundary conditions at the base and the presence of a second horizontal component in addition to one horizontal component have negligible effect on the sloshing response of cylindrical tanks when subjected to earthquake motions.

Z. Ozdemir (✉)
Department of Civil and Structural Engineering, University of Sheffield,
Sheffield S1 3JD, UK
e-mail: z.ozdemir@sheffield.ac.uk

Y.M. Fahjan
Department of Earthquake and Structural Engineering, Gebze Institute of Technology,
41400 Kocaeli, Turkey

M. Souli
Laboratoire de Mécanique de Lille, Université de Lille, UMR CNRS 8107,
Villeneuve D'Ascq, France

M. Papadrakakis et al. (eds.), *Computational Methods in Earthquake Engineering*,
Computational Methods in Applied Sciences 44,
DOI 10.1007/978-3-319-47798-5_3

1 Introduction

Sloshing damage to steel liquid storage tanks has caused serious consequences following several past major earthquakes. During the 1979 Imperial Valley earthquake, failure of roof-shell connections of tanks due to the sloshing of contained liquid resulted in the release of hazardous materials and environmental pollution. Large amplitude sloshing action in floating-roof tanks storing combustible materials led to extensive fires after the 2003 Tokachi-oki (Japan) and 1999 Kocaeli (Turkey) earthquakes. Past experience has demonstrated that widespread sloshing damage to liquid storage tanks is mainly caused by poor prediction of hydrodynamic forces acting on tanks.

Liquid sloshing in tanks during earthquakes may represent violent fluid motion involving high-speed impacts on tank walls and roof in oblique sense, breaking waves, and liquid droplet formation. The amplitude of the sloshing, in general, depends on the nature, amplitude and frequency of the earthquake motion, liquid fill level, liquid properties and tank geometry. When the frequency of the motion is close to one of the natural frequencies of liquid sloshing, large amplitudes sloshing waves can be expected. High hydrodynamic forces generated by sloshing waves on tank affect the overall response of the tank and cause a complicated fluid-structure interaction (FSI) phenomenon between two materials. Therefore, sloshing is a difficult mathematical problem to solve analytically.

Early treatments of sloshing were carried out with analytical methods established on potential flow theory disregarding all viscous effects. In these studies, the irrotational motion of inviscid and incompressible fluid inside the rigid container was represented with Laplace equation. The first approximate solution for a rigid cylindrical tank under horizontal motion was provided by Jacobsen [1] on the basis of a closed-form solution of the Laplace equation that satisfies specified boundary conditions. Housner [2–4] used an approximate method idealizing the liquid as being constraint by rigid membranes to compute the hydrodynamic pressures developed in a rigid cylinder and rectangular fluid container subjected to horizontal accelerations. Veletsos and Yang [5] split hydrodynamic effects obtained from Laplace equation in two parts namely the “impulsive” and the “convective” motions. Faltinsen [6] derived a linear analytical solution for liquid sloshing in a horizontally excited 2D rectangular tank considering damping due to viscous effects. Fischer and Rammerstorfer [7] analytically investigated the overall effect of pressure generated by interaction forces between sloshing and the wall motion modifying the free surface boundary conditions.

Numerical techniques, especially the Finite Element Method (FEM), have been widely used to predict hydrodynamic forces acting on tanks. El-Zeiny [8] formulated fluid motion with Laplace equation and developed a Finite Element (FE) program, which uses an updated Eulerian-Lagrangian description of the liquid-structure interface to enforce compatibility between structure and liquid elements. Chen and Chiang [9] studied sloshing phenomenon occurring inside a 2D

tank with rigid walls by solving incompressible Euler equation under fully nonlinear kinematic free-surface condition using a time independent finite difference method. This study was extended by Chen [10] by adding fluid viscous effects. Souli et al. [11] and Souli and Zolesio [12] developed a procedure for FSI problems based on Arbitrary Lagrangian Eulerian (ALE) algorithm of FEM and validated the applicability of the procedure for sloshing problems. Longatte et al. [13, 14] solved incompressible Navier Stokes equations with an implicit or explicit coupling to the structure for low amplitude sloshing problems. Aquelet et al. [15] developed an ALE coupling algorithm to model large structural deformations generated by large amplitude sloshing waves. The sloshing behaviors of fluid in 3D rigid cylindrical and rectangular tanks subjected to horizontal oscillations were addressed with a numerical and experimental study by Chen et al. [16]. Liu and Lin [17] adopted the finite difference method which solves Navier–Stokes equations to study 2D and 3D viscous and inviscid liquid sloshing in rectangular tanks and verified the results with the linear analytical solution and experimental data. Mitra et al. [18] used FEM to solve wave equation to quantify liquid sloshing in partially filled 2D rigid annular, horizontal cylindrical and trapezoidal containers.

Experimental studies have been extensively conducted on anchored and unanchored tanks to measure sloshing wave height and to quantify the resulting hydrodynamic pressure and shell stresses. Kana [19] measured wall stresses of cylindrical flexible tank induced by sloshing and inertial loads experimentally. Manos [20] carried out experiments to determine impulsive mode frequencies and base-overturning moments of broad and tall tanks. The sloshing wave heights in 2D and 3D rectangular tanks subjected to external loads were measured experimentally by Liu and Lin [17]. A more extensive literature review and detailed investigation of sloshing problem from basic theory to advanced analytical and experimental studies can be found in the work of Ibrahim [21].

In this chapter, current nonlinear numerical modelling strategies for the solution of coupled tank-liquid problems are presented in great detail. The governing equations for fluid and structure and their solution methodologies are clarified. The presented numerical methods are first applied to the solution of the sloshing problem in a rectangular tank under resonant harmonic motion. For the problem under consideration, the accuracy of the numerical methods is validated with the existing analytical formulation derived from potential flow theory as well as experimental data in terms of wave height of the liquid free surface. Results showed that the presented numerical algorithms are reliable and useful for the solution of sloshing problems even under resonance motions. Finally, the sloshing response of anchored and unanchored steel cylindrical liquid storage tanks under earthquake ground motions is numerically assessed by considering all nonlinear behaviour mechanisms of the tank and fluid. The relative importance of earthquake ground motion components on the seismic sloshing response of cylindrical tanks are investigated using the presented numerical modelling methods.

2 Governing Equations for Liquid Sloshing

Oscillatory movements of a liquid free surface inside a partially filled container are referred as liquid sloshing. Laplace, Euler, wave or Navier-Stokes equations can be used to describe fluid motion within a container. The irrotational motion of inviscid and incompressible fluid inside a container is represented with Laplace equation. A more realistic solution for sloshing problems can be obtained by solving Navier Stokes equations for the fluid domain, since nonlinear fluid motion is taken into account more accurately.

The Laplace equation (Eq. (1)) is formalized by combining Eqs. (2) and (3):

$$\nabla^2 \Phi = 0 \tag{1}$$

$$\boldsymbol{u}(x,t) = \nabla \Phi \tag{2}$$

$$\nabla \cdot \boldsymbol{u} = 0 \tag{3}$$

Equation (2) represents the fluid velocity field $u(x,t)$ in terms of velocity potential of the fluid $\Phi(x,t)$ and the incompressibility condition is expressed by Eq. (3). The sloshing phenomenon in a 2D rigid tank subjected to harmonic motion can be investigated by solving the Laplace Equation analytically as an initial boundary-value problem. A two-dimensional rigid rectangular tank system with a length of $2a$ is partially filled with liquid to a height of h as shown in Fig. 1. A Cartesian co-ordinate system (x, y) with the origin at the centre of the free surface of the fluid is used to solve the governing equations. The forced excitation of the tank is applied as a horizontal harmonic displacement motion at the base:

$$\boldsymbol{d_e}(t) = D \sin(\omega t) \tag{4}$$

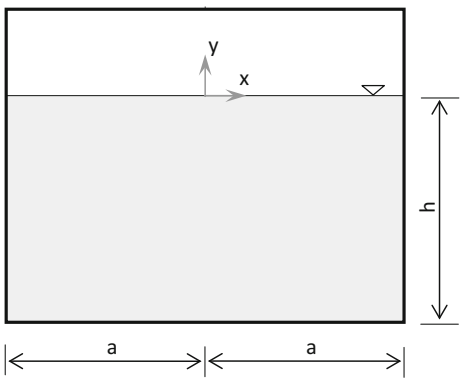

Fig. 1 2D rectangular tank

where D is the amplitude of the harmonic external force and ω is the circular frequency of the applied motion.

In order to simplify the solution, the total velocity potential function $\Phi(x,t)$ is split into a disturbance potential function due to internal sloshing flow, Φ_1, and a potential function, Φ_C, which defines the motion of the tank [6]:

$$\Phi = \Phi_1 + \Phi_C \tag{5}$$

The corresponding essential boundary conditions used for the solution of Laplace equation are linearized assuming the boundaries are rigid. The velocity boundary condition that specifies the liquid motion along the tank bottom and wall is defined as follows:

$$\frac{\partial \Phi_1}{\partial \mathrm{r}_n} = 0 \text{ on the wetted boundary} \tag{6}$$

where r_n is surface normal. Nonlinear effects are ignored assuming the wave amplitudes are very small in comparison with the wavelengths and depths. Therefore, kinematic and dynamic boundary conditions are implemented at the undisturbed free surface of the liquid, respectively, as follows:

$$\frac{\partial \boldsymbol{\eta}}{\partial t} = \frac{\partial \Phi}{\partial y} \text{ on the boundary y} = 0 \tag{7}$$

$$\frac{\partial \Phi}{\partial t} + g\boldsymbol{\eta} = 0 \text{ on the boundary y} = 0 \tag{8}$$

where $\boldsymbol{\eta}$ is free surface displacement, measured from the undisturbed liquid surface at equilibrium and g is the acceleration of gravity. The kinematic free surface boundary condition states that a fluid particle on the free surface at some time will always remain on the free surface. The dynamic free surface boundary condition states that the pressure on the free surface is zero. The combination of kinematic and dynamic boundary conditions at the free surface in terms of Φ_1 gives:

$$\frac{\partial^2 \Phi_1}{\partial t^2} + g\frac{\partial \Phi_1}{\partial y} = -\omega^3 D\cos(\omega t)x \text{ on the boundary y} = 0 \tag{9}$$

Under boundary conditions defined by Eqs. (6) and (9), the solution of Laplace equation (Eq. (3)) gives the following expression for velocity potential of fluid domain inside the tank [6]:

$$\Phi(x,y,t)=\sum_{n=0}^{\infty}\left[\sin\left\{\frac{(2n+1)\pi}{2a}x\right\}\cos h\left\{\frac{(2n+1)\pi}{2a}(y+h)\right\}(A_n\cos(\omega_n t)+C_n\cos(\omega t))\right] - \omega xD\cos(\omega t) \tag{10}$$

where n represents mode number. Coefficients A_n, C_n and K_n are defined as follows:

$$A_n=-C_n-\frac{K_n}{\omega} \tag{11}$$

$$C_n=\frac{\omega K_n}{\omega_n^2-\omega^2} \tag{12}$$

$$K_n=-\frac{\omega^2 D}{\cos h\left\{\frac{(2n+1)\pi}{2a}h\right\}}8a\left(\frac{1}{(2n+1)\pi}\right)^2(-1)^n \tag{13}$$

In the case of free vibration (i.e. if the right hand side of Eq. (9) is 0), the circular frequencies ω_n of sloshing modes are calculated as follows:

$$\omega_n^2=g\frac{(2n+1)\pi}{2a}\tanh\left(\frac{(2n+1)\pi}{2a}h\right) \tag{14}$$

The free surface displacement, $\boldsymbol{\eta}$, measured from the undisturbed liquid surface at equilibrium, and pressure, p, can be defined in terms of velocity potential function as follows:

$$p(x,y,t)=-\rho\frac{\partial\Phi}{\partial t} \tag{15}$$

$$\boldsymbol{\eta}(x,t)=\frac{1}{g}\frac{\partial\Phi}{\partial t} \tag{16}$$

where ρ is the mass density of the liquid.

As demonstrated here, the variation of pressure and sloshing wave height in time (Eqs. (15) and (16)) for an irrotational flow of an incompressible, inviscid fluid in a rigid 2D tank can be obtained by solving Laplace Equation analytically. However, sloshing problem in a flexible tank becomes far more complex to find an analytical solution. In this case, numerical methods, such as the boundary element method, the FEM, the volume of fluid method or the smoothed particle hydrodynamics method, can be employed to quantify sloshing effects in tanks. The most popular approach for the analysis of sloshing problems occurring in tanks is currently to solve Navier-Stokes equations by employing FSI algorithms of the FEM. Details of this technique are presented in the following sections.

3 Mesh Description Algorithms for the Numerical Analysis of Fluid-Tank Systems

In order to solve complex tank-fluid interaction problems, an appropriate numerical simulation method, which can cope with large deformations of fluid free surface and the structure and accurately predicts the hydrodynamic forces due to impulsive fluid motion effects and the high-speed impacts of sloshing liquid on a tank wall and roof, is required. The nonlinear FE techniques with either Lagrangian, Eulerian or Arbitrary Lagrangian-Eulerian (ALE) formulations may be employed as a numerical method to analyze tank problems.

3.1 Lagrangian Algorithm

In Lagrangian systems, mainly used for structural mechanics, all nodes of the computational mesh follow the movement of the associated material nodes, since the mesh nodes are embedded in the material nodes. In the Lagrangian algorithm, materials with history-dependent constitutive relations can be treated easily. Free surfaces and interfaces between the different types of materials are tracked automatically. Boundary conditions are easily imposed because the edges of the mesh represent the limits of the physical domain during calculation. However, it has a major drawback: the Lagrangian algorithm cannot cope with large distortions of the computational domain without remeshing frequently.

3.2 Eulerian Algorithm

In Eulerian systems, which are most commonly used in fluid dynamic modelling, the computational mesh and associated nodes are fixed in position, but the material nodes are free to move with respect to the Eulerian grid. This enables the ability to handle large distortions in the modelling, but at the cost of flow detail resolution and the accurate definition of the interface.

3.3 Arbitrary Lagrangian-Eulerian (ALE) Algorithm

The Arbitrary Lagrangian-Eulerian (ALE) was developed to combine the positive aspects of the Lagrangian and Eulerian algorithms. In this algorithm, computational nodes of the mesh can move with the material nodes as in Lagrangian systems, remain fixed like in Eulerian systems, or move arbitrarily with respect to the

material nodes in order to limit mesh distortion [22]. The ALE can handle high deformation problems with less mesh distortion than the Lagrangian algorithm and with higher accuracy than the Eulerian algorithm.

3.4 SPH Algorithm

As an alternative to the FE analysis, coupled fluid-structure problems can also be analyzed using the Smooth Particle Hydrodynamics (SPH) method. In this method, the fluid region is represented with particles, which carry information about mass conservation and their hydrodynamic and thermo-dynamic behavior. Therefore, SPH is a meshless Lagrangian technique used to model the fluid equations of motion. Since this is a meshless technique, problems with large amplitude fluid motions and/or complex geometries can be solved easily without having the limitations of volumetric meshing. But, the SPH method requires a large number of particles to model FSI problems, thus it is computationally expensive in terms of both memory and CPU time.

In general, for tank problems, the choice of mesh representation for the fluid domain depends on the characteristics of the specific problem. Especially for large deformation problems, the selection of an appropriate mesh description is very important to properly simulate the physical phenomenon. If the response of the fluid-tank system under earthquake motion involves small amplitude deformations of free surface and tank structure, Lagrangian formulation can be used to model fluid domain. If large amplitude deformations at the fluid free surface and fluid-structure interface are expected, an intermediate formulation is required, in which mesh of the fluid domain follows the boundary motion while keeping the mesh deformation limited. The ALE algorithm of FEM constitutes a very efficient intermediate formulation for the solution of the seismic tank problems since it can cope with large deformations of free surface of the fluid and the structure. In addition, the ALE algorithm can correctly predict the hydrodynamic forces caused by coupling of flexible tank and the fluid and the high-speed impacts of sloshing liquid on tank wall and roof. SPH method can also be used to solve tank problems with large deformations, since mesh distortion is not a problem for this algorithm. However, a large number of SPH particles need to be used to define the fluid domain.

4 ALE Description of Navier–Stokes Equations

The ALE approach is based on the arbitrary movement of a reference domain which, additionally to the common material (Lagrangian) domain and spatial (Eulerian) domain, is introduced as a third domain, as detailed in [23]. The reference domain, which will later on correspond to the FE mesh, is used to formulate

the FSI problem. The arbitrary movement of the reference frame, accompanied of course by a good "mesh moving algorithm", enables one to rather conveniently deal with moving boundaries, free surfaces, large deformations, and interface contact problems.

The total time derivative of a variable f with respect to a reference coordinate can be described as follows:

$$\frac{\mathrm{d}f(\vec{X},t)}{\mathrm{d}t} = \frac{\partial f(\vec{x},t)}{\partial t} + (\vec{\boldsymbol{v}} - \vec{\boldsymbol{w}}) \cdot \overrightarrow{grad} f(\vec{x},t) \tag{17}$$

where $\vec{X}$ is the Lagrangian coordinate, $\vec{x}$ is the ALE coordinate, $\vec{\boldsymbol{v}}$ is the particle velocity and $\vec{\boldsymbol{w}}$ is the velocity of the reference coordinate, which will represent the grid velocity for the numerical simulation, and the system of reference will be later the ALE grid.

Let $\Omega^f \in R^3$ represent the domain occupied by the fluid particles, and let $\partial\Omega^f$ denote its boundary. The equations of mass, momentum and energy conservation for a Newtonian fluid in ALE formulation in the reference domain, are given by:

$$\frac{\partial \rho}{\partial t} + (\vec{\boldsymbol{v}} - \vec{\boldsymbol{w}}) grad(\rho) + \rho\, div(\vec{\boldsymbol{v}}) = 0 \tag{18}$$

$$\rho \frac{\partial \vec{v}}{\partial t} + \rho(\vec{\boldsymbol{v}} - \vec{\boldsymbol{w}}) \cdot \overline{\overline{grad}}(\vec{\boldsymbol{v}}) = \overrightarrow{div}(\overline{\overline{\sigma}}) + \vec{f} \tag{19}$$

$$\rho \frac{\partial e}{\partial t} + \rho(\vec{\boldsymbol{v}} - \vec{\boldsymbol{w}}) \cdot \overrightarrow{grad}(e) = \overline{\overline{\sigma}} : \overline{\overline{grad}}(\vec{\boldsymbol{v}}) + \vec{f} \cdot \vec{\boldsymbol{v}} \tag{20}$$

where ρ is the density and σ is the total Cauchy stress given by:

$$\overline{\overline{\sigma}} = -p \cdot \overline{\overline{Id}} + \mu(\overline{\overline{grad}}(\vec{\boldsymbol{v}}) + \overline{\overline{grad}}(\vec{\boldsymbol{v}})^T) \tag{21}$$

where p is the pressure and μ is the dynamic viscosity. For compressible flow, Eqs. (18), (19) and (20) are completed by an equation of state that relates pressure to density and internal energy. The internal energy, e, in Eq. (20) is the energy per unit volume.

Equations (18), (19) and (20) are completed with appropriate boundary conditions. The part of the boundary, at which the velocity is specified, is denoted as $\partial\Omega_1^f$. The inflow boundary condition is:

$$\overrightarrow{v} = \overrightarrow{g}(t) \text{ on } \partial\Omega_1^f \tag{22}$$

The traction boundary condition associated with Eq. (19) is the conditions on stress components. These conditions are assumed to be imposed on the remaining part of the boundary:

$$\overline{\overline{\boldsymbol{\sigma}}}.\vec{n} = \vec{h}(t) \text{ on } \partial\Omega_2^f \tag{23}$$

where, $\vec{n}$ is the outward unit normal vector on the boundary.

One of the major difficulties in time integration of the ALE Navier-Stokes Equations (Eqs. (18), (19) and (20)) is due to the nonlinear term related to the relative velocity $(\vec{\boldsymbol{v}} - \vec{\boldsymbol{w}})$ which is usually referred to as the advection term. This term accounts for the transport of the material past the mesh and makes solving the ALE equations numerically much more difficult than the Lagrangian equations, where the relative velocity is zero. For some ALE formulations, the mesh velocity can be calculated using a remeshing and smoothing process. In the Eulerian formulation, since the problem is formulated in the spatial coordinate, the reference frame is fixed $\left(\vec{\boldsymbol{w}} = \vec{0}\right)$. This assumption eliminates the remeshing and smoothing process, but does not simplify the Eqs. (18), (19) and (20).

In order to solve ALE formulation of Navier-Stokes Equations (Eqs. (18), (19) and (20)), there are two ways, and they correspond to the two approaches taken in implementing the Eulerian viewpoint in fluid mechanics. The first way solves the fully coupled equations for computational fluid mechanics; this approach used by different authors can handle only a single material in an element. The alternative approach is referred to as an operator split method in the literature [11, 24] where the calculation, for each time step, is divided into two phases. First, a Lagrangian phase is performed using an explicit FEM, in which the mesh moves with the fluid particle. In the CFD community, the Lagrangian phase is referred to as a linear Stokes problem. In this phase, the changes in velocity, pressure and internal energy due to external and internal forces are computed. The equilibrium equations of the Lagrangian phase are given as follows:

$$\rho \frac{\mathrm{d}\vec{\boldsymbol{v}}}{\mathrm{d}t} = \overrightarrow{div}(\overline{\overline{\boldsymbol{\sigma}}}) + \vec{f} \tag{24}$$

$$\rho \frac{\mathrm{d}e}{\mathrm{d}t} = \overline{\overline{\boldsymbol{\sigma}}} : \overline{\overline{grad}}(\vec{\boldsymbol{v}}) + \vec{f} \cdot \vec{\boldsymbol{v}} \tag{25}$$

In the second phase, the displaced mesh from the Lagrangian phase is remapped into the initial mesh for an Eulerian formulation, or an arbitrary distorted mesh for an ALE formulation. The transportation of mass, momentum and energy across element boundaries are computed. This may be thought of as remapping the displaced mesh at the Lagrangian phase back to its initial position. The transport equations for the advection phase are given as follows:

$$\frac{\partial \phi}{\partial t} + \vec{\boldsymbol{c}} \cdot \overrightarrow{grad}(\phi) = 0 \tag{26}$$

$$\phi(\vec{x}, 0) = \phi_0(x) \tag{27}$$

where $\vec{c} = \vec{v} - \vec{w}$ is the difference between the fluid velocity $\vec{v}$, and the velocity of the computational domain $\vec{w}$, which will represent the mesh velocity in the FE formulation. In some papers $\vec{c}$ is referred as the convective velocity.

Equation (26) is solved successively for the conservative variables: mass, momentum and energy with initial condition $\phi_0(x)$, which is the solution from the Lagrangian calculation of Eqs. (24) and (25) at the current time. In Eq. (26), the time t is a fictitious time; here, time step is not updated when solving for the transport equation. There are different ways of splitting the Navier-Stokes problems. In some split methods, each of the Stokes problem and transport equation are solved successively for half time step. The hyperbolic equation system (26) is solved for mass, momentum and energy by using a finite volume method. Either a first order upwind method or second order Van Leer advection algorithm [25] can be used to solve Eq. (26).

5 Governing Equations for Structure

Let $\Omega^S \in R^3$ be the domain occupied by the structure, and let $\partial\Omega^S$ denote its boundary. An updated Lagrangian FE formulation is considered: the movement of the structure Ω^S described by $x_i(t)$ (i = 1, 2, 3) can be expressed in terms of the reference coordinates $X_\alpha(t)$ (α = 1, 2, 3) and time t:

$$x_i = x_i(X_\alpha, t) \tag{28}$$

The solution of Eq. (24) satisfies the displacement boundary condition (Eq. (29)) on the boundary $\partial\Omega_1^S$ and the traction boundary condition (Eq. (30)) on the boundary $\partial\Omega_2^S$:

$$\vec{x}(\vec{X}, t) = \vec{D}(t) \text{ on } \partial\Omega_1^S \tag{29}$$

$$\overline{\overline{\sigma}} \cdot \vec{n} = \vec{\tau}(t) \text{ on } \partial\Omega_2^S \tag{30}$$

6 Numerical Algorithms for FSI

The main concern in fluid–structure interaction problems is the computation of the fluid forces that act on a rigid or deformable structure. Accurate computation of these forces is essential to provide structural safety. In fact, the application of fluid–structure interaction technology allows to correctly predict the hydrodynamic forces that act on a structure due to motion of the fluid by solving the hydrodynamic equations and to communicate the forces between fluid and structure for dynamic equilibrium. The numerical FSI algorithms by means of FEM have been developed

using either Lagrangian, Eulerian or Arbitrary Lagrangian-Eulerian (ALE) mesh descriptions to model fluid motion that interacts with a Lagrangian structure. Therefore, in the following sections, first, the interface conditions for FSI problems are explained. Then, FSI algorithms are presented in detail.

6.1 Interface Conditions

Let us assume that a fluid Ω^f and a structure Ω^S are in contact as shown in Fig. 2. Therefore, the gap, d, normal to the common interface is zero. However, for clarity, the contacting surfaces are depicted in this figure separately. This sketch sums up Eqs. (18)–(23) for the fluid and the Eqs. (24), (25), (29) and (30) for the structure. In a fluid–structure interaction problem, two conditions applied on the interface $\partial\Omega_2^C$ common to $\partial\Omega_2^S$ and $\partial\Omega_2^f$ are added to the previous equations: the fluid–structure traction conditions and the impenetrability condition. The traction condition observes the balance of momentum across the fluid–structure interface. Since this interface has no mass, the sum of traction forces on the fluid and structure must vanish (Newton's third law). Since a frictionless model is considered, the tangential tractions vanish too. Thus, the traction condition is simply the normal traction relation:

$$\overline{\overline{\boldsymbol{\sigma}}}^S \cdot \vec{n}^S + \overline{\overline{\boldsymbol{\sigma}}}^f \cdot \vec{n}^f = 0 \text{ on } \partial\Omega_2^C \tag{31}$$

where $\vec{n}^S$ and $\vec{n}^f$ are normals at the contact point for Ω^S and Ω^f, respectively, $\overline{\overline{\boldsymbol{\sigma}}}^S$ and $\overline{\overline{\boldsymbol{\sigma}}}^f$ are the stress fields of the fluid and structure, respectively.

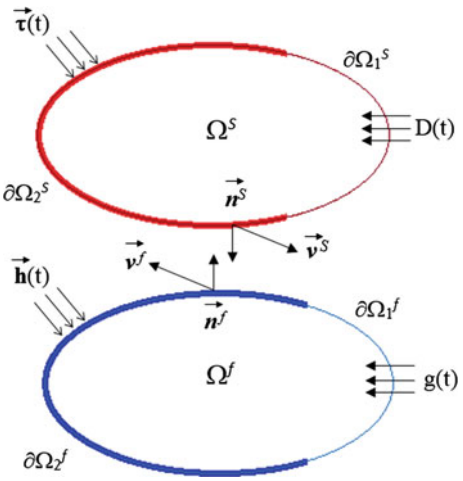

Fig. 2 Interaction between structure domain Ω^S and fluid domain Ω^f (the contacting surfaces are sketched separately for clarity)

The impenetrability conditions for Ω^f and Ω^S can be stated as

$$\Omega^f \cap \Omega^S = 0 \text{ on } \partial\Omega_2^C \tag{32}$$

Since $\vec{n}^f = -\vec{n}^S$, it is convenient to express the condition Eq. (32) in terms of penetration rate $\dot{d}$:

$$\dot{d} = \vec{v}^S \cdot \vec{n}^S + \vec{v}^f \cdot \vec{n}^f = (\vec{v}^S - \vec{v}^f) \cdot \vec{n}^S \leq 0 \text{ on } \partial\Omega_2^C \tag{33}$$

where $\vec{v}^S$ and $\vec{v}^f$ are the contact point velocities of the fluid and structure, respectively.

The condition Eq. (33) expresses the fact that the fluid and structure must either remain in contact $\left(\dot{d} = 0\right)$ or separate $\left(\dot{d} < 0\right)$. It may appear inconsistent to speak of a penetration rate $\dot{d}$ when impenetrability is an important condition on the solution. However, in many numerical methods, a small amount of interpenetration is allowed: $d < 0$. Then, the condition Eq. (33) will not be observed with exactitude. In the penalty method, the impenetrability constraint is imposed as a penalty normal traction along the fluid–structure interface.

6.2 *Interaction Between Lagrangian Structure and Lagrangian Fluid Elements*

For tank problems, a purely Lagrangian modelling strategy, in which both tank and fluid are represented with two independent Lagragian meshes, can be employed. Therefore, a contact algorithm needs to be used to transfer interaction forces between structure and fluid domains (Fig. 3a). Although this modelling technique can be implemented with ease, large deformations of the tank and fluid and construction of new fluid free surfaces cannot be handled with the same Lagrangian mesh during the entire simulation. Severely distorted elements have low accuracy and their stable time step sizes are small for explicit time integration algorithms to continue the simulation [24]. In this case, a new mesh must be generated and the old solution must be transferred from the old mesh onto the new mesh. This remeshing process can be achieved by a rezoning method where automatic mesh generators are called internally to create a new mesh with a new topology [25]. In the rezoning methods, the dependent variables, such as velocity, pressure, internal energy, stress components and plastic strain, are updated on the new mesh by using a remap algorithm.

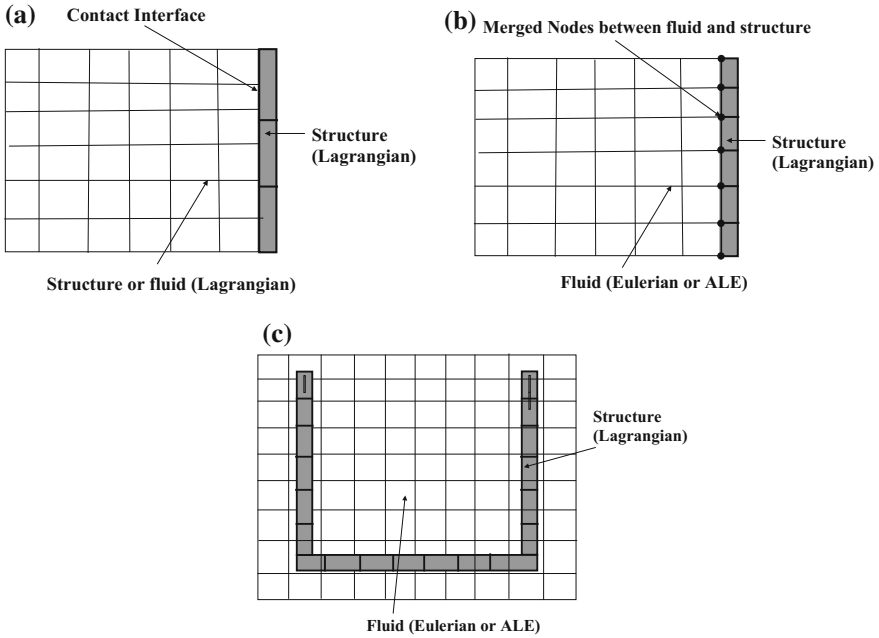

Fig. 3 Modelling strategies for FSI problems **a** contact algorithms, **b** FSI with common fluid and structure nodes at the interface and **c** fluid-structure coupling

6.3 Interaction Between Lagrangian Structure and ALE Fluid Elements

As an alternative, the ALE algorithm can be used to model fluid domain. Unlike a rezoning method, the topology of the mesh is fixed in the ALE algorithm where only the mesh nodes are relocated to obtain a homogeneous and undistorted mesh. The accuracy of an ALE calculation is often superior to the accuracy of a rezoned calculation because the algorithms used to remap the solution from the distorted to the undistorted mesh is second order accurate for the ALE formulation when using second order advection algorithms, while the algorithm for the remap in the rezoning is only first order accurate. If fluid domain is modelled with the ALE algorithm, interaction forces between fluid and tank can be transferred by merging nodes lying on the fluid and structure interface (Fig. 3b). In this method, the fluid region is treated on a moving mesh using an ALE formulation whereas the structure is discretized with a deformable mesh using a Lagrangian formulation. This method is suitable for fluid structure interaction problems where structure deforms considerably moderate.

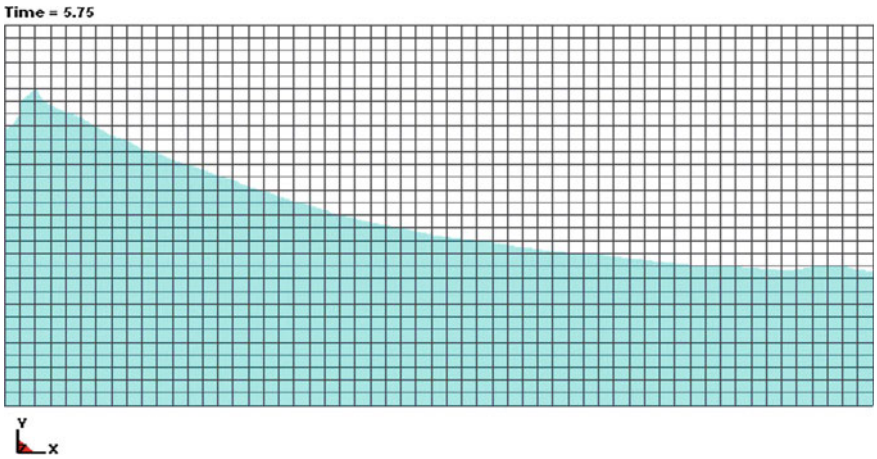

Fig. 4 FE model for a rigid tank problem simulated using the ALE algorithm with common nodes at the interface

For tank problems with large deformations, ALE mesh with common nodes at the interface cannot accord the deformations of Lagrangian structural mesh at the fluid structure interface and stable time step size is not high enough for explicit time integration algorithms to continue. In this case, a coupling algorithm, where the fluid and structure are represented with two independent meshes, can be employed to solve fluid–tank interaction problems (Fig. 3c). The coupling algorithm computes interface forces applied from the fluid to the structure and conversely. These forces are imposed to the fluid and structure nodes lying on the interface in order to prevent a node from passing through fluid–structure interface. For explicit methods, nodal forces at the fluid–structure interface are updated at each time step to account for interface forces. In contact problems, the slave and master meshes geometrically define the contact interface, whereas in the fluid–structure coupling method, the fluid coupling interface is defined by the material surface. From a mechanical point of view, the Euler–Lagrange coupling algorithm is similar to penalty contact algorithm of Lagrangian analysis because the coupling method is mainly based on force equilibrium, and energy conservation. Penalty contact algorithm is explained in detail in Sect. 6. Figures 4 and 5 show examples of FE models for a rectangular tank problem simulated using the ALE method with common nodes at the interface and fluid-structure coupling algorithm, respectively.

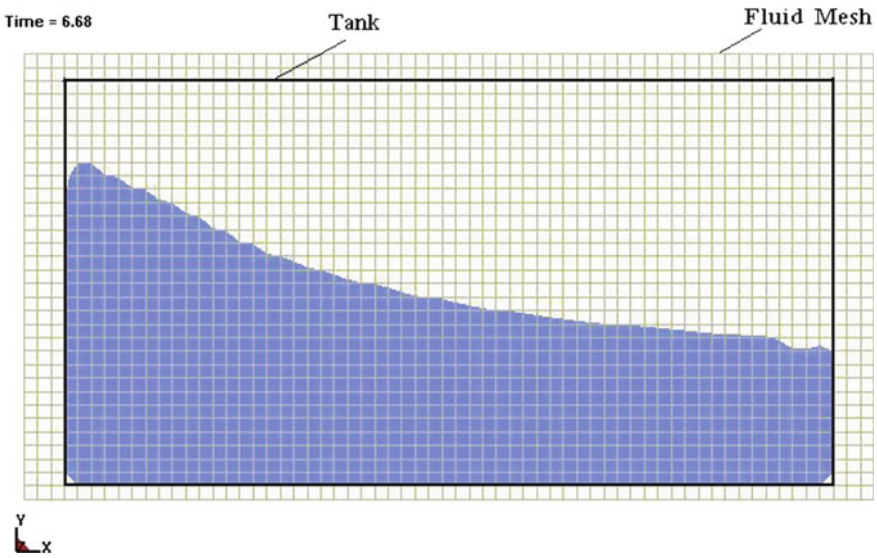

Fig. 5 FE model for a rigid rectangular tank problem simulated using the ALE coupling method

7 Boundary Conditions of Tanks at the Base

Liquid storage tanks can be grouped into two categories as anchored and unanchored tanks depending on the boundary conditions at the base. Anchored tanks are rigidly fixed to a substantial foundation. However, anchoring of a tank is not practical to construct and considerably expensive because it needs a large number of bolts and suitable attachments onto the tank wall. Improperly designed bolts can tear the tank wall. Also, a massive foundation is required especially for large tanks. In practice, it is more common to construct tank shell on a simple ringwall foundation or directly on the compacted soil due to these disadvantages of anchoring. Yet, the dynamic behavior of unanchored tanks is quite different than that of anchored tanks.

Seismic response of unanchored tanks is highly nonlinear, because of the partial uplift of the tank bottom plate caused by overturning moments. Since uplift represents stiffness loss of the whole system, the frequencies of the coupled fluid-tank system decreases and the axial compression forces in the tank wall increases. This increment in axial compression stress makes an unanchored tank more prone to buckling than an anchored. Uplift may also affect tank mode shapes, system damping and hydrodynamic pressure distribution acting on an unanchored tank. On the other hand, anchored tanks have the ability to resist seismic overturning moment and respond to this moment in a manner like a circular cylinder shell moving in its modal forms (shell buckling modes) with out-of-round cross-sectional distortions (circumferential cos $n\theta$-type modes, $n > 1$). These higher order distortions increase the axial compressive stress on the wall which, in turn, accelerates

buckling. These higher order distortions of the tank cross section are of considerable importance for the overall structural response.

In numerical models, boundary conditions of anchored tanks are implemented by ideally restraining all translational and rotational degrees of freedom of the tank baseplate nodes to its rigid foundation, whereas unanchored tank is assumed to be resting directly on ground. The interface between soil and unanchored tank in many cases involve lift off and reclosure of tank base as well as frictional sliding. The successive contact and separation between the tank baseplate and its rigid foundation, along with the friction effects, are modelled using a contact algorithm. Contact problems are among the most difficult and expensive nonlinear problems because the parameters of the contact region, which include the sliding state, the frictional stress distribution, the shape and the size of the region, etc., and deformation status of the media in contact, are unknown before the analysis. However, FEM offers a convenient solution to treat contact problems.

Numerical algorithms usually use either the constraint method or the penalty method for the enforcement of contact conditions. In the kinematical constraint method, the impermeability condition is imposed directly by kinematical boundary conditions insuring momentum conservation. Since the penetration is not permitted during the procedure in this method, the equations of motion remain uncoupled. As oppose to constraint base method, the penalty method allows penetrations between contracting boundaries where the penetrating node is referred to as the slave node whereas the penetrated segment is referred to as master segment. A master surface consists of multiple segments and a single shell element or a single face of a solid element can be thought as a segment.

In the penalty method, penetration between slave nodes and master segments are searched in every time step. When a slave node penetrates a master segment two forces are applied to that node: a restoring force normal to the penetrated segment, $\boldsymbol{F_N}$, and a shear force parallel to the penetrated segment, $\boldsymbol{F_C}$. The shear force is called as the coulomb friction force or the sliding friction force. The restoring force, $\boldsymbol{F_N}$, which is proportional to the penetration depth is applied to slave node to prevent its penetration though the master segment. This method can be represented as placing normal interface linear springs between penetrating nodes and their respective surfaces (Fig. 6). The restoring spring force $\boldsymbol{F_N}$ is computed by the following relationship:

$$\boldsymbol{F_N} = kd \tag{34}$$

where k is the spring (contact) stiffness or penalty factor, and d is the penetration distance. The penalty factor k is computed by Eqs. (35) and (36) for solid elements and segments on solid element faces, respectively:

$$k = \frac{\alpha K A^2}{V} \tag{35}$$

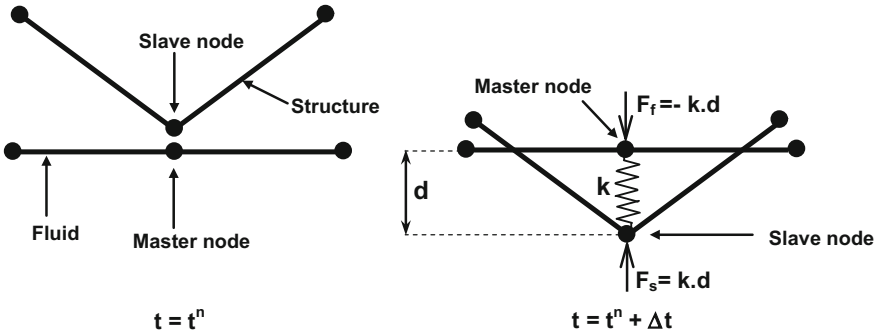

Fig. 6 Sketch of contact algorithm

$$k = \frac{\alpha K A}{d_d} \tag{36}$$

where α, K, A, V and d_d represent penalty scale factor, bulk material modulus, area of the segment contacted by the slave node, volume of the element being penetrated and minimum diagonal distance between penetrated node and master segment, respectively.

Friction plays an important role in the interaction effects between tank and soil. Sliding of the tank over its foundation which occurs when the lateral inertial force (base shear) exceeds the static friction force is prevented by friction. In general, friction is an integral part of the contact algorithms and it is based on a Coulomb formulation, where the magnitude of the friction force is proportional to the normal force, but its direction is always opposite to that of the sliding velocity. The Coulomb friction law neglects the elasticity between the particles and a rigid plastic contact behavior is assumed.

The Coulomb friction forces are approximately represented by equivalent fictitious elastic-plastic springs which are connected to the nodes that make contact with a surface. The Coulomb friction force can be defined by the following formulation:

$$\boldsymbol{F_C} = \mu_C \boldsymbol{F_N} \tag{37}$$

where $\boldsymbol{F_N}$ is the normal force, μ_C the instantaneous coefficient of friction and $\boldsymbol{F_C}$ the frictional force. The instantaneous frictional coefficient, μ_C, is assumed to depend on relative velocity v_{rel} of the surfaces in contact and an exponential interpolation function with a decay coefficient is used for transition from static to dynamic friction:

$$\mu_c = \mu_d + (\mu_s - \mu_d) e^{-D|v_{rel}|} \tag{38}$$

where, μ_s is the static coefficient of friction, μ_d the dynamic coefficient of friction, and D the exponential decay coefficient which determines the rate at which the

instantaneous friction coefficient transitions from μ_s to μ_d with increasing slip velocity. According to Eq. (38), if a decay coefficient of zero is specified, instantaneous coefficient of friction μ_C is equal to the static friction coefficient μ_s for all slip velocities. On the other hand, if a very large decay coefficient is specified, the result is nearly an instantaneous, or step, transition between μ_s and μ_d, which could potentially result in an undesired and unrealistic dynamic system response. This equation also reveals that as the velocity increases, the instantaneous coefficient of friction decreases and thus, the slip force decreases in direct proportion. The instantaneous friction coefficient, and thus the slip force are highly dependent on the decay factor, as well as the relative sliding velocity between the contacting surfaces [26].

The penalty method does not introduce new unknowns, therefore the system of equations to be solved is not expanded. Due to the symmetry of the approach, small amount of hourglassing is excited. Momentum is exactly conserved without the necessity of imposing impact and release conditions and the energy conservation spontaneously occurs in contrast to the kinematical constraint method. No special treatment is given to intersecting interfaces. Also, the computed time step is not affected by the existence of the interfaces, since the interface stiffness is chosen to be approximately the same order of magnitude as the stiffness of the interface element normal to the interface. However, large interface pressure may produce unacceptable penetration. This problem can be remedied by scaling up the stiffness or scaling down the time step at the cost of increasing solution time [27].

8 Applications

The sloshing response of a rectangular tank when subjected to harmonic motion and a cylindrical tank under earthquake motions is assessed using the ALE algorithm as implemented in general purpose FE code LS-DYNA. Two boundary conditions are considered for the cylindrical tank: anchored and unanchored. Sloshing wave height time histories observed in rigid, elastic and nonlinear cylindrical tanks are compared to quantify the effect of tank material on the sloshing response. Different combinations of the selected earthquake record components are used for the seismic analysis of tanks. The anchored tank model is assumed to be located on two different soil types: rock and stiff clay to investigate the influence of soil condition on the sloshing response of tanks.

8.1 Sloshing Response of a Rigid Rectangular Tank

The sloshing event inside a rigid rectangular tank subjected to resonant harmonic motion is investigated with fully nonlinear FSI algorithms of the FEM based on ALE approach. The tank, which has a width of 0.57 m, breath of 0.31 m and total

height of 0.30 m, is filled with water ($\rho_w = 1000\,\mathrm{kg/m^3}$) up to a height of 0.15 m. The tank is fixed at its base and harmonic motion is applied as displacement. The excitation frequency is taken as the same as the first fundamental frequency of sloshing ω_0 (Eq. (14)). The amplitude of the horizontal harmonic excitation is considered as 0.005 m. Hydrostatic pressure field is generated by gradually increasing pressure until 1 s [17].

Two different FSI methods based on the ALE algorithm are applied to the tank problem and the results are evaluated in terms of sloshing wave height observed at specific locations at the free surface. In the first method, the fluid-structure interface is described by the interface nodes, which are common for the fluid and the structure domains [28]. In the second method, the ALE coupling algorithm, in which the fluid and structure are represented with independent meshes, is employed to compute the interaction forces at the fluid-structure interface [29]. In both methods, the fluid is represented by solving Navier–Stokes equations with an ALE formulation and the structure is treated on a deformable mesh using a Lagrangian formulation. In the numerical models, the influence of the third dimension is ignored and the tank-fluid system is modeled as 2D. The liquid domain is discretized with uniform solid mesh. In order to reduce the number of elements in the fluid mesh, a moving ALE mesh that follows the structure motion is employed in the numerical analyses. The time step size is 1×10^{-4} s throughout the simulation. The average computation time for analysing sloshing problem in the 2D tank using ALE common nodes was approximately 3 min, on a six core 64 bit workstation with 16 GB memory. The finite element analysis of the same problem using ALE coupling took around 3 min on the same computer.

Figure 7 presents the time history response of free surface elevations obtained by both numerical methods at three measurement locations which were located near left (i.e. $x = -0.265, \mathrm{y} = 0$) and right (i.e. $x = 0.265, \mathrm{y} = 0$) ends of tank and at the middle of the free surface (i.e. $x = 0, y = 0$). There is a strong correlation between the results of both methods; the free surface time history results are almost the same in terms of peak level timing, shape and amplitude of sloshing wave.

Numerical simulation results for the ALE algorithm with common fluid and structure nodes at the interface are also compared with the corresponding results of analytical formulation and the shaking-table test results of Liu and Lin [17]. For all solution types, as it is expected, the wave height is almost zero at the middle of the free surface for each method. The wave height increases continuously over time at the near left and right end of the tank. The comparison of three solution methods reveals that the analytical method overestimates negative surface amplitudes, whereas it underestimates the positive ones (Fig. 8). Numerical and experimental results are highly consistent in terms of peak level timing, shape and amplitude of sloshing wave. The free surface displacement time histories obtained from numerical and experimental studies show that the positive (upward) sloshing wave amplitudes are always larger than the negative (downward) ones. This phenomenon is a classical indication of a nonlinear behavior of sloshing and caused by

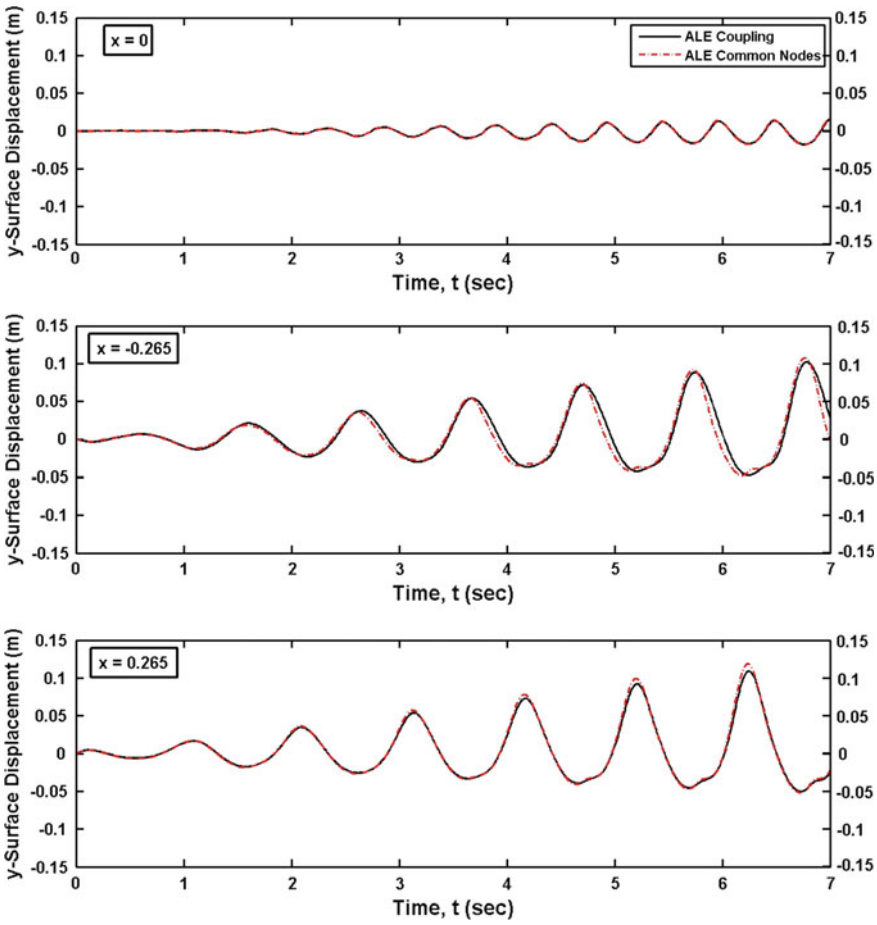

Fig. 7 Comparisons of the time histories of surface elevation for the ALE algorithm with common fluid and structure nodes at the interface and the ALE coupling algorithm

suppression effect of the tank base on the waves with negative amplitude. Although the gravity effects exist for both upward and downward fluid motion, the downward motion of fluid is blocked by the tank bottom. The ratio of positive amplitude to absolute negative amplitude increases as the fluid depth decreases. This phenomenon cannot be observed from analytical solution since it is derived under linearized assumptions. This verifies that the analytical method is not reliable for resonant frequencies where nonlinear sloshing behavior is extremely dominant. On the other hand, the present numerical algorithms can be used for the analysis of sloshing problems practically for every frequency range of external excitation.

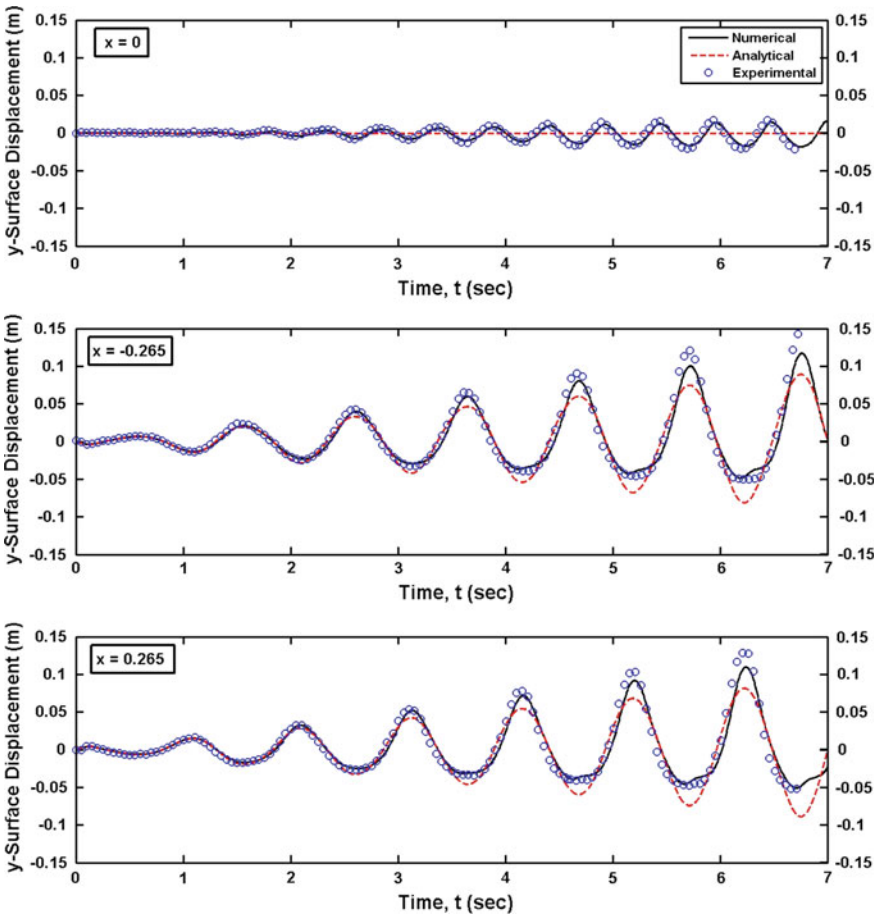

Fig. 8 Comparisons of the time histories of surface elevation for the ALE algorithm with common fluid and structure nodes at the interface, the analytical solution and experimental data

8.2 Sloshing Response of 3D Cylindrical Anchored and Unanchored Tanks

The tank model under consideration has a radius of 24 m and a total height of 18 m. The flat tank roof is constructed on a set of radial beams and rafters which are supported by columns (Fig. 9). The tank shell consists of 9 courses which are tapered from bottom to top. The thicknesses of the bottom plate and the first shell course nearest to the bottom are 0.007 and 0.020 m, respectively. The thickness of the tank shell decreases 0.002 m at each two courses and it reaches 0.012 m at the top course. The steel of cylindrical shell, roof, base plate, columns and roof rafters has a modulus of elasticity $E = 200$ GPa, Poisson's ratio of $v = 0.30$, and mass

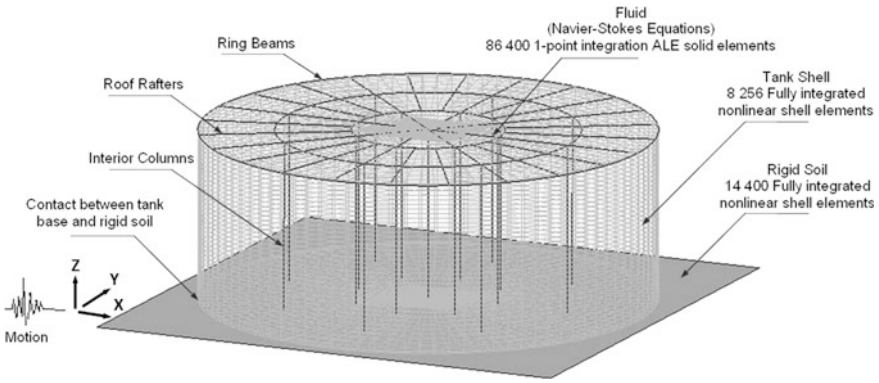

Fig. 9 FE model of the unanchored tank [30]

density of $\rho = 7800\,\mathrm{kg/m^3}$. The tank model under consideration is analyzed with three different material types: rigid, linear elastic and elastic-perfectly plastic. For elastic-perfectly plastic steel material, yield stress is assumed to be $\sigma_y = 355\,\mathrm{MPa}$. Water $(\rho_w = 1000\,\mathrm{kg/m^3})$ is filled up to a height of 14 m. Bulk modulus and dynamic viscosity of water are considered as $K = 2.2 \times 10^9\,\mathrm{N/m^2}$ and $\eta_v = 10^{-3}\,\mathrm{Pa\,s}$, respectively [30].

The analyses are performed on the same tank model under two support conditions, anchored and unanchored. Numerical analysis parameters such as friction coefficients, shell and fluid element formulations have a key importance for the accurate simulation of the physical phenomenon. The parameters of the anchored and unanchored tank models were studied and calibrated with existing experimental models in a previous study [31]. The calibrated parameters are employed to model the real size anchored and unanchored tanks under consideration. Static and dynamic friction are taken into account with coefficients of 0.50 and 0.45, respectively. The ALE description is employed for the fluid domain and the nodes at the interface of fluid and structure are merged. Four noded fully integrated shell elements with 3 integration points through the thickness are used for the discretization of the tank. In the numerical simulations, both material and geometric nonlinearities are considered in order to accurately determine stress, strain and strain rate distributions throughout the tank. Initially, a vertical acceleration field of 1 g is applied to give the correct hydrostatic pressure in the fluid. Anchored tank model is assumed to be placed on two different soil types: rock and stiff clay. Local site classes Z1 and Z3 of the Turkish Seismic Design Code (TSDC) [32] are considered for rock and stiff clay, respectively. The subgrade modulus of stiff clay is taken as $20\,\mathrm{MN/m^3}$ and two noded spring elements are employed to represent stiff clay in numerical models. For unanchored tank, soil is considered to be rigid.

In this study, real earthquake records, that satisfy seismological and geological conditions (faulting type, magnitude, distance to the fault, site conditions, etc.), are first processed with a time domain scaling procedure [33]. Each component of

records, which are selected from the Pacific Earthquake Engineering Research (PEER) Center strong-motion database [34], are independently scaled to match the target response spectrum specified in TSDC [32]. In all numerical analyses, anchored and unanchored tanks are assumed to be located on the 1st degree earthquake zone (effective ground acceleration coefficient, $A_0 = 0.4$), which corresponds to very high seismic risk. The importance factor, I of the tank is assumed to be 1.5. Response modification factor, R is taken as 1. Due to the fact that a vertical design spectrum is not specified in the TSDC [32], two thirds of the horizontal spectrum coefficients are used for the vertical spectrum coefficients. Damping of the impulsive and convective modes is assumed to be 5 % and 0.5 %, respectively, in the code implementation. Response spectrum values for 0.5 % damping for the convective mode are 1.5 times the 5 %-damped spectral values. As a second step, two records, one for rock and one for stiff clay, that best match the corresponding target spectra after time domain scaling process, are reprocessed with the computer program RSPMATCH [35]. Therefore, earthquake records, that are consistent with the target design spectra both in short-period and long-period ranges, are generated. Selected earthquake records along with their time domain scaling factors are listed in Table 1. Acceleration time histories of the RSPMATCH generated records that are used in the nonlinear transient analyses of the tanks located on rock and stiff clay are shown in Figs. 10 and 11. Numerical analyses are extended up to 40 s in order to observe the variation in sloshing wave height after motion subsides. The average computation time for analysing sloshing problem in the 3D anchored and unanchored cylindrical tanks using ALE common nodes was approximately 66 and 83 h, respectively, on a dual-core 64 bit PC with 1 GB memory. The finite element analysis of the sloshing problem in the 3D unanchored cylindrical tank located on stiff clay took around 104 h on the same computer.

In order to evaluate the relative importance of earthquake ground-motion components on the response of anchored and unanchored tanks, analyses are carried out for different combinations of the selected record components as shown in Table 2. Loading Case 1 represents the horizontal component applied at $\theta = 0^\circ$ while the second horizontal component of the selected earthquake motion is applied perpendicular to the 1st component $(\theta = 90^\circ)$. Circumferential angle, (θ), represents the angle from $+X$ axis and it increases counterclockwise. Loading Case 2 includes concurrently application of both of two horizontal components of the selected record. Loading Case 3 consists of simultaneously presence of the horizontal component used in Loading Case 1 and vertical component of ground motion while Loading Case 4 characterizes the three-dimensional nature of the earthquake motion.

Following the development of the FE model of tanks, a mesh sensitivity analysis was carried out to ensure that the results are not sensitive to the mesh size. The converged model includes 8256 shell elements, 729 beam elements and 86400 ALE single material fluid elements with a total of 90,613 nodes. The number of shell elements which represents soil underlying the unanchored tank is 14,400. The resulting FE model of the unanchored tank is shown in Fig. 9.

Table 1 The selected earthquake records and scaling factors (α_{AT})

Soil	Record No.	Earthquake	Date	Station	Record			Closest to fault rupture	Duration			Fault type	Scaling factor (α_{AT})		
					# 1	# 2	# 3		Record	Significant	Bracketed		# 1	# 2	# 3
Z1	P1087	Kocaeli, TR	17.08.1999	Arcelik	ARC000	ARC090	ARCDWN	17	30.0	11.0	9.7	SS	3.82	3.53	4.70
Z3	P1114	Kocaeli, TR	17.08.1999	Yarimca	YPT060	YPT330	YPT-UP	2.6	35	15.34	17.00	SS	1.95	1.98	1.94

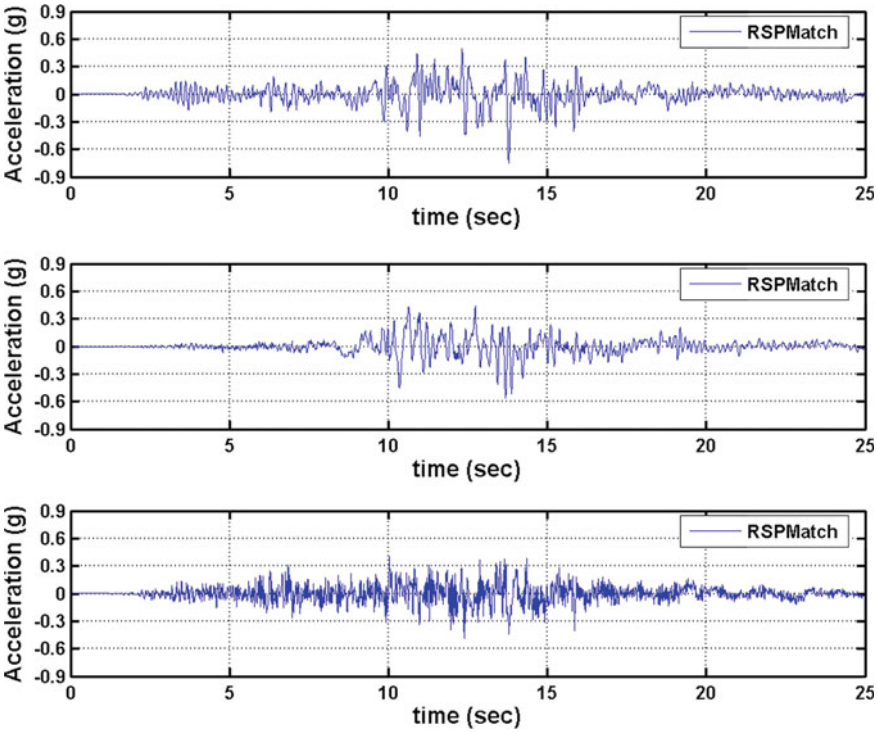

Fig. 10 Acceleration time histories of RSPMATCH generated **a** P1087-ARC000, **b** P1087-ARC090 and **c** P1087-ARCDWN records

Figure 12 shows time history plots of the free surface elevation at $X = R(\theta = 0^\circ)$ and $X = -R(\theta = 180^\circ)$ in tanks with different material types (rigid, linear elastic and elastic-perfectly plastic) and support conditions. As can be seen from these figures, the sloshing response is almost identical for all tank material types and support conditions. Hence, the general acceptance in the literature regarding the insensitivity of sloshing response to the tank base support conditions is validated by using the fully nonlinear algorithm.

Time-history plots of free-surface elevation at $\theta = 180^\circ$ and $X = R$ for the anchored and unanchored tanks under different combinations of the components of P1087-ARC record are shown in Fig. 13. As can be seen in this figure, the sloshing response is very similar for different combinations of earthquake ground-motion components and the sloshing response of anchored and unanchored tanks is almost identical. The average maximum sloshing wave height is around 3.60 m. The free-surface height decreases slowly after the motion stops and never exceeds its maximum value during the effective duration of the earthquake (30 s).

Figure 14 shows free surface time history at $X = -R$ and $\theta = 180^\circ$ when the anchored tank is founded on Z3 soil type. In this case, sloshing response is different than that when tank is settled on rigid foundation. Maximum free surface wave

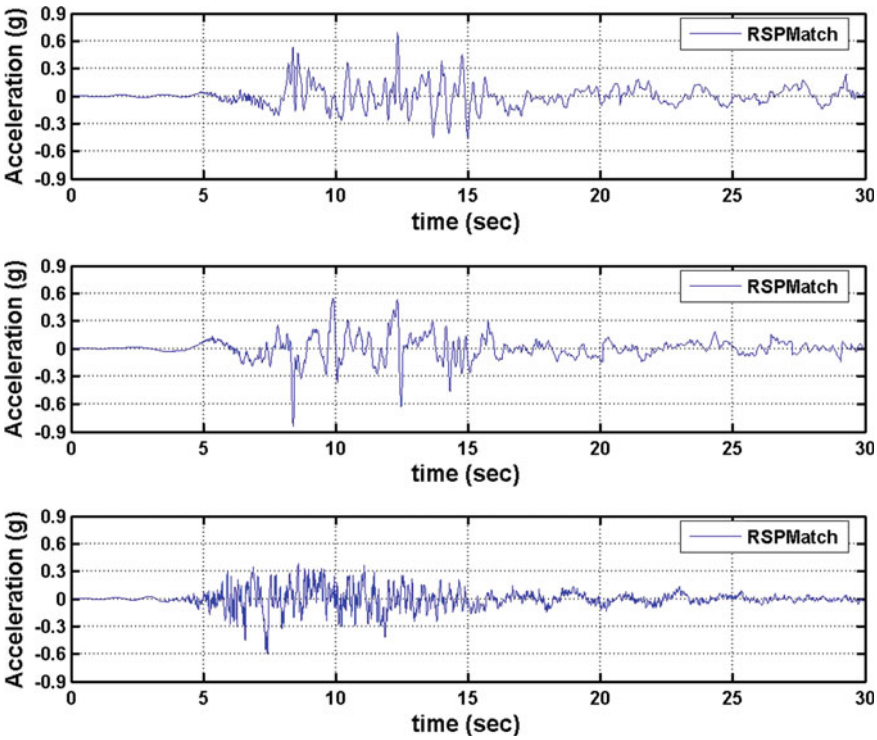

Fig. 11 Acceleration time histories of RSPMATCH generated **a** P1114-YPT060, **b** P1114-YPT330 and **c** P1114-YPT-UP records

Table 2 Combinations of ground motion components used in the transient analyses

Loading name	Record combinations
Loading case 1	Horizontal component of the selected earthquake ground motion
Loading case 2	Concurrently presence of two horizontal components of the selected earthquake ground motion
Loading case 3	Concurrently presence of one horizontal and vertical components of the selected earthquake ground motion
Loading case 4	Three components of the selected earthquake ground motion

height for anchored tank supported on Z3 soil type exceeds 4 m. Sloshing waves in the anchored tank impact to the roof of the tank and cause high joint stresses at the junction between the tank wall and tank roof and sloshing damage at the tank roof. Therefore, regular harmonic behaviour of sloshing waves is disturbed.

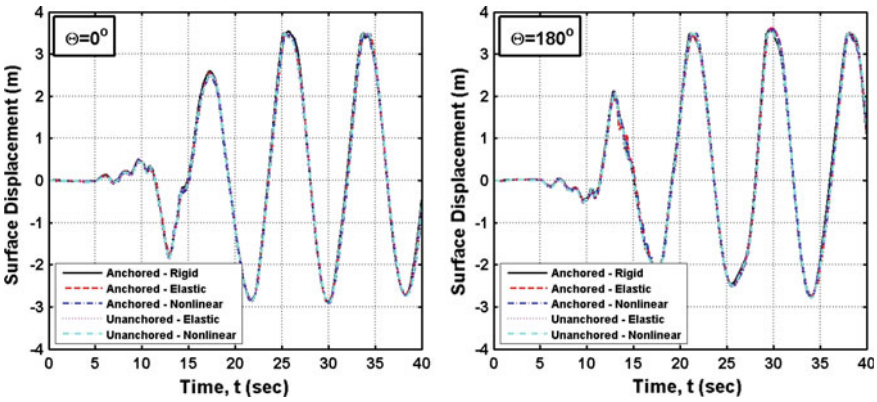

Fig. 12 Comparisons of free surface time histories of the anchored and unanchored tanks with different tank materials when subjected to RSPMATCH generated P1087-ARC000 record

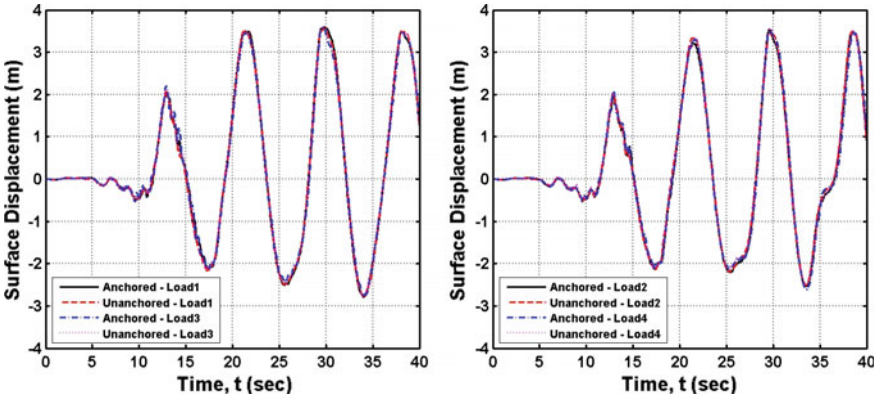

Fig. 13 Comparisons of free surface time histories of the anchored and unanchored tanks when subjected to different combinations of RSPMATCH generated P1087-ARC record $(\theta = 180^{\circ})$

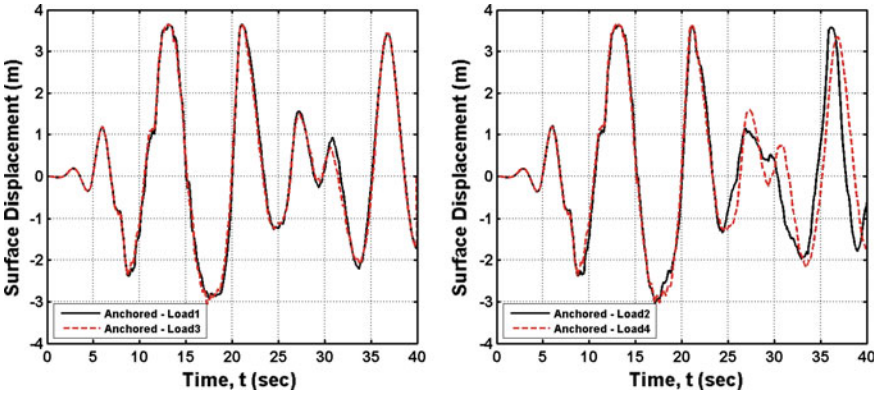

Fig. 14 Comparisons of free surface time histories of the anchored tank when subjected to different combinations of RSPMATCH generated P1114-YPT record $(\theta = 180^{\circ})$

9 Conclusions

This chapter presents a survey of nonlinear numerical modeling strategies that are used for the sloshing analysis of liquid storage tanks considering FSI effects. The governing equations for the fluid and structure and their solution methodologies are first clarified. Current nonlinear FE modelling algorithms for interaction between liquid, tank and rigid soil are presented in great detail. Then, the sloshing in a rectangular and cylindrical tanks under external motions is analysed using the presented numerical modelling schemes. Strong correlation between experimental and numerical results is obtained in terms of sloshing wave height for the rectangular tank model when subjected to resonant harmonic motion. However, the linear analytical solution based on potential flow theory shows deviations from the experimental data. The consistency of numerical and experimental results suggest that the FEM can be used as a reliable tool for the sloshing analysis of tanks when subjected to external motions. Finally, the presented numerical modelling methods are used to simulate sloshing response of broad anchored and unanchored cylindrical steel liquid storage tanks when subjected to earthquake ground motions. The complex interaction phenomenon occurring between the unanchored tank base plate and soil is taken into account with contact algorithm including friction forces. Analysis results showed that the sloshing response of anchored and unanchored tanks under consideration is insensitive to tank materials. Moreover, the presence of other ground motion components in addition to one horizontal component has ignorable importance on the sloshing response of cylindrical tanks for both support conditions. Second horizontal component affects temporal and spatial distributions of free surface wave height, but it does not substantially affect maximum sloshing response. The vertical component of the earthquake motion has a negligible effect on the sloshing response. Soft soil conditions influence the sloshing response of tanks and causes high joint stresses at the junction between tank wall and tank roof and sloshing damage at the tank roof.

References

1. Jacobsen LS (1949) Impulsive hydrodynamics of fluid inside a cylindrical tank and of fluid surrounding a cylindrical pier. Bull Seismol Soc Am 39(3):189–204
2. Housner GW (1954) Earthquake pressures on fluid containers. In: The 8th technical report under office of naval research. California Institute of Technology, Pasadena, California
3. Housner GW (1957) Dynamic pressures on accelerated fluid containers. Bull Seismol Soc Am 47(1):15–35
4. Housner GW (1963) The dynamic behavior of water tanks. Bull Seismol Soc Am 53(2): 381–387
5. Veletsos AS, Yang JY (1977) Earthquake response of liquid storage tanks. Advances in civil engineering through engineering mechanics. In: Proceedings of the engineering mechanics division specialty conferences. ASCE, Raleigh, North Carolina, pp 1–24

6. Faltinsen OM (1978) A numerical nonlinear method of sloshing in tanks with two-dimensional flow. J Ship Res 22:193–202
7. Fischer FD, Rammerstorfer FG (1999) A refined analysis of sloshing effects in seismically excited tanks. Int J Press Vessels Pip 76:693–709
8. El-Zeiny A (1995) Nonlinear time-dependent seismic response of unanchored liquid storage tanks. PhD Dissertation, Department of Civil and Environmental Engineering, University of California, Irvine
9. Chen BF, Chiang HW (1999) Complete 2D and fully nonlinear analysis of ideal fluid in tanks. J Eng Mech ASCE 125(1):70–78
10. Chen BF (2005) Viscous fluid in tank under coupled surge, heave, and pitch motions. J Waterw Port Coast Ocean Eng ASCE 131(5):239–256
11. Souli M, Ouahsine A, Lewin L (2000) ALE formulation for fluid-structure interaction problems. Comput Methods Appl Mech Eng 190:659–675
12. Souli M, Zolesio JP (2001) Arbitrary Lagrangian-Eulerian and free surface methods in fluids mechanics. Comput Methods Appl Mech Eng 191:451–466
13. Longatte E, Benddjedou Z, Souli M (2003) Methods for numerical study of tube bundle vibrations in cross-flows. J Fluids Struct 18(5):513–528
14. Longatte E, Bendjeddou Z, Souli M (2003) Application of Arbitrary Lagrange Euler formulations to flow-induced vibration problems. J Press Vessel Technol 125:411–417
15. Aquelet N, Souli M, Olovson L (2005) Euler Lagrange coupling with damping effects: application to slamming problems. Comput Methods Appl Mech Eng 195:110–132
16. Chen YH, Hwang WS, Ko CH (2007) Sloshing behaviours of rectangular and cylindrical liquid tanks subjected to harmonic and seismic excitations. Earthq Eng Struct Dyn 36:1701–1717
17. Liu D, Lin P (2008) A numerical study of three-dimensional liquid sloshing in tanks. J Comput Phys 227:3921–3939
18. Mitra S, Upadhyay PP, Sinhamahapatra KP (2008) Slosh dynamics of inviscid fluids in two-dimensional tanks of various geometry using finite element method. Int J Numer Meth Fluids 56:1625–1651
19. Kana DD (1979) Seismic response of flexible cylindrical liquid storage tanks. Nucl Eng Des 52:185–199
20. Manos GC (1986) Dynamic response of a broad storage tank model under a variety of simulated earthquake motions. In: Proceedings of the 3rd U.S. National Conference on Earthquake Engrg. Earthquake Engineering Research Institute, E1 Cerrito, CA, pp 2131–2142
21. Ibrahim RA (2005) Liquid sloshing dynamics: theory and applications. Cambridge University Press, New York, USA
22. Belytschko T, Liu WK, Moran B (2000) Nonlinear finite elements for continua and structures. Wiley, New York
23. Hughes TJR, Liu WK, Zimmerman TK (1981) Lagrangian Eulerian finite element formulation for viscous flows. J Comput Methods Appl Mech Eng 29:329–349
24. Benson DJ (1992) Computational methods in Lagrangian and Eulerian Hydrocodes. Comput Methods Appl Mech Eng 99:235–394
25. Van Leer B (1977) Towards the ultimate conservative difference scheme. IV. A new approach to numerical convection. J Comput Phys 23:276–299
26. Reid JD, Hiser NR (2004) Friction modelling between solid elements. Int J Crashworthiness 9 (1):65–72
27. Hallquist JO (2005) LS-DYNA theoretical manual. Livermore Software Technology Corporation, Livermore, CA
28. Ozdemir Z, Moatamedi M, Fahjan YM, Souli M (2009) ALE and fluid structure interaction for sloshing analysis. Int J Multiphys 3(3)
29. Ozdemir Z, Souli M, Fahjan YM (2010) FSI methods for seismic analysis of sloshing tank problems. Mécanique et Industries 11(2):133–147

30. Ozdemir Z, Fahjan YM, Souli M (2012) Numerical evaluation of non-linear response of broad cylindrical steel tanks under multi-dimensional earthquake motion. Earthq Spectra 28(1):217–238
31. Ozdemir Z, Souli M, Fahjan YM (2010) Application of nonlinear fluid-structure interaction methods to seismic analysis of anchored and unanchored tanks. Eng Struct 32:409–423
32. TSDC (Turkish Seismic Design Code) (2007) Specification for buildings to be built in seismic zones (TSC). Earthquake Research Department, Ministry of Public Works and Settlement, Government of Republic of Turkey, Ankara. http://www.deprem.gov.tr (in Turkish)
33. Fahjan YM (2008) Selection and scaling of real earthquake accelerograms to fit the Turkish design spectra. Teknik Dergi Tech J Turk Chamber Civ Eng (TCCE) Digest 19, 1231–1250
34. PEER (Pacific Earthquake Engineering Research Center) (2006) PEER strong motion database. http://peer.berkeley.edu/smcat/
35. Abrahamson NA (1993) Non-stationary spectral matching. Seismol Res Lett 63:30

Seismic Analysis of Structural Systems Subjected to Fully Non-stationary Artificial Accelerograms

Giuseppe Muscolino and Tiziana Alderucci

Abstract In seismic engineering, the earthquake-induced ground motion is generally represented in the form of pseudo-acceleration or displacement response spectra. There are, however, situations in which the response spectrum is not considered appropriate, and a fully dynamic analysis is required. In this case, the most effective approach is to define artificial spectrum-compatible stationary accelerograms, which are generated to match the target elastic response spectrum. So a Power Spectral Density (PSD) function is derived from the response spectrum. However, the above approach possesses the drawback that the artificial accelerograms do not manifest the variability in time and in frequency observed from the analysis of real earthquakes. Indeed, the recorded accelerograms can be considered sample of a fully non-stationary process. In this study a procedure based on the analysis of a set of accelerograms recorded in a chosen site to take into account their time and frequency variability is described. In particular the generation of artificial fully non-stationary accelerograms is performed in three steps. In the first step the spectrum-compatible PSD function, in the hypothesis of stationary excitations, is derived. In the second step the spectrum-compatible Evolutionary Power Spectral Density (EPSD) function is obtained by an iterative procedure to improve the match with the target response spectrum starting from the PSD function, once a time-frequency modulating function is chosen. In the third step the artificial accelerograms are generated by the well-known Shinozuka and Jan (J Sound Vib 25:111–128, 1972) formula and deterministic analyses can be performed to evaluate the structural response. Once the EPSD spectrum-compatible function is derived, a method recently proposed by the authors (Muscolino and Alderucci in Probab Eng

G. Muscolino (✉)
Department of Engineering and Inter-University Centre of Theoretical and Experimental Dynamics (C.I.Di.S.), University of Messina, Messina, Italy
e-mail: gmuscolino@unime.it

T. Alderucci
Department of Engineering, University of Messina, Messina, Italy
e-mail: talderucci@unime.it

M. Papadrakakis et al. (eds.), *Computational Methods in Earthquake Engineering*,
Computational Methods in Applied Sciences 44,
DOI 10.1007/978-3-319-47798-5_4

Mech 40:75–89, 2015), is adopted to evaluate the EPSD response function of linear structural systems subjected to fully non-stationary excitations by very handy explicit closed-form.

1 Introduction

For earthquake-resistant design of structures, the earthquake-induced ground motion is generally represented in the form of a response spectrum of pseudo-acceleration or displacement. The spectrum used as input is usually obtained by scaling an elastic spectrum by factors that account for, amongst other phenomena, the influence of inelastic structural response [1]. There are, however, situations in which the scaled response spectrum is not considered appropriate, and a fully dynamic analysis is required. These situations may include structures with configuration in plan or elevation that is highly irregular; structures for which higher modes are likely to be excited; structures with special devices to reduce the dynamic response; buildings designed for a high degree of ductility and so on. Faced with these special situations, the engineer will generally have to employ time-history analysis, for which the requirements are appropriate linear or non-linear models for the structure and a suitable suite of accelerograms to represent the seismic excitation [2].

There are three basic options available to the engineer in terms of obtaining suitable accelerograms. The first approach requires the generation of *synthetic accelerograms* from seismological source models and accounting for path and site effects [3, 4]. In general, there are actual difficulties in defining appropriate input parameters such as the source, path, and site characteristics. Moreover, to generate synthetic accelerograms there is a need for a definition of a specific earthquake scenario in terms of magnitude, rupture mechanism in addition to geological conditions and location of the site. Generally, most of these parameters are not often available, particularly when using seismic design codes. It follows that the main limit of this approach is that practitioners cannot always accurately characterize the seismological threat to generate appropriate synthetic signals.

The second approach adopts *real accelerograms* recorded during earthquakes [5, 6]. Real accelerograms contain a wealth of information about the nature of the ground shaking and carry all the ground-motion characteristics (amplitude, frequency, and energy content, duration and phase characteristics), and reflect all the factors that influence accelerograms (characteristics of the source, path, and site). Due to the increase of available strong ground motion acceleration records, using and scaling real recorded accelerograms becomes one of most referenced contemporary research issues in this field. Despite the continued growth of the global strong motion database, there are many combinations of earthquake parameters such as magnitude, rupture mechanism, source-to-site distance and site classification that are not well represented. It follows that their manipulation is relatively simple but often confusing and it is difficult to obtain suitable records in some circumstances.

The third approach uses *artificial spectrum-compatible accelerograms*. Artificial accelerograms are generated to match a target elastic response spectrum by obtaining a Power Spectral Density (PSD) function from the smoothed response spectrum, and then to derive harmonic signals having random phase angles [7–11]. The attraction of these approaches is obvious because it is possible to obtain acceleration time-series that are almost completely compatible with the elastic design spectrum, which in some cases will be the only information available to the design engineer regarding the nature of the ground motions to be considered. However, the above approaches possess the common drawback that the artificial accelerograms do not manifest the variability observed in real earthquakes.

It is now widely accepted that the evaluation of the spectrum-compatible PSD function leads to stationary artificial accelerograms which generally have an excessive number of cycles of strong motion and consequently they possess unreasonably high energy content [12]. Furthermore, the stationary model suffers the major drawback of neglecting the non-stationary characteristics of the real records: the changes in amplitude and frequency content. Indeed, the time-varying amplitude is due to the natural evolution of the earthquake ground motion, while the time-varying frequency content is prevalently due to different arrival times of the primary, secondary and surface waves that propagate at different velocities through the earth crust. Moreover, it has been shown that the non-stationarity in frequency content can have significant effects on the response of non-linear structures [12]. The stochastic processes involving both the amplitude and the frequency changes are referred in literature as *fully non-stationary* random processes while the so-called *quasi-stationary* (or *uniformly modulated*) random processes present changes in amplitude only. The spectral characterization of the fully non-stationary processes is usually performed by introducing the *Evolutionary Power Spectral Density* (*EPSD*) function [13]. On the contrary of the stationary case the EPSD function cannot be defined univocally. Then, several models have been proposed in literature. In particular Preumont [14] derived the EPSD function by imposing to the non-stationary model the equality of the average energy for each frequency with respect the stationary case. An alternative approach has been proposed by Cacciola [15] that evaluates the artificial fully non-stationary accelerograms by the superposition of two independent contributions: the first one is a fully non-stationary counterpart assumed to be known and modeled by a record; the second one is a corrective term represented by a quasi-stationary zero-mean Gaussian process that adjusts the response-spectrum of the non-stationary signal in order to make it spectrum-compatible. Cacciola and Zentner [16] extended the procedure proposed by Preumont [14] introducing an EPSD function with random coefficients and compatible with the given target response spectrum. This procedure has been extended by Cacciola et al. [17] to include enhanced variability models accounting for the correlation of spectral accelerations.

Another powerful strategy to analyse the evolutionary frequency content is based on the wavelet analysis [18–20]. Wavelet analysis is well suited to identify and preserve non-stationarity because the wavelet basis consist of compact functions of varying lengths. Each wavelet function corresponds to a finite portion of the time

domain and has a different bandwidth in the frequency domain. The multiscale nature of wavelet analysis facilitates the simultaneous evaluation of non-stationarity in the time and frequency domains. Wavelet analysis has been performed by Suàrez and Montejo [21] to simulate non-stationary ground motions. Moreover, several studies have been carried out to obtain fully non-stationary spectrum-compatible artificial accelerograms [22–24]. However, through the wavelet analysis the statistics of the response process cannot be obtained immediately.

In this study in order to generate artificial fully non-stationary accelerograms, a procedure based on the analysis of a set of accelerograms recorded in a chosen site is described. In particular for the analysis of the recorded accelerograms the following mean parameters are derived: the *peak ground acceleration* (PGA); the *total seismic duration*; the *HUSID diagram*; *the strong motion duration* (SMD); as well as the *mean frequency* derived as the arithmetic average of the up-crossing rate in time of the time axis of the recorded accelerograms. The last parameter evidences the frequency content change of the set of accelerograms while the previous ones characterize the time variation. The generation of fully non-stationary accelerograms is performed in three steps. In the first step the spectrum-compatible PSD function in the hypothesis of stationary excitations is derived. In the second step the spectrum-compatible EPSD function is obtained by an iterative procedure to improve the match with the target response spectrum starting from the PSD, function once a time-frequency modulating function is chosen. In the third step the accelerograms are generated by the Shinozuka and Jan [25] formula and deterministic analyses can be performed to evaluate the structural response.

Following the procedure previously described, the generated artificial accelerograms are derived as samples of a fully non-stationary spectrum-compatible process. However, for linear structures, methods of stochastic dynamics can be also adopted, to avoid long time consuming deterministic analyses. For this reason, in the last section of this study, a method, recently proposed by the authors [26], is described to evaluate in closed-form the *EPSD* response function of linear structural systems subjected to fully non-stationary excitations by very handy explicit closed-form.

2 Preliminary Definitions

2.1 Definition of the Fully Non-stationary Stochastic Input

In the framework of seismic engineering it is well known that only a probabilistic approach can afford a rigorous representation of earthquake ground motion. Accordingly, a ground motion accelerogram recorded at a given location can be seen as a sample of a fully non-stationary zero-mean stochastic process. Indeed, both a time-varying amplitude and frequency content is observed in actual accelerogram records. In order to define the ground motion as a realization of a zero-mean *fully non-stationary* Gaussian stochastic process the Priestley spectral

representation of non-stationary processes is usually adopted [13]. According to this representation, the non-stationary stochastic process is defined by the following *Fourier-Stieltjes integral* [13, 27]:

$$\overline{F}(t) = \int_{-\infty}^{\infty} \exp(\mathrm{i}\omega t)\, a(\omega, t)\, \mathrm{d}N(\omega) \tag{1}$$

where $a(\omega, t)$ is a slowly varying complex deterministic time-frequency modulating function which has to satisfy the condition: $a(\omega, t) \equiv a^*(-\omega, t)$; the asterisk denotes the complex conjugate quantity. In Eq. (1) $N(\omega)$ is a process with orthogonal increments satisfying the condition:

$$\mathrm{E}\langle \mathrm{d}N(\omega_1)\, \mathrm{d}N^*(\omega_2)\rangle = \delta(\omega_1 - \omega_2)\, S_0(\omega_1)\, \mathrm{d}\omega_1\, \mathrm{d}\omega_2 \tag{2}$$

where $\mathrm{E}\langle\cdot\rangle$ denotes the stochastic average operator, $\delta(\cdot)$ is the Dirac delta and the asterisk indicates the complex conjugate quantity. In this equation $S_0(\omega)$ is the PSD function of the so-called "embedded" stationary counterpart process [28]. It is a real and symmetric function: $S_0(-\omega) = S_0(\omega)$. It follows that the zero-mean Gaussian non-stationary random process $\overline{F}(t)$ is completely defined by the knowledge of the autocorrelation function $R_{\overline{FF}}(t_1, t_2) = R_{\overline{FF}}(t_2, t_1) = \mathrm{E}\langle \overline{F}(t_1)\, \overline{F}(t_2)\rangle$, which is a real symmetric function given as:

$$\begin{aligned} R_{\overline{FF}}(t_1, t_2) &= \int_{-\infty}^{\infty} \exp[\mathrm{i}\omega(t_1 - t_2)] a(\omega, t_1)\, a^*(\omega, t_2) S_0(\omega)\, \mathrm{d}\omega \\ &= \int_{-\infty}^{\infty} \exp[\mathrm{i}\omega(t_1 - t_2)] S_{\overline{FF}}(\omega, t_1, t_2)\, \mathrm{d}\omega \end{aligned} \tag{3}$$

where $\mathrm{i}^2 = -1$ is the imaginary unit and

$$S_{\overline{FF}}(\omega, t_1, t_2) = a(\omega, t_1)\, a^*(\omega, t_2) S_0(\omega) \tag{4}$$

In the Priestley evolutionary process model, the function

$$S_{\overline{FF}}(\omega, t) = |a(\omega, t)|^2 S_0(\omega) \tag{5}$$

is called *Evolutionary PSD* (EPSD) function of the non-stationary process $\overline{F}(t)$. In the previous equation the symbol $|\cdot|$ denotes the modulus of the function in brackets. The processes characterized by the EPSD function, $S_{\overline{FF}}(\omega, t)$, given in Eq. (5), are called *fully non-stationary* random processes, since both time and frequency content change. If the modulating function is a real time dependent function, $a(\omega, t) \equiv a(t)$, the non-stationary process is called *quasi-stationary* (or *uniformly modulated*) random

process. In this case only, the amplitude of the stochastic process changes in time and the EPSD function assumes the following expression:

$$S_{\overline{FF}}(\omega,t) = a^2(t)\, S_0(\omega) \tag{6}$$

In the stochastic analysis the *one-sided PSD* function is generally used; the latter, in the Priestley representation, can be suitably defined by the following relationships:

$$G_{FF}(\omega,t_1,t_2) = \begin{cases} a\,(\omega,t_1)\, a^*(\omega,t_2)\, G_0(\omega) \equiv 2S_{\overline{FF}}(\omega,t_1,t_2), & \omega \geq 0; \\ 0, & \omega < 0. \end{cases} \tag{7}$$

where $G_0(\omega)$ $(G_0(\omega) = 2S_0(\omega),\ \omega \geq 0;\ G_0(\omega) = 0,\ \omega < 0)$ is the one-sided PSD function of the stationary counterpart of input process $F(t)$. It follows that the corresponding autocorrelation function is given by:

$$R_{FF}(t_1,t_2) = \int_0^\infty \exp[\mathrm{i}\omega\,(t_1 - t_2)]a\,(\omega,t_1)\, a^*(\omega,t_2) G_0(\omega)\,\mathrm{d}\omega \tag{8}$$

Note that since the one-sided PSD function $G_0(\omega)$ is not symmetric, the corresponding autocorrelation function is a complex function [10], whose real part coincides with the function defined in Eq. (3): $\mathrm{Re}\{R_{FF}(t_1,t_2)\} \equiv R_{\overline{FF}}(t_1,t_2)$. It has been proved that the complex function (8) can be also defined as the autocorrelation function of a complex process $F(t)$ defined as [29]:

$$F(t) = \sqrt{2} \int_0^\infty \exp(\mathrm{i}\omega t)\, a\,(\omega,t)\,\mathrm{d}N(\omega) \tag{9}$$

The real part of $F(t)$ is proportional to the process $\overline{F}(t)$, while the imaginary part of $F(t)$, $\widetilde{F}(t)$, is a process having stationary counterpart proportional to the Hilbert transform of the real part of the stationary counterpart of the complex process itself [29–31]. The complex process, $F(t)$, which generates the complex autocorrelation function (8) has been called *pre-envelope process* [30].

2.2 *Definition of Response Spectrum-Compatible Artificial Stationary Earthquake Accelerograms*

The problem of simulating response spectrum-compatible earthquake accelerograms is addressed on a probabilistic basis under the assumption that an earthquake accelerogram is considered as a sample of a random process. The simulation of artificial accelerograms is usually based upon a stationary stochastic zero-mean

Gaussian process assumption. Several methods for generating a spectrum-consistent PSD function are available in the literature [7– 11].

Here the method proposed by Cacciola et al. [11] is briefly described. This method considers the ground-acceleration as a sample of a zero-mean stationary Gaussian process. It approximates the pseudo-acceleration response spectrum as the 50 % fractile of the peak maxima distribution of the response process obtaining the following very handy recursive expression of the PSD function of the earthquake acceleration zero-mean process, $\ddot{U}_g(t)$, compatible with the assigned pseudo-acceleration response spectrum [11]:

$$G_{\ddot{U}_g}^{\mathrm{ST}}(\omega_k) = 0, \quad 0 \le \omega_k \le \omega_i;$$
$$G_{\ddot{U}_g}^{\mathrm{ST}}(\omega_k) = \frac{4\zeta_0}{\omega_k \pi - 4\zeta_0 \omega_{k-1}} \left(\frac{S_{\mathrm{pa}}^2(\omega_k, \zeta_0)}{\eta^2(\omega_k, \zeta_0)} - \Delta\omega \sum_{j=1}^{k-1} G_{\ddot{U}_g}^{\mathrm{ST}}(\omega_j) \right), \quad \omega_i \le \omega_k \le \omega_f; \tag{10}$$

where the apex ST evidences that the PSD function is evaluated in the hypothesis of stationary random processes, $\omega_i \le 1$ (rad/s) [11] and ω_f are chosen as bounds of the existence domain of the PSD function $G_{\ddot{U}_g}^{\mathrm{ST}}(\omega)$. In Eq. (10) $S_{\mathrm{pa}}(\omega_k, \zeta_0)$ is the target pseudo-acceleration elastic response spectrum for a given natural frequency ω_k and damping ratio $\zeta_0 = 0.05$ and $\eta(\omega_k, \zeta_0)$ is the peak factor given as [32]:

$$\eta(\omega_k, \zeta_0) = \sqrt{2 \ln \left\{ \frac{T_s\, \omega_k}{\pi} (-\ln 0.5)^{-1} \left[1 - \exp\left[-\delta^{1.2} \sqrt{\pi \ln \left(\frac{T_s\, \omega_k}{\pi} (-\ln 0.5)^{-1} \right)} \right] \right] \right\}} \tag{11}$$

In the previous equation T_S is the time observing window, assumed equals to the strong motion phase of the ground motion process and δ is the bandwidth factor evaluated in the hypothesis of white noise process. The latter quantities can be written as [32]:

$$\delta = \left[1 - \frac{1}{1 - \zeta_0^2} \left(1 - \frac{2}{\pi} \arctan \frac{\zeta_0}{\sqrt{1 - \zeta_0^2}} \right)^2 \right]^{1/2} = 0.246 \quad (\zeta_0 = 0.05) \tag{12}$$

Once the PSD function is obtained by Eq. (10), the N stationary spectrum-compatible artificial earthquake accelerograms are obtained by the formula proposed by Shinozuka and Jan [25]:

$$\ddot{u}_{i,\mathrm{g}}^{\mathrm{ST}}(t) = \sum_{r=1}^{m_c} \sqrt{2\, G_{\ddot{U}_g}^{\mathrm{ST}}(r\Delta\omega)\, \Delta\omega} \sin\left(r\Delta\omega\, t + \theta_r^{(i)} \right); \quad 0 \le t \le t_d \tag{13}$$

where $m_c = \omega_f/\Delta\omega$, $\ddot{u}_{i,g}^{ST}(t)$, is the ith sample of the stationary zero-mean spectrum-compatible acceleration stochastic process, $\theta_r^{(i)}$ are independent random phases uniformly distributed in the interval $[0, 2\pi)$ and $t_d > T_s$ is the duration of spectrum-compatible accelerogram.

The main problem of the stationary model of the ground motion acceleration process is that it is unable to catch the characteristics of real earthquakes, such as the amplitude and frequency modulation of the signal. In particular it can be easily proved that the mean frequency, $\nu_{\ddot{U}_g}^{+}(t)$, which evaluates the variation in time of the mean up-crossing rate of the time axis, is a constant quantity for the stationary spectrum-compatible acceleration random process $\ddot{U}_g(t)$. This result is in contrast with the analysis of recorded accelerograms. Furthermore, the energy, $E_{\ddot{U}_g}^{ST}(t_d)$, of the spectrum-compatible stationary acceleration random process is proportional to the variance. Indeed the following relationship holds:

$$E_{\ddot{U}_g}^{ST}(t_d) = \int_0^{t_d} \int_0^{+\infty} G_{\ddot{U}_g}^{ST}(\omega)\, \mathrm{d}\omega\, \mathrm{d}t = t_d\, \sigma_{\ddot{U}_g}^2, \quad [\mathrm{m}^2/\mathrm{s}^3] \tag{14}$$

where $\sigma_{\ddot{U}_g}^2 = \int_0^{\infty} G_{\ddot{U}_g}^{ST}(\omega)\, \mathrm{d}\omega$ is the variance of the stationary spectrum-compatible stationary stochastic process $\ddot{U}_g(t)$. Moreover, Eq. (14) shows that the energy of the spectrum-compatible stationary acceleration random process is proportional to the duration of the process itself. This confirms that a stationary stochastic process, as well as its generic realization, possesses infinite energy. Even though this result from a mathematically point of view is strictly coherent, it is physically unrealistic.

3 Analysis of Recorded Ground Motion Accelerograms

Earthquakes are vibrations of the earth surface caused by sudden movements of the earth crust which consists of rock plates that float on the earth mantle. The ground motion is due to the rupture of the rock when the shear stress exceeds the strength of the rock and the energy is released in the form of seismic waves. Two of the most common parameters related to a seismic event are the earthquake *magnitude* (M) and *distance* (R) (in km) of the rupture zone from the site of interest.

For engineering purposes, the ground motion caused by seismic waves is measured by accelerometers or accelerographs which record three components of the ground acceleration, two horizontal and one vertical. The earthquake accelerograms by themselves provide general information among which the *peak ground acceleration* (PGA) and the *total seismic duration* t_d. The PGA is the most simple and widely used intensity index for seismic structural analysis purposes. It is

also adopted in many structural design codes or provisions worldwide. Although PGA is an important intensity index, its scope of application is limited because a single measure is unable to fully describe the complex earthquake characteristics. For further information an elaboration of the accelerograms is necessary. The results of this elaboration are characteristic parameters either in the time or in the frequency domain. Some parameters in the time domain are the *ARIAS intensity*, the *HUSID diagram*, *the strong motion duration* (SMD). On the other hand, some parameters in the frequency domain are the s*pectral intensities* and the *Fourier spectra*. The ARIAS intensity is a measure of the strength of a ground motion and it is usually defined by the following relationship:

$$I_{\mathrm{A}} = \frac{\pi}{2\,\mathrm{g}} \int_0^{t_d} \ddot{u}_{\mathrm{g}}^2(t)\,\mathrm{d}t,\ [\mathrm{m/s}] \tag{15}$$

where g is the acceleration due to gravity and $\ddot{u}_{\mathrm{g}}(t)$ is the recorded accelerogram. The HUSID diagram, $H(t)$, is the time history of the seismic energy content scaled to the total energy content and it is defined by the following relation:

$$H(t) = \frac{\int_0^t \ddot{u}_{\mathrm{g}}^2(\tau)\,\mathrm{d}\tau}{\int_0^{t_d} \ddot{u}_{\mathrm{g}}^2(t)\,\mathrm{d}t} \tag{16}$$

By means of the HUSID diagram it is possible to define the SMD, T_s, as the time elapsed between the 5 and 95 % of the HUSID diagram defined by the following relation:

$$T_s = t_{0.95} - t_{0.05} \tag{17}$$

where $t_{0.95}$ is the time elapsed at the 95 % of the HUSID diagram and $t_{0.05}$ the time elapsed at the 5 % of the HUSID diagram. In order to define a procedure to generate fully non-stationary artificial spectrum-compatible earthquake time-histories, a set of accelerograms recorded in the Imperial Valley (California, USA) is analyzed. In Table 1 the main characteristics of 30 of these accelerograms are reported. Namely: the station name, the date of the recorded event, the magnitude, the PGA, the energy, the strong motion duration as well as $t_{0.05}$ and $t_{0.95}$. From the analysis of these accelerograms the following average parameters are obtained: $\overline{T}_s = 14.40$ [s], $\bar{t}_{0.05} = 5.04$ [s], and $\bar{t}_{0.95} = 19.44$ [s]. Furthermore in Fig. 1 the mean frequency, $\bar{\nu}^{+}_{\ddot{U}_{\mathrm{g}}}(t)$ derived as the arithmetic average of the up-crossing rate in time of the time axis of the 30 recorded accelerograms is depicted. This figure shows both the time-varying amplitude and frequency content of recorded accelerogram.

Table 1 Main characteristics of the accelerograms recorded in the Imperial Valley (California, USA)

Station	Date	Magnitude	PGA a_{max} [m/s^2]	Energy $\frac{2g}{\pi} I_A$ [m^2/s^3]	Duration t_d [s]	SMD T_s [s]	$t_{0.05}$ [s]	$t_{0.95}$ [s]
El Centro Array #9	19/05/1940	6.53	3.07	10.30	40.00	23.50	1.96	25.47
El Centro Array #9	24/01/1951	6.53	0.28	0.12	40.00	25.44	0.99	26.44
El Centro Array #9	17/12/1955	6.53	0.55	0.18	40.00	16.82	0.77	17.59
El Centro Array #12	15/10/1979	6.53	1.40	2.38	39.01	19.16	6.41	25.58
Niland Fire Station	15/10/1979	6.53	1.07	1.14	39.98	22.20	5.83	28.03
Calipatria Fire Station	15/10/1979	6.53	1.26	0.89	39.52	22.35	7.52	29.87
Parachute Test Site	15/10/1979	6.53	1.09	1.25	39.33	17.52	6.91	24.44
Brawley Airport	15/10/1979	6.53	1.57	1.81	37.82	11.89	6.12	18.01
El Centro Array #1	15/10/1979	6.53	1.37	1.68	39.03	12.84	6.25	19.09
El Centro Array #2	15/10/1979	5.01	3.09	7.82	39.52	8.59	7.12	15.71
El Centro Array #3	15/10/1979	6.53	2.61	7.11	39.54	12.48	6.13	18.61
El Centro Array #4	15/10/1979	6.53	4.76	8.33	39.00	6.72	4.80	11.52
El Centro Array #5	15/10/1979	6.53	5.09	10.08	39.28	6.07	4.36	10.43
El Centro Array #6	15/10/1979	6.53	4.02	9.07	39.03	10.65	2.51	13.16
El Centro Array #7	15/10/1979	6.53	3.31	5.33	36.82	6.50	4.78	11.28
El Centro Array #8	15/10/1979	6.53	5.90	9.90	37.56	6.68	5.39	12.08
EC Country Center FF	15/10/1979	6.53	2.09	4.70	39.98	11.01	6.04	17.06
El Centro Diff. Array	15/10/1979	6.53	3.45	10.66	38.96	6.92	5.31	12.24
El Centro Array #10	15/10/1979	6.53	1.68	3.52	36.97	12.36	5.42	17.78
Holtville Post Office	15/10/1979	5.62	2.48	5.40	37.74	11.59	4.72	16.31
	15/10/1979	6.53	3.08	5.34	39.98	8.16	3.87	12.03

(continued)

Table 1 (continued)

Station	Date	Magnitude	PGA a_{max} [m/s^2]	Energy $\frac{2g}{\pi} I_A$ [m^2/s^3]	Duration t_d [s]	SMD T_s [s]	$t_{0.05}$ [s]	$t_{0.95}$ [s]
El Centro-Mel. Geot. Array								
Station	Date	Magnitude	PGA	Energy	Duration	SMD	$t_{0.05}$	$t_{0.95}$
El Centro Array #11	15/10/1979	6.53	3.57	12.19	39.03	8.48	6.17	14.65
Westmorland Fire Station	16/10/1979	5.62	1.68	1.05	40.00	8.82	2.81	11.64
Victoria	15/10/1979	6.53	1.19	1.21	40.00	20.85	9.12	29.97
Chihuahua	15/10/1979	6.53	2.65	7.17	40.00	19.17	5.36	24.54
Compuertas	15/10/1979	6.53	1.83	2.71	36.00	28.29	5.40	33.70
Bonds Corner	15/10/1979	6.53	5.77	24.20	37.60	9.36	3.09	12.46
Calexico Fire Station	15/10/1979	6.53	2.69	5.34	37.80	11.77	4.71	16.49
El Centro Array #13	15/10/1979	6.53	1.15	1.66	39.50	21.96	5.89	27.86
Westmorland Fire Station	15/10/1979	6.53	0.73	0.76	39.98	23.76	5.22	28.98

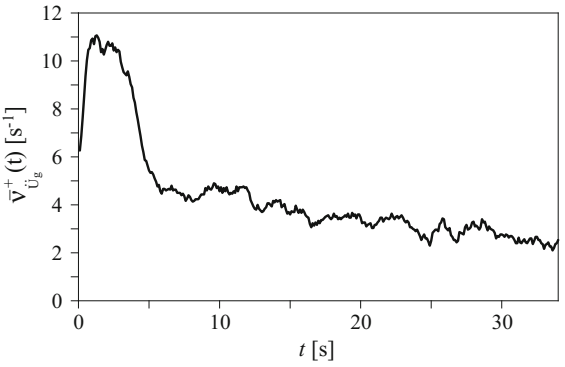

Fig. 1 Arithmetic average of the up-crossing time axis rate, $\bar{\nu}^+_{\ddot{U}_g}(t)$, of the 30 accelerograms recorded in the Imperial Valley (California, USA)

4 Generation of Response Spectrum-Compatible Artificial Fully Non-stationary Earthquake Accelerograms

4.1 Definition of Spectrum-Compatible Evolutionary Power Spectral Density

The main problem of the stationary model of the ground motion acceleration process is the inability to catch the characteristics of real earthquakes, such as the amplitude and frequency modulation of the signal. Moreover it has been shown that

the energy of the stationary acceleration random process is proportional to the duration of the process itself. This confirms that a stationary stochastic process, as well as its generic realization, possesses infinite energy. Then the most suitable model of the ground motion acceleration is the fully non-stationary process model.

In this section the procedure proposed by Cacciola and co-workers [15–17] is extended to generate artificial spectrum-compatible fully non-stationary earthquake accelerograms. In order to do this the characteristic parameters derived in the previous section are used to define the non-stationary process. On the contrary of the stationary case the EPSD function cannot be defined univocally; here the following Priestley evolutionary model of the one-sided *Evolutionary PSD* (EPSD) function of the fully non-stationary process is chosen:

$$G_{\ddot{U}_g}^{\mathrm{NST}}(\omega,t)=|a\,(\omega,t)|^2 G_{\ddot{U}_g}^{\mathrm{STC}}(\omega) \tag{18}$$

where $G_{\ddot{U}_g}^{\mathrm{STC}}(\omega)$ is the stationary counterpart of the fully non-stationary process $\ddot{U}_g(t)$ and $a\,(\omega,t)$ is a slowly varying deterministic time-frequency modulating function chosen coherently to the Spanos and Solomos [33] model that is:

$$\begin{aligned} a\,(\omega,t) &= \varphi(t)\,\varepsilon(\omega)\exp\left[-\frac{1}{2}\left(0.15+\frac{\omega^2}{500\pi^2}\right)t\right]; \\ \varepsilon\,(\omega) &= \frac{1}{\alpha}\frac{\omega\sqrt{2}}{5\pi} \end{aligned} \tag{19}$$

with $\varphi\,(t)$ a piecewise function, which models the time-amplitude variation of the non-stationary accelerograms, here assumed step-wise as in the Jennings et al. [34] model:

$$\varphi\,(t) = t\left[\left(\frac{t}{\bar{t}_{0.05}}\right)^2 \mathbb{W}(0,\bar{t}_{0.05}) + \mathbb{W}(\bar{t}_{0.05},\bar{t}_{0.95}) + \exp[-\gamma(t-\bar{t}_{0.95})]\mathbb{U}(t-\bar{t}_{0.95})\right] \tag{20}$$

where $\mathbb{W}\,(t_i,t_j)$ and $\mathbb{U}\,(t)$ are the window and the unit-step functions defined respectively as:

$$\mathbb{W}\,(t_i,t_j) = \begin{cases} 1, & t_i < t \le t_j; \\ 0, & t \le t_i,\ t > t_j; \end{cases} \qquad \mathbb{U}(t-t_0) = \begin{cases} 0, & t \le t_0; \\ 1, & t > t_0; \end{cases} \tag{21}$$

In Eq. (19) the parameter α normalizes the exponential modulating function so that the maximum is unity, while the parameter γ, in Eq. (20) is an adjustable parameter which has to be chosen to match the mean duration of the recorded accelerograms. This parameter is here assumed $\gamma = 0.13$. In order to obtain artificial spectrum-compatible EPSD function the procedure proposed by Cacciola [15] is

herein applied to evaluate the stationary counterpart PSD function of the fully non-stationary evolutionary process. This method evaluates the spectrum-compatible PSD function of the stationary counterpart, $G^{\mathrm{STC}}_{\ddot{U}_{\mathrm{g}}}(\omega)$, modifying the PSD function evaluated by Eq. (10) under the hypothesis of stationary spectrum-compatible process, $G^{\mathrm{ST}}_{\ddot{U}_{\mathrm{g}}}(\omega)$, adding an additional term $\Delta G^{\mathrm{ST}}_{\ddot{U}_{\mathrm{g}}}(\omega_k)$, namely:

$$\begin{aligned} G^{\mathrm{STC}}_{\ddot{U}_{\mathrm{g}}}(\omega_k) &= 0, \quad 0 \le \omega_k \le \omega_i; \\ G^{\mathrm{STC}}_{\ddot{U}_{\mathrm{g}}}(\omega_k) &= G^{\mathrm{ST}}_{\ddot{U}_{\mathrm{g}}}(\omega_k) + \Delta G^{\mathrm{ST}}_{\ddot{U}_{\mathrm{g}}}(\omega_k), \quad \omega_i \le \omega_k \le \omega_f \end{aligned} \tag{22}$$

The term $\Delta G^{\mathrm{ST}}_{\ddot{U}_{\mathrm{g}}}(\omega_k)$ is evaluated to reduce the gap between the target spectrum and the average one, that is:

$$\begin{aligned} \Delta G^{\mathrm{ST}}_{\ddot{U}_{\mathrm{g}}}(\omega_k) = \frac{4\zeta_0}{\omega_k \pi - 4\zeta_0 \omega_{k-1}} \left(\frac{S^2_{\mathrm{pa}}(\omega_k, \zeta_0) - \left(\varepsilon\, \overline{S}^{\mathrm{NST}}_{\mathrm{pa}}(\omega_k, \zeta_0) \right)^2}{\eta^2(\omega_k, \zeta_0)} - \Delta\omega \sum_{j=1}^{k-1} \Delta G^{\mathrm{ST}}_{\ddot{U}_{\mathrm{g}}}(\omega_j) \right) \\ \times\, \mathbb{U} \left(\frac{S^2_{\mathrm{pa}}(\omega_k, \zeta_0) - \left(\varepsilon\, \overline{S}^{\mathrm{NST}}_{\mathrm{pa}}(\omega_k, \zeta_0) \right)^2}{\eta^2(\omega_k, \zeta_0)} - \Delta\omega \sum_{j=1}^{k-1} \Delta G^{\mathrm{ST}}_{\ddot{U}_{\mathrm{g}}}(\omega_j) \right) \end{aligned} \tag{23}$$

where $\mathbb{U}(\cdot)$ is the unit step function defined in Eq. (21), $S_{\mathrm{pa}}(\omega_k, \zeta_0)$ is the target pseudo-acceleration elastic response spectrum and

$$\varepsilon = 1 \quad \text{if} \quad S_{\mathrm{pa}}(\omega_k, \zeta_0) \ge \overline{S}^{\mathrm{NST}}_{\mathrm{pa}}(\omega_k, \zeta_0) \quad \text{or else} \quad \varepsilon = \min \left\{ \frac{S_{\mathrm{pa}}(\omega_k, \zeta_0)}{\overline{S}^{\mathrm{NST}}_{\mathrm{pa}}(\omega_k, \zeta_0)} \right\} \tag{24}$$

Finally, in the previous equations, $\overline{S}^{\mathrm{NST}}_{\mathrm{pa}}(\omega_k, \zeta_0)$ is the average pseudo-acceleration response spectrum obtained as the arithmetic average of the response of SDoF oscillators with natural circular frequency ω_k and damping ratio ζ_0 subjected to N fully non-stationary artificial earthquake accelerograms generated as:

$$\begin{aligned} \ddot{u}^{\mathrm{NST}}_{i,\mathrm{g}}(t) &= \sum_{r=1}^{m_c} \sqrt{2 G^{\mathrm{NST}}_{\ddot{U}_{\mathrm{g}}}(r\Delta\omega, t)\, \Delta\omega} \sin\left(r\, \Delta\omega\, t + \theta^{(i)}_r\right) \\ &= \sum_{r=1}^{m_c} \sqrt{2 |a\,(\omega, t)|^2 G^{\mathrm{STC}}_{\ddot{U}_{\mathrm{g}}}(r\Delta\omega) \Delta\omega} \sin\left(r\, \Delta\omega\, t + \theta^{(i)}_r\right) \end{aligned} \tag{25}$$

where $G^{\mathrm{NST}}_{\ddot{U}_{\mathrm{g}}}(r\Delta\omega, t)$ is the EPSD defined in Eq. (18). Notice that, according to the Eurocode 8 (EC8) instructions [35], the spectrum compatibility is verified if no value of the mean elastic spectrum, $\overline{S}^{\mathrm{NST}}_{\mathrm{pa}}(\omega, \zeta_0)$, calculated from all time histories,

is less than 90 % of the corresponding value of the target response spectrum, $S_{\mathrm{pa}}(\omega,\zeta_0)$ in a selected range of periods. If the spectrum compatibility is not verified it is necessary to modify the stationary counterpart PSD function by adopting the following iterative scheme:

$$G_{\ddot{U}_{\mathrm{g}}}^{\mathrm{STC}\,(j)}(\omega)=G_{\ddot{U}_{\mathrm{g}}}^{\mathrm{STC}\,(j-1)}(\omega)\left[\frac{S_{\mathrm{pa}}(\omega,\zeta_0)}{\overline{S}_{\mathrm{pa}}^{\mathrm{NST}(j-1)}(\omega,\zeta_0)}\right]^2 \tag{26}$$

where $G_{\ddot{U}_{\mathrm{g}}}^{\mathrm{STC}\,(j-1)}(\omega)$ and $\overline{S}_{\mathrm{pa}}^{\mathrm{NST}\,(j-1)}(\omega,\zeta_0)$ are the PSD function of the stationary counterpart and the average simulated pseudo-acceleration response spectrum, respectively, both evaluated at the $(j-1)$ iteration. Furthermore, the energy of the spectrum-compatible fully non-stationary acceleration random process is given as:

$$E_{\ddot{U}_{\mathrm{g}}}^{\mathrm{NST}}(t_d)=\int_0^{t_d}\int_0^{\infty}G_{\ddot{U}_{\mathrm{g}}}^{\mathrm{NST}}(\omega,t)\,\mathrm{d}\omega\,\mathrm{d}t,\quad [\mathrm{m}^2/\mathrm{s}^3] \tag{27}$$

4.2 Evaluation of Spectrum-Compatible Spectral Parameters and Functions

In order to verify the previously described procedure, to generate fully non-stationary artificial spectrum-compatible earthquake time histories, the set of accelerograms recorded in the Imperial Valley (California, USA) is analyzed. Since all the events, except the one recorded at the station "El Centro Array #2" at the date of 15/10/1979, have a magnitude superior than 5.5 (see Table 1) and according to the (EC8) instructions [35] a spectrum of type 1 (see Fig. 4) is chosen as target spectrum. The peak ground acceleration is assumed equal to the average of the PGA of the recorded events $a_g = 2.483$ [m/s^2] and, following the values of the parameters describing the recommended Type I elastic response spectra [35] for the type "C" of soil, the parameters $S = 1.15$, $T_B = 0.2$ [s] $T_C = 0.6$ [s], and $T_D = 2.0$ [s] are selected.

Following the iterative procedure described before the spectrum-compatible PSD function $G_{\ddot{U}_{\mathrm{g}}}^{\mathrm{STC}}(\omega)$ of the stationary counterpart of the fully non-stationary process $\ddot{U}_{\mathrm{g}}(t)$ is obtained. In Fig. 2 $G_{\ddot{U}_{\mathrm{g}}}^{\mathrm{STC}}(\omega)$ is then compared (in logarithmic scale) with the PSD $G_{\ddot{U}_{\mathrm{g}}}^{\mathrm{ST}}(\omega)$ evaluated by Eq. (10) under the hypothesis of stationary spectrum-compatible process.

From the analysis of Fig. 2 it is evident that at the lower frequencies the spectrum-compatible PSD function of the stationary counterpart, $G_{\ddot{U}_g}^{STC}(\omega)$, is bigger than the stationary spectrum-compatible PSD function, $G_{\ddot{U}_g}^{ST}(\omega)$, on the contrary of the higher frequencies.

The EPSD function of the spectrum-compatible fully non-stationary process evaluated by Eq. (18) is depicted in Fig. 3.

The arithmetic average of the up-crossing time axis rate is also obtained from the 500 artificial spectrum-compatible fully non-stationary accelerograms and compared, in Fig. 5, with the average of the up-crossing time axis rate derived from the set of the recorded time histories. From the analysis of this figure it is evident that the described model is able to catch both the time-varying amplitude and frequency content of actual accelerogram records. It is important to notice that the gap between the average mean frequency of the real accelerograms and of the artificial set cannot be regained because it depends on the spectrum compatible PSD function of the stationary counterpart (Fig. 4).

Finally, in Table 2 the following quantities are reported: the average of the energy, $2\,g\overline{I}_A/\pi$, evaluated as a function of the average of Arias intensity, $\overline{I}_A$, of the recorded accelerograms in the Imperial Valley; the average energy of the 500 artificial earthquakes, $\overline{E}_{\ddot{U}_g}^{NST}(t_d)$, as well as the average energy, $\overline{E}_{\ddot{U}_g}^{ST}(t_d)$, of a set of 500 spectrum-compatible stationary acceleration random process.

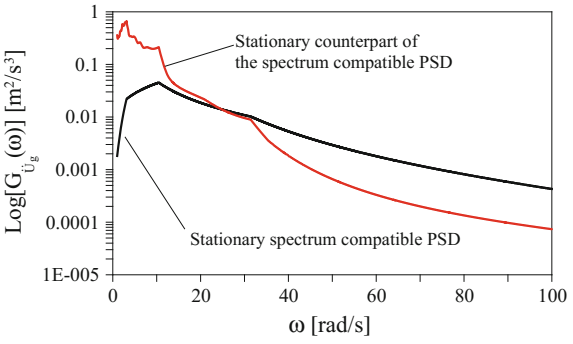

Fig. 2 Spectrum-compatible PSDs. Stationary assumption (*red line*) and stationary counterpart in the fully non-stationary assumption (*black line*)

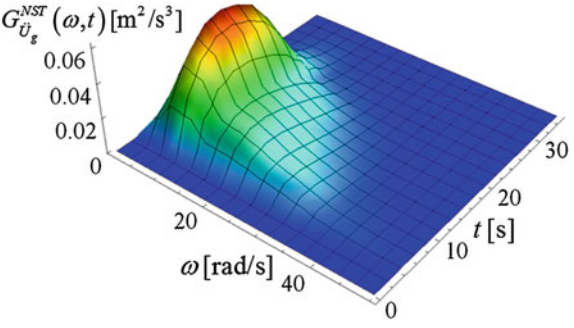

Fig. 3 EPSD function of the spectrum-compatible fully non-stationary process $\ddot{U}_g(t)$

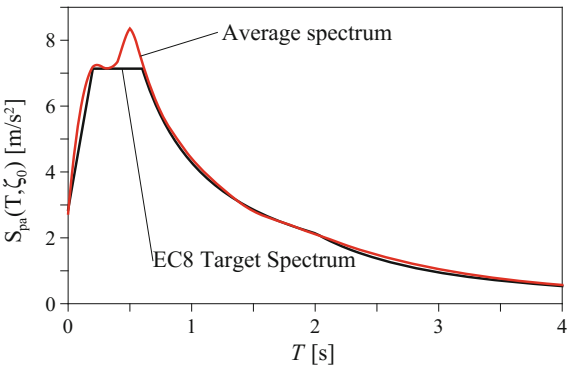

Fig. 4 Comparison between the selected EC8 target pseudo-acceleration spectrum $S_{pa}(T,\zeta_0)$ (*black line*) and the average of 500 pseudo-acceleration spectra $\overline{S}_{pa}^{NST}(T,\zeta_0)$ (*red line*)

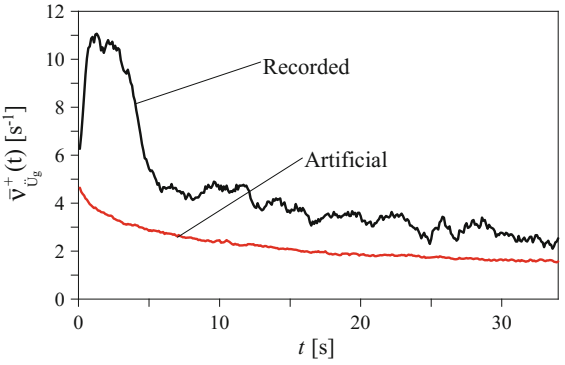

Fig. 5 Comparison between the average mean frequency (*black line*) and the average mean frequency of the artificial spectrum-compatible fully non-stationary accelerograms (*red line*)

From the analysis of the results reported in Table 2 it is evident that the energy associated to the spectrum-compatible stationary model is much higher than the energy evaluated by applying the other ones. On the contrary the spectrum-compatible fully non-stationary process model is able to catch also the energetic aspects of the recorded earthquakes.

5 Closed Form Solutions of the EPSD Response Function Matrix

5.1 Equations of Motion

In this section an explicit closed-form expression of the EPSD response function matrix is evaluated as a function of the *evolutionary frequency response vector function*. In order to do this, let us consider a linear quiescent classically damped structural system with n unconstrained degree-of-freedom (n-DoF) subjected to *seismic excitation* $\ddot{u}_g(t)$ whose dynamic behaviour is governed by the following equation of motion:

Table 2 Energy characteristics of the set of accelerograms and of the stationary and fully non-stationary spectrum compatible acceleration processes

Recorded accelerograms		Artificial accelerograms			
		Non-stationary spectrum compatible model		Stationary spectrum compatible model	
Total mean energy	Standard deviation	Total mean energy	Standard deviation	Total mean energy	Standard deviation
$\frac{2g}{\pi}\bar{I}_A$ [m^2/s^3]	$\frac{2g}{\pi}\sigma_{I_A}$ [m^2/s^3]	$\overline{E}^{\mathrm{NST}}_{\ddot{U}_g}(t_d)$ [m^2/s^3]	$\sigma_{\overline{E}^{\mathrm{NST}}_{\ddot{U}_g}(t_d)}$ [m^2/s^3]	$\overline{E}^{\mathrm{ST}}_{\ddot{U}_g}(t_d)$ [m^2/s^3]	$\sigma_{\overline{E}^{\mathrm{ST}}_{\ddot{U}_g}(t_d)}$ [m^2/s^3]
5.44	5.02	13.17	1.46	34.30	1.43

$$\mathbf{M}\,\ddot{\mathbf{u}}\,(t)+\mathbf{C}\dot{\mathbf{u}}\,(t)+\mathbf{K}\mathbf{u}\,(t)=-\mathbf{M}\,\boldsymbol{\tau}\,\ddot{u}_{\mathrm{g}}(t) \tag{28}$$

where $\mathbf{M}$, $\mathbf{C}$, and $\mathbf{K}$ are the $n\times n$ mass, damping, and stiffness matrices of the structure; $\mathbf{u}(t)$ is the vector, of order $n\times 1$, collecting the displacements of the n-DoF of the structure with respect to the ground, having for rth element $u_r(t)$ and a dot over a variable denotes differentiation with respect to time. Furthermore, in Eq. (28) $\boldsymbol{\tau}$ is the influence vector, of order n, while the seismic excitation $\ddot{u}_{\mathrm{g}}(t)$ is modelled as zero-mean Gaussian fully non-stationary random process. Under the assumption of classically damped systems the equation of motion can be decoupled by applying modal analysis. Therefore we introduce the modal coordinate transformation:

$$\mathbf{u}\,(t)=\boldsymbol{\Phi}\,\mathbf{q}(t)=\sum_{j=1}^{m}\boldsymbol{\phi}_j q_j(t)\Rightarrow u_i(t)=\sum_{j=1}^{m}\phi_{\,ij}\,q_j(t) \tag{29}$$

In this equation, $\boldsymbol{\Phi}=[\,\boldsymbol{\phi}_1\quad\boldsymbol{\phi}_2\quad\cdots\quad\boldsymbol{\phi}_m\,]$ is the modal matrix, of order $n\times m$, collecting the m eigenvectors $\boldsymbol{\phi}_k$, normalized with respect to the mass matrix $\mathbf{M}$. These are the solutions of the following eigenproblem:

$$\mathbf{K}^{-1}\,\mathbf{M}\,\boldsymbol{\Phi}=\boldsymbol{\Phi}\,\boldsymbol{\Omega}^{-2};\quad\boldsymbol{\Phi}^{T}\mathbf{M}\,\boldsymbol{\Phi}=\mathbf{I}_m \tag{30}$$

where $\boldsymbol{\Omega}$ is a diagonal matrix listing the undamped natural circular frequency ω_j, $\mathbf{I}_m$ is the identity matrix of order m and the superscript T denotes the transpose matrix operator. Once the modal matrix $\boldsymbol{\Phi}$ is evaluated, by applying the coordinate transformation (29) to Eq. (28), the following set of decoupled second order differential equations is obtained:

$$\ddot{\mathbf{q}}(t)+\boldsymbol{\Xi}\,\dot{\mathbf{q}}(t)+\boldsymbol{\Omega}^2\mathbf{q}(t)=\mathbf{p}\,\ddot{u}_{\mathrm{g}}(t) \tag{31}$$

where $\mathbf{p}$ is the vector collecting the participation factors

$$\mathbf{p}=-\boldsymbol{\Phi}^{T}\,\mathbf{M}\,\boldsymbol{\tau} \tag{32}$$

while $\boldsymbol{\Xi}$ is a the generalized damping matrix given by:

$$\boldsymbol{\Xi}=\boldsymbol{\Phi}^{T}\mathbf{C}\,\boldsymbol{\Phi} \tag{33}$$

For classically damped structures the modal damping matrix $\boldsymbol{\Xi}$ is a diagonal matrix listing the quantities $2\zeta_k\omega_k$, ζ_k being the modal damping ratio. It follows that the kth differential Eq. (31) can be written as:

$$\ddot{q}_k(t)+2\zeta_k\omega_k\,\dot{q}_k(t)+\omega_k^2\,q_k(t)=p_k\,\ddot{u}_{\mathrm{g}}(t),\quad k=1,2,\ldots,m; \tag{34}$$

where p_k is the kth element of the vector $\mathbf{p}$. In the state space, Eq. (34) can be written as a set of two first order differential equations:

$$\dot{\mathbf{y}}_k(t) = \mathbf{D}_k\,\mathbf{y}_k(t) + \mathbf{v}_k\,\ddot{u}_g(t) \tag{35}$$

where

$$\mathbf{y}_k(t) = \begin{bmatrix} q_k(t) \\ \dot{q}_k(t) \end{bmatrix}; \quad \mathbf{D}_k = \begin{bmatrix} 0 & 1 \\ -\omega_k^2 & -2\zeta_k\omega_k \end{bmatrix}; \quad \mathbf{v}_k = \begin{bmatrix} \mathbf{0} \\ \mathbf{p}_k \end{bmatrix} \tag{36}$$

For quiescent systems at time $t = t_0$, the solution of Eq. (35) can be written in integral form as follows:

$$\mathbf{y}_k(t) = \int_{t_0}^{t} \mathbf{\Theta}_k(t-\tau)\;\mathbf{v}_k\;\ddot{u}_g(\tau)\;\mathrm{d}\tau \tag{37}$$

where $\mathbf{\Theta}_k(t)$ is the so-called transition matrix of the kth modal oscillator [36]:

$$\mathbf{\Theta}_k(t) = \exp\left(\mathbf{D}_k\,t\right) = \begin{bmatrix} -\omega_k^2\,g_k(t) & h_k(t) \\ -\omega_k^2\,h_k(t) & \dot{h}_k(t) \end{bmatrix} \tag{38}$$

with

$$\begin{aligned} g_k(t) &= -\frac{1}{\omega_k^2}\exp\left(-\zeta_k\,\omega_k\,t\right)\left[\cos\left(\bar{\omega}_k t\right) + \frac{\zeta_k\,\omega_k}{\bar{\omega}_k}\sin\left(\bar{\omega}_k t\right)\right]; \\ h_k(t) &= \dot{g}_k(t) = \frac{1}{\bar{\omega}_k}\exp\left(-\zeta_k\,\omega_k\,t\right)\sin\left(\bar{\omega}_k t\right); \\ \dot{h}_k(t) &= \exp\left(-\zeta_k\,\omega_k\,t\right)\left[\cos\left(\bar{\omega}_k t\right) - \frac{\zeta_k\,\omega_k}{\bar{\omega}_k}\sin\left(\bar{\omega}_k t\right)\right] \end{aligned} \tag{39}$$

and $\bar{\omega}_k = \omega_k\sqrt{1-\zeta_k^2}$ is the kth damped natural circular frequency.

According to the coordinate transformation (29), the rth nodal displacement response, $u_r(t)$ in terms of state variable $\mathbf{z}_r = \left[u_r\;\dot{u}_r\right]^T$, can be evaluated as:

$$\mathbf{z}_r = \sum_{j=1}^{m} \phi_{rj}\,\mathbf{y}_j(t) \tag{40}$$

where the jth modal state variable vector, $\mathbf{y}_j(t)$, has been defined in Eq. (36) and ϕ_{rj} is the rth, jth element of the modal matrix $\mathbf{\Phi}$. It follows that, for the quiescent structural system, after some algebra, the one-sided EPSD function matrix of the rth state variable nodal displacement response $\mathbf{z}_r(t)$ can be evaluated as [37]:

$$\mathbf{G}_{\mathbf{z}_r\,\mathbf{z}_r}(\omega,t)=\sum_{k=1}^{m}\sum_{\ell=1}^{m}p_k\,p_\ell\,\phi_{r\,k}\,\phi_{r\,\ell}\,\mathbf{G}_{k\,\ell}\,(\omega,t) \tag{41}$$

where the matrix $\mathbf{G}_{k\,\ell}(\omega,t_1,t_2)$, of order 2×2, is the one-sided EPSD function matrix between the zero-mean kth and ℓth modal "purged" response processes This matrix, in the spectral representation, can be written as [26]:

$$\mathbf{G}_{k\,\ell}(\omega,t_1,t_2)=\mathbf{Y}_k^{*}(\omega,t_1)\;G_0(\omega)\;\mathbf{Y}_\ell^{T}(\omega,t_2) \tag{42}$$

where $\mathbf{Y}_j(\omega,t)$ is the *modal evolutionary frequency response vector function*, which, for quiescent systems at time $t=t_0$, can be written as:

$$\mathbf{Y}_j(\omega,t)=\int_{t_0}^{t}\mathbf{\Theta}_j(t-\tau)\;\mathbf{v}\,\exp\left(\mathrm{i}\omega\tau\right)a\,(\omega,\tau)\;\mathrm{d}\tau;\quad j=k,\ell; \tag{43}$$

where $a\,(\omega,t)$ is the modulating function of the evolutionary process and $\mathbf{v}=[\,0\quad 1\,]^T$.

As recently proposed by the authors [26], the *modal evolutionary frequency response vector functions* $\mathbf{Y}_j(\omega,t)$ for the commonly adopted expressions of the time-frequency varying modulating functions can be obtained in closed form solution as the solution of the following set of first order differential equations:

$$\dot{\mathbf{Y}}_j(\omega,t)=\mathbf{D}_j\,\mathbf{Y}_j(\omega,t)+\mathbf{v}\,\exp\left(\mathrm{i}\omega t\right)a\,(\omega,t) \tag{44}$$

with the initial conditions $\mathbf{Y}_j(\omega,t_0)=\mathbf{0}$. It follows that, for fully non-stationary stochastic excitations, the closed-form solution of the cross-EPSD function matrix of zero-mean kth ℓth, modal "purged" response processes is evaluated by means of Eq. (41), once Eq. (44) are solved. Equation (44) represents the equation of motion, in state variable, of the jth quiescent oscillator subjected to the pseudo-force: $\exp\left(\mathrm{i}\omega t\right)a\,(\omega,t)$. If the particular solution of this equation, $\mathbf{Y}_{\mathrm{p},j}(\omega,t)$, can be determined in explicit form, the solution of Eqs. (44), can be written respectively as [36, 38]:

$$\mathbf{Y}_j(\omega,t)=\mathbf{Y}_{\mathrm{p},j}(\omega,t)+\mathbf{\Theta}_j(t-t_0)\left[\mathbf{Y}_j(\omega,t_0)-\mathbf{Y}_{\mathrm{p},j}(\omega,t_0)\right] \tag{45}$$

Furthermore, the contribution of the last term in the right member of Eq. (45) decreases with time because the transition matrix, defined in Eq. (38) satisfies the condition:

$$\lim_{t\to\infty}\mathbf{\Theta}_j(t)=\mathbf{0} \tag{46}$$

5.2 Analytical Expression for the Response EPSD Function Matrix of the Adopted Fully Non-stationary Model

In this section explicit closed-form solutions of the evolutionary frequency response vector function are evaluated for the adopted model of the spectrum-compatible fully non-stationary input having the one-sided EPSD defined in Eq. (18). The particular solution vector of Eq. (44), forced by the function $f(\omega,t)=\exp(\mathrm{i}\omega\, t)\, a(\omega,t)$, with the step wise function $a(\omega,t)$ defined in Eq. (19), can be evaluated in closed form solution as [26]:

$$\mathbf{Y}_{\mathrm{p},j}(\omega,t)=\begin{cases}-\frac{\varepsilon(\omega)}{t_1^2}\exp[-\beta_1(\omega)\,t]\sum\limits_{s=0}^{3}\left[\frac{3!}{s!}t^s\,\mathbf{B}_{1j}^{3-s+1}(\omega)\right]\mathbf{v}, & 0<t\le t_1;\\ -\varepsilon(\omega)\exp[-\beta_2(\omega)\,t]\sum\limits_{s=0}^{1}\left[t^s\,\mathbf{B}_{2j}^{2-s}(\omega)\right]\mathbf{v}, & t_1<t\le t_2;\\ -\varepsilon(\omega)\exp[-\beta_2(\omega)\,t-\gamma\,(t-t_2)]\sum\limits_{s=0}^{1}\left[t^s\,\mathbf{B}_{3j}^{2-s}(\omega)\right]\mathbf{v}, & t>t_2.\end{cases} \tag{47}$$

where $t_1=\bar{t}_{0.05}$, $t_2=\bar{t}_{0.95}$ and

$$\beta_1(\omega)=\beta_2(\omega)=\frac{1}{2}\left(0.15+\frac{\omega^2}{500\,\pi^2}\right)-\mathrm{i}\omega;\quad \beta_3(\omega)=\beta_2(\omega)+\gamma;$$
$$\mathbf{B}_{rj}(\omega)=\left[\mathbf{D}_j+\beta_r(\omega)\,\mathrm{I}_2\right]^{-1}=\chi_{rj}(\omega)\begin{bmatrix}\beta_r(\omega)-2\,\zeta_j\omega_j & -1\\ \omega_j^2 & \beta_r(\omega)\end{bmatrix};\quad (r=1,2,3) \tag{48}$$

In these equations I_2 is the identity matrix of order 2 and

$$\chi_{rj}(\omega)=\frac{1}{\beta_r(\omega)^2-2\,\zeta_j\omega_j\,\beta_r(\omega)+\omega_j^2};\quad (r=1,2,3) \tag{49}$$

Substituting Eqs. (47) into Eq. (45) the state variable vector of the *modal evolutionary frequency response vector function*, $\mathbf{Y}_j(\omega,t)$, of the quiescent jth oscillator (at time $t=0$), can be evaluated in explicit closed form.

Once the state variable function vector, $\mathbf{Y}_k(\omega,t)$ and $\mathbf{Y}_\ell(\omega,t)$, of the k, ℓth oscillators are determined it is possible to evaluate in explicit form the corresponding *one-sided EPSD function matrix* $\mathbf{G}_{k\ell}(\omega,t)=G_0(\omega)\,\mathbf{Y}_k^*(\omega,t)\mathbf{Y}_\ell^T(\omega,t)$ as the sum of three contributions: the first in the time interval $(0,t_1]$, the second in the time interval $(t_1,t_2]$, the third for $t>t_2$. Substituting the function matrix $\mathbf{G}_{k\ell}(\omega,t)$ into Eq. (41) the one-sided EPSD function matrix of the rth state variable nodal displacement response $\mathbf{z}_r(t)$ is evaluated.

It has to be emphasized that this very remarkable result is obtained because the state variable formulation has been adopted.

6 Numerical Results

In this section four benchmark linear classically damped multi-degree of freedoms (MDoFs) structural systems, composed by a three-story one-bay shear-type frame, are considered. These frames have a uniform story height $H = 3.2$ m and a bay width $L = 6.0$ m, as shown in Fig. 6. The beams are considered rigid to enforce a typical shear building behaviour. The tributary mass per story and the column stiffness are reported in Table 3. Under these assumptions, the shear-type frames are modelled as a 3-DoF linear system. The damping ratio $\zeta_0 = 0.05$ is assumed equal for all three modes of vibration.

The modal periods and circular frequencies for the four linear elastic undamped shear-type frames are summarized in Table 4. Notice that the modal mass ratios are the same for all structures and are given for the three modes 91.41, 7.49 and 1.10 % respectively.

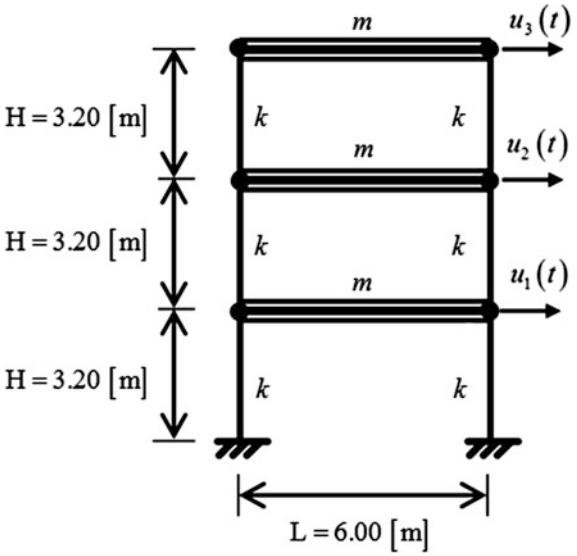

Fig. 6 Geometric configuration of benchmark three-storey one-bay shear-type frame

Table 3 Mass and column stiffness of the four benchmark linear classically damped shear type frames

Shear type frame	m [kg]	k [N/m]
1	5×10^4	1.5×10^7
2	3.5×10^4	2.03×10^7
3	2×10^4	4.5×10^7
4	1×10^4	6.3×10^7

Table 4 Modal periods and frequencies of the four benchmark linear classically damped shear type frames

Shear type frame	T_1 [s]	T_2 [s]	T_3 [s]	ω_1 [rad/s]	ω_2 [rad/s]	ω_3 [rad/s]
1	0.58	0.21	0.14	10.90	30.54	44.14
2	0.41	0.15	0.1	15.15	42.45	61.34
3	0.21	0.07	0.05	29.85	83.65	120.9
4	0.13	0.04	0.03	49.95	139.97	202.27

The benchmark structural shear-type frames are subjected to a stochastic earthquake base excitation, modelled by the zero mean Gaussian spectrum-compatible fully non-stationary process; the input is obtained following the procedure explained in Sects. 4.1 and 4.2. The EPSD function $G_{\ddot{U}_g}^{\mathrm{NST}}(\omega, t)$ is obtained as in Eq. (18).

In order to evidence the influence of the corrective term of the PSD function of the stationary counterpart $G_{\ddot{U}_g}^{\mathrm{STC}}(\omega)$ at different frequencies, for each of the considered frames, the variance of the nodal displacement response, $\sigma_{u_i u_i}^2(t) = \int_0^\infty G_{u_i u_i}(\omega, t)\,\mathrm{d}\omega$, is evaluated and compared with the results obtained under the hypothesis of stationary process model (see Figs. 7, 8, 9 and 10). In this case the EPSD function is obtained by replacing in Eq. (18) the Unit Step function $\mathbb{U}(t)$ as

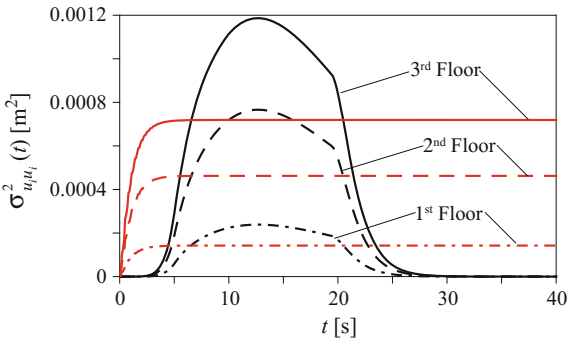

Fig. 7 Shear type frame 1: time histories of the variance of the nodal displacements for spectrum-compatible fully non-stationary process (*black line*) and spectrum-compatible stationary process (*red line*)

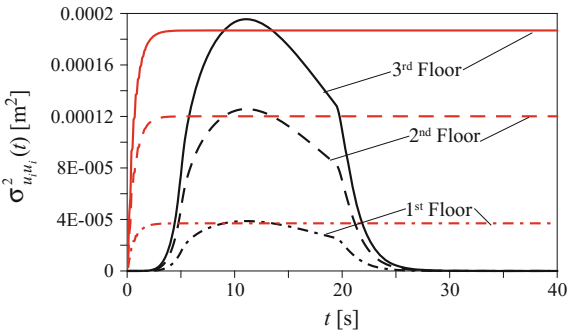

Fig. 8 Shear type frame 2: time histories of the variance of the nodal displacements for spectrum-compatible fully non-stationary process (*black line*) and spectrum-compatible stationary process (*red line*)

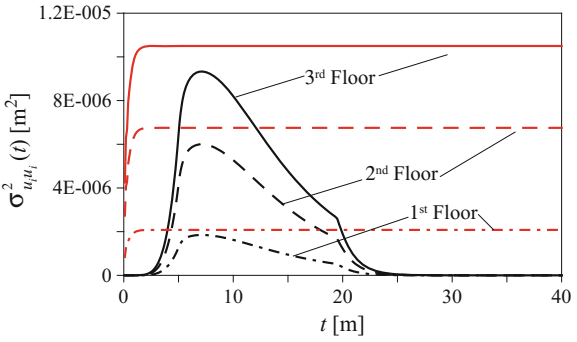

Fig. 9 Shear type frame 3: time histories of the variance of the nodal displacements for spectrum-compatible fully non-stationary process (*black line*) and spectrum-compatible stationary process (*red line*)

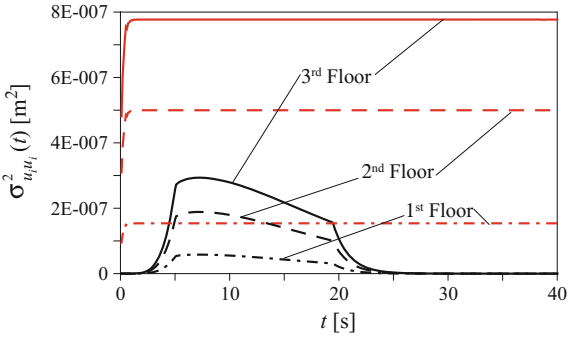

Fig. 10 Shear type frame 4: time histories of the variance of the nodal displacements for spectrum-compatible fully non-stationary process (*black line*) and spectrum-compatible stationary process (*red line*)

modulating function and selecting the PSD function of the stationary spectrum compatible process.

From the analysis of the Figs. 7, 8, 9 and 10 it is evident that, even if the energy associated to the spectrum-compatible stationary process model is much higher than the one associated to the fully non-stationary process model, in some cases the spectrum-compatible stationary model gives non-conservative results. This is prevalently due to the fact that, at the lower frequencies the stationary counterpart, $G^{\mathrm{STC}}_{\ddot{U}_g}(\omega)$, of the spectrum-compatible EPSD function is bigger than the stationary spectrum-compatible PSD function, $G^{\mathrm{ST}}_{\ddot{U}_g}(\omega)$, as shown in Fig. 2. This is a very remarkable result that should be taken into account in the in the prediction of the safety of structural systems.

7 Concluding Remarks

In seismic engineering, the most effective approach to evaluate the structural response is to define artificial spectrum-compatible accelerograms, which are generated to match the target elastic response spectrum. Usually the stationary

model, which leads to a spectrum-compatible Power Spectral Density (PSD) function, is adopted. However, the above approach possesses the drawback that the artificial accelerograms do not manifest the variability in time and in frequency observed from the analysis of real earthquakes. Indeed, the recorded accelerograms can be considered as samples of a fully non-stationary process.

In this study a procedure based on the analysis of a set of accelerograms recorded in a chosen site to take into account their time-frequency variability has been described. In particular the generation of artificial spectrum-compatible fully non-stationary accelerograms has been performed in three steps. In the first step the spectrum-compatible PSD function in the hypothesis of stationary excitations is derived. In the second step the spectrum-compatible Evolutionary Power Spectral Density (EPSD) function is obtained by an iterative procedure to improve the match with the target response spectrum, starting from the PSD function once a time-frequency modulating function is chosen. In the third step the artificial accelerograms are generated by the well-known Shinozuka and Jan [25] formula and deterministic analyses can be performed to evaluate the structural response.

Once the EPSD spectrum-compatible function is derived, a method, recently proposed by the authors [26], is adopted to evaluate in closed-form the EPSD response function of linear structural systems subjected to fully non-stationary excitations by very handy explicit closed-form. In the "Numerical results" section it is evidenced that the spectrum-compatible stationary model in some cases gives non-conservative results with respect to the ones obtained by the fully non-stationary spectrum-compatible model, even if the energy associated to the spectrum-compatible stationary process model is higher than the one associated to the fully non-stationary process model.

References

1. Chopra AK (1995) Dynamics of structures—theory and applications to earthquake engineering. Prentice Hall, Upper Saddle River, N.J, USA
2. Bommer JJ, Acevedo AB (2004) The use of real earthquake accelerograms as input to dynamic analysis. J Earthquake Eng 8:43–91
3. Lam N, Wilson J, Hutchinson G (2000) Generation of synthetic earthquake accelerograms using seismological modelling: a review. J Earthq Eng 4:321–354
4. Rezaeian S, Der Kiureghian A (2010) Simulation of synthetic ground motions for specified earthquake and site characteristics. Earthq Eng Struct Dyn 39:1155–1180
5. Iervolino I, Galasso C, Cosenza E (2010) REXEL: computer aided record selection for code-based seismic structural analysis. Bull Earthq Eng 8:339–362
6. Katsanos EI, Sextos AG, Manolis GD (2010) Selection of earthquake ground motion records: a state-of-the-art review from a structural engineering perspective. Soil Dyn Earthq Eng 30:157–169
7. Vanmarcke EH, Gasparini DA (1977) Simulated earthquake ground motions. In: Proceedings of the 4th international conference on Smirt, K1/9 San Francisco
8. Kaul MJ (1978) Stochastic characterization of earthquakes through their response spectrum. Earthq Eng Struct Dyn 6:497–509

9. Pfaffinger DD (1983) Calculation of power spectra from response spectra. J Eng Mechan (ASCE) 109:357–372
10. Preumont A (1984) The generation of spectrum compatible accelerograms for the design of nuclear power plants. Earthq Eng Struct Dyn 12:481–497
11. Cacciola P, Colajanni P, Muscolino G (2004) Combination of modal responses consistent with seismic input representation. J Struct Eng (ASCE) 130:47–55
12. Wang J, Fan L, Qian S, Zhou J (2005) Simulations of non-stationary frequency content and its importance to seismic assessment of structures. Earthq Eng Struct Dyn 31:993–1005
13. Priestley MB (1965) Evolutionary spectra and non-stationary processes. J R Stat Soc Ser B (Methodol) 27:204–237
14. Preumont A (1985) The generation of nonseparable artificial earthquake accelerograms for the design of nuclear power plants. Nucl Eng Des 88:59–67
15. Cacciola P (2010) A stochastic approach for generating spectrum-compatible fully nonstationary earthquakes. Comput Struct 88:889–901
16. Cacciola P, Zentner I (2012) Generation of response spectrum-compatible artificial earthquake accelerograms with random joint time frequency distributions. Probab Eng Mech 28:52–58
17. Cacciola P, D'Amico L, Zentner I (2014) New insights in the analysis of the structural response to response spectrum-compatible accelerograms. Eng Struct 78:3–16
18. Spanos PD, Failla G (2004) Evolutionary spectra estimation using wavelets. J Eng Mechan (ASCE) 130:952–960
19. Spanos PD, Tezcan J, Tratskas P (2005) Stochastic processes evolutionary spectrum estimation via harmonic wavelets. Comput Methods Appl Mech Eng 194:1367–1383
20. Mallat SG (2009) A wavelet tour of signal processing: the sparse way. 3rd ed. Academic Press
21. Suàrez LE, Montejo LA (2005) Generation of artificial earthquakes via the wavelet transform. Int J Solids Struct 42:5905–5919
22. Mukherjee S, Gupta VK (2002) Wavelet-based generation of spectrum-compatible time-histories. Soil Dyn Earthq Eng 22:799–804
23. Giaralis A, Spanos PD (2009) Wavelet-based response spectrum compatible synthesis of accelerograms—Eurocode application (EC8). Soil Dyn Earthq Eng 29:219–235
24. Cecini D, Palmeri A (2015) Spectrum-compatible accelerograms with harmonic wavelet. Comput Struct 147:26–35
25. Shinozuka M, Jan C-M (1972) Digital simulation of random processes and its application. J Sound Vib 25:111–128
26. Muscolino G, Alderucci T (2015) Closed-form solutions for the evolutionary frequency response function of linear systems subjected to separable or non-separable non-stationary stochastic excitations. Probab Eng Mech 40:75–89
27. Priestley MB (1967) Power spectral analysis of non-stationary random processes. J Sound Vib 6:86–97
28. Michaelov G, Sarkani S, Lutes LD (1999) Spectral Characteristics of Nonstationary Random Processes – A Critical Review. Struct Saf 21:223–244
29. Di Paola M, Petrucci G (1990) Spectral moments and pre-envelope covariances of nonseparable processes. J Appl Mechan (ASME) 57:218–224
30. Di Paola M (1985) Transient spectral moments of linear systems. SM Arch 10:225–243
31. Di Paola M, Muscolino G (1988) Analytic evaluation of spectral moments. J Sound Vib 124:479–488
32. Vanmarcke EH (1972) Properties of spectral moments with applications to random vibrations. J Eng Mechan (ASCE) 98:425–446
33. Spanos P, Solomos GP (1983) Markov approximation to transient vibration. J Eng Mechan (ASCE) 109:1134–1150
34. Jennings PC, Housner GW, Tsai C (1969) Simulated earthquake motions for design purpose. In: Proceedings of 4th world conference on earthquake engineering, Santiago, A-1, pp 145–160

35. Eurocode 8 (2003) European committee for standardization: design of structures for earthquake resistance—part 1: general rules, seismic actions and rules for buildings. Brussels, Belgium
36. Borino G, Muscolino G (1986) Mode-superposition methods in dynamic analysis of classically and non-classically damped linear systems. Earthquake Eng Struct Dynam 14:705–717
37. Lutes LD, Sarkani S (1997) Stochastic analysis of structural and mechanical vibrations. Prentice-Hall, Upper Saddle River
38. Muscolino G (1996) Dynamically modified linear structures: deterministic and stochastic response. J Eng Mechan (ASCE) 122:1044–1051

Elastic and Inelastic Analysis of Frames with a Force-Based Higher-Order 3D Beam Element Accounting for Axial-Flexural-Shear-Torsional Interaction

João P. Almeida, António A. Correia and Rui Pinho

Abstract When one of the dimensions of a structural member is not clearly larger than the two orthogonal ones, engineers are usually compelled to simulate it with refined meshes of shell or solid finite elements that typically impose a large computational burden. The alternative use of classical beam theories, either based on Euler-Bernoulli or Timoshenko's assumptions, will in general not accurately capture important deformation mechanisms such as shear, warping, distortion, flexural-shear-torsional interaction, etc. However, higher-order beam theories are a still largely disregarded avenue that requires an acceptable computational demand and simultaneously has the potential to account for the above mentioned deformation mechanisms, some of which can also be relevant in slender members. This chapter starts by recalling the main theoretical features of a recently developed higher-order beam element, which was combined for the first time with a force-based formulation. The latter strictly verifies the advanced form of beam equilibrium expressed in the governing differential equations. The main innovative theoretical aspects of the proposed element are accompanied by an illustrative application to members with linear elastic behaviour. In particular, the ability of the model to simulate the effect of different boundary conditions on the response of an axially loaded member is addressed, which is then followed by an application to a case where flexural-shear-torsional interaction takes place. The beam performance is assessed by comparison against refined solid finite element analyses, classical

J.P. Almeida (✉)
École Polytechnique Fédérale de Lausanne, EPFL ENAC IIC EESD, GC B2 515 (Bâtiment GC), Station 18, 1015 Lausanne, Switzerland
e-mail: joao.almeida@epfl.ch

A.A. Correia
Department of Structures, National Laboratory for Civil Engineering (LNEC), LNEC-DE/NESDE, Av. do Brasil 101, 1700-066 Lisbon, Portugal

R. Pinho
Department of Civil Engineering and Architecture, University of Pavia, c/o EUCENTRE, Via Ferrata 1, 27100, Pavia, Italy

M. Papadrakakis et al. (eds.), *Computational Methods in Earthquake Engineering*, Computational Methods in Applied Sciences 44,
DOI 10.1007/978-3-319-47798-5_5

beam theory results, and approximate numerical solutions. Finally, with a view to a future extension to earthquake engineering, an example of the element behaviour with inelastic response is also carried out.

1 Introduction

Many structures are modelled with beam elements since it is well-known that the latter typically provide reliable simulation results when one of the dimensions of the member (the one along its longitudinal axis) is considerably larger than its two other orthogonal dimensions. In such circumstances, the use of other structural mechanics' theories that involve less assumptions with respect to the three-dimensional problem are often not justified as they require a finer discretisation of the structure and a comparatively much larger number of degrees of freedom (and hence computational time).

However, classical beam theories such as Euler-Bernoulli's and Timoshenko's are often not sufficiently accurate to predict the global member response and its internal stress-strain state. For instance, in the Timoshenko beam theory (TBT), the shear strain distribution is incorrectly assumed to be constant throughout the beam height; e.g., considering a simple rectangular cross-section, such hypothesis does not respect the zero shear strain and stress boundary conditions at its top and bottom. Therefore, a shear correction factor is required to accurately determine the strain energy of deformation, which has deserved the attention of researchers since the 1950s up to the present day [9, 10, 14, 16]. Within the framework of this chapter, classical beam theories are considered to be of the first-order, i.e., those in which the displacement fields inside the cross-section are linear functions on each of the cross-sectional coordinates. Shear deformation effects are best considered through higher-order beam theories (HOBTs), wherein the displacement field inside the cross-section is represented by a power series expansion in the cross-sectional coordinates, thus relaxing the constraint in the cross-sectional warping. Therefore, out-of-plane warping displacements of the cross-sectional points are allowed by using shape functions for the cross-sectional displacements which are at least quadratic in one coordinate or bilinear in both. Moreover, in-plane deformations of the cross-section are also directly considered.

Many HOBTs have been proposed over the past decades for both planar and spatial beams; a brief review of some of the most relevant contributions is presented in Correia et al. [8]. The points on which they differ include the order of the theory, the number and definition of the cross-sectional displacement modes, the approach used to derive the corresponding beam governing equations, and the chosen finite element formulation. Regarding this latter issue, the so-called stiffness or displacement-based methods (DB, as they will be henceforth called, see Bathe [4]), which make use of compatible displacement interpolation functions along the element length and the principle of virtual work (or virtual displacements), are still the most commonly used. They are also known as pure compatibility models in the literature [18], and are popular since the inter-element continuity of the displacement

field is trivially satisfied. On the other hand, the latter is difficult to enforce in flexibility or force-based formulations (FB, as they will be henceforth called), which are built on the derivation of self-equilibrated stress interpolation functions and the principle of complementary virtual work (or virtual forces). These approaches are also known as pure equilibrium models, and within their framework it is possible to find an exact solution to the beam equilibrium differential equations. Hence, the main advantage of FB beam-column formulations, over the more common DB counterparts, is that equilibrium is always strictly verified. Such property holds even when a material nonlinear response takes place, explaining why flexibility methods have been progressively adopted by the structural engineering community for the inelastic analysis of frame members. Another advantage of FB formulations is that no shear-locking phenomena exist, contrary to what occurs in DB approaches. Although frame finite elements based on force interpolation functions alone have been in use for many decades [6, 15], the development of efficient and stable state determination algorithms, wherein nodal compatibility is respected, is more recent [17, 20].

Comparative studies between FB and DB formulations can be found elsewhere [1, 17]. Of further interest are considerations on the bounding of the solution associated with these two different types of formulation, which are carried out in Almeida et al. [2]. Equally fundamental is to understand the relationship between DB and FB approaches, as they have been herein described, and energy principles. Such comparison should be carried out not just at the theoretical level, but also regarding numerical implementation and computational performance. While the application of the Hu-Washizu three-field functional seems to be a promising avenue [11], trade-offs between classical DB methods and mixed methods are far from being completely clarified [12]. The merit of FB beam models is however clearly undisputed [13], and the beam element of the present work relies on it.

To the authors' knowledge, pure equilibrium (FB) approaches have only been used, up to now, in association with classical beam theory. In other words, the finite elements that have been developed within the context of the HOBTs are, in their essence, displacement-based formulations. A higher-order beam element developed within the framework of a pure force-based formulation has been proposed, for the first time, by Correia et al. [8]. Following a short review on the main theoretical aspects of this latter approach, the present chapter presents new numerical applications that evidence the ability of the model to simulate physical effects, such as axial-flexural-shear-torsional interaction, which typically can only be reproduced by refined meshes of shell or solid finite elements.

2 Theoretical Features of the Force-Based Higher-Order Beam Element

Following the basic idea from Vlassov [23], the distinctive trace in all beam theories is the assumption of a displacement field composed of cross-sectional displacement modes defined a priori and multiplied by functions of the beam

coordinate axis only. In other words, the beam displacement field **u** (whose vector components are u_x, u_y, and u_z) can be separated into a component function of the axis x of the beam and another varying in the cross-section (whose coordinate axes are y and z):

$$\mathbf{u}(x,y,z) = \mathbf{U}(y,z)\mathbf{d}(x) \tag{1}$$

where $\mathbf{U}(y,z)$ is the matrix of the displacement interpolation functions over the cross-section (the cross-sectional displacement modes), and $\mathbf{d}(x)$ is the vector of weights associated to the interpolation functions, also called generalised displacements. For the HOBT of the present work, which is derived for a solid rectangular cross-section of dimensions h (height) $\times$ b (width), the previous expression takes the form:

$$\mathbf{u}(x,y^*,z^*) = \sum_{i=0}^{n}\sum_{j=0}^{n} \mathbf{U}^{*,ij}(y^*,z^*)\boldsymbol{d}^{*,ij}(x) = \mathbf{U}^*(y^*,z^*)\mathbf{d}^*(x) \tag{2}$$

where the normalized cross-sectional coordinates $y^* = 2y/b$ and $z^* = 2z/h$ are adopted, the cross-sectional interpolation functions are defined as

$$\mathbf{U}^{*,ij}(y^*,z^*) = \begin{bmatrix} P_i(y^*)P_j(z^*) & 0 & 0 \\ 0 & P_{i-1}(y^*)P_j(z^*) & 0 \\ 0 & 0 & P_i(y^*)P_{j-1}(z^*) \end{bmatrix} \tag{3}$$

and $\boldsymbol{d}^{*,ij}(x) = \begin{bmatrix} u_x^{*,ij} & u_y^{*,ij} & u_z^{*,ij} \end{bmatrix}^{\boldsymbol{T}}$ are the normalised generalised displacements. They replace the classical beam theory generalised displacements $\boldsymbol{d}^{ij}(x) = \begin{bmatrix} u_x^{ij} & u_y^{ij} & u_z^{ij} \end{bmatrix}^{\boldsymbol{T}}$, for reasons that are apparent below.

In Eq. (3), $P_n(s)$ represents Legendre polynomials for $n = 0, 1, 2, \ldots$, which are nth-degree polynomials that can be expressed using Rodrigues' formula:

$$P_n(s) = \frac{1}{2^n n!}\frac{d^n}{ds^n}\left[\left(s^2-1\right)^n\right] \tag{4}$$

The latter form a complete orthogonal set in the interval $-1 \leq s \leq 1$, which is a fundamental property in the development of the current finite element since it enables the definition of generalised stress-resultants that are not only independent but also orthogonal to one another. This leads to an unambiguous definition of the generalised stress-resultants and to a minimisation of the coupling between the resulting equilibrium equations. The use of y^* and z^* defined above, instead of y and z, is related to the interval where the orthogonality property holds. Note that any set of orthogonal displacement functions could be used instead of Legendre polynomials. The application of a Gram–Schmidt orthogonalisation procedure to a set of independent base functions would produce such orthogonal set, and further it could be applied in order to extend this formulation to different cross-sectional geometries.

$$
\begin{array}{ccccccccc}
 & & & & 1 & & & & \\
 & & & & y^* & & z^* & & \\
 & & & P_2(y^*) & & y^*z^* & & P_2(z^*) & \\
 & & P_3(y^*) & & P_2(y^*)z^* & & y^*P_2(z^*) & & P_3(z^*) \\
 & P_4(y^*) & & P_3(y^*)z^* & & & & y^*P_3(z^*) & & P_4(z^*) \\
 & & P_4(y^*)z^* & & & & & & y^*P_4(z^*)
\end{array}
$$

Fig. 1 Polynomial terms considered for the longitudinal displacement u_x

From Eq. (3), it can be observed that the transverse displacements have a one degree lower polynomial function than the axial displacements. This results in the same degree of approximation for the shear strain fields, considering the contributions of both the axial and transverse displacements in each set of modes *ij*.

The number of terms and the combination of indices *ij* adopted in the present beam-column model was based on a balance between intended accuracy and computational cost: all terms $\mathbf{U}^{*,ij}(y^*, z^*)$ up to the fourth-order in one coordinate and first-order in the other were considered. As demonstrated in the application examples of Sects. 3 to 5, the selected terms are sufficient to retrieve the intended axial-flexural-shear-torsional interaction. Figure 1 represents all 16 terms considered for the longitudinal displacement u_x in a Pascal triangle type of representation. The transverse displacements u_y and u_z contain 11 terms each, with one degree less in y^* and z^* respectively than the corresponding terms in u_x, resulting in a total of 38 displacement terms.

The matrix $\mathbf{U}^*(y^*, z^*)$ in Eq. 2 is a (3 × 38) matrix which is not depicted due to space limitations, while the normalised generalised displacements $\mathbf{d}^*(x)$ is the following (38 × 1) vector:

$$
\begin{aligned}
\mathbf{d}^*(x) = [&u^*_{x0}\ u^*_{y0}\ u^*_{z0}\ \theta^*_x\ \theta^*_y\ \theta^*_z\ \eta^*\gamma^* u^{*,20}_x\ u^{*,20}_y\ u^{*,02}_x\ u^{*,02}_z\ u^{*,21}_x\ u^{*,21}_y\ u^{*,21}_z \\
&\ldots u^{*,12}_x\ u^{*,12}_y\ u^{*,12}_y\ u^{*,12}_z\ u^{*,30}_x\ u^{*,30}_y\ u^{*,03}_x\ u^{*,03}_z\ u^{*,31}_x\ u^{*,31}_y\ u^{*,31}_z\ u^{*,13}_x \\
&\ldots u^{*,13}_y\ u^{*,13}_z\ u^{*,40}_x\ u^{*,40}_y\ u^{*,04}_x\ u^{*,04}_z\ u^{*,41}_x\ u^{*,41}_y\ u^{*,41}_z\ u^{*,14}_x\ u^{*,14}_y\ u^{*,14}_z]^T
\end{aligned}
\tag{5}
$$

It is noted that there is a compatibility matrix which converts the classical generalised displacements vector $\mathbf{d}(x)$ (38 × 1) into the previous normalized generalised displacements vector $\mathbf{d}^*(x)$ (38 × 1). Considering common engineering reasoning, the meaningful classical generalised displacements are those of the first-order $\mathbf{d}^{1st\ order}(x) = [u_{x0}\ u_{y0}\ u_{z0}\ \theta_x\ \theta_y\ \theta_z\ \eta\ \gamma]$; hence, the components of vector $\mathbf{d}(x)$ related to the higher-order generalised displacements are considered here to be identical to the corresponding normalised generalised displacements. The complete set of cross-sectional displacement shapes for a square section, which will be used in the numerical applications of Sects. 3 to 5, is included in Fig. 2. Each mode is defined by a column of the matrix $\mathbf{U}(y, z)$ in Eq. (1). The first-order modes 1 through 8 are composed of the six modes corresponding to classical Timoshenko beam theory, followed by two related to warping and distortion. The remaining 30 higher-order displacement modes are defined in Eq. (3) based on normalised

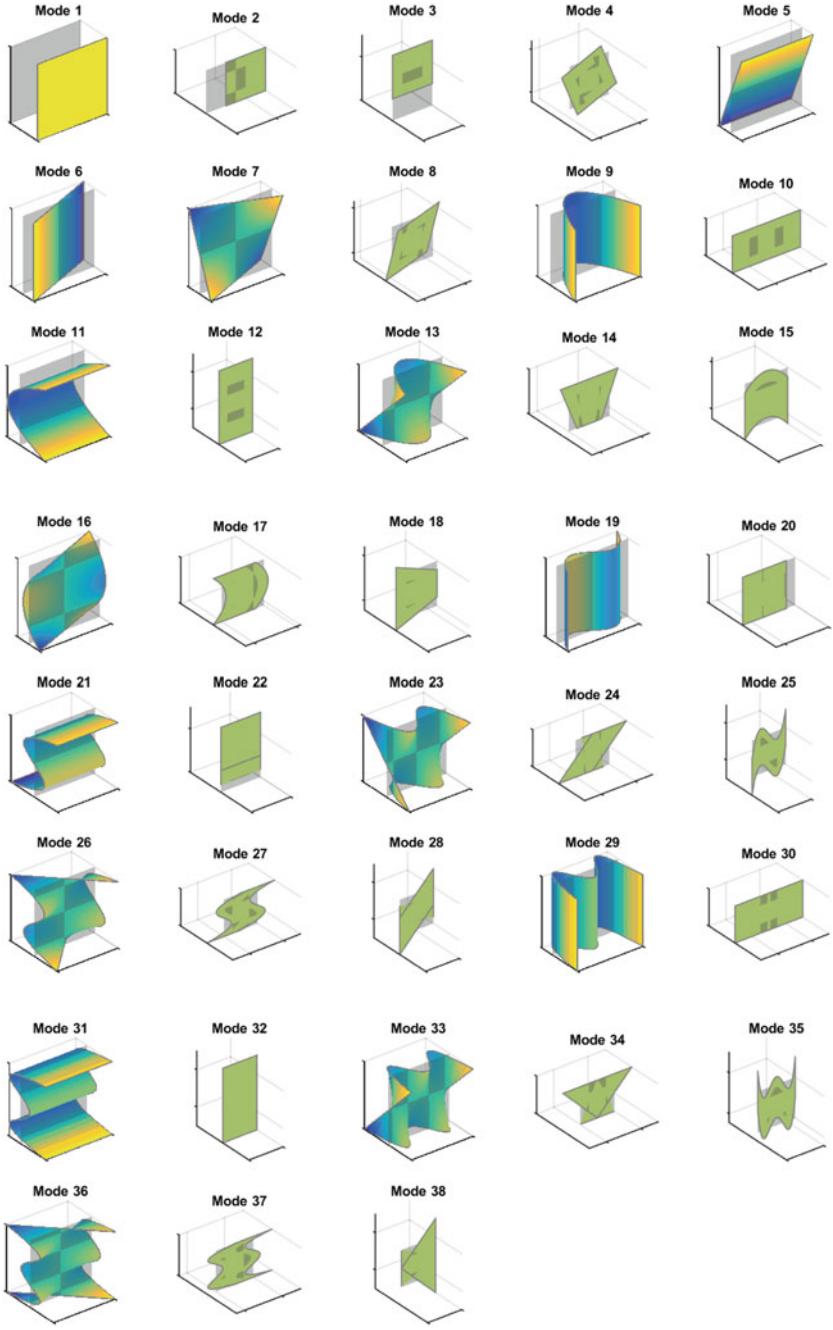

Fig. 2 Complete set of cross-sectional displacement modes for a square cross-section

Legendre polynomials and therefore reflect a product of polynomials of different degree along the two orthogonal cross-sectional coordinate axes.

In the process of derivation of the beam compatibility equations, Legendre polynomials and their derivatives appear in the definition of the generalised strains. However, those derivatives are not orthogonal either to the Legendre polynomials or between each other. Consequently, the generalised strains thus obtained would be independent from one another but they would not constitute an orthogonal set. Such lack of orthogonality would lead to a dubious definition for the generalised stress-resultants and to a large coupling of the equilibrium equations. This is undesirable in a FB approach since it would become extremely complex to obtain the self-equilibrated interpolation functions for the generalised stress-resultants. Moreover, the nodal boundary conditions (BCs) would also be coupled, which would unnecessarily increase the model's complexity. Hence, in order to have a unique definition for the generalised stress-resultants and to reduce the coupling of the equilibrium equations and boundary conditions to a minimum, those derivatives may and should be decomposed on the basis of Legendre polynomials. Every single generalised strain will then be associated to a unique Legendre polynomial in each direction. The derivation of the first and higher-order compatibility equations can be found in Correia et al. [8].

In order to obtain power-conjugated generalised stress-resultants, the beam equilibrium equations are obtained through a projection of the classical local equilibrium equations on the functional space of the cross-sectional displacement modes defined in Eq. (3) [21]. Such operation may also be regarded as weighting the residuals of the classical local equilibrium equations, where the cross-sectional displacement modes are taken as weighting functions. The complete beam equilibrium equations are a highly indeterminate system of differential equations represented by a (38 × 57) differential equilibrium operator (adjoint to the differential compatibility operator), a (38 × 1) vector of normalised distributed loads, and the following (57 × 1) vector of normalised generalised stress-resultants $\mathbf{s}^*$:

$$\mathbf{s}^*(x) = \begin{bmatrix} N\ M_y^*\ M_z^*\ B^*\ \mathbf{N}^{*,ij}\ (12\times 1)\ \mathbf{N}_y^{*,ij}\ (6\times 1)\ \mathbf{N}_z^{*,ij}\ (6\times 1) \\ \ldots V_y T^*\ Q^*\ \mathbf{V}_y^{*,ij}\ (9\times 1)\ V_z\ \mathbf{V}_z^{*,ij}\ (9\times 1)\ V_{yz}\ \mathbf{V}_{yz}^{*,ij}\ (6\times 1) \end{bmatrix}^T \tag{6}$$

where the first-order components $\mathbf{s}^{*,1st\,order}(x) = \left[N\ V_y\ V_z\ T^* M_y^*\ M_z^*\ B^*\ Q^*\ V_{yz}\right]^T$ relate to the classical generalised stress-resultants $\mathbf{s}^{*,1st\,order}(x) = \left[N\ V_y\ T\ M_y\ M_z\ B\ Q\ V_{yz}\right]^T$, and conversely, through:

$$\begin{cases} M_y^* = \frac{2}{h} M_y \\ M_z^* = \frac{2}{b} M_z \\ B^* = \frac{4}{bh} B \\ Q^* = Q\left(\frac{1}{b} + \frac{1}{h}\right) + T\left(\frac{1}{b} - \frac{1}{h}\right) \\ T^* = Q\left(\frac{1}{b} - \frac{1}{h}\right) + T\left(\frac{1}{b} + \frac{1}{h}\right) \end{cases} \quad \begin{cases} M_y = \frac{h}{2} M_y^* \\ M_z = \frac{b}{2} M_z^* \\ B = \frac{bh}{4} B^* \\ Q = Q^*\left(\frac{b}{4} + \frac{h}{4}\right) + T^*\left(\frac{b}{4} - \frac{h}{4}\right) \\ T = Q^*\left(\frac{b}{4} - \frac{h}{4}\right) + T^*\left(\frac{b}{4} + \frac{h}{4}\right) \end{cases} \tag{7}$$

and the higher-order components are given by:

$$\left.\begin{aligned} N^{*,ij} &= \int_A P_i(y^*)P_j(z^*)\sigma_x da \quad (12\,terms) \\ N_y^{*,ij} &= \int_A P_{i-2}(y^*)P_j(z^*)\sigma_y da \quad (6\,terms) \\ N_z^{*,ij} &= \int_A P_i(y^*)P_{j-2}(z^*)\sigma_z da \quad (6\,terms) \end{aligned}\right\} for\ i \geq 2\ or\ j \geq 2$$

$$\left.\begin{aligned} V_y^{*,ij} &= \int_A P_{i-1}(y^*)P_j(z^*)\tau_{xy} da \quad (9\,terms) \\ V_z^{*,ij} &= \int_A P_i(y^*)P_{j-1}(z^*)\tau_{xz} da \quad (9\,terms) \end{aligned}\right\} for\ i \geq 1\ or\ j \geq 1$$

$$V_{yz}^{*,ij} = \int_A P_{i-1}(y^*)P_{j-1}(z^*)\tau_{yz} da \quad (6\,terms)\ for\ i \geq 1\ and\ j \geq 1 \tag{8}$$

The compatibility and equilibrium boundary conditions can be found in Correia et al. [8]. It is noted that V_{yz}, $\mathbf{N}_y^{*,ij}$, $\mathbf{N}_z^{*,ij}$, and $\mathbf{V}_{yz}^{*,ij}$ are related to the stress components σ_y, σ_z, and τ_{yz}, which are not applied in the cross-section of the beam. Consequently, these 19 generalised stress-resultants do not appear in the static boundary conditions at the beam element ends.

As previously stressed, a FB formulation is employed in this work. Hence, the field of generalised stress-resultants should respect the beam local equilibrium conditions. In order to determine the complementary solution of the homogeneous equilibrium equations, and since there are a total of 38 local equilibrium equations involving 57 unknown generalised stress-resultants, a few assumptions have to be made concerning the functions describing the evolution of some generalised stress-resultants. Given that the differential equations of equilibrium require only one boundary condition each (as they involve only first derivatives), a total of 38 BCs are needed for this purpose. On the other hand, there are $38 \times 2 = 76$ available BCs at both extremities of the beam, corresponding to the nodal values of the 38 generalised stress-resultants related to the cross-sectional stresses σ_x, τ_{xy}, and τ_{xz}. Moreover, six of these nodal values are dependent on the remaining ones since they are related to the six rigid-body motions of the beam. Hence, from the remaining $76 - 6 = 70$ BCs, there are 32 which will not be used to solve the equations of equilibrium and that may be applied instead for defining a priori an assumed variation for the 19 generalised stress-resultants related to the stresses σ_y, σ_z, and τ_{yz}. Such assumed variation is not unique, which means that different self-equilibrated approximations can be envisaged. In the current formulation, the field of those 19 generalised stress-resultants is approximated by the simplest possible polynomial functions, namely linear and constant ones, and the necessary assumptions on their variations are briefly indicated in Appendix B of Correia et al. [8]. The latter reference also depicts the compact expression of the solution corresponding to such self-equilibrated higher-order stress-resultants.

With the above mentioned approximation, equilibrium in the domain and at the boundary is automatically satisfied. However, compatibility in the domain and at the boundary has to be likewise satisfied. So as to maintain power-conjugacy, the domain compatibility equations are verified in a weighted form using the

generalised stress-resultants' interpolation matrix as weighting functions. Finally, it is possible to derive the corresponding incremental equations required for nonlinear constitutive behaviour, including the beam tangent flexibility matrix. Although the complete theoretical developments of the present FB higher-order element cannot be included in the current chapter due to space limitations, they can be found in Correia et al. [8].

The first applications of the current model can be seen in the work by Almeida et al. [2], including: a cantilever subjected to a tip lateral load / imposed torsional rotation, and a simply supported beam with distributed loads. The following Sect. 3 illustrates the ability of the model to simulate the interaction between the different strain and stress components when a member is subjected to an imposed axial displacement. Section 4, on the other hand, includes a first example wherein a simultaneous flexural-shear-torsional loading is applied, while Sect. 5 shows the influence of material inelastic behaviour in such response. The structural analysis code *SAGRES* (*Software for Analysis of GRadient Effects on Structures*), developed by the authors and implemented in the MATLAB platform [22], was used to run the analyses.

3 Effect of Boundary Conditions on the Response of an Axially Loaded Member

In classical theories (Euler-Bernoulli or Timoshenko), stress-resultants and boundary conditions are of straightforward understanding and definition. However, in a higher-order model, the large number of generalised stress- and strain-resultants —well beyond the six classical ones—are much less intuitive from the engineering standpoint; they relate with the also large number of element nodal displacements and forces that are controlled by appropriate BCs. As observed by other researchers [5, 19], HOBTs are subjected to specific effects that require careful interpretation and a study of their influence on the accuracy of the results. These so-called higher-order boundary effects—which also show up in displacement-based formulations, although with distinct traits—play a relevant role in the response. They are intrinsically related to the boundary conditions assumed, which for this model consist of a combination of imposed generalised nodal displacements and/or forces, in a total of 76 (38 at each extremity), as discussed above. The special nature of such effects when applied together with a flexibility formulation naturally requires a careful analysis, which was carried out by Almeida et al. [2] to expose this yet undisclosed behaviour. Therein, the uncommon effects that the higher-order boundary conditions can cause on the stress-strain distributions—particularly near the member extremities—were highlighted, and an appropriate interpretation of the physical meaning of the generalised stress-resultants was made.

On the other hand, the number of BCs and stress-resultants also reflect the significant adaptability of the model in simulating physical phenomena that would

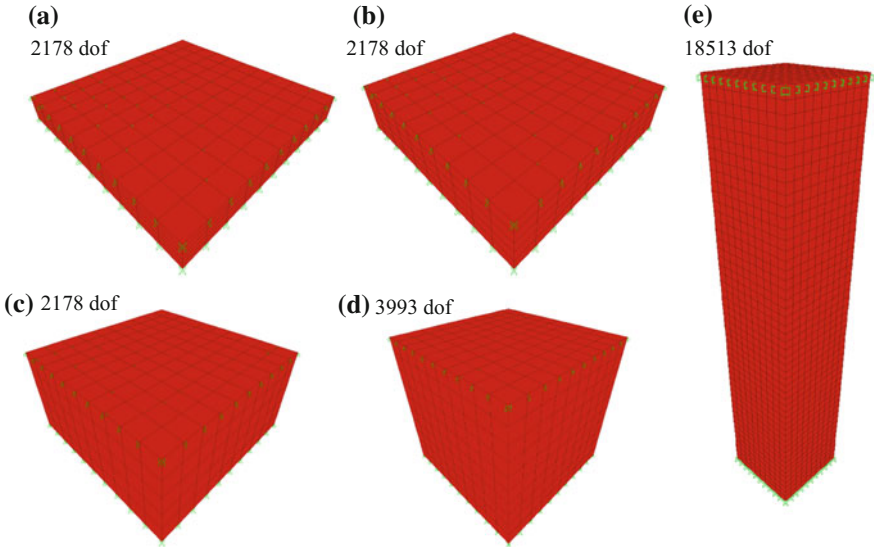

Fig. 3 Solid finite element mesh used to model the response for member lengths L equal to: **a** 0.125 (m); **b** 0.25 (m); **c** 0.5 (m); **d** 1 (m), and **e** 5 (m) [7]

pass unnoticed with traditional beam theories, even for very simple loading cases as the one that follows. This first numerical application analyses the response of a structural member subjected to an imposed end-node axial displacement, focusing on the comparison between the results of a refined mesh of solid finite elements, a classical beam theory, and the proposed higher-order one.

Five different member lengths L are analysed: 0.125, 0.25, 0.5, 1, and 5 (m). Additionally, a square cross-sectional geometry with unitary area 1×1 (m $\times$ m) is assumed and a linear elastic isotropic constitutive model was assigned, with Young's modulus $E = 200 \times 10^9$ (N/m^2) and Poisson's ratio $\nu = 0.3$. Regarding the solid finite element simulations [7], the meshes represented in Fig. 3 were employed, which had between 2178 and 18513 degrees of freedom (dof). All nodes in both member extremities were fully restrained and an axial displacement $\Delta_{axial} = 1 \times 10^{-3}$ (m) was applied to all nodes in one end. Concerning the frame models, a single element was used to model the member using both the classical beam theory (12 dof) and the proposed higher-order one (76 dof). Two sets of boundary conditions were considered for the higher-order element: (i) 'Max. Fixity': at each node all the 38 generalised displacements were restrained, while simultaneously an axial displacement $\Delta_{axial} = 1 \times 10^{-3}$ (m) was imposed at one node; this case corresponds to the maximum possible degree of fixity which is possible to assign to this higher-order beam model and is the one that better simulates the above mentioned joint restraints applied to the extremity nodes of the solid finite element mesh; (ii) 'Min. Fixity': at one node, only the six rigid-body displacements corresponding to the Timoshenko beam theory are restrained $\left(u_{x0} = u_{y0} = u_{z0} = \theta_x = \theta_y = \theta_z = 0\right)$, leaving the remaining 32 dof as

force-controlled and equal to zero; at the other node, the 38 dof were also force-controlled and kept equal to zero, except the one corresponding to the dof of axial displacement, on which a value of $\Delta_{axial} = 1 \times 10^{-3}$ (m) was again imposed; this case corresponds to the minimum possible degree of fixity provided by the model. It is noted that the geometry and loading herein defined are not intended to be realistic and have the sole purpose of illustrating the qualitative features of the proposed beam theory. The results presented in the following, namely the distribution of stresses, thus only have a numerical meaning.

Regarding the material properties, the HOBT model adopted the ones described above for the solid FE model, while the axial rigidity as used by classical beam theories (Timoshenko or Euler-Bernoulli) is equal to $(EA)_{classical} = 200 \times 10^9$ (N) and it is obviously independent of the member length L. However, for the HOBT and the solid FE model, the effect of fully restrained sections at the member extremities is expected to play a role in the increase of the equivalent axial rigidity, as computed by $(EA)_{equiv.} = F_{axial}/(\Delta_{axial}/L)$, where F_{axial} is the reaction along the axial degree of freedom (for the HOBT), or the summation of all extremity joint reactions along the member axis (for the solid FE model). This physical effect is well-known, for instance, as a frictional confinement effect on the results of compression tests of concrete cylinder or cube specimens. Figure 4 shows the ratio of

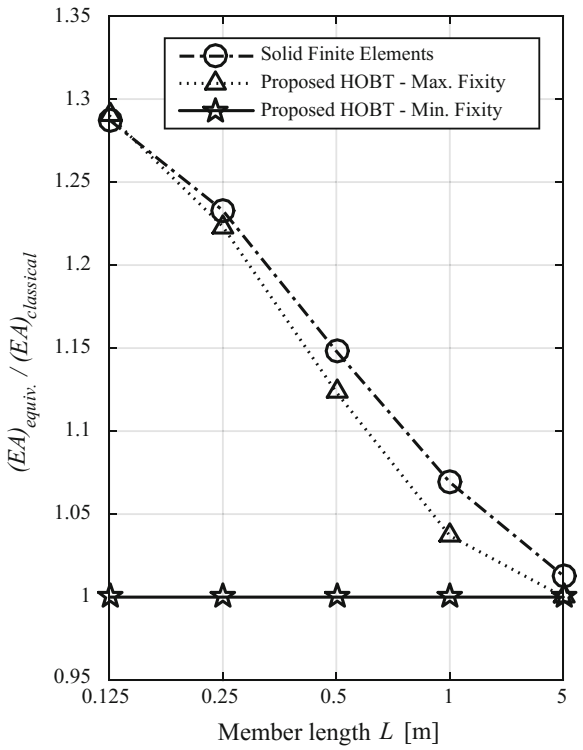

Fig. 4 Ratio of the equivalent axial rigidity $(EA)_{equiv.}$ to the axial rigidity given by classical beam theory $(EA)_{classical}$, for the five distinct member lengths shown in Fig. 3

the equivalent axial rigidity $(EA)_{equiv.}$ to the axial rigidity given by classical beam theory $(EA)_{classical}$, for the values of member length L indicated above. For the higher-order beam theory, both BCs 'Max. Fixity' and 'Min. Fixity' are analysed.

Taking the results obtained with the solid finite element mesh as the reference solution, it can be observed that for members with smaller lengths there is a significant increase in the equivalent axial rigidity due to the comparatively larger relevance of the boundary confining effects in the response with respect to longer members. Such increase is of around 15 % for a member length that is half the section side [i.e., $L = 0.5$ (m)], while for $L = 0.125$ (m) it goes up to close to 30 %.

Figure 4 also shows that the proposed HOBT, when the BCs 'Max. Fixity' are used, manages to capture accurately the increase of equivalent axial rigidity, closely reproducing the results from the solid finite element analyses. On the other hand, the BCs 'Min. Fixity' output the same results than classical beam theory, as the extremity sections are free to distort in their own plane. Other BCs corresponding to intermediate cases of fixity could have been considered as well, which would inevitably lead to estimations of the equivalent axial rigidity in-between those of the foregoing extreme scenarios.

Considering the BCs 'Max. Fixity', it is interesting to list the components of the stress-resultants $\mathbf{s}^*$ that for this case influence the behaviour of the element, i.e., those that are non-negligible from a quantitative viewpoint: $N, N^{*,20}, N^{*,02}, N^{*,40}, N^{*,04}, N_y^{*,20}, N_z^{*,02}, N_y^{*,40}, N_z^{*,04}, V_y^{*,20}, V_z^{*,02}, V_y^{*,40}, V_z^{*,04}$, see Eq. (8). The latter are all the variables that take part in the coupled differential equilibrium equations included in systems (1), (5) and (6) of Appendix A in Correia et al. [8]. System (1) corresponds simply to the differential equation from classical beam theory involving the axial force N. On the other hand, systems (5) and (6) involve the resultants $N^{*,ij}$ of the stress component σ_x that are symmetric within the cross-section (namely $N^{*,20}, N^{*,02}, N^{*,40}, N^{*,04}$, see also modes 9, 11, 29 and 31 in Fig. 2), which are expected to be non-null in view of the loading and geometric symmetry properties of the analysed problem. The additional presence, in the systems of coupled differential Eqs. (5) and (6), of some higher-order resultants of $\sigma_y, \sigma_z, \tau_{xy}$ and τ_{xz} (namely $N_y^{*,20}, N_z^{*,02}, N_y^{*,40}, N_z^{*,04}, V_y^{*,20}, V_z^{*,02}, V_y^{*,40}, V_z^{*,04}$), ensures that an advanced interaction between normal and shear stresses is considered in the proposed HOBT.

The extent to which the proposed element can also capture the distribution of stresses is now analysed. Figures 5 and 6 show the distribution of axial stresses at the extremity of the axially loaded member for $L = 5$ (m) and $L = 0.125$ (m) respectively. The results obtained with the solid finite element mesh are compared with those of the proposed higher-order element (again considering the BCs 'Max. Fixity'); the legend colour code was adjusted so that it is approximately similar to that of the solid FE output.

Figure 5b, c show that, for $L = 5$ (m), the proposed FB higher-order beam element encouragingly manages to reproduce the general qualitative distribution of axial stresses obtained from the refined finite element analyses. From a quantitative viewpoint, the beam model is not able to recover the peak stress concentrations

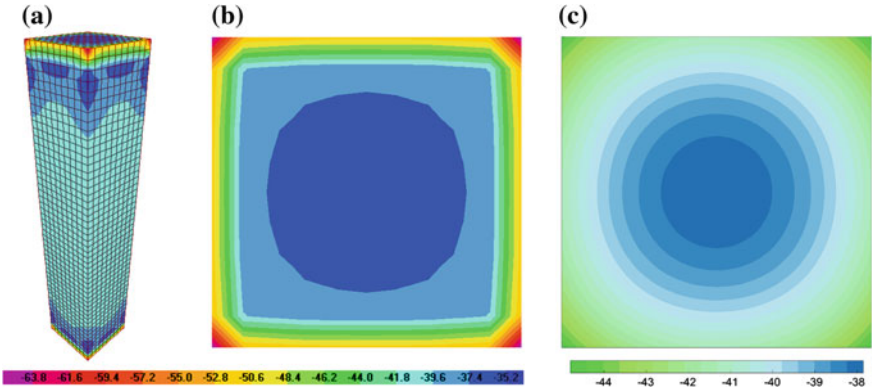

Fig. 5 Distribution of axial stresses [$\times$ 10^6 (N/m^2)] for L = 5 (m): **a** along the member, from solid FE model [7]; At the extremity, from **b** solid FE model and **c** proposed HOBT

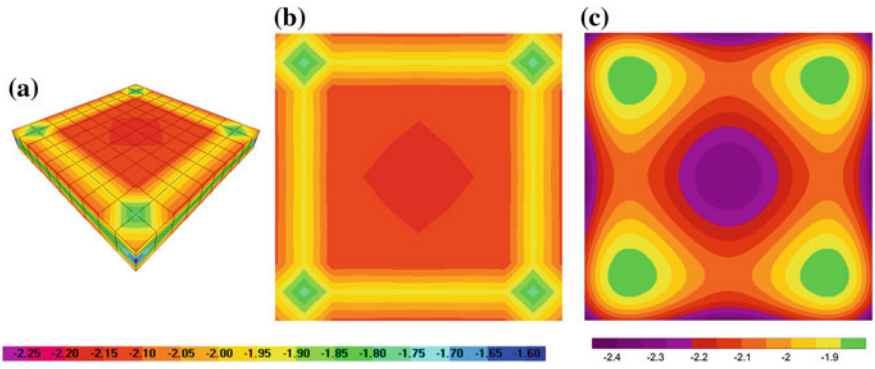

Fig. 6 Distribution of axial stresses [$\times$ 10^9 (N/m^2)] for L = 0.125 (m): **a** along the member, from solid FE model [7]; At the extremity, from **b** solid FEs and **c** proposed HOBT

taking place at the four cross-sectional corners (the solid FE mesh outputs peak values of almost -64×10^6 (N/m^2), while the counterpart values given by the HOBT are of -45×10^6 (N/m^2)). A more enriched set of cross-sectional displacement modes would be required to better estimate such stress peaks. However, one should also note that FE mesh outputs at corners and other geometric or loading discontinuities oftentimes fail to produce realistic results. In fact, they output exaggerated peak stresses at those regions and require a much finer discretization or some output averaging to give results of practical significance. On the other hand, a better agreement is achieved for the stress values in the larger central part of the cross-section (-36.5×10^6 (N/m^2) from the solid FE analyses *vs* -38×10^6 (N/m^2) from the HOBT). It is noted that, both with a classical beam theory or the present HOBT using the BCs 'Min. Fixity', a constant value of $\sigma_x = -40 \times 10^6\,(\mathrm{N/m^2})$ would be obtained throughout the entire cross-section,

which is far off from the stress distribution occurring at the extremity sections. Finally, at the member mid-span, the referred constant stress profile is retrieved both with the solid FE model—see Fig. 5a—and with the HOBT (not represented).

The effects of the boundary conditions become predominant for smaller member lengths, which is apparent from contrasting Figs. 6a with 5a. Again, comparing the results of Fig. 6b with those of Fig. 6c, it is clear that the new beam formulation approximately reproduces the qualitative distribution of the axial stresses at the member extremities. Furthermore, the agreement now extends to a quantitative comparison as well: the refined solid FE model outputs a value of $\sigma_x = -1.9 \times 10^9\,(\mathrm{N/m^2})$ for the central value in the four corner regions, *vs* $\sigma_x = -1.8 \times 10^9\,(\mathrm{N/m^2})$ given by the HOBT. Around the cross-sectional geometrical centre, the solid FE model outputs an axial stress of -2.15×10^9 ($\mathrm{N/m^2}$), while the current beam element indicates a value of -2.33×10^9 ($\mathrm{N/m^2}$). Classical beam theory, or the current HOBT with BCs 'Min. Fixity', would provide a constant value of $\sigma_x = -1.6 \times 10^9\,(\mathrm{N/m^2})$ throughout the entire cross-section.

4 Flexural-Shear-Torsional Interaction: Linear Elastic Behaviour

In this second group of examples, a member with the same mechanical and cross-sectional geometric characteristics of the previous Sect. 3 is subjected to a simultaneously imposed transversal displacement Δ and a torsional rotation θ at midspan (on a 1:1 ratio). Five different member lengths L are analysed: 0.25, 0.5, 1, 2, and 10 (m). Again, a comparison between a refined solid finite element mesh, the present HOBT, and results from classical beam theory and approximate solutions for the torsional constant is performed. Regarding the solid finite element simulations [7], the adopted meshes were resembling to those of Fig. 3 and had a total number of degrees of freedom ranging from 1782 to 3402. All the nodes at both member extremities were restrained. At each node at the midspan, a bidirectional (along y and z) translational displacement was assigned so that the imposed deformed shape combined the effects of the aforementioned imposed transverse displacement and torsional rotation. Concerning the frame models, four higher-order FB elements were used to model the member, in a total of 190 degrees of freedom. The boundary conditions corresponding to the previously discussed case 'Max. Fixity' were considered.

Figure 7 summarises the results of the analyses carried out, which are split into torsional and bending components and compared with the output of classical approaches. With regards to the latter, it is noted that whilst the second moment of the cross-sectional area I to compute the bending rigidity $(EI)_{classical}$ is clearly defined, there are no exact analytical formulations for calculating the sectional torsion constant J. Approximate solutions have however been found for many shapes and the expression $J \approx 2.25a^4$ (a is the side length of a square section) was

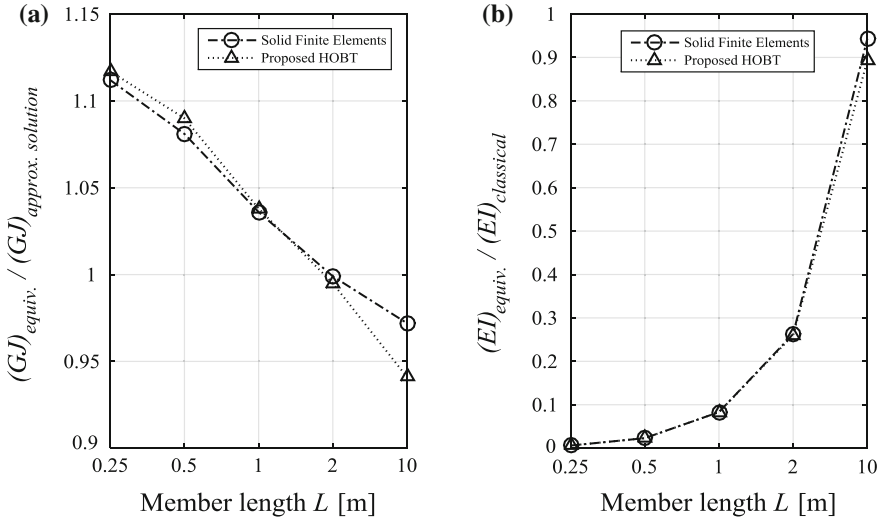

Fig. 7 **a** Ratio of the equivalent torsional rigidity $(GJ)_{equiv.}$ to the torsional rigidity given by available approximate solutions $(GJ)_{approxim.\ solution}$; **b** Ratio of the equivalent flexural rigidity $(EI)_{equiv.}$ to the flexural rigidity given by classical beam theory $(EI)_{classical}$

used to estimate the torsional rigidity $(GJ)_{approxim.\ solution}$, where $G = E/[2(1+\nu)]$ is the shear modulus. In particular, Fig. 7 (a) shows the ratio of the equivalent torsional rigidity $(GJ)_{equiv.}$—as derived both for the solid FE mesh and the HOBT—to the torsional rigidity given by the approximate solution mentioned above $(GJ)_{approxim.\ solution}$, for the considered values of member length L. Similarly, Fig. 7b shows the ratio of the equivalent bending rigidity $(EI)_{equiv.}$ to the bending rigidity given by classical beam theory $(EI)_{classical}$. The equivalent torsional rigidity is computed as $(GJ)_{equiv.} = T \times (L/2)/\theta$, where T is the torsional moment at each member extremity, i.e., the reaction along the torsional degree of freedom (for the HOBT) or the summation of the torsional moments for every joint reaction using the appropriate lever arm (for the solid FE model). Analogously, the equivalent bending rigidity is computed as $(EI)_{equiv.} = 2 \times V \times L^3/(192 \times \Delta)$, where V is the reaction shear force, i.e., the reaction along the transverse degree of freedom (for the HOBT) or the summation of the extremity joint reactions along that same direction (for the solid FE model).

It is observed that the proposed higher-order theory closely follows the results of the solid finite element models. Figure 7a shows that the increase in torsional stiffness associated to the warping restraints provided at the member extremity sections, which assumes a particular relevance for the shorter members, is accurately simulated. On the other hand, Fig. 7b indicates that, as expected, the contribution of classical flexural beam-type deformations are very small for members

with a short span; as the shear span increases, so does the relative contribution of these flexural deformations and, for L = 10 (m), the latter are roughly responsible for about 90–95 % of the overall deformations.

5 Flexural-Shear-Torsional Interaction: Multiaxial J2 Linear Plasticity

The present section expands the previous case-study [considering L = 10 (m)] to account for material nonlinear behaviour. Namely, the flexural-shear-torsional interaction is now assessed in the inelastic range, for the first time using the current FB higher-order beam element. The following ratios of torsional rotation θ to transversal displacement Δ at midspan were imposed: $\theta/\Delta = 0.5, 1, 2$, as well as the two bounds corresponding to the imposition of only θ and only Δ respectively. For this latter loading case, a classical FB Euler-Bernoulli beam theory (EBBT) is also employed for comparative purposes. It considers inelasticity through a cross-sectional discretisation by fibres to which one-dimensional nonlinear material models are assigned. As in the previous Sect. 3, the boundary conditions corresponding to 'Max. Fixity' were assigned to the HOBT model while, for the Euler-Bernoulli beam, the three translational displacements and the three rotations at each extremity were blocked.

In order to validate the comparison between these beam theories, it should be possible to relate the distinct material models under specific states of stress and strain. On the other hand, to ease the interpretation of the results, the latter should be as simple as possible. Therefore, the following models were employed: (i) a one-dimensional plastic model with hardening, for the EBBT simulation, whose behaviour is defined by the Young's modulus E, the uniaxial yield stress $\sigma_y^{uniaxial}$, and the strain hardening ratio $b = E_p/E$ (E_p stands for the plastic modulus); (ii) the multiaxial J2 linear plasticity model described by Auricchio and Taylor [3], for the HOBT simulation, which is based on linear evolutionary rules for both the plastic strain and the hardening mechanisms. The parameters that define this model are the isotropic and kinematic hardening (defined respectively by the parameters H_{iso} and H_{kin}), the initial yield stress in the three-dimensional context $\sigma_{y,0}$, which relates to $\sigma_y^{uniaxial}$ through $\sigma_{y,0} = \sqrt{2/3}\ \sigma_y^{uniaxial}$, the shear modulus G, and the bulk modulus K. The last two parameters are herein obtained from the Young's modulus E and the Poisson's ratio v.

In the present application, the following material parameters are considered for the one-dimensional material used in the force-based EBBT element: $\sigma_y^{uniaxial} = 500 \times 10^6\ (\mathrm{N/m^2})$, $E = 200 \times 10^9\ (\mathrm{N/m^2})$, and b = 0.01. On the other hand, the analyses carried out with the proposed force-based HOBT element employ the following parameters for the multiaxial J2 linear plasticity:

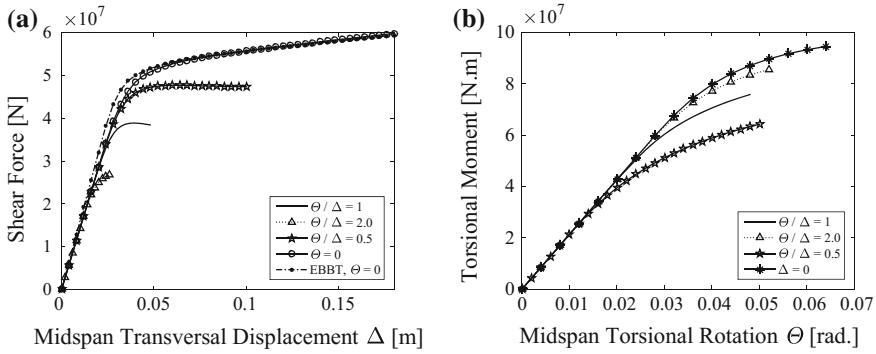

Fig. 8 **a** Reaction shear force *vs* imposed midspan displacement Δ, including the results for the EBBT; **b** Reaction torsional moment *vs* imposed midspan torsional rotation θ

$\sigma_{y,0} = \sqrt{2/3} \times 500 \times 10^6\ (\mathrm{N/m^2})$, $E = 200{\times}10^9\ (\mathrm{N/m^2})$, $H_{kin} = 1.34 \times 10^9$, $H_{iso} = 0$, and $\nu = 0.3$.

For each of the four elements in the mesh, the numerical integration was carried out with a Gauss-Lobatto scheme with eight integration sections. Geometrical nonlinear effects are neglected. The cross-sectional area integration was performed with a grid of 16 × 16 quadrilaterals (along the height × along the width), each one featuring a total of 4 × 4 Gauss-Lobatto integration points. The midspan loads Δ and/or θ were applied through a suite of monotonic increments in order to trace the nonlinear response up to a level where the member is mainly responding plastically. Figure 8a, b depict the $V{-}\Delta$ and the $T{-}\theta$ curves respectively (where V stands for the reaction shear force and T for the reaction torsional moment), obtained for the different loading ratios and beam theories.

The following main comments can be made to the several plots above. Firstly, the output of the proposed element and the EBBT in Fig. 8a, when subjected to an imposed midspan transversal displacement Δ (i.e., without torsion), show a very close match. Such expected outcome relates to the fact that, due to the long shear span of the analysed member, flexural deformations—which are appropriately simulated by the EBBT as well—are predominant. Further, they increase during the inelastic range of the response, heightening the aforementioned match. On the other hand, the role of the additional flexibility conferred by the enriched displacement modes accounted for in the HOBT is also clearly visible during the elastic behavioural phase (i.e., by the slightly lower initial stiffness due to shear deformability).

Secondly, the effects of the flexural-shear-torsional interaction in the inelastic range are clearly depicted. Figure 8a shows that the maximum member shear capacity is attained under bending without torsion, and that as the ratio of the imposed midspan torsional rotation to the transversal displacement at the midspan θ/Δ increases (for 0.5, 1 and 2 respectively), the shear capacity progressively reduces. This lowered plateau of maximum shear force capacity is associated with

the decrease of torsional stiffness with increased imposed torsional rotations, depicted in Fig. 8b. The same figure also shows that, as expected, the reduction of torsional stiffness is more pronounced for smaller ratios θ/Δ.

6 Conclusions

The present chapter started by recalling the theoretical framework of a recently developed higher-order force-based beam element that simulates the axial-flexural-shear-torsional interaction in three-dimensional frames. The explicit and direct interaction between three-dimensional shear and normal stresses is enabled by the considered set of higher-order deformation modes. In particular, cross-sectional displacement and strain fields are composed of independent and orthogonal modes, which results in unambiguously defined generalised cross-sectional stress-resultants and in a minimisation of the coupling between the equilibrium equations. On the basis of work-equivalency to three-dimensional continuum theory, dual one-dimensional higher-order equilibrium and compatibility equations are derived that govern an advanced form of beam equilibrium. The former are solved by using a force-based formulation, hence inherently avoiding shear-locking problems and allowing to account for the effects of span loads accurately. The proposed formulation is developed independently of the assumed constitutive behaviour (elastic or inelastic).

New numerical applications that capture a number of distinct physical phenomena were then presented. Firstly, the ability of the model in simulating the effect of different boundary conditions on the response of an axially loaded member under elastic response was addressed. The comparison against the results of solid finite element analyses showed the ability of the proposed formulation in adequately simulating the previous effect in the global response of members with different lengths, while using a total number of degrees of freedom one to two orders of magnitude smaller. Additionally, those examples showed that the proposed higher-order beam theory allows to simulate qualitatively the complex stress distribution occurring at the sectional level. From the quantitative viewpoint the matching is acceptable although the stress concentrations cannot be accurately reproduced, as expected. It is noted that the effects above cannot be simulated by classical beam theories. Secondly, an application to a case where flexural-shear-torsional interaction takes place was carried out. The beam performance was again assessed by comparison against refined solid finite element analyses, which confirmed the very good results of the present formulation for a wide range of member lengths wherein classical beam theory results and approximate numerical solutions are inadequate. Finally, the previous case was extended to account for inelastic material behaviour. Namely, the response of a relatively long member subjected to different ratios of imposed torsional rotation to transversal displacement at midspan was analysed. The current beam element simulated the progressive reduction of the shear force capacity due to larger

torsional rotations, as well as the progressive decrease of torsional stiffness in the inelastic range. Moreover, the response of the member when only bending was applied closely matches the results of an Euler-Bernoulli force-based fibre beam approach with an equivalent inelastic uniaxial material model.

References

1. Alemdar BN, White DW (2005) Displacement, flexibility, and mixed beam-column finite element formulations for distributed plasticity analysis. J Struct Eng 131:1811–1819
2. Almeida JP, Correia AA, Pinho R (2015) Force-based higher order beam element with flexural-shear-torsional interaction in 3D frames. Part II: Applications. Eng Struct 89:218–235
3. Auricchio F, Taylor RL (1995) Two material models for cyclic plasticity: nonlinear kinematic hardening and generalized plasticity. Int J Plast 11:65–98
4. Bathe K-J (1996) Finite element procedures. Prentice Hall
5. Bickford WB (1982) A consistent higher order beam theory. Dev Theor Appl Mech 11:137–150
6. Ciampi V, Carlesimo L (1986) A nonlinear beam element for seismic analysis of structures. In: Eighth European Conference on Earthquake Engineering. Lisbon, Portugal, pp 73–80
7. Computers and Structures Inc. (2013) SAP2000—Version 16.0.1
8. Correia AA, Almeida JP, Pinho R (2015) Force-based higher order beam element with flexural-shear-torsional interaction in 3D frames. Part I: Theory. Eng Struct 89:204–217
9. Cowper GR (1966) The shear coefficient in Timoshenko's beam theory. J Appl Mech 33:335–340
10. Dong SB, Alpdogan C, Taciroglu E (2010) Much ado about shear correction factors in Timoshenko beam theory. Int J Solids Struct 47:1651–1665
11. Frischkorn J, Reese S (2013) A solid-beam finite element and non-linear constitutive modelling. Comput Methods Appl Mech Eng 265:195–212
12. Hjelmstad KD (2002) Mixed methods and flexibility approaches for nonlinear frame analysis. J Constr Steel Res 58:967–993
13. Hjelmstad KD, Taciroglu E (2005) Variational basis of nonlinear flexibility methods for structural analysis of frames. J Eng Mech 131:1157–1169
14. Kaneko T (1975) On Timoshenko's correction for shear in vibrating beams. J Phys D Appl Phys 8:1927–1936
15. Menegotto M, Pinto PE (1973) Method of analysis for cyclically loaded RC plane frames including changes in geometry and non-elastic behaviour of elements under combined normal force and bending. In: IABSE Symposium on resistance and ultimate deformability of structures acted on by well defined repeated loads—Final report
16. Mindlin RD, Deresiewicz H (1953) Timoshenko's shear coefficient for flexural vibrations of beams, technical report No. 10, ONR Project NR064–388. New York
17. Neuenhofer A, Filippou FC (1997) Evaluation of nonlinear frame finite-element models. J Struct Eng 123:958–966
18. Pian THH, Tong P (1968) Rationalization in deriving element stiffness matrix by assumed stress approach. In: Conference on matrix methods in structural analysis (2nd), pp 441–469
19. Prathap G, Vinayak RU, Naganarayana BP (1996) Beam elements based on a higher order theory—II. Boundary layer sensitivity and stress oscillations. Comput Struct 58:791–796
20. Spacone E, Ciampi V, Filippou FC (1996) Mixed formulation of nonlinear beam finite element. Comput Struct 58:71–83

21. Teixeira de Freitas JA, Moitinho de Almeida JP, Ribeiro Pereira EMB (1999) Non-conventional formulations for the finite element method. Comput Mech 23:488–501
22. The MathWorks Inc., 2009. MATLAB—Version 7.9
23. Vlassov BZ (1962) Pièces Longues en Voiles Minces. Éditions Eyrolles, Paris, France

Improved Method for the Calculation of Plastic Rotation of Moment-Resisting Framed Structures for Nonlinear Static and Dynamic Analysis

Kevin K.F. Wong and Matthew S. Speicher

Abstract Given the vast advancements in computing power in the last several decades, nonlinear dynamic analysis has gained wide acceptance by practicing engineers as a useful way of assessing and improving the seismic performance of structures. Nonlinear structural analysis software packages give engineers the ability to directly model nonlinear component behavior in detail, resulting in improved understanding of how a building will respond under strong earthquake shaking. One key component, in particular, for understanding the behavior of moment-resisting frames is the plastic rotation of the flexural hinges. Performance-based standards typically use plastic rotation as the primary parameter for defining the acceptance criteria in moment-resisting frames. Since plastic rotation is a key parameter in the seismic damage assessment, the concept as well as the method to calculate this quantity must be understood completely. Though engineers rely on the plastic rotation output from seismic structural analysis software packages to determine acceptable performance, the actual calculation methods used in achieving such plastic rotation quantities usually lay within a so-called "black box". Based on the outputs obtained from most structural analysis software packages, it can be shown that running an algorithm considering material nonlinearity by itself will produce reasonably accurate results. Moreover, separately running an algorithm considering geometric nonlinearity also can produce accurate results. However, when material nonlinearity is combined with geometric nonlinearity in an analysis, obtaining accurate results or even stable solutions is more difficult. The coupling effect between the two nonlinearities can significantly affect the global response and the local plastic rotation obtained from the analysis and therefore needs to be verified through some analytical means. Yet, the verification process is difficult because a robust analytical framework for calculating plastic rotation is currently unavailable and urgently needed. In view of this gap, an improved analytical approach based on small displacement theory is derived to

K.K.F. Wong (✉) · M.S. Speicher
National Institute of Standards and Technology, Gaithersburg, MD 20899, USA
e-mail: kfwong@nist.gov

M.S. Speicher
e-mail: speicher@nist.gov

M. Papadrakakis et al. (eds.), *Computational Methods in Earthquake Engineering*,
Computational Methods in Applied Sciences 44,
DOI 10.1007/978-3-319-47798-5_6

calculate the plastic rotations of plastic hinges at various locations of moment-resisting frames. Both static and dynamic analysis with nonlinear geometric effects will be incorporated in the derivation. Here the element stiffness matrices are first rigorously derived using a member with plastic hinges in compression, and therefore the coupling of geometric and material nonlinearity effects is included from the beginning of the derivation. Additionally, plastic rotation is handled explicitly by considering this rotation as an additional nonlinear degree-of-freedom. Numerical simulation is performed to calculate the nonlinear static and dynamic responses of simple benchmark models subjected to seismic excitations. Results are compared with various software packages to demonstrate the feasibility of the proposed method in light of the output results among software packages in calculating plastic rotations.

1 Introduction

Plastic rotation is one of the most fundamental structural performance metrics for moment-resisting frames. Current performance-based standards such as ASCE/SEI 41 [1] use plastic rotation as the primary performance measure in the assessment of flexure components in moment-resisting frames for the life safety and collapse prevention performance levels. Relatively large lateral displacement is expected to occur due to the flexibility of moment-resisting frames. Therefore, structural analysis software packages should possess the capability of handling both material nonlinearity and geometric nonlinearity in order to provide the needed output used to gauge acceptable performance.

Geometric nonlinearity causes a reduction in stiffness due to the axial compressive force acting on the entire length in the member, while material nonlinearity causes a reduction in stiffness concentrated at the plastic hinges of the member. These two nonlinear phenomena interact with one another in moment-resisting frames, but this interaction may have not been captured in all of the structural analysis software packages and algorithms that are currently available today. Yet, there have been studies concerning moment-resisting frames that involve the use of geometric nonlinearity with material nonlinearity in dynamic analysis (e.g., [2–6]) where the interaction is not explicitly handled but rather is left up to the software packages used in the analysis.

When addressing material nonlinearity, the plastic rotation action is often handled through a plastic reduction matrix, which represents the change in stiffness due to inelastic system behavior. This reduction matrix is derived using principles from the theory of plasticity and assuming an appropriate yield surface. It is often combined with the geometric stiffness matrix to account for both material and geometric nonlinearities and the behavior can then be traced incrementally by solving simultaneous linear algebraic equations to arrive at a solution. In other words, many of these seismic analysis software packages use one algorithm for

performing material nonlinearity analysis and another algorithm for performing geometric nonlinearity analysis.

Handling material nonlinearity and geometrically nonlinearity independently is often viewed as the most efficient approach for performing the analysis. It can be shown that running an algorithm considering material nonlinearity by itself will produce reasonably accurate results using most structural analysis software packages. Moreover, separately running an algorithm considering geometric nonlinearity also can produce reasonably accurate results. However, when material nonlinearity is combined with geometric nonlinearity in an analysis, software packages often neglect the interactions between these nonlinearities, resulting in limited consistency, reduced accuracy, and solution instability. As a result, plastic rotation, as the end product of the analysis, can differ significantly based on the approach taken in the nonlinear algorithm.

One reason for this shortcoming in addressing the nonlinear interaction is because currently there is no analytical theory that can be used to capture this interaction exactly. Therefore, a numerical solution is often employed that assumes the nonlinear interaction is automatically taken into account when both material and geometric nonlinearities are captured independently and then combined. The results presented here propose a method to accurately calculate the plastic rotation while capturing the interaction of material nonlinearity and geometric nonlinearity using an analytical theory based on basic principles of structural mechanics. Element stiffness matrices are first derived using a column member with plastic hinges subjected to axial compression; therefore, both geometric nonlinearity and material nonlinearity along with their interactions are captured from the beginning of the formulation. The element stiffness matrices are then assembled in the global stiffness matrices to perform nonlinear static analysis, and the global stiffness matrices are used in the dynamic equilibrium equations to perform nonlinear dynamic analysis. Numerical simulations are then performed on a simple moment-resisting frame. Both global responses such as the displacement and local responses including plastic rotations are obtained and compared with those obtained from various structural analysis software packages.

2 Element Stiffness Formulations

The stability theory of using stability functions is used to derive the element stiffness matrices of framed members with plastic hinges at both ends in a two-dimensional frame analysis. This theory was first developed for elastic structures in the 1960s [7–9], but it found limited application because of its complexity in the closed-form solution as compared to those using either the $P-\Delta$ approach [10] or the geometric stiffness approach [11]. Even with the advance in computing technology, only one research publication was found in the recent literature on the analysis of framed structures using stability functions [12]. For structures with significant lateral deflection, large geometric nonlinearity is expected, and linear or

second-order approximation of the geometric nonlinearity may not be able to capture the nonlinear behavior accurately. Therefore, stability functions are rigorously derived in this chapter to include both geometric and material nonlinearities in the element stiffness formulations.

2.1 Element Stiffness Matrix [$\mathbf{k}_i$]

The element stiffness matrix $\mathbf{k}_i$ for bending relates the displacement at the two ends of the ith member [commonly labeled as degrees of freedom (DOFs)] with the forces applied at these DOFs. For moment-resisting frame members, these displacement quantities include the lateral displacement and rotations at the two ends. This gives 4 DOFs for the bending stiffness of each element in a two-dimensional plane analysis, and these DOFs are labeled as:

- Case 1—Lateral displacement at the '1' end or 'near' end,
- Case 2—Rotation at the '1' end or 'near' end,
- Case 3—Lateral displacement at the '2' end or 'far' end, and
- Case 4—Rotation at the '2' end or 'far' end.

To compute the element stiffness matrix $\mathbf{k}_i$, each of the 4 DOFs is displaced independently by one unit as shown in Fig. 1 while subjected to an axial compressive load P. Here, V_{1l}, M_{1l}, V_{2l}, and M_{2l} represent the required shears and moments at the two ends of the member to cause the deflection in the prescribed pattern, and $l = 1, \ldots, 4$ represents the four cases of unit displacement patterns of member deflection.

Using the classical Bernoulli-Euler beam theory on homogeneous and isotropic material where the moment is proportional to the curvature and plane sections are assumed to remain plane, the governing equilibrium equation describing the deflected shape of the member can be written as

$$(EIv'')'' + Pv'' = 0 \tag{1}$$

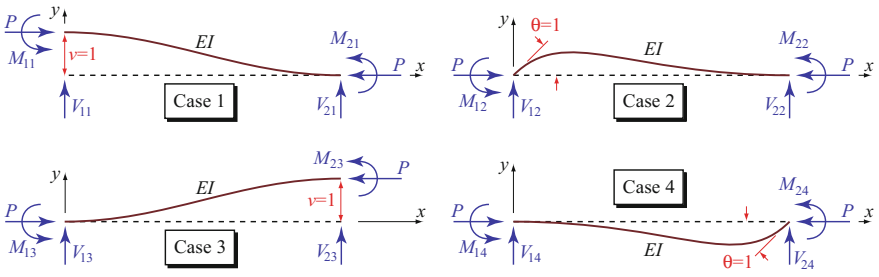

Fig. 1 Displacement patterns and the corresponding fixed-end forces

where E is the elastic modulus, I is the moment of inertia, v is the lateral deflection, P is the axial compressive force of the member, and each prime represents taking derivatives of the corresponding variable with respect to the x-direction of the member. By assuming EI is constant along the member, the solution to the fourth-order ordinary differential equation becomes:

$$v = A\ \sin kx + B\ \cos kx + Cx + D \tag{2}$$

where $k^2 = P/EI$. Let $\lambda = kL$ to simplify the derivations, where L is the length of the member. The following four cases of boundary conditions (in reverse order) are now considered.

Case 4 of Fig. 1: Imposing the boundary conditions $v(0) = 0$, $v'(0) = 0$, $v(L) = 0$, and $v'(L) = 1$ gives

$$v(0) = 0: \quad B + D = 0 \tag{3a}$$

$$v'(0) = 0: \quad kA + C = 0 \tag{3b}$$

$$v(L) = 0: \quad A\ \sin\lambda + B\ \cos\lambda + CL + D = 0 \tag{3c}$$

$$v'(L) = 1: \quad kA\ \cos\lambda - kB\ \sin\lambda + C = 1 \tag{3d}$$

Solving simultaneously for the constants in Eqs. 3a–3d gives

$$A = \frac{L(1-\cos\lambda)}{\lambda(\lambda\ \sin\lambda + 2\ \cos\lambda - 2)}, \quad B = \frac{L(\sin\lambda - \lambda)}{\lambda(\lambda\ \sin\lambda + 2\ \cos\lambda - 2)}, \quad C = -kA, \quad D = -B \tag{4}$$

Therefore, Eq. 2 along with the constants in Eq. 4 gives the deflected shape for Case 4. The shears (i.e., V_{14} and V_{24}) and moments (i.e., M_{14} and M_{24}) at the two ends of the member (see Fig. 1) are then evaluated using the classical Bernoulli-Euler beam theory formula:

$$M(x) = EIv'', \quad V(x) = EIv''' + Pv' \tag{5}$$

Now taking derivatives of Eq. 2 and substituting the results into Eq. 5 while using the constants calculated in Eq. 4, the shears and moments at the two ends for Case 4 in Fig. 1 are calculated as:

$$M_{14} = -EIv''(0) = EIk^2B = scEI/L \tag{6a}$$

$$V_{14} = EIv'''(0) + Pv'(0) = -EIk^3A + P \times 0 = \bar{s}EI/L^2 \tag{6b}$$

$$M_{24} = EIv''(L) = -EIk^2(A\ \sin\lambda + B\ \cos\lambda) = sEI/L \tag{6c}$$

$$V_{24} = -EIv'''(L) - Pv'(L) = EIk^3(A\cos\lambda - B\sin\lambda) - P \times 1 = -\bar{s}EI/L^2 \quad (6d)$$

where

$$s = \frac{\lambda(\sin\lambda - \lambda\cos\lambda)}{2 - 2\cos\lambda - \lambda\sin\lambda}, \quad c = \frac{\lambda - \sin\lambda}{\sin\lambda - \lambda\cos\lambda}, \quad \bar{s} = s + sc = \frac{\lambda^2(1 - \cos\lambda)}{2 - 2\cos\lambda - \lambda\sin\lambda} \quad (7)$$

The minus signs appear in front of the equations for M_{14} in Eq. 6a and V_{24} in Eq. 6d because there is a difference in sign convention between the classical Bernoulli-Euler beam theory and the theory for the stiffness method in structural analysis.

Case 3 of Fig. 1: Imposing the boundary conditions $v(0) = 0$, $v'(0) = 0$, $v(L) = 1$, and $v'(L) = 0$ gives

$$v(0) = 0: \quad B + D = 0 \quad (8a)$$

$$v'(0) = 0: \quad kA + C = 0 \quad (8b)$$

$$v(L) = 1: \quad A\sin\lambda + B\cos\lambda + CL + D = 1 \quad (8c)$$

$$v'(L) = 0: \quad kA\cos\lambda - kB\sin\lambda + C = 0 \quad (8d)$$

Solving simultaneously for the constants in Eqs. 8a–8d gives

$$A = -\frac{\sin\lambda}{\lambda\sin\lambda + 2\cos\lambda - 2}, \quad B = \frac{1 - \cos\lambda}{\lambda\sin\lambda + 2\cos\lambda - 2}, \quad C = -kA, \quad D = -B \quad (9)$$

Therefore, Eq. 2 along with the constants in Eq. 9 gives the deflected shape for Case 3. Now taking derivatives of Eq. 2 and substituting the results into Eq. 5 while using the constants calculated in Eq. 9, the shears and moments at the two ends for Case 3 in Fig. 1 are calculated as:

$$M_{13} = -EIv''(0) = EIk^2B = -\bar{s}EI/L^2 \quad (10a)$$

$$V_{13} = EIv'''(0) + Pv'(0) = -EIk^3A + P \times 0 = -s'EI/L^3 \quad (10b)$$

$$M_{23} = EIv''(L) = -EIk^2(A\sin\lambda + B\cos\lambda) = -\bar{s}EI/L^2 \quad (10c)$$

$$V_{23} = -EIv'''(L) - Pv'(L) = EIk^3(A\cos\lambda - B\sin\lambda) - P \times 0 = s'EI/L^3 \quad (10d)$$

where

$$s' = 2\bar{s} - \lambda^2 = \frac{\lambda^3 \sin\lambda}{2 - 2\cos\lambda - \lambda\sin\lambda} \tag{11}$$

and $\bar{s}$ is given in Eq. 7.

Case 2 of Fig. 1: Imposing the boundary conditions $v(0) = 0$, $v'(0) = 1$, $v(L) = 0$, and $v'(L) = 0$ gives

$$v(0) = 0: \quad B + D = 0 \tag{12a}$$

$$v'(0) = 1: \quad kA + C = 1 \tag{12b}$$

$$v(L) = 0: \quad A\sin\lambda + B\cos\lambda + CL + D = 0 \tag{12c}$$

$$v'(L) = 0: \quad kA\cos\lambda - kB\sin\lambda + C = 0 \tag{12d}$$

Solving simultaneously for the constants in Eqs. 12a–12d gives

$$A = \frac{L(\lambda\sin\lambda + \cos\lambda - 1)}{\lambda(\lambda\sin\lambda + 2\cos\lambda - 2)}, \quad B = \frac{L(\lambda\cos\lambda - \sin\lambda)}{\lambda(\lambda\sin\lambda + 2\cos\lambda - 2)}, \quad C = 1 - kA, \quad D = -B \tag{13}$$

Therefore, Eq. 2 along with the constants in Eq. 13 gives the deflected shape for Case 2. Now taking derivatives of Eq. 2 and substituting the results into Eq. 5 while using the constants calculated in Eq. 13, the shears and moments at the two ends for Case 2 in Fig. 1 are calculated as:

$$M_{12} = -EIv''(0) = EIk^2B = sEI/L \tag{14a}$$

$$V_{12} = EIv'''(0) + Pv'(0) = -EIk^3A + P \times 1 = \bar{s}EI/L^2 \tag{14b}$$

$$M_{22} = EIv''(L) = -EIk^2(A\sin\lambda + B\cos\lambda) = scEI/L \tag{14c}$$

$$V_{22} = -EIv'''(L) - Pv'(L) = EIk^3(A\cos\lambda - B\sin\lambda) - P \times 0 = -\bar{s}EI/L^2 \tag{14d}$$

where s, c, and $\bar{s}$ are given in Eq. 7.

Case 1 of Fig. 1: Finally, imposing the boundary conditions $v(0) = 1$, $v'(0) = 0$, $v(L) = 0$, and $v'(L) = 0$ gives

$$v(0) = 1: \quad B + D = 1 \tag{15a}$$

$$v'(0) = 0: \quad kA + C = 0 \tag{15b}$$

$$v(L) = 0: \quad A \sin\lambda + B \cos\lambda + CL + D = 0 \tag{15c}$$

$$v'(L) = 0: \quad kA \cos\lambda - kB \sin\lambda + C = 0 \tag{15d}$$

Solving simultaneously for the constants in Eqs. 15a–15d gives

$$A = \frac{\sin\lambda}{\lambda \sin\lambda + 2\cos\lambda - 2}, \quad B = \frac{\cos\lambda - 1}{\lambda \sin\lambda + 2\cos\lambda - 2}, \quad C = -kA, \quad D = 1 - B \tag{16}$$

Therefore, Eq. 2 along with the constants in Eq. 16 gives the deflected shape for Case 1. Now taking derivatives of Eq. 2 and substituting the results into Eq. 5 while using the constants calculated in Eq. 16, the shears and moments at the two ends for Case 1 in Fig. 1 are calculated as:

$$M_{11} = -EIv''(0) = EIk^2 B = \bar{s}EI/L^2 \tag{17a}$$

$$V_{11} = EIv'''(0) + Pv'(0) = -EIk^3 A + P \times 0 = s'EI/L^3 \tag{17b}$$

$$M_{21} = EIv''(L) = -EIk^2(A \sin\lambda + B \cos\lambda) = \bar{s}EI/L^2 \tag{17c}$$

$$V_{21} = -EIv'''(L) - Pv'(L) = EIk^3(A \cos\lambda - B \sin\lambda) - P \times 0 = -s'EI/L^3 \tag{17d}$$

where $\bar{s}$ is given in Eq. 7 and s' is given in Eq. 11.

In summary, based on Eqs. 6a–6d, 10a–10d, 14a–14d, and 17a–17d for the above four cases, the element stiffness matrix of the ith member $\mathbf{k}_i$ after incorporating axial compressive force using stability functions becomes:

$$\mathbf{k}_i = \frac{EI}{L^3}\begin{bmatrix} s' & \bar{s}L & -s' & \bar{s}L \\ \bar{s}L & sL^2 & -\bar{s}L & scL^2 \\ -s' & -\bar{s}L & s' & -\bar{s}L \\ \bar{s}L & scL^2 & -\bar{s}L & sL^2 \end{bmatrix} \begin{matrix} \leftarrow v(0) \\ \leftarrow v'(0) \\ \leftarrow v(L) \\ \leftarrow v'(L) \end{matrix} \tag{18}$$

2.2 *Element Stiffness Matrix* $[\mathbf{k}'_i]$

The element stiffness matrix $\mathbf{k}'_i$ relates the plastic rotations at the plastic hinge locations (PHLs) of the ith member with the restoring forces applied at the DOFs. Two plastic hinges typically occur at the two ends of the member, and they are

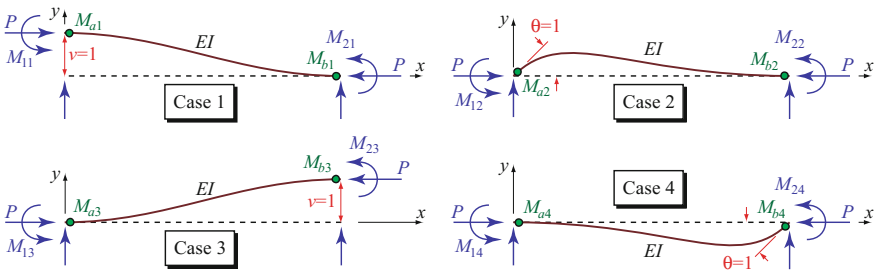

Fig. 2 Displacement patterns for computation of moments at the plastic hinge locations

labeled as 'a' for plastic hinge at the 'near' end (or '1' end) and 'b' for plastic hinge at the 'far' end (or '2' end) as shown in Fig. 2. To compute the element stiffness matrix $\mathbf{k}_i'$, a unit plastic rotation at each PHL can be independently applied to the member and then determine the shear and moment at each of the two ends. However, this is a difficult process because imposing a unit plastic rotation requires the discontinuity of $v'(x)$ to be addressed. To avoid this problem, the $\mathbf{k}_i'^T$ matrix is constructed instead. The $\mathbf{k}_i'^T$ matrix relates the lateral displacements and rotations at the two ends of the member (i.e., the four cases of unit displacements at each DOF) with the moments at the PHLs (i.e., M_{al} and M_{bl}, $l = 1, \ldots, 4$).

Consider the four cases of unit displacements of the member independently as shown in Fig. 2, where the moment at the plastic hinges 'a' and 'b' (i.e., M_{al} and M_{bl}, $l = 1, \ldots, 4$) represent the desired quantities. Note that the moments at the two ends of the member (i.e., M_{1l} and M_{2l}, $l = 1, \ldots, 4$) have already been calculated using the unit displacement patterns in Fig. 1 and summarized in the second and fourth rows of the element stiffness matrix $\mathbf{k}_i$ given in Eq. 18. Therefore, based on Fig. 2, the moments M_{al} and M_{bl} at the two plastic hinges for each of the four cases become:

Case 1 of Fig. 2: Imposing the boundary conditions $v(0) = 1$, $v'(0) = 0$, $v(L) = 0$, and $v'(L) = 0$ gives

$$M_{a1} = M_{11} = \bar{s}EI/L^2, \quad M_{b1} = M_{21} = \bar{s}EI/L^2 \tag{19}$$

Case 2 of Fig. 2: Imposing the boundary conditions $v(0) = 0$, $v'(0) = 1$, $v(L) = 0$, and $v'(L) = 0$ gives

$$M_{a2} = M_{12} = sEI/L, \quad M_{b2} = M_{22} = scEI/L \tag{20}$$

Case 3 of Fig. 2: Imposing the boundary conditions $v(0) = 0$, $v'(0) = 0$, $v(L) = 1$, and $v'(L) = 0$ gives

$$M_{a3} = M_{13} = -\bar{s}EI/L^2, \quad M_{b3} = M_{23} = -\bar{s}EI/L^2 \tag{21}$$

Case 4 of Fig. 2: Finally, imposing the boundary conditions $v(0) = 0$, $v'(0) = 0$, $v(L) = 0$, and $v'(L) = 1$ gives

$$M_{a4} = M_{14} = scEI/L, \quad M_{b4} = M_{24} = sEI/L \tag{22}$$

Therefore, from Eqs. 19 to 22, the transpose of stiffness matrix $\mathbf{k}_i'$ for the ith member becomes

$$\mathbf{k}_i'^T = \begin{bmatrix} \bar{s}EI/L^2 & sEI/L & -\bar{s}EI/L^2 & scEI/L \\ \bar{s}EI/L^2 & scEI/L & -\bar{s}EI/L^2 & sEI/L \end{bmatrix} \begin{matrix} \leftarrow \theta_a'' \\ \leftarrow \theta_b'' \end{matrix} \tag{23}$$

Once the $\mathbf{k}_i'^T$ matrix in Eq. 23 is derived, the $\mathbf{k}_i'$ matrix can be written as:

$$\mathbf{k}_i' = \begin{bmatrix} M_{a1} & M_{b1} \\ M_{a2} & M_{b2} \\ M_{a3} & M_{b3} \\ M_{a4} & M_{b4} \end{bmatrix} = \begin{bmatrix} \bar{s}EI/L^2 & \bar{s}EI/L^2 \\ sEI/L & scEI/L \\ -\bar{s}EI/L^2 & -\bar{s}EI/L^2 \\ scEI/L & sEI/L \end{bmatrix} \begin{matrix} \leftarrow v(0) \\ \leftarrow v'(0) \\ \leftarrow v(L) \\ \leftarrow v'(L) \end{matrix} \tag{24}$$

2.3 *Element Stiffness Matrix* $[\mathbf{k}_i'']$

The element stiffness matrix $\mathbf{k}_i''$ relates the moments at the PHLs 'a' and 'b' with a corresponding unit plastic rotation at each of these PHLs of the ith member. To determine the $\mathbf{k}_i''$ matrix, the goal is to compute the plastic hinge moments M_{aa}, M_{ab}, M_{ba}, and M_{bb} as shown in Fig. 3.

The moments computed in the process of determining the 4×2 $\mathbf{k}_i'$ matrix shown in Eq. 24 can be used to calculate the element stiffness matrix $\mathbf{k}_i''$. For example, the first column of the $\mathbf{k}_i'$ matrix in Eq. 24 represents the shears ($V_{near} = M_{a1} = \bar{s}EI/L^2$ and $V_{far} = M_{a3} = -\bar{s}EI/L^2$) and moments ($M_{a2} = sEI/L$ and $M_{a4} = scEI/L$) at the two ends of the member due to a unit plastic rotation at PHL 'a', as shown in Fig. 3. Similarly, the second column of the $\mathbf{k}_i'$ matrix in Eq. 24 represents the shears ($V_{near} = M_{b1} = \bar{s}EI/L^2$ and $V_{far} = M_{b3} = -\bar{s}EI/L^2$) and moments ($M_{b2} = scEI/L$ and $M_{b4} = sEI/L$) at the two ends of the member due to a unit plastic rotation at PHL 'b', as shown in Fig. 3. Then the plastic hinge moments M_{aa}, M_{ab}, M_{ba}, and M_{bb} at the PHLs for each of the two cases (i.e., 'a' and 'b') can be evaluated as:

Case '*a*' of Fig. 3: Imposing a unit plastic rotation $\theta_a'' = 1$ and $\theta_b'' = 0$ gives

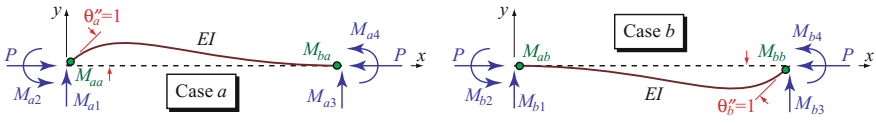

Fig. 3 Displacement patterns for computation of moments due to unit plastic rotations

$$M_{aa} = M_{a2} = sEI/L, \quad M_{ba} = M_{a4} = scEI/L \tag{25}$$

Case '*b*' of Fig. 3: Imposing a unit plastic rotation $\theta''_a = 0$ and $\theta''_b = 1$ gives

$$M_{ab} = M_{b2} = scEI/L, \quad M_{bb} = M_{b4} = sEI/L \tag{26}$$

Therefore, from Eqs. 25 and 26, the element stiffness matrix $\mathbf{k}''_i$ for the ith member becomes

$$\mathbf{k}''_i = \begin{bmatrix} sEI/L & scEI/L \\ scEI/L & sEI/L \end{bmatrix} \begin{matrix} \leftarrow \theta''_a \\ \leftarrow \theta''_b \end{matrix} \tag{27}$$

3 Global Stiffness Matrices

By using the element stiffness matrices computed in Eqs. 18, 24, and 27, the assembly of these matrices into the global stiffness matrices $\mathbf{K}$, $\mathbf{K}'$, and $\mathbf{K}''$ is a straightforward procedure; many textbooks (e.g., [11, 13, 14]) have discussed this procedure in great detail. The procedure is to map each DOFs and PHLs of the element stiffness matrices to the corresponding DOFs and PHLs of the global stiffness matrices. Consider a framed structure having a total of n DOFs and m PHLs, the resulting global stiffness matrices can then be obtained and are often written in the form:

$$\mathbf{K} = \left[\textit{Collection of } \mathbf{k}_i \right]_{n\times n} \begin{matrix} \leftarrow DOF\ \#1 \\ \vdots \\ \leftarrow DOF\ \#n \end{matrix} \tag{28a}$$

$$\mathbf{K}' = \left[\textit{Collection of } \mathbf{k}'_i \right]_{n\times m} \begin{matrix} \leftarrow DOF\ \#1 \\ \vdots \\ \leftarrow DOF\ \#n \end{matrix} \tag{28b}$$

$$\mathbf{K}'' = \left[\textit{Collection of } \mathbf{K}''_i \right]_{m\times m} \begin{matrix} \leftarrow PHL\ \#1 \\ \vdots \\ \leftarrow PHL\ \#m \end{matrix} \tag{28c}$$

However, consistencies of the global stiffness matrices depend on the consistencies of the element stiffness matrices, and therefore it is worth spending the effort to investigate the properties of the element stiffness matrix $\mathbf{k}_i$ computed in Eq. 18 and its relationship with the global stiffness matrix $\mathbf{K}$ in Eq. (28a).

The element stiffness matrix $\mathbf{k}_i$ is obtained by solving the fourth order differential equation, and therefore it is the exact solution based on small displacement theory. It is a nonlinear relationship with sine and cosine functions of the axial compressive force P, and it is capable of capturing both large $P-\Delta$ (i.e., geometric nonlinearity due to sidesway of the member) and small $P-\delta$ (i.e., geometric nonlinearity due to local deformation of the member) effects. One can perform Taylor series expansion of Eq. 18 with respect to P and then truncating the higher-order terms. Doing so gives

$$\mathbf{k}_{i(GS)} = \frac{EI}{L^3}\begin{bmatrix} 12 & 6L & -12 & 6L \\ 6L & 4L^2 & -6L & 2L^2 \\ -12 & -6L & 12 & -6L \\ 6L & 2L^2 & -6L & 4L^2 \end{bmatrix} + \frac{P}{L}\begin{bmatrix} -6/5 & -L/10 & 6/5 & -L/10 \\ -L/10 & -2L^2/15 & L/10 & L^2/30 \\ 6/5 & L/10 & -6/5 & L/10 \\ -L/10 & L^2/30 & L/10 & -2L^2/15 \end{bmatrix} \tag{29}$$

where $\mathbf{k}_{i(GS)}$ is commonly known as the second-order geometric stiffness of the member, with the first term representing the initial elastic stiffness matrix and the second term representing the geometric stiffness matrix. Since $\mathbf{k}_{i(GS)}$ is obtained by Taylor series expansion, both large $P-\Delta$ and small $P-\delta$ effects are also captured in this formulation.

Further simplification of Eq. 29 can be performed by ignoring the small $P-\delta$ effect, and the resulting element stiffness matrix becomes

$$\mathbf{k}_{i(P\Delta)} = \frac{EI}{L^3}\begin{bmatrix} 12 & 6L & -12 & 6L \\ 6L & 4L^2 & -6L & 2L^2 \\ -12 & -6L & 12 & -6L \\ 6L & 2L^2 & -6L & 4L^2 \end{bmatrix} + \frac{P}{L}\begin{bmatrix} -1 & 0 & 1 & 0 \\ 0 & 0 & 0 & 0 \\ 1 & 0 & -1 & 0 \\ 0 & 0 & 0 & 0 \end{bmatrix} \tag{30}$$

where $\mathbf{k}_{i(P\Delta)}$ is here known as the $P-\Delta$ stiffness of the member. While geometric nonlinearity due to sidesway can be captured using $\mathbf{k}_{i(P\Delta)}$ in Eq. 30, the magnification of response due to local deformation with an axial compressive force is totally ignored in one element model. But the $P-\delta$ effect of local deformation can be captured using several element $P-\Delta$ stiffnesses by subdividing the member into several elements in the model. The following example presents a simple illustration on the improvement of accuracy of $P-\Delta$ stiffness by subdividing a member into three elements. It also illustrates the consistencies of using stability functions in the formulation and the lack of consistencies in other element stiffness formulations.

Consider a member of length $3L$ with elastic modulus E and moment of inertia I subjected to an axial compressive force $P = 0.3 \times EI/L^2$ as shown in Fig. 4. No boundary condition needs to be applied to the member because only the element stiffness matrix is considered. Following Eqs. 18, 29, and 30, different forms of element stiffness matrices $\mathbf{k}_i$ using one long element with length $3L$ in the model with DOFs #1 to #4 can be written as

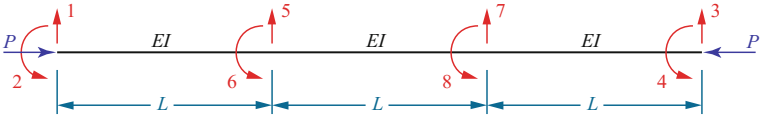

Fig. 4 Member subdivided into three elements

$$\mathbf{k}_{i(SF)} = \frac{EI}{L^3}\begin{bmatrix} 0.32405 & 0.63607L & -0.32405 & 0.63607L \\ 0.63607L & 1.20883L^2 & -0.63607L & 0.69938L^2 \\ -0.32405 & -0.63607L & 0.32405 & -0.63607L \\ 0.63607L & 0.69938L^2 & -0.63607L & 1.20883L^2 \end{bmatrix} \begin{matrix} \leftarrow \text{DOF\#1} \\ \leftarrow \text{DOF\#2} \\ \leftarrow \text{DOF\#3} \\ \leftarrow \text{DOF\#4} \end{matrix} \tag{31a}$$

$$\mathbf{k}_{i(GS)} = \frac{EI}{L^3}\begin{bmatrix} 0.32444 & 0.63667L & -0.32444 & 0.63667L \\ 0.63667L & 1.21333L^2 & -0.63667L & 0.69667L^2 \\ -0.32444 & -0.63667L & 0.32444 & -0.63667L \\ 0.63667L & 0.69667L^2 & -0.63667L & 1.21333L^2 \end{bmatrix} \begin{matrix} \leftarrow \text{DOF\#1} \\ \leftarrow \text{DOF\#2} \\ \leftarrow \text{DOF\#3} \\ \leftarrow \text{DOF\#4} \end{matrix} \tag{31b}$$

$$\mathbf{k}_{i(P\Delta)} = \frac{EI}{L^3}\begin{bmatrix} 0.34444 & 0.66667L & -0.34444 & 0.66667L \\ 0.66667L & 1.33333L^2 & -0.66667L & 0.66667L^2 \\ -0.34444 & -0.66667L & 0.34444 & -0.66667L \\ 0.66667L & 0.66667L^2 & -0.66667L & 1.33333L^2 \end{bmatrix} \begin{matrix} \leftarrow \text{DOF\#1} \\ \leftarrow \text{DOF\#2} \\ \leftarrow \text{DOF\#3} \\ \leftarrow \text{DOF\#4} \end{matrix} \tag{31c}$$

where $\mathbf{k}_{i(SF)}$ is the same as $\mathbf{k}_i$ in Eq. 18 but with the subscript '*SF*' added to denote that it is computed using the stability function method.

Now assume that the same member is subdivided into three elements of equal lengths L. The element stiffness matrices $\mathbf{k}_i$ with geometric nonlinearity for each of the three members are formulated, then by assembling each term into the global stiffness matrices according to DOFs #1 to #8 as labeled in Fig. 4, the final global stiffness matrices $\mathbf{K}_{SF}$, $\mathbf{K}_{GS}$, and $\mathbf{K}_{P\Delta}$ can be written as

$$\mathbf{K}_{SF} = \frac{EI}{L^3}\left[\begin{array}{cccc:cccc} 11.64 & 5.97L & 0 & 0 & -11.64 & 5.97L & 0 & 0 \\ 5.97L & 3.96L^2 & 0 & 0 & -5.97L & 2.01L^2 & 0 & 0 \\ 0 & 0 & 11.64 & -5.97L & 0 & 0 & -11.64 & -5.97L \\ 0 & 0 & -5.97L & 3.96L^2 & 0 & 0 & 5.97L & 2.01L^2 \\ \hdashline -11.64 & -5.97L & 0 & 0 & 23.28 & 0 & -11.64 & 5.97L \\ 5.97L & 2.01L^2 & 0 & 0 & 0 & 7.92L^2 & -5.97L & 2.01L^2 \\ 0 & 0 & -11.64 & 5.97L & -11.64 & -5.97L & 23.28 & 0 \\ 0 & 0 & -5.97L & 2.01L^2 & 5.97L & 2.01L^2 & 0 & 7.92L^2 \end{array}\right] \tag{32a}$$

$$\mathbf{K}_{GS} = \frac{EI}{L^3}\left[\begin{array}{cccc:cccc} 11.64 & 5.97L & 0 & 0 & -11.64 & 5.97L & 0 & 0 \\ 5.97L & 3.96L^2 & 0 & 0 & -5.97L & 2.01L^2 & 0 & 0 \\ 0 & 0 & 11.64 & -5.97L & 0 & 0 & -11.64 & -5.97L \\ 0 & 0 & -5.97L & 3.96L^2 & 0 & 0 & 5.97L & 2.01L^2 \\ \hdashline -11.64 & -5.97L & 0 & 0 & 23.28 & 0 & -11.64 & 5.97L \\ 5.97L & 2.01L^2 & 0 & 0 & 0 & 7.92L^2 & -5.97L & 2.01L^2 \\ 0 & 0 & -11.64 & 5.97L & -11.64 & -5.97L & 23.28 & 0 \\ 0 & 0 & -5.97L & 2.01L^2 & 5.97L & 2.01L^2 & 0 & 7.92L^2 \end{array}\right] \tag{32b}$$

$$\mathbf{K}_{P\Delta} = \frac{EI}{L^3}\left[\begin{array}{cccc:cccc} 11.7 & 6L & 0 & 0 & -11.7 & 6L & 0 & 0 \\ 6L & 4L^2 & 0 & 0 & -6L & 2L^2 & 0 & 0 \\ 0 & 0 & 11.7 & -6L & 0 & 0 & -11.7 & -6L \\ 0 & 0 & -6L & 4L^2 & 0 & 0 & 6L & 2L^2 \\ \hdashline -11.7 & -6L & 0 & 0 & 23.4 & 0 & -11.7 & 6L \\ 6L & 2L^2 & 0 & 0 & 0 & 8L^2 & -6L & 2L^2 \\ 0 & 0 & -11.7 & 6L & -11.7 & -6L & 23.4 & 0 \\ 0 & 0 & -6L & 2L^2 & 6L & 2L^2 & 0 & 8L^2 \end{array}\right] \begin{array}{l} \leftarrow \text{DOF\#1} \\ \leftarrow \text{DOF\#2} \\ \leftarrow \text{DOF\#3} \\ \leftarrow \text{DOF\#4} \\ \leftarrow \text{DOF\#5} \\ \leftarrow \text{DOF\#6} \\ \leftarrow \text{DOF\#7} \\ \leftarrow \text{DOF\#8} \end{array} \tag{32c}$$

where $\mathbf{K}_{SF}$, $\mathbf{K}_{GS}$, and $\mathbf{K}_{P\Delta}$ are the global stiffness matrices computed using the stability function method, geometric stiffness method, and $P-\Delta$ stiffness method, respectively.

Static condensation is now used to eliminate DOFs #5 to #8 from the global stiffness matrices in Eqs. 32a–32c based on the equation

$$\mathbf{K} = \left[\begin{array}{c:c} \mathbf{K}_{11} & \mathbf{K}_{12} \\ \hdashline \mathbf{K}_{21} & \mathbf{K}_{22} \end{array}\right] \quad , \quad \overline{\mathbf{K}} = \mathbf{K}_{11} - \mathbf{K}_{12}\mathbf{K}_{22}^{-1}\mathbf{K}_{21} \tag{33}$$

where $\mathbf{K}_{11}$, $\mathbf{K}_{12}$, $\mathbf{K}_{21}$, and $\mathbf{K}_{22}$ are submatrices partitioned according to the dotted lines of those full stiffness matrices shown in Eqs. 32a–32c and 33, and $\overline{\mathbf{K}}$ represents the condensed global stiffness matrix. It can be seen that each of these submatrices is a 4×4 matrix, with subscript '2' denoting DOFs #5 to #8 to be eliminated and subscript '1' denoting DOFs #1 to #4 to remain after condensation. Now substituting these submatrices presented in Eqs. 32a–32c into Eq. 33 and performing the matrix multiplications gives

$$\overline{\mathbf{K}}_{SF} = \frac{EI}{L^3}\left[\begin{array}{cccc} 0.32405 & 0.63607L & -0.32405 & 0.63607L \\ 0.63607L & 1.20883L^2 & -0.63607L & 0.69938L^2 \\ -0.32405 & -0.63607L & 0.32405 & -0.63607L \\ 0.63607L & 0.69938L^2 & -0.63607L & 1.20883L^2 \end{array}\right] \begin{array}{l} \leftarrow \text{DOF\#1} \\ \leftarrow \text{DOF\#2} \\ \leftarrow \text{DOF\#3} \\ \leftarrow \text{DOF\#4} \end{array} \tag{34a}$$

$$\overline{\mathbf{K}}_{GS} = \frac{EI}{L^3}\begin{bmatrix} 0.32410 & 0.63615L & -0.32410 & 0.63615L \\ 0.63615L & 1.20899L^2 & -0.63615L & 0.69945L^2 \\ -0.32410 & -0.63615L & 0.32410 & -0.63615L \\ 0.63615L & 0.69945L^2 & -0.63615L & 1.20899L^2 \end{bmatrix} \begin{matrix} \leftarrow \text{DOF\#1} \\ \leftarrow \text{DOF\#2} \\ \leftarrow \text{DOF\#3} \\ \leftarrow \text{DOF\#4} \end{matrix} \tag{34b}$$

$$\overline{\mathbf{K}}_{P\Delta} = \frac{EI}{L^3}\begin{bmatrix} 0.33429 & 0.65143L & -0.33429 & 0.65143L \\ 0.65143L & 1.24030L^2 & -0.65143L & 0.71399L^2 \\ -0.33429 & -0.65143L & 0.33429 & -0.65143L \\ 0.65143L & 0.71399L^2 & -0.65143L & 1.24030L^2 \end{bmatrix} \begin{matrix} \leftarrow \text{DOF\#1} \\ \leftarrow \text{DOF\#2} \\ \leftarrow \text{DOF\#3} \\ \leftarrow \text{DOF\#4} \end{matrix} \tag{34c}$$

Comparing the stiffness matrices in Eqs. 31a–31c using one-element formulation with those in Eqs. 34a–34c using three-element formulation shows that only the stability functions approach gives exactly the same stiffness matrix regardless of whether one long element is used or three subdivided elements are used (i.e., $\mathbf{k}_{i(SF)} = \overline{\mathbf{K}}_{SF}$, but $\mathbf{k}_{i(GS)} \approx \overline{\mathbf{K}}_{GS}$ and $\mathbf{k}_{i(P\Delta)} \neq \overline{\mathbf{K}}_{P\Delta}$). This indicates that while all three geometric nonlinearity approaches address large $P{-}\Delta$ appropriately, only the stability functions approach consistently captures the small $P{-}\delta$ effect. Note that the difference between $\mathbf{k}_{i(P\Delta)}$ in Eq. 31c and $\mathbf{k}_{i(SF)}$ in Eq. 31a is quite significant, but the difference becomes smaller when $\overline{\mathbf{K}}_{P\Delta}$ in Eq. 34c is compared to $\overline{\mathbf{K}}_{SF}$ in Eq. 34a. This indicates that capturing small $P{-}\delta$ effect using the $P{-}\Delta$ stiffness matrix is possible by subdividing the member into several elements, but it also indicates that subdividing into three elements at an axial compressive force of $P = 0.3 \times EI/L^2$ is insufficient to capture the small $P{-}\delta$ effect using the $P{-}\Delta$ stiffness matrix only.

4 Nonlinear Static Analysis of Framed Structures

Once the global stiffness matrices $\mathbf{K}$, $\mathbf{K}'$, and $\mathbf{K}''$ in Eqs. 28a–28c are assembled from the element stiffness matrices $\mathbf{k}_i$, $\mathbf{k}'_i$, and $\mathbf{k}''_i$ in Eqs. 18, 24, and 27, respectively, they can be used to perform static analysis of moment-resisting framed structures with both geometric and material nonlinearities. For the structure modeled as a multi-degree of freedom (MDOF) system, the derivation of the analysis procedure begins with the concept of inelastic displacements. Considering a structure having n DOFs, the displacement can be written in vector form as

$$\mathbf{x} = \mathbf{x}' + \mathbf{x}'' = \begin{Bmatrix} x'_1 \\ x'_2 \\ \vdots \\ x'_n \end{Bmatrix} + \begin{Bmatrix} x''_1 \\ x''_2 \\ \vdots \\ x''_n \end{Bmatrix} \tag{35}$$

where $\mathbf{x}$ represents the total displacement vector, $\mathbf{x}'$ is the elastic displacement vector, and $\mathbf{x}''$ is the inelastic displacement vector. For moment-resisting framed structures, let the total moment vector $\mathbf{M}$ at the plastic hinge locations (PHLs) be described in vector form as

$$\mathbf{M} = \mathbf{M}' + \mathbf{M}'' = \begin{Bmatrix} M_1' \\ M_2' \\ \vdots \\ M_m' \end{Bmatrix} + \begin{Bmatrix} M_1'' \\ M_2'' \\ \vdots \\ M_m'' \end{Bmatrix} \tag{36}$$

where $\mathbf{M}'$ is the elastic moment vector due to elastic displacement $\mathbf{x}'$, and $\mathbf{M}''$ is the inelastic moment vector due to inelastic displacement $\mathbf{x}''$ that is caused by plastic rotations. The value m represents the total number of PHLs in the moment-resisting frame.

4.1 Residual Components Due to Plastic Rotations

Consider first the inelastic moment vector $\mathbf{M}''$ that is caused by plastic rotations in the moment-resisting frame. Define the plastic rotation vector $\boldsymbol{\Theta}''$ as

$$\boldsymbol{\Theta}'' = \begin{Bmatrix} \theta_1'' \\ \theta_2'' \\ \vdots \\ \theta_m'' \end{Bmatrix} \tag{37}$$

An example of having plastic rotations developed at two PHLs of the ith member is shown in Fig. 5a. This state of the structure can never exist because this member violates either the compatibility or the equilibrium condition with the adjacent joints. Without any force applied to this member, it should remain straight, yet the plastic rotations induce incompatibility with the adjacent joints that have no rotation. On the other hand, if the member is deformed in a compatible way with the adjacent joint, forces must be applied to this member resulting in violation of the equilibrium condition of the joint. To ensure the member deforms in a compatible way with the rest of the structure while satisfying the equilibrium condition, this member with plastic rotations $\boldsymbol{\Theta}''$ is first isolated from the structure and restoring forces are applied to restore this member back to the original undeformed shape, as shown in Fig. 5b. This induces internal restoring forces $\mathbf{F}_{RF}$ and the fixed-end shears and moments on the member. At the global degree of freedom level, the restoring force is an $n \times 1$ vector of the form:

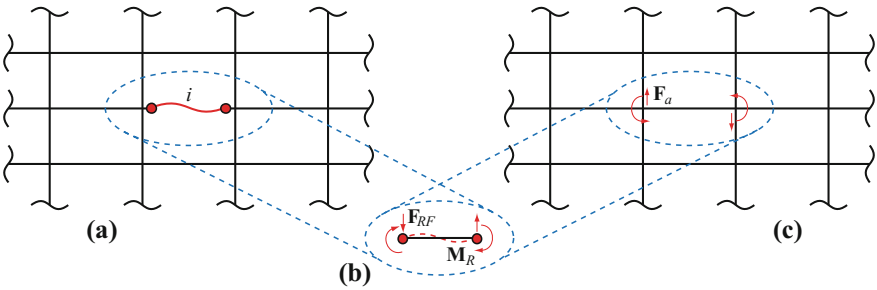

Fig. 5 Satisfying compatibility and equilibrium conditions in nonlinear static analysis

$$\mathbf{F}_{RF} = \begin{Bmatrix} F_{RF1} \\ F_{RF2} \\ \vdots \\ F_{RFn} \end{Bmatrix} = -\mathbf{K}'\boldsymbol{\Theta}'' \tag{38}$$

where $\mathbf{K}'$ is the $n \times m$ assembled global stiffness matrix defined in Eq. 28b. In addition to the restoring forces $\mathbf{F}_{RF}$ that are applied at the global DOFs, plastic rotations $\boldsymbol{\Theta}''$ induce residual moments $\mathbf{M}_R$ at the PHLs as shown in Fig. 5b. At the local PHL, the residual moment is an $m \times 1$ vector in the form:

$$\mathbf{M}_R = \begin{Bmatrix} M_{R,1} \\ M_{R,2} \\ \vdots \\ M_{R,m} \end{Bmatrix} = -\mathbf{K}''\boldsymbol{\Theta}'' \tag{39}$$

where $\mathbf{K}''$ is the $m \times m$ global stiffness matrix defined in Eq. 28c. The minus signs appear in Eqs. 38 and 39 because negative actions must be applied in order to rotate a positive plastic rotation back to zero, which results in negative restoring forces and negative residual moments.

Now the member is assembled back into the structure and the deformation of this *i*th member is compatible with the rest of the structure. However, the restoring forces $\mathbf{F}_{RF}$ as shown in Fig. 5b are actually not present globally as shown in Fig. 5a, and as a result equal and opposite forces $\mathbf{F}_a = -\mathbf{F}_{RF}$ must be applied to the structure's DOFs to cancel these restoring forces, as shown in Fig. 5c. Substituting Eq. 38 into the equation gives

$$\mathbf{F}_a = -\mathbf{F}_{RF} = \mathbf{K}'\boldsymbol{\Theta}'' \tag{40}$$

Applying the equivalent forces $\mathbf{F}_a$ results in a permanent deformation of the structure, which is exactly the inelastic displacement $\mathbf{x}''$. The relationship can be obtained through conducting the matrix structural analysis for MDOF systems as:

$$\mathbf{F}_a = \mathbf{K}\mathbf{x}'' \tag{41}$$

where $\mathbf{K}$ is the $n \times n$ global stiffness matrix defined in Eq. 28a. Through this process, the structure remains in equilibrium in addition to being compatible. Equating $\mathbf{F}_a$ in both Eqs. 40 and 41 and solving for the inelastic displacements $\mathbf{x}''$ gives

$$\mathbf{x}'' = \mathbf{K}^{-1}\mathbf{K}'\boldsymbol{\Theta}'' \tag{42}$$

Due to the induced equivalent forces $\mathbf{F}_a$, which produce inelastic displacements $\mathbf{x}''$ in the structure, additional moments are also induced at the PHLs. Denoting this induced moment vector as $\mathbf{M}_P$, it is related to the inelastic displacement $\mathbf{x}''$ by the equation

$$\mathbf{M}_P = \mathbf{K}'^T\mathbf{x}'' \tag{43}$$

where $\mathbf{K}'^T$ is the transpose of the $\mathbf{K}'$ matrix in Eq. 28b. Then substituting Eq. 42 into Eq. 43 gives

$$\mathbf{M}_P = \mathbf{K}'^T\mathbf{K}^{-1}\mathbf{K}'\boldsymbol{\Theta}'' \tag{44}$$

Finally, the inelastic moment vector $\mathbf{M}''$ at the PHLs in Fig. 5a is determined by summing the residual moments $\mathbf{M}_R$ at the PHLs shown in Fig. 5b and the induced moments $\mathbf{M}_P$ shown in Fig. 5c, i.e.,

$$\mathbf{M}'' = \mathbf{M}_R + \mathbf{M}_P \tag{45}$$

Substituting Eqs. 39 and 44 into Eq. 45 gives the equation for inelastic moments $\mathbf{M}''$ as a function of plastic rotations $\boldsymbol{\Theta}''$:

$$\mathbf{M}'' = -\left(\mathbf{K}'' - \mathbf{K}'^T\mathbf{K}^{-1}\mathbf{K}'\right)\boldsymbol{\Theta}'' \tag{46}$$

Equations 42 and 46 represent the inelastic displacement and inelastic moment vectors due to the plastic rotations within the structure with no externally applied force. This can be interpreted as the case when an earthquake causes plastic rotations within the structure, then the inelastic displacements represent the permanent deformation (or sometimes known as the residual drift) of the structure and inelastic moments represent the forces remaining in the members after the earthquake motion subsides.

4.2 *Elastic Components Due to Elastic Displacements*

Now consider the relationship between the elastic moments $\mathbf{M}'$ and the elastic displacements $\mathbf{x}'$ due to the external applied static load $\mathbf{F}_o$. Similar to Eq. 41 where

the inelastic displacements $\mathbf{x}''$ are due to the application of the induced equivalent loads $\mathbf{F}_a$, the elastic displacements $\mathbf{x}'$ of the structure are the result of applying the external static loads $\mathbf{F}_o$. Again by using the matrix structural analysis for multi-degree of freedom systems, the external static loads $\mathbf{F}_o$ are related to the elastic displacements $\mathbf{x}'$ through the $n \times n$ global stiffness matrix $\mathbf{K}$, i.e.,

$$\mathbf{F}_o = \mathbf{K}\mathbf{x}' \tag{47}$$

Similarly from Eq. 43, where the induced moments $\mathbf{M}_P$ are related to the inelastic displacements $\mathbf{x}''$ due to the application of the induced equivalent load $\mathbf{F}_a$, the elastic moments $\mathbf{M}'$ are related to the elastic displacements $\mathbf{x}'$ through the $\mathbf{K}'^T$ matrix, i.e.,

$$\mathbf{M}' = \mathbf{K}'^T\mathbf{x}' \tag{48}$$

4.3 Analysis Procedure Using Total Responses

Once the elastic and inelastic portions of the structures are characterized, the objective now is to apply Eqs. 35 and 36 and represent the analytical procedure using the total displacements $\mathbf{x}$, total moments $\mathbf{M}$, plastic rotation $\boldsymbol{\Theta}''$, and the external applied static load $\mathbf{F}_o$. Equation 35 is first considered by solving for the elastic displacements $\mathbf{x}'$, i.e., $\mathbf{x}' = \mathbf{x} - \mathbf{x}''$, and substituting this result into Eqs. 47 and 48 gives

$$\mathbf{F}_o = \mathbf{K}[\mathbf{x} - \mathbf{x}''], \quad \mathbf{M}' = \mathbf{K}'^T[\mathbf{x} - \mathbf{x}''] \tag{49}$$

Then substituting the inelastic displacements $\mathbf{x}''$ in Eq. 42 into Eq. 49 gives

$$\mathbf{F}_o = \mathbf{K}\left[\mathbf{x} - \mathbf{K}^{-1}\mathbf{K}'\boldsymbol{\Theta}''\right], \quad \mathbf{M}' = \mathbf{K}'^T\left[\mathbf{x} - \mathbf{K}^{-1}\mathbf{K}'\boldsymbol{\Theta}''\right] \tag{50}$$

Simplifying the first equation of Eq. 50 gives

$$\mathbf{F}_o = \mathbf{K}\mathbf{x} - \mathbf{K}'\boldsymbol{\Theta}'' \tag{51}$$

Now based on Eq. 36, the total moment vector $\mathbf{M}$ at all the PHLs is calculated by substituting the elastic moments $\mathbf{M}'$ in Eq. 50 and the inelastic moments $\mathbf{M}''$ in Eq. 46 in the equation. Doing so gives

$$\mathbf{M} = \mathbf{M}' + \mathbf{M}'' = \mathbf{K}'^T\left[\mathbf{x} - \mathbf{K}^{-1}\mathbf{K}'\boldsymbol{\Theta}''\right] - \left[\mathbf{K}'' - \mathbf{K}'^T\mathbf{K}^{-1}\mathbf{K}'\right]\boldsymbol{\Theta}'' = \mathbf{K}'^T\mathbf{x} - \mathbf{K}''\boldsymbol{\Theta}'' \tag{52}$$

Combining Eqs. 51 and 52 gives the governing equation of the analysis procedure for solving nonlinear static problems:

$$\left[\begin{array}{c|c} \mathbf{K} & \mathbf{K}' \\ \hline \mathbf{K}'^{T} & \mathbf{K}'' \end{array}\right]\left\{\begin{array}{c} \mathbf{x} \\ \hline -\boldsymbol{\Theta}'' \end{array}\right\}=\left\{\begin{array}{c} \mathbf{F}_o \\ \hline \mathbf{M} \end{array}\right\} \tag{53}$$

Equation 53 shows both the $n \times 1$ total displacement vector $\mathbf{x}$ (n unknowns for the DOFs) and the $m \times 1$ plastic rotation vector $\boldsymbol{\Theta}''$ (m unknowns for the PHLs) make up the unknown vector that is typically required to be solved in the nonlinear structural analysis problem. However, because material nonlinearity is involved in this equation, the solution requires performing an iterative procedure. To illustrate this iterative procedure, the goal is to solve for the unknowns $\mathbf{x}$, $\boldsymbol{\Theta}''$, and $\mathbf{M}$ for any applied static force pattern $\mathbf{F}_o$. This adds up to a total of $n+2m$ unknowns, and therefore the solution requires $n+2m$ equations provided as follows:

- Equation 53 by itself gives $n+m$ independent equations that satisfy both global equilibrium and compatibility conditions.
- Each plastic hinge contains its own moment versus plastic rotation relationship, which gives additional m equations that follows the local hysteretic behavior of the plastic hinges.

Using these $n+2m$ equations, the $n+2m$ unknowns (i.e., $\mathbf{x}$, $\boldsymbol{\Theta}''$, and $\mathbf{M}$) in Eq. 53 can be solved uniquely. Once these unknowns are calculated, the inelastic displacements $\mathbf{x}''$ can be determined using Eq. 42. This completes the calculations for the nonlinear static analysis.

4.4 Implementation of the Analysis Procedure with Updates to Geometric Nonlinearity

The following example is used to illustrate the procedure for statically analyzing moment-resisting framed structure with geometric and material nonlinearities. Consider a one-story one-bay moment-resisting steel frame shown in Fig. 6. Assume that axial deformation is ignored for all three members, this results in a system with 3 DOFs $(n=3)$ and 6 PHLs $(m=6)$ as labeled in the figure. Also assume that a lateral force of F_o is applied at x_1. This gives $F_1 = F_o$ and $F_2 = F_3 = 0$, and therefore

$$\mathbf{F}_o = \left\{\begin{array}{c} F_1 \\ F_2 \\ F_3 \end{array}\right\} = \left\{\begin{array}{c} F_o \\ 0 \\ 0 \end{array}\right\} \tag{54}$$

Let the gravity load on the frame be $P = 890$ kN and the lengths of the members be $L_b = 6.10$ m and $L_c = 4.27$ m. For W14 $\times$ 82 columns, the cross-sectional area

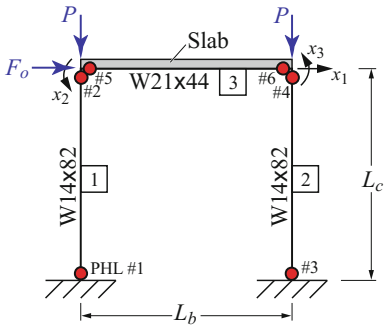

Fig. 6 One-story one-bay moment-resisting steel frame

is $A_c = 15,500$ mm^2, the moment of inertia is $I_c = 3.67 \times 10^8$ mm^4, and the plastic section modulus is $Z_c = 2,278,000$ mm^3. For the W21 × 44 beam, the moment of inertia is $I_b = 3.47 \times 10^8$ mm^4, and the plastic section modulus is $Z_b = 1,876,000$ mm^3, while the cross-sectional area of the beam is not used in the calculation. A elastic modulus of $E = 200$ GPa and a yield stress of $f_Y = 248$ MPa for steel are used.

Since the axial force in Member 1 (denoted as P_1) will be different from that of Member 2 (denoted as P_2) due to overturning induced by the lateral applied force F_o, the resulting stability coefficients will be different as well. The axial force in Member 3 is assumed to be negligible (i.e., $P_3 \approx 0$) due to the presence of slab. Therefore, let

$$\lambda_1 = \sqrt{P_1/EI_c} \times L_c, \quad \lambda_2 = \sqrt{P_2/EI_c} \times L_c \tag{55}$$

It follows that the global stiffness matrices for this one-story frame become:

$$\mathbf{K} = \begin{bmatrix} s_1' EI_c/L_c^3 + s_2' EI/L_c^3 & \bar{s}_1 EI_c/L_c^2 & \bar{s}_2 EI_c/L_c^2 \\ \bar{s}_1 EI_c/L_c^2 & s_1 EI_c/L_c + 4EI_b/L_b & 2EI_b/L_b \\ \bar{s}_2 EI_c/L_c^2 & 2EI_b/L_b & s_2 EI_c/L_c + 4EI_b/L_b \end{bmatrix} \begin{matrix} \leftarrow x_1 \\ \leftarrow x_2 \\ \leftarrow x_3 \end{matrix} \tag{56a}$$

$$\mathbf{K}' = \left[\begin{array}{cc|cc|cc} \bar{s}_1 EI_c/L_c^2 & \bar{s}_1 EI_c/L_c^2 & \bar{s}_2 EI_c/L_c^2 & \bar{s}_2 EI_c/L_c^2 & 0 & 0 \\ s_1 c_1 EI_c/L_c & s_1 EI_c/L_c & 0 & 0 & 4EI_b/L_b & 2EI_b/L_b \\ 0 & 0 & s_2 c_2 EI_c/L_c & s_2 EI_c/L_c & 2EI_b/L_b & 4EI_b/L_b \end{array}\right] \begin{matrix} \leftarrow x_1 \\ \leftarrow x_2 \\ \leftarrow x_3 \end{matrix} \tag{56b}$$

$$\mathbf{K}'' = \left[\begin{array}{cc|cc|cc} s_1 EI_c/L_c & s_1 c_1 EI_c/L_c & 0 & 0 & 0 & 0 \\ s_1 c_1 EI_c/L_c & s_1 EI_c/L_c & 0 & 0 & 0 & 0 \\ \hline 0 & 0 & s_2 EI_c/L_c & s_2 c_2 EI_c/L_c & 0 & 0 \\ 0 & 0 & s_2 c_2 EI_c/L_c & s_2 EI_c/L_c & 0 & 0 \\ \hline 0 & 0 & 0 & 0 & 4EI_b/L_b & 2EI_b/L_b \\ 0 & 0 & 0 & 0 & 2EI_b/L_b & 4EI_b/L_b \end{array}\right] \begin{matrix} \leftarrow \theta_1'' \\ \leftarrow \theta_2'' \\ \leftarrow \theta_3'' \\ \leftarrow \theta_4'' \\ \leftarrow \theta_5'' \\ \leftarrow \theta_6'' \end{matrix} \tag{56c}$$

where s_1, c_1, $\bar{s}_1$, and s_1' are the stability coefficients of Member 1 as functions of λ_1 and P_1, and s_2, c_2, $\bar{s}_2$, and s_2' are the stability coefficients of Member 2 as functions of λ_2 and P_2. Then Eq. 53 becomes

$$\left[\begin{array}{c|c} \mathbf{K}(3\times3) & \mathbf{K}'(3\times6) \\ \hline \mathbf{K}'^{T}(6\times3) & \mathbf{K}''(6\times6) \end{array}\right] \left\{\begin{array}{c} x_1 \\ x_2 \\ x_3 \\ \hline -\theta_1'' \\ -\theta_2'' \\ -\theta_3'' \\ -\theta_4'' \\ -\theta_5'' \\ -\theta_6'' \end{array}\right\} = \left\{\begin{array}{c} F_o \\ 0 \\ 0 \\ \hline M_1 \\ M_2 \\ M_3 \\ M_4 \\ M_5 \\ M_6 \end{array}\right\} \tag{57}$$

The yielding characteristics of each plastic hinge must also be defined. Assume the material exhibits elastic-plastic behavior, and an elliptical yield surface is used with the interaction between axial force and moment of the column and beam members following the relationships:

$$\text{Columns}: \left(\frac{P_k}{f_Y A_c}\right)^2 + \left(\frac{M_k}{f_Y Z_c}\right)^2 \le 1, \quad k = 1, \ldots, 4 \tag{58a}$$

$$\text{Beam}: \left|\frac{M_k}{f_Y Z_b}\right| \le 1, \quad k = 5, 6 \tag{58b}$$

Following Eqs. 58a, 58b, this gives the moment versus plastic rotation relationships for the 6 PHLs as

$$\text{if} \begin{cases} M_k \le M_{Yc,k} \\ M_k > M_{Yc,k} \end{cases}, \quad \text{then} \quad \begin{cases} \theta_k'' = 0 \\ M_k = M_{Yc,k} \end{cases} \quad i = 1, 2, 3, 4 \tag{59a}$$

$$\text{if} \begin{cases} M_i \le f_Y Z_b \\ M_i > f_Y Z_b \end{cases}, \quad \text{then} \quad \begin{cases} \theta_i'' = 0 \\ M_i = f_Y Z_b \end{cases} \quad i = 5, 6 \tag{59b}$$

where $M_{Yc,k}$ is the moment capacity of the kth column plastic hinge computed based on a specified axial compressive force and the yield surface equation given in Eq. 58a.

To demonstrate the nonlinear static analysis procedure using the currently proposed improved method, a pushover curve is now constructed for the frame by taking the following steps.

Step U1: The frame is initially assumed to respond in the linearly elastic range i.e., $\theta_1'' = \theta_2'' = \theta_3'' = \theta_4'' = \theta_5'' = \theta_6'' = 0$. At an applied force of $F_o = 414.8$ kN and $P_1 = P_2 = 890$ kN, extracting the first three equations of Eq. 57 gives

$$\begin{bmatrix} 22145 & 24069 & 24069 \\ 24069 & 114253 & 23017 \\ 24069 & 23017 & 114253 \end{bmatrix} \begin{Bmatrix} x_1 \\ x_2 \\ x_3 \end{Bmatrix} = \begin{Bmatrix} 414.8 \\ 0 \\ 0 \end{Bmatrix} \tag{60}$$

Solving for the displacements at the DOFs gives

$$x_1 = 0.0303\,\text{m}, \quad x_2 = x_3 = -0.00531\,\text{rad} \tag{61}$$

Then substituting the results in Eq. 61 back into the last six equations of Eq. 57 gives the moments

$$\begin{Bmatrix} M_1 \\ M_2 \\ M_3 \\ M_4 \\ M_5 \\ M_6 \end{Bmatrix} = \begin{bmatrix} 24069 & 34491 & 0 \\ 24069 & 68219 & 0 \\ 24069 & 0 & 34491 \\ 24069 & 0 & 68219 \\ 0 & 46034 & 23017 \\ 0 & 23017 & 46034 \end{bmatrix} \begin{Bmatrix} 0.0303 \\ -0.00531 \\ -0.00531 \end{Bmatrix} = \begin{Bmatrix} 545.5 \\ 366.5 \\ 545.5 \\ 366.5 \\ -366.5 \\ -366.5 \end{Bmatrix} \tag{62}$$

Based on the setup of the frame as shown in Fig. 5, the column axial forces are determined by computing the shear forces at the two ends of the beam member by using equilibrium of the beam and directly transfer to the columns, i.e.,

$$P_1 = P + (M_5 + M_6)/L_b = 890 + (-366.5 - 366.5)/6.10 = 769\,\text{kN} \tag{63a}$$

$$P_2 = P - (M_5 + M_6)/L_b = 890 - (-366.5 - 366.5)/6.10 = 1010\,\text{kN} \tag{63b}$$

Then using Eq. 59a to check for yielding at PHLs #1 and #3 gives

$$\text{PHL } \#1: \ (769/3843)^2 + (545.5/565.4)^2 = 0.971 \tag{64a}$$

$$\text{PHL } \#3: \ (1010/3843)^2 + (545.5/565.4)^2 = 1.000 \tag{64b}$$

which indicates that PHL #3 reaches its yield surface, where any additional loading will cause yielding at this plastic hinge.

Step U2: The analysis continues with PHL #3 yielded, i.e., $\theta_1'' = \theta_2'' = \theta_4'' = \theta_5'' = \theta_6'' = 0$. The lateral force is applied up to $F_o = 418.7$ kN. Rows 1, 2, 3, and 6 are extracted from Eq. 57 with updated geometric nonlinearity based on the column axial forces obtained in Eqs. 63a, 63b:

$$\left[\begin{array}{ccc:c} 22145 & 24082 & 24057 & 24057 \\ 24082 & 114322 & 23017 & 0 \\ 24057 & 23017 & 114184 & 34508 \\ \hdashline 24057 & 0 & 34508 & 68150 \end{array}\right] \left\{\begin{array}{c} x_1 \\ x_2 \\ x_3 \\ \hdashline -\theta_3'' \end{array}\right\} = \left\{\begin{array}{c} 418.7 \\ 0 \\ 0 \\ \hdashline 545.5 \end{array}\right\} \tag{65}$$

Solving for the displacements at the DOFs and plastic rotations in Eq. 65 gives

$$x_1 = 0.0307\,\text{m}, \quad x_2 = -0.00540\,\text{rad}, \quad x_3 = -0.00535\,\text{rad}, \quad \theta_3'' = 0.00014\,\text{rad} \tag{66}$$

Then substituting the results in Eq. 66 back into the last six equations of Eq. 57 gives the moments

$$\begin{Bmatrix} M_1 \\ M_2 \\ M_3 \\ M_4 \\ M_5 \\ M_6 \end{Bmatrix} = \left[\begin{array}{cccc:c} 24082 & 34473 & 0 & 0 \\ 24082 & 68288 & 0 & 0 \\ 24057 & 0 & 34508 & 68150 \\ 24057 & 0 & 68150 & 34508 \\ 0 & 46034 & 23017 & 0 \\ 0 & 23017 & 46034 & 0 \end{array}\right] \left\{\begin{array}{c} 0.0307 \\ -0.00540 \\ -0.00535 \\ \hdashline -0.00014 \end{array}\right\} = \begin{Bmatrix} 554.0 \\ 371.5 \\ 545.5 \\ 370.3 \\ -371.5 \\ -370.3 \end{Bmatrix} \tag{67}$$

and the column axial forces are updated as

$$P_1 = P + (M_5 + M_6)/L_b = 890 + (-371.5 - 370.3)/6.10 = 768\,\text{kN} \tag{68a}$$

$$P_2 = P - (M_5 + M_6)/L_b = 890 - (-371.5 - 370.3)/6.10 = 1011\,\text{kN} \tag{68b}$$

Then using Eq. 59a to check for yielding at PHLs #1 and #3 gives

$$\text{PHL } \#1: \ (768/3843)^2 + (554.0/565.4)^2 = 1.000 \tag{69a}$$

$$\text{PHL } \#3: \ (1011/3843)^2 + (545.5/565.4)^2 = 1.000 \tag{69b}$$

which indicates that PHL #1 reaches its capacity and PHL #3 continues yielding at this step.

Step U3: The analysis continues with PHLs #1 and #3 yielded, i.e., $\theta_2'' = \theta_4'' = \theta_5'' = \theta_6'' = 0$. The lateral force is applied up to $F_o = 457.0$ kN. Rows 1, 2, 3, 4, and 6 are extracted from Eq. 57 with updated geometric nonlinearity based on the column axial forces obtained in Eqs. 68a, 68b:

$$\left[\begin{array}{ccc:cc} 22145 & 24082 & 24057 & 24082 & 24057 \\ 24082 & 114323 & 23017 & 34473 & 0 \\ 24057 & 23017 & 114183 & 0 & 34508 \\ \hdashline 24082 & 34473 & 0 & 68289 & 0 \\ 24057 & 0 & 34508 & 0 & 68150 \end{array}\right] \left\{\begin{array}{c} x_1 \\ x_2 \\ x_3 \\ \hdashline -\theta_1'' \\ -\theta_3'' \end{array}\right\} = \left\{\begin{array}{c} 457.0 \\ 0 \\ 0 \\ \hdashline 554.0 \\ 545.5 \end{array}\right\} \tag{70}$$

Solving for the displacements at the DOFs and plastic rotations in Eq. 70 gives

$$x_1 = 0.0445\,\text{m}, \quad x_2 = -0.00676\,\text{rad}, \quad x_3 = -0.00671\,\text{rad}$$

$$\theta_1'' = 0.00415\,\text{rad}, \quad \theta_3'' = 0.00429\,\text{rad} \tag{71}$$

Then substituting the results in Eq. 71 back into the last six equations of Eq. 57 gives the moments

$$\begin{Bmatrix} M_1 \\ M_2 \\ M_3 \\ M_4 \\ M_5 \\ M_6 \end{Bmatrix} = \left[\begin{array}{ccc:cc:c} 24082 & 34473 & 0 & 68289 & 0 & \\ 24082 & 68289 & 0 & 34473 & 0 & \\ 24057 & 0 & 34508 & 0 & 68150 & \\ 24057 & 0 & 68150 & 0 & 34508 & \\ 0 & 46034 & 23017 & 0 & 0 & \\ 0 & 23017 & 46034 & 0 & 0 & \end{array}\right] \left\{\begin{array}{c} 0.0445 \\ -0.00676 \\ -0.00671 \\ \hdashline -0.00415 \\ -0.00429 \end{array}\right\} = \begin{Bmatrix} 553.9 \\ 465.6 \\ 545.4 \\ 464.3 \\ -465.6 \\ -464.3 \end{Bmatrix} \tag{72}$$

At this point, the moment at PHL #5 reaches its capacity of $f_Y Z_b = 465.6$ kN-m, and the column axial forces are updated as

$$P_1 = P + (M_5 + M_6)/L_b = 890 + (-465.6 - 464.3)/6.10 = 737\,\text{kN} \tag{73a}$$

$$P_2 = P - (M_5 + M_6)/L_b = 890 - (-465.6 - 464.3)/6.10 = 1042\,\text{kN} \tag{73b}$$

Step U4: The analysis continues with PHLs #1, #3, and #5 yielded, i.e., $\theta_2'' = \theta_4'' = \theta_6'' = 0$. The lateral force is applied up to $F_o = 457.1$ kN. Rows 1, 2, 3, 4, 6, and 8 are extracted from Eq. 57 with updated geometric nonlinearity based on the column axial forces obtained in Eqs. 73a, 73b:

$$\left[\begin{array}{ccc:ccc} 22145 & 24085 & 24054 & 24085 & 24054 & 0 \\ 24085 & 114340 & 23017 & 34469 & 0 & 46034 \\ 24054 & 23017 & 114166 & 0 & 34513 & 23017 \\ \hdashline 24085 & 34469 & 0 & 68306 & 0 & 0 \\ 24054 & 0 & 34513 & 0 & 68132 & 0 \\ 0 & 46034 & 23017 & 0 & 0 & 46034 \end{array}\right] \left\{\begin{array}{c} x_1 \\ x_2 \\ x_3 \\ \hdashline -\theta_1'' \\ -\theta_3'' \\ -\theta_5'' \end{array}\right\} = \left\{\begin{array}{c} 457.1 \\ 0 \\ 0 \\ \hdashline 553.9 \\ 545.4 \\ -465.6 \end{array}\right\} \tag{74}$$

Solving for the displacements at the DOFs and plastic rotations in Eq. 70 gives

$$x_1 = 0.0448\,\text{m}, \quad x_2 = -0.00685\,\text{rad}, \quad x_3 = -0.00674\,\text{rad}$$

$$\theta_1'' = 0.00421\,\text{rad}, \quad \theta_3'' = 0.00441\,\text{rad}, \quad \theta_5'' = -0.00011\,\text{rad} \tag{75}$$

Then substituting the results in Eq. 75 back into the last six equations of Eq. 57 gives the moments

$$\begin{Bmatrix} M_1 \\ M_2 \\ M_3 \\ M_4 \\ M_5 \\ M_6 \end{Bmatrix} = \left[\begin{array}{ccc:ccc} 24085 & 34469 & 0 & 68306 & 0 & 0 \\ 24085 & 68306 & 0 & 34469 & 0 & 0 \\ 24054 & 0 & 34513 & 0 & 68134 & 0 \\ 24054 & 0 & 68132 & 0 & 34513 & 0 \\ 0 & 46034 & 23017 & 0 & 0 & 46034 \\ 0 & 23017 & 46034 & 0 & 0 & 23017 \end{array}\right] \left\{\begin{array}{c} 0.0448 \\ -0.00685 \\ -0.00674 \\ -0.00421 \\ -0.00441 \\ 0.00011 \end{array}\right\} = \begin{Bmatrix} 554.9 \\ 465.6 \\ 544.2 \\ 465.6 \\ -465.6 \\ -465.6 \end{Bmatrix} \tag{76}$$

At this point, the moment at PHL #6 reaches its capacity of $f_Y Z_b = 465.6$ kN-m, and the column axial forces are updated as

$$P_1 = P + (M_5 + M_6)/L_b = 890 + (-465.6 - 465.6)/6.10 = 737\,\text{kN} \tag{77a}$$

$$P_2 = P - (M_5 + M_6)/L_b = 890 - (-465.6 - 465.6)/6.10 = 1042\,\text{kN} \tag{77b}$$

Step U5: Now that a mechanism has developed with the formation of plastic hinges at PHLs #1, #3, #5, and #6, the frame will continue to deflect without any additional load. But as the displacement increases, the gravity loads of $P = 890$ kN cause an increase in column moments due to P−Δ effect, resulting in a reduction of the amount of lateral load that can be withstood by the frame. This effect can be captured easily in the current analysis procedure. Let the analysis continue with PHLs #1, #3, #5, and #6 yielded, i.e., $\theta_2'' = \theta_4'' = 0$. By using any applied lateral force less than $F_o = 457.1$ kN (from Step U4) to capture the lateral load reduction, say $F_o = 434.1$ kN, Rows 1, 2, 3, 4, 6, 8, and 9 are extracted from Eq. 57 with updated geometric nonlinearity based on the column axial forces obtained in Eqs. 77a, 77b:

$$\left[\begin{array}{ccc:ccc:c} 22145 & 24085 & 24054 & 24085 & 24054 & 0 & 0 \\ 24085 & 114340 & 23017 & 34469 & 0 & 46034 & 23017 \\ 24054 & 23017 & 114165 & 0 & 34513 & 23017 & 46034 \\ \hdashline 24085 & 34469 & 0 & 68307 & 0 & 0 & 0 \\ 24054 & 0 & 34513 & 0 & 68132 & 0 & 0 \\ 0 & 46034 & 23017 & 0 & 0 & 46034 & 23017 \\ 0 & 23017 & 46034 & 0 & 0 & 23017 & 46034 \end{array}\right] \left\{\begin{array}{c} x_1 \\ x_2 \\ x_3 \\ \hdashline -\theta_1'' \\ -\theta_3'' \\ -\theta_5'' \\ -\theta_6'' \end{array}\right\} = \left\{\begin{array}{c} 434.1 \\ 0 \\ 0 \\ \hdashline 554.9 \\ 544.2 \\ -465.6 \\ -465.6 \end{array}\right\} \tag{78}$$

Solving for the displacements at the DOFs and plastic rotations in Eq. 78 gives

$$x_1 = 0.1000\,\text{m}, \quad x_2 = -0.01979\,\text{rad}, \quad x_3 = -0.01968\,\text{rad}$$

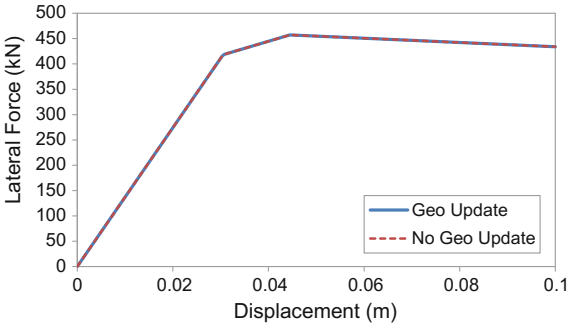

Fig. 7 Comparison of pushover curves with and without updates to geometric nonlinearity

$$\theta_1'' = 0.01715\,\text{rad}, \quad \theta_3'' = 0.01735\,\text{rad}, \quad \theta_5'' = -0.01305\,\text{rad}, \quad \theta_6'' = -0.01294\,\text{rad} \tag{79}$$

Then substituting the results in Eq. 79 back into the last six equations of Eq. 57 gives the moments

$$\begin{Bmatrix} M_1 \\ M_2 \\ M_3 \\ M_4 \\ M_5 \\ M_6 \end{Bmatrix} = \left[\begin{array}{ccc:ccc} 24085 & 34469 & 0 & 68307 & 0 & 0 & 0 \\ 24085 & 68307 & 0 & 34469 & 0 & 0 & 0 \\ 24054 & 0 & 34513 & 0 & 68132 & 0 & 0 \\ 24054 & 0 & 68132 & 0 & 34513 & 0 & 0 \\ 0 & 46034 & 23017 & 0 & 0 & 46034 & 23017 \\ 0 & 23017 & 46034 & 0 & 0 & 23017 & 46034 \end{array}\right] \begin{Bmatrix} 0.1000 \\ -0.01979 \\ -0.01968 \\ -0.01715 \\ -0.01735 \\ 0.01305 \\ 0.01294 \end{Bmatrix} = \begin{Bmatrix} 554.9 \\ 465.6 \\ 544.2 \\ 465.6 \\ -465.6 \\ -465.6 \end{Bmatrix} \tag{80}$$

and the column axial forces remain as

$$P_1 = P + (M_5 + M_6)/L_b = 890 + (-465.6 - 465.6)/6.10 = 737\,\text{kN} \tag{81a}$$

$$P_2 = P - (M_5 + M_6)/L_b = 890 - (-465.6 - 465.6)/6.10 = 1042\,\text{kN} \tag{81b}$$

Finally, the pushover curve can be plotted as shown in Fig. 7 for the case where geometric nonlinearity are updated due to the change in axial forces in the columns.

4.5 *Implementation of the Analysis Procedure with no Update to Geometric Nonlinearity*

As shown in Eqs. 60, 65, 70, 74, and 78, it is observed that the first entry to the stiffness matrices remain at 22,145 kN/m even when there are changes to the column axial forces. This suggests that a reduction in stiffness due to an increase in

axial force in Column 2 is offset by an increase in stiffness due to a reduction in axial force in Column 1, as presented in the stiffness matrix in Eq. 56a. Therefore, it may be interesting to investigate the differences in response when geometric nonlinearity is updated at every step of the analysis or not.

Now consider the case where geometric nonlinearity is not updated when there is a change in the column axial forces. This is achieved by using constant stiffness matrices $\mathbf{K}$, $\mathbf{K}'$, and $\mathbf{K}''$ in Eq. 57 that are computed based on the initial column axial forces throughout the analysis. By using the same one-story frame as shown in Fig. 6 with column axial loads of $P_1 = P_2 = 890$ kN, Eq. 57 becomes

$$\left[\begin{array}{ccc:ccc:cc:cc} 22145 & 24069 & 24069 & 24069 & 24069 & 24069 & 24069 & 0 & 0 \\ 24069 & 114253 & 23017 & 34491 & 68219 & 0 & 0 & 46034 & 23017 \\ 24069 & 23017 & 114253 & 0 & 0 & 34491 & 68219 & 23017 & 46034 \\ \hdashline 24069 & 34491 & 0 & 68219 & 34491 & 0 & 0 & 0 & 0 \\ 24069 & 68219 & 0 & 34491 & 68219 & 0 & 0 & 0 & 0 \\ 24069 & 0 & 34491 & 0 & 0 & 68219 & 34491 & 0 & 0 \\ 24069 & 0 & 68219 & 0 & 0 & 34491 & 68219 & 0 & 0 \\ 0 & 46034 & 23017 & 0 & 0 & 0 & 0 & 46034 & 23017 \\ 0 & 23017 & 46034 & 0 & 0 & 0 & 0 & 23017 & 46034 \end{array}\right] \left\{\begin{array}{c} x_1 \\ x_2 \\ x_3 \\ \hdashline -\theta_1'' \\ -\theta_2'' \\ -\theta_3'' \\ -\theta_4'' \\ -\theta_5'' \\ -\theta_6'' \end{array}\right\} = \left\{\begin{array}{c} F_o \\ 0 \\ 0 \\ \hdashline M_1 \\ M_2 \\ M_3 \\ M_4 \\ M_5 \\ M_6 \end{array}\right\} \tag{82}$$

Step N1: The same calculation in Step U1 above can be applied to this step, where $F_o = 414.8$ kN and $x_1 = 0.0303$ m. The moment M_3 reaches its moment capacity of 545.5 kN-m and the axial forces in the columns are $P_1 = 769$ kN and $P_2 = 1010$ kN.

Step N2: The analysis continues with PHL #3 yielded, i.e., $\theta_1'' = \theta_2'' = \theta_4'' = \theta_5'' = \theta_6'' = 0$. The lateral force is applied up to $F_o = 418.7$ kN. Rows 1, 2, 3, and 6 are extracted from Eq. 82:

$$\left[\begin{array}{ccc:c} 22145 & 24069 & 24069 & 24069 \\ 24069 & 114253 & 23017 & 0 \\ 24069 & 23017 & 114253 & 34491 \\ \hdashline 24069 & 0 & 34491 & 68219 \end{array}\right] \left\{\begin{array}{c} x_1 \\ x_2 \\ x_3 \\ \hdashline -\theta_3'' \end{array}\right\} = \left\{\begin{array}{c} 418.7 \\ 0 \\ 0 \\ \hdashline 545.5 \end{array}\right\} \tag{83}$$

Solving for the displacements at the DOFs and plastic rotations in Eq. 83 gives

$$x_1 = 0.0308\,\text{m}, \quad x_2 = -0.00540\,\text{rad}, \quad x_3 = -0.00534\,\text{rad}, \quad \theta_3'' = 0.00015\,\text{rad} \tag{84}$$

Then substituting the results in Eq. 84 back into the last six equations of Eq. 82 gives the moments

$$\begin{Bmatrix} M_1 \\ M_2 \\ M_3 \\ M_4 \\ M_5 \\ M_6 \end{Bmatrix} = \left[\begin{array}{cccc:c} 24069 & 34491 & 0 & 0 & 0 \\ 24069 & 68219 & 0 & 0 & 0 \\ 24069 & 0 & 34491 & 68219 & 0 \\ 24069 & 0 & 68219 & 34491 & 0 \\ 0 & 46034 & 23017 & 0 & 0 \\ 0 & 23017 & 46034 & 0 & 0 \end{array}\right] \left\{\begin{array}{c} 0.0308 \\ -0.00540 \\ -0.00534 \\ -0.00015 \end{array}\right\} = \begin{Bmatrix} 554.0 \\ 371.7 \\ 545.5 \\ 370.4 \\ -371.7 \\ -370.4 \end{Bmatrix} \tag{85}$$

and the column axial forces are updated as

$$P_1 = P + (M_5 + M_6)/L_b = 890 + (-371.7 - 370.4)/6.10 = 768\,\text{kN} \tag{86a}$$

$$P_2 = P - (M_5 + M_6)/L_b = 890 - (-371.7 - 370.4)/6.10 = 1011\,\text{kN} \tag{86b}$$

Then using Eq. 59a to check for yielding at PHLs #1 and #3 gives

$$\text{PHL } \#1: \ (768/3843)^2 + (554.0/565.4)^2 = 1.000 \tag{87a}$$

$$\text{PHL } \#3: \ (1011/3843)^2 + (545.5/565.4)^2 = 1.000 \tag{87b}$$

which indicates that PHL #1 reaches its capacity and PHL #3 continues yielding at this step.

Step N3: The analysis continues with PHLs #1 and #3 yielded, i.e., $\theta_2'' = \theta_4'' = \theta_5'' = \theta_6'' = 0$. The lateral force is applied up to $F_o = 457.0$ kN. Rows 1, 2, 3, 4, and 6 are extracted from Eq. 82:

$$\left[\begin{array}{ccc:cc} 22145 & 24069 & 24069 & 24069 & 24069 \\ 24069 & 114253 & 23017 & 34491 & 0 \\ 24069 & 23017 & 114253 & 0 & 34491 \\ \hdashline 24069 & 34491 & 0 & 68219 & 0 \\ 24069 & 0 & 34491 & 0 & 68219 \end{array}\right] \left\{\begin{array}{c} x_1 \\ x_2 \\ x_3 \\ \hdashline -\theta_1'' \\ -\theta_3'' \end{array}\right\} = \left\{\begin{array}{c} 457.0 \\ 0 \\ 0 \\ \hdashline 554.0 \\ 545.5 \end{array}\right\} \tag{88}$$

Solving for the displacements at the DOFs and plastic rotations in Eq. 88 gives

$$x_1 = 0.0445\,\text{m}, \quad x_2 = -0.00676\,\text{rad}, \quad x_3 = -0.0670\,\text{rad}$$

$$\theta_1'' = 0.00415\,\text{rad}, \quad \theta_3'' = 0.00430\,\text{rad} \tag{89}$$

Then substituting the results in Eq. 89 back into the last six equations of Eq. 82 gives the moments

$$\begin{Bmatrix} M_1 \\ M_2 \\ M_3 \\ M_4 \\ M_5 \\ M_6 \end{Bmatrix} = \left[\begin{array}{ccc:cc:c} 24069 & 34491 & 0 & 68219 & 0 & \\ 24069 & 68219 & 0 & 34491 & 0 & \\ 24069 & 0 & 34491 & 0 & 68219 & \\ 24069 & 0 & 68219 & 0 & 34491 & \\ 0 & 46034 & 23017 & 0 & 0 & \\ 0 & 23017 & 46034 & 0 & 0 & \end{array}\right] \left\{\begin{array}{c} 0.0445 \\ -0.00676 \\ -0.00670 \\ \hdashline -0.00415 \\ -0.00430 \end{array}\right\} = \begin{Bmatrix} 553.9 \\ 465.6 \\ 545.4 \\ 464.3 \\ -465.6 \\ -464.3 \end{Bmatrix} \tag{90}$$

At this point, the moment at PHL #5 reaches its capacity of $f_Y Z_b = 465.6$ kN-m, and the column axial forces are updated as

$$P_1 = P + (M_5 + M_6)/L_b = 890 + (-465.6 - 464.3)/6.10 = 737\,\text{kN} \tag{91a}$$

$$P_2 = P - (M_5 + M_6)/L_b = 890 - (-465.6 - 464.3)/6.10 = 1042\,\text{kN} \tag{91b}$$

Step N4: The analysis continues with PHLs #1, #3, and #5 yielded, i.e., $\theta_2'' = \theta_4'' = \theta_6'' = 0$. The lateral force is applied up to $F_o = 457.1$ kN. Rows 1, 2, 3, 4, 6, and 8 are extracted from Eq. 82:

$$\left[\begin{array}{ccc:ccc} 22145 & 24069 & 24069 & 24069 & 24069 & 0 \\ 24069 & 114253 & 23017 & 34491 & 0 & 46034 \\ 24069 & 23017 & 114253 & 0 & 34491 & 23017 \\ \hdashline 24069 & 34491 & 0 & 68219 & 0 & 0 \\ 24069 & 0 & 34491 & 0 & 68219 & 0 \\ 0 & 46034 & 23017 & 0 & 0 & 46034 \end{array}\right] \left\{\begin{array}{c} x_1 \\ x_2 \\ x_3 \\ \hdashline -\theta_1'' \\ -\theta_3'' \\ -\theta_5'' \end{array}\right\} = \left\{\begin{array}{c} 457.1 \\ 0 \\ 0 \\ \hdashline 553.9 \\ 545.4 \\ -465.6 \end{array}\right\} \tag{92}$$

Solving for the displacements at the DOFs and plastic rotations in Eq. 92 gives

$$x_1 = 0.0448\,\text{m}, \quad x_2 = -0.00685\,\text{rad}, \quad x_3 = -0.00674\,\text{rad}$$

$$\theta_1'' = 0.00420\,\text{rad}, \quad \theta_3'' = 0.00442\,\text{rad}, \quad \theta_5'' = -0.00011\,\text{rad} \tag{93}$$

Then substituting the results in Eq. 93 back into the last six equations of Eq. 82 gives the moments

$$\begin{Bmatrix} M_1 \\ M_2 \\ M_3 \\ M_4 \\ M_5 \\ M_6 \end{Bmatrix} = \left[\begin{array}{ccc:ccc} 24069 & 34491 & 0 & 68219 & 0 & 0 \\ 24069 & 68219 & 0 & 34491 & 0 & 0 \\ 24069 & 0 & 34491 & 0 & 68219 & 0 \\ 24069 & 0 & 68219 & 0 & 34491 & 0 \\ 0 & 46034 & 23017 & 0 & 0 & 46034 \\ 0 & 23017 & 46034 & 0 & 0 & 23017 \end{array}\right] \left\{\begin{array}{c} 0.0448 \\ -0.00685 \\ -0.00674 \\ \hdashline -0.00420 \\ -0.00442 \\ 0.00011 \end{array}\right\} = \begin{Bmatrix} 554.9 \\ 465.6 \\ 544.2 \\ 465.6 \\ -465.6 \\ -465.6 \end{Bmatrix} \tag{94}$$

At this point, the moment at PHL #6 reaches its capacity of $f_Y Z_b = 465.6$ kN-m, and the column axial forces are updated as

$$P_1 = P + (M_5 + M_6)/L_b = 890 + (-465.6 - 465.6)/6.10 = 737\,\text{kN} \quad (95a)$$

$$P_2 = P - (M_5 + M_6)/L_b = 890 - (-465.6 - 465.6)/6.10 = 1042\,\text{kN} \quad (95b)$$

Step N5: Now that a mechanism has developed with the formation of plastic hinges at PHLs #1, #3, #5, and #6, the frame will continue to deflect without any additional load. Let the analysis continue with PHLs #1, #3, #5, and #6 yielded, i.e., $\theta_2'' = \theta_4'' = 0$. By using any applied lateral force less than $F_o = 457.1$ kN (from Step N4), say $F_o = 434.1$ kN, Rows 1, 2, 3, 4, 6, 8, and 9 are extracted from Eq. 82:

$$\left[\begin{array}{ccc:cccc} 22145 & 24069 & 24069 & 24069 & 24069 & 0 & 0 \\ 24069 & 114253 & 23017 & 34491 & 0 & 46034 & 23017 \\ 24069 & 23017 & 114253 & 0 & 34491 & 23017 & 46034 \\ \hdashline 24069 & 34491 & 0 & 68219 & 0 & 0 & 0 \\ 24069 & 0 & 34491 & 0 & 68219 & 0 & 0 \\ 0 & 46034 & 23017 & 0 & 0 & 46034 & 23017 \\ 0 & 23017 & 46034 & 0 & 0 & 23017 & 46034 \end{array}\right] \left\{\begin{array}{c} x_1 \\ x_2 \\ x_3 \\ \hdashline -\theta_1'' \\ -\theta_3'' \\ -\theta_5'' \\ -\theta_6'' \end{array}\right\} = \left\{\begin{array}{c} 434.1 \\ 0 \\ 0 \\ \hdashline 554.9 \\ 544.2 \\ -465.6 \\ -465.6 \end{array}\right\} \quad (96)$$

Solving for the displacements at the DOFs and plastic rotations in Eq. 96 gives

$$x_1 = 0.1000\,\text{m}, \quad x_2 = -0.01979\,\text{rad}, \quad x_3 = -0.01968\,\text{rad}$$

$$\theta_1'' = 0.01714\,\text{rad}, \quad \theta_3'' = 0.01735\,\text{rad}, \quad \theta_5'' = -0.01305\,\text{rad}, \quad \theta_6'' = -0.01294\,\text{rad} \quad (97)$$

Then substituting the results in Eq. 97 back into the last six equations of Eq. 57 gives the moments

Table 1 Comparison of plastic rotations with and without updates to geometric nonlinearity

Step	Plastic rotation (rad) with geo update				Plastic rotation (rad) with no update			
	PHL #1	PHL #3	PHL #5	PHL #6	PHL #1	PHL #3	PHL #5	PHL #6
1	0	0	0	0	0	0	0	0
2	0	0.00014	0	0	0	0.00015	0	0
3	0.00415	0.00429	0	0	0.00415	0.00430	0	0
4	0.00421	0.00441	0.00011	0	0.00420	0.00442	0.00011	0
5	0.01715	0.01735	0.01305	0.01294	0.01714	0.01735	0.01305	0.01294

$$\begin{Bmatrix} M_1 \\ M_2 \\ M_3 \\ M_4 \\ M_5 \\ M_6 \end{Bmatrix} = \left[\begin{array}{ccc:ccc:c} 24069 & 34491 & 0 & 68219 & 0 & 0 & 0 \\ 24069 & 68219 & 0 & 34491 & 0 & 0 & 0 \\ 24069 & 0 & 34491 & 0 & 68219 & 0 & 0 \\ 24069 & 0 & 68219 & 0 & 34491 & 0 & 0 \\ 0 & 46034 & 23017 & 0 & 0 & 46034 & 23017 \\ 0 & 23017 & 46034 & 0 & 0 & 23017 & 46034 \end{array}\right] \left\{\begin{array}{c} 0.1000 \\ -0.01979 \\ -0.01968 \\ \hdashline -0.01714 \\ -0.01735 \\ 0.01305 \\ 0.01294 \end{array}\right\} = \begin{Bmatrix} 554.9 \\ 465.6 \\ 544.2 \\ 465.6 \\ -465.6 \\ -465.6 \end{Bmatrix} \quad (98)$$

and the column axial forces remain as

$$P_1 = P + (M_5 + M_6)/L_b = 890 + (-465.6 - 465.6)/6.10 = 737\,\text{kN} \quad (99a)$$

$$P_2 = P - (M_5 + M_6)/L_b = 890 - (-465.6 - 465.6)/6.10 = 1042\,\text{kN} \quad (99b)$$

The pushover curve is plotted as shown in Fig. 7 for the case where the update of stiffness matrix due to geometric nonlinearity is ignored when axial forces in the columns change. It is observed that there is practically no difference in the "global" response between whether geometric nonlinearity due to changes in axial forces in the columns for the one-story frame is updated or not. The reason is that while the induced lateral displacement imposes overturning moment on the entire framed structure, global equilibrium requires that there will be an increase in column compression on one side of the frame and an equal amount of reduction in column compression on the opposite side of the frame in order to resist the imposed overturning moment. While an increase in column compression on one side of the frame reduces the lateral stiffness of these columns, a reduction in column compression on the opposite side of the frame increases the lateral stiffness of those columns by a similar amount. The end result is that the net change in total lateral stiffness of the entire frame becomes negligible, and this can be observed when the stiffness matrix in Eq. 65 (**Step U2**) is compared with that in Eq. 83 (**Step N2**). Similar observations can also be made when the stiffness matrix in Eq. 70 (**Step U3**) is compared with that in Eq. 88 (**Step N3**). Therefore, an assumption to keep the geometrically nonlinear stiffness matrices unchanged throughout the analysis even as loading increases is reasonable, and this is consistent with the recommendation by Wilson [15] that P–Δ analysis method "does not require iteration because the total axial force at a story level is equal to the weight of the building above that level and does not change during the application of lateral loads". This observation is important in nonlinear dynamic analysis of moment-resisting frames because significant computational effort can be reduced with reasonable accuracy by using the approximation of constant geometrically nonlinear stiffness matrices.

Table 1 summarizes the plastic rotation results obtained in the above analysis procedure. It can be seen that the differences in plastic rotations between whether geometric nonlinearity is updated or not updated is negligible. This suggests that there is practically no difference in the "local" response between whether geometric nonlinearity due to changes in axial forces in the columns for the one-story frame is updated or not, even at a drift ratio of 1.6 % (i.e., $0.10/6.10 = 0.0164$).

5 Nonlinear Dynamic Analysis of Framed Structures

In the previous section, the global stiffness matrices incorporating both geometric and material nonlinearities are used to determine the static behavior and plastic rotation response of structures. In this section, the analysis procedure with plastic rotation calculations is extended to nonlinear dynamic analysis. For an n-DOF system subjected to earthquake ground motions, the equation of motion can be written as

$$\mathbf{m}\ddot{\mathbf{x}}(t) + \mathbf{c}\underline{\dot{\mathbf{x}}}(t) + \mathbf{K}(t)\mathbf{x}'(t) = -\mathbf{m}\ddot{\mathbf{g}}(t) - \mathbf{F}_a(t) \tag{100}$$

where $\mathbf{m}$ is the $n \times n$ mass matrix, $\mathbf{c}$ is the $n \times n$ damping matrix, $\dot{\mathbf{x}}(t)$ is the $n \times 1$ velocity vector, $\ddot{\mathbf{x}}(t)$ is the $n \times 1$ acceleration vector, $\mathbf{K}(t)$ is the time-varying $n \times n$ stiffness matrix derived in Eq. 28a while subjected to time-varying column axial compressive forces, $\ddot{\mathbf{g}}(t)$ is the $n \times 1$ earthquake ground acceleration vector corresponding to the effect of ground motion at each DOF, and $\mathbf{F}_a(t)$ is the $n \times 1$ vector of additional forces imposed on the frame due to geometric nonlinearity of all the gravity columns in the structure (mainly the P−Δ effect). This nonlinearity can often be modeled using a leaning column (or sometimes called a P−Δ column) in a two-dimensional analysis but may require more detailed modeling of all gravity columns in a three-dimensional analysis that may affect the response due to torsional irregularity of the structure. In a two-dimensional analysis, the relationship between this lateral force $\mathbf{F}_a(t)$ and the lateral displacement can be written as:

$$\mathbf{F}_a(t) = \mathbf{K}_a\mathbf{x}(t) \tag{101}$$

where $\mathbf{K}_a$ is an $n \times n$ stiffness matrix that is a function of the gravity loads on the leaning column and the corresponding story height, but it is not a function of time. For two-dimensional frames with horizontal degrees of freedom only, this $\mathbf{K}_a$ matrix often takes the form:

$$\mathbf{K}_a = \begin{bmatrix} -Q_1/h_1 - Q_2/h_2 & Q_2/h_2 & 0 & \cdots & 0 \\ Q_2/h_2 & -Q_2/h_2 - Q_3/h_3 & \ddots & \ddots & \vdots \\ 0 & \ddots & \ddots & Q_{n-1}/h_{n-1} & 0 \\ \vdots & \ddots & Q_{n-1}/h_{n-1} & -Q_{n-1}/h_{n-1} - Q_n/h_n & Q_n/h_n \\ 0 & \cdots & 0 & Q_n/h_n & -Q_n/h_n \end{bmatrix} \tag{102}$$

where Q_i is the total axial force due to gravity on the leaning column of the ith floor, and h_i is the story height of the ith floor.

While the lateral force $\mathbf{F}_a(t)$ takes care of the nonlinear geometric effects from all the gravity columns in the structure, the stiffness matrix $\mathbf{K}(t)$ in Eq. 100 considers both large P−Δ and small P−δ effects of geometric nonlinearity on the

moment-resisting frame itself. Let this time-dependent global stiffness matrix $\mathbf{K}(t)$ be represented in the form:

$$\mathbf{K}(t) = \mathbf{K}_L + \mathbf{K}_G(t) \tag{103}$$

where $\mathbf{K}_L$ denotes the linearized elastic stiffness of the frame due to the gravity loads only, and $\mathbf{K}_G(t)$ denotes the change in stiffness due to the change in axial load on members during the dynamic loading. Since the $\mathbf{K}_L$ matrix is computed by using the gravity loads on the columns (which means $\mathbf{K}_L = \mathbf{K}(t_0) = \mathbf{K}(0)$, i.e., the stiffness matrix computed at time step 0) only, it is not a function of time and therefore remains as a constant throughout the dynamic analysis.

The state space method of dynamic analysis uses explicit formulation, which is a desirable method when nonlinearity is involved. Therefore it is used here in the derivation of the analysis procedure. However, it requires that the mass matrix $\mathbf{m}$ in Eq. 100 be invertible. In many practical structural analysis problems, masses at certain DOFs are intentionally set to zero in order to reduce the number of DOFs in the structural model. When the mass is zero at certain DOFs, such as those DOFs related to the vertical translation and joint rotations, the mass matrix in Eq. 100 will become singular and therefore the state space method cannot be readily employed. To overcome this problem with non-invertible (or singular) mass matrix, static condensation is first applied in order to eliminate those DOFs with zero mass or mass moment of inertia before solving the dynamic problem.

5.1 Static Condensation for Nonlinear Dynamic Analysis

Consider a moment-resisting frame with n DOFs and m PHLs as presented in Eq. 100, the equation of motion can be partitioned in the matrix form as

$$\begin{bmatrix} \mathbf{m}_{dd} & \mathbf{0} \\ \mathbf{0} & \mathbf{0} \end{bmatrix} \begin{Bmatrix} \ddot{\mathbf{x}}_d(t) \\ \ddot{\mathbf{x}}_r(t) \end{Bmatrix} + \begin{bmatrix} \mathbf{c}_{dd} & \mathbf{0} \\ \mathbf{0} & \mathbf{0} \end{bmatrix} \begin{Bmatrix} \dot{\mathbf{x}}_d(t) \\ \dot{\mathbf{x}}_r(t) \end{Bmatrix} + \begin{bmatrix} \mathbf{K}_{dd}(t) & \mathbf{K}_{dr}(t) \\ \mathbf{K}_{rd}(t) & \mathbf{K}_{rr}(t) \end{bmatrix} \begin{Bmatrix} \mathbf{x}'_d(t) \\ \mathbf{x}'_r(t) \end{Bmatrix} = -\begin{bmatrix} \mathbf{m}_{dd} & \mathbf{0} \\ \mathbf{0} & \mathbf{0} \end{bmatrix} \begin{Bmatrix} \ddot{\mathbf{g}}_d(t) \\ \mathbf{0} \end{Bmatrix} - \begin{Bmatrix} \mathbf{F}_a(t) \\ \mathbf{0} \end{Bmatrix} \tag{104}$$

where $\mathbf{m}_{dd}$ is the mass matrix associated with DOFs with mass only, $\mathbf{c}_{dd}$ is the damping matrix associated with DOFs with mass only, and $\mathbf{K}_{dd}(t)$, $\mathbf{K}_{dr}(t)$, $\mathbf{K}_{rd}(t)$, and $\mathbf{K}_{rr}(t)$ are the stiffness submatrices partitioned according to the DOFs with mass and those with zero mass. The vector $\mathbf{x}'(t)$ is the elastic displacement response, $\dot{\mathbf{x}}(t)$ is the velocity response, $\ddot{\mathbf{x}}(t)$ is the acceleration response, $\mathbf{F}_a(t)$ is the $d \times 1$ vector of additional forces imposed on the translational DOFs due to geometric nonlinearity of gravity columns, and the earthquake ground acceleration vector $\ddot{\mathbf{g}}_d(t)$ corresponds to the effect of a ground motion on each DOF associated with nonzero mass. The subscript d denotes the number of degrees of freedom that have nonzero mass, and subscript r denotes the number of degrees of freedom that

have zero mass and zero moment of inertia. This gives $n = d + r$ in an n-DOF system.

Equations 52 and 42 related to material nonlinearity can similarly be partitioned as follows:

$$\mathbf{M}(t) + \mathbf{K}''(t)\boldsymbol{\Theta}''(t) = \left[\mathbf{K}'_d(t)^T \;\vdots\; \mathbf{K}'_r(t)^T\right]\left\{\begin{matrix}\mathbf{x}_d(t)\\ \hdashline \mathbf{x}_r(t)\end{matrix}\right\} \tag{105}$$

$$\left\{\begin{matrix}\mathbf{x}''_d(t)\\ \hdashline \mathbf{x}''_r(t)\end{matrix}\right\} = \left[\begin{matrix}\mathbf{K}_{dd}(t) & \vdots & \mathbf{K}_{dr}(t)\\ \hdashline \mathbf{K}_{rd}(t) & \vdots & \mathbf{K}_{rr}(t)\end{matrix}\right]^{-1}\left[\begin{matrix}\mathbf{K}'_d(t)\\ \hdashline \mathbf{K}'_r(t)\end{matrix}\right]\boldsymbol{\Theta}''(t) \tag{106}$$

where

$$\mathbf{K}'(t) = \left[\begin{matrix}\mathbf{K}'_d(t)\\ \hdashline \mathbf{K}'_r(t)\end{matrix}\right] \quad , \quad \mathbf{x}''(t) = \left\{\begin{matrix}\mathbf{x}''_d(t)\\ \hdashline \mathbf{x}''_r(t)\end{matrix}\right\} \quad , \quad \left\{\begin{matrix}\mathbf{x}_d(t)\\ \hdashline \mathbf{x}_r(t)\end{matrix}\right\} = \left\{\begin{matrix}\mathbf{x}'_d(t)\\ \hdashline \mathbf{x}'_r(t)\end{matrix}\right\} + \left\{\begin{matrix}\mathbf{x}''_d(t)\\ \hdashline \mathbf{x}''_r(t)\end{matrix}\right\} \tag{107}$$

Static condensation is now performed on Eq. 104. The second equation of Eq. 104 is extracted and written in the long form as

$$\mathbf{K}_{rd}(t)\mathbf{x}'_d(t) + \mathbf{K}_{rr}(t)\mathbf{x}'_r(t) = \mathbf{0} \tag{108}$$

Solving for $\mathbf{x}'_r(t)$ in Eq. 108 gives

$$\mathbf{x}'_r(t) = -\mathbf{K}_{rr}^{-1}(t)\mathbf{K}_{rd}(t)\mathbf{x}'_d(t) \tag{109}$$

Now substituting Eq. 109 back into the first equation of Eq. 104 gives

$$\begin{aligned}&\mathbf{m}_{dd}\ddot{\mathbf{x}}_d(t) + \mathbf{c}_{dd}\dot{\mathbf{x}}_d(t) + \mathbf{K}_{dd}(t)\mathbf{x}'_d(t) - \mathbf{K}_{dr}(t)\mathbf{K}_{rr}^{-1}(t)\mathbf{K}_{rd}(t)\mathbf{x}'_d(t)\\ &\quad = -\mathbf{m}_{dd}\ddot{\mathbf{g}}_d(t) - \mathbf{F}_a(t)\end{aligned} \tag{110}$$

Define

$$\overline{\mathbf{K}}(t) = \mathbf{K}_{dd}(t) - \mathbf{K}_{dr}(t)\mathbf{K}_{rr}^{-1}(t)\mathbf{K}_{rd}(t) \tag{111}$$

Then Eq. 110 becomes

$$\mathbf{m}_{dd}\ddot{\mathbf{x}}_d(t) + \mathbf{c}_{dd}\dot{\mathbf{x}}_d(t) + \overline{\mathbf{K}}(t)\mathbf{x}'_d(t) = -\mathbf{m}_{dd}\ddot{\mathbf{g}}_d(t) - \mathbf{F}_a(t) \tag{112}$$

which represents the equation of motion in the statically condensed form.

Since Eqs. 105 and 106 contain both DOFs with mass (i.e., $\mathbf{x}_d(t)$ and $\mathbf{x}''_d(t)$) and DOFs without mass (i.e., $\mathbf{x}_r(t)$ and $\mathbf{x}''_r(t)$), static condensation must also be applied to these two equations to reduce the DOFs to those with mass only. Considering Eq. 106 and pre-multiplying both sides of this equation by the stiffness matrix $\mathbf{K}(t)$ gives

$$\left[\begin{matrix}\mathbf{K}_{dd}(t) & \vdots & \mathbf{K}_{dr}(t)\\ \hdashline \mathbf{K}_{rd}(t) & \vdots & \mathbf{K}_{rr}(t)\end{matrix}\right]\left\{\begin{matrix}\mathbf{x}''_d(t)\\ \hdashline \mathbf{x}''_r(t)\end{matrix}\right\} = \left[\begin{matrix}\mathbf{K}'_d\\ \hdashline \mathbf{K}'_r\end{matrix}\right]\boldsymbol{\Theta}''(t) \tag{113}$$

Extracting the second equation of Eq. 113 and solving for $\mathbf{x}''_r(t)$ gives

$$\mathbf{x}_r''(t) = -\mathbf{K}_{rr}^{-1}(t)\mathbf{K}_{rd}(t)\mathbf{x}_d''(t) + \mathbf{K}_{rr}^{-1}(t)\mathbf{K}_r'(t)\boldsymbol{\Theta}''(t) \tag{114}$$

Now substituting Eq. 114 back into the first equation of Eq. 113 gives

$$\mathbf{K}_{dd}(t)\mathbf{x}_d''(t) + \mathbf{K}_{dr}(t)\left[-\mathbf{K}_{rr}^{-1}(t)\mathbf{K}_{rd}(t)\mathbf{x}_d''(t) + \mathbf{K}_{rr}^{-1}(t)\mathbf{K}_r'(t)\boldsymbol{\Theta}''(t)\right] = \mathbf{K}_d'\boldsymbol{\Theta}''(t) \tag{115}$$

and rearranging the terms gives

$$\left[\mathbf{K}_{dd}(t) - \mathbf{K}_{dr}(t)\mathbf{K}_{rr}^{-1}(t)\mathbf{K}_{rd}(t)\right]\mathbf{x}_d''(t) = \left[\mathbf{K}_d'(t) - \mathbf{K}_{dr}(t)\mathbf{K}_{rr}^{-1}(t)\mathbf{K}_r'(t)\right]\boldsymbol{\Theta}''(t) \tag{116}$$

Define

$$\overline{\mathbf{K}}'(t) = \mathbf{K}_d'(t) - \mathbf{K}_{dr}(t)\mathbf{K}_{rr}^{-1}(t)\mathbf{K}_r'(t) \tag{117}$$

Substituting Eqs. 111 and 117 into Eq. 116 gives

$$\overline{\mathbf{K}}(t)\mathbf{x}_d''(t) = \overline{\mathbf{K}}'(t)\boldsymbol{\Theta}''(t) \tag{118}$$

Finally, pre-multiplying both sides of Eq. 118 by the inverse of the condensed global stiffness matrix in Eq. 111 (i.e., $\overline{\mathbf{K}}(t)^{-1}$) gives

$$\mathbf{x}_d''(t) = \overline{\mathbf{K}}(t)^{-1}\overline{\mathbf{K}}'(t)\boldsymbol{\Theta}''(t) \tag{119}$$

which represents the condensed form of Eq. 106.

Finally, considering Eq. 105 and expanding the right hand side this equation gives

$$\mathbf{M}(t) + \mathbf{K}''(t)\boldsymbol{\Theta}''(t) = \mathbf{K}_d'(t)^T\mathbf{x}_d(t) + \mathbf{K}_r'(t)^T\mathbf{x}_r(t) \tag{120}$$

The term $\mathbf{x}_r(t)$ in Eq. 120 must be first calculated. Since $\mathbf{x}_r(t) = \mathbf{x}_r'(t) + \mathbf{x}_r''(t)$ according to Eq. 107, substituting Eqs. 109 and 114 into this equation gives

$$\begin{aligned}\mathbf{x}_r(t) &= \mathbf{x}_r'(t) + \mathbf{x}_r''(t) \\ &= -\mathbf{K}_{rr}^{-1}(t)\mathbf{K}_{rd}(t)\mathbf{x}_d'(t) - \mathbf{K}_{rr}^{-1}(t)\mathbf{K}_{rd}(t)\mathbf{x}_d''(t) + \mathbf{K}_{rr}^{-1}(t)\mathbf{K}_r'(t)\boldsymbol{\Theta}''(t)\end{aligned} \tag{121}$$

Also, since $\mathbf{x}_d'(t) + \mathbf{x}_d''(t) = \mathbf{x}_d(t)$ according to Eq. 107, substituting this equation in Eq. 121 gives

$$\mathbf{x}_r(t) = -\mathbf{K}_{rr}^{-1}(t)\mathbf{K}_{rd}(t)\mathbf{x}_d(t) + \mathbf{K}_{rr}^{-1}(t)\mathbf{K}_r'(t)\boldsymbol{\Theta}''(t) \tag{122}$$

Now substituting Eq. 122 into Eq. 120 and rearranging the terms gives

$$\begin{aligned}\mathbf{M}(t) + \left[\mathbf{K}''(t) - \mathbf{K}_r'(t)^T \mathbf{K}_{rr}^{-1}(t)\mathbf{K}_r'(t)\right] \boldsymbol{\Theta}''(t) \\ = \left[\mathbf{K}_d'(t)^T - \mathbf{K}_r'(t)^T \mathbf{K}_{rr}^{-1}(t)\mathbf{K}_{rd}(t)\right] \mathbf{x}_d(t)\end{aligned} \tag{123}$$

Define

$$\overline{\mathbf{K}}''(t) = \mathbf{K}''(t) - \mathbf{K}_r'(t)^T \mathbf{K}_{rr}^{-1}(t)\mathbf{K}_r'(t) \tag{124}$$

Substituting Eqs. 117 and 124 into Eq. 123 gives

$$\mathbf{M}(t) + \overline{\mathbf{K}}''(t)\boldsymbol{\Theta}''(t) = \overline{\mathbf{K}}'(t)^T \mathbf{x}_d(t) \tag{125}$$

which represents the condensed form of Eq. 105.

5.2 Nonlinear Dynamic Analysis Procedure

By applying static condensation to eliminate the DOFs associated with zero mass and zero mass moment of inertia (i.e., $\mathbf{x}_r(t)$), the resulting equations for nonlinear dynamic analysis are presented in Eqs. 112, 125, and 119, which are rewritten here:

$$\mathbf{m}_{dd}\ddot{\mathbf{x}}_d(t) + \mathbf{c}_{dd}\dot{\mathbf{x}}_d(t) + \overline{\mathbf{K}}(t)\mathbf{x}_d'(t) = -\mathbf{m}_{dd}\ddot{\mathbf{g}}_d(t) - \mathbf{F}_a(t) \tag{126a}$$

$$\mathbf{M}(t) + \overline{\mathbf{K}}''(t)\boldsymbol{\Theta}''(t) = \overline{\mathbf{K}}'(t)^T \mathbf{x}_d(t) \tag{126b}$$

$$\mathbf{x}_d''(t) = \overline{\mathbf{K}}(t)^{-1}\overline{\mathbf{K}}'(t)\boldsymbol{\Theta}''(t) \tag{126c}$$

where according to Eqs. 111, 117, and 124, the statically condensed global stiffness matrices are:

$$\overline{\mathbf{K}}(t) = \mathbf{K}_{dd}(t) - \mathbf{K}_{dr}(t)\mathbf{K}_{rr}^{-1}(t)\mathbf{K}_{rd}(t) \tag{127a}$$

$$\overline{\mathbf{K}}'(t) = \mathbf{K}_d'(t) - \mathbf{K}_{dr}(t)\mathbf{K}_{rr}^{-1}(t)\mathbf{K}_r'(t) \tag{127b}$$

$$\overline{\mathbf{K}}''(t) = \mathbf{K}''(t) - \mathbf{K}_r'(t)^T \mathbf{K}_{rr}^{-1}(t)\mathbf{K}_r'(t) \tag{127c}$$

and Eqs. 101 and 103 can be written in the forms:

$$\mathbf{F}_a(t) = \mathbf{K}_a\mathbf{x}_d(t), \quad \overline{\mathbf{K}}(t) = \overline{\mathbf{K}}_L + \overline{\mathbf{K}}_G(t) \tag{128}$$

where again $\mathbf{K}_a$ denotes the lateral stiffness due to the gravity columns and $\overline{\mathbf{K}}_L$ denotes the linearized elastic stiffness of the moment-resisting frame only. Solving for the elastic displacement $\mathbf{x}_d'(t)$ in Eq. 107 gives $\mathbf{x}_d'(t) = \mathbf{x}_d(t) - \mathbf{x}_d''(t)$, and substituting the result into Eq. 126a gives

$$\mathbf{m}_{dd}\ddot{\mathbf{x}}_d(t) + \mathbf{c}_{dd}\dot{\mathbf{x}}_d(t) + \overline{\mathbf{K}}(t)\mathbf{x}_d(t) = -\mathbf{m}_{dd}\ddot{\mathbf{g}}_d(t) - \mathbf{F}_a(t) + \overline{\mathbf{K}}(t)\mathbf{x}''_d(t) \tag{129}$$

Then substituting Eq. 128 into Eq. 129, the equation of motion after considering both large $P-\Delta$ and small $P-\delta$ effects of geometric nonlinearity of the entire structure becomes

$$\mathbf{m}_{dd}\ddot{\mathbf{x}}_d(t) + \mathbf{c}_{dd}\dot{\mathbf{x}}_d(t) + \overline{\mathbf{K}}_L\mathbf{x}_d(t) = -\mathbf{m}_{dd}\ddot{\mathbf{g}}_d(t) - \mathbf{K}_a\mathbf{x}_d(t) - \overline{\mathbf{K}}_G(t)\mathbf{x}_d(t) + \overline{\mathbf{K}}(t)\mathbf{x}''_d(t) \tag{130}$$

Define

$$\overline{\mathbf{K}}_e = \overline{\mathbf{K}}_L + \mathbf{K}_a \tag{131}$$

where $\overline{\mathbf{K}}_e$ represents the elastic stiffness of the entire structure (i.e., the sum of elastic stiffness of the moment-resisting frame and that of the gravity columns). Substituting Eq. 131 into Eq. 130, it follows that

$$\mathbf{m}_{dd}\ddot{\mathbf{x}}_d(t) + \mathbf{c}_{dd}\dot{\mathbf{x}}_d(t) + \overline{\mathbf{K}}_e\mathbf{x}_d(t) = -\mathbf{m}_{dd}\ddot{\mathbf{g}}_d(t) - \overline{\mathbf{K}}_G(t)\mathbf{x}_d(t) + \overline{\mathbf{K}}(t)\mathbf{x}''_d(t) \tag{132}$$

This equation of motion can now be solved using the state space method. To represent Eq. 132 in state space form, let the state vector $\mathbf{z}(t)$ be defined as

$$\mathbf{z}(t) = \begin{Bmatrix} \mathbf{x}_d(t) \\ \dot{\mathbf{x}}_d(t) \end{Bmatrix} \tag{133}$$

which is a $2d \times 1$ vector with a collection of states of the responses. It follows from Eq. 132 that

$$\begin{aligned} \dot{\mathbf{z}}(t) = \begin{Bmatrix} \dot{\mathbf{x}}_d(t) \\ \ddot{\mathbf{x}}_d(t) \end{Bmatrix} &= \begin{bmatrix} \mathbf{0} & \mathbf{I} \\ -\mathbf{m}_{dd}^{-1}\overline{\mathbf{K}}_e & -\mathbf{m}_{dd}^{-1}\mathbf{c}_{dd} \end{bmatrix} \begin{Bmatrix} \mathbf{x}_d(t) \\ \dot{\mathbf{x}}_d(t) \end{Bmatrix} \\ &+ \begin{bmatrix} \mathbf{0} \\ -\mathbf{h} \end{bmatrix} \mathbf{a}(t) + \begin{bmatrix} \mathbf{0} \\ \mathbf{m}_{dd}^{-1} \end{bmatrix} \left(\overline{\mathbf{K}}_e(t)\mathbf{x}''_d(t) - \overline{\mathbf{K}}_G(t)\mathbf{x}_d(t)\right) \end{aligned} \tag{134}$$

where $\mathbf{h}$ is a $d \times 3$ matrix that relates the directions of each DOF with the global X-, Y-, and Z-directions (i.e., a collection of 0's and 1's in all entries), and $\mathbf{a}(t)$ is the 3×1 ground acceleration vector in the three global directions of $\ddot{g}_X(t)$, $\ddot{g}_Y(t)$, and $\ddot{g}_Z(t)$. The relationship between the ground acceleration vector $\ddot{\mathbf{g}}_d(t)$ for each DOF in Eq. 132 and the three-component ground acceleration vector $\mathbf{a}(t)$ in Eq. 134 can be expressed as

$$\ddot{\mathbf{g}}_d(t) = \mathbf{h}\mathbf{a}(t) = \mathbf{h}\begin{Bmatrix} \ddot{g}_X(t) \\ \ddot{g}_Y(t) \\ \ddot{g}_Z(t) \end{Bmatrix} \tag{135}$$

To simplify Eq. 134, let

$$\mathbf{A} = \begin{bmatrix} \mathbf{0} & \mathbf{I} \\ -\mathbf{m}_{dd}^{-1}\overline{\mathbf{K}}_e & -\mathbf{m}_{dd}^{-1}\mathbf{c}_{dd} \end{bmatrix}, \quad \mathbf{H} = \begin{bmatrix} \mathbf{0} \\ -\mathbf{h} \end{bmatrix}, \quad \mathbf{B} = \begin{bmatrix} \mathbf{0} \\ -\mathbf{m}_{dd}^{-1} \end{bmatrix} \tag{136a}$$

$$\mathbf{f}_G(t) = -\overline{\mathbf{K}}_G(t)\mathbf{x}_d(t), \quad \mathbf{f}_M(t) = \overline{\mathbf{K}}(t)\mathbf{x}_d''(t) \tag{136b}$$

where $\mathbf{A}$ is the $2d \times 2d$ state transition matrix in the continuous form, $\mathbf{H}$ is the $2d \times 3$ ground motion transition matrix in the continuous form, $\mathbf{B}$ is the $2d \times d$ nonlinearity transition matrix in the continuous form, $\mathbf{f}_G(t)$ is the $d \times 1$ equivalent force vector due to geometric nonlinearity, and $\mathbf{f}_M(t)$ is the $d \times 1$ equivalent force vector due to material nonlinearity. Then Eq. 134 becomes

$$\dot{\mathbf{z}}(t) = \mathbf{A}\mathbf{z}(t) + \mathbf{H}\mathbf{a}(t) + \mathbf{B}\mathbf{f}_G(t) + \mathbf{B}\mathbf{f}_M(t) \tag{137}$$

Solving for the first-order linear differential equation in Eq. 137 gives

$$\mathbf{z}(t) = \mathbf{e}^{\mathbf{A}(t-t_o)}\,\mathbf{z}(t_o) + \mathbf{e}^{\mathbf{A}t}\int_{t_o}^{t} \mathbf{e}^{-\mathbf{A}s}[\,\mathbf{H}\mathbf{a}(s) + \mathbf{B}\mathbf{f}_G(s) + \mathbf{B}\mathbf{f}_M(s)]ds \tag{138}$$

where t_o is the time of reference when the integration begins, which is typically the time when the states are known. In a recursive analysis procedure, the known states are often taken at the current time step $\mathbf{z}(t_o)$ and the objective is to calculate the states at the next time step $\mathbf{z}(t)$. Therefore, let $t_{k+1} = t$, $t_k = t_o$, and $\Delta t = t_{k+1} - t_k$, and the subscript k denotes the kth time step, then it follows from Eq. 138 that

$$\mathbf{z}_{k+1} = \mathbf{e}^{\mathbf{A}\Delta t}\,\mathbf{z}_k + \mathbf{e}^{\mathbf{A}t_{k+1}}\int_{t_k}^{t_{k+1}} \mathbf{e}^{-\mathbf{A}s}\,[\mathbf{H}\mathbf{a}(s) + \mathbf{B}\mathbf{f}_G(s) + \mathbf{B}\mathbf{f}_M(s)]\,ds \tag{139}$$

By using the Dirac delta function approximation for the variables in the integral for the purpose of carrying out the integration, the ground acceleration vector $\mathbf{a}(s)$, equivalent geometric nonlinear force vector $\mathbf{f}_G(s)$, and equivalent material nonlinear force vector $\mathbf{f}_M(s)$ take the form:

$$\mathbf{a}(s) = \mathbf{a}_k\delta(s - t_k)\Delta t \quad , \quad t_k \le s < t_{k+1} \tag{140a}$$

$$\mathbf{f}_G(s) = \mathbf{f}_{G,k}\delta(s - t_k)\Delta t \quad , \quad t_k \le s < t_{k+1} \tag{140b}$$

$$\mathbf{f}_M(s) = \mathbf{f}_{M,k}\delta(s - t_k)\Delta t \quad , \quad t_k \le s < t_{k+1} \tag{140c}$$

Substituting Eqs. 140a–140c into Eq. 139 and performing the integration gives

$$\mathbf{z}_{k+1} = \mathbf{e}^{\mathbf{A}\Delta t}\,\mathbf{z}_k + \Delta t\,\mathbf{e}^{\mathbf{A}\Delta t}\mathbf{H}\mathbf{a}_k + \Delta t\,\mathbf{e}^{\mathbf{A}\Delta t}\mathbf{B}\mathbf{f}_{G,k} + \Delta t\,\mathbf{e}^{\mathbf{A}\Delta t}\mathbf{B}\mathbf{f}_{M,k} \tag{141}$$

where $\mathbf{z}_k$, $\mathbf{a}_k$, $\mathbf{f}_{G,k}$, and $\mathbf{f}_{M,k}$ are the discretized forms of $\mathbf{z}(t)$, $\mathbf{a}(t)$, $\mathbf{f}_G(t)$, and $\mathbf{f}_M(t)$, respectively. Let

$$\mathbf{F}_d = \mathbf{e}^{\mathbf{A}\Delta t}, \quad \mathbf{H}_d = \mathbf{e}^{\mathbf{A}\Delta t}\mathbf{H}\Delta t, \quad \mathbf{B}_d = \mathbf{e}^{\mathbf{A}\Delta t}\mathbf{B}\Delta t \tag{142}$$

Then Eq. 141 becomes

$$\mathbf{z}_{k+1} = \mathbf{F}_d\mathbf{z}_k + \mathbf{H}_d\mathbf{a}_k + \mathbf{B}_d\mathbf{f}_{G,k} + \mathbf{B}_d\mathbf{f}_{M,k} \tag{143}$$

In Eq. 143, both equivalent force terms $\mathbf{f}_{G,k}$ and $\mathbf{f}_{M,k}$ are functions of the column axial forces at time step k. Therefore, Eq. 143 represents the recursive equation for calculating the dynamic response of moment-resisting framed structures while considering updates on geometric nonlinearity as the axial compressive force in columns changes with time.

For the case where updates on geometric nonlinearity are ignored in the nonlinear dynamic analysis, the $\overline{\mathbf{K}}_G(t)$ matrix as given in Eq. 128 becomes $\overline{\mathbf{K}}_G(t) = \mathbf{0}$. Therefore, from the same equation, $\overline{\mathbf{K}}(t) = \overline{\mathbf{K}}_L$. Then it follows from Eq. 136b that

$$\mathbf{f}_G(t) = [\mathbf{0}] \cdot \mathbf{x}_d(t) = \mathbf{0} \tag{144a}$$

$$\mathbf{f}_M(t) = \overline{\mathbf{K}}(t)\mathbf{x}_d''(t) = \overline{\mathbf{K}}_L\mathbf{x}_d''(t) \tag{144b}$$

and Eq. 143 becomes

$$\mathbf{z}_{k+1} = \mathbf{F}_d\mathbf{z}_k + \mathbf{H}_d\mathbf{a}_k + \mathbf{G}_d\mathbf{x}_{d,k}'' \tag{145}$$

where

$$\mathbf{G}_d = \mathbf{B}_d\overline{\mathbf{K}}_o = \mathbf{e}^{\mathbf{A}\Delta t}\begin{bmatrix}\mathbf{0}\\ \mathbf{m}_{dd}^{-1}\end{bmatrix}\overline{\mathbf{K}}_o\Delta t = \mathbf{e}^{\mathbf{A}\Delta t}\begin{bmatrix}\mathbf{0}\\ \mathbf{m}_{dd}^{-1}\overline{\mathbf{K}}_L\end{bmatrix}\Delta t \tag{146}$$

and $\mathbf{x}_{d,k}''$ representing the discretized forms of $\mathbf{x}_d''(t)$. Equation 145 represents the recursive equation for calculating the nonlinear dynamic response of moment-resisting framed structures without updates on geometric nonlinearity as the axial compressive force in columns changes with time.

To perform nonlinear dynamic analysis, either Eq. 143 or Eq. 145 is used in conjunction with Eqs. 126b and 126c, rewritten here in discretized forms:

$$\mathbf{M}_{k+1} + \overline{\mathbf{K}}_{k+1}''\Delta\boldsymbol{\Theta}'' = \overline{\mathbf{K}}_{k+1}'^{T}\mathbf{x}_{d,k+1} - \overline{\mathbf{K}}_{k+1}''\boldsymbol{\Theta}_k'' \tag{147}$$

$$\mathbf{x}_{d,k+1}'' = \overline{\mathbf{K}}_{k+1}^{-1}\overline{\mathbf{K}}_{k+1}'\boldsymbol{\Theta}_{k+1}'' \tag{148}$$

where $\mathbf{x}_{d,k}$, $\boldsymbol{\Theta}_k''$, and $\mathbf{M}_k$ are the discretized forms of $\mathbf{x}_d(t)$, $\boldsymbol{\Theta}''(t)$, and $\mathbf{M}(t)$, respectively, $\Delta\boldsymbol{\Theta}'' = \boldsymbol{\Theta}_{k+1}'' - \boldsymbol{\Theta}_k''$, and $\overline{\mathbf{K}}_k$, $\overline{\mathbf{K}}_k'$, and $\overline{\mathbf{K}}_k''$ are the stiffness matrices at

time step k computed using the axial forces in columns at the same time step. Note that the stiffness matrices in Eqs. 147 and 148 are written in terms of time step $k+1$. However, the axial forces in columns at time step $k+1$ are unknown prior to the calculation of moments and change in plastic rotations, which means Eq. 147 requires an iterative procedure in the solution and may be difficult to execute. Therefore, the stiffness matrices in these two equations are approximated by replacing with those at time step k, i.e.,

$$\mathbf{M}_{k+1} + \overline{\mathbf{K}}_k'' \Delta\boldsymbol{\Theta}'' = \overline{\mathbf{K}}_k'^T \mathbf{x}_{k+1} - \overline{\mathbf{K}}_k'' \boldsymbol{\Theta}_k'' \tag{149}$$

$$\mathbf{x}_{k+1}'' = \overline{\mathbf{K}}_k^{-1} \overline{\mathbf{K}}_k' \boldsymbol{\Theta}_{k+1}'' \tag{150}$$

If updates to geometric nonlinearity are ignored throughout the time history analysis, further approximation can be performed (as demonstrated in the comparison of responses in Sects. 4.4 and 4.5) by simplifying the stiffness matrices as:

$$\overline{\mathbf{K}}_k = \overline{\mathbf{K}}(0) = \overline{\mathbf{K}}_L, \quad \overline{\mathbf{K}}_k' = \overline{\mathbf{K}}'(0) = \overline{\mathbf{K}}_L', \quad \overline{\mathbf{K}}_k'' = \overline{\mathbf{K}}''(0) = \overline{\mathbf{K}}_L'' \tag{151}$$

where $\overline{\mathbf{K}}_L'$ and $\overline{\mathbf{K}}_L''$ (and $\overline{\mathbf{K}}_L$ as previously defined in Eq. 131) are the linearized condensed stiffness matrices with geometric nonlinearity derived from the gravity load on the frame only. Then Eqs. 149 and 150 become

$$\mathbf{M}_{k+1} + \overline{\mathbf{K}}_L'' \Delta\boldsymbol{\Theta}'' = \overline{\mathbf{K}}_L'^T \mathbf{x}_{d,k+1} - \overline{\mathbf{K}}_L'' \boldsymbol{\Theta}_k'' \tag{152}$$

$$\mathbf{x}_{d,k+1}'' = \overline{\mathbf{K}}_L^{-1} \overline{\mathbf{K}}_L' \boldsymbol{\Theta}_{k+1}'' \tag{153}$$

Equations 145, 152, and 153 represent the set of equations for solving the nonlinear dynamic analysis problems when no update to geometric nonlinearity due to changes in axial force is performed.

Finally, the absolute acceleration vector (i.e., $\ddot{\mathbf{y}}_d(t) = \ddot{\mathbf{x}}_d(t) + \ddot{\mathbf{g}}_d(t)$) can be computed by rewriting Eq. 126a in discretized form as

$$\ddot{\mathbf{y}}_{d,k} = -\mathbf{m}_{dd}^{-1} \mathbf{c}_{dd} \dot{\mathbf{x}}_{d,k} - \mathbf{m}_{dd}^{-1} \overline{\mathbf{K}}_k \left(\mathbf{x}_{d,k} - \mathbf{x}_{d,k}'' \right) - \mathbf{m}_{dd}^{-1} \mathbf{K}_a \mathbf{x}_{d,k} \tag{154}$$

where $\dot{\mathbf{x}}_{d,k}$ and $\ddot{\mathbf{y}}_{d,k}$ are the discretized forms of $\dot{\mathbf{x}}_d(t)$ and $\ddot{\mathbf{y}}_d(t)$, respectively.

5.3 *Implementation of the Dynamic Analysis Procedure to the One-Story Frame*

As an example of the above derivation, consider the same configuration of a one-story one-bay moment-resisting frame as shown in Fig. 6 but with different

member properties. First, let the members be axially rigid. This gives a total of 3 DOFs (i.e., $n = 3$) and 6 PHLs (i.e., $m = 6$) as shown in the figure. The global stiffness matrices have been presented in Eqs. 56a–56c.

Assume that the frame has a mass of $m_{dd} = 318.7$ Mg and a damping of 0 % (i.e., $c_{dd} = 0.0$) at DOF #1, while the mass moment of inertia at DOFs #2 and #3 are ignored. This gives $d = 1$ and $r = 2$. Note that $d + r = n$. Therefore, static condensation can be applied to eliminate the DOFs for x_2 and x_3. For the beam and columns, let $E = 200$ GPa, $I_b = I_c = 4.995 \times 10^8$ mm^4, $L_b = 7.62$ m, and $L_c = 4.57$ m. Assume that the plastic hinges exhibit elastic-plastic behavior with plastic moment capacities of $M_b = 3130$ kN-m for the beam and $M_c = 3909$ kN-m for the two columns. Also, let the gravity load be $P = 5338$ kN. Assuming no update of geometric nonlinearity due to changes in axial forces in columns is performed, the condensed stiffness matrices $\overline{\mathbf{K}}_L$, $\overline{\mathbf{K}}'_L$, and $\overline{\mathbf{K}}''_L$ based on Eqs. 127a–127c become:

$$\overline{K}_L = \overline{K}_e = 10018\,\text{kN/m} \tag{155a}$$

$$\overline{\mathbf{K}}'_L = [\,16907 \quad 11331 \quad 16907 \quad 11331 \quad -11331 \quad -11331\,]\,\text{kN} \tag{155b}$$

$$\overline{\mathbf{K}}''_L = \begin{bmatrix} 56761 & 13494 & 2458 & 4585 & -13494 & -4585 \\ 13494 & 25173 & 4585 & 8554 & -25173 & -8554 \\ 2458 & 4585 & 56761 & 13494 & -4585 & -13494 \\ 4585 & 8554 & 13494 & 25173 & -8554 & -25173 \\ -13494 & -25173 & -4585 & -8554 & 25173 & 8554 \\ -4585 & -8554 & -13494 & -25173 & 8554 & 25173 \end{bmatrix} \text{kN} - \text{m/rad} \tag{155c}$$

The period of vibration T is calculated as:

$$T = 2\pi\sqrt{m_{dd}/\overline{K}_L} = 2\pi\sqrt{318.7/10017} = 1.121\,\text{s} \tag{156}$$

With a time step size of $\Delta t = 0.01$ s and assuming no updates to the geometric nonlinearity is performed, the transition matrices are calculated as:

$$\mathbf{A} = \begin{bmatrix} 0 & 1 \\ -31.43 & 0 \end{bmatrix}, \quad \mathbf{H} = \begin{bmatrix} 0 \\ -1 \end{bmatrix}, \quad \mathbf{B} = \begin{bmatrix} 0 \\ 0.5495 \end{bmatrix} \tag{157a}$$

$$\mathbf{F}_d = \mathbf{e}^{\mathbf{A}\Delta t} = \begin{bmatrix} 0.998429 & 0.009995 \\ -0.31415 & 0.998429 \end{bmatrix}, \mathbf{H}_d = \begin{bmatrix} -0.00010 \\ -0.00998 \end{bmatrix}, \mathbf{G}_d = \begin{bmatrix} 0.00314 \\ 0.31381 \end{bmatrix} \tag{157b}$$

and Eqs. 145, 152, and 153 for performing the nonlinear dynamic analysis become

$$\begin{Bmatrix} x_1 \\ \dot{x}_1 \end{Bmatrix}_{k+1} = \begin{bmatrix} 0.998429 & 0.009995 \\ -0.31415 & 0.998429 \end{bmatrix} \begin{Bmatrix} x_1 \\ \dot{x}_1 \end{Bmatrix}_k + \begin{bmatrix} -0.00010 \\ -0.00998 \end{bmatrix} a_k + \begin{bmatrix} 0.00314 \\ 0.31381 \end{bmatrix} x''_{d,k} \tag{158a}$$

$$\begin{Bmatrix} M_1 \\ M_2 \\ M_3 \\ M_4 \\ M_5 \\ M_6 \end{Bmatrix}_{k+1} + \begin{bmatrix} 56761 & 13494 & 2458 & 4585 & -13494 & -4585 \\ 13494 & 25173 & 4585 & 8554 & -25173 & -8554 \\ 2458 & 4585 & 56761 & 13494 & -4585 & -13494 \\ 4585 & 8554 & 13494 & 25173 & -8554 & -25173 \\ -13494 & -25173 & -4585 & -8554 & 25173 & 8554 \\ -4585 & -8554 & -13494 & -25173 & 8554 & 25173 \end{bmatrix} \begin{Bmatrix} \Delta\theta''_1 \\ \Delta\theta''_2 \\ \Delta\theta''_3 \\ \Delta\theta''_4 \\ \Delta\theta''_5 \\ \Delta\theta''_6 \end{Bmatrix}$$

$$= \begin{bmatrix} 16907 \\ 11329 \\ 16907 \\ 11329 \\ -11329 \\ -11329 \end{bmatrix} x_{1,k+1} - \begin{bmatrix} 56761 & 13494 & 2458 & 4585 & -13494 & -4585 \\ 13494 & 25173 & 4585 & 8554 & -25173 & -8554 \\ 2458 & 4585 & 56761 & 13494 & -4585 & -13494 \\ 4585 & 8554 & 13494 & 25173 & -8554 & -25173 \\ -13494 & -25173 & -4585 & -8554 & 25173 & 8554 \\ -4585 & -8554 & -13494 & -25173 & 8554 & 25173 \end{bmatrix} \begin{Bmatrix} \theta''_1 \\ \theta''_2 \\ \theta''_3 \\ \theta''_4 \\ \theta''_5 \\ \theta''_6 \end{Bmatrix}_k \tag{158b}$$

$$x''_{d,k+1} = \frac{1}{10017} \begin{bmatrix} 16907 & 11329 & 16907 & 11329 & -11329 & -11329 \end{bmatrix} \begin{Bmatrix} \theta''_1 \\ \theta''_2 \\ \theta''_3 \\ \theta''_4 \\ \theta''_5 \\ \theta''_6 \end{Bmatrix}_{k+1} \tag{158c}$$

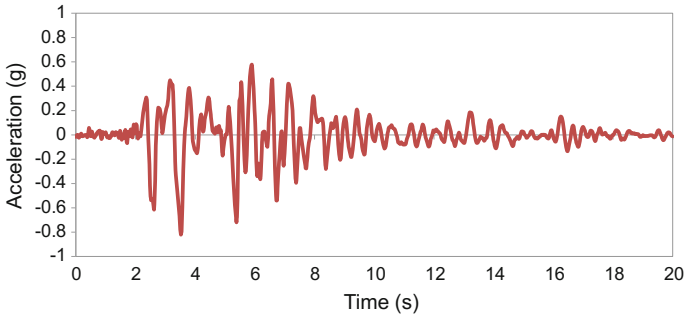

Fig. 8 1995 Kobe earthquake ground acceleration at Kajima station, component 000, with a peak ground acceleration of 0.821 g

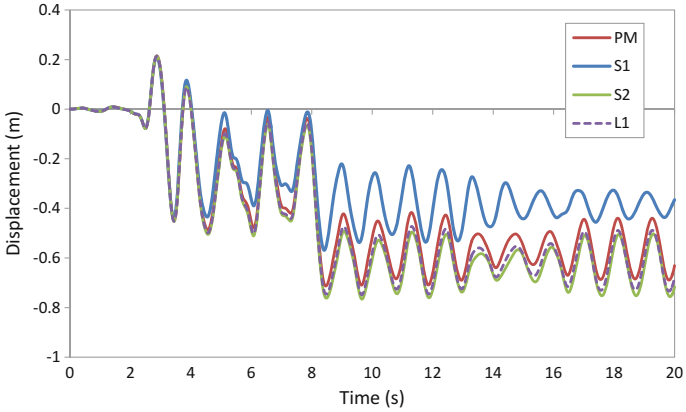

Fig. 9 Displacement response comparisons of the one-story frame using the proposed method (PM) with two small-displacement-based structural analysis software packages (S1 and S2) and a large-displacement-based finite element software package (L1)

Equation 158a–158c represents the set of recursive equations used for the entire nonlinear dynamic analysis. Note that the method for solving Eq. 158b is similar to those discussed in Sects. 4.4 and 4.5, where an iterative procedure is used to determine whether each plastic hinges is at the loading phase (i.e., plastic rotation becomes the unknown) or at the unloading phase (i.e., moment becomes the unknown).

The frame is now subjected to the 1995 Kobe earthquake ground motion as shown in Fig. 8 but magnified with a scale factor of 1.3 to produce larger displacement response and more yielding in the plastic hinges. The global displacement response at DOF #1 is plotted in Fig. 9 using the currently proposed method (PM) of nonlinear analysis. In addition, two small-displacement-based structural analysis software packages (here labeled as S1 that uses $P-\Delta$ stiffness as shown in Eq. 30 and S2 that uses geometric stiffness as shown in Eq. 29) and a large-displacement-based finite element analysis software package (here labeled as L1) are used to develop the same one-story one-bay moment-resisting frame model as shown in Fig. 6, and the undamped displacement responses obtained from S1 and S2 are also plotted in Fig. 9 for comparisons. Note that even though using 0 % damping is an idealized situation, it helps eliminate the potentially differing effects of using damping parameters on the responses that may occur due to differences in damping formulations used in various software packages.

As shown in Fig. 9, it is observed that the proposed method (PM) produces a "global" response that is comparable to other software packages that use different material nonlinearity and geometric nonlinearity formulations. At such a large displacement response of the frame, the large-displacement-based finite element analysis software package L1 is assumed to give accurate results; therefore, it serves as a benchmark for other small-displacement-based software packages. It is

observed that while S1 differs noticeably from the L1 prediction, S2 performs slightly better than the PM in the displacement response.

Figure 10 shows the plastic hinge moment responses at PHLs #1, #3, #5, and #6 of the one-story one-bay frame among the same software packages used in the study. As shown in this figure, the L1 results show that the moment responses at all the plastic hinges should be skewed to the positive direction. However, only the proposed method (PM) captures this behavior, while S1 captures this behavior to a lesser extent and S2 misses the behavior completely. This suggests that starting from the basic principles at the element level is important in capturing the local responses of the structure.

Finally, Fig. 11 shows the plastic rotations responses at PHLs #1, #3, #5, and #6 of the one-story one-bay frame using the small-displacement-based structural analysis software packages. The large-displacement-based finite element software package L1 produces plastic strain as the output, yet the conversion from plastic strain to plastic rotation is not readily available. Therefore, the output from L1 is not plotted in the figure. By comparing the proposed method (PM) with S1 in Fig. 11, it can be seen that even though the local plastic rotation responses change suddenly (jumps) due to yielding at the same time steps, the magnitudes of the changes are different. Given the performance accuracy of PM in Fig. 10, this suggests that the software package S1 may not have addressed the effect of plastic rotation on the residual response of the structure appropriately. Finally, at such a large displacement response as shown in Fig. 9, software package S2 predicts only a slight

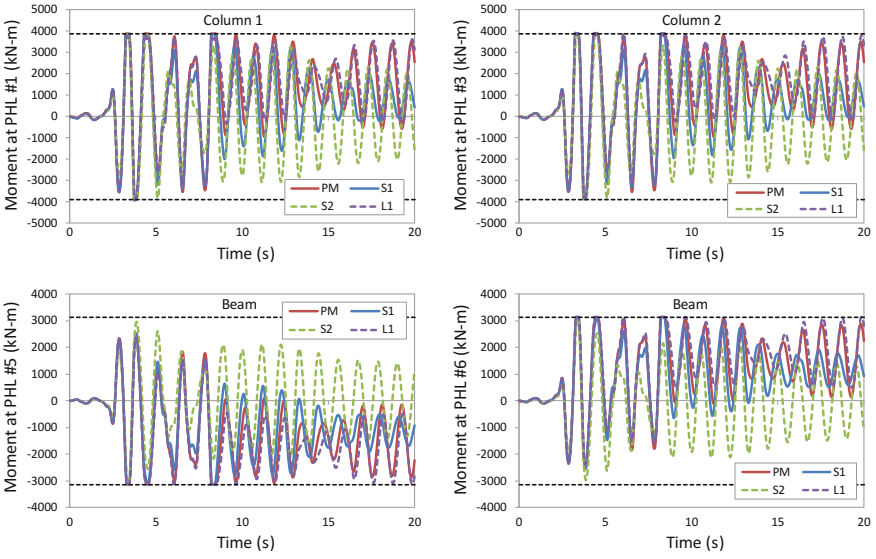

Fig. 10 Moment response comparisons at various plastic hinge locations using the proposed method (PM) with two small-displacement-based structural analysis software packages (S1 and S2) and a large-displacement-based finite element software package (L1)

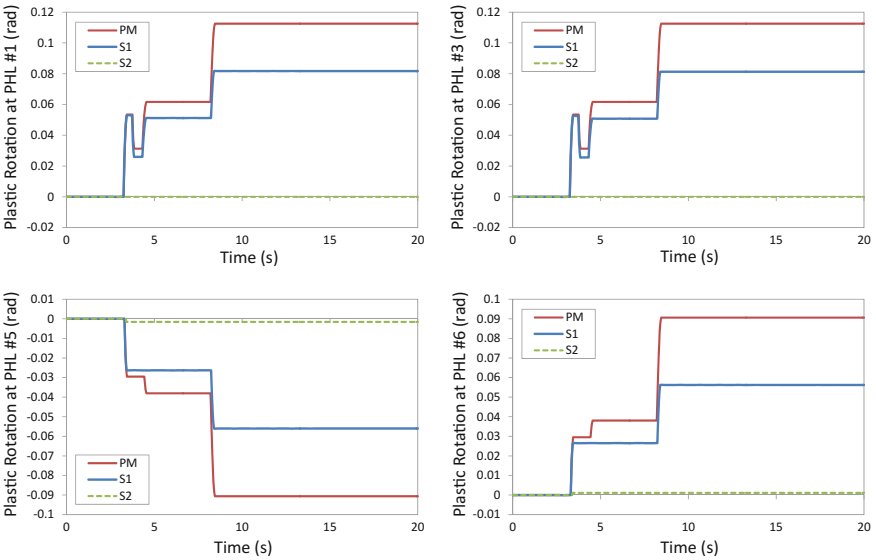

Fig. 11 Plastic rotation response comparisons at various plastic hinge locations using the proposed method (PM) with two small-displacement-based structural analysis software packages (S1 and S2) and a large-displacement-based finite element software package (L1)

damage in the plastic rotation responses shown in Fig. 11 with fairly elastic moment responses in Fig. 10 throughout the analysis. This suggests that there may be a fundamental issue in calculating the local response that software package S1 may have missed.

6 Conclusion

Plastic rotation in moment-resisting frame is an important parameter in the assessment process for performance-based seismic engineering, and therefore it needs to be calculated correctly. In this research, basic principles were used to derive the stiffness matrices of a column member with axial load to capture the interaction between geometric nonlinearity and material nonlinearity. This results in a method for capturing the plastic rotation demand for both nonlinear static analysis and nonlinear dynamic analysis that produces displacement results comparable with the large-displacement-based finite element software package L1 used in the study. It also suggests that this method is an improvement to the two small-displacement-based software packages S1 and S2 used in the study. While there are many structural analysis software packages available that consider both geometric and material nonlinearities, it is unclear which ones have addressed the interaction appropriately. Therefore, engineers should be careful in assessing plastic

rotation responses in moment-resisting frames with large displacement, where significant material nonlinearity is coupled with significant geometric nonlinearity. This leads to a bigger question as to the accuracy and reliability on assessing damages in moment-resisting framed structures based on the ASCE/SEI 41-13 recommendations, which is something that eventually must be addressed in the future updates of the standard.

The method for calculating plastic rotations developed in this research was based on two-dimensional analysis. Two-dimensional stiffness matrices for beams seem appropriate, but these matrices may need to be extended to three-dimensions for columns when biaxial bending is significant. In addition, elastic-plastic behavior was used in the examples for simplicity of illustrations on the calculation method. However, in order to capture the actual behavior more accurately, a hysteretic bilinear model with post-capping degrading strength may be necessary. Therefore, further research in these areas are needed.

References

1. ASCE/SEI 41-13 (2013) Seismic evaluation and retrofit of existing buildings. American Society of Civil Engineers, Reston, VA
2. Domizio M, Ambrosini D, Curadelli O (2015) Experimental and numerical analysis to collapse of a framed structure subjected to seismic loading. Eng Struct 82:22–32
3. Eads L, Miranda E, Krawinkler H, Lignos DG (2013) An efficient method for estimating the collapse risk of structures in seismic regions. Earthquake Eng Struct Dyn 42(1):25–41
4. Grigorian M, Grigorian CE (2012) Lateral displacements of moment frames at incipient collapse. Eng Struct 44:174–185
5. Lignos DG, Krawinkler H, Whittaker AS (2011) Prediction and validation of sidesway collapse of two scale models of a 4-story steel moment frame. Earthquake Eng Struct Dyn 40 (7):807–825
6. Zareian F, Krawinkler H (2007) Assessment of probability of collapse and design for collapse safety. Earthquake Eng Struct Dyn 36(13):1901–1914
7. Bazant ZP, Cedolin L (2003) Stability of structures. Dover Publication, New York
8. Horne MZ, Merchant W (1965) The stability of frames. Pergamon Press, New York
9. Timoshenko SP, Gere JM (1961) Theory of elastic stability, 2nd edn. McGraw Hill, New York
10. Powell GH (2010) Modeling for structural analysis: behavior and basics. Computers and Structures Inc., California
11. McGuire W, Gallagher RH, Ziemian RD (2000) Matrix structural analysis. John Wiley and Sons, New York
12. Park JW, Kim SE (2008) Nonlinear inelastic analysis of steel-concrete composite beam-columns using the stability functions. Struct Eng Mech 30(6):763–785
13. Hibbeler RC (2012) Structural analysis, 8th edn. Prentice Hall, New Jersey, USA
14. Leet KM, Uang CM, Gilbert AM (2010) Fundamentals of structural analysis, 4th edn. McGraw Hill, New York, USA
15. Wilson EL (2010) Static and dynamic analysis of structures. Computers and Structures Inc., California

Seismic Demand on Acceleration-Sensitive Nonstructural Components

Gennaro Magliulo, Crescenzo Petrone and Gaetano Manfredi

Abstract Nonstructural components should be subjected to a careful and rational seismic design, in order to reduce economic loss and to avoid threats to the life safety, as well as what concerns structural elements. The design of nonstructural components is based on the evaluation of the maximum inertial force, which is related to the floor spectral accelerations. The question arises as to whether the European Building Code, i.e. Eurocode 8, is able to predict actual floor response spectral accelerations occurring in structures designed according to its provisions. A parametric study is therefore conducted on five RC frame structures designed according to Eurocode 8. It shows that Eurocode formulation for the evaluation of the seismic demand on nonstructural components does not well fit the analytical results for a wide range of periods, particularly in the vicinity of the higher mode periods of vibration of the reference structures. The inconsistent approach of current European building codes to the design of nonstructural components is also highlighted. For this reason a parametric study is conducted in order to evaluate the seismic demand on light acceleration-sensitive nonstructural components caused by frequent earthquakes. The above mentioned RC frame structures are therefore subjected to a set of frequent earthquakes, i.e. 63 % probability of exceedance in 50 years. A novel formulation is proposed for an easy implementation in future building codes based on the actual Eurocode provisions.

G. Magliulo (✉) · C. Petrone · G. Manfredi
Department of Structures for Engineering and Architecture, University of Naples Federico II, Via Claudio 21, 80125 Naples, Italy
e-mail: gmagliul@unina.it

C. Petrone
e-mail: crescenzo.petrone@unina.it

G. Manfredi
e-mail: gamanfre@unina.it

M. Papadrakakis et al. (eds.), *Computational Methods in Earthquake Engineering*, Computational Methods in Applied Sciences 44,
DOI 10.1007/978-3-319-47798-5_7

1 Introduction

Nonstructural components should be subjected to a careful and rational seismic design, in order to reduce economic loss and to avoid threat to the life safety, as well as what concerns structural elements. Nonstructural components are subjected to severe seismic actions due to the dynamic interaction with the primary system. Several research studies were conducted in the past concerning the evaluation of the floor acceleration and the floor response spectra.

Rodriguez et al. [24] conducted an analytical investigation for the evaluation of the earthquake-induced floor horizontal accelerations in cantilever wall buildings built with rigid diaphragms. They described several methods prescribed by design standards and proposed a new method for deriving the design horizontal forces. Singh et al. [26, 27] proposed two methods for calculating the seismic design forces for flexible and rigid nonstructural components. The validity of such methods was verified by comparing their floor response spectra with the ones obtained for an ensemble of earthquakes exciting several buildings with different numbers of stories. Sankaranarayanan and Medina [25] evaluated the main factors that influence the variation of the floor response spectrum values caused by the inelasticity in the primary structure. Analyses were carried out on moment-resisting frame structures with 3, 6, 9, 12, 15, and 18 stories. It was found that the main factors that influence the "inelastic" floor response spectrum are the location of the NSC in the supporting structure, the periods of component and building, the damping ratio of the component, and the level of inelasticity of the supporting structure. The influence was evaluated through the assessment of an acceleration response modification factor, that addressed both the decrease and the increase in elastic floor response spectral values due to the yielding of the supporting structure. Wieser et al. [31] analyzed a set of special moment resisting frame (SMRF) buildings using the incremental dynamic analysis procedure. They proposed an improved estimation for the PFA/PGA ratio by incorporating the elastic natural period of the structure and the expected level of ductility. Moreover, they debated the use of a constant component amplification factor and proposed an alternative design approach that directly amplifies the ground acceleration spectrum to achieve the desired floor acceleration spectrum.

Very limited studies have been performed concerning the Eurocode 8 [4] formulation for the evaluation of the floor spectral acceleration, according to which the seismic demand on a given nonstructural component is evaluated. Moreover, past studies were usually focused on steel buildings or wall structures. The question arises as to whether EC8 is able to predict actual floor response spectral accelerations occurring at the design seismic intensity level on EC8-designed structures. Indeed, the structural overstrength due to the Eurocode 8 provisions may significantly influence the floor response spectra.

For this reason a set of benchmark RC frame structures are selected and designed according to Eurocode 8. In Sect. 2 dynamic nonlinear analyses are performed on the benchmark structures in order to validate the Eurocode formulation for the

seismic demand on nonstructural components. Dynamic analyses are performed both on elastic and inelastic models of the benchmark structures, in order to evaluate the influence of the inelasticity on the definition of the floor response spectrum. The floor response spectra are compared to the ones of Eurocode 8; some considerations on the peak floor acceleration and the maximum floor spectral acceleration are also given.

In Sect. 3 a parametric study is conducted in order to evaluate the seismic demand on light acceleration-sensitive nonstructural components caused by frequent earthquakes. The study is motivated by the inconsistent approach of current European and Italian Building Codes. The above mentioned nonstructural damage exhibited after low intensity earthquakes also encouraged such a study. Dynamic nonlinear analyses are performed on the benchmark structures for a set of frequent earthquakes. The floor response spectra are compared to the ones of Eurocode 8. Finally, a novel formulation is proposed for a future implementation in building codes.

2 Floor Response Spectra in RC Frame Structures Designed According to Eurocode 8

A parametric study is conducted on five RC frame structures in order to evaluate the floor response spectra. The structures, designed according to Eurocode 8, are subjected to a set of earthquakes compatible with the design response spectrum. Time-history analyses are performed both on elastic and inelastic models of the considered structures in order to assess the accuracy of Eurocode formulation for the evaluation of the seismic demand on nonstructural components.

2.1 Methodology

Description of the parametric study. A parametric study is conducted to investigate the seismic demand to which a light acceleration-sensitive nonstructural component may be subjected in multi-story RC frames. 2D frame structures are considered: they are representative of a tridimensional structure with a double symmetric plan and with three frames arranged in each direction (Figs. 1 and 2). Benchmark structures with different number of stories are considered: one-, two-, three-, five- and ten-story buildings, with a 3 m interstory height and two 5 m wide bays.

The benchmark structures are designed according to Eurocode 8 (EC8) [4] provisions, using the default EC8 values. A 0.25 g design ground acceleration a_g is considered. The horizontal elastic response spectrum is defined referring to a 5 % damping ratio and to a 1.2 soil factor, i.e. soil type B.

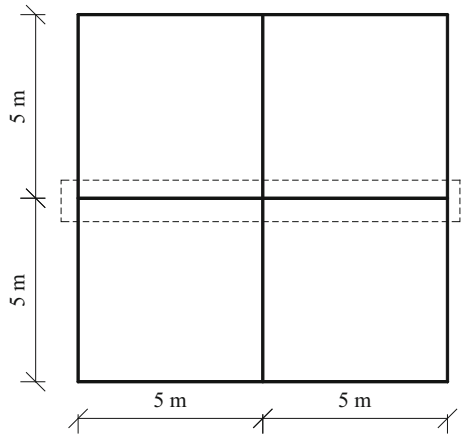

Fig. 1 Plan view of the benchmark structures

The seismic design meets the ductility class "high" (DCH) requirements: the behavior factor is equal to 4.95 for one-story building and 5.85 for multi-story frames. The sizing of primary elements is strongly influenced, especially for tall structures, by the restricted value of normalized design axial force, i.e. the ratio between the average compressive stress and the concrete compression design strength, which must not exceed 0.55. Moreover, the seismic detailing requirements in terms of longitudinal and transversal reinforcements provide an amount of reinforcement which is larger than the one strictly required by the design analysis. They produce high overstrength ratios which influence the structural response, as discussed in the following. A half moment of inertia is considered for the primary elements during the design phase, according to EC8, in order to take into account the effect of cracking. The fundamental period of the benchmark structures, evaluated according to such a "reduced" flexural stiffness, are listed in Fig. 2.

Modeling. Both elastic and inelastic structural responses are investigated. Dynamic analyses are carried out for a set of seven earthquake records, on both linear and nonlinear models. Rigid diaphragms are considered for each floor; a third of the seismic mass of the corresponding 3D building is assigned to a master joint at each floor. Analyses are performed using the OpenSees program [16].

The linear modeling allows that the primary elements be modeled as elastic beam-column elements with the gross moment of inertia. Concrete is modelled as an elastic material with a Modulus of Elasticity equal to 31,476 MPa according to the C25/30 class concrete assumed during the design phase.

A lumped plasticity nonlinear approach is also considered: it is assumed that the primary elements have an elastic behavior and that any inelasticity source is lumped in plastic hinges at their ends. Moment–rotation envelopes in the plastic hinges are defined according to the formulation suggested by Haselton [12]. The nonlinear behavior of the plastic hinges is defined by peak-oriented hysteretic rules, which simulate the modified Ibarra-Medina-Krawinkler [13] deterioration model. In order to determine the moment-curvature diagrams, appropriate cross sections are defined

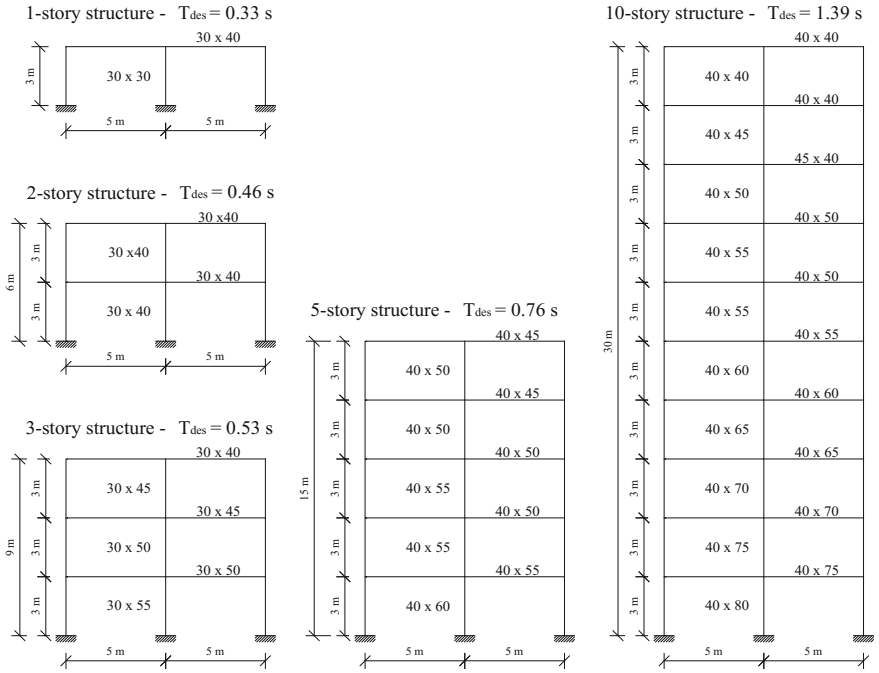

Fig. 2 Lateral view of the considered building models and their design fundamental period (T_{des}) —dimensions of the cross sections are in cm

for each element considering the actual geometry and steel reinforcement. The cross section is divided into fibers and a stress-strain relationship is defined for each fiber. Different constitutive laws are applied to three different kinds of fibers: unconfined concrete law is associated to cover fibers, confined concrete law is associated to core fibers and steel law is associated to the longitudinal reinforcement fibers. The stress–strain relationship proposed by Mander et al. [15] is used both for unconfined and confined concrete. The B450C steel class is adopted with a bilinear with hardening material law. The steel mechanical characteristics are calculated according to Eurocode 2 (Table C.1, "Properties of reinforcement") [3].

Table 1 shows the comparison between the first and second natural periods of vibration of the structures, which can be obtained with either the design-approximated stiffness assumption ($T_{i,des}$) or gross section elastic stiffness ($T_{i,el}$) or inelastic yielding secant stiffness ($T_{i,nl}$). The period range in Table 1 points out the large uncertainty in the assessment of the structural period during the design phase. This range would have been even wider if the infill contribution to the lateral stiffness had been considered. It is especially valid in case of brick infills, widespread in the European area [18].

Ground motion records. The structural response is investigated through time history analyses. Therefore, a suitable set of 7 accelerograms (Table 2) is provided,

Table 1 Comparison of the first and second vibrational periods evaluated according to different models of the considered structures

No. story	$T_{1,des}$	$T_{1,el}$	$T_{1,nl}$	$T_{2,el}$	$T_{2,nl}$
[-]	[s]	[s]	[s]	[s]	[s]
1	0.33	0.23	0.42	–	–
2	0.46	0.32	0.64	0.11	0.22
3	0.53	0.37	0.78	0.14	0.26
5	0.76	0.52	1.11	0.18	0.37
10	1.39	0.95	2.12	0.36	0.78

Table 2 Waveform ID, earthquake ID (Eqk ID) and name, date, moment magnitude (MW), epicentral distance (R), horizontal direction (Dir.) and peak ground acceleration (PGA) of the accelerograms selected for dynamic analyses [1]

Waveform	Eqk ID	Earthquake name	Date	M_W [–]	R [km]	Dir.	PGA [m/s^2]
146	65	Friuli (aftershock)	15/09/1976	6.0	14	y	3.30
197	93	Montenegro	15/04/1979	6.9	24	x	2.88
413	192	Kalamata	13/09/1986	5.9	10	y	2.91
414	192	Kalamata	13/09/1986	5.9	11	x	2.35
414	192	Kalamata	13/09/1986	5.9	11	y	2.67
4673	1635	South Iceland	17/06/2000	6.5	15	y	4.68
6334	2142	South Iceland (aftershock)	21/06/2000	6.4	11	y	7.07

matching the design spectrum at the life safety limit state, i.e. 475 years return period earthquake, according to the EC8 recommendations [14]:

- the mean of zero-period spectral response acceleration values, that is equal to 3.69 m/s^2, is larger than the design value, i.e. $a_g \cdot S$;
- the mean elastic spectrum of the selected ground motions is larger than 90 % of the design elastic response spectrum in the range of periods between $0.2T_{1,min}$ and $2T_{1,max}$, where $T_{1,min}$ and $T_{1,max}$ are, respectively, the minimum and the maximum fundamental period of the benchmark 2D structures (Fig. 3).

Preliminary nonlinear static analyses. The acceleration demand on non-structural components depends on both the dynamic interaction with the primary structure and the structural energy dissipation [21, 24] . The energy dissipation tends to reduce the intensity of the acceleration time history at a given floor. Structural overstrength, instead, makes the structure dissipate less energy and reduce the ductility demand compared to the ductility assumed during the design phase. The smaller the ductility demand is, the larger the floor accelerations are and they tend to be equal to the floor accelerations evaluated on the elastic structure [17].

In order to estimate the effective structural response and evaluate the over-strength ratios, nonlinear static analyses are performed applying a pattern of lateral forces proportional to the first mode displacement shape. For each structure, the

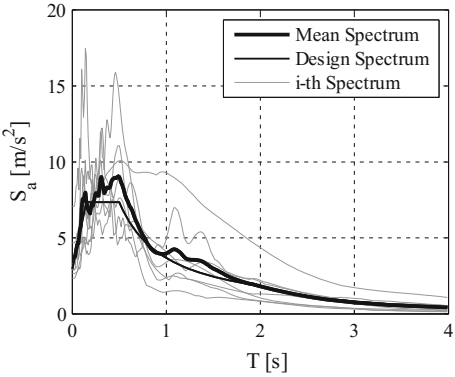

Fig. 3 Comparison between the mean acceleration response spectrum of the adopted set of accelerograms and the design spectrum according to EC8

relationship between the base shear force and the roof displacement is determined. The pushover curve, evaluated on the MDOF system, is converted in the capacity curve for the equivalent SDOF system; the idealized bilinear force–displacement relationships are obtained in accordance to the Italian Building Code [7] (Fig. 4): the ultimate displacement d_u is the SDOF displacement corresponding to a strength reduction equal to the 15 %; the bilinear curve initial stiffness and yielding shear force are obtained imposing that the first branch intersects the capacity curve at 0.6 F_u and imposing the equality of the areas under the actual and the bilinear curves until the ultimate displacement d_u.

The bilinear curve can be plotted in the ADRS (*Acceleration-Displacement Response Spectrum*) plane, where the design spectrum is plotted. In order to investigate the different sources of overstrength, the following ratios are evaluated for each structure (Fig. 5):

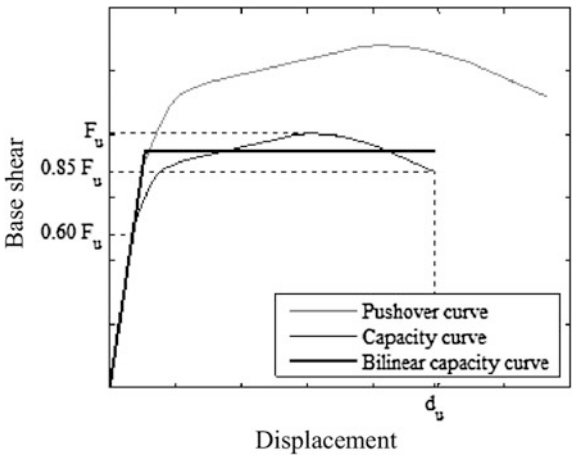

Fig. 4 Evaluation of the bilinear capacity curve according to the Italian Building Code [7]

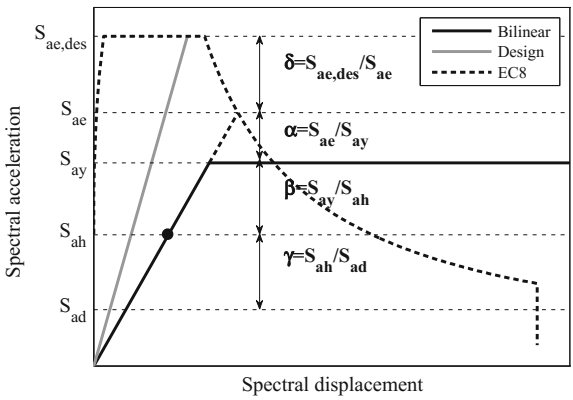

Fig. 5 Overstrength ratios definition

- α, the ratio between the spectral acceleration evaluated for the equivalent SDOF structure with a linear behavior (S_{ae}) and the spectral acceleration corresponding to the yielding of the SDOF system (S_{ay}). This ratio represents the reduction of spectral acceleration demand due to the non-linear behavior of the structure and, therefore, provides an estimation of the global ductility demand;
- β, the ratio between the spectral acceleration value corresponding to the yielding of the SDOF system (S_{ay}) and the spectral acceleration that produces the first plastic hinge yielding (S_{ah}). This ratio takes into account the overstrength caused by the structural redundancy;
- γ, the ratio between the value of spectral acceleration corresponding to the first plastic hinge (S_{ah}) and the design spectral acceleration (S_{ad}). This ratio represents the overstrength due to materials and design or detailing of RC members;
- δ, the ratio between the spectral acceleration demand considered during the design phase ($S_{ae,des}$) and the spectral acceleration evaluated for the equivalent SDOF structure with a linear behavior (S_{ae}). This ratio takes into account the reduction of the stiffness in the nonlinear model.

In Fig. 6 the bi-linearized capacity curves of the different structures are plotted in the ADRS plane and compared to the EC8 design spectrum. The first plastic hinge yielding is highlighted by a circle. Table 3 includes the overstrength ratios for the different structures. It shows that RC frames designed according to Eurocode 8 are characterized by a large overstrength [20]. A low ductility demand is expected, which is very far from the assumed behavior factor q; hence, the effective floor acceleration time histories are likely to be not significantly reduced with respect to the ones evaluated with the elastic model [21].

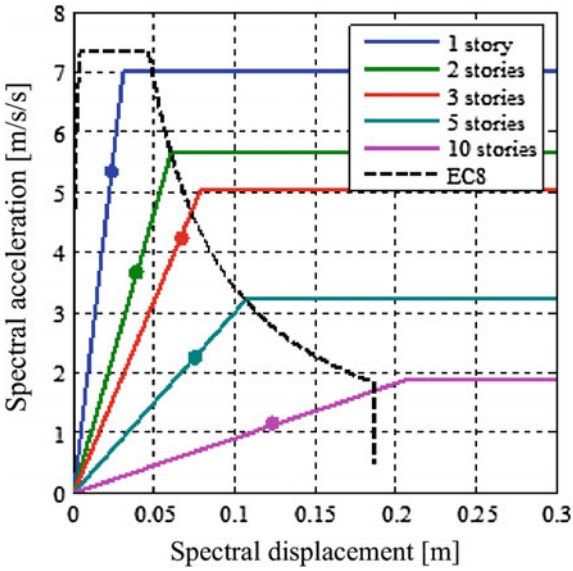

Fig. 6 Capacity curves of the benchmark structures plotted in the acceleration displacement response spectrum plane

Table 3 Overstrength ratios values for the analyzed structures

No. story	α	β	γ	δ
1	1.05	1.31	3.59	1.00
2	1.00	1.55	2.91	1.30
3	0.92	1.19	3.50	1.52
5	1.03	1.45	2.67	1.47
10	0.88	1.66	2.46	1.63

2.2 *Results and Discussion*

Elastic and inelastic floor response spectra. Dynamic analyses on both elastic and inelastic models are performed and the horizontal acceleration time-histories at different levels are recorded for each selected accelerogram. Floor response spectra are obtained for each floor accelerogram with a 5 % damping ratio and a mean response spectrum is plotted for each floor (Fig. 7). These spectra provide the acceleration demand of nonstructural components that are connected to the floor and exhibit a fundamental period *T*. Figure 7 shows the mean floor response spectra, evaluated on both the elastic (dotted line) and inelastic (solid lines) models for the 5-story structure.

Due to the dynamic interaction, the primary structure modifies the frequency content of the earthquake so that the floor accelerogram, amplified with respect to the base accelerogram, has a large frequency content for periods close to the vibration periods of the elastic model. If the nonstructural component period corresponds to one of the vibration periods of the structure, a double-resonance phenomenon occurs; the floor response spectra exhibit peaks which may exceed five

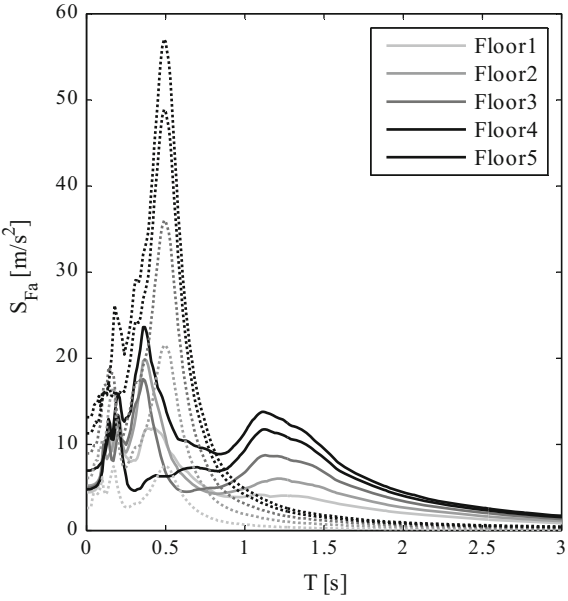

Fig. 7 Floor response spectra of the 5-story structure evaluated on both the elastic (*dotted line*) and inelastic models (*solid line*)

times the acceleration of gravity, i.e. about 20 times the base acceleration, at the top floor of the structure. Two main peaks are recorded corresponding to periods, i.e. $T_{1,el\text{-}eff}$ and $T_{2,el\text{-}eff}$, very close to the periods associated to the first and second vibration modes, i.e. $T_{1,el}$ and $T_{2,el}$ (Table 1).

The inelastic floor response spectra (solid lines in Fig. 7), show that the curves exhibit peaks at periods, i.e. $T_{1,nl\text{-}eff}$ and $T_{2,nl\text{-}eff}$, much larger than the elastic ones, due to the different initial stiffness of the two models. Figure 8 shows the comparison between elastic and inelastic floor response spectra for the remaining structures. The following comments can be drawn:

- a significant period elongation is exhibited, comparing the peak related to the first structural mode of the elastic model with the inelastic one;
- the comparison of the peak related to the first structural mode of the elastic model with the inelastic one also shows a substantial reduction of the peak spectral ordinate: the maximum spectral values of the inelastic model are less than 3 g for the various structures. The reduction is caused by both the period elongation phenomenon and the ductility demand experienced by the structure. This phenomenon is not exhibited by the one-story structure, because the period elongation does not modify the base response spectral ordinate, as denoted by the δ factor in Table 3;
- higher modes effect is significant in the 10-story structure. Moreover, the peak spectral values associated with the higher modes are slightly reduced in the inelastic model. At lower stories, the spectral values associated with higher modes can be even larger than the elastic ones, as also pointed out by [5] in a

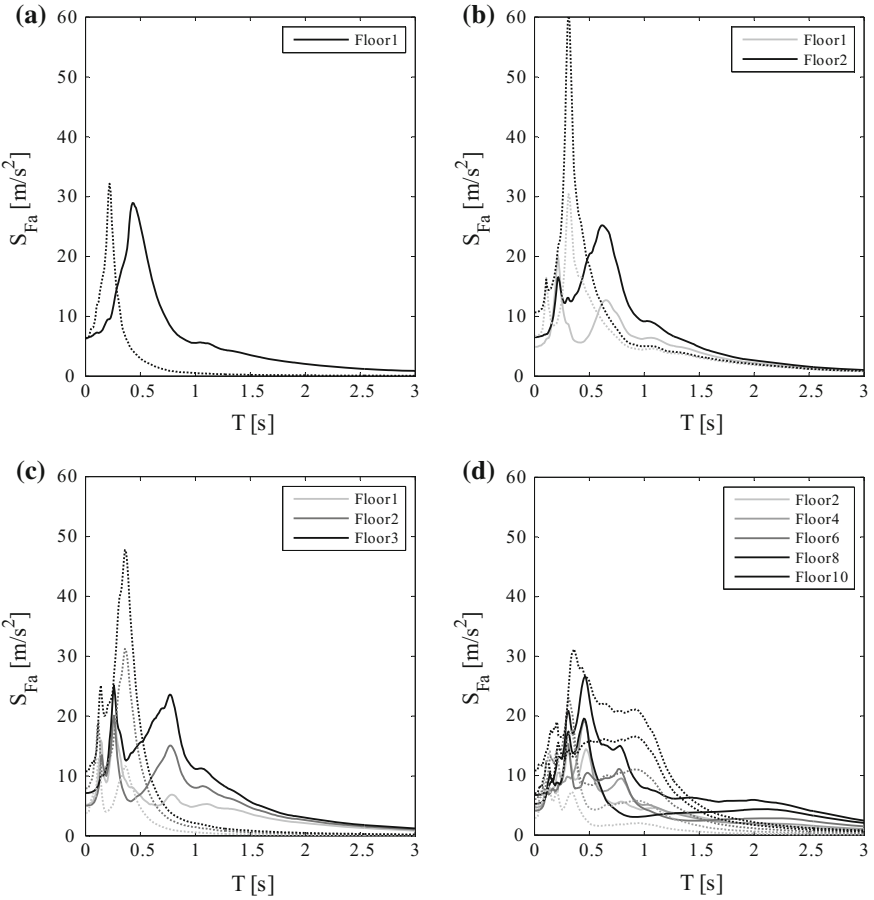

Fig. 8 Floor response spectra of the **a** 1-story, **b** 2-story, **c** 3-story and **d** 10-story structures evaluated on both the elastic (*dotted line*) and inelastic models (*solid line*)

research study on steel moment-resisting frames. This phenomenon confirms that the higher mode influence becomes more significant in the inelastic range [10, 23].

It can be observed that the inelastic spectral acceleration demand reduction is significantly far from the assumed behavior factor, due to the large structural overstrength. It is also confirmed that the energy dissipation is mostly related to the first mode; indeed the peak value associated to $T_{2,nl\text{-}eff}$ may exceed the peak value associated to $T_{1,nl\text{-}eff}$. It can be concluded that when inelastic models are considered, higher modes give a larger contribution to the definition of the floor spectral ordinates.

Floor amplification evaluation. The ratio between peak floor acceleration (PFA) and peak ground acceleration (PGA) is plotted versus the relative height in

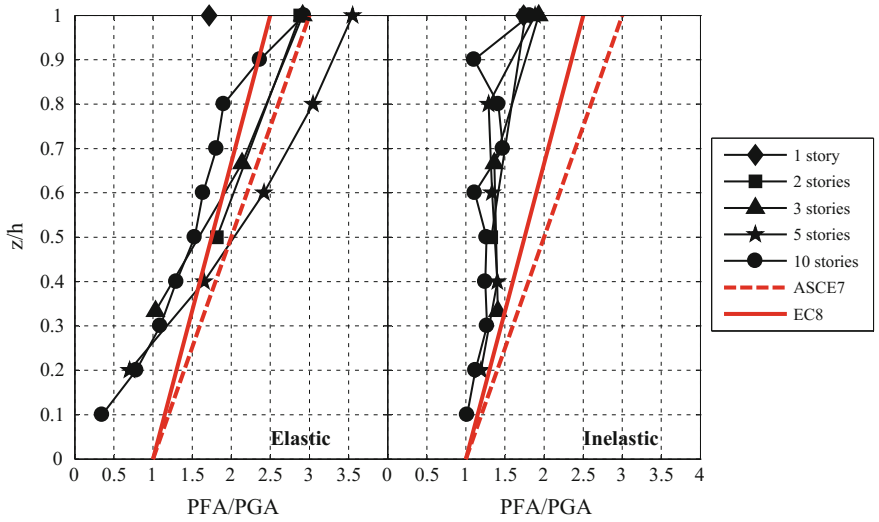

Fig. 9 Ratio between peak floor acceleration (PFA) and peak ground acceleration (PGA), versus the relative height (z/h) for the different considered structures compared to the provisions included in ASCE7 and EC8

Fig. 9 for the benchmark structures, in order to study the floor acceleration magnification with height. The PFA over PGA trend with the relative structural height is shown for both elastic and inelastic models.

The elastic model diagrams, which represent the average response of each structure, show an almost linear trend and they reach values of PFA/PGA close to three at the top floor. At the same relative height, the values of the ratio PFA/PGA are larger for structures with a larger number of floors, except for the tallest structure. At the lower stories of tall structures, PFA values are smaller than PGA values.

The inelastic model diagrams also show a linear trend. In this case the amplification is smaller than the one of the elastic models: the PFA/PGA values are always greater than one and they reach the maximum value, close to 2, at the top story. As pointed out by Wieser et al. [31] and Ray-Chaudhuri and Hutchinson [22], the yielding of the structure and the period elongation cause a significant reduction of the peak floor accelerations.

Both the elastic and inelastic trends are compared to ASCE7 (American Society of Civil Engineers [2] and Eurocode 8 provisions (Fig. 9). Such a comparison shows that both the ASCE7 and EC8 provisions are safe-sided for the inelastic diagrams, which are the most realistic ones. Finally, a linear trend that goes form 1 at the base to 2 at the top would better fit the outcomes of the nonlinear analyses.

Component amplification evaluation. The ratio between the maximum floor spectral acceleration and the PFA, i.e. a_p, is plotted versus the relative floor height for each floor of the analyzed structures in order to study the floor acceleration

magnification on the component (Fig. 10). This ratio represents the amplification of the floor acceleration demand for a nonstructural component that is in tune with the primary structure.

The inelastic floor magnifications on nonstructural components are slightly smaller than the elastic ones. For the 10-story structure, the inelastic a_p values are larger than the elastic ones. This is due to the fact that the largest spectral ordinate value is given by higher modes, which are only slightly influenced by the nonlinearity experienced by the structure (Fig. 8d) [23]; the PFA values, instead, are influenced by the first mode, and they significantly decrease in the inelastic model (Fig. 9). Hence, the ratio between the maximum floor spectral acceleration and the PFA could be larger in inelastic models in tall structures.

Assuming both elastic and inelastic models, the trend is almost constant with the height and the a_p values are greater than 2.5, which is the value recommended by ASCE7 and EC8, and it is close to 4.5. A significant underestimation of the a_p values in the current building codes is clearly highlighted, confirming the results included in Medina et al. [17].

Comparison with EC8 formula and limitations. In order to take into account the realistic behavior of the primary structures, inelastic floor spectra should be considered. These curves are compared with the ones obtained by Eurocode 8 formulation [4] for the evaluation of the floor response spectrum acceleration S_a acting on a nonstructural component:

$$S_a = \alpha \cdot S \cdot \left[\frac{3 \cdot (1 + z/H)}{1 + (1 - T_a/T_1)^2} - 0.5 \right] \cdot g \geq \alpha \cdot S \cdot g \tag{1}$$

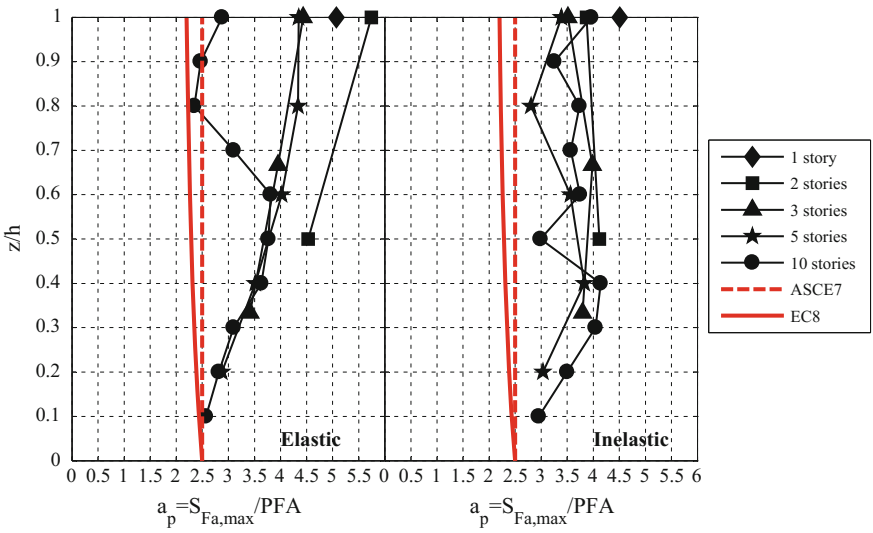

Fig. 10 Floor acceleration magnification on nonstructural components

where:

- α is the ratio between the ground acceleration and the gravity acceleration g;
- S is a soil amplification factor;
- z/H is the relative structural height at which the component is installed;
- T_a is the nonstructural component period;
- T_1 is the fundamental period of the primary structure, assumed during the design phase.

The design floor response spectrum depends on the ratio between the nonstructural component period and the structural period, as well as by the level at which the nonstructural component is installed. The formulation does not identify separately the different factors that affect the floor spectral accelerations, as provided, instead, by ASCE7 formulation [2]. However, it implicitly assumes that the PFA linearly ranges from PGA at the base to 2.5 times PGA at the top of the structure, whereas a_p linearly ranges from 2.5 at the base to 2.2 at the top of the structure. Moreover, the maximum S_a value is equal to 5.5 times the PGA, i.e. the spectral acceleration acting on a component placed at the top floor which is in tune with the structure.

For different values of T_a and for each floor, the Eurocode formulation provides a curve that shows the maximum value for T_a equal to T_1. In Fig. 11 both inelastic floor spectra and design Eurocode 8 floor spectra are plotted for the benchmark structures. This comparison underlines that Eurocode formulation underestimates the maximum floor acceleration demand for a wide range of nonstructural component periods, whereas it may overestimate the acceleration demand on nonstructural components with a period close to the design period of the structure (T_{des} in Fig. 2). Moreover the peak of the Eurocode curve is reached at the design period, which is lower than the effective one for all inelastic models.

Eurocode formulation does not take into account higher modes: a significant underestimation is recorded in the range of periods close to the higher modes periods of vibration. The effective floor spectrum acceleration can be significantly underestimated, especially for tall structures, e.g. the 10-story structure in Fig. 11e, in which higher modes are predominant.

The effect of the higher modes in the floor response spectra is clearly influenced by the nonlinear excursion that the structure experiences during the earthquake motion. However, both European and US codes do not explicitly take into account the reduction of the floor response spectra due to the nonlinear behavior of structures, even though the adoption of a low a_p value, i.e. from 2.2 to 2.5, could include the reduction due to the nonlinear behavior of the main structure. Indeed, the a_p values recorded in structures that experience large ductility demand are typically smaller than the ones recorded in Fig. 10, due to the low level of ductility demand experienced by the benchmark structures.

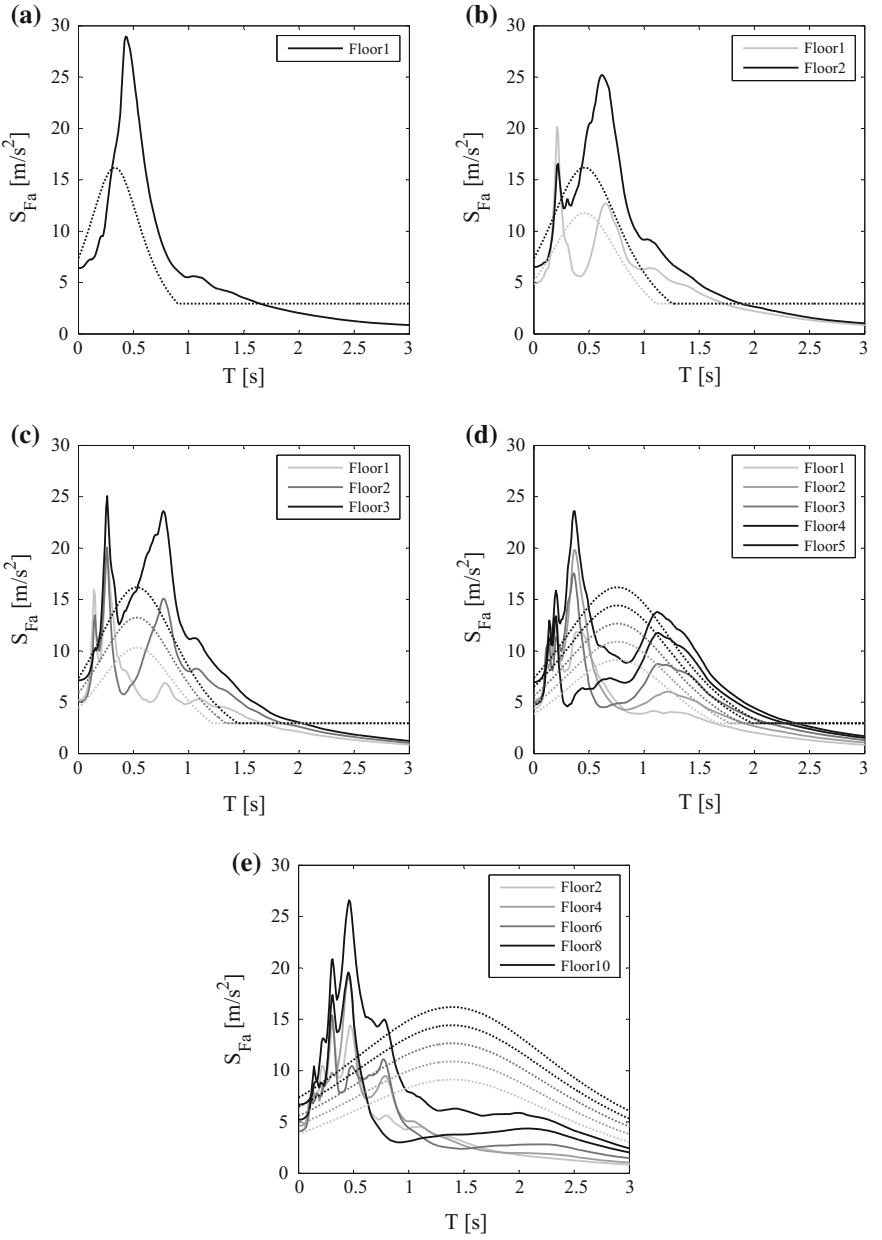

Fig. 11 Comparison between effective inelastic floor response spectra (*solid lines*) and floor response spectra evaluated according to Eurocode 8 (*dashed lines*) for the **a** 1-story, **b** 2-story, **c** 3-story, **d** 5-story and **e** 10-story structures

Finally, it is concluded that the Eurocode could not adequately address the design of acceleration-sensitive nonstructural components, as pointed out by Velasquez et al. [30] who analyzed the floor time-history accelerations recorded during a shake-table test campaign.

3 Code-Oriented Evaluation of the Seismic Demand on Light Acceleration-Sensitive Nonstructural Components in Ordinary Buildings

A parametric study is conducted in order to evaluate the seismic demand on light acceleration-sensitive nonstructural components caused by frequent earthquakes. The study is motivated by the inconsistent approach of current building codes to the design of nonstructural components; moreover, the extensive nonstructural damage recorded after recent low intensity earthquakes also encouraged such a study. The selected set of benchmark RC frame structures are therefore subjected to a set of frequent earthquakes.

3.1 Why Investigate Floor Spectra Caused by Frequent Earthquakes?

Current building codes, such as Eurocode 8 (EC8) [4] and Italian Building Code (NTC 08) [6], provide that ultimate limit states are not achieved for a rare earthquake, e.g. 475-year return period earthquakes for ordinary buildings, and damage/serviceability limit state are not overcome for a frequent earthquake, e.g. 50-year return period earthquakes for ordinary buildings, according to the approach included in [28]. Ultimate limit states concern the safety of the people and the structure whereas serviceability limit states concern the functioning of the structure.

The Italian Building Code accurately defines the two limit states considered during the design phase. Ultimate limit state is reached in case nonstructural components fail and structural components are damaged but the structure still has a safety margin with respect to collapse. Damage limit state, instead, is reached in case structural components, nonstructural components and contents exhibit a minor damage level that does not threaten the life safety and reduce the safety of the building.

The "damage limitation requirement" is deemed to be satisfied by just limiting the structural interstory drifts for frequent earthquakes; the limitation implies that displacement-sensitive nonstructural components are not damaged in case a frequent earthquake occurs. Both EC8 and NTC 08 provide that acceleration-sensitive nonstructural components, instead, are designed in order to withstand the seismic demand caused by a rare earthquake, e.g. a 475-year return period event for

ordinary buildings. This approach is inconsistent: hence, while it is implicitly accepted that displacement-sensitive nonstructural components may collapse for a rare earthquake, acceleration-sensitive components should not collapse for such an intense motion.

It is definitely important to verify that nonstructural components do not exhibit major damage for a frequent earthquake, considering the limit state definitions mentioned above. Moreover, it is questionable to verify such components against a rare earthquake; it does not make sense to verify their safety while, according to the definition of the ultimate limit state, it is accepted that they can collapse for a rare earthquake. The verification for a rare earthquake could be conducted only for nonstructural components that can threaten the life safety in case of failure. Therefore it seems reasonable to design also acceleration-sensitive nonstructural components in ordinary buildings according to frequent earthquakes. For this reason, the research study aims at evaluating the seismic demand on acceleration-sensitive nonstructural components caused by frequent earthquakes. It should be underlined that the such considerations are limited to ordinary buildings. Nonstructural components inserted in strategic facilities, such as hospitals, must remain operational even for rare earthquakes [11].

3.2 Methodology

Modeling of benchmark structures. Dynamic analyses are carried out for a set of seven earthquake records, on both linear and nonlinear models. Both linear and nonlinear analyses are performed on the selected benchmark structures.

A distributed plasticity approach is selected in order to define the nonlinear model of the structures. This approach allows investigating pre- and post-cracking behavior of the elements. Primary elements are modeled as nonlinear force-based elements [16]. For each element appropriate cross sections are defined considering the actual geometry and steel reinforcement. The cross section is divided into fibers and a unixial stress-strain relationship is defined for each of them. The stress–strain relationship for both unconfined and confined concrete are evaluated according to Mander et al. [15]. The tensile concrete strength is also considered. A bilinear with hardening relationship is adopted for the steel.

Ground motion records. A set of accelerograms representative of the frequent earthquake ground motion at the considered site is defined based on the motivations included in Sect. 3.1. Eurocode 8 does not provide a formulation for the definition of the spectrum corresponding to a frequent earthquake. The Italian Building Code, instead, provides detailed hazard maps (a grid of more than 16,000 points) corresponding to different probabilities of exceedance in 50 years; the maps allow defining the spectrum that envelopes the uniform hazard spectrum at the site characterized by a given probability of exceedance. The maps are defined upon a probabilistic seismic hazard assessment (PSHA) of Italy performed by Stucchi et al. [29].

In order to be consistent with the spectrum adopted during the design phase, the selected point of the Italian grid exhibits a 475-y return period spectrum very close to the one assumed during the design phase. The point, located close to the epicenter of (6.9 M_w) 1980 Irpinia earthquake, is characterized by a peak ground acceleration on stiff soil equal to 0.25 g for a 10 % probability of exceedance in 50 years, i.e. a return period equal to 475 years. According to the Italian Building Code, a frequent earthquake is characterized by a 63 % probability of exceedance, i.e. a 50-year return period; for the selected grid point the peak ground acceleration on stiff soil, characterized by a 63 % probability of exceedance in 50 years is equal to 0.078 g.

A suitable set of 7 European accelerograms recorded on soil type B is then provided, according to the EC8 recommendations [14], matching the 50-year return period spectrum [19].

3.3 Results and Discussion

Elastic and inelastic floor response spectra. Dynamic analyses on elastic and inelastic models are performed. The floor response spectrum at a given story is evaluated as the mean of the floor response spectra evaluated subjecting the structure to the 7 selected accelerograms. A 5 % damping ratio is considered. The floor response spectra resulting from elastic and inelastic models are plotted and compared in Fig. 12.

However, for inelastic models the peaks do not correspond to natural periods because the primary elements, subjected both to vertical loads and horizontal seismic action, exhibit a stiffness reduction due to the cracking, leading to the natural period elongation phenomenon.

The influence of higher modes is more evident in tall buildings, whose floor spectral accelerations, associated to the higher modes, are greater than the ones corresponding to the first mode. This phenomenon is more evident for inelastic models, in which the reduction of the floor spectral ordinates mainly involves the first mode peak, whereas the peaks corresponding to the higher modes are only slightly reduced.

Floor amplification evaluation. The trends of the ratio between the peak floor acceleration (PFA) and the peak ground acceleration (PGA) are plotted in Fig. 13, in order to study the acceleration amplification at the different story levels.

Both elastic and inelastic models show almost linear trends, excepting the 10-story structure, where the shape of the PFA/PGA trend is influenced by the second mode displacement shape at the top stories. A reduction of the PFA/PGA ratio is exhibited in the inelastic models with respect to the elastic ones, due to the cracking of the primary elements; however, at lower stories of the tallest buildings, i.e. 5- and 10-story structures, a slight increase is recorded. This latter phenomenon could be caused by the great influence that higher modes have when structural nonlinearity, i.e. cracking, occurs [9, 23].

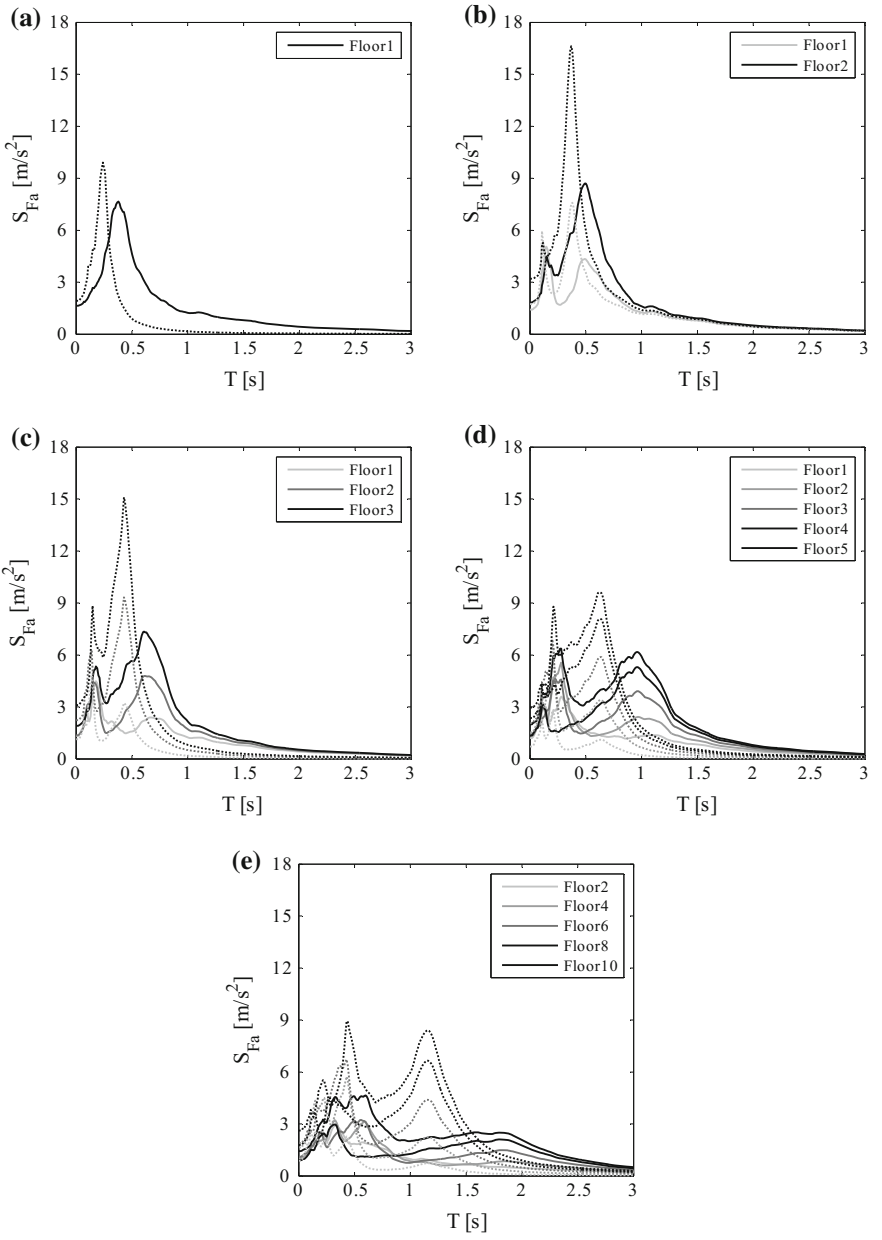

Fig. 12 Floor response spectra in elastic (*dotted lines*) and inelastic (*solid lines*) models for **a** 1-story, **b** 2-story, **c** 3-story, **d** 5-story and **e** 10-story structures

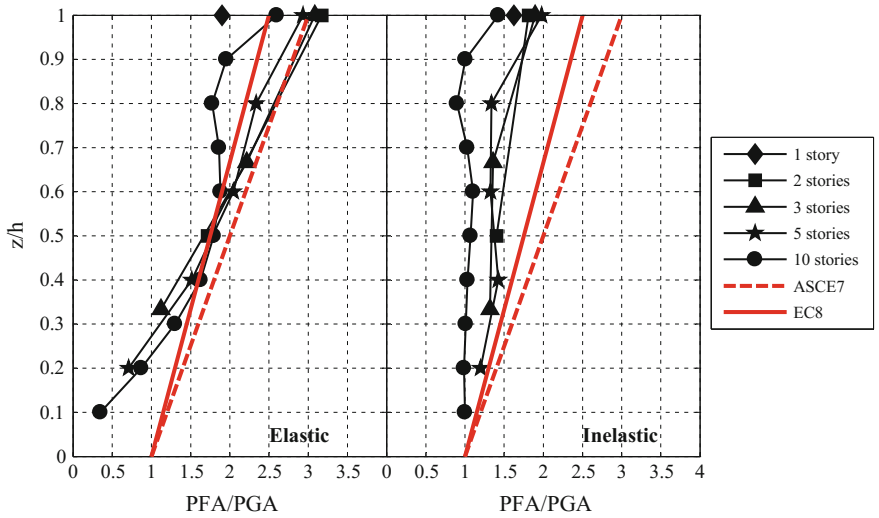

Fig. 13 Ratio between peak floor acceleration (PFA) and peak ground acceleration (PGA), versus the relative height (z/h) compared to the provisions included in ASCE7 and EC8

Both EC8 and ASCE 7 envelopes overestimate the numerical outcomes; it is noted that inelastic models are considered, since they better predict the actual behavior of the structures through the inclusion of the cracking in the elements.

Component amplification evaluation. The trends of the ratio a_p between the maximum floor spectrum acceleration ($S_{fa,max}$) and the PFA with respect to relative height are shown in Fig. 14, in order to study the component acceleration magnification of the floor accelerations. The outcomes corresponding to the elastic and inelastic models are compared: only slight differences are exhibited. The a_p ratio ranges from 3.0 to 5.2 in elastic models whereas it ranges from 2.6 to 4.8 in inelastic models. The component acceleration magnifications in tall buildings are generally smaller than the ones in short structures.

A noteworthy underestimation of the a_p values in the current building codes is highlighted, as shown in Medina et al. [17].

Comparison with EC8 formula and limitations. The Eurocode 8 floor response spectrum could be then compared to the floor spectra resulting from the analyses, assuming a peak ground acceleration on stiff soil equal to 0.078 g, i.e. the 50-year return period peak ground acceleration. In Fig. 15 the floor spectra are compared to Eurocode 8 floor spectra for the different structures considered in this study. In order to take into account the realistic behavior of the primary structures, floor spectra in inelastic models are considered.

This comparison underlines that Eurocode 8 typically underestimates the acceleration demand on nonstructural components for a wide range of periods, especially for periods close to the structural natural periods. Eurocode floor spectra give a good approximation, typically safe-sided, of the floor spectra for period

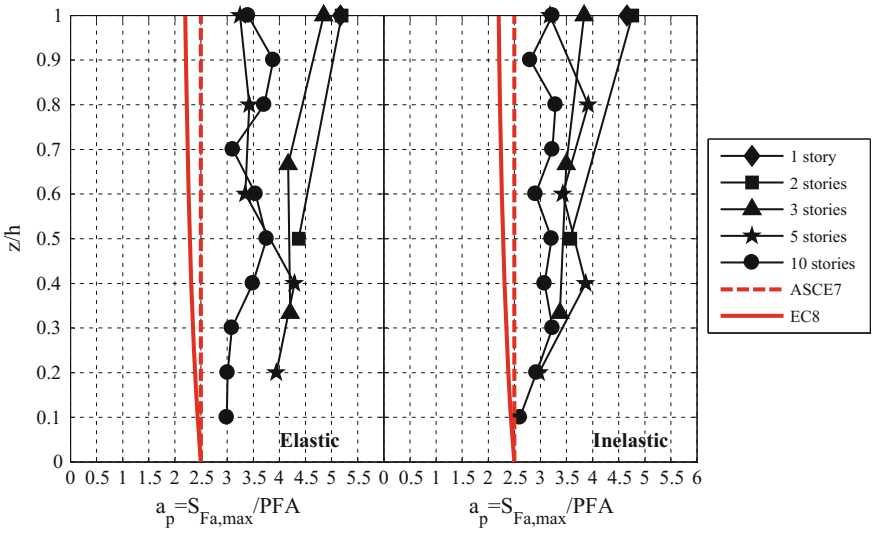

Fig. 14 Floor acceleration magnification on nonstructural components versus the relative height (z/h) compared to the provisions included in ASCE7 and EC8

sufficiently larger than the fundamental period of the structure. They also give a good approximation of the period at which the maximum floor spectral acceleration occurs; this is caused by the assumption of halved inertia during the design phase, in order to take into account the effects of cracking.

Higher mode effects are not considered in Eurocode formulation: a significant underestimation is recorded in the range of periods close to the higher mode periods of vibration. The effective floor spectrum acceleration can be significantly underestimated, especially for tall buildings, i.e. the 5- and the 10-story structures, in which higher modes are predominant. An urgent need to include higher modes in the code formulation is highlighted.

3.4 Definition of a Code Formula

The previous sections highlighted the inadequacy of Eurocode provisions for the evaluation of the seismic demand on acceleration-sensitive nonstructural components. The main issues of the EC8 formulation can be summarized in: (a) the slight overestimation of the peak floor acceleration, (b) the significant underestimation of the component acceleration magnification at a given floor, (c) the non-inclusion of the higher mode effects in the formulation, that leads to a significant underestimation of the floor spectral acceleration for small periods. However, the shape of the Eurocode floor spectrum is found to suitably catch the shape of typical floor response spectra.

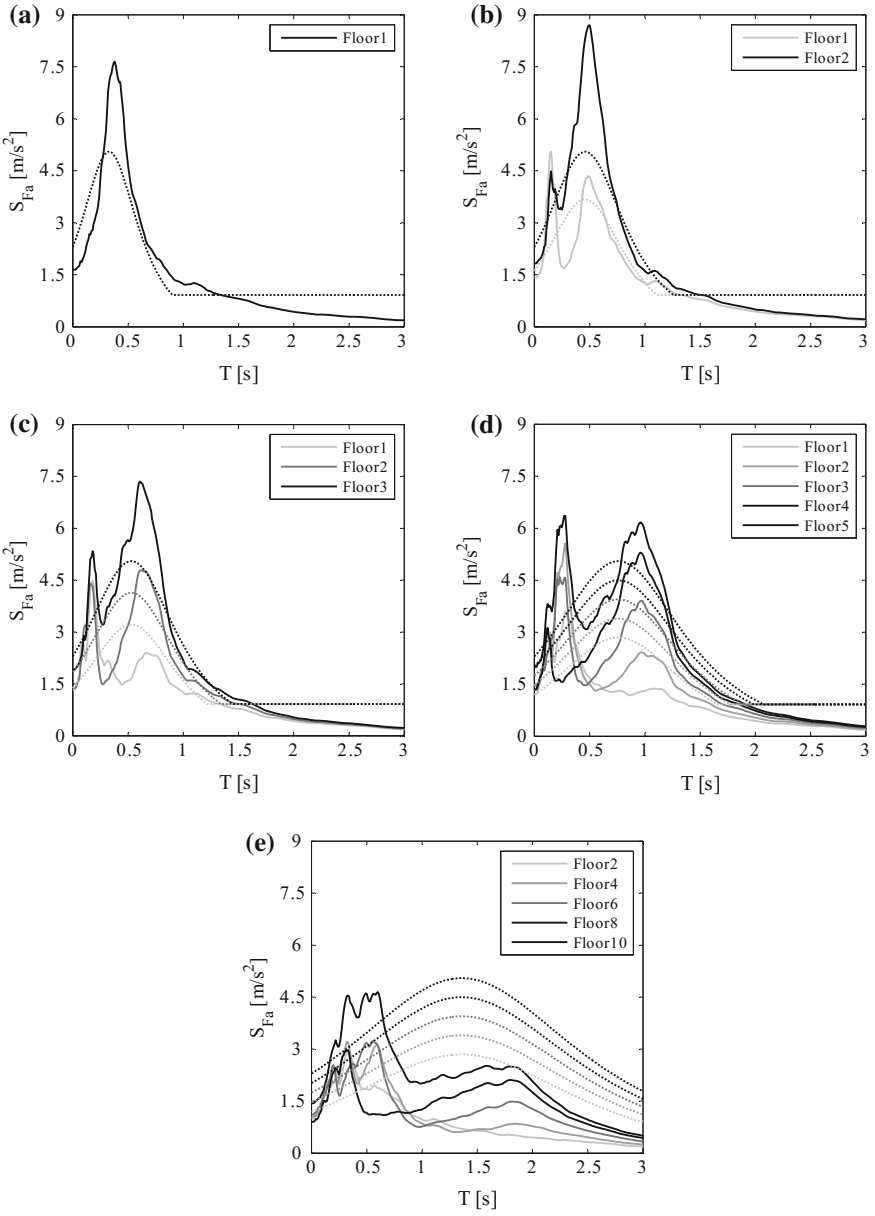

Fig. 15 Floor response spectra (*solid lines*) on inelastic models compared to EC8 floor spectra (*dashed lines*) for the **a** 1-story, **b** 2-story, **c** 3-story, **d** 5-story and **e** 10-story structures

In this Section a novel formulation is proposed (Fig. 16): it is based on the Eurocode formulation and to some suggestions included in [8].

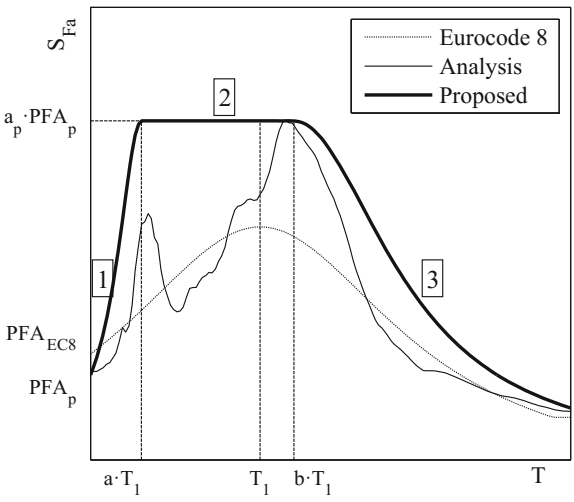

Fig. 16 Proposed floor spectral shape compared to the Eurocode 8 floor spectral shape and to a typical analytical floor spectrum

Table 4 Values of the parameters of the proposed formulation for different ranges of structural periods

	a [–]	b [–]	a_p [–]
$T_1 < 0.5$ s	0.8	1.4	5.0
0.5 s < T_1 < 1.0 s	0.3	1.2	4.0
$T_1 > 1.0$ s	0.3	1.0	2.5

A formula similar to the one already included in the Eurocodes is defined, both for the sake of simplicity and in order to facilitate the implementation in future building codes.

- A three-branch floor response spectrum is defined (branches from 1 to 3 in Fig. 16), in order to include the peaks corresponding to higher mode effect. Branches no. 1 and no. 3 have a shape similar to Eurocode 8 floor spectrum. The definition of the flat branch no. 2 is also capable to include the uncertainty in the evaluation of the structural periods.
- The formula included in EC8 is slightly modified in order to directly distinguish the different terms, i.e. ground acceleration, floor amplification and component amplification, that influence the definition of the floor response spectrum.
- The PFA over PGA ratio trend is modified according to the analysis results. The proposed ratio trend goes from 1 at the base of the structure to 2 at its top.
- The amplification factor a_p is increased up to 5 for short buildings and is reduced for tall ones (Table 4), according to the analysis results (Fig. 14).

The proposed response spectra is defined according to the following formulation:

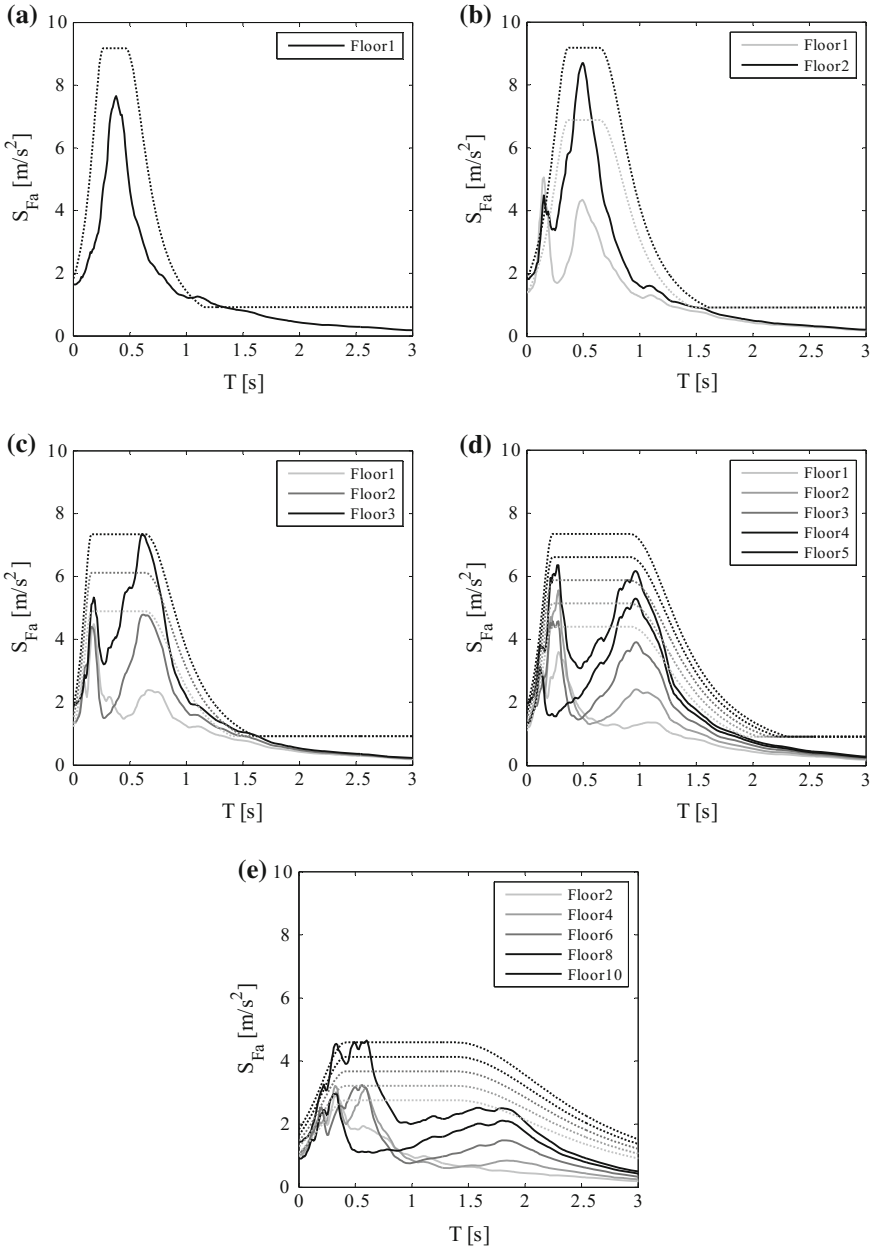

Fig. 17 Floor response spectra (*solid lines*) on inelastic models compared to formulation *(3)* (*dashed lines*) for the **a** 1-story, **b** 2-story, **c** 3-story, **d** 5-story and **e** 10-story structures

$$S_{Fa,proposed}(T) = \begin{cases} \alpha \cdot S \cdot g \cdot (1 + z/H) \cdot \left[\frac{a_p}{1 + (a_p - 1)(1 - T/a \cdot T_1)^2} \right] \geq \alpha \cdot S \cdot g & \text{for } T < a \cdot T_1 \\ \alpha \cdot S \cdot g \cdot (1 + z/H) \cdot a_p & \text{for a} \cdot T_1 < T < b \cdot T_1 \\ \alpha \cdot S \cdot g \cdot (1 + z/H) \cdot \left[\frac{a_p}{1 + (a_p - 1)(1 - T/b \cdot T_1)^2} \right] \geq \alpha \cdot S \cdot g & \text{for } T > b \cdot T_1 \end{cases} \tag{2}$$

The parameters a, b and a_p are defined according to the fundamental period of the structure T_1 according to Table 4. They are based on the indications included in [8] and they are then calibrated in order to ensure a good match between the analytical floor response spectra and the proposed floor spectra. The other parameters are the same as in Eurocode.

The floor spectra are evaluated according to the proposed formulation and compared to the analytical floor spectra evaluated on the inelastic models (Fig. 17). The proposed floor spectra are typically safe-sided with respect to the analytical results. They are also capable to include the peaks related to the structural higher modes; the reduction of the seismic demand on very flexible nonstructural components is also caught.

The proposed formulation yields conservative floor spectral accelerations for a wide range of periods, especially for periods close to the fundamental period; however, this overestimation could cover the uncertainty in the estimation of the structural period due to, for instance, the presence of stiff infill walls and partition walls [18], as well as the uncertainty in the estimation of the nonstructural component period during the design phase.

4 Conclusions

A parametric study for the evaluation of the floor response spectra in European RC frame structures, i.e. 1-2- 3-5- and 10-story structures, is conducted. The structures, designed according to Eurocode 8, are subjected to a set of earthquakes that are compatible with the elastic design response spectrum for a life safety limit state. Preliminary nonlinear static analyses show that the benchmark structures are characterized by a significant overstrength, due to some geometric limitations included in the Eurocode 8. Time-history analyses are performed both on elastic and inelastic models of the benchmark structures. The comparison between elastic and inelastic floor response spectra shows a substantial reduction of the peak spectral ordinate associated to the first mode; moreover, the peak occurs at a longer period due to the period elongation phenomenon. The peak spectral values associated with the higher modes are only slightly reduced in the inelastic model. At lower stories, the spectral values associated to higher modes can be even larger than the elastic ones. The ratio between PFA and PGA trend with the relative structural height shows that both the ASCE7 and EC8 provisions are safe-sided. A linear trend that goes from 1 at the base of the structure to 2 at the top would better fit the

outcome of the analyses. The yielding of the structure gives a significant contribution to the peak floor acceleration reduction. The component amplification, i.e. the ratio between the maximum floor spectral value and the PFA, is almost constant with the height for both elastic and inelastic models. An unsafe-sided estimation of the a_p values in the actual building codes is clearly highlighted: the component amplification a_p values are significantly greater than 2.5, which is the value recommended by ASCE7 and EC8, and close to 4.5. It is found that Eurocode formulation for the evaluation of the seismic demand on nonstructural components does not fit well the results of the analyses. It underestimates the maximum floor acceleration demand for a wide range of nonstructural component periods, whereas it overestimates the acceleration demand on nonstructural components with a period close to the design period of the structure. The underestimation is significant for nonstructural component periods close to the higher modes structural periods, since the Eurocode formulation does not include higher modes effect.

Furthermore, the floor spectra are evaluated according to a set of accelerograms compatible to a frequent seismic input motion. The investigation of floor response spectra induced by frequent earthquakes is motivated by a detailed analysis of the limit states definition in the actual European and Italian Building Codes. Both elastic and inelastic models of the benchmark structures are considered. A period elongation phenomenon is shown in floor spectra of the inelastic models, which is mainly caused by the cracking of the primary elements. The peak floor acceleration shows an almost linear trend with the structural relative height. The predictions included both in EC8 and ASCE 7 are conservative, i.e. they provide larger values of peak floor acceleration compared to the accelerations that result from the analyses. The peak component acceleration, i.e. the maximum floor spectral acceleration value at a given story, normalized to the peak floor acceleration exhibits an almost constant trend with the structural relative height. Moreover, the taller the structure is, the smaller the component amplification factor becomes. A significant unsafe-sided prediction of both EC8 and ASCE 7 provisions is demonstrated. The comparison of the floor spectra of inelastic models with the EC8 provisions clearly underlines that Eurocode 8 typically underestimates the acceleration demand on nonstructural component for a wide range of periods. Eurocode floor spectra give a good approximation, typically safe-sided, of the floor spectra for periods sufficiently larger than the fundamental period of the structure. A significant underestimation is recorded in the range of periods close to the higher mode periods of vibration of the benchmark structures.

A novel formulation is then proposed, based on the Eurocode actual formulation for an implementation in the future building codes. The proposed formulation is shown to be able to envelope the floor spectral peaks due to the higher modes. Moreover, it yields conservative floor spectral acceleration for a wide range of periods, especially for periods close to the fundamental period. However, such an overestimation could cover the uncertainty in the estimation of the structural and the nonstructural component periods during the design phase.

It should be underlined that the above presented results and conclusions are related and limited to a set of five RC “simple” structures designed according to

Eurocode 8. A larger set of structures should be considered in a future study to further validate the proposed formulation.

References

1. Ambraseys N, Smit P, Sigbjornsson R, Suhadolc P, Margaris B (2002) Internet-Site for European strong-motion data. European Commission, Research-Directorate General, Environment and Climate Programme
2. American Society of Civil Engineers (2010) ASCE/SEI 7-10: minimum design loads for buildings and other structures. Reston, Virginia, US
3. CEN (2004a) Eurocode 2: Design of concrete structures—Part 1–1: general rules and rules for buildings. EN 1992-1-1. Brussels, Belgium
4. CEN (2004b) Eurocode 8: design of structures for earthquake resistance—Part 1: general rules, seismic actions and rules for buildings. EN 1998-1. Brussels, Belgium
5. Chaudhuri S, Villaverde R (2008) Effect of building nonlinearity on seismic response of nonstructural components: a parametric study. J Struct Eng 134(4):661–670. doi:10.1061/(ASCE)0733-9445
6. Consiglio Superiore dei Lavori Pubblici (2008) Decreto Ministeriale del 14/01/2008, Approvazione delle nuove norme tecniche per le costruzioni. G.U. n. 29 del 4/2/2008 (in Italian)
7. Consiglio Superiore dei Lavori Pubblici (2009) Circolare 2 febbraio 2009, n. 617, Istruzioni per l'applicazione delle «Nuove norme tecniche per le costruzioni». G.U. n. 27 del 26-2-2009 (in Italian)
8. Fathali S, Lizundia B (2011) Evaluation of current seismic design equations for nonstructural components in tall buildings using strong motion records. Struct Des Tall Spec Buildings 20:30–46. doi:10.1002/tal.736
9. Fischinger M, Ercolino M, Kramar M, Petrone C, Isakovic T (2011a) Inelastic seismic shear in multi-storey cantilever columns. Paper presented at the 3rd international conference on computational methods in structural dynamics and earthquake engineering, COMPDYN 2011, Corfu, Greece, 25–28 May 2011
10. Fischinger M, Ercolino M, Kramar M, Petrone C, Isakovic T (2011b) Inelastic seismic shear in multi-storey cantilever columns. In: ECCOMAS Thematic conference—COMPDYN 2011: 3rd international conference on computational methods in structural dynamics and earthquake engineering: an IACM special interest conference, programme
11. Gatscher JA, Bachman R (2012) Elements of 2012 IBC/ASCE 7–10 Nonstructural seismic provisions: bridging the implementation gap. Paper presented at the 15th world conference on earthquake engineering, Lisboa, Portugal
12. Haselton CB (2006) Assessing seismic collapse safety of modern reinforced concrete moment frame buildings. Ph.D. thesis, Stanford University, California, US
13. Ibarra LF, Medina RA, Krawinkler H (2005) Hysteretic models that incorporate strength and stiffness deterioration. Earthq Eng Struct Dyn 34(12):1489–1511. doi:10.1002/eqe.495
14. Maddaloni G, Magliulo G, Cosenza E (2012) Effect of the seismic input on non-linear response of R/C building structures. Adv Struct Eng 15(10):1861–1877
15. Mander J, Priestley M, Park R (1988) Theoretical stress-strain model for confined concrete. J Struct Eng 114(8):1804–1826 10.1061/(ASCE)0733-9445
16. McKenna F, Fenves GL (2013) OpenSees Manual. Pacific Earthquake Engineering Research Center, Berkeley, California. http://opensees.berkeley.edu
17. Medina RA, Sankaranarayanan R, Kingston KM (2006) Floor response spectra for light components mounted on regular moment-resisting frame structures. Eng Struct 28(14):1927–1940. doi:10.1016/j.engstruct.2006.03.022

18. Petrone C, Magliulo G, Manfredi G (2014) Shake table tests for the seismic assessment of hollow brick internal partitions. Eng Struct 72:203–214. doi:10.1016/j.engstruct.2014.04.044
19. Petrone C, Magliulo G, Manfredi G (2015) Seismic demand on light acceleration-sensitive nonstructural components in European reinforced concrete buildings. Earthq Eng Struct Dyn 44:1203–1217. doi:10.1002/eqe.2508
20. Petrone C, Magliulo G, Manfredi G (2016) Floor response spectra in RC frame structures designed according to Eurocode 8. Bull Earthq Eng 14(3):747–767. doi:10.1007/s10518-015-9846-7
21. Politopoulos I (2010) Floor spectra of MDOF nonlinear structures. J Earth Eng 14(5):726–742. doi:10.1080/13632460903427826
22. Ray-Chaudhuri S, Hutchinson TC (2011) Effect of nonlinearity of frame buildings on peak horizontal floor acceleration. J Earth Eng 15(1):124–142. doi:10.1080/13632461003668046
23. Rejec K, Isaković T, Fischinger M (2012) Seismic shear force magnification in RC cantilever structural walls, designed according to Eurocode 8. Bull Earthq Eng 10(2):567–586. doi:10.1007/s10518-011-9294-y
24. Rodriguez ME, Restrepo JI, Carr AJ (2002) Earthquake-induced floor horizontal accelerations in buildings. Earthq Eng Struct Dyn 31(3):693–718. doi:10.1002/eqe.149
25. Sankaranarayanan R, Medina RA (2007) Acceleration response modification factors for nonstructural components attached to inelastic moment-resisting frame structures. Earthq Eng Struct Dyn 36(14):2189–2210. doi:10.1002/eqe.724
26. Singh M, Moreschi L, Suárez L, Matheu E (2006) Seismic design forces. I: rigid nonstructural components. J Struct Eng 132(10):1524–1532 10.1061/(ASCE)0733-9445
27. Singh M, Moreschi L, Suárez L, Matheu E (2006) Seismic design forces. II: flexible nonstructural components. J Struct Eng 132(10):1533–1542 10.1061/(ASCE)0733-9445
28. Structural Engineers Association of California (SEAOC) (1995) Vision 2000—a framework for performance-based design. California Office of Emergency Services
29. Stucchi M, Meletti C, Montaldo V, Crowley H, Calvi GM, Boschi E (2011) Seismic hazard assessment (2003–2009) for the Italian building code. Bull Seismol Soc Am 101(4):1885–1911. doi:10.1785/0120100130
30. Velasquez JF, Restrepo J, Blandon CA (2012) Floor response spectra for the design of acceleration sensitive light nonstructural systems in buildings. Paper presented at the 15th world conference on earthquake engineering, Lisboa, Portugal, 24–28 Sept 2013
31. Wieser J, Pekcan G, Zaghi AE, Itani A, Maragakis M (2013) Floor accelerations in yielding special moment resisting frame structures. Earthq Spectra 29(3):987–1002. doi:10.1193/1.4000167

Design of RC Sections with Single Reinforcement According to EC2-1-1 and the Rectangular Stress Distribution

Vagelis Plevris and George Papazafeiropoulos

Abstract Nowadays, the design of concrete structures in Europe is governed by the application of Eurocode 2 (EC2). In particular, EC2—Part 1-1 deals with the general rules and the rules for concrete buildings. An important aspect of the design is specifying the necessary tensile (and compressive, if needed) steel reinforcement required for a Reinforced Concrete (RC) section. In this study we take into account the equivalent rectangular stress distribution for concrete and the bilinear stress-strain relation with a horizontal top branch for steel. This chapter presents three detailed methodologies for the design of rectangular cross sections with tensile reinforcement, covering all concrete classes, from C12/15 up to C90/105. The purpose of the design is to calculate the necessary tensile steel reinforcement. The first methodology provides analytic formulas and an algorithmic procedure that can be easily implemented in any programming language. The second methodology is based on design tables that are provided in Appendix A, requiring less calculations. The third methodology provides again analytic formulas that can replace the use of tables and even be used to reproduce the design tables. Apart from the direct problem, the inverse problem is also addressed, where the steel reinforcement is given and the purpose is to find the maximum bending moment that the section can withstand, given also the value and position of the axial force. For each case analytic relations are extracted in detail with a step-by-step procedure, the relevant assumptions are highlighted and results for four different cross section design examples are presented.

V. Plevris (✉)
Department of Civil Engineering and Energy Technology, Oslo and Akershus University College of Applied Sciences, Pilestredet 35, 0166 Oslo, Norway
e-mail: vagelis.plevris@hioa.no

G. Papazafeiropoulos
National Technical University of Athens, Institute of Structural Analysis and Antiseismic Research, Zografou Campus, 15780 Athens, Greece
e-mail: gpapazafeiropoulos@yahoo.gr

M. Papadrakakis et al. (eds.), *Computational Methods in Earthquake Engineering*, Computational Methods in Applied Sciences 44,
DOI 10.1007/978-3-319-47798-5_8

1 Literature Review and Introduction

During the last decades, well-established procedures have been used for the design of reinforced concrete cross-sections against bending and/or axial loads [8]. Three Model Codes have been published in the past [2, 3, 5, 6], which are guiding documents for future codes, making recommendations for the design of reinforced and prestressed concrete structures. In the first two, improved models were developed for a more accurate representation of the structural behaviour of reinforced concrete structures. In Model Code 1990 [3] constitutive equations for the proper description of concrete material properties were introduced (concrete strengths up to C80 were considered), in view of the possibility of nonlinear finite element analysis of structures. Model Code 1990 [3] became the most important reference document for the future development of EC2-1-1 [4]. A detailed presentation of the Model Code 2010 [5, 6] is given in [13].

It is common knowledge that all relevant national standards of European countries regarding the design and construction of reinforced concrete structures will eventually be replaced by the Eurocode 2 (EC2), which will be valid throughout the whole Europe and not only. EC2-Part 1-1 [4] specifies the strength and deformation characteristics of 14 classes of concrete, classified according to their strength. For all of these, stress–strain relationships are defined for: (a) structural analysis, (b) design of cross-section and (c) confinement of concrete. In the second case, three stress-strain relationships are defined for concrete as follows: (a) parabolic-rectangular stress distribution (b) bi-linear stress distribution, (c) rectangular stress distribution.

In the past research has been conducted regarding the degree of simplification, conservative design, safety and equivalence in between the three above cases of stress-strain distributions, as well as their application for modern types of reinforcement (e.g. Fibre Reinforced Polymer, FRP). In [9] the design of a reinforced concrete section subjected to bending using two stress–strain relationships mentioned in EC2, namely the parabola-rectangle stress distribution and the rectangular distribution, is studied and the differences are underlined. Two dimensionless quantities are used to convert the parabola-rectangle stress distribution to an equivalent concentrated force for the concrete in compression. Also analytic relations which determine the limit between single reinforcement (only tensile) and double reinforcement (tensile and compressive) are provided. The results drawn from the use of these two stress distributions, namely, parabola–rectangle and rectangle, showed that the differences between the amounts of reinforcement are less than 1 % for singly reinforced sections and less than 2 % for doubly reinforced sections.

Due to the different characteristics of higher strength concrete (higher strain before reaching yield, and much reduced stress plateau after yield) some design procedures traditionally used in normal strength concrete structures had to be revised. In [7], Jenkins compared the results of the revised rectangular stress block specified in the Australian Standard Concrete Structures Code AS 3600-2009 [11]

regarding concrete strengths higher than 50 MPa, with those in the main international codes (e.g. ACI 318-2005 [1], EC2-1-1 [4]), and with stress-strain distributions closer to the actual behaviour of high strength concrete. It was found that the equivalent rectangular stress block derived from the parabolic-rectangular stress block of EC2 (assuming the same positions of centroids and the same resultant compressive force) gave almost identical results to the parabolic-rectangular curve of EC2 for all concrete strengths when used on a rectangular section.

In [10] the influence of the assumed stress-strain curve for concrete on the prediction of the strength of conventional and high strength concrete columns under eccentric axial load is investigated. It was concluded that the traditional parabola-rectangle stress-strain relationship of the CEB-FIP Model Code 90 (for $f_{ck} < 50$ MPa) leads to unsafe results when used for high strength concrete.

A general methodology for determining the moment capacity of FRP RC sections by using the general parabola-rectangle diagram for concrete in compression, according to the model of EC2 is proposed in [12]. Non-dimensional equations are derived independently of the characteristics of concrete and FRP reinforcement, and a simplified closed-form equation is also proposed for the case of failure due to FRP rupture. These equations can be used to obtain universal design charts and tables, which can facilitate the design process. A comparative study is also presented between the predictions of the proposed methodology and experimental results from 98 tests available in the literature.

Although the above studies deal with the application of the most suitable stress-strain diagram for concrete for the "optimal" design of cross sections using different approaches, to the authors' knowledge, there is no study in which explicit closed formulas, design charts and design tables are provided to achieve the design of RC sections according to EC2-1-1 [4]. In the present study, the case of the rectangular stress distribution of EC2-1-1 for concrete is thoroughly studied and three different but equivalent methodologies are provided for the design of RC sections with single tensile reinforcement. The first and the third of the methodologies provide analytic formulas and step-by-step instructions for the design, while the second is based on easy-to-use design tables that are provided in Appendix. In addition, the inverse problem is also investigated, again using the three methodologies, where given the steel reinforcement the aim is to find the maximum bending moment that the RC section can withstand, given also the axial force acting on the section.

2 Concrete

2.1 Concrete Properties

According to EC2-1-1 [4] the compressive strength of concrete is denoted by concrete strength classes which relate to the characteristic (5 %) cylinder strength f_{ck}, or cube strength $f_{ck,cube}$, in accordance with EN 206-1. Higher strength

Table 1 Strength classes for concrete according to EC2-1-1

f_{ck} (MPa)	12	16	20	25	30	35	40	45	50	55	60	70	80	90
$f_{ck,cube}$ (MPa)	15	20	25	30	37	45	50	55	60	67	75	85	95	105

concretes, up to the class C90/105 are covered by Eurocode 2. The strength classes for concrete are presented in Table 1 where f_{ck} is the characteristic compressive cylinder strength of concrete at 28 days and $f_{ck,cube}$, is the corresponding cube strength.

The design compressive strength is defined as

$$f_{cd} = a_{cc}\frac{f_{ck}}{\gamma_c} \tag{1}$$

where:

- γ_c is the partial safety factor for concrete at the Ultimate Limit State, which is given in Table 2.1 N of EC2-1-1 [4]. For persistent and transient design situations, $\boldsymbol{\gamma_c = 1.5}$
- a_{cc} is the coefficient taking account of long term effects on the compressive strength and of unfavourable effects resulting from the way the load is applied. The value of a_{cc} for use in a country should lie between 0.8 and 1.0 and may be found in its National Annex. **The recommended value is 1**, although various countries have adopted lower values, leading to more conservative designs.

It should be noted that higher concrete strength shows more brittle behaviour, reflected by shorter horizontal branch, as will be shown in the stress-strain relations and diagrams, later.

2.2 *Concrete Stress-Strain Relations for the Design of Cross Sections*

Eurocode 2 Part 1-1 suggests the use of three approaches for the stress-strain relations of concrete for the design of cross sections:

1. Parabola-rectangle diagram (more detailed)—EC2-1-1 Par. 3.1.7(1)
2. Bi-linear stress-strain relation (less detailed)—EC2-1-1 Par. 3.1.7(2)
3. Rectangular stress distribution (simplest approach)—EC2-1-1 Par. 3.1.7(3)

The three different approaches are described in detail in the following sections. In the present study, only the 3rd approach has been used for the design of RC sections.

2.2.1 Rectangular Stress Distribution

According to Paragraph 3.1.7(3) of EC2-1-1, a rectangular stress distribution may be assumed for concrete, as shown in Fig. 1 (Fig. 3.5 of EC2-1-1 [4]).

In the figure, d is the effective depth of the cross-section, x is the neutral axis depth, A_s is the cross sectional area of the tensile steel reinforcement, ε_s is the tensile strain at the position of the steel reinforcement, F_c is the concrete force (compressive, positive, as in the figure), F_s is the steel reinforcement force (tensile, positive, as in the figure). The factor λ defining the effective height of the compression zone and the factor η defining the effective strength, are calculated from:

$$\lambda = \begin{cases} 0.8 & \text{for} \quad f_{ck} \leq 50 \text{ MPa} \\ 0.8 - \frac{f_{ck}-50}{400} & \text{for} \quad 50 < f_{ck} \leq 90 \text{ MPa} \end{cases} \tag{2}$$

$$\eta = \begin{cases} 1.0 & \text{for} \quad f_{ck} \leq 50 \text{ MPa} \\ 1.0 - \frac{f_{ck}-50}{200} & \text{for} \quad 50 < f_{ck} \leq 90 \text{ MPa} \end{cases} \tag{3}$$

According to EC2-1-1, Table 3.1 [4] the value of ε_{cu3} is given by

$$\varepsilon_{cu3}(‰) = \begin{cases} 3.5 & \text{for} \quad f_{ck} \leq 50 \text{ MPa} \\ 2.6 + 35\left(\frac{90-f_{ck}}{100}\right)^4 & \text{for} \quad 50 < f_{ck} \leq 90 \text{ MPa} \end{cases} \tag{4}$$

Table 2 and Fig. 2 show the values of the parameters λ, η and ε_{cu3} for each concrete class.

Note: According to EC2-1-1 [4], if the width of the compression zone decreases in the direction of the extreme compression fibre, the value $\eta \cdot f_{cd}$ should be reduced by 10 %. This case is not examined in the present study, as the cross section is assumed to be rectangular and the width of the compression zone does not decrease. In any case, if needed, this correction can be very easily implemented in the calculations.

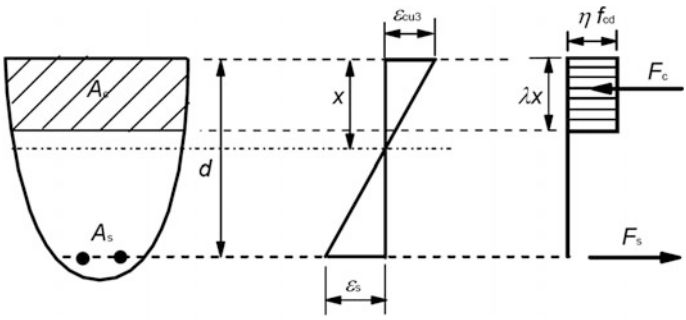

Fig. 1 Rectangular stress distribution

Table 2 The parameters λ, η and ε_{cu3} for each concrete class

Concrete Class	λ	η	ε_{cu3} (‰)
C12/15–C50/60	0.80	1.00	3.50
C55/67	0.79	0.98	3.13
C60/75	0.78	0.95	2.88
C70/85	0.75	0.90	2.66
C80/95	0.73	0.85	2.60
C90/105	0.70	0.80	2.60

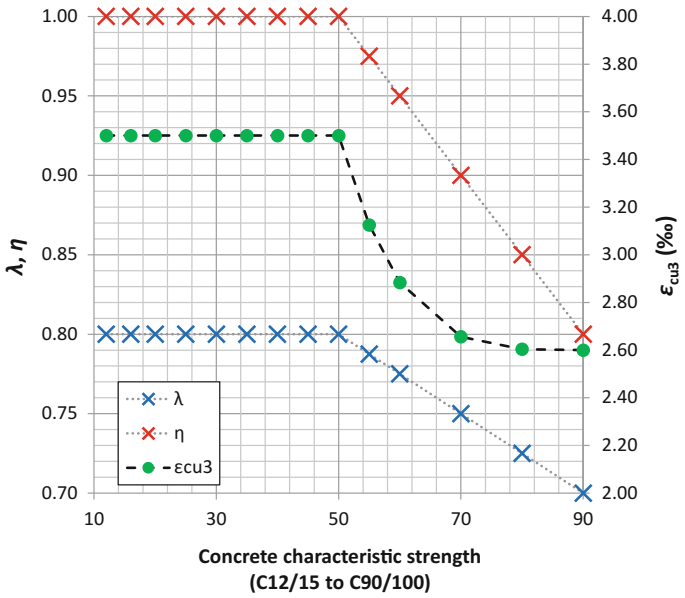

Fig. 2 The parameters λ, η and ε_{cu3} for each concrete class

3 Steel

3.1 Steel Properties

The design strength for steel is given by

$$f_{yd} = \frac{f_{yk}}{\gamma_s} \tag{5}$$

where γ_s is the partial safety factor for steel at the Ultimate Limit State, which is given in Table 2.1 N of EC2-1-1 [4] (for persistent and transient design situations, $\boldsymbol{\gamma_s = 1.15}$) and f_{yk} is the characteristic yield strength of steel reinforcement.

Table 3 Properties of steel reinforcement according to EC2-1-1

Product form	Bars and de-coiled rods			Requirement or quantile value (%)
Class	A	B	C	–
Characteristic yield strength f_{yk} or $f_{0,2k}$ (MPa)	400–600			5.0
Minimum value of $k = (f_t/f_y)_k$	≥ 1.05	≥ 1.08	≥ 1.15 <1.35	10.0
Characteristic strain at maximum force, ε_{uk} (%)	≥ 2.5	≥ 5.0	≥ 7.5	10.0

Table 3 (derived from Table C.1 of Annex C of EC2-1-1 [4]) gives the properties of reinforcement suitable for use with the Eurocode. The properties are valid for temperatures between −40 and 100 °C for the reinforcement in the finished structure. Any bending and welding of reinforcement carried out on site should be further restricted to the temperature range as permitted by EN 13670.

The application rules for design and detailing in Eurocode 2 are valid for a specified yield strength range, f_{yk} from 400 to 600 MPa. The yield strength f_{yk} is defined as the characteristic value of the yield load divided by the nominal cross sectional area. The reinforcement should have adequate ductility as defined by the ratio of tensile strength to the yield stress, $(f_t/f_y)_k$ and the characteristic strain at maximum force, ε_{uk}. Typical values of f_{yk} used in the design practice nowadays are 400 and 500 MPa.

3.2 *Steel Stress-Strain Relations for the Design of Cross-Sections*

According to Paragraph 3.2.7(2) of EC2-1-1, for normal design, either of the following assumptions may be made for the stress-strain relation for steel, as shown in Fig. 3 (Fig. 3.8 of EC2-1-1 [4]):

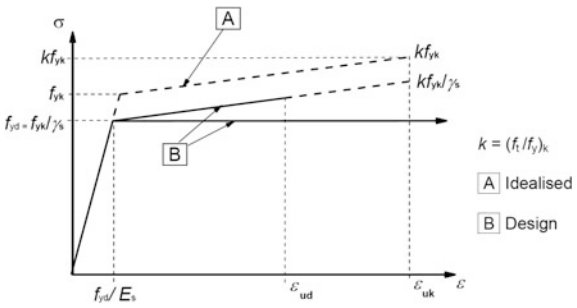

Fig. 3 Idealised and design stress-strain diagrams for reinforcing steel (for tension and compression)

Table 4 The parameters f_{yk}, f_{yd} and ε_{ys} for each steel class, assuming E_s = 200 GPa and γ_s = 1.15

Steel Class	f_{yk} (MPa)	f_{yd} (MPa)	ε_{ys} (‰)
B400	400	347.83	1.74
B500	500	434.78	2.17
B600	600	521.74	2.61

1. An inclined top branch with a strain limit of ε_{ud} and a maximum stress of $k \cdot f_{yk}/\gamma_s$ at ε_{uk}, where $k = (f_t/f_y)_k$.
2. A horizontal top branch without the need to check the strain limit.

The parameter k defines the inclination of the top branch. The special case $k = 1$ corresponds to a horizontal top branch (no inclination).

In the present study we use the second of the above approaches, i.e. a horizontal top branch for steel ($k = 1$). According to this approach, there is no need to check the strain limit of steel and as a result in the design of RC cross sections, the concrete is always assumed to be the critical material. In this case, the steel design stress is given by

$$\sigma_s = \begin{cases} f_{yd} \cdot \frac{\varepsilon_s}{\varepsilon_{ys}} = E_s \cdot \varepsilon_s & \text{if } 0 < \varepsilon_s < \varepsilon_{ys} \\ f_{yd} & \text{if } \varepsilon_s \geq \varepsilon_{ys} \end{cases} \tag{6}$$

where f_{yd} is the design steel strength given by Eq. (5) and ε_{ys} is the design yield strain given by

$$\varepsilon_{ys} = \frac{f_{yd}}{E_s} \tag{7}$$

The design value of the steel modulus of elasticity E_s may be assumed to be 200 GPa according to EC2-1-1 [4].

Table 4 shows the parameters f_{yk}, f_{yd} and ε_{ys} for each steel class (B400, B500, B600), with the assumptions E_s = 200 GPa and γ_s = 1.15, in accordance with EC2-1-1 [4].

4 Design Assumptions

The following design assumptions are made in this study, in accordance with Eurocode 2—Part 1-1:

1. The design is based on characteristic concrete cylinder strengths, not cube strengths.
2. Plane sections remain plane.
3. Strain in the bonded reinforcement, whether in tension or compression, is the same as that of the surrounding concrete.
4. The tensile strength of concrete is completely ignored.

5. The concrete stress is considered according to the simplified rectangular distribution shown in Fig. 1. This gives the opportunity to obtain elegant closed-form solutions for the design process.
6. Stress in steel reinforcement is considered according to the stress-strain relation of EC 2-1-1 [4] for steel (Fig. 3), with a horizontal top branch without the need to check the strain limit. As a result, concrete is assumed to always be the critical material, reaching its maximum strain at ULS.

5 Rectangular Stress Distribution Case Definitions

Figure 4 shows a typical rectangular cross section and the distribution of strains, stresses and corresponding forces.

Since the horizontal top branch for the steel stress-strain relationship is adopted in this study (Fig. 3), there is no need to check the strain limit of steel and at the Ultimate Limit State (ULS) the concrete is the critical material ($\varepsilon_c = \varepsilon_{cu3}$) as shown in Fig. 4, where:

- h and b are the height and width of the rectangular section, respectively
- d_1 is the distance from the lower edge of the section to the centre of the tensile reinforcement
- d is the effective depth of the rectangular section
- x is the neutral axis depth
- ε_s is the tensile strain in the steel reinforcement
- $\varepsilon_c = \varepsilon_{cu3}$ is the compressive strain in the concrete upper edge
- λ is a factor defining the effective height of the compression zone, given by Eq. (2)

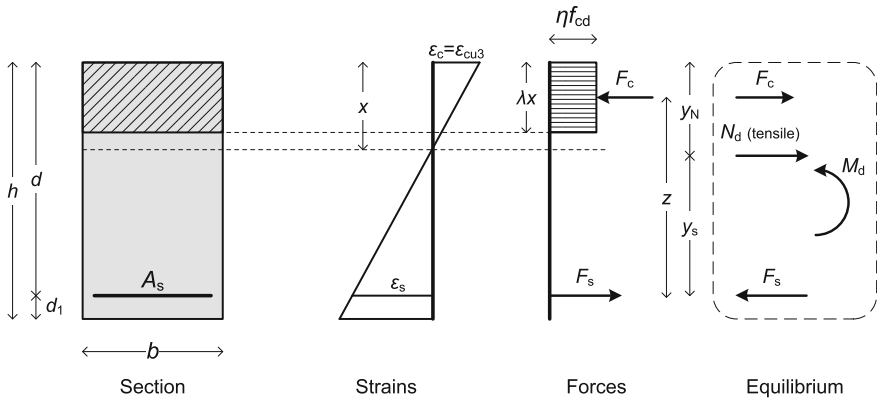

Fig. 4 Cross section, strain, stresses and forces distribution and section equilibrium, assuming $\varepsilon_c = \varepsilon_{cu3}$ (concrete at limit strain)

- η is a factor defining the effective strength of the compression zone, given by Eq. (3)
- M_d is the applied external bending moment (if positive, it puts the lower edge of the section in tension)
- N_d is the applied external axial force (tensile for the section if positive), applied at a position y_N measured from the top of the section towards the lower edge of it. Note: If the axial force is central, acting at the middle of the section height, then $y_N = h/2$
- y_s is the distance from the tensile steel reinforcement to the position of the external applied axial force
- z is the distance of the resultant concrete force F_c from the steel reinforcement
- F_c is the concrete (compressive) force
- F_s is the steel (tensile) force
- A_s is the required steel reinforcement.

5.1 Definition of the Direct and the Inverse Problem

In the direct problem, the loading conditions (bending moment M_d, axial force N_d,) are given and the purpose is to calculate the required tensile reinforcement (steel area) A_s. In the inverse problem, A_s and N_d (applied at y_N) are given and the purpose is to calculate the maximum bending moment M_d that the cross section can withstand.

6 Investigation of the Direct Problem

6.1 Analytical Calculation of the Required Tensile Reinforcement Area $\mathbf{A}_s$

In the direct problem, the loading conditions are given and the purpose is to calculate the required tensile reinforcement (steel area) A_s. In order to calculate A_s, the unknown quantities x and z for the given loading conditions have to be calculated first. After moving the external force N_d to the position of the steel reinforcement and imposing force and moment equilibrium for the cross-section, the situation is depicted in Fig. 5.

From the equilibrium of the section in the x-direction, we have:

$$\Sigma F_x = 0 \Rightarrow F_c + N_d - F_s = 0 \Rightarrow F_s = F_c + N_d \tag{8}$$

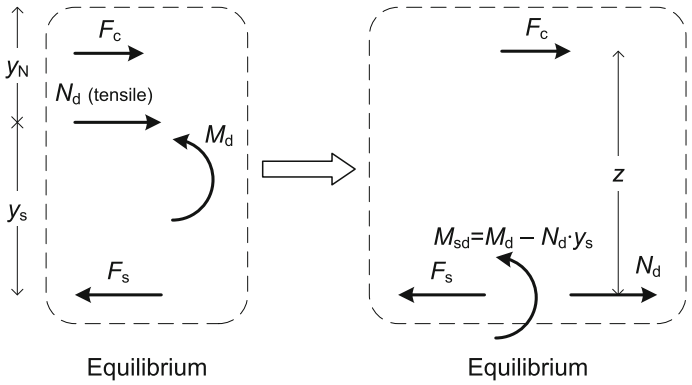

Fig. 5 Equilibrium after moving the external force N_d to the position of the steel reinforcement

We have also:

$$d_1 + d = h \Rightarrow d = h - d_1 \tag{9}$$

$$y_s + y_N = d \Rightarrow y_s = d - y_N \tag{10}$$

The effective bending moment applied at the location of the steel reinforcement is:

$$M_{sd} = M_d - N_d \cdot y_s \tag{11}$$

From the geometry of the section (Fig. 4), we have:

$$d = z + \frac{\lambda x}{2} \Rightarrow z = d - \frac{\lambda x}{2} \tag{12}$$

The concrete force, assuming a rectangular distribution of stresses, is given by:

$$F_c = \lambda x \eta b f_{cd} \tag{13}$$

From the equilibrium of moments at the position of the steel reinforcement (Fig. 5) we have (clockwise moment taken as positive):

$$\Sigma M_{steel} = 0 \Rightarrow F_c \cdot z - M_{sd} = 0 \Rightarrow M_{sd} = F_c \cdot z \tag{14}$$

By substituting Eq. (13) into Eq. (14), we obtain:

$$M_{sd} = \lambda x \eta b z f_{cd} \tag{15}$$

By substituting Eq. (12) into Eq. (15), we have:

$$M_{sd} = \lambda x \eta b f_{cd} \cdot \left(d - \frac{\lambda x}{2}\right) = x \cdot (\lambda \eta b d f_{cd}) - x^2 \cdot \left(nb \frac{\lambda^2}{2} f_{cd}\right) \Rightarrow \quad (16)$$

$$\left(\frac{\eta b \lambda^2 f_{cd}}{2}\right) \cdot x^2 - (\lambda \eta b d f_{cd}) \cdot x + M_{sd} = 0 \quad (17)$$

The above quadratic equation needs to be solved for the neutral axis depth x. All quantities except for x are known and the solution of the quadratic equation can be easily obtained as

$$x_{1,2} = \frac{d}{\lambda} \pm \frac{\sqrt{\Delta_1}}{2A_1} \quad (18)$$

where

$$A_1 = \frac{\eta b \lambda^2 f_{cd}}{2} \quad (19)$$

and Δ_1 is the discriminant of the quadratic equation:

$$\Delta_1 = \lambda^2 \eta b f_{cd} \left(\eta b d^2 f_{cd} - 2M_{sd}\right) \quad (20)$$

According to Eq. (2), it is always $\lambda < 1$, as $\lambda = 0.80$ for $f_{ck} \leq 50$ MPa and $\lambda < 0.80$ for $50 < f_{ck} \leq 90$ MPa and as a result $d/\lambda > d$ which leads to $x_2 > d$ which is not acceptable, since the requirement is that $0 \leq x \leq d$ for sections under bending. Therefore the only acceptable solution is $x = x_1$ and thus:

$$x = x_1 = \frac{d}{\lambda} - \frac{\sqrt{\Delta_1}}{2A_1} \quad (21)$$

After calculating x from Eq. (21), it is easy to calculate also z, F_c and F_s from Eqs. (12), (13), (8). The required tensile reinforcement is then calculated by

$$A_s = \frac{F_s}{\sigma_s} \quad (22)$$

where σ_s is the steel stress at the Ultimate Limit State (ULS) of the section, calculated by Eq. (6). In our case, at the ULS the concrete zone is always at the critical strain, $\varepsilon_c = \varepsilon_{cu3}$ while the steel strain ε_s can be calculated considering the geometry of Fig. 4 as follows:

$$\frac{\varepsilon_{cu3}}{x} = \frac{\varepsilon_{cu3} + \varepsilon_s}{d} \Rightarrow \varepsilon_s = \left(\frac{d}{x} - 1\right)\varepsilon_{cu3} \tag{23}$$

If the steel does not work in full stress ($\sigma_s < f_{yd}$), although the required reinforcement area A_s can be calculated, the design with a single tensile reinforcement is not economic. Either compressive reinforcement should be also added, or an increase in the dimensions of the cross section, in particular its effective depth d.

6.1.1 Maximum Effective Moment $M_{sd,max}$ that the Section Can Withstand

The maximum effective bending moment that the section can withstand (either economically, with steel working at full strength or not) can be calculated by setting $x = d$, so that the concrete compressive zone obtains its maximum value. In order to find the corresponding maximum effective bending moment $M_{sd,max}$, we set $x = d$ in Eq. (16) and we obtain:

$$M_{sd,max} = \lambda\left(1 - \frac{\lambda}{2}\right)\eta b d^2 f_{cd} \tag{24}$$

It should be noted that the maximum effective bending moment $M_{sd,max}$ is the upper limit of the effective moment, but the design for $M_{sd,max}$ is in fact impossible, as for $x = d$, it is $\varepsilon_s = 0$, $\sigma_s = 0$ and as a result an infinite amount of steel reinforcement would be needed according to Eq. (22).

The effective bending moment M_{sd} can be also expressed in general in a normalized (dimensionless) form as follows

$$\mu_{sd} = \frac{M_{sd}}{b d^2 f_{cd}} \tag{25}$$

where μ_{sd} is called the normalized effective bending moment. For the maximum normalized effective bending moment, we have

$$\mu_{sd,max} = \frac{M_{sd,max}}{b d^2 f_{cd}} = \lambda\left(1 - \frac{\lambda}{2}\right)\eta \tag{26}$$

It can be seen that $\mu_{sd,max}$ depends only on the concrete class, as λ and η are both direct functions of the concrete strength only [Eqs. (2) and (3)].

6.1.2 Critical Effective Moment $M_{sd,lim}$ that the Section Can Withstand Economically

Theoretically, the steel area can be calculated for any $M_{sd} < M_{sd,max}$ (or equivalently $\mu_{sd} < \mu_{sd,max}$) but as mentioned earlier, for the cases $M_{sd,lim} < M_{sd} < M_{sd,max}$ (or $\mu_{sd,lim} < \mu_{sd} < \mu_{sd,max}$) the design is not economic as steel works below its yield point. In order for the design to be economic, the steel reinforcement has to work above the yield limit, at full strength ($\varepsilon_s \geq \varepsilon_{ys}$ and $\sigma_s = f_{yd}$). At the limit of this condition, we set $\varepsilon_s = \varepsilon_{ys}$ in Eq. (23), and solving for x, we have the corresponding limit value x_{lim} of x:

$$x_{lim} = \frac{\varepsilon_{cu3}}{\varepsilon_{cu3} + \varepsilon_{ys}} d \tag{27}$$

In order to find the corresponding effective moment $M_{sd,lim}$, we set $x = x_{lim}$ in Eq. (16)

$$M_{sd,lim} = x_{lim} \cdot (\lambda \eta b d f_{cd}) - x_{lim}^2 \cdot \left(\eta b \frac{\lambda^2}{2} f_{cd} \right) \tag{28}$$

By substituting x_{lim} from Eq. (27) into Eq. (28), we finally obtain:

$$M_{sd,lim} = \frac{\varepsilon_{cu3}\left(1 - \frac{\lambda}{2}\right) + \varepsilon_{ys}}{\left(\varepsilon_{cu3} + \varepsilon_{ys}\right)^2} \varepsilon_{cu3} \cdot \eta \lambda b d^2 f_{cd} \tag{29}$$

The corresponding dimensionless limit value $\mu_{sd,lim}$ is then

$$\mu_{sd,lim} = \frac{M_{sd,lim}}{b d^2 f_{cd}} = \frac{\varepsilon_{cu3}(1 - \lambda/2) + \varepsilon_{ys}}{\left(\varepsilon_{cu3} + \varepsilon_{ys}\right)^2} \eta \lambda \varepsilon_{cu3} \tag{30}$$

If for a given design problem $M_{sd} \leq M_{sd,lim}$ (or equivalently $\mu_{sd} \leq \mu_{sd,lim}$) then an economic design *can* be achieved using single steel reinforcement only. On the other hand, if $M_{sd} > M_{sd,lim}$ (or $\mu_{sd} > \mu_{sd,lim}$) then an economic design cannot be achieved using only single steel reinforcement. Either double reinforcement (tensile and also compressive) is needed, or an increase in the dimensions of the cross section (especially d, but also b). As shown in Eq. (30), the value of $\mu_{sd,lim}$ depends on the concrete strength class and the steel yield strain ε_{ys} which is dependent on the steel strength, as shown in Eq. (7) and Table 4.

6.1.3 Summary of the Analytical Methodology for the Design of Cross Sections

The full methodology for the calculation of the needed steel reinforcement A_s is summarized below:

Known quantities for the design:

- **Materials properties**: f_{ck}, f_{yk}, E_s (EC2-1-1 value is 200 GPa)
- **Safety factors**: γ_c (EC2-1-1 value is 1.5), γ_s (EC2-1-1 value is 1.15), a_{cc} (EC2-1-1 recommended value is 1, National Annexes can enforce values between 0.8 and 1.0)
- **Section geometry**: b, h, d_1
- **Loading conditions**: M_d, N_d applied at y_N position

Quantities to be calculated and corresponding equation to use:

- λ: Eq. (2), η: Eq. (3)
- f_{cd},: Eq. (1), ε_{cu3}: Eq. (4), f_{yd}: Eq. (5), ε_{ys}: Eq. (7)
- d: Eq. (9), y_s: Eq. (10), M_{sd}: Eq. (11)
- $M_{sd,max}$: Eq. (24). If $M_{sd} < M_{sd,max}$ then proceed with the next calculations, otherwise stop, the design *cannot* be achieved
- $M_{sd,lim}$: Eq. (29). If $M_{sd} < M_{sd,lim}$ then the design using single steel reinforcement is economic (steel working at full strength), otherwise the design using single steel reinforcement can be achieved, but it is not economic (steel working below full strength)
- A_1: Eq. (19), Δ_1: Eq. (20), x: Eq. (21), z: Eq. (12)
- F_c: Eq. (13), F_s: Eq. (8)
- ε_s: Eq. (23), σ_s: Eq. (6), A_s: Eq. (22)

The above procedure is straightforward and can be easily implemented in any programming language. A simple spreadsheet program, such as Microsoft Excel, can be also used in order to make the necessary calculations, without even the need for any complicated programming macros.

6.2 *Design of Cross Sections Using Design Tables*

In this section, we explain how the steel reinforcement area can be calculated using the design tables that are provided in Appendix A. We define the dimensionless value ω as

$$\omega = \frac{F_c}{bdf_{cd}} \tag{31}$$

From Eq. (8) we have

$$F_c = F_s - N_d \tag{32}$$

Substituting F_s from Eqs. (22) in (32) and then substituting F_c from Eq. (32) into Eq. (31) we obtain

$$\omega = \frac{A_s \sigma_s - N_d}{bdf_{cd}} \tag{33}$$

By solving Eq. (33) for A_s, we obtain

$$A_s = \frac{1}{\sigma_s}(\omega bdf_{cd} + N_d) \tag{34}$$

It is obvious that if ω and σ_s are both known, then it is easy to calculate the needed steel reinforcement area A_s from Eq. (34). In Appendix A there are six tables which provide the values of ω and σ_s for given values of the normalized effective bending moment μ_{sd}, for each concrete class. In Sect. 6.3 we will explain how the values of the tables can be calculated. Each table gives the value of ω for a given value of μ_{sd}, together with the values of $\xi = x/d$, $\zeta = z/d$, ε_s (‰) and also σ_s for three different steel classes (B400, B500, B600). Of these parameters, only σ_s is affected by the steel quality and that's why it is given in three columns.

It should be noted that the first nine concrete classes (C12/15, C16/20, C20/25, C25/30, C30/37, C35/45, C40/50, C45/55, C50/60) share the same table (Table 10) while for the other five concrete classes (C55/67, C60/75, C70/85, C80/95 and C90/105) there are separate tables for each case.

The tables are independent of the values of the concrete parameters a_{cc} and γ_c. Of course these parameters affect the final design, but they are taken into account through the calculation of f_{cd} in Eq. (34) which affects the calculation of A_s. The first 5 columns, μ_{sd}, ω, ξ, ζ, ε_s are also independent of the steel parameters γ_s and E_s. Only the steel stress at the ultimate state (last three columns of the tables) depends on the steel parameters γ_s and E_s and these three columns have been calculated with the assumption E_s = 200 GPa and γ_s = 1.15 (in accordance with EC2-1-1 [4]). This is also the case for the limit values $\mu_{sd,lim}$ and ω_{lim} which depend also on E_s and γ_s.

6.2.1 Linear Interpolation for the ω-μ_{sd} Tables

In most cases, the value of μ_{sd} is not an exact value of the table, but rather lies between two neighbouring values μ_{sd1} and μ_{sd2} ($\mu_{sd1} < \mu_{sd} < \mu_{sd2}$). In this case linear interpolation is needed in order to obtain the value of ω that corresponds to the given μ_{sd}. This is of course an easy-to-solve problem, but nevertheless we will provide an explicit analytic solution here.

Table 5 The linear interpolation problem of the μ_{sd}-ω tables

μ_{sd} values from Table	ω values from Table
μ_{sd1}	ω_1
Our μ_{sd} ($\mu_{sd1} < \mu_{sd} < \mu_{sd2}$)	Our ω = ?
μ_{sd2}	ω_2

If ω_1 corresponds to μ_{sd1} and ω_2 corresponds to μ_{sd2} then we have the linear interpolation problem that is depicted in Table 5.

The solution is given below

$$\frac{\mu_{sd2} - \mu_{sd1}}{\omega_2 - \omega_1} = \frac{\mu_{sd} - \mu_{sd1}}{\omega - \omega_1} \Rightarrow \tag{35}$$

$$\omega = \omega_1 + \frac{\mu_{sd} - \mu_{sd1}}{\mu_{sd2} - \mu_{sd1}}(\omega_2 - \omega_1). \tag{36}$$

6.3 *Analytic Formulas and Investigation of the Design Parameters ω, ξ, ζ, ε_s*

In this section, we will investigate the parameters ω, ξ, ζ, ε_s and we will end up to closed formulas for their calculation. Using these formulas, one can easily generate the design tables of Appendix.

6.3.1 Parameter ω

Although the values of the parameter ω can be taken from the design tables using the design approach described before, it is very interesting to investigate also ω analytically, using closed formulas. From Eq. (8) we have

$$F_s = F_c + N_d \tag{37}$$

By substituting the concrete force from Eq. (13) and the steel force from Eq. (22) into Eq. (37), we have

$$A_s \cdot \sigma_s = \lambda x \cdot \eta f_{cd} \cdot b + N_d \tag{38}$$

By substituting A_s from Eq. (34) into Eq. (38), we have

$$\frac{1}{\sigma_s}(\omega b d f_{cd} + N_d) \cdot \sigma_s = \lambda x \cdot \eta f_{cd} \cdot b + N_d \Rightarrow \tag{39}$$

$$\frac{\lambda x \eta}{d} = \omega \tag{40}$$

By definition it is

$$\mu_{sd} = \frac{M_{sd}}{bd^2 f_{cd}} \tag{41}$$

By substituting M_{sd} from Eq. (15) into Eq. (41) we have

$$\mu_{sd} = \frac{\lambda x \cdot \eta f_{cd} \cdot b \cdot z}{bd^2 f_{cd}} = \frac{\lambda \eta x z}{d^2} \tag{42}$$

By substituting z from Eq. (12) into Eq. (42) we obtain

$$\mu_{sd} = \frac{\lambda \eta x\left(d - \frac{\lambda x}{2}\right)}{d^2} = \frac{\lambda x \eta}{d} - \frac{1}{2\eta}\left(\frac{\lambda x \eta}{d}\right)^2 \tag{43}$$

By substituting $\lambda x\eta/d$ from Eq. (40) into Eq. (43) we finally get

$$\mu_{sd} = \omega - \frac{1}{2\eta}\omega^2 \tag{44}$$

The above is a simple analytic formula for the calculation of μ_{sd} when ω is known. This is very useful in the inverse problem which will be investigated later. Now we will try to solve Eq. (44) for ω. It can be written in the following form:

$$\frac{1}{2\eta}\omega^2 - \omega + \mu_{sd} = 0 \tag{45}$$

The solution of the quadratic equation is:

$$\omega_{1,2} = \eta\left(1 \pm \sqrt{1 - \frac{2\mu_{sd}}{\eta}}\right) \tag{46}$$

From the above two solutions, only the one with the negative sign (ω_1) is acceptable (proof will follow) and as a result:

$$\omega = \eta\left(1 - \sqrt{1 - \frac{2\mu_{sd}}{\eta}}\right) \tag{47}$$

Proof that ω_2 (with the positive sign) is not an acceptable solution of Eq. (45)

Assuming that ω_2 is an acceptable solution, then from Eq. (40) we have

$$\omega_2 = \eta \cdot \frac{\lambda x_2}{d} \tag{48}$$

Since

$$\omega_2 = \eta\left(1 + \sqrt{1 - \frac{2\mu_{sd}}{\eta}}\right) \tag{49}$$

Then it should be

$$\eta \cdot \frac{\lambda x_2}{d} = \eta\left(1 + \sqrt{1 - \frac{2\mu_{sd}}{\eta}}\right) \Rightarrow \tag{50}$$

$$\lambda \frac{x_2}{d} = 1 + \sqrt{1 - \frac{2\mu_{sd}}{\eta}} \Rightarrow \tag{51}$$

$$x_2 = \frac{1 + \sqrt{1 - \frac{2\mu_{sd}}{\eta}}}{\lambda} \cdot d \tag{52}$$

Since the numerator is greater than 1 and the denominator λ is less than 1, then $x_2 > d$ which is not acceptable. As a result, ω_2 is *not* an acceptable solution.

Figure 6 depicts Eq. (47) showing ω as a function of the dimensionless effective bending moment μ_{sd}, for every concrete class.

Using Eq. (47) for ω and setting as μ_{sd} the values of $\mu_{sd,max}$ [Eq. (26)] and $\mu_{sd,lim}$ [Eq. (30)] for each steel class, it is easy to calculate the corresponding values ω_{max} and ω_{lim} for every steel class, and obtain the closed formulas as follows:

$$\omega_{max} = \eta\lambda \tag{53}$$

$$\omega_{lim} = \eta\left(1 - \sqrt{1 - \frac{\varepsilon_{cu3}(2-\lambda) + 2\varepsilon_{ys}}{(\varepsilon_{cu3} + \varepsilon_{ys})^2}\lambda\varepsilon_{cu3}}\right) \tag{54}$$

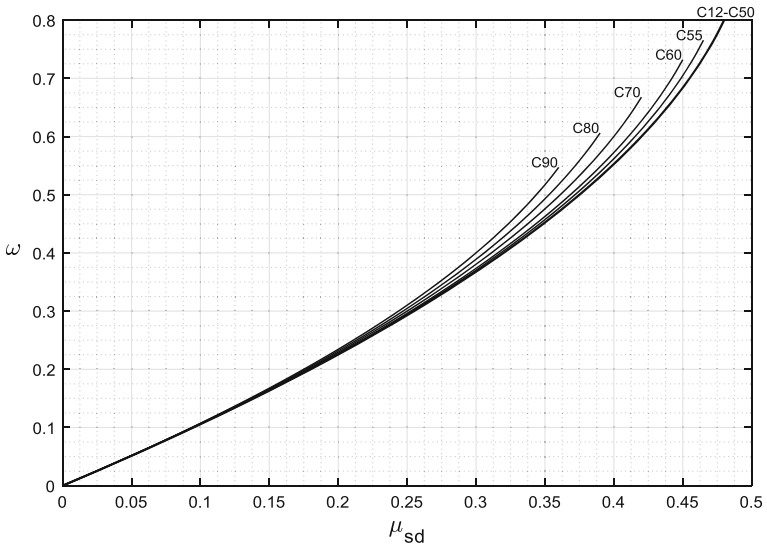

Fig. 6 ω as a function of μ_{sd} for every concrete class

Table 6 The values of the parameters $\mu_{sd,max}$, ω_{max}, $\mu_{sd,lim}$, ω_{lim}

Concrete class	max. (any steel)		lim (B400)		lim (B500)		lim (B600)	
	$\mu_{sd,max}$	ω_{max}	$\mu_{sd,lim}$	ω_{lim}	$\mu_{sd,lim}$	ω_{lim}	$\mu_{sd,lim}$	ω_{lim}
C12/15–C50/60	0.4800	0.8000	0.3916	0.5344	0.3717	0.4935	0.3533	0.4584
C55/67	0.4655	0.7678	0.3685	0.4933	0.3477	0.4528	0.3287	0.4185
C60/75	0.4510	0.7363	0.3482	0.4593	0.3270	0.4198	0.3079	0.3865
C70/85	0.4219	0.6750	0.3155	0.4079	0.2946	0.3712	0.2761	0.3405
C80/95	0.3929	0.6163	0.2892	0.3695	0.2695	0.3358	0.2521	0.3078
C90/105	0.3640	0.5600	0.2652	0.3356	0.2469	0.3050	0.2307	0.2795

Maximum and limit values for μ_{sd} and ω

Table 6 shows the values of the parameters $\mu_{sd,max}$, ω_{max} (the same for all steel classes) and $\mu_{sd,lim}$, ω_{lim} (for steel B400, B500 and B600), for every concrete class. It should be noted that the values of the limit parameters (lim) of the table have been calculated for E_s = 200 GPa and γ_s = 1.15, in accordance with EC2-1-1 [4].

Figure 7 shows the corresponding $\mu_{sd,max}$, ω_{max} and $\mu_{sd,lim}$, ω_{lim}, as functions of the concrete strength. Figure 8 depicts ω_{max} and ω_{lim} versus $\mu_{sd,max}$ and $\mu_{sd,lim}$ for each concrete and steel class.

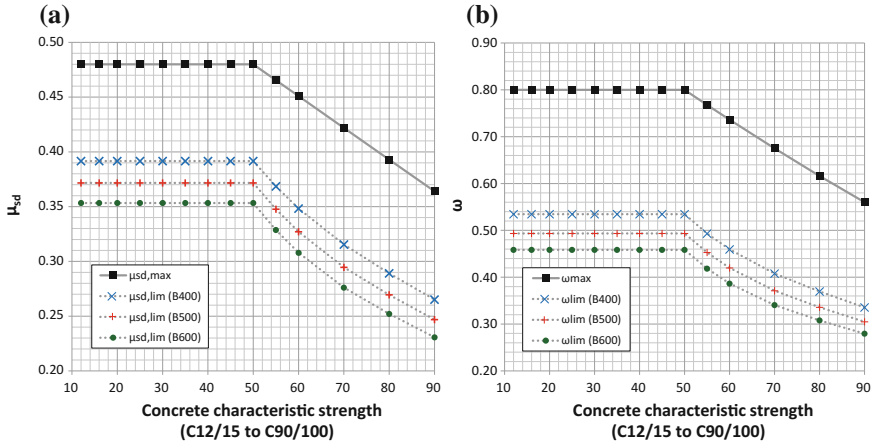

Fig. 7 For each concrete class and steel class: **a** $\mu_{sd,max}$ and $\mu_{sd,lim}$, **b** ω_{max} and ω_{lim}

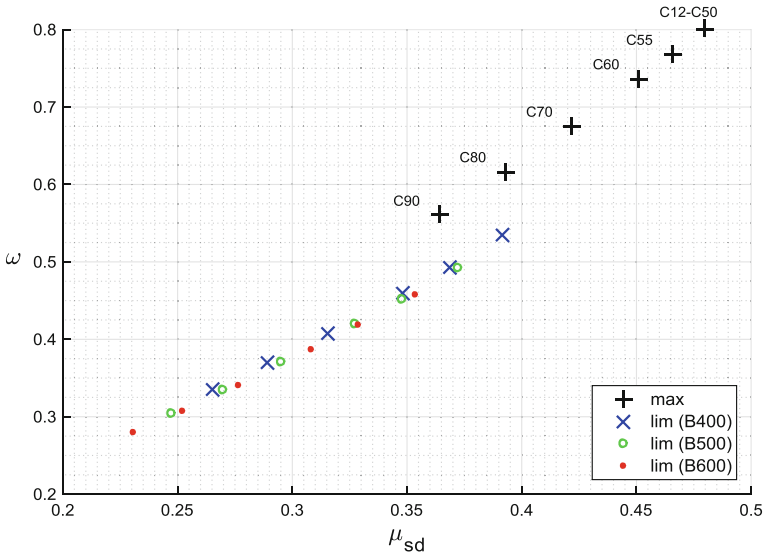

Fig. 8 ω_{max} and ω_{lim} versus $\mu_{sd,max}$ and $\mu_{sd,lim}$ for each concrete and steel class

6.3.2 Parameter ξ

The parameter ξ is the normalized neutral axis depth. The neutral axis depth is normalized with respect to the effective height d of the section and is defined as

$$\xi = \frac{x}{d} \tag{55}$$

Using Eq. (40) and also substituting ω from Eq. (47) we have

$$\xi = \frac{x}{d} = \frac{\omega}{\lambda\eta} = \frac{1}{\lambda}\left(1 - \sqrt{1 - \frac{2\mu_{sd}}{\eta}}\right) \tag{56}$$

The corresponding values $\xi_{\max}$ and $\xi_{\lim}$ are

$$\xi_{max} = 1 \tag{57}$$

$$\xi_{lim} = \frac{1}{\lambda}\left(1 - \sqrt{1 - \frac{\varepsilon_{cu3}(2-\lambda) + 2\varepsilon_{ys}}{\left(\varepsilon_{cu3} + \varepsilon_{ys}\right)^2}\lambda\varepsilon_{cu3}}\right) \tag{58}$$

In Fig. 9 ξ is shown as a function of the normalized moment μ_{sd} for various concrete strength classes. It is apparent that for higher concrete classes, the normalized neutral axis depth is higher, for the same value of μ_{sd}. All curves increase with increasing normalized moment, until ξ gets equal to one ($x = d$).

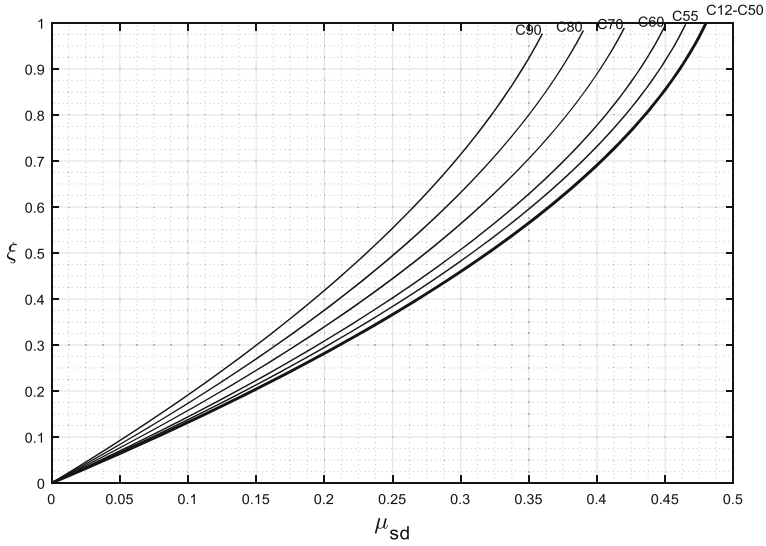

Fig. 9 ξ as a function of μ_{sd} for every concrete class

6.3.3 Parameter ζ

The parameter ζ is the normalized distance of the resultant concrete force from the tensile reinforcement z with respect to the effective section height d and is defined as

$$\zeta = \frac{z}{d} \tag{59}$$

Using Eq. (12) and also Eq. (56) we have

$$\zeta = \frac{z}{d} = \frac{\left(d - \frac{\lambda x}{2}\right)}{d} = 1 - \frac{\lambda}{2} \cdot \frac{x}{d} = 1 - \frac{\lambda}{2} \cdot \xi = 1 - \frac{\omega}{2\eta} \tag{60}$$

Substituting ξ from Eq. (56) we obtain also

$$\zeta = 1 - \frac{\lambda}{2} \cdot \frac{1}{\lambda}\left(1 - \sqrt{1 - \frac{2\mu_{sd}}{\eta}}\right) = 0.5\left(1 + \sqrt{1 - \frac{2\mu_{sd}}{\eta}}\right) \tag{61}$$

The corresponding values $\zeta_{\min}$ (corresponding to $\omega_{\max}$ and $\mu_{\mathrm{sd,max}}$) and $\zeta_{\lim}$ are

$$\zeta_{min} = 1 - \frac{\lambda}{2} \tag{62}$$

$$\zeta_{lim} = 0.5\left(1 + \sqrt{1 - \frac{\varepsilon_{cu3}(2-\lambda) + 2\varepsilon_{ys}}{\left(\varepsilon_{cu3} + \varepsilon_{ys}\right)^2}\lambda\varepsilon_{cu3}}\right) \tag{63}$$

In Fig. 10 ζ is plotted against the dimensionless design bending moment μ_{sd} for various concrete strength classes. It is observed that ζ decreases with increasing concrete strength class for the same value of μ_{sd} and it decreases generally with increasing μ_{sd}.

Table 7 shows the values of the parameters $\xi_{\max}$, $\zeta_{\min}$ (the same for all steel classes) and $\xi_{\lim}$, $\zeta_{\lim}$ (for steel B400, B500 and B600), for every concrete class. It should be noted that the values of the limit parameters (lim) of the table have been calculated for E_s = 200 GPa and γ_s = 1.15, in accordance with EC2-1-1 [4].

6.3.4 Steel Strain ε_s

From the definition of ξ, it is

$$\frac{d}{x} = \frac{1}{\xi} \tag{64}$$

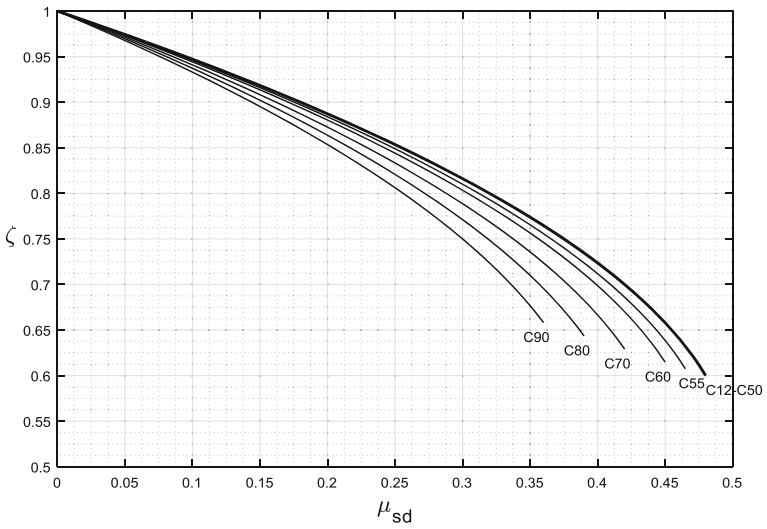

Fig. 10 ζ as a function of μ_{sd} for every concrete class

Table 7 The values of the parameters $\xi_{\max}$, $\zeta_{\min}$, $\xi_{\lim}$, $\zeta_{\lim}$

Concrete class	max./min. (any steel class)		lim (B400)		lim (B500)		lim (B600)	
	$\xi_{\max}$	$\zeta_{\min}$	$\xi_{\lim}$	$\zeta_{\lim}$	$\xi_{\lim}$	$\zeta_{\lim}$	$\xi_{\lim}$	$\zeta_{\lim}$
C12/15–C50/60	1	0.6000	0.6680	0.7328	0.6169	0.7533	0.5730	0.7708
C55/67	1	0.6063	0.6425	0.7470	0.5898	0.7678	0.5450	0.7854
C60/75	1	0.6125	0.6238	0.7583	0.5702	0.7791	0.5250	0.7966
C70/85	1	0.6250	0.6043	0.7734	0.5499	0.7938	0.5045	0.8108
C80/95	1	0.6375	0.5995	0.7827	0.5450	0.8025	0.4995	0.8189
C90/105	1	0.6500	0.5992	0.7903	0.5446	0.8094	0.4992	0.8253

Substituting Eq. (64) into Eq. (23) and also using Eq. (56) we have

$$\varepsilon_s = \left(\frac{1}{\xi} - 1\right)\varepsilon_{cu3} = \left(\frac{1}{\frac{\omega}{\lambda\eta}} - 1\right)\varepsilon_{cu3} = \left(\frac{\lambda\eta}{\omega} - 1\right)\varepsilon_{cu3} \tag{65}$$

or in terms of μ_{sd}

$$\varepsilon_s = \left(\frac{1}{\xi} - 1\right)\varepsilon_{cu3} = \left(\frac{1}{\frac{1}{\lambda}\left(1 - \sqrt{1 - \frac{2\mu_{sd}}{\eta}}\right)} - 1\right)\varepsilon_{cu3} = \left(\frac{\lambda\eta\left(1 + \sqrt{1 - \frac{2\mu_{sd}}{\eta}}\right)}{2\mu_{sd}} - 1\right)\varepsilon_{cu3} \tag{66}$$

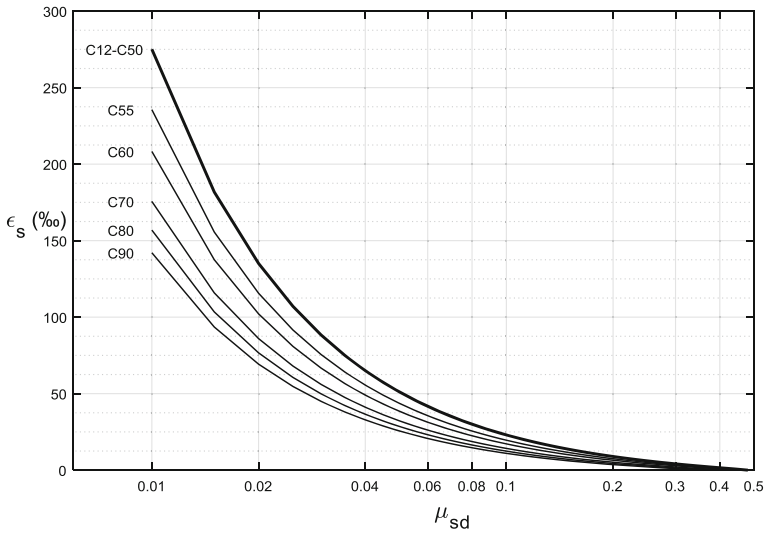

Fig. 11 ε_s as a function of μ_{sd} for every concrete class (μ_{sd} in logarithmic scale)

The strain of the reinforcement ε_s is shown in Fig. 11, as a function of the normalized design bending moment μ_{sd} (for $\mu_{sd} \geq 0.01$), for various concrete strength classes, where the x-axis (μ_{sd}) is in logarithmic scale for better clarity. In general, it is shown that the steel strain decreases for increasing normalized bending moment μ_{sd}. If the horizontal top branch of the steel stress-strain diagram is considered (as in this study), the steel strain is not supposed to have a maximum and in theory it can extend to infinity. Therefore, for very small values of the dimensionless bending moment μ_{sd} the ε_s curves tend asymptotically towards infinity. Furthermore, for higher values of μ_{sd}, the steel strain decreases and for $\mu_{sd,max}$ it becomes zero, as shown in the figure.

In Fig. 12 we zoom in the area of higher values of μ_{sd}, $0.2 \leq \mu_{sd} \leq 0.48$. The yield (limit) values for ε_s (ε_{ys}, shown in Table 4) have been plotted in this diagram also, as horizontal lines, for each steel class.

6.3.5 Analytic Formulas of μ_{sd}, ω, ξ, ζ, ε_s for Concrete Classes up to C50/60

For the special case of concrete classes up to C50/60, calculations are much simpler. For this case, it is $\eta = 1$ and $\lambda = 0.8$ and as a result we obtain the following simplified formulas.

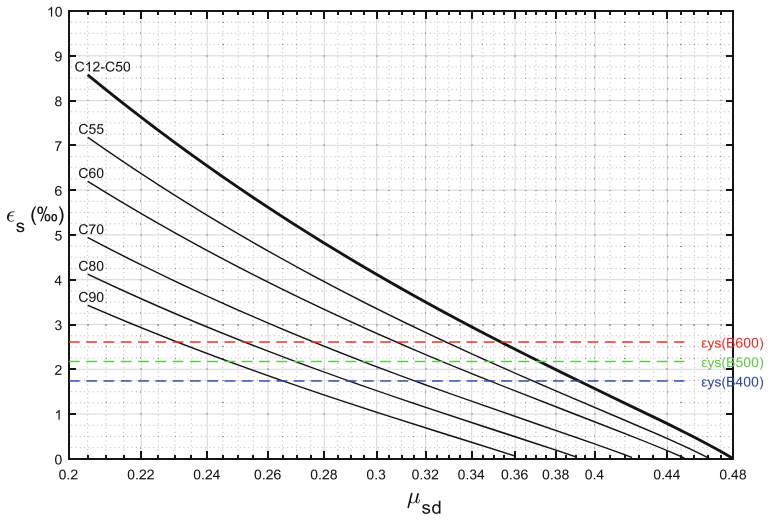

Fig. 12 ε_s as a function of μ_{sd} for every concrete class ($\mu_{sd} \geq 0.2$, μ_{sd} in logarithmic scale)

For μ_{sd}:

$$\mu_{sd} = \omega - 0.5 \cdot \omega^2 \tag{67}$$

$$\mu_{sd,max} = 0.48 \tag{68}$$

$$\mu_{sd,lim} = \frac{0.48\varepsilon_{cu3} + 0.8\varepsilon_{ys}}{\left(\varepsilon_{cu3} + \varepsilon_{ys}\right)^2}\varepsilon_{cu3} \tag{69}$$

For ω:

$$\omega = 1 - \sqrt{1 - 2\mu_{sd}} \tag{70}$$

$$\omega_{max} = 0.8 \tag{71}$$

$$\omega_{lim} = 1 - \sqrt{1 - \frac{0.96\varepsilon_{cu3} + 1.6\varepsilon_{ys}}{\left(\varepsilon_{cu3} + \varepsilon_{ys}\right)^2}\varepsilon_{cu3}} \tag{72}$$

For ξ:

$$\xi = 1.25\omega = 1.25\left(1 - \sqrt{1 - 2\mu_{sd}}\right) \tag{73}$$

$$\xi_{max} = 1 \tag{74}$$

$$\xi_{lim} = 1.25 - 1.25\sqrt{1 - \frac{0.96\varepsilon_{cu3} + 1.6\varepsilon_{ys}}{\left(\varepsilon_{cu3} + \varepsilon_{ys}\right)^2}\varepsilon_{cu3}} \tag{75}$$

For ζ:

$$\zeta = 1 - 0.5\omega = 0.5\left(1 + \sqrt{1 - 2\mu_{sd}}\right) \tag{76}$$

$$\zeta_{min} = 0.6 \tag{77}$$

$$\zeta_{lim} = 0.5 + 0.5\sqrt{1 - \frac{0.96\varepsilon_{cu3} + 1.6\varepsilon_{ys}}{\left(\varepsilon_{cu3} + \varepsilon_{ys}\right)^2}\varepsilon_{cu3}} \tag{78}$$

For ε_s:

$$\varepsilon_s = \left(\frac{0.8}{\omega} - 1\right)\varepsilon_{cu3} = \left[\frac{0.4}{\mu_{sd}}\left(1 + \sqrt{1 - 2\mu_{sd}}\right) - 1\right]\varepsilon_{cu3} \tag{79}$$

Figure 13 shows the parameters ω, ξ, ζ and ε_s as functions of the normalized bending moment μ_{sd} for concrete classes C12/15 up to C50/60.

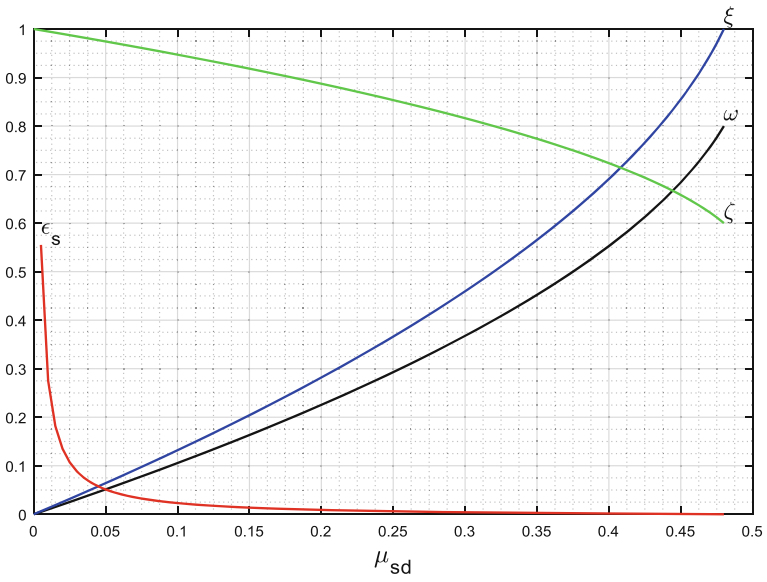

Fig. 13 ω, ξ, ζ, ε_s as functions of μ_{sd} for concrete classes C12/15 up to C50/60

7 Investigation of the Inverse Problem

In the inverse problem, the tensile reinforcement (steel area) A_s and the axial force N_d (which is applied at y_N) are given and the purpose is to calculate the maximum bending moment M_d that the cross section can withstand.

7.1 *Analytical Calculation of the Maximum Bending Moment* M_d

In this problem there are generally again two cases:

- Steel working at full strength ($\varepsilon_s \geq \varepsilon_{ys}$, $\sigma_s = f_{yd}$)
- Steel working below full strength ($\varepsilon_s < \varepsilon_{ys}$, $\sigma_s < f_{yd}$)

Case A: We assume that steel works at full strength

If steel works at full strength, then $\varepsilon_s \geq \varepsilon_{ys}$ and $\sigma_s = f_{yd}$ and we have:

$$A_s = \frac{F_s}{f_{yd}} \Rightarrow F_s = A_s \cdot f_{yd} \tag{80}$$

$$\Sigma F_x = 0 \Rightarrow F_c + N_d - F_s = 0 \Rightarrow F_c = F_s - N_d \tag{81}$$

$$F_c = \lambda x n b f_{cd} \Rightarrow x = \frac{F_c}{\lambda n b f_{cd}} \tag{82}$$

$$\frac{\varepsilon_{cu3}}{x} = \frac{\varepsilon_{cu3} + \varepsilon_s}{d} \Rightarrow \varepsilon_s = \left(\frac{d}{x} - 1\right)\varepsilon_{cu3} \tag{83}$$

Using Eq. (83) we can now check our principal assumption. If $\varepsilon_s \geq \varepsilon_{ys}$ then the assumption was right and we can continue, otherwise the assumption was not right and we have to move to Case B. By substituting Eqs. (80), (81), (82) into Eq. (83) and doing some calculations, the criterion for Case A becomes as follows:

$$\text{if } \left[\left(\frac{d\lambda n b f_{cd}}{A_s f_{yd} - N_d} - 1\right)\frac{\varepsilon_{cu3}}{\varepsilon_{ys}}\right] \geq 1 \quad \text{then} \quad \varepsilon_s \geq \varepsilon_{ys} \quad \text{otherwise} \quad \varepsilon_s < \varepsilon_{ys} \tag{84}$$

If the criterion of Eq. (84) is satisfied, then $\varepsilon_s \geq \varepsilon_{ys}$. If this is the case, then we calculate x from Eq. (82) and we continue with the Final step below, otherwise we move to Case B where $\varepsilon_s < \varepsilon_{ys}$.

Case B: Steel working below the yield limit (with less than full strength)

If the criterion of Eq. (84) is not satisfied then steel works below the yield point, $\varepsilon_s < \varepsilon_{ys}$ and $\sigma_s < f_{yd}$ and we have:

$$\sigma_s = f_{yd} \cdot \frac{\varepsilon_s}{\varepsilon_{ys}} = E_s \cdot \varepsilon_s \tag{85}$$

$$A_s = \frac{F_s}{\sigma_s} \Rightarrow F_s = A_s \cdot \sigma_s \tag{86}$$

$$\frac{\varepsilon_{cu3}}{x} = \frac{\varepsilon_{cu3} + \varepsilon_s}{d} \Rightarrow \varepsilon_s = \left(\frac{d}{x} - 1\right)\varepsilon_{cu3} \tag{87}$$

By substituting ε_s from Eq. (87) into Eq. (85) and then σ_s from Eq. (85) into Eq. (86) we obtain:

$$F_s = A_s E_s \cdot \left(\frac{d}{x} - 1\right)\varepsilon_{cu3} \tag{88}$$

We have also:

$$F_c = \lambda x n b f_{cd} \tag{89}$$

$$F_s = F_c + N_d \tag{90}$$

By substituting F_s from Eq. (88) and F_c from Eq. (89) into Eq. (90) we have:

$$A_s E_s \cdot \left(\frac{d}{x} - 1\right)\varepsilon_{cu3} = \lambda x n b f_{cd} + N_d \Rightarrow \tag{91}$$

$$(\lambda n b f_{cd}) \cdot x^2 + (N_d + A_s E_s \varepsilon_{cu3}) \cdot x - A_s E_s d \varepsilon_{cu3} = 0 \Rightarrow \tag{92}$$

The above quadratic equation needs to be solved for the neutral axis depth x. It can be written as:

$$A_2 x^2 + B_2 x + C_2 = 0 \tag{93}$$

where

$$A_2 = \lambda n b f_{cd}, \quad B_2 = N_d + A_s E_s \varepsilon_{cu3}, \quad C_2 = -A_s E_s d \varepsilon_{cu3} \tag{94}$$

The quantities A_2, B_2 and C_2 are all known, so by solving the quadratic Eq. (93) we can determine the quantity x. The discriminant Δ_2 of the quadratic equation is given by:

$$\Delta_2 = B_2^2 - 4A_2 \cdot C_2 = (N_d + A_s \cdot E_s \cdot \varepsilon_{cu3})^2 + 4\lambda \cdot n \cdot f_{cd} \cdot b \cdot A_s \cdot E_s \cdot d \cdot \varepsilon_{cu3} \quad (95)$$

The solution of the quadratic equation is:

$$x_{1,2} = \frac{-B_2 \pm \sqrt{\Delta_2}}{2A_2} \Rightarrow \begin{cases} x_1 = \frac{-B_2 - \sqrt{\Delta_2}}{2A_2} \\ x_2 = \frac{-B_2 + \sqrt{\Delta_2}}{2A_2} \end{cases} \quad (96)$$

Given that $-B_2 - \sqrt{\Delta_2} < 0$ and according to the requirement $0 \leq x \leq d$, the only acceptable solution is $x = x_2$ and thus:

$$x = x_2 = \frac{-B_2 + \sqrt{\Delta_2}}{2A_2} \quad (97)$$

After calculating x from Eq. (97), it is easy to calculate also ε_s from Eq. (87). We can now check again the validity of the principal assumption. It should certainly be $\varepsilon_s < \varepsilon_{ys}$ otherwise the assumption for Case B was not right and there must be a problem in the calculations. If indeed $\varepsilon_s < \varepsilon_{ys}$ then we continue with the Final step below, with the value of x calculated with Eq. (97).

Final step:

Having obtained the value of x, either from Case A or Case B, we continue with the following calculations:

$$M_{sd} = \lambda x \eta b f_{cd} \left(d - \frac{\lambda x}{2} \right) \quad (98)$$

$$M_{sd} = M_d - N_d \cdot y_s \Rightarrow M_d = M_{sd} + N_d \cdot y_s \quad (99)$$

7.1.1 Summary of the Analytical Methodology for the Calculation of the Maximum Bending Moment M_d

The full methodology for the calculation of the maximum bending moment M_d that the section can withstand given the existing steel reinforcement A_s and the axial force N_d (which is applied at y_N) is summarized below:

Known quantities for the calculation of the strength: The known quantities for the calculation of the cross section strength are the same as the ones of the direct problem, with the exception of the applied external bending moment M_d which is now not known (and needs to be calculated). Instead, the existing steel reinforcement A_s is now known.

Quantities to be calculated and corresponding equation to use:

- λ: Eq. (2), η: Eq. (3), f_{cd}: Eq. (1), ε_{cu3}: Eq. (4), f_{yd}: Eq. (5), ε_{ys}: Eq. (7), d: Eq. (9), y_s: Eq. (10)

- If the Criterion of Eq. (84) is satisfied, then proceed with Case A, otherwise proceed with Case B

• Case A – F_s: Eq. (80), F_c: Eq. (81), x: Eq. (82), ε_s: Eq. (83) (should be $\geq \varepsilon_{ys}$), $\sigma_s = f_{yd}$	• **Case B** – A_2, B_2, C_2: Eq. (94), Δ_2: Eq. (95), x: Eq. (97), ε_s: Eq. (87) (should be $< \varepsilon_{ys}$), σ_s: steel stress, Eq. (85)

- M_{sd}: Eq. (98), M_d: Eq. (99).

The above is again a straightforward procedure that can be very easily implemented in any programming language.

7.2 *Solution of the Inverse Problem Using Design Tables*

The inverse problem can be solved using the design tables provided in Appendix A, without any complicated analytic calculations in the usual case of economic design (steel working at full strength). In the case where the steel does not work at full strength, then it is not very easy to use the design tables, as the unknowns in this case are two (ω and σ_s) and an iterated process is needed in order to calculate the real value of ω, as described in detail in the following sections.

Case A: We assume that steel works at full strength

Setting $\sigma_s = f_{yd}$ in Eq. (33) we obtain

$$\omega = \frac{A_s f_{yd} - N_d}{bdf_{cd}} \tag{100}$$

Now we must calculate ω with Eq. (100) and then read the design table and ensure that for the given value of ω, steel works indeed above the yield limit, at full strength ($\sigma_s = f_{yd}$) so our assumption was right. For this we can also simply read the ω_{lim} value for the given steel class and check if the calculated ω is below ω_{lim} ($\omega \leq \omega_{lim}$). Otherwise, if $\omega > \omega_{lim}$ then the assumption was not right and we have to move to Case B. If indeed steel works at full strength, then for the given value of ω, we use the design table to take the corresponding value of μ_{sd} (linear interpolation may be needed) Then we calculate M_{sd} with the following formula which is derived by solving Eq. (25) for M_{sd}:

$$M_{sd} = \mu_{sd} \cdot bd^2 f_{cd} \tag{101}$$

Then, as previously, M_d can be easily calculated using Eq. (99)

Table 8 Schematic representation of how to use design tables when Steel works below the yield limit

ω (from table)	σ_s (from table)	ω (calculated from σ_s with Eq. (102))
ω_{lim}	$\sigma_s = f_{yd}$	$\omega_{calc,in}$ (from $\sigma_s = f_{yd}$) > ω_{lim}
ω_{table}	$\sigma_{s,table}$	ω_{calc} (from $\sigma_{s,table}$) > ω_{table}
…	…	…
$\omega_{1,table}$	$\sigma_{s1,table}$	$\omega_{a,calc}$ (from $\sigma_{s1,table}$) > $\boldsymbol{\omega_{1,table}}$
$\omega_{2,table}$	$\sigma_{s2,table}$	$\omega_{b,calc}$ (from $\sigma_{s2,table}$) < $\boldsymbol{\omega_{2,table}}$

Case B: Steel working below the yield limit (with less than full strength)

If using Eq. (100) for the given A_s and N_d, we obtain a value of ω equal to $\omega_{calc,in}$ for which it is $\omega_{calc,in} > \omega_{lim}$, then the assumption that steel works at full strength was wrong. In this case for the real value of ω, it is $\omega < \omega_{calc,in}$ because in fact $\sigma_s < f_{yd}$. We must start an iterative process in order to calculate the real value of ω from the values of the table. We continue with the first pair of ω_{table} and $\sigma_{s,table}$ values from the table which correspond to an uneconomic design (first $\sigma_{s,table}$ for which it is $\sigma_{s,table} < f_{yd}$). From each $\sigma_{s,table}$ we calculate ω_{calc} as follows:

$$\omega_{calc} = \frac{A_s \sigma_{s,table} - N_d}{b d f_{cd}} \tag{102}$$

and we move on with the next pairs (ω_{table}, $\sigma_{s,table}$) until we find a value of ω_{calc} for which $\omega_{calc} < \omega_{table}$. Then we stop and the real value of ω should be between the last two values from the table, as shown in Table 8.

In Table 8, the real value of ω should be between the two values ω_1 and ω_2 (the word "table" has been omitted) of the table. In order to find ω we have to find the intersection of two lines in the 2D space of (σ_s, ω), namely the line passing through points (σ_{s1}, ω_1) and (σ_{s2}, ω_2) and the line passing through points (σ_{s1}, ω_a) and (σ_{s2}, ω_b). The intersection point can be easily calculated as follows:

$$\sigma_s = \frac{\sigma_{s1}(\omega_2 - \omega_b) + \sigma_{s2}(\omega_a - \omega_1)}{\omega_2 - \omega_b + \omega_a - \omega_1} \tag{103}$$

$$\omega = \frac{\omega_2 \omega_a - \omega_1 \omega_b}{\omega_2 - \omega_b + \omega_a - \omega_1} \tag{104}$$

Having calculated ω, we read μ_{sd} from the table (linear interpolation may be needed). Then as previously, we can calculate M_{sd} and M_d, by using Eqs. (101) and (99), respectively.

7.2.1 Linear Interpolation for the ω-μ_{sd} Tables

Generally, the value of ω is not an exact value of the table, but rather lies between two neighboring values ω_1 and ω_2 ($\omega_1 < \omega < \omega_2$), corresponding to μ_{sd} values μ_{sd1} and μ_{sd2}. In this case linear interpolation is needed again. Solving Eq. (35) for μ_{sd} we obtain

$$\mu_{sd} = \mu_{sd1} + \frac{\omega - \omega_1}{\omega_2 - \omega_1}(\mu_{sd2} - \mu_{sd1}). \tag{105}$$

7.3 *Analytic Formulas of ω, ξ, ζ, ε_s for the Solution of the Inverse Problem*

Again we have two cases: Steel working at full strength and steel working below full strength.

Case A: We assume that steel works at full strength ($\mu_{sd} \leq \mu_{sd,lim}$)

Setting $\sigma_s = f_{yd}$ in Eq. (33) we obtain

$$\omega = \frac{A_s f_{yd} - N_d}{b d f_{cd}} \tag{106}$$

Substituting ω from Eq. (47) we have:

$$\eta\left(1 - \sqrt{1 - \frac{2\mu_{sd}}{\eta}}\right) = \frac{A_s f_{yd} - N_d}{b d f_{cd}} \Rightarrow \tag{107}$$

$$\mu_{sd} = \frac{\eta}{2}\left[1 - \left(1 - \frac{A_s f_{yd} - N_d}{\eta b d f_{cd}}\right)^2\right] \tag{108}$$

Now we check if the μ_{sd} calculated from Eq. (108) is indeed less than $\mu_{sd,lim}$ (see Table 6). If indeed $\mu_{sd} \leq \mu_{sd,lim}$ then the assumption was right, otherwise we move to case B. If the assumption was right, then we can calculate M_{sd} and M_d as previously, by using Eqs. (101) and (99).

Case B: Steel working below the yield limit (less than full strength, $\mu_{sd} > \mu_{sd,lim}$)

If using Eq. (108) for the given A_s and N_d, the obtained value μ_{sd} is greater than $\mu_{sd,lim}$, then steel works below yield strain and the design is not economic. In this case, we have $\varepsilon_s < \varepsilon_{ys}$ and from Eq. (6) we have

$$\sigma_s = E_s \cdot \varepsilon_s \tag{109}$$

Substituting σ_s from Eq. (109) into Eq. (33) we have

$$\omega = \frac{A_s E_s \varepsilon_s - N_d}{b d f_{cd}} \tag{110}$$

Substituting ε_s from Eq. (65) into Eq. (110) we have

$$\omega = \frac{A_s E_s \left(\frac{\lambda\eta}{\omega} - 1\right) \varepsilon_{cu3} - N_d}{b d f_{cd}} \Rightarrow \tag{111}$$

$$(b d f_{cd}) \cdot \omega^2 + (A_s E_s \varepsilon_{cu3} + N_d) \cdot \omega - \lambda\eta A_s E_s \varepsilon_{cu3} = 0 \tag{112}$$

The above quadratic equation needs to be solved for ω. It can be written in the form:

$$A_3 \omega^2 + B_3 \omega + C_3 = 0 \tag{113}$$

where

$$A_3 = b d f_{cd} \tag{114}$$

$$B_3 = A_s E_s \varepsilon_{cu3} + N_d \tag{115}$$

$$C_3 = -\lambda\eta A_s E_s \varepsilon_{cu3} \tag{116}$$

The quantities A_3, B_3 and C_3 are all known. The discriminant Δ_3 of the quadratic equation is given by:

$$\Delta_3 = B_3^2 - 4 A_3 C_3 = (A_s E_s \varepsilon_{cu3} + N_d)^2 + 4\lambda\eta b d f_{cd} A_s E_s \varepsilon_{cu3} \tag{117}$$

The solution of the quadratic equation is:

$$\omega_{1,2} = \frac{-B_3 \pm \sqrt{\Delta_3}}{2A_3} \Rightarrow \begin{cases} \omega_1 = \frac{-B_3 - \sqrt{\Delta_3}}{2A_3} \\ \omega_2 = \frac{-B_3 + \sqrt{\Delta_3}}{2A_3} \end{cases} \tag{118}$$

Of the above solutions, only the second is acceptable, as the first leads to negative values for ω. So we have

$$\omega = \frac{-B_3 + \sqrt{\Delta_3}}{2A_3} \tag{119}$$

Having calculated ω, we calculate μ_{sd} with Eq. (44) and then as previously, we can calculate M_{sd} and M_d, by using Eq. (101) and Eq. (99).

8 Numerical Examples

Four concrete sections will be examined in total. For each section, the direct and the inverse problem are solved using three methodologies:

1. Analytical calculations
2. Using the design tables provided in Appendix A
3. Using ω analytic formulas without the use of tables

Below are the common properties for all numerical examples:

- $\gamma_c = 1.50$, $a_{cc} = 1$
- Steel class B500 ($f_{yk} = 500$ MPa)
- $E_s = 200$ GPa, $\gamma_s = 1.15$

The main different characteristics of the four test examples are summarized below:

1. Concrete Class C20/25, **no axial force** (steel working at full strength).
2. Concrete Class C30/37, **with tensile axial force** (steel working at full strength).
3. **Higher Concrete Class (C70/85)**, with tensile axial force (steel working at full strength).
4. Concrete Class C30/37, with compressive axial force (**steel working below the yield limit**, with less than full strength).

8.1 Numerical Example 1

The section of the first numerical example has the following properties (Fig. 14):

- Concrete class C20/25, Height $h = 50$ cm, Width $b = 25$ cm, $d_1 = 5$ cm
- For the direct problem, we have: $M_d = 60$ kNm, $N_d = 0$ (no axial force), y_N: Not applicable.

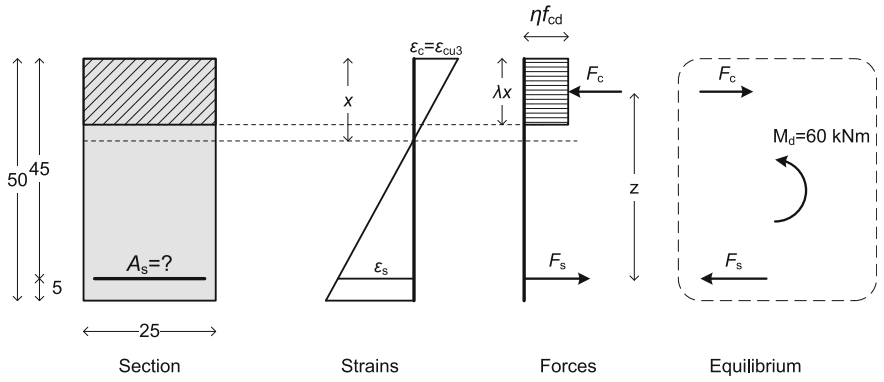

Fig. 14 The direct problem of the 1st numerical example (dimensions in cm)

8.1.1 Direct Problem

In the direct problem, the external forces are known and we need to find the required steel reinforcement area A_s.

A. Analytical calculations

1. $\lambda = 0.8$ 2. $\eta = 1$ 3. $f_{cd} = 13{,}333.33$ kPa 4. $\varepsilon_{cu3} = 3.5$ ‰ 5. $f_{yd} = 434782.61$ kPa 6. $\varepsilon_{ys} = 2.17$ ‰ 7. $d = 0.45$ m 8. y_s = Not applicable 9. $M_{sd} = 60$ kNm 10. $M_{sd,max} = 324$ kNm, $M_{sd} < M_{sd,max}$ so proceed with the next calculations 11. $M_{sd,lim} = 250.91$ kNm, $M_{sd} < M_{sd,lim}$ so the design using single steel reinforcement is economic (steel working at full strength)	12. $A_1 = 1066.67$ 13. $M_d = 60$ kNm 14. $N_d = 0$ 15. $\Delta = 1{,}184{,}000$ 16. $x = 0.052$ m 17. $z = 0.429$ m 18. $F_c = 139.85$ kN 19. $F_s = 139.85$ kN 20. $\varepsilon_s = 26.53$ ‰ 21. $\sigma_s = 434{,}782.61$ kPa 22. $\mathbf{A_s = 3.22\ cm^2}$

B. Using design tables

After calculating M_{sd} as above, we calculate μ_{sd} from Eq. (25). Then using linear interpolation we obtain the corresponding value of ω from the values of μ_{sd1}, μ_{sd2}, ω_1, ω_2 of Table 10. Finally, we read the corresponding value of σ_s from the table (linear interpolation is not needed for σ_s, unless we are in the area of $\mu_{sd} > \mu_{sd,lim}$ of uneconomic design) and we calculate the value of A_s using Eq. (34), as follows

1. $M_{sd} = 60$ kNm
2. $\mu_{sd} = 0.0889$
3. For $\mu_{sd1} = 0.08$, $\omega_1 = 0.0835$ (Table 10)
4. For $\mu_{sd2} = 0.09$, $\omega_2 = 0.0945$ (Table 10)
5. $\omega = 0.0933$ (obtained with linear interpolation)
6. $\sigma_s = 434.78$ MPa
7. $\mathbf{A_s = 3.22\ cm^2}$

C. Using ω analytic formulas without the use of tables

Again, after calculating M_{sd}, we calculate μ_{sd} from Eq. (25). Then, instead of using the design tables in order to obtain ω and σ_s, we calculate the value of ω using Eq. (47), the value of ε_s using Eq. (66) and the value of σ_s using Eq. (6). Finally, we obtain the value of A_s again using Eq. (34), as follows

1. $M_{sd} = 60$ kNm
2. $\mu_{sd} = 0.0889$
3. $\omega = 0.0932$

4. $\varepsilon_s = 26.53$ ‰ $> \varepsilon_{ys}$
5. $\sigma_s = 434.78$ MPa
6. $A_s = 3.22$ cm^2

8.1.2 Inverse Problem

In the inverse problem, the tensile reinforcement (steel area) A_s and the axial force N_d (which is applied at y_N) are given and the purpose is to calculate the maximum bending moment M_d that the cross section can withstand. We assume that we have the same problem as previously, therefore:

- $N_d = 0$, y_N: Not applicable
- $A_s = 3.22$ cm^2

A. Analytical calculations

1. $\lambda = 0.8$	9. Criterion of Eq. (84) = 12.19 $\geq$ 1, thus
2. $\eta = 1$	we have Case A, steel working at full strength
3. $f_{cd} = 13333.33$ kPa	10. $F_s = 140.00$ kN
4. $\varepsilon_{cu3} = 3.5$ ‰	11. $F_c = 140.00$ kN
5. $f_{yd} = 434782.61$ kPa	12. $x = 0.053$ m
6. $\varepsilon_{ys} = 2.17$ ‰	13. $\varepsilon_s = 26.50$ ‰ $\geq \varepsilon_{ys}$
7. $d = 0.45$ m	14. $M_{sd} = 60.06$ kNm
8. y_s = Not applicable	15. $\boldsymbol{M_d = 60.06}$ **kNm**

We see that we get a value of M_d equal to 60.06 kNm, instead of 60.00 kNm of the direct problem. This is because of the fact that in the inverse problem we set $A_s = 3.22$ cm^2 while in the direct problem, the exact value of the needed A_s had more decimal digits (3.21662 cm^2), but it was rounded to two decimal digits for the definition of the inverse problem.

B. Using design tables

We assume that steel works at full strength. We calculate ω using Eq. (100)

- $\omega = 0.0933$

We read σ_s from the table (Table 10) and we confirm that steel works at full strength ($\sigma_s = 434.78$ MPa), so we proceed with Case A. We take the value of μ_{sd} from the table (linear interpolation is needed):

- For $\omega_1 = 0.0835$, $\mu_{sd1} = 0.08$ (Table 10)
- For $\omega_2 = 0.0945$, $\mu_{sd2} = 0.09$ (Table 10)
- With linear interpolation: $\mu_{sd} = 0.0889 < \mu_{sd,lim} = 0.3717$

Then we calculate M_{sd} from Eq. (101) and M_d from Eq. (99) as follows:

- M_{sd} = 60.03 kNm
- $\boldsymbol{M_d}$ **= 60.03 kNm**

C. Using ω analytic formulas without the use of tables

We assume that steel works at full strength. We calculate μ_{sd} using Eq. (108)

- μ_{sd} = 0.0890

It is $\mu_{sd} \leq \mu_{sd,lim}$ = 0.3713, so indeed steel works at full strength and the assumption was right. We then calculate M_{sd} from Eq. (101) and M_d from Eq. (99) as follows:

- M_{sd} = 60.06 kNm
- $\boldsymbol{M_d}$ **= 60.06 kNm**.

8.2 Numerical Example 2

The section of the second numerical example has the following properties (Fig. 15):

- Concrete class C30/37, Height h = 60 cm, Width b = 30 cm, d_1 = 5 cm
- For the direct problem, we have: M_d = 100 kNm, N_d = 50 kN, $y_N = h/2$ = 30 cm.

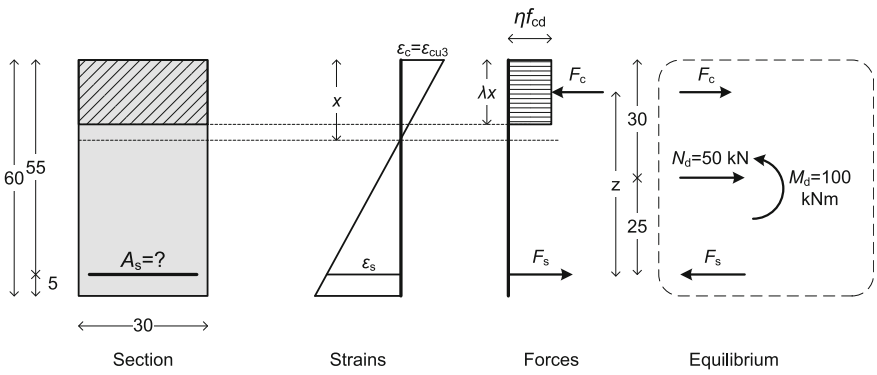

Fig. 15 The direct problem of the 2nd numerical example (dimensions in cm)

8.2.1 Direct Problem

A. Analytical calculations

1. $\lambda = 0.8$ 2. $\eta = 1$ 3. $f_{cd} = 20000$ kPa 4. $\varepsilon_{cu3} = 3.5$ ‰ 5. $f_{yd} = 434782.61$ kPa 6. $\varepsilon_{ys} = 2.17$ ‰ 7. $d = 0.55$ m 8. $y_s = 0.25$ m 9. $M_{sd} = 87.50$ kNm 10. $M_{sd,max} = 871.20$ kNm, $M_{sd} < M_{sd,max}$ so proceed with the next calculations	11. $M_{sd,lim} = 674.68$ kNm, $M_{sd} < M_{sd,lim}$ so the design using single steel reinforcement is economic (steel working at full strength) 12. $x = 0.034$ m 13. $z = 0.536$ m 14. $F_c = 163.12$ kN 15. $F_s = 213.12$ kN 16. $\varepsilon_s = 53.14$ ‰ 17. $\sigma_s = 434782.61$ kPa 18. $\boldsymbol{A_s = 4.90\ cm^2}$

B. Using design tables

Using the same methodology as in the first example, we have:

1. $M_{sd} = 87.5$ kNm
2. $\mu_{sd} = 0.0482$
3. For $\mu_{sd1} = 0.04$, $\omega_1 = 0.0408$ (Table 10)
4. For $\mu_{sd2} = 0.05$, $\omega_2 = 0.0513$ (Table 10)
5. $\omega = 0.0494$ (linear interpolation)
6. $\sigma_s = 434.78$ MPa
7. $\boldsymbol{A_s = 4.90\ cm^2}$

C. Using ω analytic formulas without the use of tables

Using the same methodology as in the first example, we have:

1. $M_{sd} = 87.50$ kNm
2. $\mu_{sd} = 0.0482$
3. $\omega = 0.0494$
4. $\varepsilon_s = 53.14$ ‰ $> \varepsilon_{ys}$
5. $\sigma_s = 434.78$ MPa
6. $\boldsymbol{A_s = 4.90\ cm^2}$.

8.2.2 Inverse Problem

We assume that we have the same problem as previously, therefore:

- $N_d = 50$ kN, $y_N = h/2 = 30$ cm
- $A_s = 4.90\ cm^2$

A. Analytical calculations

1. $\lambda = 0.8$	9. Criterion of Eq. (84) = 24.46 $\geq$ 1, thus
2. $\eta = 1$	we have Case A, steel working at full strength
3. $f_{cd} = 20{,}000$ kPa	10. $F_s = 213.04$ kN
4. $\varepsilon_{cu3} = 3.5$ ‰	11. $F_c = 163.04$ kN
5. $f_{yd} = 434782.61$ kPa	12. $x = 0.034$ m
6. $\varepsilon_{ys} = 2.17$ ‰	13. $\varepsilon_s = 53.17$ ‰ $\geq \varepsilon_{ys}$
7. $d = 0.55$ m	14. $M_{sd} = 87.46$ kNm
8. $y_s = 0.25$ m	15. $\boldsymbol{M_d = 99.96}$ **kNm**

Again, there is a small errors due to rounding A_s to two decimal digits.

B. Using design tables

We assume that steel works at full strength. We calculate ω using Eq. (100)

- $\omega = 0.0494$

We read σ_s from the table and we confirm that steel works at full strength ($\sigma_s = 434.78$ MPa), so we proceed with Case A. We take the value of μ_{sd} from the table (linear interpolation is needed):

- For $\omega_1 = 0.0408$, $\mu_{sd1} = 0.04$ (Table 10)
- For $\omega_2 = 0.0513$, $\mu_{sd2} = 0.05$ (Table 10)
- With linear interpolation: $\mu_{sd} = 0.0482 < \mu_{sd,lim} = 0.3717$

Then we calculate M_{sd} from Eq. (101) and M_d from Eq. (99) as follows:

- $M_{sd} = 87.48$ kNm
- $\boldsymbol{M_d = 99.98}$ **kNm**

C. Using ω analytic formulas without the use of tables

We assume that steel works at full strength. We calculate μ_{sd} using Eq. (108)

- $\mu_{sd} = 0.0482$

It is $\mu_{sd} \leq \mu_{sd,lim} = 0.3713$, so indeed steel works at full strength and the assumption was right. We then calculate M_{sd} from Eq. (101) and M_d from Eq. (99):

- $M_{sd} = 87.46$ kNm
- $\boldsymbol{M_d = 99.96}$ **kNm**.

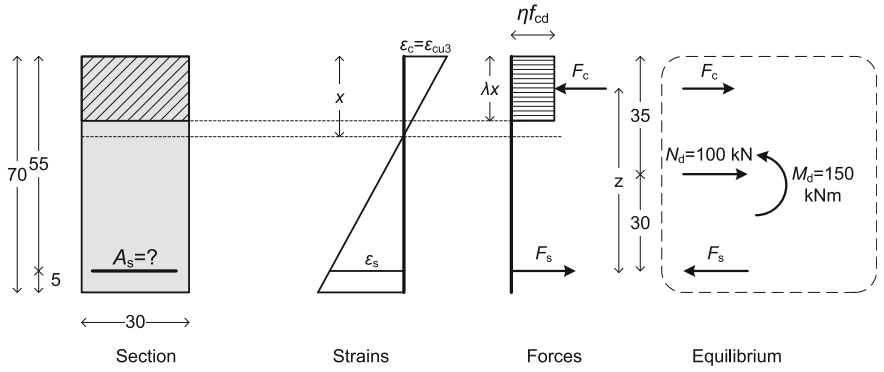

Fig. 16 The direct problem of the 3rd numerical example (dimensions in cm)

8.3 Numerical Example 3

The section of the third numerical example has the following properties (Fig. 16):

- Concrete class C70/85, Height h = 70 cm, Width b = 30 cm, d_1 = 5 cm
- For the direct problem, we have: M_d = 150 kNm, N_d = 100 kN, $y_N = h/2$ = 35 cm.

8.3.1 Direct Problem

A. Analytical calculations

1. $\lambda = 0.75$ 2. $\eta = 0.90$ 3. f_{cd} = 46,667 kPa 4. ε_{cu3} = 2.66 ‰ 5. f_{yd} = 434782.61 kPa 6. ε_{ys} = 2.17 ‰ 7. d = 0.65 m 8. y_s = 0.30 m 9. M_{sd} = 120 kNm 10. $M_{sd,max}$ = 2495.38 kNm, $M_{sd} < M_{sd,max}$ so proceed with the next calculations	11. $M_{sd,lim}$ = 1742.81 kNm, $M_{sd} < M_{sd,lim}$ so the design using single steel reinforcement is economic (steel working at full strength) 12. x = 0.020 m 13. z = 0.643 m 14. F_c = 186.74 kN 15. F_s = 286.74 kN 16. ε_s = 84.71 ‰ 17. σ_s = 434782.61 kPa 18. $\boldsymbol{A_s = 6.60\ cm^2}$

B. Using design tables

Using the same methodology as in the previous examples, we have:

1. M_{sd} = 120 kNm
2. μ_{sd} = 0.0203

3. For $\mu_{sd1} = 0.02$, $\omega_1 = 0.0202$ (Table 13)
4. For $\mu_{sd2} = 0.03$, $\omega_2 = 0.0305$ (Table 13)
5. $\omega = 0.0205$ (linear interpolation)
6. $\sigma_s = 434.78$ MPa
7. $A_s = 6.59$ cm^2

C. Using ω analytic formulas without the use of tables

Using the same methodology as in the previous examples, we have:

1. $M_{sd} = 120$ kNm
2. $\mu_{sd} = 0.0203$
3. $\omega = 0.0205$
4. $\varepsilon_s = 84.71$ ‰ $> \varepsilon_{ys}$
5. $\sigma_s = 434.78$ MPa
6. $\boldsymbol{A_s = 6.60}$ **cm^2**

8.3.2 Inverse Problem

We assume that we have the same problem as previously, therefore:

- $N_d = 100$ kN, $y_N = h/2 = 35$ cm
- $A_s = 6.60$ cm^2

A. Analytical calculations

1. $\lambda = 0.75$	9. Criterion of Eq. (84) = 38.92 $\geq$ 1, thus
2. $\eta = 0.90$	we have Case A, steel working at full strength
3. $f_{cd} = 46666.67$ kPa	10. $F_s = 286.96$ kN
4. $\varepsilon_{cu3} = 2.66$ ‰	11. $F_c = 186.96$ kN
5. $f_{yd} = 434782.61$ kPa	12. $x = 0.020$ m
6. $\varepsilon_{ys} = 2.17$ ‰	13. $\varepsilon_s = 84.61$ ‰ $\geq \varepsilon_{ys}$
7. $d = 0.65$ m	14. $M_{sd} = 120.13$ kNm
8. $y_s = 0.30$ m	15. $\boldsymbol{M_d = 150.13}$ **kNm**

B. Using design tables

We assume that steel works at full strength. We calculate ω using Eq. (100)

- $\omega = 0.0205$

We read σ_s from the table and we confirm that steel works at full strength ($\sigma_s = 434.78$ MPa), so we proceed with Case A. We take the value of μ_{sd} from the table (linear interpolation is needed):

- For $\omega_1 = 0.0202$, $\mu_{sd1} = 0.02$ (Table 13)
- For $\omega_2 = 0.0305$, $\mu_{sd2} = 0.03$ (Table 13)
- $\mu_{sd} = 0.0203 < \mu_{sd,lim} = 0.2946$

Then we calculate M_{sd} from Eq. (101) and M_d from Eq. (99) as follows:

- $M_{sd} = 120.28$ kNm
- $M_d = 150.28$ kNm

C. Using ω analytic formulas without the use of tables

We assume that steel works at full strength. We calculate μ_{sd} using Eq. (108)

- $\mu_{sd} = 0.0203$

It is $\mu_{sd} \leq \mu_{sd,lim} = 0.2946$, so indeed steel works at full strength and the assumption was right. We then calculate M_{sd} from Eq. (101) and M_d from Eq. (99):

- $M_{sd} = 120.13$ kNm
- **$M_d = 150.13$ kNm**

8.4 Numerical Example 4

The section of the fourth numerical example has the following properties:

- Concrete class C30/37, Height $h = 50$ cm, Width $b = 25$ cm, $d_1 = 5$ cm
- For the direct problem, we have: $M_d = 378$ kNm, $N_d = -50$ kN (compressive), $y_N = h/2 = 25$ cm (Fig. 17).

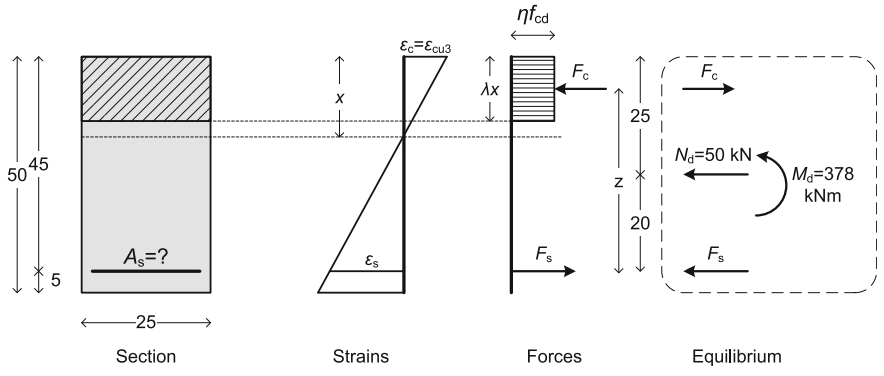

Fig. 17 The direct problem of the 4th numerical example (dimensions in cm)

8.4.1 Direct Problem

A. Analytical calculations

1. $\lambda = 0.8$ 2. $\eta = 1$ 3. $f_{cd} = 20000$ kPa 4. $\varepsilon_{cu3} = 3.5$ ‰ 5. $f_{yd} = 434782.61$ kPa 6. $\varepsilon_{ys} = 2.17$ ‰ 7. $d = 0.45$ m 8. $y_s = 0.20$ m 9. $M_{sd} = 388$ kNm 10. $M_{sd,max} = 486.00$ kNm, $M_{sd} < M_{sd,max}$ so proceed with the next calculations	11. $M_{sd,lim} = 376.37$ kNm, $M_{sd} > M_{sd,lim}$ so the design using single steel reinforcement is not economic (**steel *not* working at full strength**) 12. $x = 0.291$ m 13. $z = 0.334$ m 14. $F_c = 1162.57$ kN 15. $F_s = 1112.57$ kN 16. $\varepsilon_s = 1.92$ ‰ $< \varepsilon_{ys}$ 17. $\sigma_s = 383803.99$ kPa $< f_{yd}$ **18. $A_s = 28.99$ cm^2**

B. Using design tables

Using the same methodology as in the previous examples, we have:

1. $M_{sd} = 388$ kNm
2. $\mu_{sd} = 0.3832$
3. For $\mu_{sd1} = 0.38$, $\omega_1 = 0.5101$, $\sigma_{s1} = 397.82$ (Table 13)
4. For $\mu_{sd2} = 0.39$, $\omega_2 = 0.5310$, $\sigma_{s2} = 354.70$ (Table 13)
5. $\omega = 0.5168$ (linear interpolation)
6. $\sigma_s = 383979.01$ kPa (linear interpolation)
7. **$A_s = 28.98$ cm^2**

C. Using ω analytic formulas without the use of tables

Using the same methodology as in the previous examples, we have:

1. $M_{sd} = 388.00$ kNm
2. $\mu_{sd} = 0.3832$
3. $\omega = 0.5167$
4. $\varepsilon_s = 1.92$ ‰ $< \varepsilon_{ys}$
5. $\sigma_s = 383803.99$ kPa
6. **$A_s = 28.99$ cm^2**

8.4.2 Inverse Problem

We assume that we have the same problem as previously, therefore:

- $N_d = -50$ kN, $y_N = h/2 = 25$ cm
- $A_s = 28.99$ cm^2

A. Analytical calculations

1. $\lambda = 0.8$	9. Criterion of Eq. (84) = 0.60 < 1, thus we have Case B, **steel working *below* full strength**
2. $\eta = 1$	10. $A = 4000$, $B = 1979.30$, $C = -913.19$
3. $f_{cd} = 20{,}000$ kPa	11. $\Delta = 18{,}528{,}588$
4. $\varepsilon_{cu3} = 3.5$ ‰	12. $x = 0.291$ m
5. $f_{yd} = 434782.61$ kPa	13. $\varepsilon_s = 1.92$ ‰ < ε_{ys}
6. $\varepsilon_{ys} = 2.17$ ‰	14. $\sigma_s = 383784.87$ kPa < f_{yd}
7. $d = 0.45$ m	15. $M_{sd} = 388.00$ kNm
8. $y_s = 0.20$ m	16. $\boldsymbol{M_d = 378.00}$ **kNm**

B. Using design tables

We first assume that steel works at full strength. Setting $\sigma_s = f_{yd}$ in Eq. (33) we calculate ω from Eq. (100) as follows

- $\omega_{calc,in} = 0.5824$

According to the design table, $\omega_{lim} = 0.4935$, so it is $\omega_{calc,in} > \omega_{lim}$. Also, if we read the design table for the initially calculated $\omega = 0.5824$ we will see that steel works below full strength ($\sigma_s < f_{yd}$), which is in conflict with our assumption. This means that the design is not economic and the assumption of steel working at full strength was wrong. We must start the iterative process in order to calculate the real value of ω from the values of the table:

- We start with ω_{lim} which essentially corresponds to $\sigma_s = f_{yd} = 434.78$ MPa. From this value $\sigma_s = f_{yd}$ we calculate the new value of ω ($\omega_{calc,in}$) with Eq. (102). For ω_{lim} and $\sigma_s = f_{yd}$ the calculated value of ω_{calc} should be $\omega_{calc,in} > \omega_{lim}$. See the 2nd line of Table 9.
- We continue with the first pair of ω_{table} and $\sigma_{s,table}$ values from the table which correspond to an uneconomic design (first $\sigma_{s,table}$ for which it is $\sigma_{s,table} < f_{yd}$). In our case, this first value is $\sigma_{s1,table} = 397.82$ MPa. We calculate ω_{calc} again. In this case, it is again $\omega_{a,calc} > \omega_{1,table}$. See the 3rd line of Table 9.
- We repeat the previous calculation with the next pairs until we find a value of ω_{calc} for which $\omega_{calc} < \omega_{table}$. In our case this happens in the next pair, as shown in the 4th line of Table 9.

Then we stop and we use Eqs. (103) and (104) to calculate σ_s and ω as follows:

- $\sigma_s = 383894.86$ kPa
- $\omega = 0.5168$

Table 9 Iterative process for the solution of the inverse problem of the 4th example

ω (from table)	σ_s (from table)	ω [calculated from σ_s with Eq. (102)]
$\omega_{lim} = 0.4935$	$\sigma_s = f_{yd} = 434.78$	$\omega_{calc,in}$ (from $\sigma_s = f_{yd}$) = 0.5824 > ω_{lim}
$\omega_{1,table} = 0.5101$	$\sigma_{s1,table} = 397.82$	$\omega_{a,calc}$ (from $\sigma_{s1,table}$) = 0.5348 > $\omega_{1,table}$
$\omega_{2,table} = 0.5310$	$\sigma_{s2,table} = 354.70$	$\omega_{b,calc}$ (from $\sigma_{s2,table}$) = 0.4792 < $\omega_{2,table}$

For the calculation of μ_{sd} we then use linear interpolation:

- For $\omega_1 = 0.5101$, $\mu_{sd1} = 0.38$ (Table 13)
- For $\omega_2 = 0.5310$, $\mu_{sd2} = 0.39$ (Table 13)
- With linear interpolation we obtain: $\mu_{sd} = 0.3832 > \mu_{sd,lim} = 0.3717$

Then we calculate M_{sd} from Eq. (101) and M_d from Eq. (99) as follows:

- $M_{sd} = 388.02$ kNm
- $M_d = 378.02$ kNm

C. Using ω analytic formulas without the use of tables

We first assume that steel works at full strength. We calculate μ_{sd} using Eq. (108)

- $\mu_{sd} = 0.4128$

It is $\mu_{sd} > \mu_{sd,lim} = 0.3717$, so the assumption was wrong—steel works *below* full strength. We move to Case B. We need to solve a quadratic equation in order to calculate ω. We calculate A_3, B_3, C_3 using Eqs. (114), (115), (116). Then we calculate ω using Eq. (119).

- $A_3 = 2250.00$, $B_3 = 1979.30$, $C_3 = -1623.44$
- $\Delta_3 = 18{,}528{,}588$
- $\omega = 0.5167$
- $\mu_{sd} = 0.3832$

We then calculate M_{sd} from Eq. (101) and M_d from Eq. (99) as follows:

- $M_{sd} = 388.00$ kNm
- $\mathbf{M_d = 378.00}$ **kNm**

9 Conclusions

- Eurocode 2-Part 1-1 gives us new tools in order to design concrete cross sections. Three approaches may be used for the stress-strain relation of concrete and another two approaches for the stress-strain relation of the steel reinforcement. In this study we used the rectangular stress distribution for concrete together with the bilinear stress-strain distribution for steel with a horizontal top branch (no hardening, $k = 1$).
- EC2-1-1 allows the designer not to limit the ultimate strain for steel when a horizontal top branch is assumed for its stress-strain diagram. In this case, the concrete zone is assumed to be at the ultimate strain at the ULS and the steel strain can take any value, without any limitation. This approach is followed in the present study—in all the methodologies and the examples, concrete is the critical material in all cases.

- This chapter presents three detailed methodologies for the design of rectangular cross sections with tensile (single) reinforcement, covering all concrete classes, from C12/15 up to C90/105. The purpose in every case is to calculate the necessary tensile steel reinforcement A_s. The first methodology provides an analytical algorithmic procedure that can be easily applied in any programming language. The second methodology is based on design tables that are provided in Appendix A. The third methodology provides again analytic formulas that can replace completely the use of tables and can in fact be used to reproduce these tables.
- Apart from the direct problem, the inverse problem is also studied, where the steel reinforcement is given and the purpose is to find the maximum bending moment that the section can withstand, given also the value and position of the axial force on the section. Again, the inverse problem is solved using the same three methodologies of the direct problem.
- All methodologies provide the same results. The results of the two methodologies based on analytic formulas coincide, while the use of tables incorporates small errors that can affect the decimal digits of the final result. The solution of the inverse problem always leads to the bending moment of the direct problem. Small errors are due to the fact that the steel area is "rounded" in two decimal digits when the inverse problem is defined.
- All Eurocode parameters, such as a_{cc}, γ_c, γ_s, even E_s and many others can be adjusted according to the preferences of the designer, without any limitation. That is with the exception of the Tables of Appendix where the last columns (steel stress σs) and the limit values have been calculated for E_s = 200 GPa and γ_s = 1.15. Nevertheless, using the proposed methodology new tables can be generated where the values of these parameters can be different.
- In this study detailed guidelines are provided for reinforced concrete section design accompanied with special design curves for each case. The curves presented are based on equations which are given in closed form.
- The various regions of reinforced concrete section design are explicitly defined. Two limits are defined for the normalized design bending moment: $\mu_{sd,lim}$ and $\mu_{sd,max} > \mu_{sd,lim}$. We have three cases in general:

1. If for the direct problem, $\mu_{sd} \leq \mu_{sd,lim}$, then the design is economic and this should be the case in practice.
2. If $\mu_{sd,lim} < \mu_{sd} < \mu_{sd,max}$, then the design is possible, but not economic and it should be avoided, as steel works below its full strength.
3. If $\mu_{sd} \geq \mu_{sd,max}$ then the design is impossible. The dimensions of the section must be increased and/or compressive reinforcement must be added.

Appendix A: Tables for the Design of Cross Sections with Single Reinforcement

Assumptions (in accordance with EC2-1-1 [4]): E_s = 200 GPa and γ_s = 1.15, affecting the calculation of $\mu_{sd,lim}$, ω_{lim} and σ_s values, only (Tables 10, 11, 12, 13, 14 and 15).

Table 10 Design table for Concrete C12/15 up to C50/60

Concretes from C12/15 up to C50/60 − $\mu_{sd,max}$ = 0.4800							
μ_{sd}	ω	$\xi = x/d$	$\zeta = z/d$	ε_s (‰)	σ_s (B400) $\mu_{sd,lim}$ = 0.3916 ω_{lim} = 0.5344	σ_s (B500) $\mu_{sd,lim}$ = 0.3717 ω_{lim} = 0.4935	σ_s (B600) $\mu_{sd,lim}$ = 0.3533 ω_{lim} = 0.4584
0.01	0.0101	0.0126	0.9950	275.09	347.83	434.78	521.74
0.02	0.0202	0.0253	0.9899	135.09			
0.03	0.0305	0.0381	0.9848	88.41			
0.04	0.0408	0.0510	0.9796	65.07			
0.05	0.0513	0.0641	0.9743	51.06			
0.06	0.0619	0.0774	0.9690	41.72			
0.07	0.0726	0.0908	0.9637	35.05			
0.08	0.0835	0.1044	0.9583	30.04			
0.09	0.0945	0.1181	0.9528	26.14			
0.10	0.1056	0.1320	0.9472	23.02			
0.11	0.1168	0.1460	0.9416	20.47			
0.12	0.1282	0.1603	0.9359	18.34			
0.13	0.1398	0.1747	0.9301	16.53			
0.14	0.1515	0.1893	0.9243	14.99			
0.15	0.1633	0.2042	0.9183	13.64			
0.16	0.1754	0.2192	0.9123	12.47			
0.17	0.1876	0.2345	0.9062	11.43			
0.18	0.2000	0.2500	0.9000	10.50			
0.19	0.2126	0.2657	0.8937	9.67			
0.20	0.2254	0.2818	0.8873	8.92			
0.21	0.2384	0.2980	0.8808	8.24			
0.22	0.2517	0.3146	0.8742	7.63			
0.23	0.2652	0.3314	0.8674	7.06			
0.24	0.2789	0.3486	0.8606	6.54			
0.25	0.2929	0.3661	0.8536	6.06			
0.26	0.3072	0.3840	0.8464	5.62			
0.27	0.3218	0.4022	0.8391	5.20			
0.28	0.3367	0.4208	0.8317	4.82			
0.29	0.3519	0.4399	0.8240	4.46			
0.30	0.3675	0.4594	0.8162	4.12			
0.31	0.3836	0.4794	0.8082	3.80			
0.32	0.4000	0.5000	0.8000	3.50			
0.33	0.4169	0.5211	0.7915	3.22			
0.34	0.4343	0.5429	0.7828	2.95			

(continued)

Table 10 (continued)

Concretes from C12/15 up to C50/60 − $\mu_{sd,max}$ = 0.4800							
μ_{sd}	ω	$\xi = x/d$	$\zeta = z/d$	ε_s (‰)	σ_s (B400) $\mu_{sd,lim}$ = 0.3916 ω_{lim} = 0.5344	σ_s (B500) $\mu_{sd,lim}$ = 0.3717 ω_{lim} = 0.4935	σ_s (B600) $\mu_{sd,lim}$ = 0.3533 ω_{lim} = 0.4584
		0.5653	0.7739	2.69			
0.36	0.4708	0.5886	0.7646	2.45			*489.34*
0.37	0.4901	0.6126	0.7550	2.21			*442.63*
0.38	0.5101	0.6376	0.7449	1.99		*397.82*	*397.82*
0.39	0.5310	0.6637	0.7345	1.77		*354.70*	*354.70*
0.40	0.5528	0.6910	0.7236	1.57	*313.05*	*313.05*	*313.05*
0.41	0.5757	0.7197	0.7121	1.36	*272.67*	*272.67*	*272.67*
0.42	0.6000	0.7500	0.7000	1.17	*233.33*	*233.33*	*233.33*
0.43	0.6258	0.7823	0.6871	0.97	*194.81*	*194.81*	*194.81*
0.44	0.6536	0.8170	0.6732	0.78	*156.81*	*156.81*	*156.81*
0.45	0.6838	0.8547	0.6581	0.59	*118.99*	*118.99*	*118.99*
0.46	0.7172	0.8964	0.6414	0.40	*80.86*	*80.86*	*80.86*
0.47	0.7551	0.9438	0.6225	0.21	*41.67*	*41.67*	*41.67*

Table 11 Design table for concrete C55/60

Concrete C55/67 − $\mu_{sd,max}$ = 0.4655							
μ_{sd}	ω	$\xi = x/d$	$\zeta = z/d$	ε_s (‰)	σ_s (B400) $\mu_{sd,lim}$ = 0.3685 ω_{lim} = 0.4933	σ_s (B500) $\mu_{sd,lim}$ = 0.3477 ω_{lim} = 0.4528	σ_s (B600) $\mu_{sd,lim}$ = 0.3287 ω_{lim} = 0.4185
0.01	0.0101	0.0131	0.9948	235.60	347.83	434.78	521.74
0.02	0.0202	0.0263	0.9896	115.61			
0.03	0.0305	0.0397	0.9844	75.61			
0.04	0.0409	0.0532	0.9790	55.61			
0.05	0.0514	0.0669	0.9737	43.60			
0.06	0.0620	0.0807	0.9682	35.60			
0.07	0.0727	0.0947	0.9627	29.88			
0.08	0.0836	0.1089	0.9571	25.58			
0.09	0.0946	0.1232	0.9515	22.24			
0.10	0.1057	0.1377	0.9458	19.57			
0.11	0.1170	0.1524	0.9400	17.38			
0.12	0.1285	0.1673	0.9341	15.55			
0.13	0.1401	0.1824	0.9282	14.01			
0.14	0.1518	0.1977	0.9221	12.68			
0.15	0.1638	0.2133	0.9160	11.53			
0.16	0.1759	0.2290	0.9098	10.52			
0.17	0.1882	0.2451	0.9035	9.63			
0.18	0.2006	0.2613	0.8971	8.83			
0.19	0.2133	0.2779	0.8906	8.12			
0.20	0.2263	0.2947	0.8840	7.48			
0.21	0.2394	0.3118	0.8772	6.90			
0.22	0.2528	0.3292	0.8704	6.37			

(continued)

Table 11 (continued)

Concrete C55/67 − $\mu_{sd,max}$ = 0.4655							
μ_{sd}	ω	$\xi = x/d$	$\zeta = z/d$	ε_s (‰)	σ_s (B400) $\mu_{sd,lim}$ = 0.3685 ω_{lim} = 0.4933	σ_s (B500) $\mu_{sd,lim}$ = 0.3477 ω_{lim} = 0.4528	σ_s (B600) $\mu_{sd,lim}$ = 0.3287 ω_{lim} = 0.4185
		0.3469	0.8634	5.88			
0.24	0.2803	0.3650	0.8563	5.44			
0.25	0.2945	0.3835	0.8490	5.02			
0.26	0.3089	0.4024	0.8416	4.64			
0.27	0.3238	0.4217	0.8340	4.29			
0.28	0.3389	0.4414	0.8262	3.96			
0.29	0.3544	0.4616	0.8182	3.65			
0.30	0.3703	0.4823	0.8101	3.35			
0.31	0.3867	0.5036	0.8017	3.08			
0.32	0.4035	0.5255	0.7931	2.82			
0.33	0.4208	0.5481	0.7842	2.58			*515.41*
0.34	0.4387	0.5714	0.7750	2.34			*468.92*
0.35	0.4572	0.5954	0.7655	2.12		*424.66*	*424.66*
0.36	0.4764	0.6204	0.7557	1.91		*382.39*	*382.39*
0.37	0.4963	0.6464	0.7455	1.71	*341.89*	*341.89*	*341.89*
0.38	0.5172	0.6735	0.7348	1.51	*302.96*	*302.96*	*302.96*
0.39	0.5390	0.7020	0.7236	1.33	*265.39*	*265.39*	*265.39*
0.40	0.5619	0.7319	0.7118	1.15	*229.00*	*229.00*	*229.00*
0.41	0.5863	0.7635	0.6994	0.97	*193.57*	*193.57*	*193.57*
0.42	0.6122	0.7973	0.6861	0.79	*158.88*	*158.88*	*158.88*
0.43	0.6401	0.8337	0.6717	0.62	*124.65*	*124.65*	*124.65*
0.44	0.6707	0.8735	0.6561	0.45	*90.55*	*90.55*	*90.55*
0.45	0.7046	0.9177	0.6387	0.28	*56.09*	*56.09*	*56.09*
0.46	0.7434	0.9682	0.6188	0.10	*20.50*	*20.50*	*20.50*

Table 12 Design table for Concrete C60/75

Concrete C60/75 − $\mu_{sd,max}$ = 0.4510							
μ_{sd}	ω	ξ = x/d	ζ = z/d	ε_s (‰)	σ_s (B400) $\mu_{sd,lim}$ = 0.3482 ω_{lim} = 0.4593	σ_s (B500) $\mu_{sd,lim}$ = 0.3270 ω_{lim} = 0.4198	σ_s (B600) $\mu_{sd,lim}$ = 0.3079 ω_{lim} = 0.3865
0.01	0.0101	0.0137	0.9947	208.29	347.83	434.78	521.74
0.02	0.0202	0.0275	0.9894	102.14			
0.03	0.0305	0.0414	0.9840	66.75			
0.04	0.0409	0.0555	0.9785	49.05			
0.05	0.0514	0.0698	0.9730	38.43			
0.06	0.0620	0.0842	0.9674	31.34			
0.07	0.0728	0.0989	0.9617	26.28			
0.08	0.0837	0.1137	0.9560	22.48			

(continued)

Table 12 (continued)

Concrete C60/75 − $\mu_{sd,max}$ = 0.4510							
μ_{sd}	ω	ξ = x/d	ζ = z/d	ε_s (‰)	σ_s (B400) $\mu_{sd,lim}$ = 0.3482 ω_{lim} = 0.4593	σ_s (B500) $\mu_{sd,lim}$ = 0.3270 ω_{lim} = 0.4198	σ_s (B600) $\mu_{sd,lim}$ = 0.3079 ω_{lim} = 0.3865
		0.1287	0.9501	19.53			
0.10	0.1059	0.1438	0.9443	17.16			
0.11	0.1172	0.1592	0.9383	15.23			
0.12	0.1287	0.1748	0.9323	13.61			
0.13	0.1404	0.1907	0.9261	12.24			
0.14	0.1522	0.2067	0.9199	11.07			
0.15	0.1642	0.2230	0.9136	10.05			
0.16	0.1764	0.2396	0.9072	9.15			
0.17	0.1888	0.2564	0.9007	8.36			
0.18	0.2013	0.2735	0.8940	7.66			
0.19	0.2141	0.2908	0.8873	7.03			
0.20	0.2272	0.3085	0.8804	6.46			
0.21	0.2404	0.3266	0.8735	5.95			
0.22	0.2539	0.3449	0.8663	5.48			
0.23	0.2677	0.3636	0.8591	5.05			
0.24	0.2818	0.3827	0.8517	4.65			
0.25	0.2962	0.4023	0.8441	4.28			
0.26	0.3109	0.4222	0.8364	3.95			
0.27	0.3259	0.4426	0.8285	3.63			
0.28	0.3413	0.4636	0.8204	3.34			
0.29	0.3571	0.4851	0.8120	3.06			
0.30	0.3734	0.5071	0.8035	2.80			
0.31	0.3901	0.5298	0.7947	2.56			*511.76*
0.32	0.4073	0.5532	0.7856	2.33			*465.71*
0.33	0.4251	0.5774	0.7763	2.11		*422.07*	*422.07*
0.34	0.4435	0.6024	0.7666	1.90		*380.58*	*380.58*
0.35	0.4627	0.6284	0.7565	1.71	*341.03*	*341.03*	*341.03*
0.36	0.4826	0.6554	0.7460	1.52	*303.18*	*303.18*	*303.18*
0.37	0.5033	0.6837	0.7351	1.33	*266.85*	*266.85*	*266.85*
0.38	0.5251	0.7133	0.7236	1.16	*231.83*	*231.83*	*231.83*
0.39	0.5481	0.7445	0.7115	0.99	*197.93*	*197.93*	*197.93*
0.40	0.5725	0.7776	0.6987	0.82	*164.94*	*164.94*	*164.94*
0.41	0.5986	0.8130	0.6850	0.66	*132.64*	*132.64*	*132.64*
0.42	0.6267	0.8513	0.6701	0.50	*100.77*	*100.77*	*100.77*
0.43	0.6576	0.8932	0.6539	0.34	*68.98*	*68.98*	*68.98*
0.44	0.6921	0.9401	0.6357	0.18	*36.77*	*36.77*	*36.77*
0.45	0.7321	0.9943	0.6147	0.02	*3.30*	*3.30*	*3.30*

Table 13 Design table for Concrete C70/85

Concrete C70/85 − $\mu_{sd,max} = 0.4219$							
μ_{sd}	ω	$\xi = x/d$	$\zeta = z/d$	ε_s (‰)	σ_s (B400) $\mu_{sd,lim} = 0.3155$ $\omega_{lim} = 0.4079$	σ_s (B500) $\mu_{sd,lim} = 0.2946$ $\omega_{lim} = 0.3712$	σ_s (B600) $\mu_{sd,lim} = 0.2761$ $\omega_{lim} = 0.3405$
0.01	0.0101	0.0149	0.9944	175.62	347.83	434.78	521.74
0.02	0.0202	0.0300	0.9888	85.98			
0.03	0.0305	0.0452	0.9830	56.09			
0.04	0.0409	0.0606	0.9773	41.14			
0.05	0.0515	0.0763	0.9714	32.17			
0.06	0.0621	0.0921	0.9655	26.19			
0.07	0.0730	0.1081	0.9595	21.92			
0.08	0.0839	0.1243	0.9534	18.71			
0.09	0.0950	0.1408	0.9472	16.21			
0.10	0.1063	0.1574	0.9410	14.21			
0.11	0.1177	0.1744	0.9346	12.58			
0.12	0.1293	0.1915	0.9282	11.21			
0.13	0.1411	0.2090	0.9216	10.05			
0.14	0.1530	0.2267	0.9150	9.06			
0.15	0.1652	0.2447	0.9082	8.20			
0.16	0.1775	0.2630	0.9014	7.44			
0.17	0.1901	0.2816	0.8944	6.78			
0.18	0.2029	0.3005	0.8873	6.18			
0.19	0.2159	0.3198	0.8801	5.65			
0.20	0.2292	0.3395	0.8727	5.17			
0.21	0.2427	0.3596	0.8651	4.73			
0.22	0.2566	0.3801	0.8575	4.33			
0.23	0.2707	0.4011	0.8496	3.97			
0.24	0.2852	0.4225	0.8416	3.63			
0.25	0.3000	0.4444	0.8333	3.32			
0.26	0.3152	0.4670	0.8249	3.03			
0.27	0.3308	0.4901	0.8162	2.76			
0.28	0.3468	0.5138	0.8073	2.51			*502.63*
0.29	0.3633	0.5383	0.7981	2.28			*455.63*
0.30	0.3804	0.5635	0.7887	2.06		*411.42*	*411.42*
0.31	0.3980	0.5896	0.7789	1.85		*369.70*	*369.70*
0.32	0.4163	0.6167	0.7687	1.65	*330.18*	*330.18*	*330.18*
0.33	0.4352	0.6448	0.7582	1.46	*292.62*	*292.62*	*292.62*
0.34	0.4550	0.6741	0.7472	1.28	*256.80*	*256.80*	*256.80*
0.35	0.4757	0.7048	0.7357	1.11	*222.50*	*222.50*	*222.50*
0.36	0.4975	0.7370	0.7236	0.95	*189.51*	*189.51*	*189.51*
0.37	0.5205	0.7712	0.7108	0.79	*157.64*	*157.64*	*157.64*
0.38	0.5450	0.8075	0.6972	0.63	*126.67*	*126.67*	*126.67*
0.39	0.5714	0.8465	0.6826	0.48	*96.35*	*96.35*	*96.35*
0.40	0.6000	0.8889	0.6667	0.33	*66.40*	*66.40*	*66.40*

(continued)

Table 13 (continued)

Concrete C70/85 − $\mu_{sd,max}$ = 0.4219							
μ_{sd}	ω	$\xi = x/d$	$\zeta = z/d$	ε_s (‰)	σ_s (B400) $\mu_{sd,lim}$ = 0.3155 ω_{lim} = 0.4079	σ_s (B500) $\mu_{sd,lim}$ = 0.2946 ω_{lim} = 0.3712	σ_s (B600) $\mu_{sd,lim}$ = 0.2761 ω_{lim} = 0.3405
0.41	0.6317	0.9358	0.6491	0.18	*36.44*	*36.44*	*36.44*
0.42	0.6676	0.9891	0.6291	0.03	*5.87*	*5.87*	*5.87*

Table 14 Design table for concrete C80/95

Concrete C80/95 − $\mu_{sd,max}$ = 0.3929							
μ_{sd}	ω	$\xi = x/d$	$\zeta = z/d$	ε_s (‰)	σ_s (B400) $\mu_{sd,lim}$ = 0.2892 ω_{lim} = 0.3695	σ_s (B500) $\mu_{sd,lim}$ = 0.2695 ω_{lim} = 0.3358	σ_s (B600) $\mu_{sd,lim}$ = 0.2521 ω_{lim} = 0.3078
0.01	0.0101	0.0163	0.9941	156.89	347.83	434.78	521.74
0.02	0.0202	0.0328	0.9881	76.66			
0.03	0.0305	0.0496	0.9820	49.92			
0.04	0.0410	0.0665	0.9759	36.54			
0.05	0.0516	0.0837	0.9697	28.51			
0.06	0.0623	0.1011	0.9634	23.16			
0.07	0.0731	0.1187	0.9570	19.33			
0.08	0.0842	0.1366	0.9505	16.46			
0.09	0.0953	0.1547	0.9439	14.22			
0.10	0.1067	0.1731	0.9372	12.43			
0.11	0.1182	0.1918	0.9305	10.97			
0.12	0.1299	0.2108	0.9236	9.74			
0.13	0.1418	0.2302	0.9166	8.71			
0.14	0.1539	0.2498	0.9094	7.82			
0.15	0.1663	0.2698	0.9022	7.05			
0.16	0.1788	0.2902	0.8948	6.37			
0.17	0.1916	0.3109	0.8873	5.77			
0.18	0.2046	0.3321	0.8796	5.24			
0.19	0.2179	0.3537	0.8718	4.76			
0.20	0.2315	0.3757	0.8638	4.33			
0.21	0.2454	0.3983	0.8556	3.93			
0.22	0.2597	0.4214	0.8473	3.58			
0.23	0.2742	0.4450	0.8387	3.25			
0.24	0.2892	0.4693	0.8299	2.94			
0.25	0.3046	0.4942	0.8208	2.66			
0.26	0.3204	0.5199	0.8115	2.40			*480.87*
0.27	0.3367	0.5463	0.8020	2.16		*432.38*	*432.38*
0.28	0.3535	0.5737	0.7921	1.93		*386.99*	*386.99*
0.29	0.3709	0.6019	0.7818	1.72	*344.35*	*344.35*	*344.35*
0.30	0.3890	0.6313	0.7712	1.52	*304.14*	*304.14*	*304.14*
0.31	0.4078	0.6618	0.7601	1.33	*266.07*	*266.07*	*266.07*

(continued)

Table 14 (continued)

Concrete C80/95 − $\mu_{sd,max}$ = 0.3929							
μ_{sd}	ω	$\xi = x/d$	$\zeta = z/d$	ε_s (‰)	σ_s (B400) $\mu_{sd,lim}$ = 0.2892 ω_{lim} = 0.3695	σ_s (B500) $\mu_{sd,lim}$ = 0.2695 ω_{lim} = 0.3358	σ_s (B600) $\mu_{sd,lim}$ = 0.2521 ω_{lim} = 0.3078
0.32	0.4275	0.6937	0.7485	1.15	*229.89*	*229.89*	*229.89*
0.33	0.4481	0.7272	0.7364	0.98	*195.35*	*195.35*	*195.35*
0.34	0.4699	0.7625	0.7236	0.81	*162.22*	*162.22*	*162.22*
0.35	0.4929	0.7999	0.7100	0.65	*130.27*	*130.27*	*130.27*
0.36	0.5176	0.8399	0.6955	0.50	*99.26*	*99.26*	*99.26*
0.37	0.5442	0.8831	0.6799	0.34	*68.91*	*68.91*	*68.91*
0.38	0.5734	0.9305	0.6627	0.19	*38.90*	*38.90*	*38.90*
0.39	0.6061	0.9835	0.6435	0.04	*8.74*	*8.74*	*8.74*

Table 15 Design table for concrete C90/105

Concrete C90/105 − $\mu_{sd,max}$ = 0.3640							
μ_{sd}	ω	$\xi = x/d$	$\zeta = z/d$	ε_s (‰)	σ_s (B400) $\mu_{sd,lim}$ = 0.2652 ω_{lim} = 0.3356	σ_s (B500) $\mu_{sd,lim}$ = 0.2469 ω_{lim} = 0.3050	σ_s (B600) $\mu_{sd,lim}$ = 0.2307 ω_{lim} = 0.2795
0.01	0.0101	0.0180	0.9937	142.08	347.83	434.78	521.74
0.02	0.0203	0.0362	0.9873	69.28			
0.03	0.0306	0.0546	0.9809	45.01			
0.04	0.0411	0.0733	0.9743	32.87			
0.05	0.0517	0.0923	0.9677	25.58			
0.06	0.0624	0.1115	0.9610	20.72			
0.07	0.0734	0.1310	0.9541	17.25			
0.08	0.0845	0.1508	0.9472	14.64			
0.09	0.0957	0.1709	0.9402	12.61			
0.10	0.1072	0.1914	0.9330	10.98			
0.11	0.1188	0.2122	0.9257	9.65			
0.12	0.1307	0.2333	0.9183	8.54			
0.13	0.1427	0.2549	0.9108	7.60			
0.14	0.1550	0.2768	0.9031	6.79			
0.15	0.1675	0.2992	0.8953	6.09			
0.16	0.1803	0.3220	0.8873	5.47			
0.17	0.1934	0.3453	0.8791	4.93			
0.18	0.2067	0.3691	0.8708	4.44			
0.19	0.2203	0.3935	0.8623	4.01			
0.20	0.2343	0.4184	0.8536	3.61			
0.21	0.2486	0.4440	0.8446	3.26			
0.22	0.2633	0.4703	0.8354	2.93			
0.23	0.2785	0.4973	0.8260	2.63			
0.24	0.2940	0.5251	0.8162	2.35			*470.36*
0.25	0.3101	0.5538	0.8062	2.10		*419.05*	*419.05*
0.26	0.3267	0.5834	0.7958	1.86		*371.30*	*371.30*

(continued)

Table 15 (continued)

Concrete C90/105 − $\mu_{sd,max}$ = 0.3640							
μ_{sd}	ω	$\xi = x/d$	$\zeta = z/d$	ε_s (‰)	σ_s (B400) $\mu_{sd,lim}$ = 0.2652 ω_{lim} = 0.3356	σ_s (B500) $\mu_{sd,lim}$ = 0.2469 ω_{lim} = 0.3050	σ_s (B600) $\mu_{sd,lim}$ = 0.2307 ω_{lim} = 0.2795
0.27	0.3439	0.6142	0.7850	1.63	*326.68*	*326.68*	*326.68*
0.28	0.3618	0.6461	0.7739	1.42	*284.82*	*284.82*	*284.82*
0.29	0.3805	0.6794	0.7622	1.23	*245.36*	*245.36*	*245.36*
0.30	0.4000	0.7143	0.7500	1.04	*208.00*	*208.00*	*208.00*
0.31	0.4205	0.7509	0.7372	0.86	*172.46*	*172.46*	*172.46*
0.32	0.4422	0.7897	0.7236	0.69	*138.48*	*138.48*	*138.48*
0.33	0.4653	0.8310	0.7092	0.53	*105.78*	*105.78*	*105.78*
0.34	0.4902	0.8753	0.6936	0.37	*74.09*	*74.09*	*74.09*
0.35	0.5172	0.9235	0.6768	0.22	*43.08*	*43.08*	*43.08*
0.36	0.5470	0.9768	0.6581	0.06	*12.34*	*12.34*	*12.34*

References

1. ACI Committee 318 (2005) Building Code Requirements for Structural Concrete (ACI 318-05) and Commentary. American Concrete Institute
2. Comité Euro-International du Béton (1978) *CEB-FIP Model Code 1978: Model Code for Concrete Structures, 3rd ed.*, Lausanne
3. Comité Euro-International du Béton (1993) CEB-FIP Model Code 1990: Design Code. Thomas Telford, London
4. European Committee for Standardisation (2004) EN 1992-1-1. Eurocode 2: Design of concrete structures. Part 1-1: General rules and rules for buildings. CEN, Brussels
5. Fédération Internationale du Béton (2012a) fib Bulletin No. 65: Model Code 2010—Final draft, Vol. 1. FIB, Lausanne, Switzerland
6. Fédération Internationale du Béton (2012b) fib Bulletin No. 66: Model Code 2010—Final draft, Vol. 2. FIB, Lausanne, Switzerland
7. Jenkins D (2011) Time to Dump the Rectangular Stress Block? In: CONCRETE 2011 conference, Perth, Western Australia, 12–14 Oct 2011
8. Rüsch H (1960) Researches toward a general flexural theory for structural concrete. ACI Journal 57(7):1–28
9. Roşca B, Petru M (2009) Reinforced Concrete Section Design to Bending according to EN 1992-1-1/2004—Eurocode 2. *Buletinul Institutului Politehnic din Iasi, Sectia V. Constructii. Arhitectura*, LV (LIX)(3), 53–66
10. Shehata I, Shehata L, Mattos TS (2000) Stress-strain curve for the design of high-strength concrete elements. Mater Struct 33(231):411–418
11. Standards Australia (2009) Concrete Structures: AS 3600-2009. Sydney, Australia
12. Torres L, Neocleous K, Pilakoutas K (2012) Design procedure and simplified equations for the flexural capacity of concrete members reinforced with fibre-reinforced polymer bars. Structural Concrete 13(2):119–129
13. Walraven JC, Bigaj-van Vliet A (2011) The 2010 fib model code for structural concrete: a new approach to structural engineering. Struct Concr 12(3):139–147

Multi-storey Structures with Seismic Isolation at Storey-Levels

Marios C. Phocas and George Pamboris

Abstract Through increasing international research and application activities in the last years, seismic isolation has proven to be an innovative passive control technique in the area of performance-based design of buildings. Seismic isolation is principally based on the incorporation of flexible isolators at the base of low-rise buildings in order to shift the fundamental period outside of the dangerous for resonance, range of periods. In extending the concept of base isolation, the present contribution refers to the control of multi-storey structures under earthquake actions by means of introducing seismic isolation at different elevations of the structure. Thus, the structural response is influenced decisively by the vertically distributed seismic isolation, which at the respective storey-levels is alone capable of controlling the partial and overall stiffness, the force transmission and the energy dissipation process of the respective dynamic adaptable system. During strong earthquakes the effectiveness of the system in further enlarging the period of the building, compared to the classical method of seismic isolation at a unique level, is achieved, most often with decreased inter-storey deflections, and without introducing extensive displacements at the building base, which are often limited by practical constraints. The effectiveness of the proposed control system is investigated in parametric studies, in the time-history range, for a 6-storey building under ten selected earthquakes of the Greek-Mediterranean region, scaled to a maximum ground acceleration of 0.25 g. Most effective vertical distribution of seismic isolation at various storey-levels is proposed, based on the earthquake, structural and isolation characteristics used in the numerical study.

M.C. Phocas (✉)
Department of Architecture, University of Cyprus, 1678 Nicosia, Cyprus
e-mail: mcphocas@ucy.ac.cy

G. Pamboris
Estate Management Services, Cyprus University of Technology,
3036 Limassol, Cyprus
e-mail: george.pamboris@cut.ac.cy

M. Papadrakakis et al. (eds.), *Computational Methods in Earthquake Engineering*,
Computational Methods in Applied Sciences 44,
DOI 10.1007/978-3-319-47798-5_9

1 Introduction

The earthquake safety of building structures may be achieved with the isolation of the building from the ground through isolation-damping devices. In this way the input earthquake energy of the structure is itself minimized, and the earthquake impacts are transmitted from the low tuned bearings to the building as smaller shear forces, through oscillations of lower frequency. A limitation for the utilization of base isolation is the seismic gap that must be provided around the structure to accommodate the large relative displacements at the isolation level [1]. Furthermore, base isolation is usually not applicable in medium- to high-rise buildings, since the natural period of such buildings is already relatively long. Otherwise, this would require for optimal adjustment of the systems seismic performance, an isolation mechanism with large flexibility, but also high vertical load capacity [2].

In extending the concept of base isolation, the present contribution refers to the control of multi-storey structures under earthquake actions by means of introducing seismic isolation at different elevations of the structure, as originally proposed in [3, 4]. The isolation-damping devices are herewith defined as controllable complex connections that provide in a compact technique different transmission characteristics in accordance with the loading conditions. Conceptually, it is assumed that the structural deformability is influenced decisively by the vertically distributed seismic isolation, which at the respective storey-levels is alone able to control the partial and overall stiffness, the force transmission and the energy dissipation process during an earthquake event.

Limited research activities have been undertaken up to now on the distribution of seismic isolation over the building height. The concept of partial mass isolation was proposed for the utilization of seismic and wind energy transfer into sub-systems of mega-structures [5] and in connection with the application of viscous damping devices, as an economical approach for the seismic design of medium height- and tall buildings [6]. Roof level isolation of multi-storey buildings for the reduction of storey displacements and inter-storey deflections has been investigated analytically and experimentally [7, 8]. The detached building roof is hereby utilized as an absorber mass, which is connected to the building body over isolation-damping mechanisms. The seismic response of isolated superstructures of base isolated buildings, subjected to deterministic earthquake input and random excitations, has been investigated in [9, 10]. The segmented buildings showed significant reduction of the base displacements.

Following a brief presentation of the control concept of vertically distributed seismic isolation in multi-storey buildings, the aim of the study is to investigate its effectiveness under ten scaled earthquake motions of the Greek Mediterranean region. In this frame multiple isolated configurations of a 6-storey symmetrical structure with two possible isolation system characteristics are compared to the original fixed supported system, with regard to the storey displacements, accelerations and shear forces. The seismic response analyses of the isolated systems seek

to comprehend relevant investigations made in [11]. In this respect [12] already formulated favourable isolators' configurations as a single-objective optimization task through application of genetic algorithms. The proposed optimization procedure has been verified in [13], while several recorded strong earthquake motions were considered, which were applied either individually or in sets to the building in the framework of time-history analyses.

Principally, the parametric studies conducted prove that the designer is provided with numerous options to adjust the seismic response of the building. In terms of most favorable isolation configurations over the height, the results obtained in the present study are not in support of a straightforward decisions-making design task. Due to different response parameters that need to be considered and their complex effect on the structural behaviour, overall favorable solutions may be derived at first place through a multi-criteria analysis, as exemplified in the final part of the paper.

2 Isolation Mechanism Parameters

The adaptable earthquake isolators with progressive nonlinear deformability, developed and documented in [14, 15], serve as passive adaptable multi-functional connections for the purposes of this study, Fig. 1. The devices consist of two coupled elements in a single unit with different mechanical properties: A primary bearing element, responsible for the vertical load transfer and the isolation and a secondary bearing element, responsible for the displacement control, the unloading of the primary element under large displacements and the provision of additional damping. The primary element is a conventional steel plate reinforced elastomere, formed as a single ring bearing (RL) or in 4 to 12 columns (SL). The secondary element consists of a glass-fiber reinforced epoxy resin ball, embedded in a double concave elastomeric pillow.

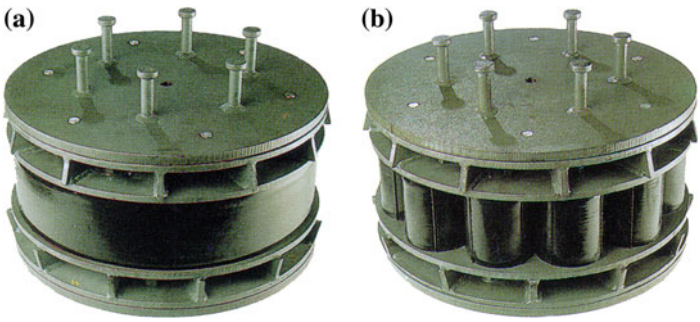

Fig. 1 Adaptable earthquake isolator with: **a** Ring bearing (RL700), **b** 12 columns bearing (12SL468)

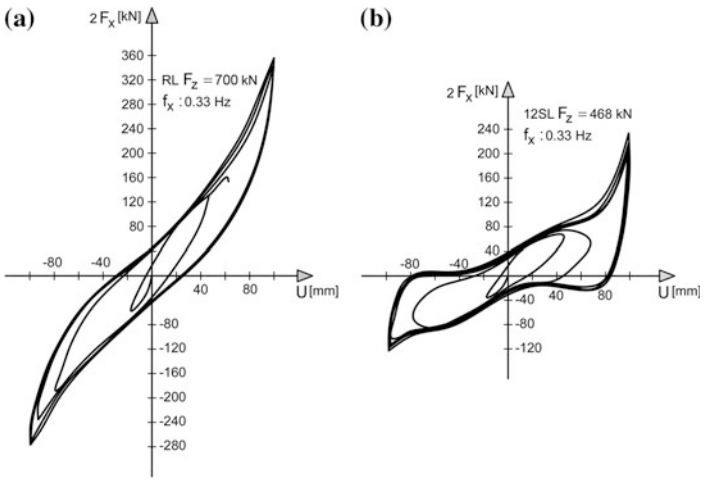

Fig. 2 Isolators' hysteretic behaviour under dynamic horizontal loading and differing vertical load: **a** $F_Z = 700$kN (RL700), **b** $F_Z = 468$kN (12SL468)

The registered hysteretic loops of the isolators, derived from dynamic laboratory tests, are characterized by a progressive nonlinearity with increasing resistance under growing displacements, which affects favorably their stability. The maximum deformation of the isolators accounts to $DU_{i,max} = 10.0$ cm. The load-deformation diagrams of the isolators, obtained from laboratory dynamic tests, under constant vertical loads of 700 and 468 kN respectively and a load frequency of 0.33 Hz are shown in Fig. 2. In the present work, for simplicity, isolator forces behaviour is modeled using an equivalent linear elastic model, which is characterized by an effective stiffness and an effective damping coefficient. These parameters were calculated based on the characteristic isolators' skeleton curve as shown in Fig. 3, [14, 15], and summarized in Table 1.

The isolator type with primary ring bearing and a normal vertical load of 700 kN (RL700) was applied for the parametric analysis of a 6-storey building. Subsequently, the isolator type with a twelve column bearing as primary element and a vertical load of 468 kN (12SL468) was considered for the analysis, meaning a relative reduction of the equivalent stiffness of each isolator of 41.51 % and an increase of the damping ratio of 88.9 %.

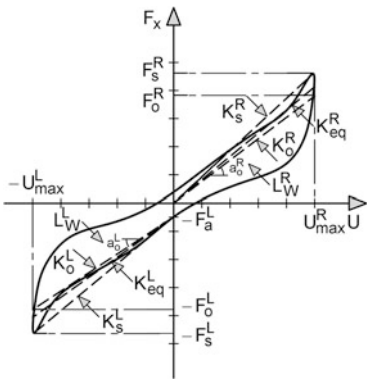

Fig. 3 Isolators' typical hysteretic loop

Table 1 Mechanical properties of passive adaptable isolators

Isolation type	Vertical load F_Z [kN]	Eq. stiffness K_{eq} [kN/cm]	Frequency ω [1/s]	Hysteretic area L_W [kNcm]	Damping ratio ζ [%]	Damping coefficient C [kNs/cm]
RL	700	12.02	4.10	748	9.91	0.58
12SL	468	7.03	3.83	810	18.72	0.69

3 Isolated Structural Systems

The seismically isolated buildings are modeled as shear-beam buildings with lumped masses at the floor levels, assuming that the structures remain elastic during an earthquake excitation. Such an assumption is reasonable, considering the intention of seismic isolation to avoid inelastic deformations of the superstructure. The inertia, damping and elastic forces depend on total accelerations, relative velocities and relative displacements, respectively. The damping and elastic forces at an isolation level depend on the type and mechanical characteristics of the isolation system.

For the numerical analyses, a 6-storey structure is considered, with possible seismic isolation at the base (SL0), at any upper storey or several storeys (SL1–SL5). The isolation levels of the upper storeys are introduced underneath the respective storey masses, Fig. 4. Considering a six to six bay symmetrical structural system, the concentrated masses for each storey are set to $M_s = 500$ tons, a constant column stiffness of the MDF model was defined to $K_i = 1000\text{MN/m}$, and the damping ratio to $\zeta_i = 0.02$. The respective additional mass as to the introduction of isolation accounts to $M_i = 100$ tons, i.e. $M_i = 0.20M_s$. This results from the mass of the devices and the mass of the required stiffening steel members underneath. The properties of the seismic isolators account to a stiffness of a single device of

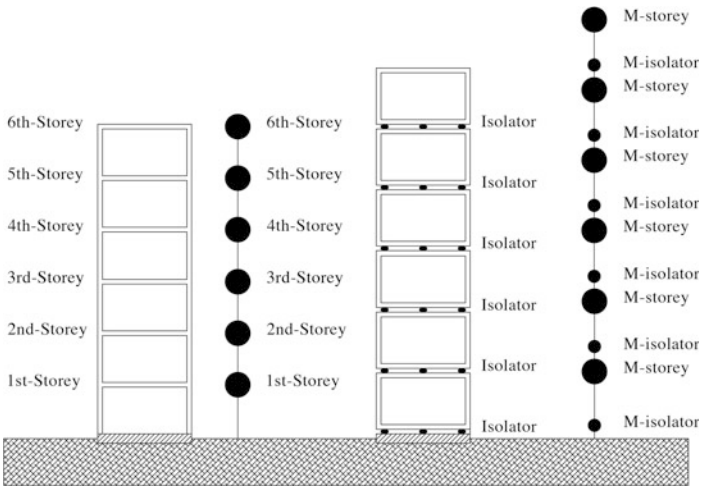

Fig. 4 Isolators configurations for a 6-storey building

$K_i = 1202\,\mathrm{kN/m}$ for the RL700 prototype and $K_i = 703\,\mathrm{kN/m}$ for the 12SL468 prototype. The stiffness of the isolator elements, introduced at a specific level refers to the number of isolators used, as to the resulting vertical load from the upper storeys, by taking into account a single device's vertical loading of 700 kN for the first analysis cycle and 468 kN for the second analysis cycle. The damping coefficient of the isolator level results also from the number of isolators used, as to the damping coefficient of a single device of 0.58 and 0.69 kNs/cm respectively.

In terms of the dynamic behaviour, the multiple isolated structures are to be treated as non-stationary dynamic models, whose response can only be investigated by means of time-history dynamic analysis. The analysis assumes in general form the step-by-step integration of the system of 2nd order differential equations of motion:

$$\boldsymbol{M} \cdot \ddot{\boldsymbol{u}}(t) + C \cdot \dot{\boldsymbol{u}}(t) + K \cdot \boldsymbol{u}(t) = -\boldsymbol{M} \cdot 1 \cdot \ddot{\boldsymbol{u}}_{\boldsymbol{g}}(t) \tag{1}$$

where $\boldsymbol{M,C,K}$ are the mass, damping and stiffness matrices, respectively. $\ddot{\boldsymbol{u}}_{\boldsymbol{g}}(t)$ is the vector of ground acceleration at each time t, while $1 = [1 \ldots 1]^T$ when considering a building with shear-beam behaviour oscillating in the one horizontal direction. $\boldsymbol{u}, \dot{\boldsymbol{u}}, \ddot{\boldsymbol{u}}$ are the vectors of the relative displacements, velocities and accelerations, respectively, of the lumped masses of the building.

The Central Difference Method (CDM), an explicit direct integration method, is used to compute the relative displacements and absolute accelerations at time $t + \Delta t$

by numerically integrating the equations of motion at time t. In particular, assuming that we know the relative displacements up to time t, the following equations are used to approximate the corresponding relative velocities and accelerations:

$$\dot{\boldsymbol{u}}(t) = \frac{\boldsymbol{u}(t+\Delta t) - \boldsymbol{u}(t-\Delta t)}{2\Delta t} \tag{2}$$

$$\ddot{\boldsymbol{u}}(t) = \frac{\boldsymbol{u}(t+\Delta t) - 2\cdot\boldsymbol{u}(t) + \boldsymbol{u}(t-\Delta t)}{\Delta t^2} \tag{3}$$

In order to calculate relative displacements at time $t+\Delta t$, the equations of motion can be expressed in matrix form:

$$\widehat{\boldsymbol{K}}\cdot\boldsymbol{u}(t+\Delta t) = \widehat{\boldsymbol{P}}(t) \tag{4}$$

with

$$\widehat{\boldsymbol{K}} = \frac{1}{\Delta t^2}\boldsymbol{M} + \frac{1}{2\cdot\Delta t}\boldsymbol{C} \tag{5}$$

$$\widehat{\boldsymbol{P}}(t) = -\boldsymbol{M}\cdot 1\cdot\ddot{\boldsymbol{u}}_{\boldsymbol{g}}(t) - \left(\boldsymbol{K} - \frac{2}{\Delta t^2}\boldsymbol{M}\right)\cdot\boldsymbol{u}(t) - \left(\frac{1}{\Delta t^2}\boldsymbol{M} - \frac{1}{2\cdot\Delta t}\boldsymbol{C}\right)\cdot\boldsymbol{u}(t-\Delta t) \tag{6}$$

Thus, relative displacements, velocities and accelerations at time $t+\Delta t$ are computed using Eqs. (4), (2) and (3), respectively.

A sufficiently small time step is used, in order to ensure the stability of the numerical method (CDM). Specifically, a time step Δt much smaller than the critical time step Δt_{cr} is selected and used in the numerical simulations, based on the smallest eigenperiod T_{min} of the seismically isolated building:

$$\Delta t \ll \Delta t_{cr} = \frac{T_{min}}{\pi} \tag{7}$$

To facilitate the description in the numerical investigation, an index vector $\boldsymbol{I}$ is defined to indicate the positions of isolators within the building under consideration. The terms of vector $\boldsymbol{I}$ take values as follows, referring to the positions of isolators within the height of the building under consideration:

$$\mathbf{I}_i = \begin{cases} 0 \Rightarrow \textit{without isolation at level } i \\ 1 \Rightarrow \textit{with isolation at level } i \end{cases} \tag{8}$$

Vector $\boldsymbol{I}$ has n_{storey} terms $(I_0, I_1, \ldots, I_{n_{storey}})$, where n_{storey} is the number of storeys of the building. I_0 refers to the base isolator or isolator '0' (i.e. storey '0' represents the base of the building), while the remaining terms I_i, $i = 1, 2, \ldots, n-1_{storey}$, are

associated with the isolators at storeys 1, 2, …, $n - 1_{storey}$, respectively. The two extreme configurations refer to a non-isolated building ($I_i = 0\,\forall_i$) and a fully isolated building ($I_i = 1\,\forall_i$), respectively. Base isolation is a special case of partial isolation with $I_0 = 1$ and $I_i = 0\ \forall_i \neq 0$. Thus, vector $\boldsymbol{I}$ holds the necessary information regarding states (active/inactive) of isolators at the potential isolation levels, which are just below the base and the slabs of the five storeys of the building.

4 Modal Properties

In contrast to traditional design methods that aim at increasing the earthquake resistance capacity of structures, seismic isolation reduces the induced seismic loads by shifting the natural period of the structure away from the period range of the dominant components of the earthquake excitations. The period shift in an isolated structure causes a reduction of the absolute accelerations, while increased displacements are controlled only at the isolation levels. The effectiveness of the isolated structural systems may be initially estimated, based on their natural period. The number of isolators applied at different levels of the structure and the resulting modes indicate respective contribution of inertial forces. Modal analysis of the governing modes was performed for all systems (Table 2).

The fixed supported structure obtains a fundamental period of $T_1 = 0.583$s, while the following two modes, with $T_2 = 0.198$ and $T_3 = 0.124$, also have a significant contribution in the dynamic behaviour. The base isolated structure with a fundamental period of $T_1 = 0.764$s has a most relatively predominant first mode compared to the possible configurations of the isolated systems. This proves that the first mode of the structure is dominated by the deformation of the isolator only at the base level. By shifting the single seismic isolation towards the top storey-level, a small reduction of the respective first period results, up to $T_1 = 0.708$s. The contribution of higher modes with predominant deformations below the isolation level seems to be substantial. The structures with two and three seismic isolation levels develop relatively higher natural periods than the single mid-height isolated system, in the range of 10–35 % higher. In accordance to the number of seismic isolators of each system, the participation of higher modes is evident. The highest fundamental period of the structure can be achieved, when all storey-levels are isolated, i.e. $T_1 = 1.256$s. This system has the highest contribution of higher modes.

The increase of the fundamental period of the isolated structures and most importantly the development of higher modes, in several cases with a considerable amount of effective mass participation, is an indication of the importance of the damping properties of the isolation mechanism at the respective storey levels. Since all major mode shapes exhibit large relative displacements at the isolation levels, providing high velocity values between the adjacent storeys, the damping properties

Table 2 Natural periods of favorable isolated 6-storey structures [s]

Eigen-form	000000	100000	010000	001000	000100	110000	010001	001100	001001	000110
1	0.583	0.764	0.772	0.771	0.763	0.913	0.849	0.910	0.853	0.891
2	0.198	0.236	0.215	0.208	0.256	0.243	0.433	0.274	0.420	0.325
3	0.124	0.137	0.130	0.163	0.139	0.173	0.175	0.171	0.192	0.212
4	0.094	0.099	0.113	0.100	0.110	0.117	0.123	0.137	0.132	0.110
5	0.079	0.081	0.087	0.086	0.082	0.087	0.098	0.086	0.086	0.102
6	0.072	0.073	0.074	0.076	0.078	0.074	0.076	0.082	0.081	0.078
7		0.049	0.050	0.051	0.052	0.051	0.056	0.053	0.056	0.054
8						0.049	0.050	0.051	0.051	0.052
	000011	111000	100110	101010	111100	110011	111110	111011	111111	
1	0.852	1.033	0.994	0.997	1.129	1.062	1.204	1.165	1.256	
2	0.391	0.292	0.404	0.393	0.364	0.500	0.442	0.509	0.520	
3	0.262	0.178	0.233	0.237	0.208	0.283	0.260	0.294	0.327	
4	0.136	0.152	0.127	0.104	0.151	0.189	0.188	0.231	0.236	
5	0.091	0.100	0.102	0.100	0.137	0.126	0.147	0.153	0.182	
6	0.075	0.076	0.081	0.093	0.082	0.081	0.102	0.097	0.145	
7	0.056	0.052	0.054	0.054	0.053	0.056	0.054	0.056	0.056	
8	0.054	0.050	0.052	0.051	0.051	0.054	0.053	0.054	0.054	
9		0.049	0.049	0.049	0.050	0.050	0.051	0.051	0.053	
10					0.048	0.048	0.049	0.050	0.051	
11							0.048	0.048	0.050	
12									0.048	

of the isolation mechanism refer primarily to the dissipation of the input seismic energy to the upper storeys.

5 Time-History Analysis

The MDOF-systems were used in the dynamic analysis in the time-history range (first 30 s) for ten representative earthquake components of the Greek Mediterranean region, Table 3. The recorded peak ground accelerations amount 0.10g ÷ 0.50g and the large majority of the earthquake motions develop in their response spectra amplification values in the frequency area of $\omega = 4$ to $8s^{-1}$, [16]. These values have been considered for the earthquake inputs in preliminary parametric analyses, conducted by the authors [11]. In the present study all earthquake records have been scaled to acquire a maximum acceleration of 0.25g, in compliance with the recommended maximum ground acceleration in the elastic response spectrum for ground type A (rock formation) of Cyprus, CYS EN1998-1:2005 [17], in order to facilitate a direct comparison of the earthquake responses as to the respective seismic input characteristics.

For the purposes of the parametric response study an algorithm has been developed with the program Matlab, enabling the calculation of the earthquake induced total storey displacements (U), inter-storey deflections (DU), absolute storey accelerations (A_g) and storey shear forces (F). The analysis has been conducted for the ten selected scaled earthquake input motions and all possible combinations of the isolated structural systems (system alternatives).

In particular, limitation of horizontal displacements may be required also for certain (or even all) floor slabs of a building. As an example, when the building under consideration has a basement, then poundings with the surrounding moat wall

Table 3 Earthquake input components for the time-history analysis

Earthquake (record station, hor. direction)	Rec. max. acceleration $\ddot{U}_g$ [g]	Scale factor to obtain $\ddot{U}_g$ = 0.25 g
E1: Aigio 95 (Aigio, 0°)	0.50	0.50
E2: Athens 99 (Sepolia, 0°)	0.33	0.76
E3: Ionian 83 (Argostoli, 90°)	0.24	1.04
E4: Kalamata 86 (Kalamata, 0°)	0.22	1.14
E5: Heraklio 84 (Heraklio, 90°)	0.21	1.19
E6: Aigio 90 (Aigio, 90°)	0.20	1.25
E7: Etolia 88 (Valsamata, 90°)	0.18	1.39
E8: Killini 88 (Zakinthos, 90°)	0.15	1.67
E9: Preveza 81 (Preveza, 0°)	0.14	1.79
E10: Gulf of Corinth 93 (Nafpaktos, 90°)	0.10	2.50

need to be prevented both for the isolated base slab and for the slab of 'storey 1'. Thus, with the provided seismic gap the aim is to facilitate the horizontal displacements of both aforementioned slabs. Another example is the potential of impact with adjacent buildings. In that case, we need to control the horizontal displacements of floor slabs, which may collide with components of neighbouring structures.

Inter-storey deflections are widely accepted as response parameters, with which we can effectively measure structural damage as a result of seismic action. Inter-storey deflections are also associated with damage of non-structural components, as well as with damage or loss of building contents.

On the other side, seismic isolation is often applied as a mitigation measure to allow critical facilities to remain safe and operational during and after a strong earthquake. Frequently, these facilities house sensitive and expensive equipment, which is also required to remain operational during and after the earthquake. Other building contents may include important items of high (e.g. historical) value. Damage to such contents is most commonly linked with the acceleration induced to the contents during the earthquake. Thus, it is important to control the absolute accelerations at the floors of a building, where these contents reside.

Finally, storey shear forces developed during an earthquake are directly related to the necessary sizes of the primary structural members and therefore influence decisively the resulting construction costs of the seismic isolated structures, compared to the non-isolated ones.

In each analysis cycle, according to the characteristics of the isolation system used (RL700 and 12SL468), the algorithm selects for every system alternative the maximum respective induced responses for three different analysis cases: In the first case, the maximum values of the four response parameters (U, DU, A_g, F) are registered, that correspond to the maximum inter-storey deflection of every system alternative under any of the ten earthquake motions; in the second case, to the maximum absolute acceleration; in the third case, to the maximum shear forces. Figures 5, 6, 7, 8, 9 and 10 present the favorable configurations of the isolated systems as to their seismic response, in respect to each isolation system used and analysis cases.

With a single isolation level over the height of the building, minimum relative deformations of the isolators are favored by the base isolated alternative, "100000", followed by the alternatives as to the sequence of storeys over the height, irrespectively of the specific characteristics of the isolation system. With regard to the maximum accelerations of the single isolated alternatives, most effective is the system alternative "010000" with the RL700 isolation system and the alternative "000100" with the 12SL468 isolation system. The maximum reduction of the base shear force takes place, when the isolation level is at the fourth storey, "000100".

By having two isolation levels over the height all maximum response criteria are further reduced compared to the single case ("110000" for DU with both isolation systems, "001001" with the RL700- and "010001" with the 12SL468 isolation

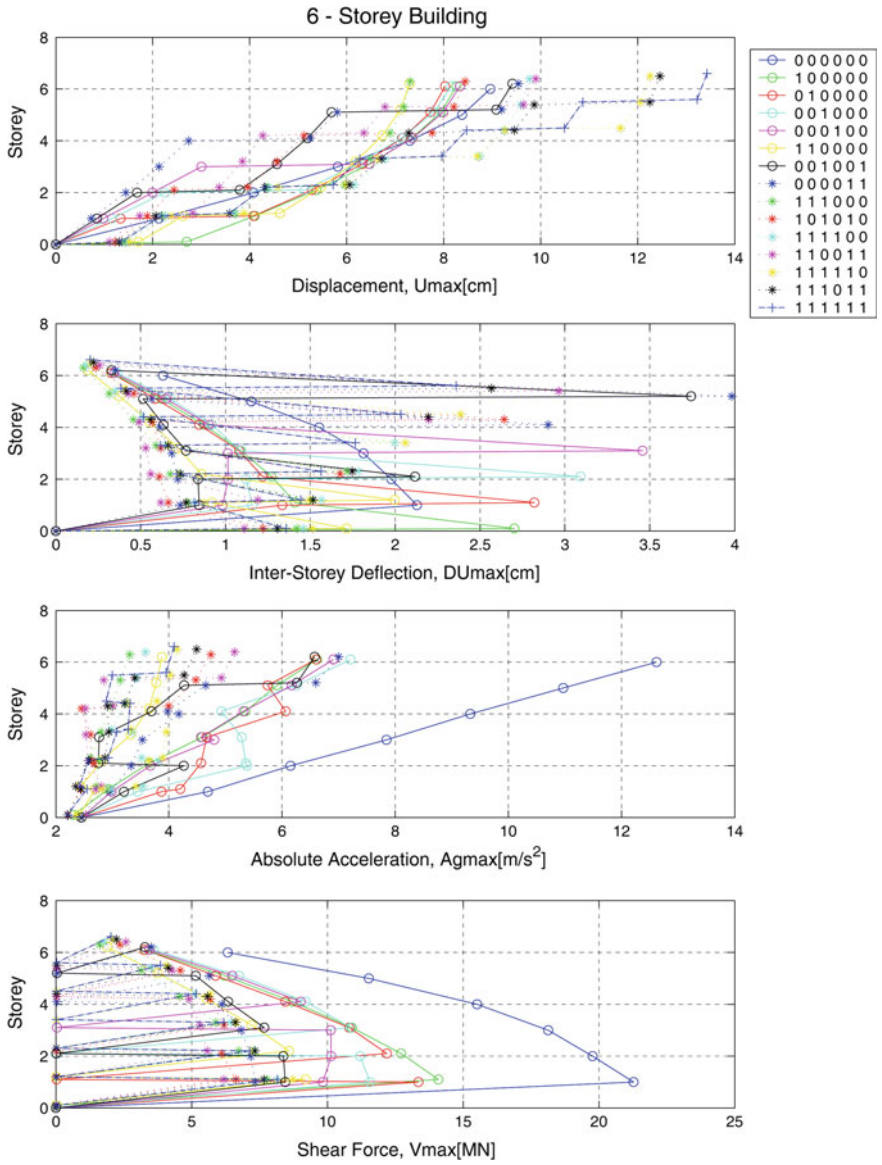

Fig. 5 Analysis case 1, seismic responses of 6-storey structures with favorable multiple possible isolation levels of the RL700 system, corresponding to a maximum inter-storey deflection of the systems

system for A_g, and "000011" with the RL700- and "000110" with the 12SL468 isolation system for F), while the total displacements remain in the same range. The same applies to the case of having three isolation levels ("111000" with both

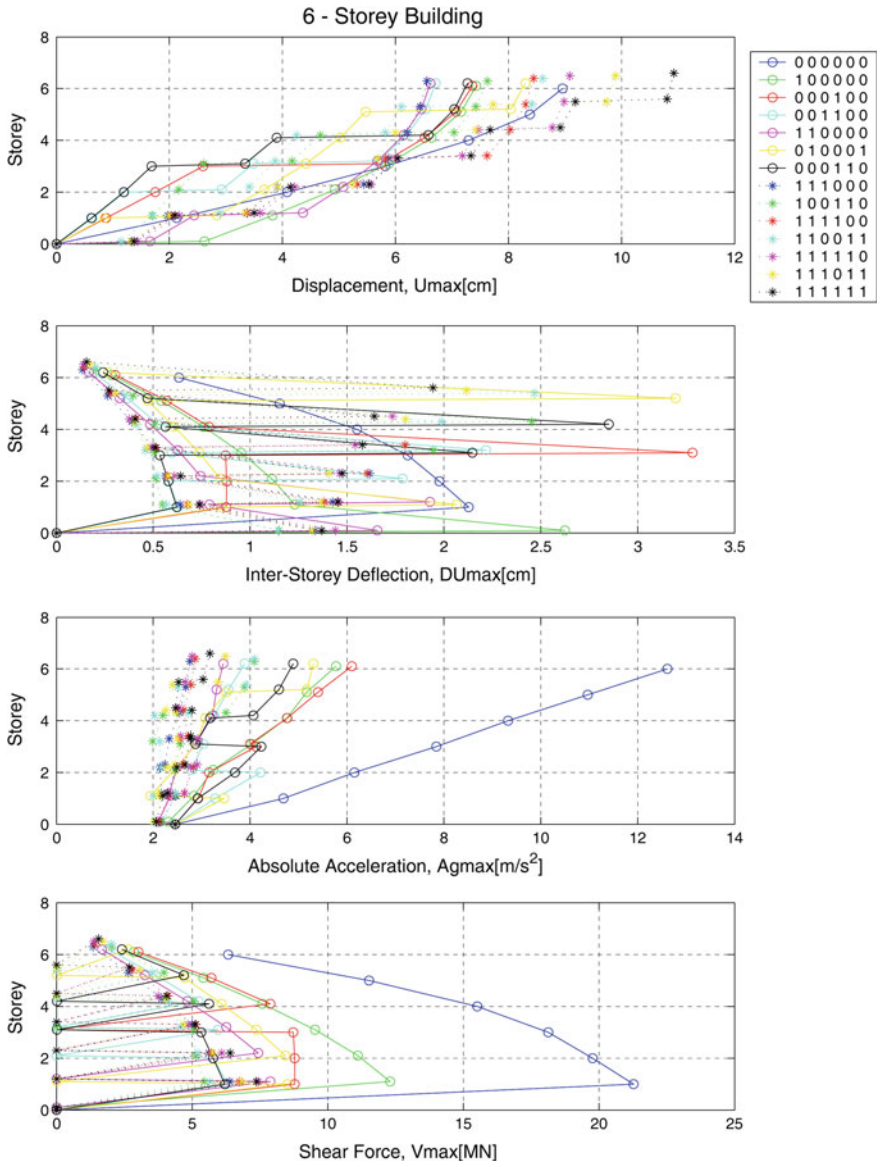

Fig. 6 Analysis case 1, seismic responses of 6-storey structures with favorable multiple possible isolation levels of the 12SL468 system, corresponding to a maximum inter-storey deflection of the systems

isolation systems for *DU* and A_g, and "101010" with the RL700- and "100110" with the 12SL468 isolation system for *F*).

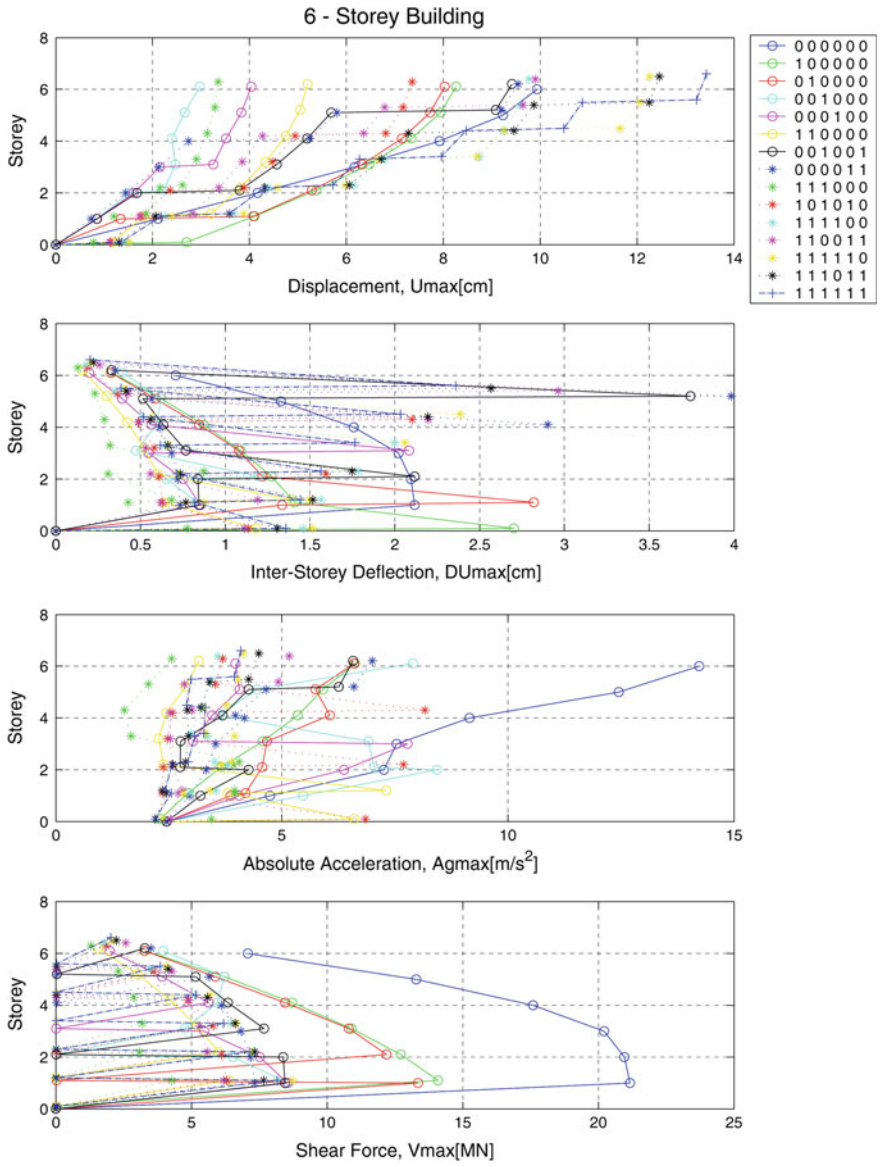

Fig. 7 Analysis case 2, seismic responses of 6-storey structures with favorable multiple possible isolation levels of the RL700 system, corresponding to a maximum absolute acceleration of the systems

Structures having more than three isolation levels develop insignificant further reductions in their maximum responses compared to the three isolation levels alternatives. In particular, lowest relative deformations of the isolators and lowest absolute accelerations develop when the isolation levels are placed at the lower

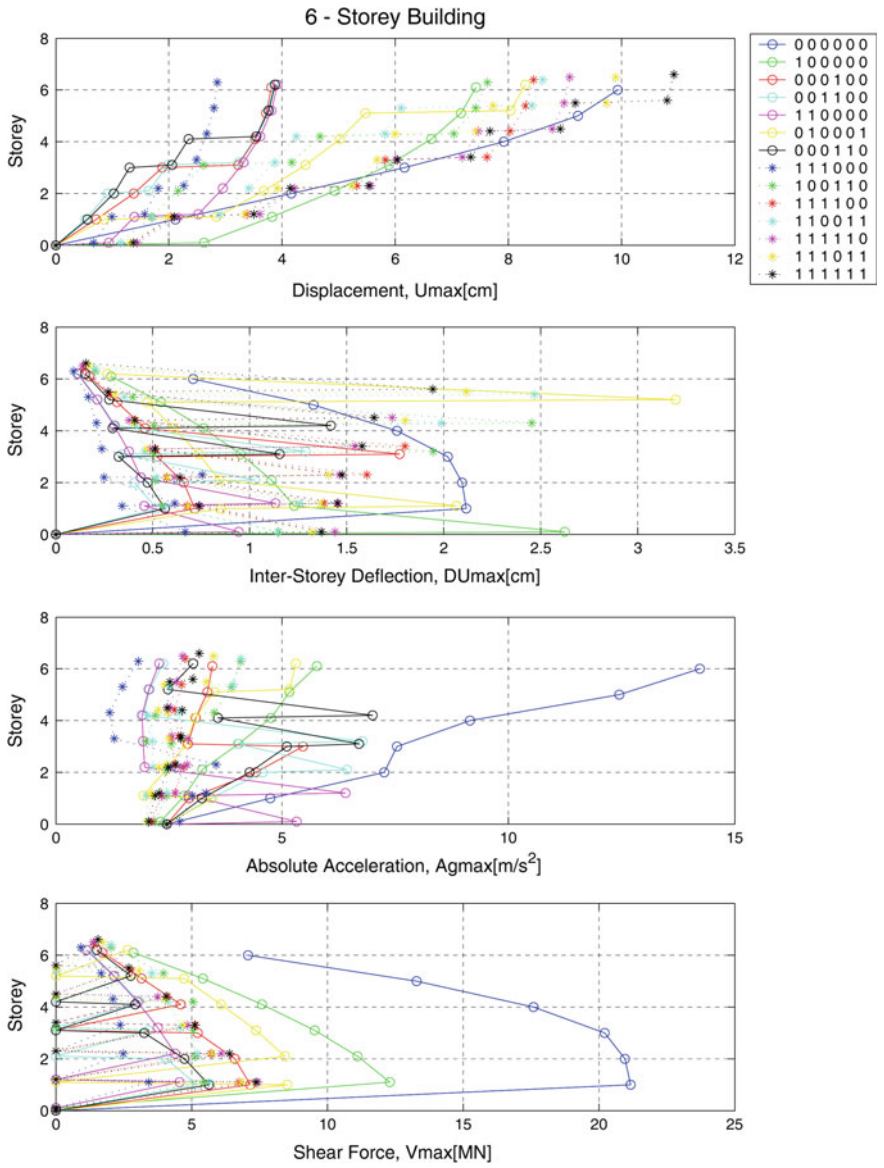

Fig. 8 Analysis case 2, seismic responses of 6-storey structures with favorable multiple possible isolation levels of the 12SL468 system, corresponding to a maximum absolute acceleration of the systems

storeys, i.e. "111100". An optimized response with regard to the base shear develops with both isolation levels, when the systems have most high stiffness values at mid-height ("110011" and "111011"). In all cases the maximum relative deformations of the isolation levels do not exceed the value of $DU_{max} = 5.0$cm,

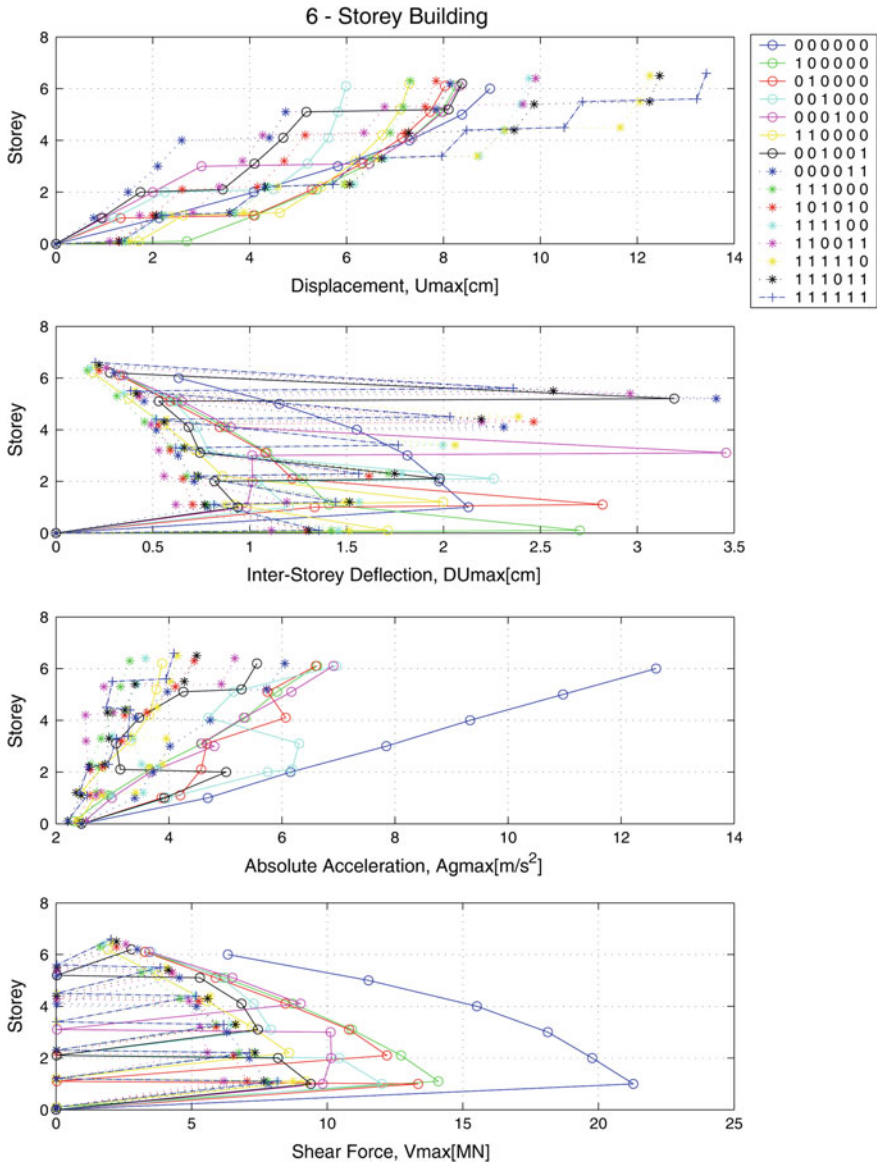

Fig. 9 Analysis case 3, seismic responses of 6-storey structures with favorable multiple possible isolation levels of the RL700 system, corresponding to a maximum shear force of the systems

which is significantly lower than the actual maximum deformation capacity of the isolators used in the study.

The numerical results of the most suitable isolated system configurations, as described above, are included in Table 4. Based on the stiffness and damping

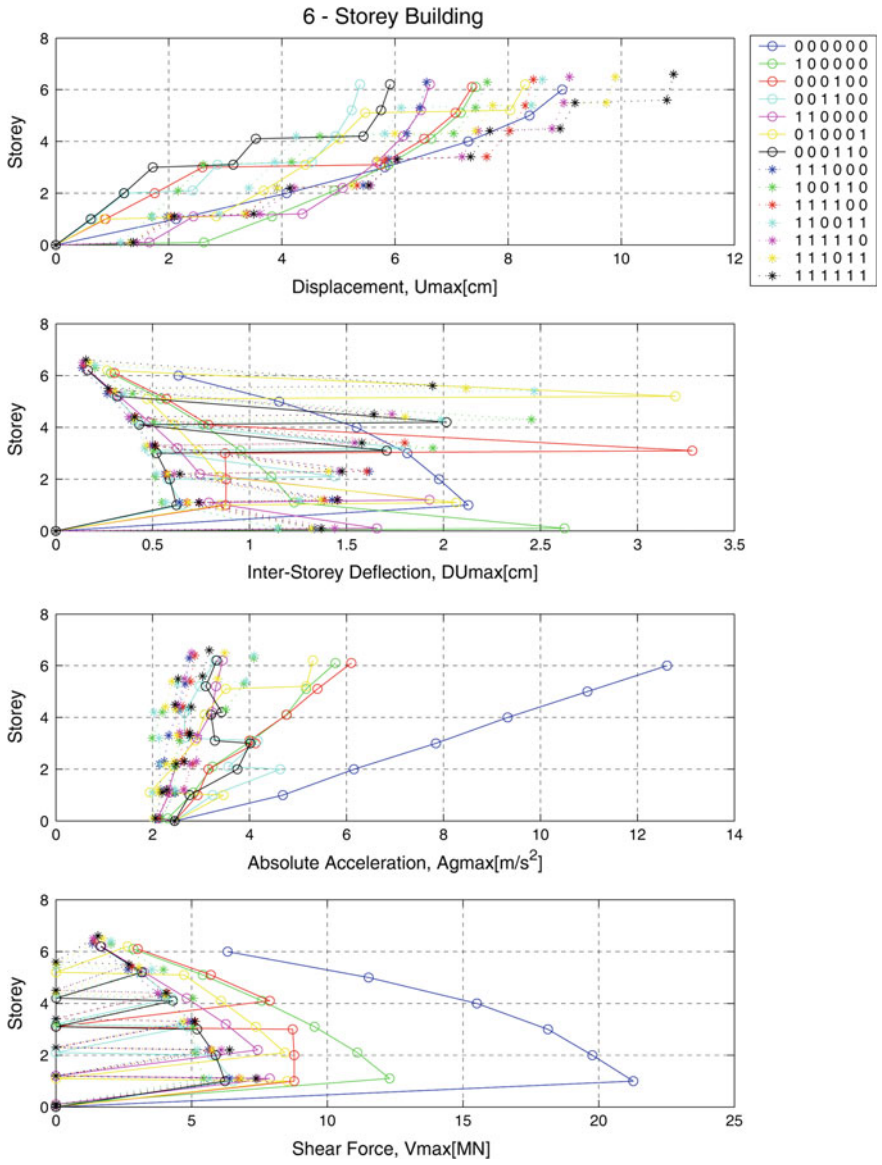

Fig. 10 Analysis case 3, seismic responses of 6-storey structures with favorable multiple possible isolation levels of the 12SL468 system, corresponding to a maximum shear force of the systems

properties of the isolators used for the analyses, the respective calculated values of the isolation levels of the MDOF-systems are included in Table 5 and 6, for the most suitable isolated system configurations.

Table 4 Isolated 6-storey structures (ISC) with selected seismic responses

A/A	ISC	U_{max} [cm]	DU_{max} [cm]	$A_{g,\max}$ [m/s^2]	F_{max} [MN]	$\frac{F_{000000,max}-F_{i,max}}{F_{000000,max}}$[%]
Isolation System RL700						
1	000000	8.961	2.129	12.619	21.285	0
2	100000	8.264	2.703	6.620	14.097	66.23
3	010000	8.032	2.821	6.602	13.354	62.74
4	001000	5.992	2.260	6.959	12.018	56.46
5	000100	8.333	3.458	6.911	10.152	47.69
6	110000	7.293	1.998	3.880	9.209	43.27
7	001001	8.384	3.191	5.556	9.397	44.15
8	000011	8.139	3.408	6.051	7.831	36.79
9	111000	7.313	1.718	3.309	7.789	36.59
10	101010	7.848	2.466	4.448	7.054	33.14
11	111100	9.769	1.998	3.818	8.156	38.32
12	110011	9.902	2.963	5.164	6.188	29.07
13	111110	12.262	2.386	4.147	8.738	41.05
14	111011	12.462	2.567	4.492	7.673	36.05
15	111111	13.429	2.360	4.090	8.167	38.37
Isolation System 12SL468						
1	000000	8.961	2.129	12.619	21.285	0
2	100000	7.430	2.625	5.771	12.310	57.83
3	000100	7.365	3.283	6.103	8.795	41.32
4	110000	6.616	1.929	3.445	7.894	37.09
5	001100	5.379	1.807	4.632	6.529	30.67
6	010001	8.303	3.197	5.307	8.525	40.05
7	000110	5.915	2.016	4.016	6.236	29.30
8	111000	6.557	1.616	2.757	6.399	30.06
9	100110	7.627	2.454	4.086	5.471	25.70
10	111100	8.449	1.800	2.863	6.752	31.72
11	110011	8.608	2.468	4.094	5.664	26.61
12	111110	9.084	1.734	2.919	7.441	34.96
13	111011	9.893	2.117	3.487	6.835	32.11
14	111111	10.924	1.944	3.170	7.376	34.65

A comparison of all individual earthquake responses of the 6-storey structures for the three respective analysis cases (DU, A_g, F) proves a reduction of all three response criteria in the range of 10–30 %, achieved through the respective decrease of the isolation stiffness and increase of the -damping coefficient, Fig. 11. In particular, in MDOF-systems with three isolation levels, the 12SL468 isolation system leads compared to the RL700 isolation system, to a response parameters reduction of on average approximately 20–30 %. In three other cases (structures with 1, 4, 5-isolation levels) the 12SL468 isolation system reduces further the maximum

Table 5 Isolated 6-storey structure's stiffness [N/m]

A/A	ISC	1-Isolation level	2-Isolation levels	3-Isolation levels	4-Isolation levels	5-Isolation levels	6-Isolation levels
Isolation System RL700							
1	000000						
2	100000	5.2E+08					
3	010000	4.4E+08					
4	001000	3.5E+08					
5	000100	2.7E+08					
6	110000	5.4E+08	4.4E+08				
7	001001	3.7E+08	1.0E+08				
8	000011	2.0E+08	1.0E+08				
9	111000	5.6E+08	4.5E+08	3.5E+08			
10	101010	5.6E+08	3.7E+08	1.9E+08			
11	111100	5.7E+08	4.7E+08	3.7E+08	2.7E+08		
12	110011	5.7E+08	4.7E+08	2.0E+08	1.0E+08		
13	111110	5.9E+08	4.9E+08	3.9E+08	2.9E+08	1.9E+08	
14	111011	5.9E+08	4.9E+08	3.9E+08	2.0E+08	1.0E+08	
15	111111	6.1E+08	5.1E+08	4.0E+08	3.0E+08	2.0E+08	1.0E+08
Isolation System 12SL468							
1	000000						
2	100000	4.6E+08					
3	000100	2.4E+08					
4	110000	4.7E+08	3.8E+08				
5	001100	3.2E+08	2.4E+08				
6	010001	4.0E+08	8.8E+07				
7	000110	2.5E+08	1.6E+08				
8	111000	4.9E+08	4.0E+08	3.1E+08			
9	100110	4.9E+08	2.5E+08	1.6E+08			
10	111100	5.0E+08	4.1E+08	3.2E+08	2.4E+08		
11	110011	5.0E+08	4.1E+08	1.8E+08	8.8E+07		
12	111110	5.2E+08	4.3E+08	3.4E+08	2.5E+08	1.6E+08	
13	111011	5.2E+08	4.3E+08	3.4E+08	1.8E+08	8.8E+07	
14	111111	5.3E+08	4.4E+08	3.5E+08	2.7E+08	1.8E+08	8.8E+07

accelerations. By having more than three isolation levels, the lower stiffness and higher damping coefficient of the isolators influence increasingly higher the inter-storey deflections (for the cases with 4 and 5-isolation levels), but less the shear forces of the systems (for the cases with 4, 5 and 6-isolation levels).

Table 6 Isolated 6-storey structure's damping [Ns/m]

A/A	ISC	1-Isolation level	2-Isolation levels	3-Isolation levels	4-Isolation levels	5-Isolation levels	6-Isolation levels
Isolation System RL700							
1	000000						
2	100000	6.4E+06					
3	010000	5.8E+06					
4	001000	5.2E+06					
5	000100	4.6E+06					
6	110000	6.6E+06	5.8E+06				
7	001001	5.4E+06	2.6E+06				
8	000011	4.0E+06	2.6E+06				
9	111000	6.8E+06	6.0E+06	4.9E+06			
10	101010	6.8E+06	5.4E+06	3.5E+06			
11	111100	7.0E+06	6.2E+06	5.1E+06	3.9E+06		
12	110011	7.0E+06	6.2E+06	3.8E+06	2.4E+06		
13	111110	7.2E+06	6.4E+06	5.3E+06	4.1E+06	3.0E+06	
14	111011	7.2E+06	6.4E+06	5.3E+06	3.5E+06	2.2E+06	
15	111111	7.4E+06	6.7E+06	5.5E+06	4.4E+06	3.2E+06	1.9E+06
Isolation System 12SL468							
1	000000						
2	100000	1.3E+07					
3	000100	9.0E+06					
4	110000	1.3E+07	1.2E+07				
5	001100	1.1E+07	8.4E+06				
6	010001	1.2E+07	5.2E+06				
7	000110	9.5E+07	7.0E+07				
8	111000	1.3E+07	1.2E+07	9.7E+06			
9	100110	1.3E+07	9.5E+06	7.0E+06			
10	111100	1.4E+07	1.2E+07	1.0E+07	7.8E+06		
11	110011	1.4E+07	1.2E+07	7.4E+06	4.8E+06		
12	111110	1.4E+07	1.3E+07	1.0E+07	8.2E+06	5.9E+06	
13	111011	1.4E+07	1.3E+07	1.0E+07	6.9E+06	4.3E+06	
14	111111	1.5E+07	1.3E+07	1.1E+07	8.6E+06	6.3E+06	3.9E+06

6 Multi-criteria Analysis

A multi-criteria analysis of the numerical results obtained from the parametric response-studies of the analysis cases has been conducted with the software program Dlab, for all values of the response parameters of the systems (DU, A_g, F). The classification as to each analysis case and response parameter may depend on specific weight coefficients of all criteria applied in the analysis. The weight coefficients have been set, based on a preliminary estimation made by the authors

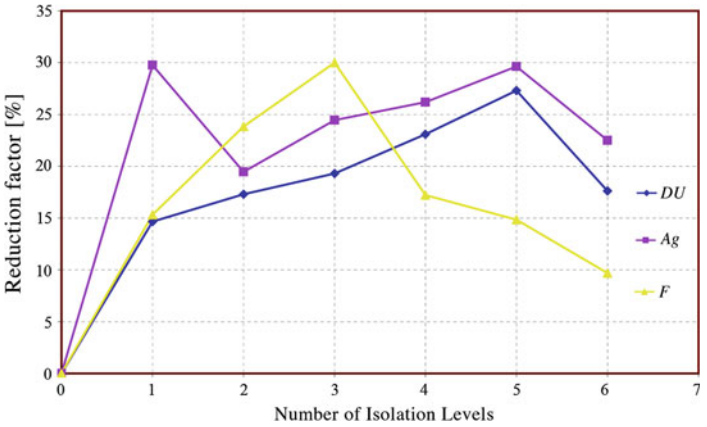

Fig. 11 Earthquake performance of multiple isolated 6-storey structures with the 12SL468- compared to the RL700 isolation system for all maximum responses

Table 7 Classification results of the structural systems seismic performance as derived from the multi-criteria analysis

A/A	RL700	12SL468	A/A	RL 700	12SL 468	A/A	RL 700	12SL 468
1	111000	111000	20	000111	110111	39	111111	010100
2	001101	010110	21	011000	101101	40	010111	011111
3	010110	101010	22	001100	110110	41	100100	010111
4	101100	111010	23	011110	001111	42	010010	111110
5	111001	011100	24	011011	111100	43	010011	000101
6	100110	111001	25	101001	000110	44	000101	000011
7	001110	011110	26	110110	000111	45	100011	100010
8	010101	110011	27	001111	110000	46	100010	100011
9	101010	011101	28	010100	101001	47	001001	010011
10	110101	001101	29	100111	111101	48	000100	001000
11	011100	110101	30	110000	101000	49	010001	001001
12	111010	011011	31	111101	100100	50	000011	010000
13	110011	101011	32	110111	010010	51	001000	000100
14	011101	100110	33	101000	101111	52	100001	010001
15	000110	010101	34	101111	100111	53	010000	100000
16	101011	101100	35	111011	111111	54	100000	100001
17	001010	111011	36	111110	001011	55	000010	000000
18	101101	001010	37	001011	001100	56	000000	000010
19	111100	001110	38	011111	011000	57	000001	000001

with regard to the significance of each criterion; e.g. the shear force in respect to the design of the structural members, the storey accelerations in respect to the safety of the storey equipment, the inter-storey deflections in respect to the maximum relative deformation values of the isolation devices, and the total displacements in respect to the possibility for example of poundings with adjacent buildings.

For providing an evaluation example, based on the results obtained from the time-history analyses of the systems, the weight coefficient for the first analysis case (DU_{max}) is set to 8 %, for the second analysis case ($A_{g,\,max}$), to 28 %, and for the third analysis case (F_{max}), to 64 %. The weight coefficients of the response parameters account to 6 % for U, 12 % for DU, 26 % for A_g and 56 % for F. In the evaluation example, the method PROMETHEE II of the program has been used, a ranking procedure that is based on the determination of the individual criteria and the comparison of the analysis cases in pairs, i.e. outranking approach [18]. The method consists of the complete ranking, whereas a net outranking flow is the balance between the positive and the negative outranking flows. An indicative classification of the structural systems seismic performance is provided in Table 7.

The results obtained from the multi-criteria analysis comply adequately with those of the parametric studies, while the isolation of the first three storeys of the building is to be favored, irrespectively of the isolation system used. Nevertheless, in the specific numerical example, the fixed supported, the base and the single top-storey isolated system alternative are the least favored.

7 Conclusions

The intention of this paper is to extend the approach of base isolation and to investigate the potential effectiveness of multi-storey structures with seismic isolators at different storey-levels. The control concept provides numerous options for the designer in respect to the desired seismic performance of the building. The respective fundamental period increases substantially, even with slight decrease of the displacements. In the parametric studies conducted, the dynamic behaviour of a 6-storey structure has been substantially improved over the fixed supported- and base isolated system, with regard to the inter-storey deflections, the absolute storey accelerations and the base shear force. In particular, main improvements in the response of the isolated 6-storey structures have been observed with three isolation levels over the height. This has been also verified in relative terms, through a multi-criteria analysis, based on the herewith defined weight coefficients of the analysis cases and response parameters. Based on two different isolation systems used in the analyses, the dynamic response of the isolated structures is indeed substantially influenced by the isolation mechanisms characteristics. In contrast to the concept of base isolation, relatively low stiffness values of the respective isolation levels and increased damping act positively on the system's seismic response.

In order to obtain a thorough insight into the characteristics of the dynamic response of the isolated systems, further design variables for the primary structures and the earthquake isolators are to be determined and evaluated in parametric studies. Finally the construction design of the proposed systems is a major influence factor for any application potentials of the concept.

Acknowledgments The research study in the current chapter has been conducted in the frame of the 'OPTARCH' research project.

References

1. Komodromos P, Polycarpou P, Papaloizou L, Phocas MC (2005) Response of seismically isolated buildings considering poundings. Earthq Eng Struct Dyn 36:1605–1622
2. Pocanschi A, Phocas MC (2003) Forces in motion: the technologies of earthquake resistant structural building design. Teubner, Wiesbaden in German
3. Phocas MC, Komodromos P (2006) Multi-storey structures with vertically distributed seismic isolation. In: First European conference on earthquake engineering, Geneva
4. Earl CL, Ryan KL (2006) Effectiveness and feasibility of inter-storey isolation systems. In: Eighth U.S. national conference on earthquake engineering. managing risk in earthquake country, San Francisco, California
5. Mita A, Kaneko M (1994) Vibration control of tall buildings utilizing energy transfer into sub-structural systems. In: First World conference on structural control, Los Angeles, California
6. Ziyaeifar M, Noguchi H (1998) Partial mass isolation in tall buildings. Earthq Eng Struct Dyn 27:49–65
7. Villaverde R (1998) Roof isolation system to reduce the seismic response of buildings: a preliminary assessment. Earthq Spectra 14(3):521–532
8. Villaverde R, Aguirre M, Hamilton C (2005) Aseismic roof isolation system built with steel oval elements: exploratory study. Earthq Spectra 21(1):225–241
9. Pan T-C, Ling S-F, Cui W (1995) Seismic response of segmental buildings. Earthq Eng Struct Dyn 24:1039–1048
10. Pan T-C, Cui W (1998) Response of segmental buildings to random seismic motions. Earthq Technol 35(4):105–112
11. Phocas MC, Pamboris G (2013) Structures with multiple seismic isolation levels. In: Syngellakis S (ed) Seismic control systems. Design and performance assessment. WIT Press, Southampton, pp 77–86
12. Charmpis DC, Komodromos P, Phocas MC (2012) Optimized earthquake response of multi-storey buildings with seismic isolation at various elevations. Earthq Eng Struct Dyn 41 (15):2289–2310
13. Charmpis DC, Phocas MC, Komodromos P (2015) Optimized retrofit of multi-storey buildings using seismic isolation at various elevations: assessment for several earthquake excitations. Bull Earthq Eng 13(9):2745–2768
14. Phocas MC, Pocanschi A (2005) Adaptable earthquake bearings for compact buildings. Eur Earthq Eng XIX 2:40–50
15. Pocanschi A, Phocas MC (2007) adaptable earthquake isolator with progressive nonlinear deformability. Eng Struct 29(10):2586–2592
16. Ambraseys N, Smit P, Berardi R, Rinaldis D, Cotton F, Berge-Thierry C (2000) Dissemination of European strong-motion data. CD-ROM Collection. European Council, Environment and Climate Research Programme, Brussels

17. CYS EN1998-1:2005 Eurocode 8: Design of structures for earthquake resistance. Part 1: General rules, seismic actions and rules for buildings. Eurocodes Committee, Ministry of Interior/Scientific Technical Chamber of Cyprus
18. Brans JP, Mareschal B (2005) PROMETHEE methods. In: Figueira J, Greco S, Ehrgott M (eds) Multiple criteria decisions analysis: state of the art surveys. Springer, Boston, pp 163–196

Integration Step Size and Its Adequate Selection in Analysis of Structural Systems Against Earthquakes

Aram Soroushian

Abstract True behaviour of an arbitrary structural system is dynamic and nonlinear. To analyze this behaviour in many real cases, e.g. structures in regions under high seismic risk, a versatile approach is to discretize the mathematical model in space, and use direct time integration to solve the resulting initial value problem. Besides versatility in application, simplicity of implementation is an advantage of direct time integration, while, inexactness of the response and the high computational cost are the weak points. Considering the sizes of the integration steps as the main parameters of time integration, and concentrating on transient analysis against ground acceleration, this chapter presents discussions on:

(1) the role of integration step size in time integration analysis, specifically, from the points of view of accuracy and computational cost,
(2) conventionally accepted comments, codes/standards' regulations, and some modern methods for assigning adequate values to the integration step sizes in constant or adaptive time integration,

and concludes with some challenges on time integration analysis and integration step size selection in structural dynamics and earthquake engineering.

1 From Structural Analysis to Time Integration

Our lives and civilization rely on different construction we daily pass by. In order to have sustainable buildings, bridges, tunnels, railways, infrastructures, etc., the structures should be designed considering their lifetime behaviour. Even, regardless of the randomness and stochastic nature of severe conditions and the complexity existing in prediction of these conditions, the study of structural behaviour at severe conditions is not simple. Theoretical and experimental approaches can be addressed

A. Soroushian (✉)
Structural Engineering Research Centre, International Institute of Earthquake Engineering and Seismology (IIEES), Tehran, Iran
e-mail: aramsoro@yahoo.com; a.soroushian@iiees.ac.ir

M. Papadrakakis et al. (eds.), *Computational Methods in Earthquake Engineering*, Computational Methods in Applied Sciences 44,
DOI 10.1007/978-3-319-47798-5_10

as means to study the structural behaviour. Nevertheless, mainly with attention to their simplicity, versatility, and inexpensiveness, numerical computations are the widely accepted and generally the superior tool.

With an initiation point in the seventeenth century (i.e. the Hooke's law), analysis of structural systems, as taken into account in the soft ware packages, started less than a century ago, by relating behaviour and excitation, via the structural property, i.e.

$$\mathbf{KX} = \mathbf{F} \tag{1}$$

In Eq. (1), **X** stands for the vector of unknowns, **F** represents the known external information (in general the excitation), and the structural geometry, topology, and material are reflected in **K**. (In time dependent problems, the initial status affects both **K** and **F**, and the solution implies the behaviour at a specific time instant.) In computerized structural analysis, the behaviour is being represented by the unknown general displacement, as the vector **X** in Eq. (1). For structural behaviour not representable by finite number of unknowns, in the mid of the past century, methods (mainly discretization methods) were developed to systematically replace continuous systems, with systems with finite number of unknowns or DOFs (degrees of freedoms). Finite difference, finite volume, finite element, and boundary element methods, are some of the major discretization methods. Development of these methods, specifically the finite elements, and the invention of computers, at 1950s, led to significant rise in the size and complexity of structural systems. For instance, the dependence of **K** and **F** in Eq. (1) to **X** causing nonlinearity could be simply tackled by incremental consideration of **F** and when needed implementation of different definitions for strain and stress. Not much later, attention to time dependent phenomena, including structural behaviour against earthquakes, aerodynamics, etc., increased significantly. In study and analysis of arbitrary structural dynamic behaviour, the inertial force, and even in cases the damping effects, are of high importance. The linear dynamic behaviour of semi-discretized structural systems can be expressed as [1–3]:

$$\begin{aligned} &\mathbf{M}\ddot{\mathbf{u}} + \mathbf{C}\dot{\mathbf{u}} + \mathbf{K}\mathbf{u} = \mathbf{f}(t) \quad 0 \le t < t_{end} \\ &\mathbf{u}(t=0) = \mathbf{u}_0 \\ &\dot{\mathbf{u}}(t=0) = \dot{\mathbf{u}}_0 \end{aligned} \tag{2}$$

where, **M**, **C**, and **K**, respectively denote the mass, damping, and stiffness matrices, **f** stands for the dynamic excitation, each top dot implies once differentiation with respect to time, **u** is the unknown general displacement, t represents the time, $\mathbf{u}_0$ and $\dot{\mathbf{u}}_0$ introduce the initial conditions, and t_{end} is the length of the time interval under consideration. In 1950, the first broadly accepted method to solve Eq. (2), in a step-by-step manner, also addressed as a time integration method, was proposed by J.C. Houbolt [4–6] (see Fig. 1, where $\mathbf{f}_{\text{int}}$ implies the internal force, essential in presence of material nonlinearity and discussed later in this chapter). The history of

step-by-step integration of initial value problems returns to the eighteenth century and the Euler method [7, 8] (see also [9], for the implementation of different Runge Kutta methods in structural dynamics); Houbolt suggested the first method, specifically dedicated to the solution of the equation of motion in structural dynamics [4]. For the Houbolt method, as well as many other time integration methods, the basic idea is to approximate the solution of Eq. (2), with sufficient accuracy, while avoiding complex mathematical functions, e.g. exp, sinh, cosh. The general approach is to carry out the analysis in a step-by-step manner, using simple relations instead of the exact computationally complex relations [10, 11]. The new relations are generally linear algebraic equations, set such that to maintain the adequacy of some mainly accuracy-related features. On this basis, many time integration methods have been proposed in the past decades [4–6, 12–17]; still, investigations for better approximate methods are in progress, in different disciplines and branches of engineering and science; see [18–26]. The most practically important and broadly accepted time integration methods are the Newmark family [1, 9–11, 27–32], central difference [1, 9–11, 14, 28–32], Wilson-Theta [9, 10, 15–17, 32], Houbolt [4–6], HHT [12, 30–32] and C-H [13] methods. All these methods convert Eq. (2) to (see also Eq. (1)):

$$\mathbf{K}_{eff}\mathbf{u} = \mathbf{f}_{eff} \tag{3}$$

or equivalently to the equation below:

$$\bar{\mathbf{K}}_{eff}\Delta\mathbf{u} = \Delta\mathbf{f}_{eff} \tag{4}$$

(considering the dynamic effect in $\mathbf{K}_{eff}$, $\mathbf{f}_{eff}$, $\bar{\mathbf{K}}_{eff}$, and $\Delta\mathbf{f}_{eff}$), to be solved for the status $(\mathbf{u}, \dot{\mathbf{u}}, \ddot{\mathbf{u}}, \ldots \text{and } \mathbf{f}_{\text{int}})$ at sequential integration stations, starting from the initial conditions; see Fig. 1. ($\Delta\mathbf{u}$ and $\Delta\mathbf{f}_{eff}$ respectively represent the increment or to say better the increase of $\mathbf{u}$ and $\mathbf{f}_{eff}$ from the previous integration station to the current integration station.) Equation (4) can be treated in a way conceptually identical to Eq. (1). However, because of the approximation existing in the time integration formulation, the results are inexact depending on the integration formulation. This, plus the versatility of time integration analysis, has caused broad and continuous studies on time integration e.g. see [19–26, 33–38]. In the next section, after a brief review on time integration analysis, the parameters, and specifically the most important parameter, i.e. the integration step size, are discussed. In Sect. 3, the influence of the integration step size, on different features of time integration, is studied. In Sects. 4 and 5, conventional and modern comments and approaches to assign adequate values to the integration step size are addressed. Later, in Sects. 6 and 7, techniques for more efficient analysis against digitized excitations are reviewed, and the seemingly most successful technique is introduced in detail. Finally, the chapter is concluded, in Sect. 8, with a brief look on the key points, and addressing some of the challenges existing on time integration and step size selection.

2 Time Integration and Its Parameters

As implied in Sect. 1, time integration is the most versatile tool to analyze Eq. (2) and its nonlinear counterpart, stated below [31]:

$$\begin{aligned} &\mathbf{M}\ddot{\mathbf{u}} + \mathbf{f}_{\text{int}} = \mathbf{f}(t) \quad 0 \le t < t_{end} \\ &\mathbf{u}(t=0) = \mathbf{u}_0 \\ &\dot{\mathbf{u}}(t=0) = \dot{\mathbf{u}}_0 \\ &\mathbf{f}_{\text{int}}(t=0) = \mathbf{f}_{\text{int}_0} \\ &\mathbf{Q} \end{aligned} \tag{5}$$

In Eqs. (5), the new parameter, **Q**, implies additional restrictions representing the nonlinear behaviour (see [39, 40]), and the essentiality of $\mathbf{f}_{\text{int}}$, as an initial condition, is explained in [41, 42]. In the analysis process, the status or indeed the responses, i.e. $\mathbf{u}, \dot{\mathbf{u}}, \ddot{\mathbf{u}}, \ldots$ and $\mathbf{f}_{\text{int}}$ are being computed, for distinct sequential time instants, starting from the station just after the initial conditions, using simple algebraic formulation (see Fig. 1). No eigen-solution is essential in ordinary direct time integration analysis. The determination of the status proceeds, in a step-by-step manner, and at each time instant, the status of the structural system is being determined approximately [10, 28, 31, 32]. In nonlinear analyses, after the computation associated with each step, occurrence of nonlinearity is being checked. When a nonlinearity is detected, some iterations are generally implemented (see Fig. 1), by methods such as Newton Raphson, to decrease the error in modelling the nonlinearity (see [1, 2, 43–46]). The

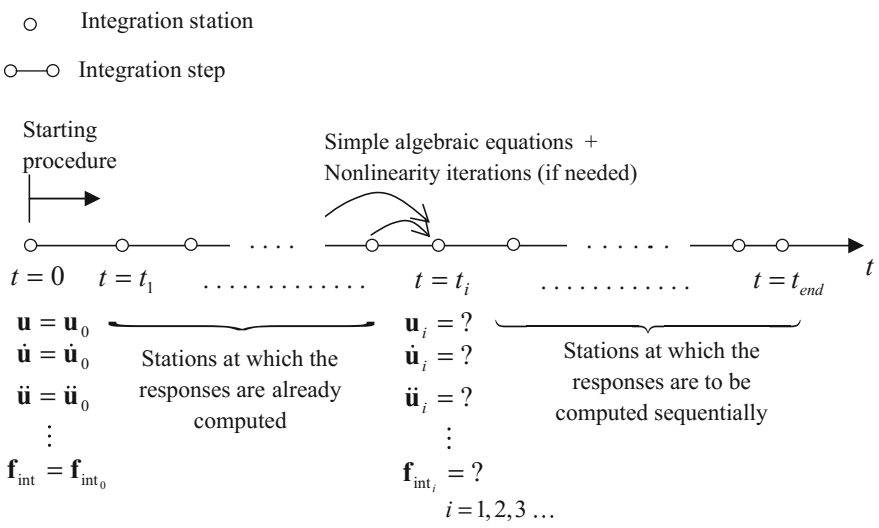

Fig. 1 Typical process of time integration analysis

step-by-step procedure continues, till the end of the integration interval, t_{end}. Considering these, time integration is a simple step-by-step computational tool. The simplicity of the step-by-step computation and the algebraic formulation bring about positive and negative consequences; some are listed below [31, 32]:

1. Approximation in the obtained responses.
2. Versatility of application to different equations of motion, and even to initial value problems originated in other branches of engineering and science, e.g. see [13, 19–23, 26, 34–37].
3. Existence of many different time integration methods, e.g. see [1, 11, 12, 14–17, 24–34, 47, 48].
4. Considerably high computational cost [31, 32, 49].

The negative features are the approximation and the high computational cost (respectively the first and forth points above). Especially the first is very important; without sufficient accuracy, implementation of time integration analysis loses its explanation. Provided acceptable accuracy, we are interested in: (1) low computational cost, where computational cost implies the in-core storage of the hardware involved in the computation [50, 51], and (2) the capability to increase the accuracy and/or decrease the computational cost. Other features of time integration analysis are also directly or indirectly associated with the inexactness of the response; numerical stability, order of accuracy, numerical damping, and overshoot, are the most important features [31–33, 52]. These features are under the control of some parameters, to which, the remainder of this section is dedicated.

In exact computations, the parameters affecting the results imply real notions. For instance, in the computation of the integral below:

$$I = \int_a^b \frac{dx}{1+x^2} = \arctan\, b - \arctan\, a \tag{6}$$

a and b are parameters with real meaning (see Fig. 2), appearing in the definition of the problem, as well as, in its exact solution; see the ending part of Eq. (6). Similarly, when using the analytical relations below [53, 54]:

$$\begin{aligned} R_A &= \tfrac{W}{l^3}(l-a)^2(l+2a), \quad & R_B &= \tfrac{Wa^2}{l^3}(3l-2a) \\ M_A &= \tfrac{-Wa}{l^2}(l-a)^2, & M_B &= \tfrac{-Wa^2}{l^2}(l-a) \end{aligned} \tag{7}$$

for determining the end moments and end shears of the beam in Fig. 3, l, a, and W, are real parameters, defining the problem and its exact solution. Returning to time integration and Eqs. (2) and (5), the initial conditions, the mass, the damping, the stiffness, the excitations, the parameters defining the nonlinear behaviour (implied specifically in Q in Eqs. (5)), and finally the t_{end}, are the real parameters.

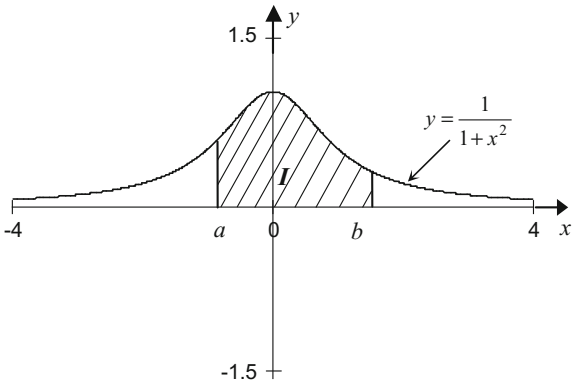

Fig. 2 An illustration of Eq. (6)

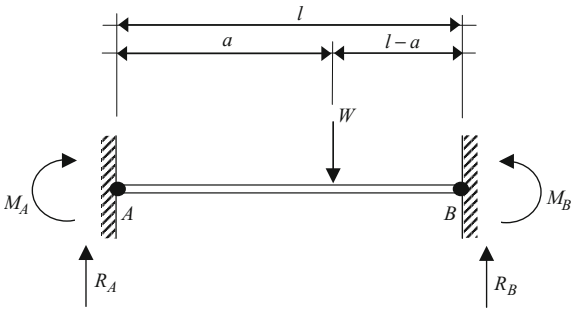

Fig. 3 A fixed-fixed two dimensional beam

There are many problems, for which, analytical solutions are either not derived (yet unavailable) or the analytical solutions are mathematically/numerically complicated, e.g. problems with analytical solutions in terms of special infinite series. To solve these problems, numerical approximate computation is the broadly accepted tool [7, 8, 55]. In approximate computations, besides real parameters, there exist parameters, essential (and even crucial) for the computation, that have no real meaning and no role in the definition of the problem and the exact solution; see [55, 56]. For instance, when using Simpson or Trapezoidal integration, for determining the value of I in Eq. (6), as apparent in the relations below [57, 58]:

$$\begin{aligned} \text{Simpson:} \quad & I = \frac{h}{6}\left\{ y_0 - y_N + 2\sum_{i=1}^{N}\left(2y\left(\frac{x_i + x_{i-1}}{2}\right) + y_i\right)\right\} \\ \text{Trapezoidal:} \quad & I = \frac{h}{2}\left\{ y_0 - y_N + 2\sum_{i=1}^{N} y_i \right\} \\ & h = \frac{b-a}{N} \quad , \quad y_i = y(x_i) = \frac{1}{1+{x_i}^2} \end{aligned} \tag{8}$$

the total number of integration steps, N, or equivalently the integration step size, h, is an additional parameter. Although the division of the integration interval to integration steps can be displayed in Fig. 2, the number of the divisions, N, and the integration step size, h, are not real parameters of the problem, and do not affect the exact solution. These parameters, having main role in the computation and no role in the definition of the problems and their exact solutions, are generally addressed as analysis or algorithmic parameters [55, 56]. It is meanwhile worth noting that it is conventional to define/redefine the algorithmic parameters, such that convergence [59, 60] of the approximate solutions to the exact solutions can be studied in the neighbourhood of zero values of the algorithmic parameter [49, 55, 56, 61]. As implied above, in the numerical integrations addressed in Eq. (8), h (or N) is the algorithmic parameter. In static analysis of the beam in Fig. 3 by specific finite elements, the size or number of the elements is a parameter, defining the computation and its accuracy [1, 30]. Accordingly, considering the basics of finite elements [1, 2], we can address the element size as the algorithmic parameter.

In time integration analysis, the main analysis (algorithmic) parameters are the sizes of integration steps throughout the integration interval; considered either constantly (as one parameter) or adaptively (according to a specific criterion). It is a broad convention to consider the integration time step Δt as a parameter linearly controlling the sizes of integration steps throughout the integration interval [49]. In view of Eqs. (2) or (5), and Fig. 1, Δt is a parameter, with no effect on the exact solution, but main role in the time integration analysis. For nonlinear problems, there exist algorithmic parameters, in addition to Δt, affecting the features of the analysis, again independent from the problem and its exact response. These parameters are:

1. Nonlinearity continuation method and the special parameters to be set for implementation of the nonlinearity iterations [1, 2, 44–46, 62–64].
2. Nonlinearity tolerance [1, 44–46, 63, 64], $\bar{\delta}$, as an indicator for the accuracy of nonlinearity iterations.
3. Maximum number of iterations (e.g. see [63–65]), as a representative for the computational facilities available, essential with attention to the always-existing round-off.

We would rather address the above parameters as nonlinearity analysis or nonlinearity algorithmic parameters. (Practically, the second parameter, i.e. $\bar{\delta}$, is the most important parameter.) Besides Δt and nonlinearity analysis parameters, parameters precisely defining the integration method are of the algorithmic parameters of time integration and can be addressed as method algorithmic parameters. These parameters do not exist for all time integration methods. For instance, equations governing the one-step Houbolt method [4–6], stated below:

$$
\begin{aligned}
&\mathbf{M}\ddot{\mathbf{u}}_i + \mathbf{f}_{\text{int}_i} = \mathbf{f}_i \\
&\mathbf{u}_i = \mathbf{q}_0 + b_0\,\dddot{\Delta\mathbf{u}}_{i-1} \\
&\dot{\mathbf{u}}_i = \mathbf{q}_1 + b_1\,\dddot{\Delta\mathbf{u}}_{i-1} \\
&\ddot{\mathbf{u}}_i = \mathbf{q}_2 + b_2\,\dddot{\Delta\mathbf{u}}_{i-1} \\
&\dddot{\mathbf{u}}_i = \mathbf{q}_3 + b_3\,\dddot{\Delta\mathbf{u}}_{i-1} \\
&\mathbf{q}_0 = \mathbf{u}_{i-1} + \dot{\mathbf{u}}_{i-1}\Delta t + \frac{1}{2}\ddot{\mathbf{u}}_{i-1}\Delta t^2 + \frac{1}{6}\dddot{\mathbf{u}}_{i-1}\Delta t^3 \\
&\mathbf{q}_1 = \dot{\mathbf{u}}_{i-1} + \ddot{\mathbf{u}}_{i-1}\Delta t + \dddot{\mathbf{u}}_{i-1}\frac{\Delta t^2}{2} \\
&\mathbf{q}_2 = \ddot{\mathbf{u}}_{i-1} + \dddot{\mathbf{u}}_{i-1}\Delta t \\
&\mathbf{q}_3 = \dddot{\mathbf{u}}_{i-1} \\
&b_0 = \Delta t^3, \quad b_1 = \frac{11}{6}\Delta t^2, \quad b_2 = 2\Delta t, \quad b_3 = 1, \qquad i = 1, 2, 3, \ldots
\end{aligned}
\tag{9}
$$

are not parametric (for $\dddot{\mathbf{u}}_0$, see [6]), while, the relations defining the HHT method [12, 30–32], stated below:

$$
\begin{aligned}
&\mathbf{M}\ddot{\mathbf{u}}_i + ((1+\alpha)\mathbf{f}_{\text{int}_i} - \alpha\,\mathbf{f}_{\text{int}_{i-1}}) = ((1+\alpha)\mathbf{f}_i - \alpha\,\mathbf{f}_{i-1}) \\
&\dot{\mathbf{u}}_i = \dot{\mathbf{u}}_{i-1} + \Delta t((1-\gamma)\ddot{\mathbf{u}}_{i-1} + \gamma\ddot{\mathbf{u}}_i) \\
&\mathbf{u}_i = \mathbf{u}_{i-1} + \Delta t\,\dot{\mathbf{u}}_{i-1} + \Delta t^2\left(\left(\frac{1}{2} - \beta\right)\ddot{\mathbf{u}}_{i-1} + \beta\,\ddot{\mathbf{u}}_i\right), \qquad i = 1, 2, 3, \ldots
\end{aligned}
\tag{10}
$$

depend on α, β, and γ, and hence, α, β, and γ are the method parameters of the HHT time integration method, precisely defining the integration method, and highly affecting the approximate response, with no effect on Eqs. (2) or (5) and the exact response. (Inequality restrictions on these parameters, for issues such as numerical stability (e.g. see [30, 31]), do not reduce the number of these parameters.) Consequently, time integration analysis, according to a specific time integration method, while implementing a specific nonlinearity continuation method [44], potentially depends on three groups of analysis parameters:

1. The main analysis parameter: Δt (or parameters defining the sizes of integration steps in adaptive time integration; see [66]).
2. Nonlinearity analysis parameter: $\bar{\delta}$ and some less important parameters, e.g. maximum number of nonlinearity iterations.
3. Method analysis parameters: parameters completing the definition of the integration methods.

From the above parameters, the main parameters, controlling different features of the analyses (specifically the computational cost and accuracy-related features, e.g. numerical stability), are Δt and $\bar{\delta}$ (shortly disregarding the method parameters).

With regard to accuracy, since implementation of an approximate method implies that the exact solution is at least not simply available, the accuracy instead of being studied in view of the definition of error, E [67], i.e.

$$E = \|\mathbf{U}^a - \mathbf{U}\| \tag{11}$$

(a as a right superscript implies that the argument is an approximation and $\|\|$ denotes an arbitrary norm [68]) needs to be evaluated indirectly, in terms of convergence [1, 7, 30–32, 56, 59–61, 67], i.e.

$$\lim_{\Delta t \to 0} E = 0 \quad \equiv \quad \lim_{\Delta t \to 0} \mathbf{U}^a = \mathbf{U} \tag{12}$$

For an arbitrary time integration analysis, Eq. (12) is theoretically equivalent to Figs. 4, as well as Fig. 5. E_i stands for the error of the response $\mathbf{U}_i^a$, obtained from time integration analysis with step sizes equal to Δt_i, L and L' denote the length of the region in the two plots implying decrease of error with positive integer slopes (not precisely defined and determinable yet), and D_i, is defined below:

$$D_i = \frac{\left\|\mathbf{U}_i^a - \mathbf{U}_{i-1}^a\right\|}{\left(\frac{\Delta t_{i-1}}{\Delta t_i}\right)^q - 1} \tag{13}$$

and addressed as pseudo-error [69, 70]. For many problems, the convergence of D_i to zero is equivalent to Eq. (12). Similarly, Figs. 4 and 5 are equivalent in the sense that either both E_i and D_i imply convergence to zero or neither do so. Furthermore,

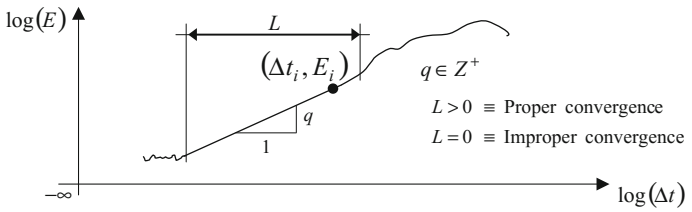

Fig. 4 Typical changes of errors for converging approximate solutions

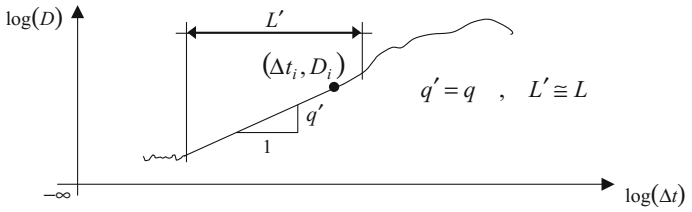

Fig. 5 A substitute for the study of convergence via Fig. 4

either the convergence trends in both convergence and pseudo convergence plots (displayed in Figs. 4 and 5, respectively) are as straight lines (with positive integer slopes towards zero errors/pseudo-errors at zero Δt) or neither display such a convergence trend. Even more, when both of the trends are as lines with positive integer slopes, the slopes in the two plots are identical and equal to the order of accuracy (in cases, less than the order of accuracy [32, 49, 71]); see [55, 69, 70]. In Eq. (13), q is a positive integer, introducing the rate of convergence (see Figs. 4 and 5), and $\mathbf{U}_{i-1}^{a}$ and $\mathbf{U}_{i}^{a}$ are named such that $\Delta t_{i-1} > \Delta t_i > 0$; see [70]. In nonlinear analyses, for maintaining Fig. 4 (with $L > 0$) and specifically to ensure the equivalence between Figs. 4 and 5 and Eqs. (12), or even the validity of

$$\lim_{\substack{\Delta t \to 0 \\ \bar{\delta} \to 0}} E = 0 \quad \equiv \quad \lim_{\substack{\Delta t \to 0 \\ \bar{\delta} \to 0}} \mathbf{U}^{a} = \mathbf{U} \tag{14}$$

we can assign very small values (depending on the problem), or values consistent with Δt, to $\bar{\delta}$ [2, 42, 63, 72].

And regarding computational cost, in analysis of a specific linear problem, by a specific time integration method, and on a specific computer, the computational cost depends on the total number of integration steps; and since t_{end} is a constant value known in advance, the computational cost increases when Δt decreases. This implies a contradiction with the accuracy, for which, it is beneficial to assign smaller values to Δt (while larger values of Δt are beneficial for computational cost). Considering this and the fact that different from $\bar{\delta}$, Δt affects both linear and nonlinear analyses, the remainder of this chapter is dedicated to Δt and the approaches to select Δt (see also [72, 73]).

3 Integration Step Size and Its Influence on Analysis Quality

As the major algorithmic parameter of time integration, the integration step size or Δt affects almost all features of arbitrary linear or nonlinear time integration analysis. The features under study in this section are accuracy, convergence, order of accuracy, stability, artificial damping, overshoot, and computational cost.

You can generally increase the accuracy, by reducing the integration step size. "Smaller integration steps lead to more accuracy" is a practically general rule (see Fig. 6 and Tables 1 and 2), with the potential to be obviated in analysis of nonlinear or complex behaviours (see Figs. 7 and Tables 3; the units are all in S.I. and each dash-dot-dash centreline, marked with CL, is associated with one mass). The nonlinear structural model is set such that the exact solution can be simply derived; see Fig. 8 [63]. Disagreement with the above-mentioned general rule corresponds to $L = 0$, in Figs. 4 and 5. Meanwhile, Tables 2 and 3 evidence that the amount of error depends also on the response under consideration. In analysis of nonlinear

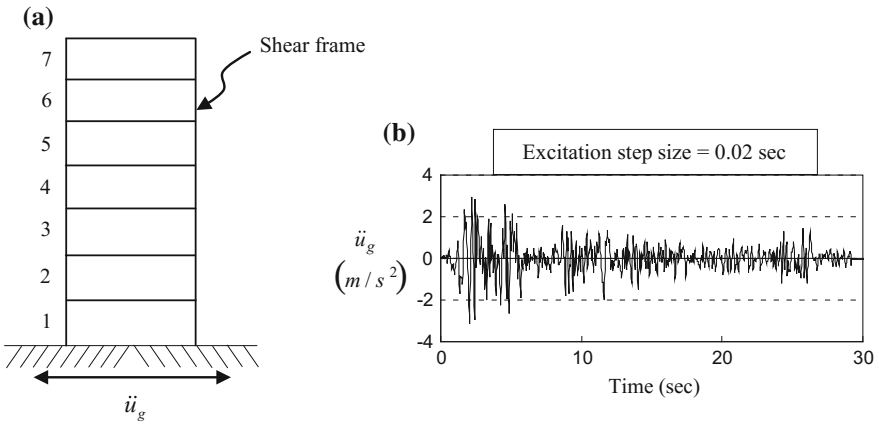

Fig. 6 An example to display the general rule of less error in analysis with smaller integration step: **a** structural system, **b** ground acceleration

Table 1 Characteristics of the undamped structural system introduced in Fig. 6

Floor	1	2	3	4	5	6	7
Mass (ton)	2068	2064	2060	2056	2052	2048	2044
Stiffness (MN/m)	840	820	700	680	660	640	620

Table 2 Changes of error with respect to step size in average acceleration time integration analysis [27] of the system introduced in Fig. 6 and Table 1

Δt (s)		0.02	0.01	0.005	0.0025	0.00125	0.000625
E (%)	Top displacement (L_2 norm)	23.5	6.89	1.99	0.508	0.127	0.0319
	Maximum mid-height drift	6.16	1.83	0.153	0.095	0.0141	0.0029
	Final base shear	107	94.2	43.3	6.93	2.04	0.51

structural dynamic systems, the details of the iterative nonlinearity analysis can significantly affect the accuracy as well as the changes of accuracy with respect to the integration step size; see [63, 72–78]. No general rule seems to exist for the changes of Δt and $\bar{\delta}$, or other analysis parameters (addressed in Sect. 2), guaranteeing more accuracy for arbitrary nonlinear or complex analysis; some comments exist, for piece-wisely linear systems, e.g. see [42, 63]. (Accordingly, the responses computed for nonlinear problems or problems with complex behaviour are in general unreliable [42, 63, 72–80].)

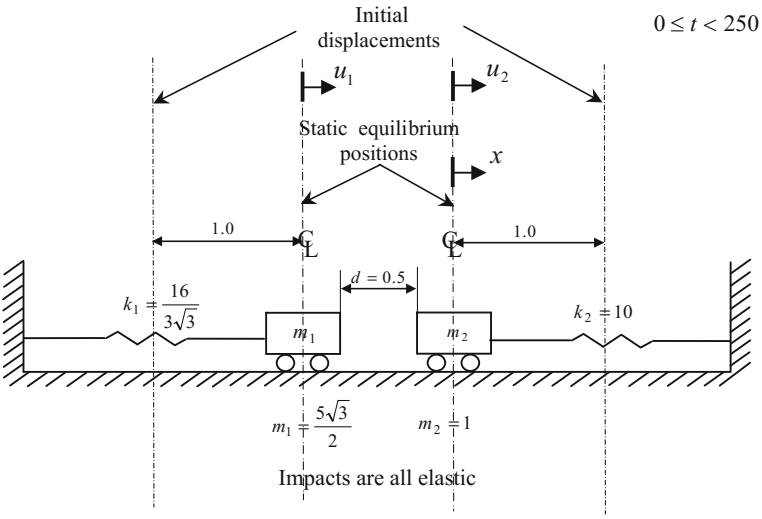

Fig. 7 An example to display the possibility of more error in time integration analysis with smaller integration step [63]

Table 3 Changes of error with respect to the step size in average acceleration analysis [27] of the system introduced in Fig. 7, where, the continuation method is fractional time stepping [62, 65], $\bar{\delta} = 10^{-2}$, and 0.1 and 5 are the scaling factor and maximum number of iterations

Δt (s)		$\frac{1}{80}$	$\frac{1}{160}$	$\frac{1}{320}$	$\frac{1}{640}$	$\frac{1}{1280}$	$\frac{1}{2560}$
E (%)	Force in the left spring (L_∞ norm)	7.17	4.83	6.15	6.15	3.49	2.85
	Maximum velocity of the centre of mass	0.0539	0.568	0.744	0.744	0.443	0.317
	Final spaces between Mass 1 and Mass 2	121	26.8	2.70	2.70	1.92	1.37

Regarding convergence and order of accuracy, in view of the Lax-Richtmyer equivalence theorem [59, 60, 81], for well-posed problems [31, 32, 81] (including almost all real engineering problems), convergence is equivalent to consistency plus numerical stability. Consistency implies that the order of accuracy is not less than one [31, 32], and order of accuracy of a time integration method is the highest rate, by which, the responses computed by the integration method converge to the exact response; see also [7, 31, 32, 49, 56], equivalently definable in terms of local truncation errors [31, 32]. Numerical stability can be defined as the capability of time integration methods to lead to responses (for physically stable problems [82])

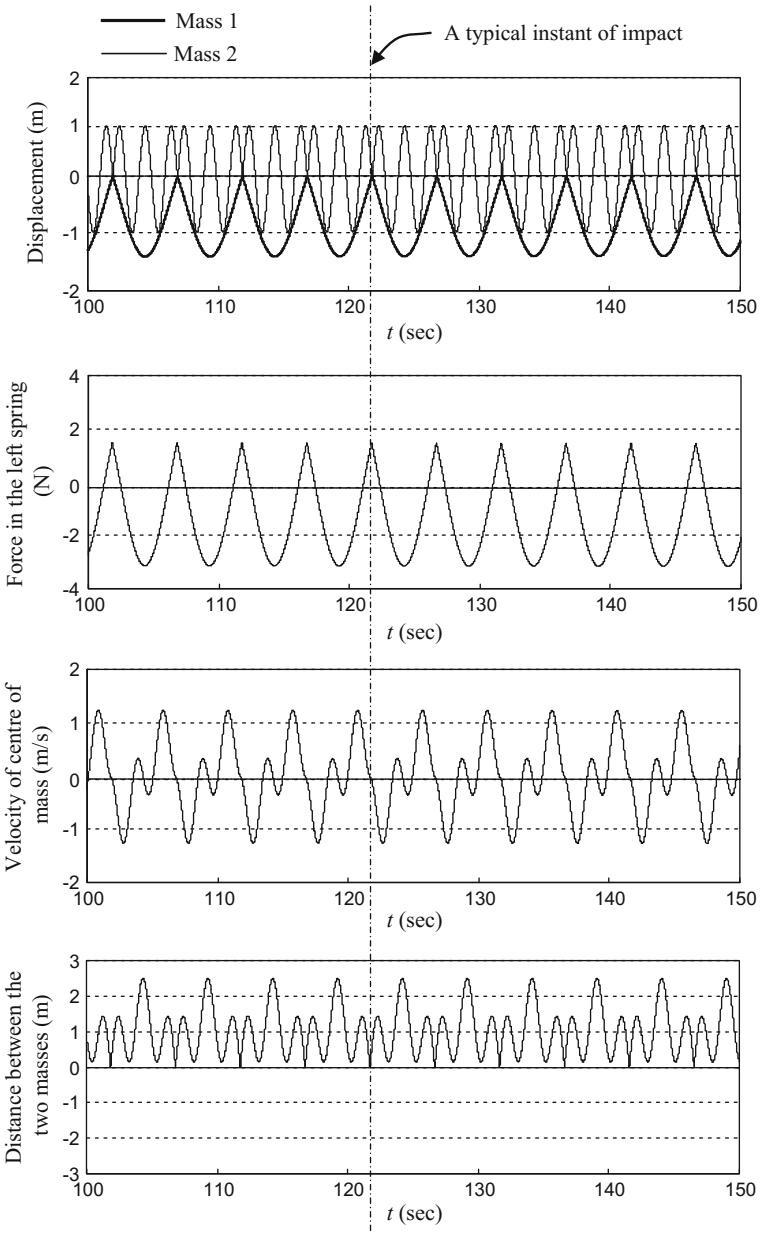

Fig. 8 Mid 50s of the exact response for the system introduced in Fig. 7

that do not diverge, even after arbitrary large number of integration steps [1, 30–33, 52, 59, 60, 81, 83]. Therefore, it is reasonable to expect the convergence to be influenced, from Δt, via numerical stability and order of accuracy.

Taking into account terms like "conditionally stable", the effect of Δt on numerical stability might be crucial [1, 10, 11, 28–33, 52]. By concentrating on one-step time integration methods (recommended in the literature [30–32]), for SDOF (Single-Degree-Of-Freedom) systems, the free vibration time integration computation, can be expressed, as stated below (multi-step methods can in many cases be rewritten as one-step methods, e.g. central difference and Houbolt methods [4–6, 32]):

$$\begin{bmatrix} u \\ \dot{u}\,\Delta t \\ \ddot{u}\,\Delta t^2 \\ \vdots \\ u^{(\alpha)}\,\Delta t^{\alpha} \end{bmatrix}_i = \mathbf{A} \begin{bmatrix} u \\ \dot{u}\,\Delta t \\ \ddot{u}\,\Delta t^2 \\ \vdots \\ u^{(\alpha)}\,\Delta t^{\alpha} \end{bmatrix}_{i-1}, \quad i = 1, 2, 3\ldots \tag{15}$$

where, α implies the highest order of time differentiation in the one-step integration, e.g. $\alpha = 3$ for the one-step Houbolt method [4–6], and $\alpha = 2$ for the HHT method [12, 30–32, 84], the right subscripts represent the same subscript for u, the temporal derivatives of u, and Δt, inside the brackets, i denotes the number of the integration step under study, and $\mathbf{A}$ is the amplification matrix, with members depending on the natural angular frequency, ω, the integration step size Δt_i, and the coefficient of viscous damping ξ [31, 32], i.e.

$$\mathbf{A} = \left[A_{j,k}(\omega, \xi, \Delta t_i)\right] \tag{16}$$

Numerical stability is provided, when the spectral radius [68] of $\mathbf{A}$, is not more than one throughout the analysis, i.e.

$$\rho = \mathrm{Max}(|\lambda_1|, |\lambda_2|, \ldots |\lambda_\alpha|) \not> 1 \tag{17}$$

In Eq. (17), ρ stands for the spectral radius, and $\lambda_{i=1,2,\ldots\alpha}$ implies the i th eigen-value of $\mathbf{A}$ (a real or complex number [57]). In more detail, for numerical stability, the absolute values of the eigen-values of $\mathbf{A}$ are to be less than one, when with multiplicity more than one, and less than or equal to one, when not repeated [29–33, 52]. The discussion is valid for forced vibrations and MDOF (Multi-Degree-Of-Freedom) systems, when considering all natural modes separately [1, 29–32]. In practice, it is conventional to study numerical stability, based on the changes of spectral radius, with respect to $\omega\,\Delta t$ (where, ω and Δt respectively imply an arbitrary natural frequency of the structural system and the constant step size in the analysis), preferably for different values of ξ; see [29–33, 52, 57] and Fig. 9. In Fig. 9, T stands for arbitrary natural period of the MDOF system, $T = 2\pi\omega^{-1}$ [31–33, 52], and the steps sizes are considered constant throughout the integration interval. (For non-proportionally damped MDOF systems, Eq. (15) can be considered directly for the whole MDOF system based on which the remainder of the discussion remains unchanged; see [84]). Consequently, $\rho < 1$ or $\rho \leq 1$ is necessary and sufficient for the stability of linear analyses, and is necessary for the stability of nonlinear time integration analyses; see [33, 63, 72]. The outcome restricts $\omega\,\Delta t$, generally leading to:

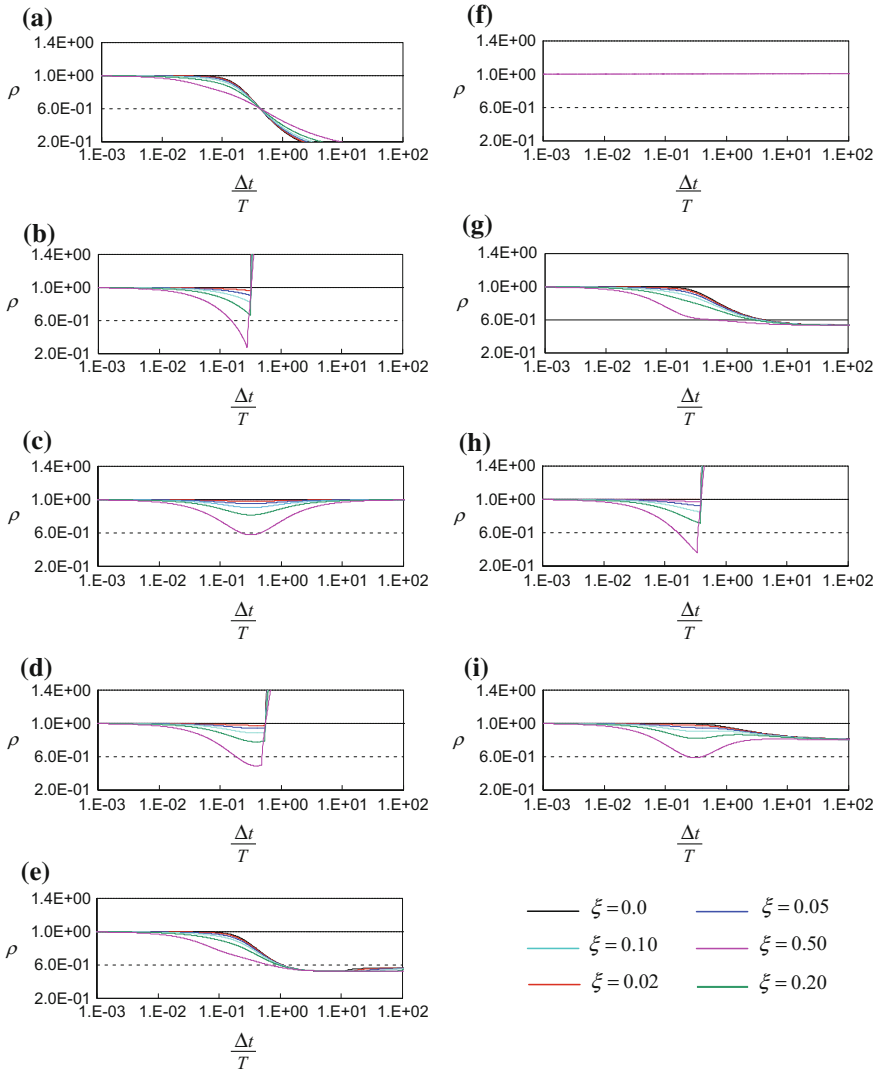

Fig. 9 Changes of spectral radius with respect to $\frac{\Delta t}{T}$ for several time integration methods: **a** Houbolt [4–6], **b** Central difference [14], **c** Average acceleration [27], **d** Linear acceleration [10, 27], **e** Wilson-θ [15–17] ($\theta = 1.42$), **f** Quasi-Wilson-θ [24] ($\theta = 1.5$), **g** HHT [12] ($\alpha = -0.3$), **h** Fox-Goodwin [85], **i** C–H [13] ($\rho_\infty = 0.8$)

$$\Delta t < \Delta t_{cr}(\omega, \xi) \quad \text{or} \quad \Delta t \leq \Delta t_{cr}(\omega, \xi) \tag{18}$$

where, Δt_{cr} stands for the integration step size corresponding to $\rho = 1$; see Fig. 9b, d, h. In view of the Lax-Richtmyer equivalence theorem [32, 59, 60, 81, 86, 87], Eq. (18) needs to be satisfied, in order to maintain responses stability and

convergence. Accordingly, unconditional stability (for linear analyses) is recommended by times [30–33, 52] and many conventional time integration methods are unconditionally stable, i.e.

$$\forall \omega,\ \forall \xi: \quad \Delta t_{cr} \to \infty \tag{19}$$

Consequently, and as displayed in Eq. (18) and Fig. 9, the effect of integration step size, on numerical stability, can be described as that, the smaller the integration step size, the more the analysis has the chance to be numerically stable. In view of the Lax-Richtmyer equivalence theorem [32, 59, 60, 81, 86, 87], and since order of accuracy is a constant value computable theoretically independent from the integration step size [32, 60], a similar claim sounds reasonable, for the influence of integration step size on convergence. Nevertheless, with attention to the inequality sign in Eq. (18) and the definition of convergence in Eqs. (12) and (14), convergence is independent from Δt, unless when $\Delta t_{cr} = 0$, i.e. the unconditionally unstable condition. The trend of convergence however depends on Δt; see Figs. 4 and 5 and the Taylor series [57] correspondence between convergence and these figures [30–32, 55]. From the standpoint of Lax-Richtmyer equivalence theorem, the above-mentioned different effects of Δt on convergence and numerical stability, while order of accuracy is not under the effect of Δt may cause questions. To avoid ambiguities, it is worth noting that in numerical determination of the order of accuracy [84], we need to carry out the time integration analyses with steps smaller than Δt_{cr}. (Sufficient smallness of Δt is also implied in the theoretical computation of the order of accuracy [32, 60].) Meanwhile, though order of accuracy is conceptually independent from numerical stability, restrictions exist that relate order of accuracy and numerical stability, depending on the number of steps involved in the computation for each new station, e.g. Dalquist Barriers [32].

Models resulted from discretization in space, by methods, such as finite elements, are different from the original continuous models, specifically in the higher modes of oscillation [30–32, 88]. To say better, though the piece-wise exact analyses [10, 11] can lead to exact responses for Eq. (2), the so-called exact responses are different from the exact responses of the PDE (Partial Differential Equation) models prior to the semi-discretization. The difference can be considerable in the higher modes of oscillations. A way to omit or reduce the errors is to somehow eliminate the higher modes with trivial contribution in the response, and time integrate the lower modes with sufficient accuracy. An assumption in this approach is the existence of higher modes with trivial contribution in the response; this is a valid assumption at least in many real structural systems [10, 31, 32, 89–91]. Numerical or artificial damping is the capability of some time integration methods, in controlling the errors of semi-discretization [1, 11, 28–33, 52]. Artificial damping provides the capability to eliminate the higher modes and analyze the lower modes with sufficient accuracy (in direct time integration of the total structural system). Time step size affects artificial damping. If, in view of the modal description of linear proportionally damped MDOF systems, we concentrate on an arbitrary SDOF system, the amplitude of the plot of the spectral radius of $\mathbf{A}$, i.e. ρ,

with respect to $\omega \Delta t$ (or equivalently $\frac{\Delta t}{T}$), inversely represents the capability to damp out the higher modes (see Fig. 9) [30–32]. In more detail, when $\rho < 1$, smaller values of ρ imply more elimination of the higher frequency oscillations [29–31] ($\rho = 0$ implies complete elimination). The general trend displayed in Fig. 9, and the presented explanation, regarding the more elimination at larger values of $\omega \Delta t$, are valid for MDOF and SDOF linear systems, considering the modes under consideration (and the corresponding values of ω or T), separately. However, the numerical details are different for different time integration methods and different values of viscous damping, and meanwhile, are differently desired for different behaviours with different contributions of higher modes of oscillation [30–33, 52]. With these considerations, and specifically, from Fig. 9, provided proper artificial damping, values of Δt larger than essential to damp out the higher modes may lead to the elimination of lower modes (see Fig. 9a, e, g, i; the last when physically damped slightly). (Proper artificial damping implies guaranteed more numerical damping for higher values of $\frac{\Delta t}{T}$, addressed here as proper artificial damping for the first time.) In other words, with assigning larger/smaller values to the integration step size, more/less oscillatory modes (starting from the highest modes) will be affected and eliminated. This can entail undesired inaccuracy. The presented discussion is valid, only for linear analysis of MDOF systems damped proportionally. Nevertheless, for many practical applications (e.g. seismic analysis), the nonlinear behaviour is of piecewise-linear type (e.g. linear-elastic/perfect-plastic and pounding [10, 28, 78, 91–94]) and meanwhile proportional damping is a broadly accepted assumption [28, 52]. Accordingly, expressions such as $\omega \Delta t$, spectral radius ρ, and artificial damping, can be defined/considered in a piece-wise manner. Therefore, in many practical cases, depending on the selection of the parameters of nonlinearity analysis and the severity of nonlinear behaviour, we can use the linear theory of artificial damping to build up an idea about the artificial damping in analysis of nonlinear structural systems. Still, in nonlinear as well as linear analyses, special attention should be paid to selection of parameters of the integration method controlling artificial damping. Alternatively, and even preferably, the results are to be checked for accuracy [7, 28, 55, 95–97], also to prevent elimination of the important lower modes from the final response.

Overshoot is the tendency of integration methods to cause significant errors in the few steps after the start of the oscillations or after abrupt changes of the status or the excitation. Accordingly, smaller integration step sizes would likely cause less error, originated in overshoot; see [30–33, 52].

Regarding computational cost, assigning smaller values to the integration step size, without changing the computer (computational facility), increases the number of integration steps, while the computational cost per integration step remains unchanged. Accordingly, the runtime, the total usage of the in-core memory, and hence the computational cost, C_C, will increase, i.e. considering $\propto$ as a sign for "dependence",

$$C_C \propto \Delta t^{-1} \tag{20}$$

In more detail, in linear time integration analysis of an arbitrary system, with equally sized integration steps,

$$\frac{C_{C_1}}{C_{C_2}} = \frac{\Delta t_2}{\Delta t_1} \tag{21}$$

where, C_{C_1} and C_{C_2} denote the computational costs of two arbitrary analyses (on one computer and when disregarding the pre- and post-processing), respectively, with steps equal to Δt_1 and Δt_2 ($\Delta t_1 \neq \Delta t_2$). To say better,

$$C_{C_1}\Delta t_1 = C_{C_2}\Delta t_2 = \cdots = C = \text{Const.} \tag{22}$$

where, C is a positive-definite constant, representing a scale of the computational cost per integration step C_C^* (C can also be defined as the computational cost of the analysis carried out with integration steps equal to one), i.e.

$$C_C^* = \frac{C_C}{N} = \frac{\Delta t\, C_C}{t_{end}} = \frac{C}{t_{end}} \tag{23}$$

N stands for the total number of integration steps, C_C is the associated computational cost of the analysis, and t_{end} is defined in Eq. (2). The computational cost associated with an integration step C_C^*, depends on the semi-discretized model, the computational facility (capabilities), i.e. how powerful is our computer?, and the integration method. Different from accuracy (including stability) and overshoot, for the sake of which, we prefer to assign smaller values to the integration step size, for reducing the computational cost, it is beneficial to time integrate with larger steps; the case is in between, when talking about artificial damping.

In an arbitrary nonlinear analysis, it is essential to check the occurrence of nonlinearity after determination of the status at each integration station. When nonlinearity is detected, appropriate changes should be implemented in the characteristics of the system [see the $\mathbf{Q}$ in Eq. (5)]. Furthermore, and before the changes, it is conventional to localize the nonlinearity by implementing some nonlinearity iterations [2, 42–46]. Accordingly, Eqs. (21) and (22) are not valid, in time integration analysis of nonlinear systems. Even, without nonlinearity iterations, because of the essentiality of status check and characteristics change, it is reasonable to consider

$$\begin{aligned} C_{C_1} &\cong \tilde{C}_{C_1} + n_{NL_1} C_Q \\ C_{C_2} &\cong \tilde{C}_{C_2} + n_{NL_2} C_Q \end{aligned} \tag{24}$$

In Eq. (24), $\tilde{C}_{C_1}$ and $\tilde{C}_{C_2}$ imply computational costs, not including nonlinearity iterations and status change, i.e.

$$\tilde{C}_{C_{i=1,2}} = \left(C_{C_{i=1,2}}\right)_{\text{Linear}} + C_{\text{Status Check}} \tag{25}$$

n_{NL_1} and n_{NL_2} stand for the number of nonlinearity detections in analysis with steps sized Δt_1 and Δt_2 respectively, C_Q is an indicator for the computational cost at a nonlinearity detection averaged out among all nonlinearities detected in the analysis, and includes the costs of nonlinearity iterations and change of status. It is worth noting that the independency of C_Q from Δt is a reasonable assumption, implemented in Eqs. (24), and leading to the approximation signs in Eqs. (24).

A special case happens when the nonlinear behaviour is piece-wisely linear (e.g. linear-elastic/perfect-plastic behaviour, impact, simple friction) [63], and no non-linearity iteration is implemented. In this case,

$$n_{NL_1} \cong n_{NL_2} \cong n_{NL} \tag{26}$$

and in view of Eqs. (24) and (26) and provided analysis with equally sized steps,

$$\frac{C_{C_1}}{C_{C_2}} \cong \frac{\tilde{C}_{C_1} + x}{\tilde{C}_{C_2} + x}, \quad x = n_{NL} C_Q > 0 \tag{27}$$

Taking into account that $\tilde{C}_{C_{i=1,2}} > 0$, and the fact that in view of Eq. (25), similar to Eq. (21),

$$\frac{\tilde{C}_{C_1}}{\tilde{C}_{C_2}} = \frac{\Delta t_2}{\Delta t_1} \tag{28}$$

Eq. (27) implies that, in analysis of piece-wisely linear systems on a specific computer, when we do not implement nonlinearity iterations and C_Q is sufficiently smaller than $\tilde{C}_{C_{i=1,2}}$, the computational cost resists against changes because of Δt. To say better, in the special case addressed above,

$$\left|\frac{C_{C_2} - C_{C_1}}{C_{C_1}}\right| < \left|\frac{\Delta t_2 - \Delta t_1}{\Delta t_2}\right| \tag{29}$$

(the above-mentioned smallness of C_Q is generally valid, for implicit analyses [1, 30, 31], recommended for many real nonlinear dynamic analyses; see [1, 43]). Another special case occurs, when nonlinearities are detected at almost all integration steps, regardless of the integration step size, and no non-linearity iteration is being implemented. In this case, provided analysis with equally sized steps,

$$\begin{aligned} C_{C_1} &= \tilde{C}_{C_1} + \frac{t_{end}}{\Delta t_1} C_Q \\ C_{C_2} &= \tilde{C}_{C_2} + \frac{t_{end}}{\Delta t_2} C_Q \end{aligned} \tag{30}$$

and, in view of Eq. (28),

$$\frac{C_{C_1}}{C_{C_2}} = \frac{\Delta t_2}{\Delta t_1} \tag{31}$$

comparable with Eq. (21). Equation (31) implies that, in a nonlinear analysis with equally sized steps and nonlinearities detected at all integration steps, if we do not implement nonlinearity iterations, the changes of computational cost with respect to the integration step size would be very similar to linear analyses. The discussion above seems new, and presented for the first time, in this chapter. Accordingly, further study is surely essential, not followed here, for the sake of brevity. Extension of the discussion to general nonlinear behaviour/analysis is being recommended for further research.

4 Practical Comments for Integration Step Size Selection

The most conventional and broadly accepted comment for selection of integration step sizes, specifically, when the steps are equally sized, is as stated in Eq. (32) [1, 10, 28, 49, 66, 97–99]:

$$\Delta t = \text{Min}\left(\Delta t_{cr}, {}_f\Delta t, \Delta t_d, \frac{T_r}{\chi}\right) \tag{32}$$

The new parameters are defined below:

- ${}_f\Delta t$: Step size, by which, the excitation is digitized (${}_f\Delta t = \infty$, when the excitation is continuous)
- Δt_d: Largest step size, according to which, we accept to obtain the history of the response (generally unimportant)
- T_r: Smallest period of oscillations with considerable contribution in the response
- χ: A factor, changing from 10 (or even 5) in linear simple analyses to 1000 in analyses involving impact, severe nonlinearity, complex or mathematically stiff behaviour, etc., such that $\frac{T_r}{\chi}$ turns to be an integration step size sufficient for accuracy

The definitions of Δt_{cr} [see Eq. (18)], ${}_f\Delta t$, and Δt_d, are clear. However, the definitions of T_r and χ are somehow imprecise and vague, and furthermore, serious arguments can be made on the typology of Eq. (32) and the computation of Δt_{cr}. This section is dedicated to these ambiguities.

The typology of Eq. (32) has five major deficiencies. First, with the exception of period elongation and amplitude decay [1, 10, 29, 33, 52], no theoretical relevance seems to exist between $\frac{T_r}{\chi}$ and accuracy, and period elongation and amplitude decay

cannot well explain the role of $\frac{T_r}{\chi}$ in Eq. (32); see [1, 29–32]. Secondly, the integration step size should be set, such that, with negligible additional inaccuracy, for the lower modes, the higher erroneous modes of oscillation can be eliminated (when Eq. (5) is obtained from discretization in space). Accordingly, in view of Fig. 9, artificial damping and the origin of Eq. (5) would rather be included in Eq. (32). Alternatively, since the details of Fig. 9 are different, for different integration methods, the integration method needs to be taken into account in Eq. (32); as a third alternative, the obtained responses are to be controlled, also for adequate selection of the parameters. Neither of these approaches seems to be properly addressed in Eq. (32) (or its implementation). In addition, the existing ambiguities on the notion of small and large modes highlight the ambiguities on the role of artificial damping in Eq. (32). Thirdly, a deficiency in the typology of Eq. (32) is the fact that, when the excitation is available as a digitized record (i.e. ${}_f\Delta t$ is finite), and the consequence of Eq. (32) is such that:

$$\Delta t <_f \Delta t \tag{33}$$

it is not simple to carry out the time integration analysis with values of Δt satisfying Eqs. (32) and (33). A supplementary practical equation, to be satisfied, while taking into account Eq. (33), is as stated below:

$$\Delta t = \frac{{}_f\Delta t}{m}, \quad m \in Z^+ - \{1\} \tag{34}$$

An approach, to consider Eqs. (32) and (34) simultaneously, seemingly addressed for the first time in this chapter, is to replace Eq. (32) with ($\Delta t'$ is used merely for the computation of Δt):

$$\begin{aligned} \Delta t' &= \text{Min}\left(\Delta t_{cr}, \Delta t_d, \frac{T_r}{\chi}\right) \\ \Delta t &= \begin{cases} {}_f\Delta t & \text{when} \quad \Delta t' \geq {}_f\Delta t \\ \dfrac{{}_f\Delta t}{m} & \text{when} \quad \exists m \in Z^+ - \{1\}, \dfrac{{}_f\Delta t}{m} \leq \Delta t' < \dfrac{{}_f\Delta t}{m-1} \end{cases} \end{aligned} \tag{35}$$

The forth deficiency in the typology of Eq. (32) originates in χ. In fact, besides the nonlinearity and its type, it is essential to take into account the severity of the nonlinear behaviour. As a simple example, the impact between two undamped single degree of freedom systems can be neglected when the velocities are about zero at all instants of impact. This leads to the negligibility of the nonlinear behaviour. The case is completely different when the impacts occur at considerable velocities. The difference between these two cases (and in general the difference between cases with different severity of a special type of nonlinear behaviour) seems not taken into account in Eq. (32). Towards a replacement for Eq. (32), attention can be paid to the discussions reported in the literature on nonlinearity quantification and measurement, e.g. see [100].

Finally, the fifth deficiency in the typology of Eq. (32) is that, though the nonlinear behaviour and its complexity affect Eq. (32) via χ, the effect of nonlinearity analysis parameters (e.g. the tolerance, $\bar{\delta}$) on the accuracy is disregarded. Two approaches to overcome this deficiency is to take into account the value of Δt, while assigning values to the nonlinearity parameters (see [42, 63, 64, 79]), or alternatively, to control the errors after the time integration analysis [28, 55, 95–97]. The latter might be unexpectedly costly.

In practical implementation of Eqs. (32) or (35), there is no ambiguity about the values to be assigned to ${}_f\Delta t$ and Δt_d. However, Δt_{cr} is under the effect of damping, and still, we cannot guarantee that, disregarding viscous damping is necessarily on the safe side of numerical stability, resulting in larger values of Δt_{cr} [30–33, 52]. Without a safe side assumption, Δt_{cr} needs to be computed considering the amount of viscous damping in different natural modes. The smallest Δt_{cr}, not necessarily associated with a special mode, would then control the numerical stability. The computation is not only complicated and computationally expensive (because of several reasons, including determination of the natural frequencies and the corresponding viscous dampings), but also the eigen-solution is in conceptual contradiction with the nature of direct time integration. The deficiency highlights in presence of nonlinearity, where the natural frequencies change throughout the integration interval. With the safe side assumption, independent of the amount of viscous damping, the natural mode causing the smallest Δt_{cr}, mostly the last natural mode, would control the numerical stability in Eqs. (32) and (35) (see Eq. (18) and the existing conditionally stable methods [1, 10, 11, 15, 24, 28–33, 52]). Furthermore, if the help of viscous damping to numerical stability is guaranteed, the definition of unconditional stability in Eq. (19) can be changed to:

$$\forall \omega \quad : \quad \Delta t_{cr} \to \infty \tag{36}$$

The above discussion and assigning an adequate value to Δt_{cr}, in Eqs. (32) and (35), are more complex in presence of non-proportional damping; in view of the versatility of time integration in analysis of non-proportionally damped systems [28–33], this complexity is indeed a practical drawback. Considering these, it is essential to emphasize once again on the existing comment not to use integration methods with finite Δt_{cr} [30–32] (when possible regardless of the type of damping), causing the simplification below in Eq. (35):

$$\begin{aligned} \Delta t' &= \mathrm{Min}\left(\Delta t_d, \frac{T_r}{\chi}\right) \\ \Delta t &= \begin{cases} {}_f\Delta t & \text{when} \quad \Delta t' \geq {}_f\Delta t \\ \dfrac{{}_f\Delta t}{m} & \text{when} \quad \exists m \in Z^+ - \{1\}, \dfrac{{}_f\Delta t}{m} \leq \Delta t' < \dfrac{{}_f\Delta t}{m-1} \end{cases} \end{aligned} \tag{37}$$

A seemingly last and most crucial deficiency in Eqs. (32), (35), and (37), is in the notion of T_r. Theoretically, T_r implies the smallest period, with considerable contribution in the response [49, 66, 101]. The expression *considerable*

contribution is vague, and besides, while the response is not at hand before the analysis, how we can determine the periods of oscillations?! Furthermore, even if, the response could somehow be predicted, no specific comment seems to exist regarding determination of the value of T_r and besides the computation of the oscillatory modes is computationally expensive. To overcome these shortcomings partly, we can compute T_r, by using the comments on the natural modes with considerable contribution in the response, if existing (e.g. see [90, 91, 99]). This approach, though leads to determination of T_r independent from the response, lacks sufficient theoretical explanation.

A practical way (in cases costly), to lessen accuracy-related shortcomings, including those originated in T_r and χ, is to upper estimate T_r (in view of the low cost of the computation, no especial approach is essential for the upper-estimation), assign the value obtained from Eqs. (32), (35), or (37), to Δt, carry out a first analysis, repeat the analysis with half steps, compare the two responses, if the difference is not sufficiently small (the error of the response is in the size of the difference), once again repeat the analysis with half steps, and eventually, stop the repetitions, when the difference is negligible. Considering that such repetitions are recommended in the literatures of numerical solution of differential equations, and practical engineering applications specifically structural dynamics [7, 28, 55, 99, 102, 103] and considerable theoretical explanations exist for repetition-based accuracy controls, e.g. see [42, 96, 97], it is reasonable to rely on these repetitions to compensate the ambiguities and arrive at sufficient accuracy. Meanwhile, it is worth noting that implementation of the repetitions might be insufficient, because of the probable improper convergence, in problems with complex oscillatory behaviour, specifically those involved in nonlinearity [42, 74–76, 78, 104, 105]. Implementation of more advanced error control methods can cause more reliability, e.g. see [55].

5 Time Integration and Step Size Selection in Seismic Codes

The material, presented in the previous sections, was mostly theoretical, discussed in different branches of science and engineering; see [13, 17, 19–22, 26, 35, 37, 106–108]. In this section, attention is paid to seismic analysis and design, as a very important and crucial research area, with direct and indirect effects on human lives and civilization. Accordingly, with attention to seismic activities, locations in the world map and issues like how developed are codes/standards?, how developed are countries/regions?, how much populated are countries/regions?, and finally, the availability of the codes/standards for the author, the following seismic codes/standards are reviewed for issues on time integration and step size selection:

1. National code/standard of India [109, 110].
2. European code/standard [111].

3. National code/standard of Turkey [112].
4. National code/standard of Greece [113].
5. National code/standard of China [114].
6. National code/standard of New Zealand [109, 115].
7. National code/standard of Iran [90].
8. National code/standard of United States [116].
9. National code/standard of Japan [117].
10. National code/standard of Mexico [118, 119].
11. National code/standard of Chile [120, 121].
12. National code/standard of Romania [122].
13. National code/standard of Taiwan [123, 124].

The footprints of time integration in seismic codes/standards are investigated by directly looking for *integration*, *time integration*, *time domain analysis*, and *time history analysis*, or indirectly by looking for *nonlinear analysis*, *non-proportional damping*, *un-classical damping*, and provisions regarding analyses out of the scope of mode superposition analysis, e.g. analysis of systems equipped with modern control devices providing non-proportional damping.

Time integration analysis against several ground motion records and putting the results together (according to a seismic code/standard), in order to arrive at a time history record for each response (or to arrive at responses) to be used in seismic designs, is called time history analysis. All of the seismic codes/standards, with the exception of the code/standard of Chile [120, 121], consider time history analysis (and time integration) as an analysis alternative. Some of the important considerations in the seismic codes/standards are briefly addressed in Table 4; the numbers in the last column stand for the seismic codes/standards, as stated in the start of this section. (Table 4 does not present all the related regulations; it attempts to present a brief overview.) Meanwhile, the codes/standards, that in some cases consider time history analysis as the superior analysis tool, are as listed below:

- National code/standard of India [109, 110]: in stack like industrial structures,
- European code/standard [111]: when an isolation system may not be modelled with an equivalent linear method,
- National code/standard of China [114]: for buildings taller than specific heights,
- National code/standard of New Zealand [99, 115]: for long period structures and when the directivity effects (e.g. see [125]) can be significant,

Table 4 A brief look on some regulations regarding time history analysis in seismic codes

Some main considerations in implementation of time history analysis	Codes/standards
Selection of records	1–9, 12, 13
Scaling and combining the results of analyses against different records	2, 3, 5, 6, 12, 13
Type and philosophy of analysis (linear/nonlinear, safe side) and material model	1, 2, 4, 7, 10
Details of analysis	6
Control on final results	6

- National code/standard of Japan [117]: for high-rise buildings,
- National code/standard of Romania [122]: similar to European code/standard,

where, for each code/standard, cases at which time history analysis is recommended or is the only seismic analysis tool, are addressed after the code/standard. And finally, the code/standard having comments on integration step size is the national code/standard of New Zealand [99, 115], while, the code/standard explicitly addressing *integration* as the mean for time history analysis is that of the United States [116]. The information above and those in Table 4 are clear evidences for the advancement of the code/standard of New Zealand [109, 115] (the code/standard introduced with "6" in Table 4), from the point of view of time history analysis and specifically the integration step size selection.

The comment of the national code/standard of New Zealand on integration step size (see Sect. 6.4.5 in [99]) is summarized in the equation below:

$$\Delta t \leq \text{Min}\left(\Delta t_{cr}, {}_f\Delta t, \frac{T_1}{100}, T_n, 0.01\right) \tag{38}$$

In Eq. (38), T_1 is the largest translational period of the first mode, judged by the largest mass contribution, in the direction of principal component of the earthquake, and T_n denotes the period of the highest mode in the same direction required to achieve the 90 % mass as described in the modal response spectrum method [99]. The guidance of the commentary [115] regarding implementation of Eq. (38) is as stated below:

> The time step should generally be not greater than $\frac{T_1}{100}$, where T_1 is the period associated with the first mode of vibration. For analyses involving impact (building pounding, rocking walls, or uplifting foundations), the time step will need to be significantly lower and a starting value of $\frac{T_1}{1000}$ is recommended. If convergence is not obtained with a particular time step, reduce it by a factor of 2 and re-run. Once convergence is obtained, make a further reduction and compare the peak results for the target response parameter. If they are within 5 %, the longer time step (which requires less computing running time) is satisfactory [115].

The above considerations, and specifically, the selection of integration step sizes, is a significant initiation in seismic regulations (the author has not met similar details in seismic codes/standards in the past; also see [126]); and hence, the consideration in the code/standard of New Zealand [99, 115] is to be deeply appreciated and acknowledged. Still, some drawbacks and ambiguities seem to exist, to which the remainder of this section is dedicated.

As the first ambiguity, since each time history analysis is composed of several time integration analyses, the cost of time history analysis is generally considerable and the selection of step sizes in the first analysis (before any repetition) is of high importance. It is unclear why selection of the step size and the way the step size decrease in the repetitions of the first analysis disregard many features of the ground motion record (${}_f\Delta t$ is an exception), as well as, the nonlinearity analysis parameters (the nonlinear behaviour is briefly taken into account via χ). To explain better,

theoretically, depending on the excitation and the linear or nonlinear behaviour, a system may oscillate in frequencies different from its first natural frequencies, leading to different essentialities of integration step sizes. This seems not well taken into account in Eq. (38); compare Eqs. (32) and (38). Furthermore, depending on the values assigned to nonlinearity tolerances, proper convergence [105] of the analyses and reliable estimation of the errors can be considerably affected; e.g. see [42, 63, 78, 80]. Disregarding these issues in Eq. (38) may lead to additional repetitions, and accordingly considerable additional computational cost, and even in cases failure of the repetitions because of round-off.

The second ambiguity is that the theory backing the validity of the recommended accuracy control is not addressed in the code/standard and the supporting material [99, 115]. Specifically, it is worth noting that the partly theoretical backing, which is the proper convergence (see Fig. 4 and [42, 63, 105]) may not be fulfilled, in nonlinear time integration analysis; this is while the purpose of the control in the code/standard of New Zealand is nonlinear analysis; see [42, 63, 72, 74, 75, 80, 104].

Finally, after repeating an analysis and comparing the two responses, until being within 5 % difference at the peak, the seismic code/standard of New Zealand does not explicitly address the resulting response and merely mentions that the response obtained using the larger step is satisfactory [115]. As clearly stated in [115], the reason of referring to the response obtained from analysis with larger integration step size as satisfactory is that the other analysis is more costly. This implies that the comment is indeed to consider the response obtained from analysis with larger steps as final. Since, the two analyses are to be carried out, prior to checking whether the responses are in 5 % difference, it seems reasonable to pay attention to accuracy rather than computational cost and consider the response obtained from the analysis with smaller step size as the final response. (The more accuracy of the response when using smaller step sizes can be explained by the theory behind the error controlling approach; see [97].) Practically, ambiguities exist, also regarding the 5 % difference, the notion of 5 %, and the error control on the peaks, not discussed here, for the sake of brevity.

6 Efficient Step Size Selection

As implied in the previous sections, Δt affects the accuracy and computational cost in reverse manners; also see [30–33, 49, 52]. Therefore, the more we eliminate the restrictions on Δt, the better the computational cost and accuracy can be balanced.

Methods are developed to eliminate the equality of the sizes of integration steps throughout the integration interval, e.g. see [66, 127]. The resulting time integration analysis is in general addressed as adaptive time stepping or adaptive time integration analysis. Adaptive time integration analysis starts with selection of step sizes for the first or first few steps. Carrying out ordinary time integration for the starting steps, the analysis continues in a step-by-step manner. After each or each several steps, a pre-assigned criterion to determine whether the sizes of the next

steps need to be changed, and if a change is needed, to determine the amount of the change, is examined; see [66]. This process continues till the end of the integration interval, i.e. t_{end} (see Eqs. (2) and (5)). Adaptive time integration analysis started in about 1970s by the studies of Hibbit and Karlson, Oughourlian and Powell, Flippa and Park, Park and Underwood, and Underwood and Park (see the brief review reported in [66]), continued in the past decades [66, 127–129], and is in progress, specifically, for nonlinear analyses, e.g. see [22, 130–132]. Returning to the process of adaptive time integration, as explained above, implementation of a pre-assigned criterion is essential in arbitrary adaptive analysis. Some main bases for the criteria are as noted below [66, 127]:

1. Errors at the integration stations, because of the integration approximation, associated with the last integration step; or to say better, the amount of error at the end of the integration step, originated in the approximate integration formulation, assuming zero errors at the start of the integration step and linear behaviour throughout the step. This error is broadly known as the local truncation error [31, 32].
2. Periods (or equivalently frequencies) of important oscillations in the response, at the integration steps, or for large MDOF systems, the 'current characteristic frequency', defined based on expressions similar to the Rayleigh ratio [66].
3. Complexity of the transient behaviour, defined, based on a measure named curvature of the response [66].

The computational costs associated with implementation of the criterion and the step size change (factorization) negatively affect the efficiency of adaptive time integration. The significance of these effects depends on the size of the structural system, the complexity of the dynamic behaviour, the length of the integration interval $[0 \quad t_{end}]$, the adaptive time stepping criterion, and the time integration method. Consequently, from the standpoint of computational cost, analysis considering adaptive time stepping is not necessarily superior to analysis with constant time steps.

For implementation of the criteria and adaptive time stepping, sizes of the starting steps, and some analysis parameters, should be set adequately and in advance. Parameters to prevent very slight or very frequent changes of the integration step size are samples [66]. These selections complicate implementation of adaptive time integration, compared to constant time stepping. It is also worth noting that, in implementation of adaptive time stepping, we cannot predict the computational cost of the analyses; in constant time stepping the prediction is simple in linear analyses. Considering these, constant time stepping and adaptive time stepping are both broadly accepted in practice, and research in either direction is in progress [21, 34, 115, 132–134], revealing the likely balanced needs in future. In seismic analyses, that the excitations are digitized in equal steps and the digitization step size complicates the selection of integration step size even further, constant time stepping is popular, e.g. see [10, 28, 29, 99, 135]. Accordingly, the discussion in the remainder of this section is concentrated on efficient step size

selection in analysis against digitized excitations using constant time steps (i.e. ${}_f\Delta t < \infty$, and in Fig. 1, $\forall\ i:\ t_{i+1} - t_i = \text{Const.}$).

In view of Eqs. (35) and (37), conventional time integration analysis using constant time steps is more efficient, when $\Delta t_d, {}_f\Delta t, \frac{T}{\chi}$, and Δt_{cr} (in Eq. 35) are closer to each other and the largest possible. In other words, unless, when $\Delta t_{cr} \to \infty$ (unconditional stability; where Δt_{cr} disappears from the relations) or $\Delta t_{cr} = 0$ (unconditional instability; this is an impractical case), it would be ideal to guarantee

$$\begin{aligned} \Delta t = \Delta t_d = {}_f\Delta t = \Delta t_{cr} = \frac{T}{\chi}, \\ \forall\, \varepsilon > 0:\ \Delta t = \frac{T}{\chi} + \varepsilon \Rightarrow \text{Practically Unacceptable Accuracy} \end{aligned} \tag{39}$$

once again, implying the advantages of unconditionally stability. Based on this idea and towards more efficient step size selection, approaches are developed to enlarge Δt_{cr} and ${}_f\Delta t$ and close the gap between the terms in Eqs. (35), e.g. see [49, 135–138]. Considering this, the title of this chapter, and the existing comments, on using unconditionally stable methods (see Eqs. (19) and (36)), the discussion is continued, concentrated on techniques that enlarge ${}_f\Delta t$, while the integration methods are unconditionally stable, in analysis of linear systems.

Since the discussion is narrowed to transient analysis against digitized excitations (cases with finite ${}_f\Delta t$), as a practical application, it is reasonable to simplify Eq. (5), to seismic analysis against ground accelerations, by considering

$$\mathbf{f}(t) = \bar{\mathbf{O}} \tag{40}$$

and

$$\mathbf{u} = \mathbf{u}_g + \mathbf{u}_r \tag{41}$$

In Eq. (41), $\mathbf{u}_g$ stands for the static displacements of the un-supported degrees of freedom, because of the ground (support) displacement, and $\mathbf{u}_r$ denotes the displacements of the un-supported degrees of freedom, additional to the static displacements. In view of Eqs. (40) and (41), Eqs. (5) can be rewritten as stated below [10, 28, 91–93, 139]:

$$\begin{aligned} &\mathbf{M}\,\ddot{\mathbf{u}}_r + \mathbf{f}_{\text{int}} = -\mathbf{M}\boldsymbol{\Gamma}\,\ddot{u}_g(t) \quad 0 \le t < t_{end} \\ &\mathbf{u}_r(t=0) = \bar{\mathbf{O}} \\ &\dot{\mathbf{u}}_r(t=0) = \bar{\mathbf{O}} \\ &\mathbf{f}_{\text{int}}(t=0) = \mathbf{f}_{\text{int}_0} \\ &\mathbf{Q} \end{aligned} \tag{42}$$

In Eq. (42), $\ddot{u}_g(t)$ represents the ground acceleration, digitized at steps sized ${}_f\Delta t$, and Γ is a vector implying the static effect of the ground (support) displacement on the displacements of un-supported degrees of freedom [10].

Four techniques, to materialize time integration analysis with steps larger than the excitation steps without disregarding the excitations, are as briefly reviewed below:

1. Time integration of integrated problems.
   This technique, is proposed by S-Y. Chang in 2002 [137], not as a technique to enlarge the integration steps. Ordinary time integration is implemented in analysis of the original problem, modified slightly. The modified problem consists of the integral of the equation of motion and the corresponding initial conditions. Accordingly, the original digitized $\mathbf{f}(t)$ is integrated, and ${}_f\Delta t$ loses its meaning and can be eliminated from Eqs. (32), (35), and (37). This is a considerable achievement, obtained in the price of the additional computational cost essential mainly for numerical integration of $\mathbf{f}(t)$. Few examples are studied; in all, the loss of accuracy is small and the save of computational cost is considerable.
2. Convergence-based replacement of excitations.
   This technique is proposed, by the author in 2008 [49], specifically in order to replace digitized excitations with excitations digitized at larger steps, i.e.

$$ {}_f\Delta t_{new} = n_f\Delta t, \quad n \in \{2, 3, 4, \ldots\} \tag{43} $$

   and later extended to non-integer enlargements [138], i.e.

$$ {}_f\Delta t_{new} = r_f\Delta t, \quad r = \frac{n_1}{n_2}, \quad n_1 > n_2, \quad n_1 \in \{2,3,4,\ldots\}, \quad n_2 \in \{1,2,3,\ldots\} \tag{44} $$

   Both versions of the technique are successfully implemented in analysis of many real problems, including frames, short mid-rise and tall buildings, different bridges, space structures, silos, water tanks, a cooling tower, etc. [49, 135, 139–154], and undergone theoretical studies [138, 155–163]; see more details in Sect. 7.
3. Impact-based replacement of excitations.
   This technique, proposed by M. Hosseini and I. Mirzaei in 2012 [164], replaces each section of the excitation record located totally above or totally below the $\ddot{u}_g = 0$ axis, with a single data $\left(\ddot{u}_g\right)$ equal to the area of the section, above or below the $\ddot{u}_g = 0$ axis, applied at the centroid of the section (see Fig. 10). Implementation of the technique in analysis of several problems has been successful.
4. Integration after combining several sequential integration steps analytically.
   This technique, first suggested by the author in 2009 [165], combines ordinary time integration computations in p' $(p' \in Z^+ - \{1\})$ sequential steps

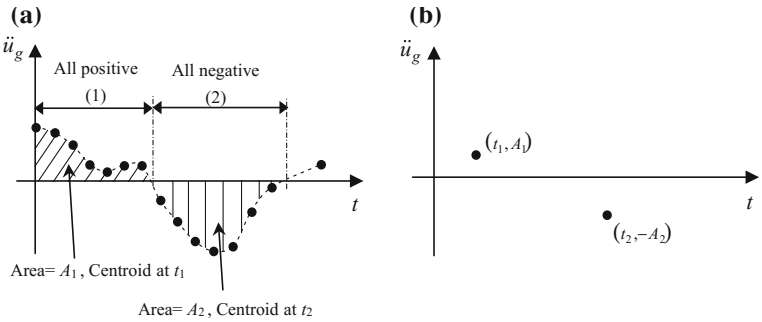

Fig. 10 Impact-based replacement [164] of two typical sequential sections of a typical digitized record respectively above and below the horizontal axis: **a** before the replacement, **b** after the replacement

analytically, in order to arrive at $(\mathbf{u}_p, \dot{\mathbf{u}}_p, \ddot{\mathbf{u}}_p)$ directly from $(\mathbf{u}_{p-p'}, \dot{\mathbf{u}}_{p-p'}, \ddot{\mathbf{u}}_{p-p'})$, and hence, provides the capability of time integration with integration steps p' times larger than the excitation steps, with no sacrifice of accuracy $(p \in Z^+ - \{1\}, p \geq p')$. However, the additional computational cost is not necessarily negligible [160, 166]. The technique, first proposed for SDOF linear systems [165], later enhanced towards further reduction of computational cost [166], afterwards, in one attempt, extended to implementation in analysis of MDOF systems [160], and in another attempt, to implementation in nonlinear analyses [167]. Though the loss of accuracy is zero, because of the additional computational cost and for the sake of efficiency, the enlargement is limited to specific values of n in Eq. (43) (four seems an appropriate upper-bound for n; Eqs. (43) and (44) are common between the second and forth techniques).

Table 5 A comparison between four techniques to enlarge the digitized excitations step sizes

Technique	1	2	3	4
Accuracy (compared to conventional analysis)	Better than Technique 3	Better than Techniques 1 and 3	Good	Excellent (perfect)
Computational cost	Negligible	Negligible	Negligible	Small (for small values of n)
Simplicity	Good	Better than Techniques 1, 3, and 4	Good	Not as good as Techniques 1–3
Numerical tests	Few	$\cong$ 150 successful tests	Few	Few
Consistency with $\Delta t = {}_f\Delta t$	No	Yes (practically)	No	Yes
Control on enlargement	Excellent (perfect)	To all positive rational numbers (practically perfect)	No	To all positive integers

A brief comparison between these four techniques is presented in Table 5, where the numbers in the first row are in accordance with the numbers introducing the techniques, introduced above. In view of Table 5 and the fact that there exists a rational number in any arbitrary neighbourhood of a real number [57] (see the last row in Table 5), the second technique can be considered as the superior technique. The next section is dedicated to a review on the second technique and its most recent advancements.

7 Recent Advancements of a Step Size Enlargement Technique

As stated in the previous section, towards more efficient seismic analysis by constant time step integration, a technique is proposed in 2008 [49], and later extended in 2013 [138]. The efficiency is provided by enlarging ${}_f\Delta t$, such that to prevent it from dominating Eqs. (35) and (37), while also bounding the induced inaccuracy. Special attention is paid to: (1) convergence, as the main essentiality of approximate computations [55, 59, 60], (2) the recommended second order of accuracy [30–32], and (3) the effect of approximations in the initial conditions, excitations, etc., on the rate of convergence [32, 49, 71]. These considerations lead to the replacement of the excitation $\mathbf{f}$, with a new excitation, $\tilde{\mathbf{f}}$, defined below:

$$\begin{aligned}
&t_i = 0: && \tilde{\mathbf{f}}_i = \tilde{\mathbf{f}}(t_i) = \mathbf{g}(t_i), \\
&0 < t_i < t'_{end}: && \tilde{\mathbf{f}}_i = \tilde{\mathbf{f}}(t_i) = \frac{1}{2}\mathbf{g}(t_i) + \frac{1}{4n'}\sum_{k=1}^{n'}\left[\mathbf{g}\left(t_{i+k/n_1}\right) + \mathbf{g}\left(t_{i-k/n_1}\right)\right], \\
& && t_i = i\,\frac{n_1}{n_2}{}_f\Delta t \quad i = 0, 1, 2, \ldots \\
&t_i = t'_{end} && \tilde{\mathbf{f}}_i = \tilde{\mathbf{f}}(t_i) = \mathbf{g}(t_i),
\end{aligned} \tag{45}$$

and digitized at steps sized ${}_f\Delta t_{new}$, introduced in Eq. (44). Regarding the new symbols in Eqs. (44) and (45), when the excitation step size, ${}_f\Delta t$, governs Eqs. (35) or (37), the replacement addressed in Eq. (45) changes the case by assigning the smallest positive integers to n_1 and n_2 satisfying

$$\frac{n_1}{n_2}{}_f\Delta t \le \mathrm{Min}\left(\Delta t_{cr}, \frac{T_r}{\chi}, \Delta t_d\right) < \frac{n_1 + 1}{n_2}{}_f\Delta t \tag{46}$$

The value of n' in Eq. (45) can be obtained from

$$
\begin{aligned}
&n' = n_1 - 1 && \text{when} \quad t = \tfrac{\Delta t}{n_2} \\
&n' = \begin{cases} \frac{n_1}{2} & n_1 = 2j, \quad j \in Z^+ \\ \frac{n_1 - 1}{2} & n_1 = 2j+1, \quad j \in Z^+ \end{cases} && \text{when} \quad \tfrac{\Delta t}{n_2} < t < t'_{end} - \tfrac{\Delta t}{n_2} \\
&n' = n_1 - 1 && \text{when} \quad t = t'_{end} - \tfrac{\Delta t}{n_2}
\end{aligned} \tag{47}
$$

t'_{end} is the only number satisfying

$$
t_{end} \le t'_{end} < t_{end} + \frac{n_1}{n_2}{}_f\Delta t, \quad \frac{t'_{end}}{\frac{n_1}{n_2}{}_f\Delta t} \in Z^+ \tag{48}
$$

and $\mathbf{g}(t)$ is available from

$$
\mathbf{g}(t_i) = \begin{cases} \bar{\mathbf{g}}(t_i) & \text{when} \quad 0 \le t \le t_{end} \\ \bar{\mathbf{O}} & \text{when} \quad t_{end} < t < t'_{end} \end{cases} \tag{49}
$$

where, $\bar{\mathbf{O}}$ is the zero vector and $\bar{\mathbf{g}}$ is a linear enrichment of $\mathbf{f}$, defined below:

$$
\begin{aligned}
&\forall\, i = 0, 1, 2, \ldots \tfrac{n_2 t'_{end}}{{}_f\Delta t}: \quad t_i = i\tfrac{{}_f\Delta t}{n_2}, \\
&\begin{cases}
\bar{\mathbf{g}}(t_i) = \mathbf{f}(t_i), & \text{when} \quad \frac{i}{n_2} \in Z^+ + \{0\} \\
\bar{\mathbf{g}}(t_i) = \mathbf{f}\big(k_1{}_f\Delta t\big) + \left(\dfrac{i - k_1}{n_2}\right)\big(\mathbf{f}\big(k_2{}_f\Delta t\big) - \mathbf{f}\big(k_1{}_f\Delta t\big)\big), & \\
\qquad k_1 = kn_2, \quad k_2 = k_1 + n_2, \quad k \le \dfrac{i}{n_2} < k+1, k \in Z^+ + \{0\} & \text{when} \quad \frac{i}{n_2} \notin Z^+ + \{0\}
\end{cases}
\end{aligned} \tag{50}
$$

Although, the technique is proposed in 2008 [49] and then extended in 2013 [138], it is now the first time that the formulation is presented in the detail stated above, considering rational number enlargements. The technique is implemented in many time integration analyses resulting in considerable reduction of computational cost in the price of negligible loss of accuracy (see Table 6). Even more, it is worth noting that, in two cases, the computational cost is reduced, while the accuracy is increased [152, 154].

A seemingly weak point in implementation of the technique is the vagueness in the notion and determination of T_r in Eq. (46), potentially entailing ambiguities in selection of n (or to say better $\frac{n_1}{n_2}$). Nevertheless, as implied in Sects. 4 and 5, these ambiguities exist, also in ordinary time integration analyses, using constant integration steps, as well as, some adaptive time stepping methods. Therefore, the ambiguities in defining and computing T_r are not deficiencies of the technique proposed in [49], but deficiencies of ordinary time integration, affecting the performance of the technique proposed in 2008. The ambiguities can be lessened by comparing the computed response with the response obtained from analysis with smaller steps [7, 28, 55, 95–97, 102], discussed in the ending parts of Sect. 4. However, questions persist. How should we set the integration step size and the

Table 6 Experiences on implementation of the technique proposed in [49] in time integration analysis against digitized ground motions

System analyzed	Cost reduced in the price of negligible errors (%)	Source
SDOF system	75	[49]
2-DOF nonlinear system	49.27	[49]
Eight storey shear frame	80	[140]
Thirty-storey building	50	[141]
3-component earthquakes	66.7	[142]
Silo	77.65	[143, 144]
Water tank	66.7	[145, 156]
Building in pounding	12.7	[146]
Bridge with linear and nonlinear behaviors	45–80	[139, 147]
Power stations	>50	[148]
Regular residential buildings	50–87	[149, 150]
Bridges with pre-stressed elements, subjected to multi-support excitation, and nonlinearities	30–70	[139]
Residential building with irregularities in height	50–80	[152]
Space Structures	>50	[151]
A cooling tower	>50	[153]
Milad telecommunication tower	>50	[154]

excitation for the analysis with smaller steps? Should the technique also contribute in the decrease of the step size (by assigning smaller values to n or $\frac{n_1}{n_2}$), or it suffices to reduce the size of the excitation step and determine the excitation by linear interpolation? What is the role of the errors originated in the technique in the total accuracy? As a brief response, or to say better comment, the repetition of the first analysis can be considered as means to control the additional errors, also because of the technique. The repetitions can be first considered with respect to the technique, and then after ensuring that the additional errors associated with the technique are sufficiently small, repetitions need to be carried out with respect to Δt; the details explained in [135, 159], imply no considerable additional cost compared to ordinary repetition-based accuracy controls.

Furthermore, the computational cost associated with Eqs. (45)–(50) is negligible compared to the cost of time integration (unless for systems with one or two degrees of freedom [49, 147, 157]). Accordingly, the amount of the computational cost reduction in linear analyses [135] can be stated as

$$A_C = 100\frac{n_1 - n_2}{n_2} \quad (\%) \tag{51}$$

and the changes of the cost reduction with respect to the enlargement, can be expressed as:

$$\frac{\partial A_C}{\partial\left(\frac{n_1}{n_2}\right)} = \frac{n_2^2}{n_1^2} \tag{52}$$

With attention to Eqs. (51) and (52), recently,

$$\frac{n_1}{n_2} \leq 5 \tag{53}$$

is suggested as a reasonable practical restriction on the selection of n (and $\frac{n_1}{n_2}$) [139, 159], changing Eqs. (46) to

$$\exists n_1' \in \{2,3,4,\ldots\}, \quad \exists n_2' \in \{1,2,3,\ldots\}: \quad \frac{n_1'}{n_2'}{}_f\Delta t \leq \text{Min}\left(\Delta t_{cr}, \frac{T_r}{\chi}, \Delta t_d\right) < \frac{n_1'+1}{n_2'}{}_f\Delta t$$

$$n_2 = n_2', \quad n_1 = \begin{cases} n_1' & \text{when} \quad \frac{n_1'}{n_2'} \leq 5 \\ 5n_2' & \text{when} \quad \frac{n_1'}{n_2'} > 5 \end{cases} \tag{54}$$

Equation (54) should be considered together with Eqs. (44), (45), (47)–(50), when the original excitation step size is the governing term in Eqs. (35) or (37) (to say better, when the technique can be implemented). The consequence is upper-bounding the computational cost reduction of linear analyses, by

$$A_C \leq 80 \quad (\%) \tag{55}$$

Another important challenge for the technique [49] is its performance, when implemented in a nonlinear time integration analysis. According to the carried out numerical studies (see Table 6), the performance of the technique is better, in implementation in analysis of linear behaviour (both from the standpoint of accuracy and also from the point of view of computational cost reduction) [135, 146, 150, 152]. Two main reasons are: (1) While convergence and second order of accuracy are the main concepts of the technique, accuracy, numerical stability, consistency, and convergence are still unresolved issues in nonlinear analyses [2, 42, 63, 72–80, 168]. (2) With larger integration steps, the number of iterations in the nonlinearity solutions may increase; the computational cost associated with these iterations can compensate the reductions of computational costs originated in the technique, and accordingly, diminish the efficiency of the technique.

Considering issues like those stated above, further study to clarify the persisting ambiguities is essential. Some main directions towards more efficient step size enlargement by the technique proposed in [49] are listed below:

1. Further clarifications regarding the values to be assigned to T_r in Eqs. (35) and (37) and more reliable selection of the enlargement scaling factor (n or $\frac{n_1}{n_2}$) to be implemented in Eq. (44),

2. Better performance, in implementation of the technique in analysis of complex (including nonlinear) structural systems.
3. Better control of accuracy.
4. Implementation in adaptive time integration analysis.

Meanwhile, the first point above can be considered of high importance in improvement of integration step size enlargement techniques other than that proposed in [49].

8 Closure

Time integration is a versatile tool to analyze semi-discretized equations of motion, and many other initial value problems from different origins. Integration step size, or to say better, Δt, is the main analysis parameter of time integration analysis which together with nonlinearity and methods' parameters, affect the analysis features, as stated below:

(a) Smaller values of Δt generally lead to more accurate responses. This is not necessarily true in analysis of nonlinear systems or systems with complex behaviour (e.g. highly oscillatory behaviour). For linear analysis, with sufficiently small integration steps not under the effect of round-off, we can guarantee more accuracy, when repeating the analysis, with smaller steps (the smallness depends on the problem, the integration method, and the computational facilities).
(b) Unless for unconditionally stable and unconditionally unstable analyses, smaller Δt can be beneficial for numerical stability.
(c) Δt has no effect on the order of accuracy.
(d) Δt has no effect on convergence, though can affect the convergence trend.
(e) Smaller values of Δt imply more computational cost for linear analyses. The case might be different for nonlinear analyses, depending on the type of nonlinear behaviour, severity of the nonlinear behaviour, the nonlinearity parameters, and the time integration method. Some special cases are discussed.
(f) Smaller values of Δt in general imply less artificial damping. This would rather be valid for both undamped and damped analyses. Values to be assigned to the parameters of artificial damping should be set carefully.

In selection of the integration step size, especially, for analysis of MDOF structural systems with constantly sized steps, emphasis is on using unconditionally stable time integration methods (the case is different for wave propagation problems; addressed in the literature by times). The requirements of numerical stability of linear analyses, obtained from spectral analysis of the amplification matrix, i.e. spectral stability, are necessary and sufficient for linear analyses, but merely necessary, for nonlinear analyses. Even in time integration analyses with unconditionally stable time integration methods, ambiguities exist in conventional step size

selection, as well as, in the comment of the national seismic code/standard of New Zealand (a code/standard with comments on integration step size selection). The ambiguities are more in nonlinear analyses. Some comments are discussed. Specifically, with attention to the ambiguities existing in the integration step size selections, control of the accuracies, for instance, by repetition of the analyses with smaller steps is necessary. Some additional details are to be satisfied in presence of nonlinearity.

From the thirteen seismic codes/standards reviewed in this chapter, many codes/standards (all with the exception of the code/standard of Chile) have considered time history analysis and time integration as tools for seismic analysis. Nevertheless, only in few codes/standards, time history analysis is recommended as the only or superior tool to analyze the semi-discretized equations of motion. There are also few codes/standards, with specific regulations on the details of time history analysis, and specifically, there is one code/standard, i.e. code/standard of New Zealand, with comments on the details of time integration analysis and the selection of integration step sizes. Although, the initiative of the seismic code/standard of New Zealand is worthy of sincere and deep appreciation and acknowledgement, ambiguities and flaws exist; some discussed in this chapter.

In time integration analysis against digitized excitations, the excitation step size should be taken into account in the selection of integration step size. In order to increase the efficiency, digitized excitations can be replaced with excitations digitized in larger steps. The existing techniques are briefly reviewed, and for the one seemingly superior, detailed explanations are presented, and the challenges are addressed.

Besides time integration analysis using constant integration steps, time integration can be carried out using steps sized adaptively, still not seriously implemented in seismic analysis. Adaptive time integration, although, directed towards more efficiency, is not necessarily more efficient compared to analysis with constantly sized steps. The efficiency depends on several parameters, including the complexity of the behaviour, the probable nonlinearity, the method of adaptive time integration and adequate selection of the details, and even the time integration method.

Some areas for further research on time integration and the step size selection are stated below:

1. Effects of viscous damping on the numerical stability of time integration methods are to be studied further.
2. The theory of numerical stability and its practical consideration are yet not well established, when the damping is not proportional.
3. The existing comments on integration step size selection need to be improved for more reliability, more rigorous supporting theory, and consideration of more issues, while preserving the simplicity.
4. Further investigation on step size selection, for implementation in nonlinear analyses, is essential.

5. More reliable still simple practical error controlling methods are to be developed and considered in seismic codes/standards. In this regard, the initiative of the code/standard of New Zealand is sincerely acknowledged.
6. Even for integration methods with numerical (artificial) damping, practical methods for selecting the parameters of the integration methods need to be developed.
7. The existing approaches for adaptive time stepping is involved in selection of parameters that are partly problem dependent. Further research for simplifications sounds essential.
8. A priori estimations do not exist for the computational cost of adaptive, as well as, nonlinear time integration analyses; accordingly, different from linear constant time-stepping analysis, the efficiencies are unclear, in the start of nonlinear or/and adaptive analyses. Further research is essential.
9. More adequate methods techniques and approaches are to be developed for time integration analysis of nonlinear systems, specifically to guarantee the simplicity, continuation, and sufficiency of accuracy, without high computational cost.
10. In view of the stochastic nature of earthquakes, the necessity to study structural systems seismic behaviour in many codes/standards, and the everyday more complexity and larger sizes of structural systems, efforts towards more efficient time history analysis and more reasonable selection of Δt are essential.

Acknowledgments The detailed comments of the reviewers who directly and indirectly caused many improvements in the chapter are sincerely appreciated. The author is also grateful to Prof. Fereydoon Arbabi, for his kind guidance, regarding the English of the chapter and Dr. Hamid Zafarani for his introducing a reference on seismology and directivity to the author. The feedbacks of Mr. George Papazafeiropoulos regarding different issues in the chapter is also sincerely acknowledged. Finally the efforts of the type-setting team, specifically Mrs. Hema Suresh and Mr. Mohammad Ali, and the kind attentions and guidance of the editors in different stages of this chapter's preparation are sincerely acknowledged and deeply appreciated.

References

1. Bathe KJ (1996) Finite element procedures. Prentice-Hall, USA
2. Belytschko T, Liu WK, Moran B (2000) Non-linear finite elements for continua and structures. Wiley, USA
3. Henrych J (1990) Finite models and methods of dynamics in structures. Elsevier, The Netherlands
4. Houbolt JC (1950) A recurrence matrix solution for the dynamic response of elastic aircraft. J Aeronaut Sci 17:540–550
5. Katona MG, Zienkiewicz OC (1985) A unified set of single step algorithms part 3: the beta-m method, a generalization of the Newmark scheme. Int J Numer Meth Eng 21:1345–1359
6. Soroushian A, Farjoodi J (2008) A unified starting procedure for the Houbolt method. Commun Numer Meth Eng 24:1–13

7. Hairer E, Wanner G (1996) Solving ordinary differential equations II: stiff and differential-algebraic problems. Springer, USA
8. Golub GH, Ortega JM (1992) Scientific computing and differential equations. Academic Press, USA
9. D'Souza AF, Garg VK (1984) Advanced dynamics: modeling and analysis. Prentice Hall, USA
10. Chopra AK (1995) Dynamics of structures: theory and application to earthquake engineering. Prentice-Hall, USA
11. Craig RR (1981) Structural dynamics: an introduction to computer methods. Wiley, USA
12. Hilber HM, Hughes TJR, Taylor RL (1977) Improved numerical dissipation for time integration algorithms in structural dynamics. Earthq Eng Struc 5:283–292
13. Chung J, Hulbert GM (1993) A time integration algorithm for structural dynamics with improved numerical dissipation: the generalized-α method. J Appl Mech-T ASME 60:371–375
14. Clough RW (1973) Numerical integration of equations of motion. Lectures on finite element methods in continuum mechanics, University of Alabama, USA
15. Wilson EL (1968) A computer program for the dynamic stress analysis of underground structures. Report No. 68-1, University of California, Berkeley, USA
16. Wilson EL, Farhoomand I, Bathe KJ (1973) Non-linear dynamic analysis of complex structures. Earthq Eng Struc 1:241–252
17. Bathe KJ, Wilson EL (1973) Stability and accuracy analysis of direct integration methods. Earthq Eng Struc 1:283–291
18. Zlatev Z, Berkowicz R, Prahm LP (1984) Implementation of a variable step size variable formula method in the time integration part of a code for treatment of long-range transport of air pollutants. J Comput Phys 55:278–301
19. Brüls O, Golinval JC (2006) The generalized-α method in mechatronic applications. Z Angew Math Phys 86:748–758
20. Erickson BA, Nordström J (2014) Stable, high order accurate adaptive schemes for long time, highly intermittent geophysics problems. J Comput Appl Math 271:328–338
21. Tang XW, Zhang XW, Uzuoka R (2015) Novel adaptive time stepping method and its application to soil seismic liquefaction analysis. Soil Dyn Earthq Eng 71:100–1013
22. Liu T, Li Q, Zhao C (2013) An efficient time-integration method for nonlinear dynamic analysis of solids and structures. Sci China: Phys, Mechan Astron 56:798–804
23. Eggl S, Dvorak R (2010) An introduction to common numerical integration codes used in dynamical astronomy. In: Dynamics of small solar system bodies and exoplanets. Springer, Germany, pp 431–480
24. Soroushian A, Saaed A, Arghavani M, Rajabi M, Sharifpour MM (2011) Two versions of the Wilson-θ time integration method. In: Proceedings of 10th biennial conference on vibration problems (ICoVP-2011), Prague, Czech Republic
25. Katsikadelis JT (2013) A new direct time integration method for the equations of motion in structural dynamics. Z Angew Math Phys 94:757–774
26. Bursi OS, He L, Bonelli A, Pegon P (2010) Novel generalized-α methods for interfield parallel integration of heterogeneous structural dynamic systems. J Comput Appl Math 234:2250–2258
27. Newmark NM (1959) A method of computation for structural dynamics. J Eng Mech-ASCE 85:67–94
28. Clough RW, Penzien J (1993) Dynamics of structures. McGraw-Hill, Singapore
29. Humar JL (1990) Dynamics of structures. Prentice-Hall, USA
30. Hughes TJR (1987) The finite element method: linear static and dynamic finite element analysis. Prentice-Hall, USA
31. Belytschko T, Hughes TJR (1983) Computational methods for transient analysis. Elsevier, The Netherlands
32. Wood WL (1990) Practical time stepping schemes. Oxford, USA

33. Geradin M, Rixen DJ (2015) Mechanical vibrations theory and applications to structural dynamics. Wiley, USA
34. Shimada M, Masuri S, Tamma KK (2015) A novel design of an isochronous integration [i Integration] framework for first/second order multidisciplinary transient systems. Int J Numer Meth Eng 102:867–891
35. Akbarzadeh-Sharbaf A, Giannacopoulos DD (2013) Finite-element time-domain solution of the vector wave equation in doubly dispersive media using Möbius transformation technique. IEEE T Antenn Propag 61:4158–4166
36. Krenk S (2007) Time integration in solid mechanics. In: Proceedings of 20th Nordic seminar on computational mechanics, Chalmers Tkniska Hoskola, Sweden
37. Artuzi WA (2005) Improving the Newmark time integration scheme in finite element time domain methods. IEEE Microw Wirel Co 15:898–900
38. Erlicher S, Bonaventura L, Bursi OS (2001) The analysis of the Generalized-α method for nonlinear dynamic problems. Comput Mech 28:83–104
39. Wriggers P (2002) Computational contact mechanics. Wiley, USA
40. Hughes TJR, Pister KS, Taylor RL (1979) Implicit-explicit finite elements in nonlinear transient analysis. Comput Meth Appl Mech Eng 17(18):159–182
41. Gavin H (2001) Structural dynamics. Class Notes CE 283, Duke University, USA
42. Soroushian A (2003) New methods to maintain responses 'convergence and control responses' errors in the analysis of nonlinear dynamic models of structural systems. PhD dissertation, University of Tehran, Iran (in Persian)
43. Soroushian A (2011) With proper convergence towards error evaluation in nonlinear analyses. In: Proceedings of 11th US national congress on computational mechanics (11th USNCCM), Minneapolis, USA
44. Allgower EL, Georg K (1980) Numerical continuation methods, an introduction. Springer, USA
45. Cook RD, Malkus DS, Plesha ME, Witt RJ (2002) Concepts and applications of finite element analysis. Wiley, USA
46. Crisfield MA, Jelenic G, Mi Y, Zhong HG, Fan Z (1997) Some aspects of the non-linear finite element method. Finite Elem Anal Des 27:19–40
47. KiaPing Y (2008) A new family of generalized-alpha time integration algorithms without overshoot for structural dynamics. Earthq Eng Struc 37:1389–1409
48. Krenk S (2006) State-space time integration with energy control and fourth-order accuracy for linear dynamic systems. Int J Numer Meth Eng 65:595–619
49. Soroushian A (2008) A technique for time integration with steps larger than the excitation steps. Commun Numer Meth Eng 24:2087–2111
50. Zhou KK, Tamma KK (2004) A new unified theory underlying time dependent first-order systems: a prelude to algorithms by design. Int J Numer Meth Eng 60:1699–1740
51. Monro DM (1987) Fortran 77. Edward Arnold, UK
52. Paultre P (2010) Dynamics of structures. Wiley, USA
53. Young WC (1989) Roark's formulas for stress and strain, 6th edn. McGraw-Hill, USA
54. Gaylord EH, Gaylord CN (1979) Structural engineering handbook, 2nd edn. McGraw-Hill, USA
55. Soroushian A, Wriggers P, Farjoodi J (2009) Asymptotic upper-bounds for the errors of Richardson extrapolation with practical application in approximate computations. Int J Numer Meth Eng 80:565–595
56. Gear CW (1971) Numerical initial value problems in ordinary differential equations. Prentice-Hall, USA
57. Apostol TM (1967) Calculus, vol I. Wiley, USA
58. Spiegel MR (1971) Advanced mathematics for engineers and scientists. McGraw-Hill, USA
59. Henrici P (1962) Discrete variable methods in ordinary differential equations. Prentice-Hall, USA
60. Srikwerda JC (1989) Finite difference schemes and partial differential equations. Wadsworth & Books/Cole, USA
61. Lambert JD (1973) Computational methods in ordinary differential equations. Wiley, UK
62. Nau JM (1983) Computation of inelastic spectra. J Eng Mech-ASCE 109:279–288

63. Soroushian A, Wriggers P, Farjoodi J (2013) Practical integration of semi-discretized nonlinear equations of motion: proper convergence for systems with piecewise linear behaviour. J Eng Mech-ASCE 139:114–145
64. Soroushian A, Farjoodi J (2002) An improvement in nonlinear analysis. In: Proceedings of 15th engineering mechanics division conference, ASCE (EM2002), New York, USA
65. Mahin SA, Lin J (1983) Construction of inelastic response spectra for single degree-of-freedom systems. Report UCB/EERC-83/17, Earthquake Engineering Research Center (EERC), University of California, Berkeley, USA
66. Rossi DF, Ferreira WG, Mansur WJ, Calenzani AFG (2014) A review of automatic time-stepping strategies on numerical time integration for structural dynamic analysis. Eng Struct 80:118–136
67. Ralston A, Rabinowitz P (1978) First course in numerical analysis. McGraw-Hill, USA
68. Noble B, Daniel JW (1977) Applied linear algebra. Prentice Hall, USA
69. Soroushian A (2010) Pseudo convergence and its implementation in engineering approximate computations. In: Proceedings of 4th international conference from scientific computing to computational engineering (IC-SCCE 2010), Athens, Greece
70. Soroushian A (2014) Equivalence between convergence and pseudo convergence when algorithmic parameters do not change geometrically. In: Proceedings of 6th international conference from scientific computing to computational engineering (IC-SCCE 2014), Athens, Greece
71. Penry SN, Wood WL (1985) Comparison of some single-step methods for the numerical solution of the structural dynamic equation. Int J Numer Meth Eng 21:1941–1955
72. Soroushian A, Wriggers P, Farjoodi J (2005) On practical integration of semi-discretized nonlinear equations of motion. Part 1: reasons for probable instability and improper convergence. J Sound Vib 284:705–731
73. Soroushian A, Wriggers P, Farjoodi J (2015) From the notions of nonlinearity tolerances towards a deficiency in commercial Transient Analysis softwares and its solution. In: Proceedings of 5th ECCOMAS thematic conference on computational methods in structural dynamics and earthquake engineering (COMPDYN 2015), Corfu, Greece
74. Xie YM, Steven GP (1994) Instability, chaos, and growth and decay of energy of time-stepping schemes for nonlinear dynamic equations. Commun Numer Meth Eng 10:393–401
75. Low KH (1991) Convergence of the numerical methods for problems of structural dynamics. J Sound Vib 150:342–349
76. Rashidi S, Saadeghvaziri MA (1997) Seismic modeling of multispan simply supported bridges using Adina. Int J Comput Struct 64:1025–1039
77. Soroushian A, Eshghi S (2006) The importance of appropriate selection of step size and nonlinearity tolerance in time history analyses. Report No. mlz-16/143, International Institute of Earthquake Engineering and Seismology (IIEES), Iran (in Persian)
78. Farjoodi J, Soroushian A (2003) Shortcomings in numerical dynamic analysis of nonlinear systems. Nashriyeh Fanni 37:269–281 (in Persian)
79. Soroushian A, Kermani AM, Chavan K, Ivanian A (2004) Responses' convergence for time integration analyses involved in linearly-elastic/perfectly-plastic behaviour and impact. In: Proceedings of 6th world conference on computational mechanics (WCCM VI in conjunction with APCOM'04), Beijing, China
80. Amiri S (2015) On the performance of the existing recommendations for time step size selection in nonlinear analysis of conventional buildings. M.Sc. dissertation, International Institute of Earthquake Engineering and Seismology (IIEES), Iran (in Persian)
81. Richtmyer RD, Morton KW (1967) Difference methods for initial value problems. Wiley, USA
82. Chen WE (2000) Structural stability: from theory to practice. Elsevier, USA
83. Poorlatifi S (2008) A method to recognize numerical instability from physical instability. M. Sc. dissertation, International Institute of Earthquake Engineering and Seismology (IIEES), Iran (in Persian)
84. Soroushian A (2015) Development of an algorithm and computer program to evaluate the numerical stability and consistency of new time integration methods. Report 7517, International Institute of Earthquake Engineering and Seismology (IIEES), Iran (in Persian)

85. Fox L, Goodwin ET (1949) Some new methods for the numerical integration of ordinary differential equations. Math Proc Cambridge 45:373–388
86. Li Y, Wu B, Ou J (2006) Stability of average acceleration method for structures with nonlinear damping. Earthq Eng Eng Vib 5:87–92
87. Giese G (2005) Nonlinear stability analysis for the method of transport for the elastic-plastic wave equation. Siam J Numer Anal 42:2569–2589
88. Kardestuncer H (1987) Finite element handbook. McGraw Hill, USA
89. Paz M (1991) Structural dynamics: theory and application, 3rd edn. Van Nostrand Reinhold, USA
90. BHRC (2015) Iranian code of practice for seismic resistant design: standard no. 2800–. Building and Housing Research Center, Iran (in Persian)
91. Zhongzhi S, Naeim F (2001) The seismic design handbook. Kluwer, USA
92. Rezaee-Pazhand M, Moayeddian M, Khajeh-Karomoddin A (2000) Seismic analysis of structures. Emam Reza University, Iran (in Persian)
93. Bargi K (1994) Principles of earthquake engineering. Majed, Iran (in Persian)
94. Basoz NI, Kiremidjian AS, King SA, Law KH (1999) Statistical analysis of bridge damage data from the 1994 Northridge, CA California. Earthq Spectra 15:25–53
95. Ruge P (1999) A priori error estimation with adaptive time-stepping. Commun Numer Meth Eng 15:479–491
96. Soroushian A, Farjoodi J (2002) Error control for step-by-step solution of linear semi-discrete equations of motion. In: Proceedings of 5th European conference on structural dynamics, Eurodyn2002, Munich, Germany
97. Soroushian A, Farjoodi J (2003) More reliable responses for time integration analyses. Struct Eng Mech 16:219–240
98. McNamara JF (1974) Solution schemes for problems of nonlinear structural dynamics. J Press Vess-T ASME 96:149–155
99. NZS (2004) Structural design actions, Part 5: earthquake actions-New Zealand. New Zealand Standard, New Zealand
100. Soroushian A, Farjoodi J, Mehrazin H (2015) A new measure for the nonlinear behaviour of piece-wisely linear structural dynamic models. In: Proceedings of the 13th International Congress on Sound and Vibration (ICSV13), Vienna, Austria
101. Chen CC, Robinson AR (1993) Improved time-history analysis for structural dynamics. I: treatment of rapid variation of excitation and material nonlinearity. J Eng Mech-ASCE 119:2496–2513
102. Collatz L (1960) The numerical treatment of differential equations. Springer, Germany
103. Fish J, Belytschko Y (2009) A first course in finite elements. Wiley, UK
104. Soroushian A (2012) On the adequacy of integration step sizes recommended for nonlinear time integration. In: Proceedings of 5th international conference from scientific computing to computational engineering (5th IC-SCCE), Athens, Greece
105. Soroushian A (2010) Proper convergence a concept new in science and important in engineering. In: Proceedings of 4th international conference from scientific computing to computational engineering (IC-SCCE 2010), Athens, Greece
106. da Costa Villar G, Menezes JC, Donadon MV (2012) Accuracy and numerical stability of direct time integration schemes applied to rotordynamics. In: Proceedings of 12th Pan-American congress of applied mechanics (PACAM XII), Port of Spain, Trinidad
107. Kpodzo K, Fourment L, Lasne P, Montmitonnet P (2016) An accurate time integration scheme for arbitrary rotation motion: application to metal forming formulation. Int J Mater Form 9:71–84
108. Bonelli A, Bursi OS (2004) Generalized-α methods for seismic structural testing. Earthq Eng Struct D 33:1067–1102
109. Bis I (2002) Criteria for earthquake resistant design of structures, Part 1. Bureau of Indian Standards, India
110. Standard DI, Criteria for earthquake resistant design of structures (Part 4) industrial stack like structures. Bureau of Indian standards, India

111. Standard B (2004) Eurocode 8: design of structures for earthquake resistance-part 1: general rules, seismic actions and rules for buildings, UK
112. Code TE (2007) Specification for buildings to be built in seismic zones. Ministry of Public Works and Settlement, Government of Republic of Turkey, Turkey
113. Code GS (2000) Earthquake resistant design of structures. Earthquake Planning and Protection Organisation, Greece
114. Standard C (2001) Code for seismic design of buildings [GB 50011-2001]. China Architectural and Building Press, China
115. Structural design actions part 5: earthquake actions–New Zealand commentary (Supplement to NZS 1170.5:2004) (2004) NZS 1170.5 Supp 1: 2004. Standards New Zealand, Wellington, New Zealand
116. American Society of Civil Engineers (2010) Minimum design loads for buildings and other structures. Amer Society of Civil Engineers, USA
117. The Building Standard Law of Japan (2004)
118. MOC-2008 (2008) Manual de diseño de obras civiles. Diseño por sismo. Recomendaciones y Comentarios. Instituto de Investigaciones Eléctricas, Comisión Federal de Electricidad, Mexico (in Spanish)
119. Tena-Colunga A, Mena-Hernández U, Pérez-Rocha L, Avilés J, Ordaz M, Vilar J (2009) Updated seismic design guidelines for model building code of Mexico. Earthq Spectra 25:869–898
120. Official Chilean Standard Nch 433 of 96 (1996) Earthquake resistant design of buildings. Instituto Nacional de Normalización INN, Chile (in English)
121. Rojas F, Lew M, Naeim F (2010) An overview of building codes and standards in Chile at the time of the 27 February 2010 Offshore Maule, Chile earthquake. Struct Des Tall Spec 19:853–865
122. Code-Part SD (2006) I: design rules for buildings. P100-1/2006, MTCT, Bucharest, Romania
123. Architecture Buildings Research Institute (ABRI) (2005) Recommended provisions for building seismic regulations. ABRI, Taiwan (in Chinese)
124. R.O.C. Construction and Planning Agency (2005) Seismic Design Code for Buildings in Taiwan. Ministry of the Interior, R.O.C, Taiwan
125. Mavroeidis GP, Papageorgiou AS (2003) A mathematical representation of near-fault ground motions. B Seismol Soc Am 93:1099–1131
126. Paz R (1994) International handbook of earthquake engineering: codes, programs, and examples. Chapman & Hall, USA
127. Ilie S, Söderlind G, Corless RM (2008) Adaptivity and computational complexity in the numerical solution of ODEs. J Complexity 341–361
128. Wanxie Z, Zhuang X, Zhu J (1998) A self-adaptive time integration algorithm for solving partial differential equations. Appl Math Comput 89:295–312
129. Lee SH, Hsieh SS (1990) Expedient implicit integration with adaptive time stepping algorithm for nonlinear transient analysis. Comput Meth Appl Mech Eng 81:151–172
130. Ilie S, Jackson KR, Enright WH (2015) Adaptive time-stepping for the strong numerical solution of stochastic differential equations. Numer Algorithms 68:791–812
131. Yaghoubi V, Khorsand Vakilzadeh M, Abrahamsson T (2014) Efficient simulation method for nonlinear structures: methodology and stability consideration. In: Proceedings of 9th international conference on structural dynamics & EURODYN 2014, Porto, Portugal
132. Liu Y, Yang H, Jiang C, Yang C (2016) A scalable fully implicit method with adaptive time stepping for unsteady compressible inviscid flows. Int. J. Comput. Struct. 176:1–12
133. Ammanagi S, Manohar CS (2016) Adaptive time stepping in pseudo-dynamic testing of earthquake driven structures. B Earthq Eng 1–28
134. Papazafeiropoulos G, Plevris V, Papadrakakis M (2016) A generalized algorithm framework for non-linear structural dynamics. B Earthq Eng 1–31
135. Soroushian A (2011) Direct time integration with steps larger than the steps by which the excitations are digitized. Report 7510, International Institute of Earthquake Engineering and Seismology (IIEES), Iran (in Persian)

136. Askes H, Nguyen DC, Tyas A (2011) Increasing the critical time step: micro-inertia, inertia penalties and mass scaling. Comput Mech 47:657–667
137. Chang SY (2002) Integrated equations of motion for direct integration methods. Struct Eng Mech 13:569–589
138. Sabzei A, Reziakolaei AY, Soroushian A (2013) On more versatility for an integration step size enlargement technique in time integration analysis. In: Proceedings of 4th ECCOMAS thematic conference on computational methods in structural dynamics and earthquake engineering (COMPDYN 2013), Kos Island, Greece
139. Azad S (2015) A study on accelerating time history analysis of bridges. M.Sc. dissertation, International Institute of Earthquake Engineering and Seismology (IIEES), Iran (in Persian)
140. Soroushian A (2010) On the performance of a conventional accuracy controlling method applied to linear and nonlinear structural dynamics. In: Proceedings of 17th international congress on sound and vibration (ICSV17), Cairo, Egypt
141. Soroushian A, Aziminejad A (2011) A more efficient seismic analysis of tall buildings by implementing a recently proposed technique. In: Proceedings of 6th international conference seismology and earthquake engineering (SEE6), Tehran, Iran
142. Bahar O, Ramezani S (2011) Faster time integration analysis for building structures subjected to 3-component earthquakes. In: Proceedings of 3rd III ECCOMAS thematic conference on computational methods in structural dynamics and earthquake engineering (COMDYN 2011), Corfu, Greece
143. Nateghi F, Yakhchalian M (2011) On less computational costs for analysis of silos seismic behaviors by time integration. In: Proceedings of 3rd ECCOMAS thematic conference on computational methods in structural dynamics and earthquake engineering (COMPDYN 2011), Corfu, Greece
144. Nateghi F, Yakhchalian M (2011) An investigation into the effectiveness of a technique proposed for reducing computational cost of time integration in the analysis of silos seismic behaviors. In: Proceedings of 11th US national congress on computational mechanics (USNCCM 2011), Minneapolis, USA
145. Soroushian A, Saaed A, Arghavani M, Rajabi M, Sharifpour MM (2011) Less computational costs in the analysis of reservoirs seismic behaviours by time integration. In: Proceedings of 10th biennial conference on vibration problems (ICoVP-2011), Prague, Czech Republic
146. Soroushian A (2011) On the performance of a recent technique for more efficient time integration in severe seismic conditions. In: Proceedings of 1st international conference on advances in structural engineering and mechanics (ASEM'11), Seoul, South Korea
147. Papadrakakis M, Fragiadakis M, Plevris V (2013) Computational methods in earthquake engineering. Springer, USA
148. Bastami M (2014) A technique for more efficient time integration applied to seismic analysis of power substation equipment. In: Proceedings of 11th world congress on computational mechanics (WCCM XI), Barcelona, Spain
149. Sabzei A (2013) On the performance of a recent technique for seismic analyses computational cost reduction when applied to buildings structural systems. M.Sc. dissertation, International Institute of Earthquake Engineering and Seismology (IIEES), Iran (in Persian)
150. Reziakolaei AY, Sabzei A, Soroushian A (2013) On the performance of a structural analysis cost reduction technique when applied to residential buildings. In: Proceedings of 4th ECCOMAS conference on computational methods in structural dynamics and earthquake engineering (COMPDYN 2013), Kos Island, Greece
151. Garakaninezhad A, Moghadas RK (2015) On the performance of a technique to accelerate time integration when applied to space structures analyses. In: Proceedings of 5th ECCOMAS thematic conference on computational methods in structural dynamics and earthquake engineering (COMPDYN 2013), Kos, Greece, June
152. Hadad AA (2015) Reducing computational costs in time integration analyses of buildings with irregularities in height because of mass. M.Sc. dissertation, International Institute of Earthquake Engineering and Seismology (IIEES), Iran (in Persian)

153. Soroushian A, Jahani Mehrnoosh A, Zarabimanesh Y, Ghondaghsaz MH, Baiani A, Zakizade A (2016) On the performance of a computational cost reduction technique when applied to cooling towers transient analysis. In: Proceedings of 7th European congress on computational methods in applied sciences and engineering (ECCOMAS VII), Crete Island, Greece
154. Zarabimanesh Y, On a recent technique for reducing the computational costs in time integration analyses when applied to the analysis of Milad Tower. M.sc. dissertation, International Institute of Earthquake Engineering and Seismology (IIEES), Iran (in Persian) (to be defended in 2017)
155. Soroushian A (2012) On the accuracy of accelerations in general implementation of a recently proposed seismic analysis computational cost reduction technique. In: Proceedings 5th international conference from scientific computing to computational engineering (5th IC-SCCE), Athens, Greece
156. Soroushian A, Garakaninezhad A, Yahyapour A, Asgarihadad A (2014) Performance of a computational cost reduction technique in lengthy time interval analyses. In: Proceedings of 11th world conference on computational mechanics (WCCM XI), Barcelona, Spain
157. Soroushian A, Farshadmanesh P, Azad S (2015) On the essentiality of techniques to enlarge analysis steps in time integration against digitized excitations. Int J Earthq Eng Seismolog (JSEE) 17:43–60
158. Majidi H (2015) Simplification of structural dynamic analyses by combining some existing approaches simplifying the records, the systems, and the analysis methods. M.Sc. dissertation, Islamic Azad University, South Tehran branch, Iran (in Persian)
159. Soroushian A (2015) A general practical procedure for a recently proposed seismic analysis computational cost reduction technique. In: Proceedings of 7th international conference on seismology and earthquake engineering (SEE7), Tehran, Iran
160. Saaed A (2012) A technique for faster seismic analysis of MDOF structural systems. M.sc. dissertation, International Institute of Earthquake Engineering and Seismology (IIEES), Tehran, Iran (in Persian)
161. Soroushian A (2015) A new excitation step size enlargement technique for seismic analyses. In: Proceedings of 5th ECCOMAS thematic conference on computational methods in structural dynamics and earthquake engineering (COMPDYN 2015), Crete, Greece
162. Soroushian A, Hosseini M, Khalkhali SMH (2016) On the frequency content of errors originated in a time integration computational cost reduction technique. In: Proceedings of 7th European congress on computational methods in applied sciences and engineering (ECCOMAS VII), Crete Island, Greece
163. Zakizadeh A Investigation on the role of the parameter representing the influence of the eliminated excitation stations in the performance of a transient analysis computational cost reduction technique. M.Sc. dissertation, International Institute of Earthquake Engineering and Seismology (IIEES), Iran (in Persian) (to be defended in 2016 or 2017)
164. Hosseini M, Mirzaei I (2012) Simplification of earthquake accelerograms for rapid time history analysis based on the impulsive load concept. In: Proceedings of the 10th international congress on computational mechanics, (WCCM X), Sao Paulo, Brazil
165. Soroushian A (2009) Time integration with step sizes less depending on the steps of excitation: I. SDOF systems. Report 7509-P89-1, International Institute of Earthquake Engineering and Seismology (IIEES), Iran (in Persian)
166. Rajabi M (2011) A new method for less expensive seismic analysis of SDOF structural systems. M.Sc. dissertation, International Institute of Earthquake Engineering and Seismology (IIEES), Iran (in Persian)
167. Sharifpour MM (2013) A method for faster time integration analysis of systems subjected to ground strong motions. M.Sc. dissertation, Islamic Azad University, West Azerbayjan Science and Research Branch, Iran (in Persian)
168. Zienkiewicz OC (2000) Achievements and some unsolved problems of the finite element method. Int J Numer Meth Eng 47:9–28

Seismic Fragility Analysis of Faulty Smart Structures

Yeesock Kim and Jong-Wha Bai

Abstract In this chapter, seismic vulnerability of smart structures is assessed using fragility analysis framework. The fragility analysis framework is effective to evaluate the performance and the vulnerability of structures under a variety of earthquake loads. To demonstrate the effectiveness of the seismic fragility analysis framework, a three-story steel frame building employing the nonlinear smart damping system is selected as a case study structure. To investigate the impact of sensor failures, various sensor damage case scenarios are considered. The seismic capacity of the smart building is determined based on the typical structural performance levels used in the literature. The unknown parameters for the seismic demand models are estimated using a Bayesian updating algorithm. Finally, the fragility curves of the smart structures under a variety of sensor damage cases are compared. It is proved from the extensive simulations that the proposed seismic fragility analysis framework is very effective in estimating the control performance of smart structures with sensor faults.

1 Introduction

In recent years, great attention has been shown to the smart structures in the society of structural engineering because smart control technology can increase the structural vibration performance without adding too much structural mass [5, 14, 15, 25, 29, 31–34, 41, 42]. Numerous studies on smart structures have tended to center around the question of how to develop effective control algorithms. However, structural reliability of smart structures has not been researched much. In particular, relatively few studies have been devoted to the analysis of the seismic vulnerability of smart control systems [10, 13, 47].

Y. Kim (✉) · J.-W. Bai
Civil Engineering, California Baptist University, Riverside, CA, USA
e-mail: yekim@calbaptist.edu; controlga@gmail.com

M. Papadrakakis et al. (eds.), *Computational Methods in Earthquake Engineering*,
Computational Methods in Applied Sciences 44,
DOI 10.1007/978-3-319-47798-5_11

In designing smart control systems, it is important to bear in mind that the control performance can degrade when sensors and/or actuators have faults. However, the systematic evaluation of seismic risk of smart structures with faulty sensor/actuators is still vastly underexplored. Choe and Baruh [16] proposed the use of the modal observers to the sensor damage detection within a linear time-invariant (LTI) dynamic system. The modal observer-based sensor fault diagnosis method needs an accurate mathematical model for the LTI systems. Plus, the approach is strictly limited in scope: linear systems only. On the contrary, neural network algorithms have also been applied to linear dynamic systems for sensor damage detection without developing an accurate analytical model [6, 39]. Sharifi et al. [45] developed an effective diagnosis approach for detecting and isolating faults of sensors and smart dampers in a nonlinear time-varying dynamic system.

Therefore, the present chapter is intended to propose a systematic analysis framework for seismic fragility evaluation of smart structures with sensor faults under a variety of seismic excitations. It is expected that the proposed fragility analysis framework may lead to better understanding of the complex behavior of smart structures. The improved understanding can be an instrument of much more effective control system design. In this study, a performance-based design method will be employed to conduct fragility analyses. The fragility analysis framework will be implemented, based on the functionality of the smart building and the seismic risk [23, 24]. It is quite clear that sensor failures in smart structures should be evaluated in a systematic way, since the seismic resisting performance of smart structures can be improved.

This chapter is organized as follows: Sect. 2 presents an analytical model for a case study smart building structure equipped with a magnetorheological (MR) damper; the fundamentals of seismic fragility analysis are described briefly in Sect. 3; seismic fragility curves are developed to assess seismic vulnerability for the case study building-MR damper systems with healthy, fully damaged, and partially damaged sensing units in Sect. 4; and concluding remarks are given in Sect. 5.

2 Smart Building Description and Analytical Model

Smart systems have been adopted from many engineering fields because the performance of structural/mechanical systems can be improved without either significantly increasing the mass of the structure or adding high costs for control power [30, 35, 43]. They may be called intelligent structures, adaptive structures, active structures, and the related technologies adaptronics, structronics, etc. [26]. In general, smart structures are developed through the integration of smart materials-based actuators/sensors, control units, signal processing units and a structural system. The smart materials might include piezoelectrics, shape memory alloys, electrostrictive and magnetostrictive materials, polymer gels, etc. Smart material-based actuators (or smart damping devices) have been proposed for large-scale civil structures because semi-active control strategies combine favorable

features of both active and passive control systems: reliable operation, low power consumption, low manufacturing cost, etc. Semi-active control devices include: variable-orifice dampers, variable-stiffness devices, variable-friction dampers, controllable-fluid dampers, shape memory alloy actuators, piezoelectrics, etc. [25, 41, 42].

2.1 Building Equipped with MR Dampers

In this section, a three-story building structure employing an MR damper is presented for use in the fragility analyses. The MR damper is installed on the 1st floor through a chevron brace as shown in Fig. 1 [2, 37].

The introduction of the MR damping device creates a nonlinear building-MR system, and the associated equations of motion are given by

$$\mathbf{M}\ddot{\mathbf{x}} + \mathbf{C}\dot{\mathbf{x}} + \mathbf{K}\mathbf{x} = \mathbf{\Gamma}\mathbf{f}_{\mathbf{MR}} - \mathbf{M}\mathbf{\Lambda}\ddot{w}_g \tag{1}$$

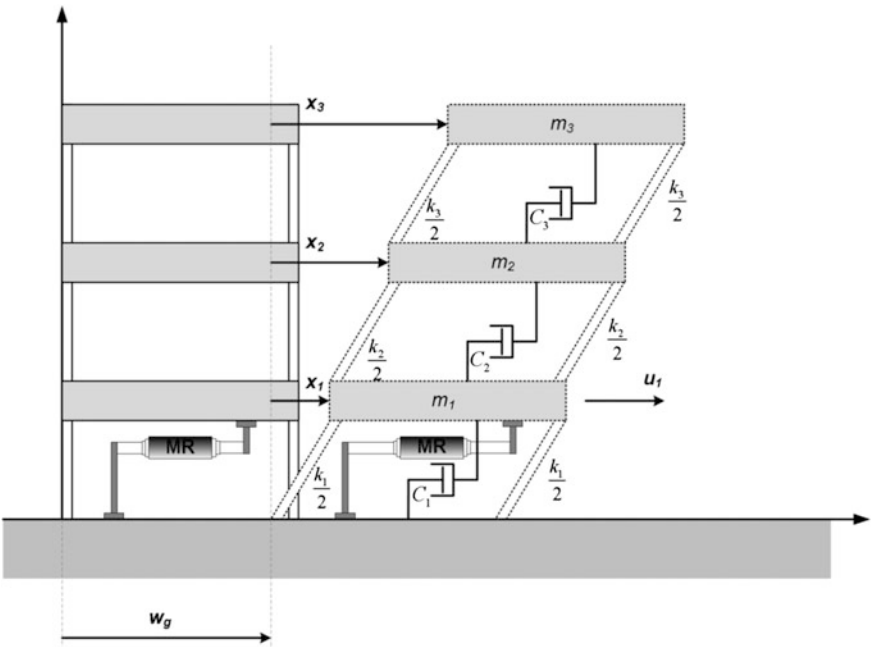

Fig. 1 Integrated building structure-MR damper system

In Eq. (1), the system matrices are given by

$$\mathbf{M} = \begin{bmatrix} m_1 & 0 & 0 \\ 0 & m_2 & 0 \\ 0 & 0 & m_3 \end{bmatrix} \tag{2}$$

$$\mathbf{C} = \begin{bmatrix} c_1 + c_2 & -c_2 & 0 \\ -c_2 & c_2 + c_3 & -c_3 \\ 0 & -c_3 & c_3 \end{bmatrix} \tag{3}$$

$$\mathbf{K} = \begin{bmatrix} k_1 + k_2 & -k_2 & 0 \\ -k_2 & k_2 + k_3 & -k_3 \\ 0 & -k_3 & k_3 \end{bmatrix} \tag{4}$$

$$\mathbf{f_{MR}}(t, x_1, \dot{x}_1, v_1) = \begin{bmatrix} f_{\mathrm{MR}}(t, x_1, \dot{x}_1, v_1) \\ 0 \\ 0 \end{bmatrix} \tag{5}$$

is the MR damper force matrix. The following notation is observed: $\ddot{w}_g$ denotes the ground acceleration; m_{i} is the mass of the ith floor; k_{i} is the stiffness of the ith floor columns; c_{i} is the damping of the ith floor columns; $\mathbf{x}$, $\dot{\mathbf{x}}$, and $\ddot{\mathbf{x}}$ are the displacement, velocity, and acceleration relative to the ground, respectively; x_1 and $\dot{x}_1$ are the displacement and the velocity at the 1st floor level, respectively, relative to the ground; v is the voltage level to be applied; and $\mathbf{\Gamma}$ and $\mathbf{\Lambda}$ are location vectors of control forces and disturbance signal, respectively. This second-order differential equation can be converted into standard state-space form

$$\begin{aligned} \dot{\mathbf{z}} &= \mathbf{A}\mathbf{z} + \mathbf{B}\mathbf{f_{MR}} - \mathbf{E}\ddot{w}_g \\ \mathbf{y} &= \mathbf{C}\mathbf{z} + \mathbf{D}\mathbf{f_{MR}} + \mathbf{n} \end{aligned} \tag{6}$$

$$\mathbf{A} = \begin{bmatrix} \mathbf{0} & \mathbf{I} \\ -\mathbf{M}^{-1}\mathbf{K} & -\mathbf{M}^{-1}\mathbf{C} \end{bmatrix} \tag{7}$$

$$\mathbf{B} = \begin{bmatrix} \mathbf{0} \\ \mathbf{M}^{-1}\mathbf{F} \end{bmatrix} \tag{8}$$

$$\mathbf{C} = \begin{bmatrix} \mathbf{I} & \mathbf{0} \\ \mathbf{0} & \mathbf{I} \\ -\mathbf{M}^{-1}\mathbf{K} & -\mathbf{M}^{-1}\mathbf{C} \end{bmatrix} \tag{9}$$

$$\mathbf{D} = \begin{bmatrix} \mathbf{0} \\ \mathbf{0} \\ \mathbf{M}^{-1}\mathbf{F} \end{bmatrix} \tag{10}$$

$$\mathbf{E} = \begin{bmatrix} \mathbf{0} \\ \mathbf{F} \end{bmatrix} \tag{11}$$

$$\mathbf{F} = \begin{bmatrix} -1 & 1 & 0 \\ 0 & -1 & 1 \\ 0 & 0 & -1 \end{bmatrix} \tag{12}$$

The dynamic properties of the three-story building structure are adopted from a scaled model [19] of a prototype building structure: the mass of each floor $m_1 = m_2 = m_3 = 98.3$ kg; the stiffness of each story $k_1 = 516{,}000$ N/m, $k_2 = 684{,}000$ N/m, and $k_3 = 684{,}000$ N/m; and the damping coefficient of each floor $c_1 = 125$ Ns/m, $c_2 = 50$ Ns/m and $c_3 = 50$ Ns/m. For this case study, SD-1000 MR damper is considered, and its parameters are given in Spencer et al. [46].

2.2 Magnetorheological (MR) Damper

Magnetorheological (MR) damper, one of the controllable-fluid dampers, has attracted attention from civil engineering in recent years because it has many attractive characteristics such as reliable operation and low power consumption [3]. In general, an MR damper consists of a hydraulic cylinder, magnetic coils, and MR fluids that consist of micron-sized magnetically polarizable particles floating within oil-type fluids as shown in Fig. 2.

To fully use the best features of the MR damper, a mathematical model that portrays the nonlinear behavior of the MR damper has to be developed first. However, this is challenging because the MR damper is a highly nonlinear hysteretic device. As shown in Fig. 3, Spencer et al. [46] proposed a modified version of the Bouc-Wen model

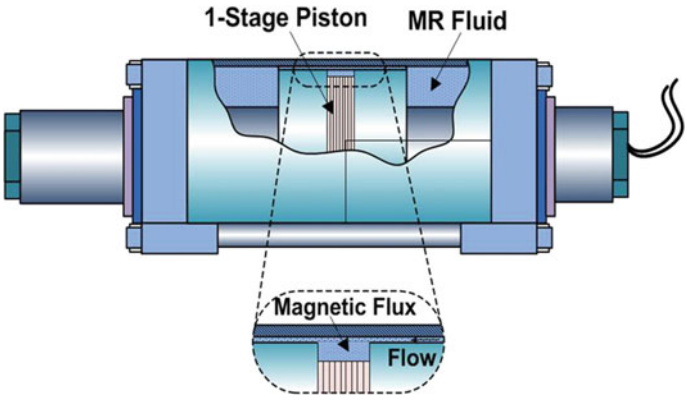

Fig. 2 Schematic of an MR damper

$$f_{\mathrm{MR}} = c_1\dot{y} + k_1(x - x_0) \tag{13}$$

$$\dot{z}_{\mathrm{BW}} = -\gamma|\dot{x} - \dot{y}|z_{\mathrm{BW}}|z_{\mathrm{BW}}|^{n-1} - \beta(\dot{x} - \dot{y})|z_{\mathrm{BW}}|^{n} + A(\dot{x} - \dot{y}) \tag{14}$$

$$\dot{y} = 1/(c_0 + c_1)\{\alpha z_{\mathrm{BW}} + c_0\dot{x} + k_0(x - y)\} \tag{15}$$

$$\alpha = \alpha_{\mathrm{a}} + \alpha_{\mathrm{b}}u \tag{16}$$

$$c_1 = c_{1\mathrm{a}} + c_{1\mathrm{b}}u \tag{17}$$

$$c_0 = c_{0\mathrm{a}} + c_{0\mathrm{b}}u \tag{18}$$

$$\dot{u} = -\eta(u - v) \tag{19}$$

where z_{BW} and α, called evolutionary variables, describe the hysteretic behavior of the MR damper; c_0 is the viscous damping parameter at high velocities; c_1 is the viscous damping parameter for force roll-off at low velocities; k_0 controls the stiffness at large velocities; k_1 represents the accumulator stiffness; the x_0 is the initial displacement of spring with stiffness k_1, γ, β and A are adjustable shape parameters of the hysteresis loops, i.e., the linearity in the unloading and the transition between pre-yielding and post-yielding regions; v and u are input and output voltages of a first-order filter, respectively; and η is the time constant of the first-order filter.

Note that nonlinear phenomena occur when the highly nonlinear MR dampers are applied to structural systems for efficient energy dissipation [1, 4, 40]. Such an integrated system behaves nonlinearly although the structure itself is usually assumed to remain linear [17, 36]. In what follows, the equations of motion for a building structure employing MR dampers are described.

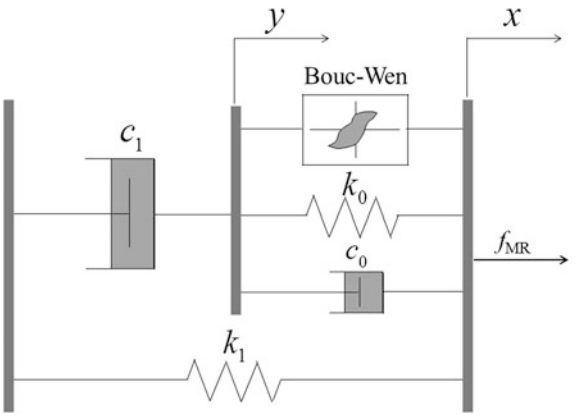

Fig. 3 Bouc-Wen model of the MR damper

2.3 Smart Control Algorithm

In the MR damper applications, the development of appropriate control algorithms has an impact on the performance of smart control systems [5, 11, 27, 31]. Effective smart control algorithms that have been commonly used for hazard mitigation of civil structures include modern control theory such as linear quadratic Gaussian (LQG) [14, 15] and intelligent controls such as fuzzy logic [29, 32, 33, 44] and neuro/emotional controls [28, 34]. In this study, H_2/LQG algorithm is used to implement controllers into the case study smart building model as shown in Fig. 4.

H_2/LQG algorithm consists of two components: Linear Quadratic Regulator (LQR) and Kalman filter. LQR is an optimization problem that finds control input signals **u**(t) to minimize a quadratic performance criterion or cost function defined in the following equation

$$J = \lim_{T\to\infty} \frac{1}{2T} E\left\{ \int_{-T}^{T} \left[\mathbf{x}^T \mathbf{Q}\mathbf{x}(t) + \mathbf{u}^T \mathbf{R}\mathbf{u}(t)\right] dt \right\} \tag{20}$$

where **Q** and **R** should be positive semi-definite state weighting matrix and positive definite control weighting matrix, respectively; T is the time; and E denotes the expected value. The full state feedback gain matrix **K** is found from

$$\mathbf{u} = -\mathbf{K}\hat{\mathbf{x}} \tag{21}$$

where $\hat{\mathbf{x}}$ is the Kalman estimate of the state vector, and **K** is given by

$$\mathbf{K} = \mathbf{R}^{-1}\mathbf{B}^T\mathbf{P} \tag{22}$$

where **B** is the input matrix (Eq. 8), and **P** denotes the solution of the matrix Riccati differential equation. The parameters of the LQR and Kalman filter are adopted

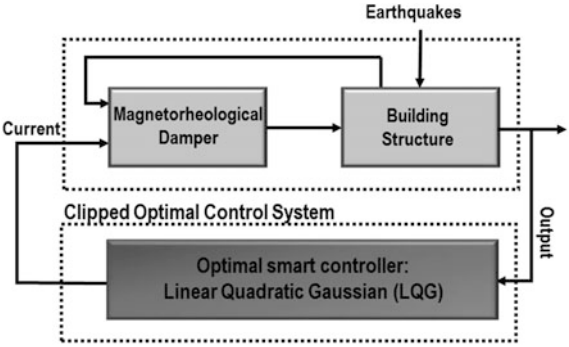

Fig. 4 Integrated building structure-MR damper system

from Dyke et al. [19]. However, the H_2/LQG algorithm should be modified to operate the MR damper for smart structure applications because it generates control force signals while current signals are used as an input signal of the MR damper. Thus, an inversion algorithm that converts the control force into current or voltage is combined with the H_2/LQG controller. The converting algorithm can be either an inverse MR damper model or a clipped algorithm. In this chapter, a clipped algorithm is utilized. A clipped algorithm proposed by Yoshida and Dyke [49] is given by

$$v = V_a \mathrm{H}\left(\left\{f_{\mathrm{H}_2/\mathrm{LQG}} - f_{\mathrm{m}}\right\} f_{\mathrm{m}}\right) \tag{23}$$

$$V_a = \begin{cases} \mu_c \cdot f_{\mathrm{H}_2/\mathrm{LQG}} & \text{for } f_{\mathrm{H}_2/\mathrm{LQG}} \leq f_{\max} \\ V_{\max} & \text{for } f_{\mathrm{H}_2/\mathrm{LQG}} > f_{\max} \end{cases} \tag{24}$$

where v is the voltage level, H is a Heaviside step function, f_{m} is a measured MR damper force, $f_{\mathrm{H2/LQG}}$ is a control force signal generated by the H_2/LQG controller, and μ_c is a value relating the MR damper force to the voltage.

2.4 Sensor Damage Scenario

The smart structure employs three accelerometers to implement the output feedback control system LQG. An accelerometer fault is introduced into the simulations to investigate the seismic hazard due to sensor fault/failures. To explore a number of representative fault conditions, the health status of the smart building is divided into four categories, defined as follows. (1) Healthy smart structure: all of the actuators and sensors are optimally operated in the smart structure. (2) Fully damaged structure: all the acceleration sensors within the smart structure have faults. (3) Partially damaged structure: in this case there is a fault in the 3rd floor accelerometer of the smart structure while there is no fault on the 1st and 2nd floor accelerometers. The reason that the 3rd floor sensor is selected as a target in this study is that it produces the worst responses, compared to either the 1st or 2nd floor accelerometer fault cases. (4) Uncontrolled structure: this is the original structure without any smart devices as a baseline of performance assessment. To mathematically model damage in the sensing units, uniform random noise signals, as shown in Fig. 5, with the signal-to-noise ratio (SNR) of 100 are added into the original acceleration responses during 2–6 s. The magnitude of the noise signal (i.e., error function) is adjusted according to structural responses to a variety of earthquake records because different earthquakes produce different levels of the magnitudes in seismic responses of smart structures.

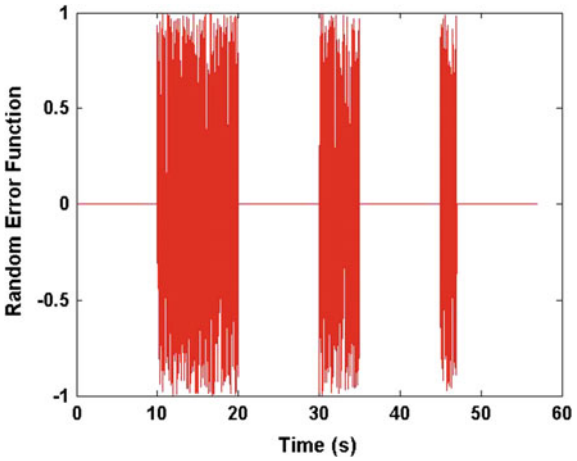

Fig. 5 Normalized error function used for simulating sensor fault/failures

3 Seismic Fragility Analysis

Seismic fragility is essential to predict potential loss estimates. It is defined as the conditional probability of attaining or exceeding a specific damage limit state during an earthquake event with a given intensity measure (*IM*), such as spectral acceleration (S_a) or peak ground acceleration (*PGA*). In this study, seismic fragility is determined as

$$F(PGA;\boldsymbol{\Theta}) = P[C - D(PGA;\boldsymbol{\Theta}) \leq 0 | PGA] \tag{25}$$

where C and D represent the capacity and seismic demand imposed on the smart building, respectively, and $\boldsymbol{\Theta}$ is a vector of unknown parameters that contribute to uncertainties in the demand model. For frame building structures, demand models and capacity limits are expressed in terms of limiting interstory drifts which are defined as relative lateral displacements between the top and the bottom of each floor. The overall maximum interstory drift over the height of a building is a convenient measure to describe the structural response of a building to lateral loads. Fragility curves can be developed from statistical methods applied to physical data gathered from building responses in past earthquake events or from analytical methods based on mathematical modeling and simulation of building responses to a series of earthquakes. Since limited historical records and physical data are available to estimate failure probabilities for smart structures of various characteristics and control systems, the following sections provide details on a proposed analytical method to determine the conditional failure probabilities or fragility functions. Herein, *PGA* is used as a measure of earthquake intensity because S_a corresponding to the fundamental period can vary during seismic excitation when the structure is equipped with a highly nonlinear hysteretic device. It is also noted that direct comparisons of fragility estimates for different structural systems are available when *PGA* is used as an earthquake intensity measure.

3.1 Fragility Curve Development

To estimate seismic fragility, two approaches can be used: (1) an approximate closed form and (2) Monte Carlo simulation. For the closed form equation, Wen et al. [48] developed the following approximate equation to estimate $F(PGA; \boldsymbol{\Theta})$:

$$F(PGA; \boldsymbol{\Theta}) \cong 1 - \Phi\left(\frac{\lambda_C - \lambda_D}{\sqrt{\sigma_D^2 + \sigma_C^2 + \sigma_M^2}}\right) \tag{26}$$

where λ_C is the median capacity limit for a given performance level in the logarithmic scale; λ_D is the median drift demand given *PGA* in the logarithmic scale;

σ_D and σ_C represent the uncertainties associated with the demand and capacity, respectively; σ_M is the modeling uncertainty.

When using the multiple demand models to consider multiple failure mechanisms, Monte Carlo simulation can be used. In this study, the seismic fragility curves for the case study structures are developed using the Monte Carlo simulations [18].

3.2 Probabilistic Capacity Limits

The structural capacity relates to a specific damage limit state, and it can be defined in terms of a maximum force or dynamic response characteristics, such as maximum displacement, maximum interstory drift, maximum acceleration, or maximum velocity. The practice of performance-based seismic design requires defining the acceptable damage limit states for a given earthquake intensity, and these limits are based on input from project stakeholders and consideration of the building's contents and function. In this research, ASCE/SEI 41-11 [7] criteria are used to express the seismic capacity of the case study smart building. ASCE/SEI 41-11 [7] provides guidance for performance-based seismic evaluation and rehabilitation of existing building structures and is based on FEMA 356 [8]. ASCE/SEI 41-11 defines a set of performance levels: Immediate Occupancy (IO), Life Safety (LS), and Collapse Prevention (CP). Defining these levels conveys expectations for the maximum damages sustained, or damage limit states. For example, structures capable of providing the IO performance level should have only minor damage. Structures exhibiting the LS performance level may have sustained significant damage, but still provide an appreciable margin against collapse. The CP performance level describes structures that are expected to remain standing, but with little margin against collapse. In addition to providing a standard vocabulary for discussing performance, ASCE/SEI 41-11 also provides both global-level (drift) limits and member-level (plastic rotation) limits to quantitatively define the damage limit states for various types of construction. For an approximate global assessment, the guidelines suggest limiting drift values for steel moment frame structures to 0.7,

2.5, and 5.0 % for the IO, LS, and CP performance levels, respectively. For braced steel frames, the corresponding drift values are 0.5, 1.5, and 2 %, respectively. For the controlled case study buildings, it is assumed that the limiting drift values are close to those for braced steel frames. For fragility curve development, uncertainty associated with the capacity model is assumed to be equal to 0.3 based on Wen et al. [48] and Bai et al. [9].

3.3 Probabilistic Demand Model Formulation

Probabilistic demand models have been developed to describe the relationship between earthquake intensity and the overall maximum interstory drift over the height of a building. Equation (27) shows the model form of a probabilistic linear model:

$$D(PGA;\boldsymbol{\Theta}) = \theta_0 + \theta_1 \ln(PGA) + \sigma\varepsilon \tag{27}$$

where $D(PGA;\boldsymbol{\Theta}) = \ln[\delta(PGA;\boldsymbol{\Theta})]$ = natural logarithm of the drift demand for a given peak ground acceleration PGA, $\boldsymbol{\Theta} = (\theta_0, \theta_1, \sigma)$ is a vector of unknown parameters; ε is a random variable representing the error in the model with zero mean and unit standard deviation, and σ is the standard deviation of the model error. The logarithmic transformation is used to approximately satisfy the normality assumption (i.e., ε has the Normal distribution) and the homoscedasticity assumption (i.e., σ is constant). The unknown parameters in this equation are estimated using the Bayesian updating rule [12].

$$f(\boldsymbol{\Theta}) = \gamma L(\boldsymbol{\Theta}) p(\boldsymbol{\Theta}) \tag{28}$$

where $p(\boldsymbol{\Theta})$ is the prior distribution of $\boldsymbol{\Theta}$, which is based on previous knowledge before obtaining the observation; $L(\boldsymbol{\Theta})$ is the likelihood function representing the objective information on $\boldsymbol{\Theta}$, which is proportional to the conditional probability for given values of $\boldsymbol{\Theta}$; γ is a normalizing factor; and $f(\boldsymbol{\Theta})$ is the posterior distribution of $\boldsymbol{\Theta}$ that incorporates the prior information in $p(\boldsymbol{\Theta})$ and the information from the observation. The mean vector, $\mathbf{M}_{\Theta}$, and the covariance matrix, $\boldsymbol{\Sigma}_{\Theta\Theta}$, can be obtained once $f(\boldsymbol{\Theta})$ is known. In the analysis presented in this section, a non-informative prior distribution is assumed to reflect that there is little or no information available about $\boldsymbol{\Theta}$ before collecting the observation.

The posterior statistics of the unknown model parameters are obtained using an adaptive MCMC simulation method, the DRAM method, which combines the Delayed Rejection (DR) method and the Adaptive Metropolis (AM) [38]. Markov chains are generated with the likelihood formulation of the demand models based on the initial points and non-informative prior distribution until a convergence criterion is met. To check the convergence of the simulated Markov chains, the Geweke convergence criterion is used [22]. More details on the formulation of the likelihood formulation can be found in Gardoni et al. [21].

4 Analytical Results

4.1 Ground Motion Records

For estimating seismic demand, synthetic ground motions for Memphis, Tennessee, developed by Fernandez and Rix [20] are used. A total of 40 ground motions are provided for each of two earthquake hazard levels: 2 and 10 % probability of exceedance in 50 years. Each hazard level has 20 ground motions for each of two types of soil conditions (lowlands and uplands) for Memphis, Tennessee. Figure 6 shows the median of response spectra for the ground motion records used in this study.

4.2 Probabilistic Seismic Demand Models

A linear regression model based on the overall maximum interstory drift for the entire building is used to predict the seismic demand relationship. Equation (27) is used to predict the seismic demands. The posterior statistics of the unknown model parameters are obtained using an adaptive MCMC simulation method. Figures 7 and 8 show the sets of the Markov chains and the corresponding probability distributions of the posterior estimates for the controlled case study structures. These are generated with the likelihood formulation of the demand models based on the initial points and non-informative prior distribution until a convergence criterion is met. To check the convergence of the simulated Markov chains, the Geweke convergence criterion is used [22]. It is based on the comparison between the mean

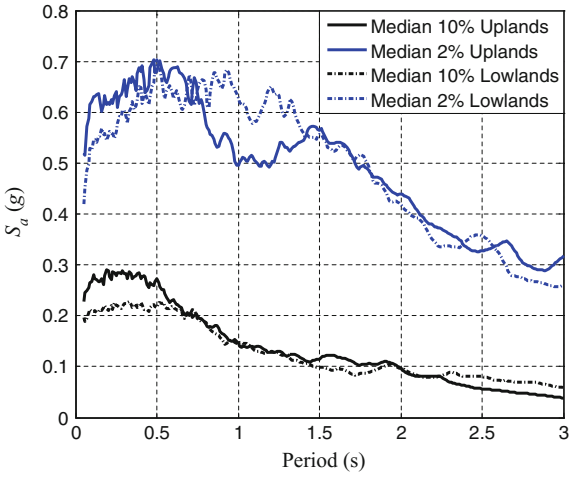

Fig. 6 Median of response spectra for Fernandez and Rix motions

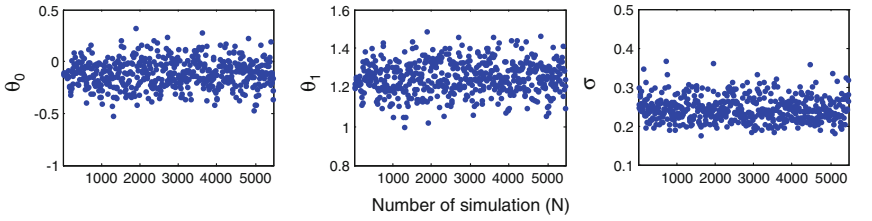

(a) Healthy smart structure

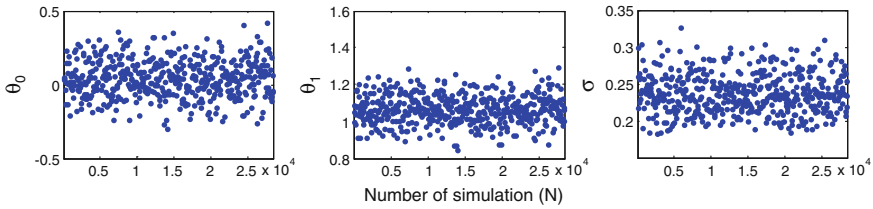

(b) Fully damaged structure

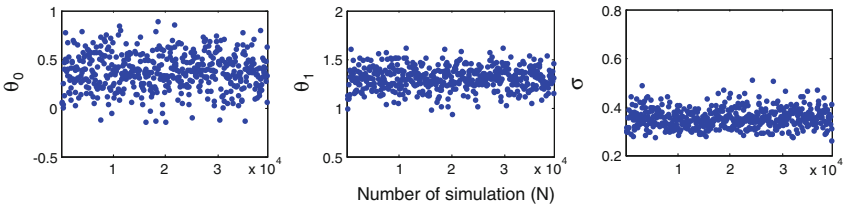

(c) Partially damaged structure

Fig. 7 Markov chains of unknown parameters for controlled structures. **a** Healthy smart structure, **b** Fully damaged structure, **c** Partially damaged structure

values of the first 10 % and last 50 % of the samples. If the difference of the mean values is less than 5 %, the MCMC simulation is terminated.

Figure 9 shows the relationship between maximum interstory drift and the corresponding *PGA* values for the case study building with the sensor damage scenarios from the simulation results. For comparison, the demand relationship for the uncontrolled structure is also presented. The regression lines are defined by Eq. (27). The predicted demands (solid line) are shown along with the one standard deviation confidence interval (dashed line) in the logarithmic space. A total of 40 points are considered, where each data point represents the demand relationship for one ground record.

As shown in Fig. 9, different slopes and variation of the demand models, which are generated based on the simulation results indicate the level of damage in terms of the maximum interstory drift values. Figure 10 shows the comparison between the computed and the predicted drifts using the probabilistic demand models. The dashed lines represent uncertainty based on standard deviation (σ) in Eq. (27).

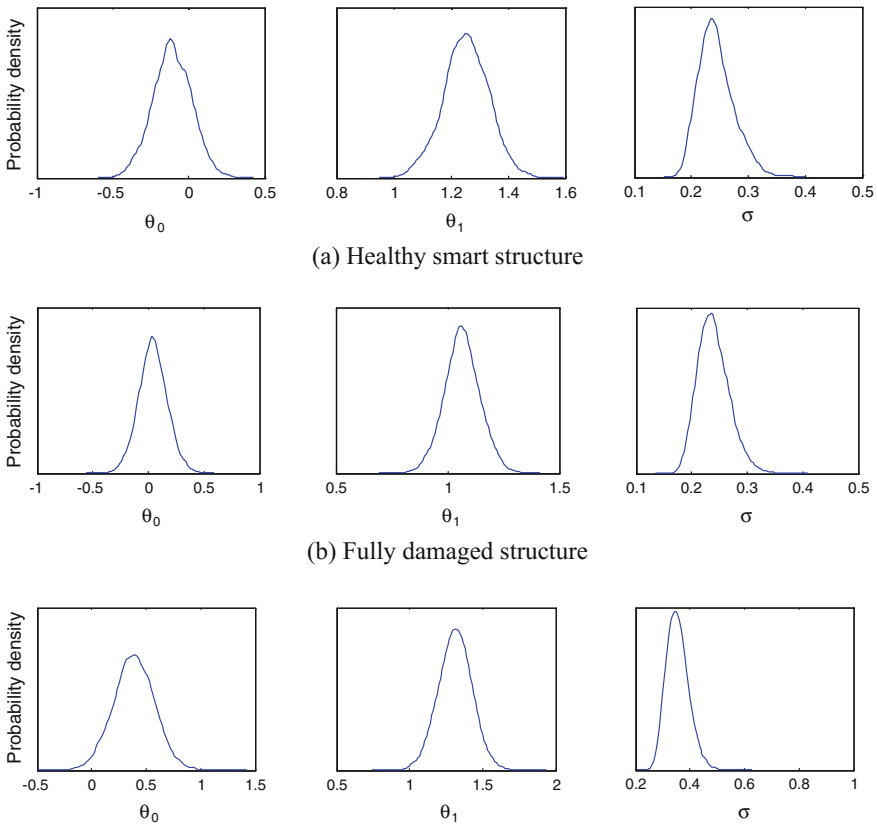

Fig. 8 Probability distributions of unknown parameters for controlled structures. **a** Healthy smart structure, **b** Fully damaged structure, **c** Partially damaged structure

Based on Fig. 10, median drifts with the controlled cases (a) through (c) have lower values than those with the uncontrolled case (d). In addition, the uncertainty for the partially damaged case is the highest among those from the controlled structures. Tables 1 and 2 show the posterior statistics of the unknown parameters and the correlation coefficient values for all the scenarios. Based on the posterior statistics, partially damaged structure has the highest uncertainty (σ) in the demand model.

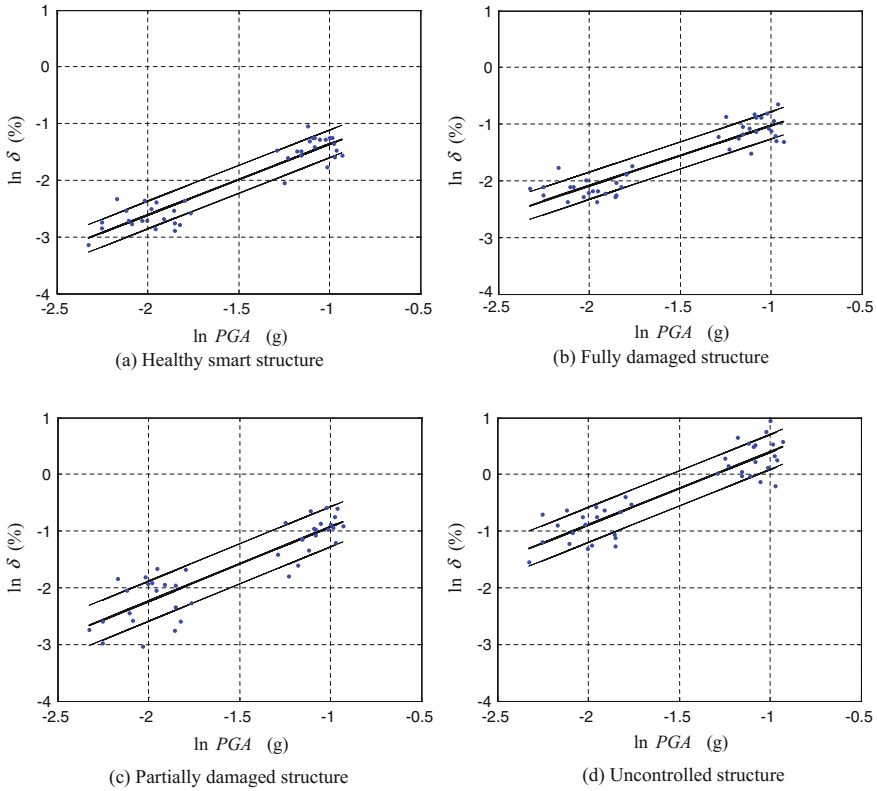

Fig. 9 Probabilistic demand models for the case study structures. **a** Healthy smart structure, **b** Fully damaged structure, **c** Partially damaged structure, **d** Uncontrolled structure

4.3 Seismic Fragility Analysis

In this study, the seismic fragility curves for the case study structures are developed using Monte Carlo simulations [18]. As shown in Eq. (25), probabilistic models of the structural capacity limits and seismic demand are needed to develop seismic fragility curves. Figure 11 shows the fragility curves based on the ASCE/SEI 41-11 global-level limits for the smart structure equipped with healthy, fully damaged, and partially damaged sensors while the uncontrolled system is used as a baseline. It can be observed that the four building categories are similar to a certain extent. For instance, the fragility curves tend to flatten as the ground motion intensity levels increase and as the performance level shifts from IO to LS to CP. The steeper curves for the IO performance level represents much more variability of maximum drift than for the other two performance levels. All four structures have higher sensitivities to exceeding the IO performance level.

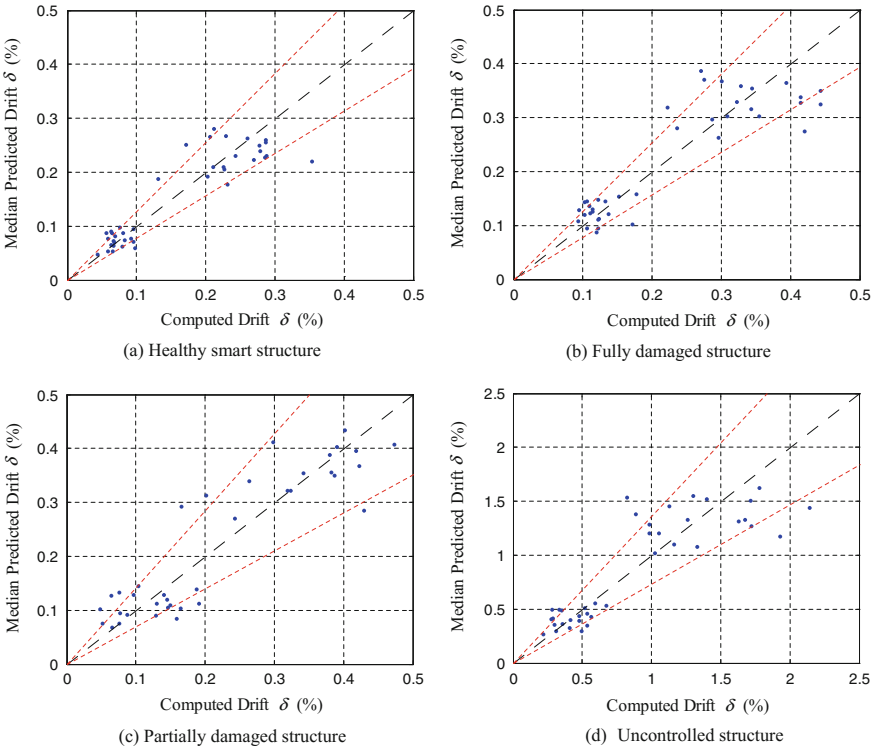

Fig. 10 Predicted versus computed drift for the case study structures. **a** Healthy smart structure, **b** Fully damaged structure, **c** Partially damaged structure, **d** Uncontrolled structure

Table 1 Posterior statistics of unknown parameters for the demand models

Case study structures	Parameters	Mean	Standard deviation
Healthy smart structure	θ_0	−0.108	0.127
	θ_1	1.250	0.079
	σ	0.244	0.031
Fully damaged structure	θ_0	0.041	0.128
	θ_1	1.070	0.080
	σ	0.239	0.029
Partially damaged structure	θ_0	0.388	0.188
	θ_1	1.310	0.116
	σ	0.353	0.042
Uncontrolled structure	θ_0	1.680	0.168
	θ_1	1.290	0.104
	σ	0.309	0.036

Table 2 Correlation coefficients of unknown parameters for the demand models

Case study structures		Correlation coefficient		
		θ_0	θ_1	σ
Healthy smart structure	θ_0	1		
	θ_1	0.950	1	
	σ	0.022	−0.005	1
Fully damaged smart structure	θ_0	1		
	θ_1	0.955	1	
	σ	0.027	0.030	1
Partially damaged smart structure	θ_0	1		
	θ_1	0.955	1	
	σ	−0.021	−0.023	1
Uncontrolled structure	θ_0	1		
	θ_1	0.956	1	
	σ	−0.002	0.005	1

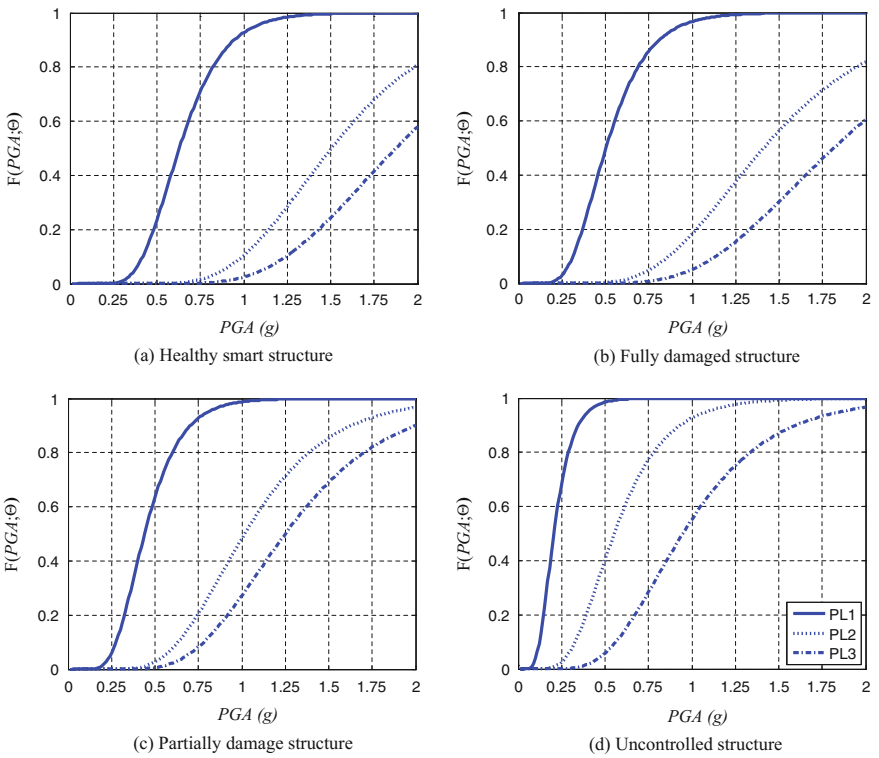

(a) Healthy smart structure

(b) Fully damaged structure

(c) Partially damage structure

(d) Uncontrolled structure

Fig. 11 Seismic fragility curves for the case study structures. **a** Healthy smart structure, **b** Fully damaged structure, **c** Partially damaged structure, **d** Uncontrolled structure

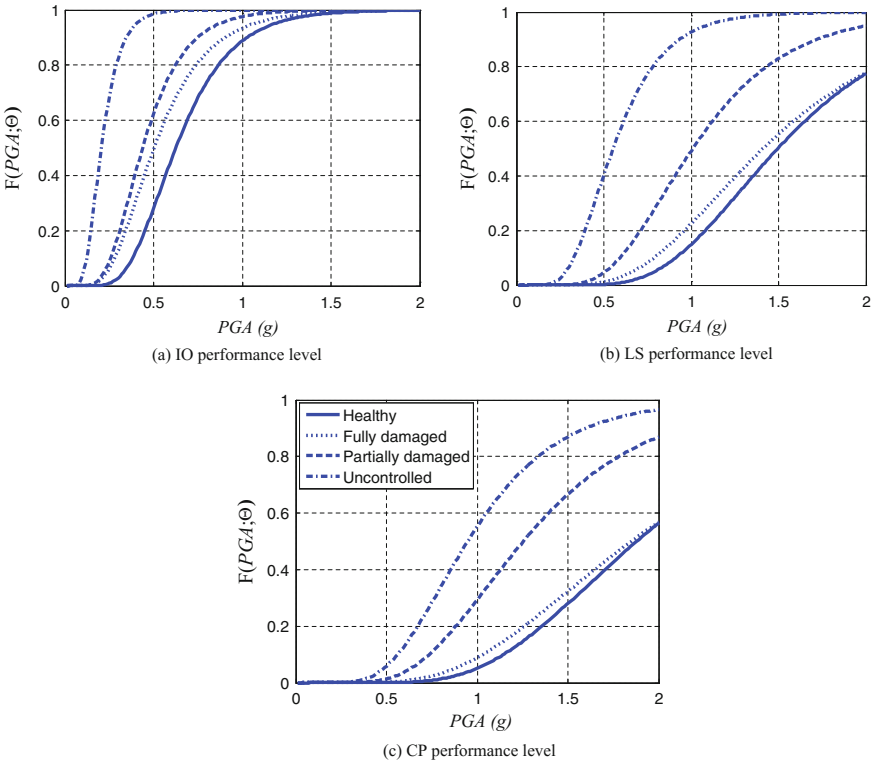

Fig. 12 Comparisons of seismic fragility curves. **a** IO performance level, **b** LS performance level, **c** CP performance level

It is noted that direct comparison of fragility estimates is available when *PGA* is used as an earthquake intensity measure. Therefore, the impact of the sensor fault within smart structures on the fragility curves for each limit state can be assessed. Figure 12 provides comparisons of fragility curves for each performance level Immediate Occupancy (PL1), Life Safety (PL2), and Collapse Prevention (PL3). In all three figures, the fragility curves for the healthy smart structure provide lower probabilities of exceedance for comparable limit states than those for the smart system with faulty sensors. Additionally, the unhealthy smart structures provide lower probabilities of exceedance for comparable limit states than those for the uncontrolled system. This shows the impact of the smart controller in terms of the seismic fragility to prove that smart structures are effective in reducing the fragility for all the performance levels.

As shown in the figures, the fragilities of the smart control system with fully faulty sensors are lower than those of the ones with partially faulty sensors. These comparisons also show that the fragilities of the smart control system with fully faulty sensors are marginally higher than the healthy smart control system for LS and CP performance levels. The reason could be found in the estimated state values

that serve as feedback to the linear quadratic regulator. The Kalman filter estimates all the state values from three contaminated acceleration responses measured from the fully damaged sensing units (i.e., three accelerometers). Because the damaged signals are created through the addition of random noise signals (SNR of 100) into original accelerations, the higher level of acceleration outputs are applied to the Kalman filter estimator. The much larger acceleration responses might be led to the larger displacement and velocity response estimations. The larger state estimations would cause the control algorithm to calculate larger control forces, i.e., higher levels of current signals to be fed to the MR damper, eventually lead to larger control forces (i.e., close to passive-on status). Although the larger control forces would be effective in reducing the drift responses of the smart structures, larger control forces would also increase the absolute acceleration at the installed location of the MR dampers because the passive-on system attempts to lock up the floor on which the MR damper is installed [27]. Thus, the passive-on status would increase seismic base shear forces in the smart structures. In near future, the research team plans to study systematically the impact of the state estimator on the performance of the smart control systems.

5 Conclusion

This chapter has attempted to present a framework to develop seismic fragility assessments and to investigate the impact of faulty sensors on the smart structure performance under a variety of seismic excitations, using fragility analysis techniques. A case study of a three-story building equipped with highly nonlinear hysteretic control devices, magnetorheological (MR) dampers, is investigated. The current signals providing feedback to the MR dampers are determined by a linear quadratic Gaussian (LQG) control algorithm. Probabilistic demand models using a Bayesian approach are constructed. The fragility curves for the smart control system with partially faulty sensors, with fully faulty sensors, and with no sensor fault are developed. Fragility curves for the original three-story building without any smart devices are also established as baselines. It is confirmed from the fragility analysis that: (1) seismic fragilities of buildings can be reduced by adopting smart control technology as previous studies have demonstrated, (2) smart control system shows improvement in seismic performance even if the sensing units have some faults, and (3) based on the comparison on fragility among the controlled structures, seismic performance is still enhanced when the sensors are fully damaged because semiactive control techniques are always stable in general.

References

1. Arsava SK, Kim Y, El-Korchi T, Park HS (2013) Nonlinear system identification of smart structures under high impact loads. J Smart Mater Struct 22. doi:10.1088/0964-1726/22/5/055008
2. Arsava SK, Chong JW, Kim Y (2014) A novel health monitoring scheme for smart structures. J Vib Control. doi:10.1177/1077546314533716
3. Arsava SK, Kim Y (2015) Modeling of magnetorheological dampers under various impact forces. Shock Vib 2015, Article ID 905186, 20 p. doi:10.1155/2015/905186
4. Arsava SK, Nam Y, Kim Y (2015) Nonlinear system identification of smart reinforced concrete structures under high impact loads. J Vib Control. doi:10.1177/1077546314563966
5. Arsava SK, Kim Y, Kim KH, Shin BS (2015) Smart fuzzy control of reinforced concrete structures excited by collision-type forces. Expert Syst Appl 42(21):7929–7941
6. Ankireddi S, Yang HTY (1999) Neural networks for sensor fault correction in structural control, ASCE. J Struct Eng 125:1056–1064
7. ASCE/SEI (2011) Seismic rehabilitation of existing buildings, ASCE/SEI 41-11, Reston, VA, American Society of Civil Engineers
8. ASCE (2000) Prestandard and commentary for the seismic rehabilitation of buildings (FEMA 356), Washington D.C., Prepared by American Society of Civil Engineers for the Federal Emergency Management Agency
9. Bai J-W, Gardoni P, Hueste MBD (2011) Story-specific demand models and seismic fragility estimates for multi-story buildings. Struct Saf 33:96–107
10. Barnawi W, Dyke SJ (2008) Fragility based analysis of a 20-story benchmark building with smart device implementation. In: Proceedings of the 11th aerospace division international conference on engineering, science, construction, and operations in challenging environments, 3–5 March, Long Beach, CA, USA
11. Bitaraf M, Ozbulut OE, Hurlebaus S, Barroso L (2010) Application of semi-active control strategies for seismic protection of buildings with MR dampers. Eng Struct 32:3040–3047
12. Box G, Tiao, GC (1992) Bayesian inference in statistical analysis, Reading, MA
13. Casciati F, Cimellaro GP, Domaneschi M (2008) Seismic reliability of a cable-stayed bridge retrofitted with hysteretic devices. Comput Struct 86:1769–1781
14. Cha YJ, Agrawal AK, Kim Y, Raich A (2012) Multi-objective genetic algorithms for cost-effective distributions of actuators and sensors in large structures. Expert Syst Appl 39:7822–7833
15. Cha YJ, Kim Y, Raich A, Agrawal AK (2013) Multi-objective optimization for actuator and sensor layouts of actively controlled 3D buildings. J Vib Control 19:942–960
16. Choe K, Baruh H (1993) Sensor failure detection in flexible structures using model observers. J Dyn Sys Meas Cont 115:411–418
17. Chong JW, Kim Y, Chon K (2014) Nonlinear multiclass support vector machine-based health monitoring system for buildings employing magnetorheological dampers. J Intell Mater Syst Struct 25:1456–1468
18. Ditlevsen O, Madsen HO (1996) Structural reliability methods. Wiley, New York
19. Dyke SJ, Spencer BF, Sain MK, Carlson JD (1996) Modeling and control of magnetorheological dampers for seismic response reduction. Smart Mat Struct 5:565–575
20. Fernandez JA, Rix GJ (2006) Soil attenuation relationships and seismic hazard analyses in the upper Mississippi embayment. In: 8th US national conference on earthquake engineering 8NCEE, San Francisco, California. http://geosystems.ce.gatech.edu/soil_dynamics/research/groundmotionsembay/
21. Gardoni P, Der Kiureghian A, Mosalam KM (2002) Probabilistic capacity models and fragility estimates for RC columns based on experimental observations. ASCE J Eng Mech 128(10):1024–1038
22. Geweke J (1992) Evaluating the accuracy of sampling-based approaches to the calculation of posterior moments. Bayesian Stat 4:164–193

23. Hueste MBD, Bai J-W (2007) Seismic retrofit of a reinforced concrete flat-slab structure: part I-seismic performance evaluation. Eng Struct 29:1165–1177
24. Hueste MBD, Bai J-W (2007) Seismic retrofit of a reinforced concrete flat-slab structure: part II-seismic fragility analysis. Eng Struct 29:1178–1188
25. Hughes JE, Kim Y, El-Korchi T (2015) Radar technology for structural hazard mitigation. J Vib Control (in press)
26. Hurlebaus S, Gaul L (2006) Smart structure dynamics. Mech Syst Signal Process 20:255–281
27. Jansen LM, Dyke SJ (2000) Semiactive control strategies for MR dampers: comparative study, ASCE. J Eng Mech 126:795–803
28. Kim DH, Seo SN, Lee IW (2004) Optimal neurocontroller for nonlinear benchmark structure. ASCE J Struct Eng 130(4):424–429
29. Kim Y, Langari R (2007) Nonlinear identification and control of a building structure with a magnetorheological damper system. In: American control conference, New York, 11–13 July
30. Kim Y, Hurlebaus S, Sharifi R, Langari R (2009) Nonlinear identification of MIMO smart structures asme dynamic systems and control conference hollywood, California, 12–14 Oct
31. Kim Y, Langari R, Hurlebaus S (2009) Semiactive nonlinear control of a building using a magnetorheological damper system. Mech Syst Signal Process 23:300–315
32. Kim Y, Hurlebaus S, Langari R (2010) Control of a seismically excited benchmark building using linear matrix inequality-based semiactive nonlinear fuzzy control. ASCE J Struct Eng 136(8):1023–1026
33. Kim Y, Langari R, Hurlebaus S (2010) Model-based multi-input, multi-output supervisory semiactive nonlinear fuzzy controller. Comput Aided Civil Infrast Eng 25:387–393
34. Kim Y, Kim C, Langari R (2010) Novel bio-inspired smart control for hazard mitigation of civil structures. J Smart Mater Struct 19:115009. doi:10.1088/0964-1726/19/11/115009
35. Kim Y, Hurlebaus S, Langari R (2011) Fuzzy identification of building-MR damper system international. J Intel Fuzzy Syst 22(4):185–205
36. Kim Y, Chong JW, Chon K, Kim JM (2013) Wavelet-based AR-SVM for health monitoring of smart structures. J Smart Mater Struct 22(1):015003. doi:10.1088/0964-1726/22/1/015003
37. Kim Y, Kim YH, Lee S (2015) Multivariable nonlinear identification of smart buildings. Mech Syst Signal Process 62–63:254–271
38. Laine M (2008) Adaptive MCMC methods with applications in environmental and geophysical models. Ph.D. dissertation. Lappeenranta University of Technology, Lappeenranta (Finland)
39. Li Z, Koh BH, Nagarajaiah S (2007) Detecting sensor failure via decoupled error function and inverse input-output model. ASCE J Eng Mech 133(11):1222–1228
40. Mitchell R, Kim Y, El-Korchi T (2012) System identification of smart structures using a wavelet neuro-fuzzy model. J Smart Mater Struct 21. doi:10.1088/0964-1726/21/11/115009
41. Mitchell R, Kim Y, El-Korchi T, Cha YJ (2013) Wavelet-neuro-fuzzy control of hybrid building-active tuned mass damper system under seismic excitations. J Vib Control 19 (12):1881–1894
42. Mitchell R, Cha YJ, Kim Y, Mahajan A (2015) Active control of highway bridges subject to a variety of earthquake loads. Earthq Eng Eng Vib 14(2):253–263
43. Mohammadzadeh S, Kim Y, Ahn J (2015) PCA-based neuro-fuzzy model for system identification of smart structures. J Smart Struct Syst 15(4):1139–1158
44. Reigles DG, Symans MD (2006) Supervisory fuzzy control of a base-isolated benchmark building utilizing a neuro-fuzzy model of controllable fluid viscous dampers. Struct Cont Health Monit 13(2–3):724–747
45. Sharifi R, Kim Y, Langari R (2010) Sensor fault isolation and detection of smart structures. J Smart Mater Struct 19. doi:10.1088/0964-1726/19/10/105001
46. Spencer BF, Dyke SJ, Sain MK, Carlson JD (1997) Phenomenological model for magnetorheological dampers. ASCE J Eng Mech 123:230–238
47. Taylor E (2007) The development of fragility relationships for controlled structures. MS thesis, Department of Civil Engineering, Washington University

48. Wen YK, Ellingwood BR, Bracci JM (2004) Vulnerability function framework for consequence-based engineering. Mid-America earthquake center project DS-4 report, Urbana, IL
49. Yoshida O, Dyke SJ (2004) Seismic control of a nonlinear benchmark building using smart dampers. ASCE J Eng Mech 130(4):386–392

Actuating Connections for Substrusture Damage Identification and Health Monitoring

Stavros Chatzieleftheriou and Nikos D. Lagaros

Abstract Vibration-based damage detection and localization are often performed aiming to relate modal analysis' results with appropriate metrics that express structural damages. The problem of structural damage identification is generally formulated as an inverse problem aiming to detect changes encountered on the global stiffness matrix of the structure's model. In most cases, the measured quantities are less than the damage parameters to be identified, thus an infinite number of possible damage configurations is expected to satisfy the measurements. Therefore, damage identification problems are often proven to be ill-conditioned. In addition, as in situ measurements are interpreted by a computer model, a number of uncertainties play an important role in the success of the identification procedure. The class of uncertainties consist of model, discretization, material and measurement errors. Furthermore, a large number of parameters need to be identified in order to assess arbitrary damage scenario and time consuming structure monitoring need to be implemented. In the majority of the developed methods the tendency is to use measurements from sensors while the vibrations are caused either by random (e.g. wind, earthquake etc.) causes or from force actuators in one or more points of the structure. In this work the implementation of actuator connections that divide a structure in several substructures is proposed. These connections can be installed on the structure during construction or retrofit. As it will be demonstrated, these connections can be controlled and excite each substructure separately and record its fundamental frequencies. In this way, each substructure can be monitored in arbitrary time while the complexity and often ill-conditioning of damage localization for large structures can be drastically reduced.

S. Chatzieleftheriou · N.D. Lagaros (✉)
Department of Structural Engineering, School of Civil Engineering,
National Technical University of Athens, Institute of Structural Analysis
and Antiseismic Research, 9, Heroon Polytechniou Str., Zografou Campus,
15780 Athens, Greece
e-mail: nlagaros@central.ntua.gr

S. Chatzieleftheriou
e-mail: stavroscha@windowslive.com

M. Papadrakakis et al. (eds.), *Computational Methods in Earthquake Engineering*,
Computational Methods in Applied Sciences 44,
DOI 10.1007/978-3-319-47798-5_12

1 Introduction—Motivation

In the last thirty years, the subject of damage identification has been studied extensively and many researchers have presented important findings. The methods proposed so far, generally belong into two categories: vibration or wave propagation based ones. Vibration based methods utilise modal data, taking advantage of the fact that some first natural frequencies (and/or the corresponding mode shapes and damping ratios) of the damaged and undamaged structural system can be attained through observation of the system over time using an array of sensors in order to record its dynamic response. Vibration-based damage identification usually utilizes eigenfrequencies and eigenmodes, often though acceleration measurements and frequency response functions are directly used in the process.

A great deal of work has been carried out in order to determine location and extent of damages in structural systems utilizing measured modal parameters (limited number of modal frequencies and/or mode shapes). The literature is vast and obviously cannot be completely covered here. A detailed survey can be found in the work by Doebling et al. [1] and in a recent one by Fan and Qiao [2]. Among others, Liang et al. [3] adopted a physical model using a massless rotational spring to represent the crack-induced local flexibility. Hassiotis and Jeong [4] correlated the changes on the eigenfrequencies with reductions on elements of the stiffness matrix using first order perturbation theory and an optimality criterion aiming to minimize the difference between the eigenvalue problem for the damaged and undamaged structural system resulting into a quadratic optimization problem. Bicanic and Chen [5] proposed a procedure for damage identification of framed structures where both location and extent of structural damage is determined using limited number of measured natural frequencies, while no knowledge of the modal shapes of the damaged structure is required. Vestroni and Capecchi [6] dealt with damage detection in beams, where damage was simulated with concentrated decrease in stiffness. In [7] Kim et al. presented a methodology to non-destructively locate and estimate the size of damage in structures for which a few natural frequencies or a few mode shapes are available. Alvandi and Cremona [8] reviewed some vibration-based damage identification techniques when used for structural damage evaluation for the case of a simply supported beam with different damage levels. Friswell [9] proposed that the first few natural frequencies can be sufficiently measured, whereas the eigenmodes are noisy data and that it is very difficult to assess the error in mode shapes. Yang [10] proposed a structural flexibility disassembly method to compute the perturbed parameters of the stiffness matrix which indicate damages. In the work by Li et al. [11], it was shown that the sensitivity method can be used in conjunction with a denser discretization in order to simulate crack-like defects. Yao and Pakzad [12] proposed two novel regression-based techniques that use local acceleration responses of a frame structure to estimate its local stiffness that were proven effective in their application to data collected from two laboratory specimens that are subjected to white noise excitation. Metaheuristic search algorithms have also been used in order to obtain solutions in such problems.

In particular, the simulated annealing algorithm was employed by He and Hwang [13], modified variants of the genetic algorithm were used by Guo and Li [14] and Jeong et al. [15], the particle swarm optimization (PSO) algorithm was applied among others by Saada et al. [16] and a hybrid PSO-simplex algorithm was used by Begambre and Laier [17].

Measurements' noise is a factor that should be taken into account during the identification procedure. In this direction Xia and Hao [18] presented a statistical damage identification procedure based on frequency changes in order to account for the effects of random noise in both vibration data and finite element model, while the effects of using different number of modal frequencies, noise level and damage level on damage identification results were also discussed. Chatzieleftheriou and Lagaros [19] presented an iterative damage identification algorithm for assessing underdetermined problems when combined with measurements' noise and model uncertainties. Furthermore, as suggested by Currie et al. [20], an important characteristic that should be taken into account when applying such procedures is the measurements' noise.

A great deal of work has been conducted in the field of substructure damage identification, indicatively Hou et al. [21, 22] presented a substructure isolation method for local structural health monitoring both in time [21] and frequency domain [22]. In order to perform substructure damage identification, measurements at the boundaries of the substructure are required along with a sufficient number of excitation forces in various positions of the global structure. In general substructure damage identification is more practical in large complex structures with hundreds of natural frequencies where only particular parts of a structure may be of interest and as the global identification schemes require a great deal of computational effort as well as time consuming monitoring.

Summarizing the literature review, most of damage identification and heath monitoring schemes adopt a semi-passive framework where the structure is monitored during ambient excitation. In order to perform damage identification, usually large scale inverse problems have to be solved and these problems are often ill-conditioned and/or sensitive to measurement noise, model and environmental uncertainties. In order to overcome these difficulties an active substructure monitoring scheme is proposed herein. The term active refers to actuating structural connections that can be installed on the global structure and selectively excite different substructures. The price one has to pay is of course the actual installation, where in many structures could be difficult or even impossible. However, the benefit is that the substructure frequency response can be directly measured. When, exciting each substructure, the natural frequencies are directly obtained and practically should be unaffected of a series of uncertainties during data acquisition, modal analysis and post processing algorithms that are usually implemented for the entire structure in most structural health monitoring schemes. In this way a direct damage localization can be achieved.

In this work the implementation of actuator connections that divide a structure in several substructures is proposed and theoretically verified. These connections can be installed on the structure during construction or retrofit (replacing existing

elements). The actuator connections as they are presented herein take the form of a flange that can actively connect beam parts. The connecting flange can be mechanically controlled (by hydraulic and piezo electric means) and can exert horizontal and vertical forces in the two beam parts it unites. Between two or more connecting elements, a substructure is defined. The objective is to use one (or more) connecting elements as a force actuator, while the others will serve as controlling elements in order to stabilize the other ends of the substructure examined. As it will be demonstrated, these connections can be controlled and excite each substructure separately and record its fundamental frequencies. The controlling forces that minimize the displacements at the nodes to be stabilized are assumed to follow an unconstrained optimization algorithm which as it will be demonstrated is effective in the control procedure.

2 Connecting Elements and Control Algorithm

In the presented work, the implementation of an actuating connecting element for damage identification and health monitoring is proposed. In Fig. 1 a brief schematic of the connecting element is presented.

When the connection is inactive, the force acting elements as well as the adjustable pins are in "locked" position forbidding the relative displacement and rotation of the two beam parts. At the activation of the connection, the forcing elements start to exert equal but opposite forces in the two beam parts. The vertical forces shall be denoted as Q. The pairs of horizontal forces are exerted in a way that are equal and opposite at all times during the excitation producing an equivalent moment that shall be denoted as M. As soon as the internal forces have been captured by the forcing elements, the adjustable pins can "move" a few mm in order

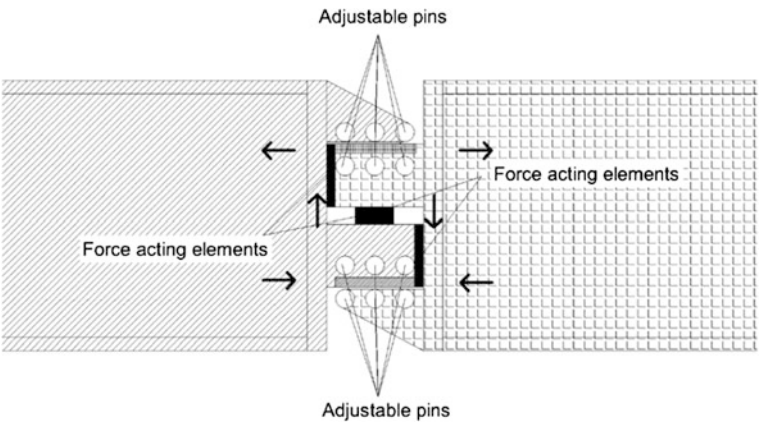

Fig. 1 Schematic of the proposed connecting element

to free the relative rotation among the beam parts. It is important for the safety of the connection, that both the adjustable pins, as well as the relative displacements of the forcing elements is small enough and that the connection is secured in case of a malfunction. At each beam part, sensors capable of recording the position, acceleration and force should be installed. The forces from the force acting elements are controlled using the sensor information as output in a feedback loop.

As the substructure excited is expected to be damaged it is not possible to extract the system transfer function from the mathematical model of the structure since the size and position of the damage(s) is not a priori known. The system performs a frequency sweep in order to capture the substructure natural frequencies. At each frequency step, the control procedure is implemented until the displacements in some nodes are minimized (zeroed) and the magnitude and phase of the controlling generalized forces (Q,M) for these nodes are recorded.

Although no numerical model for the structure is needed to perform the procedure, in order to verify the method, the analysis of the connecting system is done by numerical simulations of the structural system vibrations (see Fig. 2). In particular, the controlling forces exerted by the connecting system are fed to a numerical simulation whose output is fed back to the system that implements a control procedure by mimicking an unconstrained optimization algorithm in order to minimize a set of generalized displacements. The optimization algorithm used is of the BFGS Quasi-Newton family [23]. The same procedure can be followed in the physical implementation by calculating the gradients from recording the displacements after perturbing the control forces.

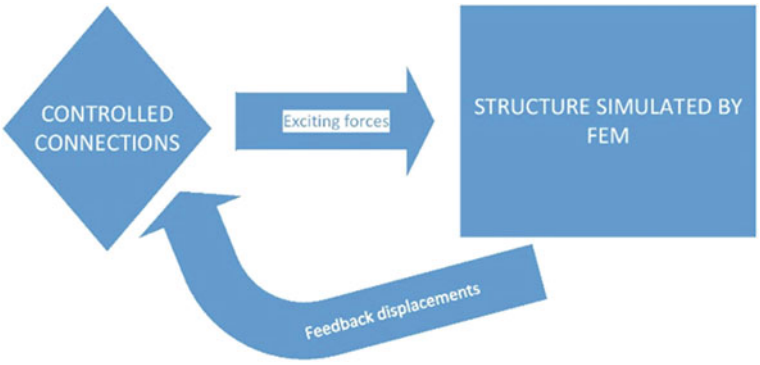

Fig. 2 Block diagram of the controlled connection system in order to stabilize certain degrees of freedom of the substructure

3 Simulation of Structure Vibration and Damage

The structure is simulated with standard finite element analysis, in particular, the generalized eigenvalue problem is formulated as follows:

$$(\boldsymbol{K} - \lambda_i \boldsymbol{M})\Phi_i = 0,\ i = 1, 2, \ldots, n \tag{1}$$

and

$$\Phi_i^{\mathrm{T}} \boldsymbol{K} \Phi_j = \lambda_j \delta_{ij}, \tag{2a}$$

$$\Phi_i^{\mathrm{T}} \boldsymbol{M} \Phi_j = \delta_{ij} \tag{2b}$$

where $\boldsymbol{K}$ and $\boldsymbol{M}$ are the global stiffness and mass matrices of the excited substructure, Φ_i (i = 1, 2,…, n) are the normalized eigenvectors with respect to the mass matrix M of the n degrees of freedom (DOFs) substructure, λ_i is the eigenvalue for the *i*th eigenmode, and δ_{ij} is the Kronecker delta. In this work a scalar damage model is implemented. The substructure is considered to be separated from the rest of the structure which implies that the first natural frequencies will be equal to zero according to the rigid body movements of the considered substructure. The global stiffness matrix of the substructure can be expressed as an assembly of the element stiffness matrices as follows:

$$\boldsymbol{K}(S) = \sum_{e=1}^{n_e} \boldsymbol{k}_e s_e = \sum_{e=1}^{n_e} \boldsymbol{k}_e (1 + \delta k_e) \tag{3}$$

where $\boldsymbol{K(S)}$ is the global stiffness matrix which is considered as a function of vector *S*, that contains the damage factors for each finite element (FE) as the residual stiffness and represent the level of damage, they are also bounded $(0 \leq s_e \leq 1)$. They can alternatively be defined as the stiffness degradation δk_e $(-1 \leq \delta k_e \leq 0)$. Each component s_e multiplies the corresponding element global stiffness matrix $\boldsymbol{k_e}$. As proposed in [11] this kind of analysis with a dense discretization, can simulate crack-like defects. The equations of motions for the structural system are given by

$$\boldsymbol{K}U + \boldsymbol{M}\ddot{U} + \boldsymbol{C}\dot{U} = F_1(t) + F_2(t) \tag{4}$$

where $\boldsymbol{C}$ is the damping matrix, $F_1(t)$, $F_2(t)$ are the steady sinusoidal and controlled regarding the magnitude and phase sinusoidal controlling forces respectively. In other words, $F_1(t)$ are considered as the excitation forces whose nodes of application are free to move while $F_2(t)$ are sinusoidal forces exerted on the nodes in order to render them "fixed". Regarding the frequency response of the system it can be written that

$$
\begin{aligned}
&(\boldsymbol{K} - \omega^2 \boldsymbol{M} + i\omega \boldsymbol{C}) U_f e^{i\omega t} = F_{f1} e^{i\omega t} + F_{f2} e^{i\omega t} \\
&U_f = \boldsymbol{A}^{-1}(F_{f1} + F_{f2}), \quad \boldsymbol{A} = \boldsymbol{K} - \omega^2 \boldsymbol{M} + i\omega \boldsymbol{C}
\end{aligned} \tag{5}
$$

While the forces that are sought by the control procedure, given that the knowledge of matrix $\boldsymbol{A}$ is not available due to damages are such that the displacements of the nodes of F_2 equal to 0.

$$
\begin{aligned}
&\boldsymbol{A} = \begin{bmatrix} \boldsymbol{A_{11}} & \boldsymbol{A_{12}} \\ \boldsymbol{A_{21}} & A_{22} \end{bmatrix} \begin{bmatrix} U_{f1} \\ U_{f2} \end{bmatrix} = \begin{bmatrix} F_{f1} \\ 0 \end{bmatrix} + \begin{bmatrix} 0 \\ F_{f2} \end{bmatrix} \\
&U_{f2} = 0 \;\Rightarrow\; F_{f2} = \boldsymbol{A_{21}} \boldsymbol{A_{11}^{-1}} F_{f1}
\end{aligned} \tag{6}
$$

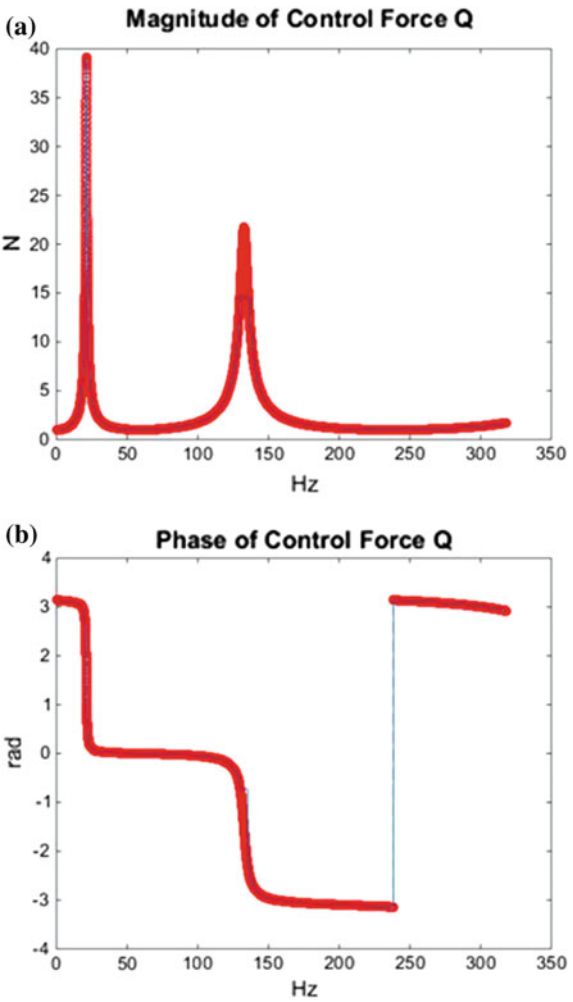

Fig. 3 **a** Magnitude of control force Q in order to stabilize the second end of the beam substructure. The *blue line* represents the results from the optimization while the *red circles* the exact solution from Eq. (6), and **b** Phase of control force Q in order to stabilize the second end of the beam substructure. The *blue line* represents the results from the optimization while the *red circles* the exact solution from Eq. (6)

4 Description of the Test Examples—Numerical Results

In order to verify the performance of the proposed control procedure a thin steel beam substructure with solid rectangular cross-section is used for the numerical verification. The beam is divided in 100 beam elements (i.e. $n_e = 100$). The Young's modulus of elasticity is equal to 200 GPa, the beam length is $L_{tot} = 0.55$ m and the density considered is equal to 7850 kg/m^3. The width of the rectangular cross-section is equal to b = 7.86 mm and the corresponding height is equal to $h = 7.86$ mm. In order to simulate an accelerometer, a small mass ($m_{accel} = 0.03$ kg) was added to the finite element model. The Rayleigh damping matrix for 2 % damping ratio is used to simulate damping.

The control procedure is performed initially for the intact structure. A frequency sweep is performed as follows: At the first end of the substructure beam a constant

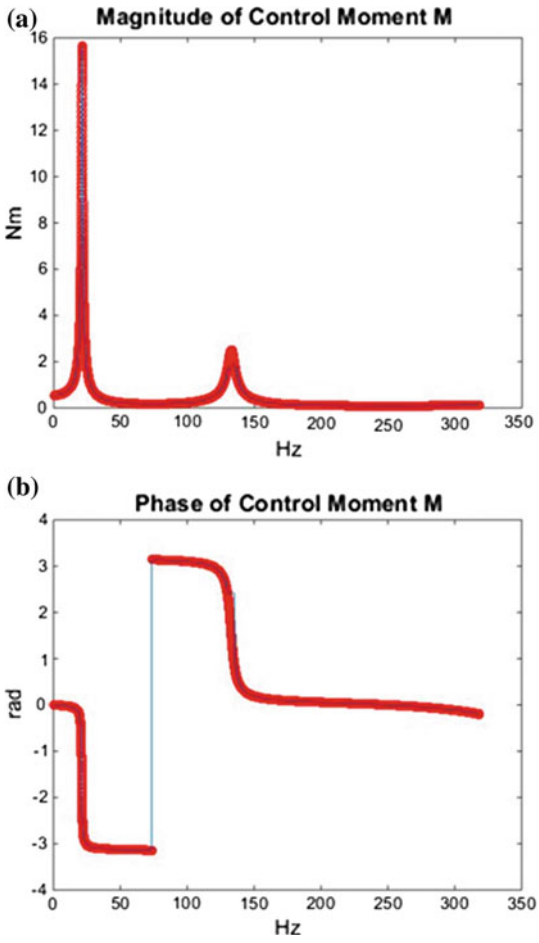

Fig. 4 **a** Magnitude of control moment M in order to stabilize the second end of the beam substructure. The *blue line* represents the results from the optimization while the *red circles* the exact solution from Eq. (6) and **b** Phase of control moment M in order to stabilize the second end of the beam substructure. The *blue line* represents the results from the optimization while the *red circles* the exact solution from Eq. (6)

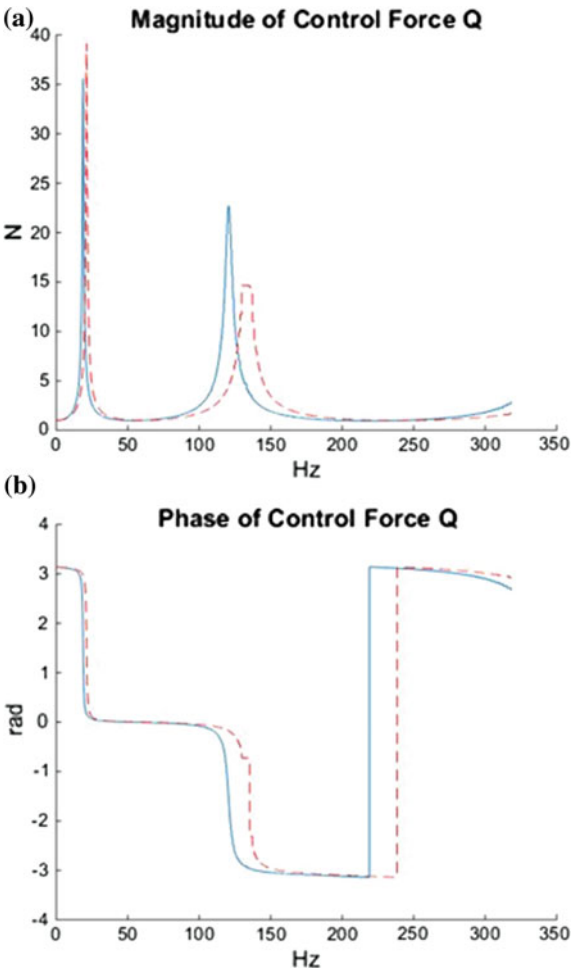

Fig. 5 **a** Magnitude of control force Q in order to stabilize the second end of the damaged and intact beam substructure. The *blue line* represents the results from damaged beam while the *red dashed line* those from the intact case and **b** Phase of control force Q in order to stabilize the second end of the damaged and intact beam substructure. The *blue line* represents the results from damaged beam while the *red dashed line* those from the intact case

regarding magnitude and phase sinusoidal force Q_1 with frequency ω is applied. At the other end the forces that minimize its displacements are sought by optimization. These forces have the same frequency ω but different magnitude and phase. The optimization algorithm starts with random values for the magnitude and phase of Q_2 and M_2 at first, but at each successive frequency step (Δω) uses the optimum values from the previous optimization procedure. The results are then compared with the exact solution from Eq. (6) as depicted in Figs. 3 and 4. It is evident that a controlling procedure mimicking the optimization algorithm can stabilize the second end of the substructure, allowing it to vibrate in essence like a cantilever. From the frequency response of the magnitude and phase of Q and M the resonant frequencies of the intact substructure are also revealed.

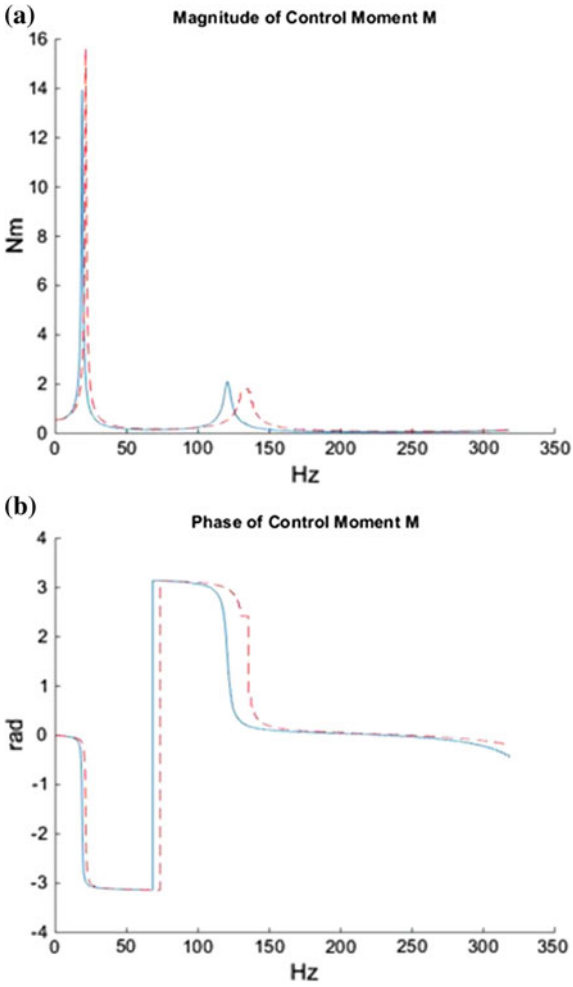

Fig. 6 **a** Magnitude of control moment M in order to stabilize the second end of the damaged and intact beam substructure. The *blue line* represents the results from damaged beam while the *red dashed line* those from the intact case and **b** Phase of control moment M in order to stabilize the second end of the damaged and intact beam substructure. The *blue line* represents the results from damaged beam while the *red dashed line* those from the intact case

In order to examine the efficiency of the proposed method in terms of damage identification, a deep crack is considered and modeled by reducing the damage factor of the 100th finite element. The procedure is than implemented again and the results are depicted in Figs. 5 and 6. It is evident from the swift of the peaks in the frequency response for the magnitude and the phase of both Q and M that the identification of damage in the particular substructure is straightforward. After the resonant frequencies of the damaged structure have been recorded, it is possible to proceed with one of the global damage identification algorithms (that uses natural frequencies) for the substructure in order to further localize the damages.

5 Conclusions

In this work the implementation of actuator connections that divide a structure in several substructures is proposed and theoretically verified. These connections can be installed on the structure during construction or retrofit. A control procedure mimicking an unconstrained optimization algorithm can be implemented that allows certain degrees of freedom of the substructure to be stabilized. In this way, real vibration data can be directly measured from the excited substructure while its natural frequencies are recorded with minimal error. The proposed procedure was numerically verified in a beam substructure and the capability of substructure damage identification was demonstrated.

Acknowledgments The research study in the current chapter has been conducted in the frame of the Research Funding Program: Marie Sklodowska-Curie Research and Innovation Staff Exchanges (RISE) "OPTARCH—Optimization Driven Architectural Design of Structures", H2020-MSCA-RISE-2015.

References

1. Doebling SW, Farrar CR, Prime MB (1998) A summary review of vibration-based damage identification methods. Shock Vib Dig 30(2):91–105
2. Fan W, Qiao P (2011) Vibration-based damage identification methods: A review and comparative study. Struct Health Monit 10(1):83–111
3. Liang RY, Hu JL, Choy F (1992) Quantitative NDE technique for assessing damages in beam structures. J Eng Mech 118(7):1468–1487
4. Hassiotis S, Jeong GD (1993) Assessment of structural damage from natural frequency measurements. Comput Struct 49(4):67–91
5. Bicanic N, Chen H-P (1997) Damage identification in framed structures using natural frequencies. Int J Numer Meth Eng 40(23):4451–4468
6. Vestroni F, Capecchi D (2000) Damage detection in beam structures based on frequency measurements. J Eng Mech 126(7):761–768
7. Kim J-T, Ryu Y-S, Cho H-M, Stubbs N (2003) Damage identification in beam-type structures: frequency-based method vs mode-shape-based method. Eng Struct 25(1):57–67
8. Alvandi A, Cremona C (2006) Assessment of vibration-based damage identification techniques. J Sound Vib 292(1–2):179–202
9. Friswell MI (2007) Damage identification using inverse methods. Philos Trans R Soc Math Phys Eng Sci 365(1851):393–410
10. Yang QW (2010) A new damage identification method based on structural flexibility disassembly. J Vib Control 17(7):1000–1008
11. Li B, Chen X, He Z (2013) Three steps meshing based multiple crack identification for structures and its experimental studies. Chin J Mech Eng 26(1):400–405
12. Yao R, Pakzad SN (2014) Time and frequency domain regression-based stiffness estimation and damage identification. Struct Control Health Monit 21(3):356–380
13. He R-S, Hwang S-F (2006) Damage detection by an adaptive real-parameter simulated annealing genetic algorithm. Comput Struct 84(31–32):2231–2243
14. Guo HY, Li ZL (2009) A two-stage method to identify structural damage sites and extents by using evidence theory and micro-search genetic algorithm. Mech Syst Signal Process 23 (3):769–782

15. Jeong M, Choi J-H, Koh B-H (2013) Performance evaluation of modified genetic and swarm-based optimization algorithms in damage identification problem. Struct Control Health Monit 20(6):878–889
16. Saada MM, Arafa MH, Nashef AO (2013) Finite element model updating approach to damage identification in beams using particle swarm optimization. Eng Optimization 45(6):677–696
17. Begambre O, Laier JE (2009) A hybrid particle swarm optimization—simplex algorithm (PSOS) for structural damage identification. Adv Eng Softw 40(9):883–891
18. Xia Y, Hao H (2003) Statistical damage identification of structures with frequency changes. J Sound Vib 263(4):853–870
19. Chatzieleftheriou S, Lagaros ND (2016) A trajectory method for vibration based damage identification of underdetermined problems. Struct Control Health Monit. Version of Record online: doi:10.1002/stc.1883
20. Currie D, Petrie N, Lu L (2012) A benchmark study of dynamic damage identification in plates. In: Proceedings of the institution of civil engineers: engineering and computational mechanics, vol 165(2), pp 103–118
21. Hou J, Jankowski L, Ou J (2011) A substructure isolation method for local structural health monitoring. Struct Control Health Monit 18(6):601–618
22. Hou J, Jankowski L, Ou J (2015) Frequency-domain substructure isolation for local damage identification. Adv Struct Eng 18(1):137–153
23. Shanno DF (1970) Conditioning of Quasi-Newton methods for function minimization. Math Comput 24:647–656

Fuzzy Neural Network Based Response of Uncertain System Subject to Earthquake Motions

S. Chakraverty and Deepti Moyi Sahoo

Abstract Earthquakes are one of the most destructive natural phenomena which consist of rapid vibrations of rock near the earth's surface. Because of their unpredictable occurrence and enormous capacity of destruction, they have brought fear to mankind since ancient times. Usually the earthquake acceleration is noted from the equipment in crisp or exact form. But in actual practice those data may not be obtained exactly at each time step, rather those may be with some error. So those records at each time step are assumed here as fuzzy. Using those fuzzy acceleration data, the structural response is found. The primary aim of the present study is to model Fuzzy Neural Network (FNN) and to compute structural response of a structural system by training the model for Indian earthquakes at Chamoli and Uttarkashi using fuzzified ground motion data. The neural network is first trained here for real fuzzy earthquake data. The trained FNN architecture is then used to simulate earthquakes by feeding various intensities and it is found that the predicted responses given by FNN model are good for practical purposes. The above may give an idea about the safety of the structural system in case of future earthquakes. The present chapter demonstrates the procedure for an example case of a simple shear structure (SDOF) but the procedure may easily be generalized for higher storey structures as well.

1 Introduction

One of the most frightening and destructive phenomena of nature is a severe earthquake and its terrible after effects. An earthquake is the sudden and rapid shaking of the earth caused by the breaking and shifting subterranean rock as it releases stress that has accumulated over a long time. Earthquakes are one of the most costly natural hazards faced by the world posing a significant risk to the public

S. Chakraverty (✉) · D.M. Sahoo
Department of Mathematics, National Institute of Technology Rourkela,
Rourkela 769008, Odisha, India
e-mail: sne_chak@yahoo.com

M. Papadrakakis et al. (eds.), *Computational Methods in Earthquake Engineering*,
Computational Methods in Applied Sciences 44,
DOI 10.1007/978-3-319-47798-5_13

safety. The risks that earthquakes pose to society, including death, injury and economic loss, can be greatly reduced by better planning, construction, mitigation practices before earthquakes happen, providing critical and timely information to improve response after they occur. There is no way to stop these natural phenomena, but seismologists have several methods so that they can estimate approximately or predict future earthquake events. By studying the amount of earthquakes and the time that they happen in a certain area, seismologist can then guess the probability of another earthquake occurring in the area within a given time. This will certainly give an idea to people about the time period of the occurrence of the next earthquake, so that they can prepare themselves for another possible quake. The prediction of the real earthquake ground motion at a particular building site is very complex and difficult. Earthquakes usually occur without warning.

When it is strong enough the earthquake ground motion sets the building in motion, starting with the foundation and transfers the motion throughout the rest of the building in a very complex way. Dynamic response of a structure to strong earthquake ground motion may be investigated by different methods. One of these methods consists of constructing a good theoretical model of a structure and calculating the exact dynamic response for an assumed known motion of the foundation. Although this approach is relatively time consuming and costly. It has frequently been used for the final design of important structures recently. The other method that has been used here may be to create a trained black box containing the characteristics of the structure and of the earthquake motion which can predict the dynamic response for any other earthquake for a particular structure.

System Identification (SI) techniques play an important role in investigating and reducing gaps between the structural systems and their structural design models. This is also true in structural health monitoring for damage detection. A great amount of research has been conducted in SI. SI techniques are also applied to determine vibration characteristics, modal shapes and damping ratios of complex structural systems so as to frame knowledge for modelling and assessing current design procedures. The result of such process identification is usually a mathematical model by which the dynamic behaviour can be estimated or predicted. Various methodologies for different types of problems in system identification were given by Masri et al. [1], Natke [2], Perry and Koh [3], Nandakumar and Shankar [4], Billmaier and Bucher [5], Chakraverty [6] and Khanmirza et al. [7]. Studies related to structural damage detection have been done by various researchers. Angeles and Alvarez-Icaza [8] used an efficient reparameterization of least-squares algorithm to identify parameters of linear models of buildings under orthogonal bi-dimensional seismic excitation in a 3 DOF system. Niu [9] proposed a structural parameter identification and damage detection approach using displacement measurement time series and the performance of this approach is validated experimentally with a frame structure model in a healthy condition and with joint connection damages. This approach also provides an alternative way for damage detection of engineering structures by direct use of structural dynamic displacement measurements. Various methods namely Derras and Bekkouche [10], Lagaros and

Papadrakakis [11], Zamani et al. [12], Robles and Hernandez-Becerril [13], Liu and Lee [14] and Ramhormozian et al. [15] were introduced for response prediction and estimation and for structural control. Hegde and Sinha [16] presented an efficient procedure to determine the natural frequencies, modal damping ratios and mode shapes for torsionally coupled shear buildings using earthquake response records. An identification of dynamic models of a building structure using multiple earthquake records has been developed by Hong et al. [17].

Artificial Neural Network (ANN) has gradually been established as a powerful tool in various fields. ANN has recently been applied to assess damage in structures. They have been successfully applied for identification and control of dynamic systems in various field of engineering because of their excellent learning capacity and high tolerance to partially inaccurate data. In this regards lots of works in structural health monitoring and damage detection using ANN have been done by various researchers. A nonparametric structural damage detection methodology based on nonlinear system identification approaches has been given by Masri et al. [18] for health monitoring of structure-unknown systems. Kao and Hung [19] considered two steps for structural damage detection. The first step involves system identification using Neural System Identification Networks (NSINs) to identify the undamaged and damaged states of a structural system and the second step involves structural damage detection using the aforementioned trained NSINs to generate free vibration responses with the same initial condition or impulsive force. A multistage identification scheme for structural damage detection with the use of modal data using a hybrid neural network strategy has been proposed by Pillai and Krishnapillai [20]. Bakhary et al. [21] presented an approach to detect structural damage using ANN method with progressive substructure zooming. This method also uses the substructure technique together with a multi-stage ANN models to detect the location and extent of the damage. The applications of neural networks to damage detection in structures are also studied by Zhang et al. [22]. To avoid the false positives of damages in the deterministic identification method induced by uncertainties in measurement noise, Zhang et al. [23] proposed a probabilistic method to identify damages of the structures with uncertainties under unknown input. The proposed probabilistic method is developed from a deterministic simultaneous identification method of structural physical parameters and input based on dynamic response sensitivity. The application of artificial neural networks and wavelet analysis to develop an intelligent and adaptive structural damage detection system has been investigated by Shi and Yu [24]. A probabilistic approach for damage identification considering measurement noise uncertainties has been given by Lei et al. [25]. The probability of identified structural damage is further derived based on the reliability theory. Hakim and Razak [26] developed an Adaptive Neuro-Fuzzy Inference System (ANFIS) and ANNs technique to identify damage in a model steel girder bridge using dynamic parameters. Other advanced studies include application of neural network techniques for damage detection are Oliva and Pichardo [27], Kerh et al. [28], Xu et al. [29], Aghamohammadi et al. [30] and Suryanita and Adnan [31]. Chakraverty et al. [32] used artificial neural network model to compute response of structural system by training the model for a

particular earthquake. In order to simulate and estimate structural response of two-storey shear building by training the model for a particular earthquake using the powerful technique of artificial neural network models has been presented by Chakraverty et al. [33]. It may be seen from above that artificial neural networks provide a fundamentally different approach to damage detection problems subjected to different earthquakes.

It is revealed from the above literature review that various authors developed different identification methodologies using ANN. They supposed that the data obtained are in exact or crisp form. But in actual practice the experimental data obtained from equipments have errors, either due to human or equipment, thereby giving uncertain form of the data. One may also use probabilistic methods to handle such problems. Yet, the probabilistic methods require huge quantity of data which may not be easy or feasible in particular to the structural parameters. In view of the above various research works are being developed using Fuzzy Neural Networks (FNN) in different fields. Ishibuchi et al. [34] developed an architecture for neural networks where the input vectors are in terms of fuzzy numbers. A methodology for fuzzy neural networks where the weights and biases are taken as fuzzy numbers and the input vectors as real numbers has been proposed by Ishibuchi et al. [35]. A fuzzy neural network with trapezoidal fuzzy weights was also presented by Ishibuchi et al. [36]. They have developed the methodology in such a way that it can handle fuzzy inputs as well as real inputs. In this respect Ishibuchi et al. [37] derived a general algorithm for training a fuzzified feed-forward neural network that has fuzzy inputs, fuzzy targets and fuzzy connection weights. The derived algorithms are also applicable to the learning of fuzzy connection weights with various shapes such as triangular and trapezoidal. Another new algorithm for learning fuzzified neural networks has also been developed by Ishibuchi et al. [38]. Sahoo and Chakraverty [39] proposed identification methodologies for multi-storey shear buildings using fuzzy neural network which can estimate the structural parameters. Pankaj and Wilscy [40] proposed a method for face recognition using a fuzzy neural network classifier based on the Integrated Adaptive Fuzzy Clustering (IAFC) method. Umoh et al. [41] developed a fuzzy-neural network model and applied the model for effective control of profitability in paper recycling to improve production accuracy, reliability, robustness and to maximize profit generated by an industry. Vijaykumar et al. [42] used T–S fuzzy neural network in speech recognition systems. Various deterrent factors influencing the supply chain to forecast the production plan have been presented by Sharma and Sinha [43]. Use of neural network combined with fuzzy logic for long term load forecasting has been given by Swaroop [44]. Zhang and Dai [45] reviewed the state of the art for the application of fuzzy neural network in diagnosis, recognition, and image processing and intelligent robot control of medicine and finally they prospected the application of fuzzy neural network in medicine. A recent work on robust fuzzy neural network for sliding mode control scheme for interior permanent magnet synchronous motor (IPMSM) drives was developed by Leu et al. [46]. Zahedi et al. [47] presented the prediction of ozone pollution as a function of meteorological parameters around the Shuaiba industrial area in Kuwait by a FNN modelling approach.

An adaptive FNN controller for missile guidance has been given by Wang and Hung [48].

For present work, Chamoli and Uttarkashi earthquake recorded at Barkot, Uttarakhand, India in NE (North-East) direction have been taken. The Chamoli earthquake occurred in 28 March 1999 and the Uttarkashi earthquake occurred in 20 October, 1991. The magnitude of Chamoli Earthquake is 6.8 Mw and its depth is about 21 km. the magnitude of Uttarkashi Earthquake is 6.8 Mw and its depth is 10 km. These earthquakes ground accelerations in fuzzified form have been considered. From the fuzzified ground acceleration, the responses in fuzzified form are computed using the proposed procedure. Then the ground acceleration and the corresponding response in fuzzified form are trained using FNN with damping and frequency parameters. After training the network with one earthquake, the converged weight matrices are stored. The earthquake acceleration data are actually both positive and negative. But due to complexities in fuzzy computation these data are transferred from bipolar to unipolar by a transformation and again it is transferred back from unipolar to bipolar by an inverse transformation. These transformations are used to reduce the computational complexity and to handle these data in α-cut form. In order to show the power of the trained networks, different intensity earthquake data (generated numerically) are used as input to predict the direct response of the structure without using any mathematical analysis of the response prediction. Similarly, various other results related to the use of these trained networks are discussed for future/other earthquakes.

2 Fuzzy Set Theory and Preliminaries

Here we briefly describe fuzzy set, fuzzy numbers and basic fuzzy arithmetic operations. The following fuzzy arithmetic operations are used in this paper for defining our fuzzified neural network Lee [49].

A. Let X be a universal set. Then the fuzzy subset A of X is defined by its membership function

$$\mu_A : X \rightarrow [0,\ 1] \tag{1}$$

which assign a real number $\mu_A(x)$ in the interval $[0,\ 1]$, to each element $x \in X$, where the value of $\mu_A(x)$ at x shows the grade of membership of x in A.

B. Given a fuzzy set A in X and any real number $\alpha \in [0,\ 1]$, then the $\alpha-$ cut or $\alpha-$ level or cut worthy set of A, denoted by A_α is the crisp set

$$A_\alpha = \{x \in X | \mu_A(x) \geq \alpha\} \tag{2}$$

C. A Triangular Fuzzy Number (TFN) A can be defined as a triplet $[\underline{a}, a\,c, \overline{a}]$. Its membership function is defined as

$$\mu_A(x) = \begin{cases} 0, & x < \underline{a} \\ \frac{x-\underline{a}}{a\,c-\underline{a}}, & \underline{a} \le x \le a\,c \\ \frac{\overline{a}-x}{\overline{a}-a\,c}, & a\,c \le x \le \overline{a} \\ 0, & x > \overline{a} \end{cases} \tag{3}$$

Above TFN may be transformed to an interval form A_α by α - cut as

$$A_\alpha = \left[\underline{a}^{(\alpha)}, \overline{a}^{(\alpha)}\right] = [(a\,c - \underline{a})\alpha + \underline{a}, -(\overline{a} - a\,c)\alpha + \overline{a}] \tag{4}$$

where $\underline{a}^{(\alpha)}$ and $\overline{a}^{(\alpha)}$ are the lower and upper limits of the α-level set A_α.

2.1 Operation of Fuzzy Numbers

In this section, we consider arithmetic operations on fuzzy numbers and the result is expressed in the membership function $\forall x, y, z \in R$ we define.

(1) Addition: $\mu_{A\,(+)\,B}\,(z) = \max\{\mu_A(x) \wedge \mu_B(y) \,|\, z = x + y\}$
(2) Multiplication: $\mu_{A\,(\cdot)\,B}\,(z) = \max\{\mu_A(x) \wedge \mu_B(y) \,|\, z = x \cdot y\}$
(3) Non Linear Mapping: $\mu_{f(Net)}\,(z) = \max\{\mu_{Net}(x) \,|\, z = f(x)\}$

Assuming A and B as two α-level sets, the operations of fuzzy numbers can be rewritten for α-level sets as follows:

(1) Addition:

$$\left[\underline{a}^{(\alpha)}, \overline{a}^{(\alpha)}\right](+)\left[\underline{b}^{(\alpha)}, \overline{b}^{(\alpha)}\right] = \left[\underline{a}^{(\alpha)} + \underline{b}^{(\alpha)}, \overline{a}^{(\alpha)} + \overline{b}^{(\alpha)}\right] \tag{5}$$

(2) Multiplication:

$$\begin{aligned}\left[\underline{a}^{(\alpha)}, \overline{a}^{(\alpha)}\right](\cdot)\left[\underline{b}^{(\alpha)}, \overline{b}^{(\alpha)}\right] = \{&\min(\underline{a}^{(\alpha)} \cdot \underline{b}^{(\alpha)}, \underline{a}^{(\alpha)} \cdot \overline{b}^{(\alpha)}, \overline{a}^{(\alpha)} \cdot \underline{b}^{(\alpha)}, \overline{a}^{(\alpha)} \cdot \overline{b}^{(\alpha)}), \\ &\max(\underline{a}^{(\alpha)} \cdot \underline{b}^{(\alpha)}, \underline{a}^{(\alpha)} \cdot \overline{b}^{(\alpha)}, \overline{a}^{(\alpha)} \cdot \underline{b}^{(\alpha)}, \overline{a}^{(\alpha)} \cdot \overline{b}^{(\alpha)})\}\end{aligned} \tag{6}$$

(3) Non Linear Mapping:

$$f(\underline{Net}^{(\alpha)}, \overline{Net}^{(\alpha)}) = \left[f(\underline{Net}^{\alpha}), f\left(\overline{Net}^{\alpha}\right)\right]. \tag{7}$$

2.2 Transformation of Data from Bipolar to Unipolar

The data are in fuzzified form, hence they are first converted to α-cut form and then the transformation is applied. The data are transferred from bipolar to unipolar i.e., from [−1, 1] to [0, 1] by the following transformation. Here the input is considered as the ground acceleration and output as the response of the structure

$$\tilde{A}_m^{\alpha} = \frac{1 + \tilde{b}_m^{\alpha}}{2} \tag{8}$$

where $\tilde{b}_m^{\alpha}$ is the output in α-cut form.

3 Fuzzy Neural Network and Learning Algorithm for FNN

Fuzzy Neural Network (FNN) is a network in which either inputs, outputs and the connection weights or all of them are in fuzzified form. The topological architecture for FNN is identical to the crisp neural network. Traditional Neural Network (NN) and Error Back Propagation (EBP) are well known but here for the sake of completeness those are developed for fuzzy numbers. The inputs, weights and biases of the standard feed forward neural network can be extended for fuzzy numbers. It may be noted that the fuzzification does not change the neural network architecture.

Here for given R training pairs $\{\tilde{Z}_1, \tilde{d}_1; \tilde{Z}_2, \tilde{d}_2; \ldots \tilde{Z}_R, \tilde{d}_R\}$ where $\tilde{Z}_i(I \times 1)$ are input and $\tilde{d}_i(M \times 1)$ are target values for the given inputs. $\tilde{Z}_i$, $\tilde{P}_j$ and $\tilde{O}_k$ are input, hidden and output layer respectively. The weights between input and hidden layers are denoted by $\tilde{v}_{ji}$ and the weights between hidden and output layers are denoted by $\tilde{w}_{mj}$ which are all in fuzzified form. The input $\tilde{Z}_i = \tilde{\ddot{a}}_i = [\underline{\ddot{a}}_i, \ddot{a}c_i, \overline{\ddot{a}}_i]$ are the ground acceleration and the output $\tilde{O}_m = \tilde{\ddot{x}}_m = [\underline{\ddot{x}}_m, \ddot{x}c_m, \overline{\ddot{x}}_m]$ are responses of the structure in fuzzified form. The procedure may easily be written for the processing of this algorithm as below.

Hence the input-output relation of the fuzzified neural networks can be written for a fuzzy input vector $\{\tilde{Z}_1, \tilde{Z}_2, \ldots \tilde{Z}_R\}$ as follows:Input units:

$$\tilde{O}_i = \tilde{Z}_i, \quad i = 1, 2, \ldots, \mathrm{I} \tag{9}$$

Hidden units:

$$\tilde{P}_j = \tilde{f}(Net_j), j = 1, 2, \ldots, \mathrm{J} \tag{10}$$

$$\left(Net_j\right) = \sum_{i=1}^{I} \tilde{v}_{ji}\, \tilde{O}_i + \tilde{\theta}_j, \quad j = 1, 2, \ldots, \mathrm{J} \tag{11}$$

where f is the unipolar activation function defined by $f(net) = 1/[1 + \exp(-\gamma\, net)]$. Output units:

$$\tilde{O}_m = \tilde{f}(Net_m), \quad m = 1, 2, \ldots, \mathrm{M} \tag{12}$$

$$(Net_m) = \sum_{j=1}^{J} \tilde{w}_{mj}\, \tilde{P}_j + \tilde{\theta}_m \, m = 1, 2, \ldots, \mathrm{M} \tag{13}$$

where $\tilde{v}_{ji}$ and $\tilde{w}_{mj}$ are fuzzy weights and $\tilde{\theta}_j$ and $\tilde{\theta}_m$ are fuzzy biases. The architecture of the fuzzified neural network is shown in Fig. 1. It should be noted that the fuzzy

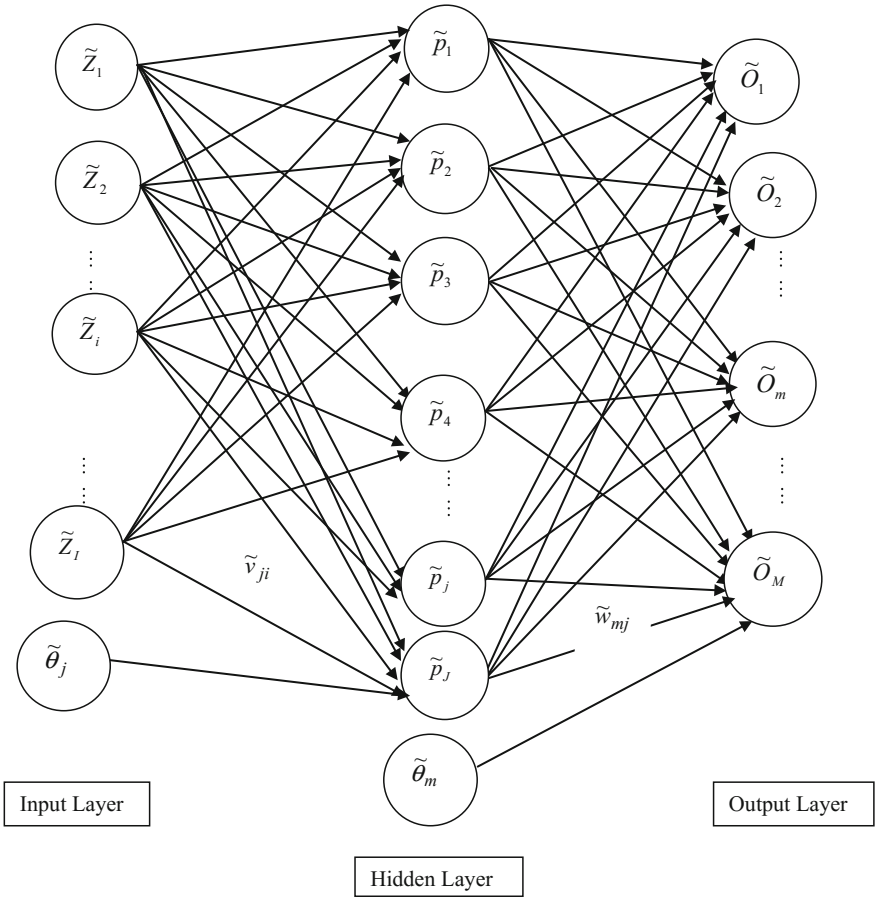

Fig. 1 Layered feed-forward fuzzy neural network

target output $\tilde{d}_m$ may be non-symmetric while fuzzy weights and the fuzzy biases are symmetric triangular fuzzy numbers. Let us denote the α-level sets of the fuzzy desired output as $\tilde{O}_m^{\alpha} = \left[\underline{O}_m^{\alpha}, \overline{O}_m^{\alpha}\right]$ and the corresponding fuzzy target output as $\tilde{d}_m^{\alpha} = \left[\underline{d}_m^{\alpha}, \overline{d}_m^{\alpha}\right]$.

The error is then computed as

$$\tilde{E} = \frac{\alpha}{2}\left[\left(\underline{d}_m^{\alpha} - \underline{O}_m^{\alpha}\right)^2 + \left(\overline{d}_m^{\alpha} - \overline{O}_m^{\alpha}\right)^2\right] m = 1, 2, \ldots, \mathrm{M} \tag{14}$$

Thus the weights between input and hidden layer are updated by the following equation

$$\begin{aligned} &\tilde{v}_{ji}^{\alpha}(New) = \left[\underline{v}_{ji}^{\alpha}(New), \overline{v}_{ji}^{\alpha}(New)\right] = \left[\underline{v}_{ji}^{\alpha}(Old), \overline{v}_{ji}^{\alpha}(Old)\right] + \left[\Delta\underline{v}_{ji}^{\alpha}, \Delta\overline{v}_{ji}^{\alpha}\right] \\ &j = 1, 2, \ldots, \mathrm{J} \text{ and } i = 1, 2, \ldots, \mathrm{I} \end{aligned} \tag{15}$$

where change in weights are calculated as

$$\Delta\tilde{v}_{ji}^{\alpha} = \left[\Delta\underline{v}_{ji}^{\alpha}, \Delta\overline{v}_{ji}^{\alpha}\right] = \left[-\eta\frac{\partial\tilde{E}}{\partial\underline{v}_{ji}^{\alpha}}, -\eta\frac{\partial\tilde{E}}{\partial\overline{v}_{ji}^{\alpha}}\right] j = 1, 2, \ldots, \mathrm{J} \text{ and } i = 1, 2, \ldots, \mathrm{I} \tag{16}$$

Consequently, weights between output and hidden layers are adjusted as,

$$\begin{aligned} &\tilde{w}_{mj}^{\alpha}(New) = \left[\underline{w}_{mj}^{\alpha}(New), \overline{w}_{mj}^{\alpha}(New)\right] = \left[\underline{w}_{mj}^{\alpha}(Old), \overline{w}_{mj}^{\alpha}(Old)\right] + \left[\Delta\underline{w}_{mj}^{\alpha}, \Delta\overline{w}_{mj}^{\alpha}\right] \\ &m = 1, 2, \ldots, \mathrm{M} \text{ and } j = 1, 2, \ldots, \mathrm{J} \end{aligned} \tag{17}$$

where change in weights for these layers are calculated as

$$\begin{aligned} \Delta\tilde{w}_{mj}^{\alpha} = \left[\Delta\underline{w}_{mj}^{\alpha}, \Delta\overline{w}_{mj}^{\alpha}\right] = \left[-\eta\frac{\partial\tilde{E}}{\partial\underline{w}_{mj}^{\alpha}}, -\eta\frac{\partial\tilde{E}}{\partial\overline{w}_{mj}^{\alpha}}\right] m = 1, 2, \ldots, \mathrm{M} \text{ and } j \\ = 1, 2, \ldots, \mathrm{J} \end{aligned} \tag{18}$$

And η is the learning constant.

All the computations and calculations are done based on the fuzzy operation defined in the above section.

4 Strategy for Response Prediction

The basic concept behind the proposed methodology is to predict the structural response (in fuzzified form) of an uncertain shear structural system subject to earthquake forces which are also in fuzzified form. Two scenarios namely, without damping and with damping have been considered for the analysis.

4.1 Without Damping

Here we discuss the procedure for an example problem of a Single Degree of Freedom (SDOF) system. Let $\tilde{M}$ be the mass of the generalized one storey structure in fuzzified form, $\tilde{K}$ the stiffness of the structure in fuzzified form and $\tilde{X}$ be the displacement relative to the ground also in fuzzified form. Then the equation of motion may be written as

$$\tilde{M}\ddot{\tilde{X}} + \tilde{K}\tilde{X} = -\tilde{M}\tilde{a} \tag{19}$$

$\ddot{\tilde{X}}$ = Acceleration in fuzzified form,
$\tilde{X}$ = Displacement in fuzzified form,
$\tilde{a}$ = Ground acceleration in fuzzified form

Equation (19) may be written as,

$$\ddot{\tilde{X}} + \tilde{\omega}^2\tilde{X} = -\tilde{a} \tag{20}$$

where $\tilde{\omega}^2$ is the fuzzified natural frequency parameter of the undamped structure. It may be noted that the above equation can be solved by Fuzzy Duhamel integral. Here to obtain the solution for Eq. (20), the Duhamel integral are considered for different sets of lower, centre and upper form. This is done to avoid complicacy raised while getting the above solution. And that is why now we will drop '$\sim$' from all notations and will consider the case for lower form first and similarly for centre and upper form.

Hence Eq. (20) in lower form is written as,

$$\ddot{\underline{X}} + \underline{\omega}^2\underline{X} = -\ddot{a} \tag{21}$$

where $\underline{\omega}^2 = \frac{\underline{K}}{\underline{M}}$ is the natural frequency parameter of the undamped structure in lower form.$\underline{K}$ is the stiffness parameter and $\underline{M}$ is the mass of the storey in lower form.

$\underline{\ddot{X}}$ = Acceleration in lower form,
$\underline{X}$ = Displacement in lower form,
$\underline{\ddot{a}}$ = Ground acceleration in lower form

Hence the solution of Eq. (21), Newmark and Rosenblueth [50] in lower form is written as

$$\underline{X(t)} = -\frac{1}{\underline{\omega}} \int_0^t \underline{\ddot{a}}(\tau) \sin[\underline{\omega}(t-\tau)] d\tau \tag{22}$$

From this solution the response of the structure namely acceleration in lower form is obtained for no damping. In a similar fashion we can compute for centre and upper form.

4.2 With Damping

Let $\tilde{M}$ be the mass of the generalized one storey structure in fuzzified form, $\tilde{K}$ the stiffness of the structure in fuzzified form, $\tilde{C}$ the damping and $\tilde{X}$ be the displacement relative to the ground all are in fuzzified form. Then the equation of motion may be written as

$$\tilde{M}\tilde{\ddot{X}} + \tilde{C}\tilde{\dot{X}} + \tilde{K}\tilde{X} = -\tilde{M}\tilde{\ddot{a}} \tag{23}$$

Equation (23) may be written in lower form as,

$$\underline{\ddot{X}} + 2\underline{\xi\omega}\underline{\dot{X}} + \underline{\omega}^2\underline{X} = -\underline{\ddot{a}} \tag{24}$$

where $\underline{\xi\omega} = \frac{\underline{C}}{\underline{M}}$ and $\underline{\omega}^2 = \frac{\underline{K}}{\underline{M}}$ are the natural frequency parameter of the damped and undamped structure in lower form. $\underline{C}$ is the damping and $\underline{\dot{X}}$ is the velocity in lower form.

Here also solution is obtained for different sets in lower, centre and upper form. Hence the solution of Eq. (24) in lower form is given as

$$\underline{X(t)} = -\frac{1}{\underline{\omega}} \int_0^t \underline{\ddot{a}}(\tau) \exp\left[-\underline{\xi}\,\underline{\omega}(t-\tau)\right] \sin[\underline{\omega}(t-\tau)] d\tau \tag{25}$$

From this solution the response of the structure namely the acceleration in lower form with damping is obtained. In a similar manner we can compute for the centre and upper form. Hence, the neural network architecture is constructed by taking the

fuzzified form of ground acceleration as input and the responses obtained from the above solution as output for each time step which is also in fuzzified form.

5 Numerical Results and Discussions

For the present study two Indian earthquakes, the Chamoli Earthquake at Barkot in NE (north east) direction and the Uttarkashi earthquake at Barkot in NE (north-east) direction have been considered for training and testing for different cases. The various cases considered are shown below:

Case (i): Without damping: Ground acceleration as well as response data in fuzzified form with crisp frequency.
Case (ii): Same as (i), but with fuzzy frequency
Case (iii): With damping: Ground acceleration as well as response data in fuzzified form with crisp frequency and fuzzy damping.
Case (iv): Same as (iii), but with fuzzy frequency
Case (v): Testing for different earthquake data with /without damping.

The earthquake acceleration data are actually both positive and negative. As mentioned in the Introduction that the transformation Eq. (8) first converts the data from bipolar to unipolar i.e., from range [−1, 1] to range [0, 1], then the data are transferred back to its bipolar form. The data in fuzzified form are converted to α-cut form first and then the transformation is applied.

As mentioned earlier for case (i), initially the system without damping is studied and for that the system is subjected to Chamoli Earthquake with maximum ground acceleration in fuzzified form as [19.088, 19.588, 20.088] cm/sec^{2}at Barkot in NE (north-east) direction. The response of the structure is obtained by solving Eq. (22). The ground acceleration in fuzzified form is converted to α-cut form and is used for training. The mass in fuzzified is taken as $\tilde{M} = [1, \quad 1, \quad 1]$ for all cases. The stiffness parameter is not used here directly as we are considering the frequency parameter in the model. Frequency parameter in crisp form is taken as ω = 0.02 with time range 0 to 14.96 s. (749 data points) for the mentioned earthquake. Comparisons between desired and FNN are shown in Fig. 2a–c. Figure 2a shows the plot for lower values, Fig. 2b shows the plot for centre values and Fig. 2c depicts the upper values. Simulations have been done for different hidden layer nodes and it was seen that the response result is almost same and good for 15 to 18 nodes in the hidden layer. However, 18 hidden layer nodes are used here to generate the results for 749 data points.

In case (ii), the system is considered without damping with the same earthquake. Here ground acceleration is taken as input and structural displacement as output. The neural network architecture is trained within the time range 0 to 14.96 s. (749 data points) taking frequency parameter in fuzzified form as $\omega = [0.4, \quad 0.5, \quad 0.6]$. Training has been done for different hidden layer nodes.

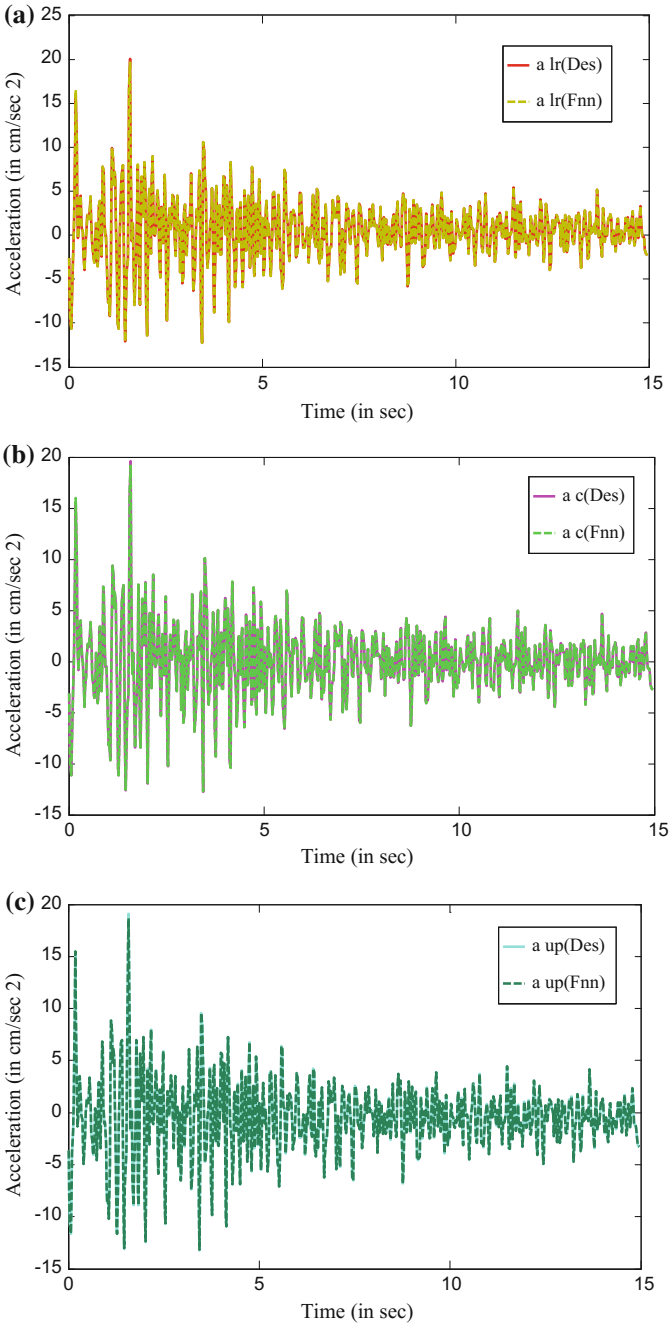

Fig. 2 **a** Comparison between the desired and FNN acceleration for lower values (without damping) **b** Comparison between the desired and FNN acceleration for centre values (without damping) **c** Comparison between the desired and FNN acceleration for upper values (without damping)

Again 18 hidden layer nodes are used to generate the results for 749 data points. The displacement time plots are plotted in Fig. 3a–c.

The system with damping is taken in case (iii). The ground acceleration of Uttarkashi earthquake at Barkot (NE) and the displacement in α-cut form are used as training patterns. The training patterns are trained by the FNN model with frequency parameter in crisp form as $\omega = 0.68981$ and damping $\tilde{C} = [1.48033, 1.58033, 1.68033]$. Training was done for a total time range of 0 to 14.96 s (749 data points). After training ground acceleration and response data for Uttarkashi earthquake for various nodes in hidden layer it was confirmed that 18 nodes are again sufficient for the prediction. So, the weights corresponding to 18 hidden nodes are stored and they are used to predict responses for various intensity earthquakes. Figure 4a–c show the displacement time plots between the desired and FNN.

For case (iv), the system is again considered with damping. The response of the structure in fuzzified form is computed using Eq. (25). Then the ground acceleration and structural response in α-cut form is used for training. Here frequency parameter in fuzzified form is taken as $\omega = [0.58981, 0.68981, 0.78981]$ and damping $\tilde{C} = [1.48033, 1.58033, 1.68033]$. The data are trained with different hidden nodes in the hidden layer and it was found that 16 hidden nodes are sufficient to get an accuracy of 0.001. Comparison between the desired and FNN is shown in Fig. 5a–c. After training the ground acceleration and response data for Uttarkashi earthquake at Barkot (NE) for different hidden nodes in hidden layer, the weights are stored and they are used to predict responses for various intensity earthquakes.

Finally in case (v) the training is extended with damping and without damping for various intensities with time range 0 to 9.98 s. (500 data points) and are tested with different hidden nodes in hidden layer. It was found that the response result is almost the same and good for 15 to 20 nodes in the hidden layer. But here 16 hidden layer nodes are used to generate the results for 500 data points without damping with frequency parameter in fuzzified form. Figure 6a–c show displacement time plot comparison between FNN and desired for 80 % of Uttarkashi earthquake at Barkot (NE) for $\omega = [0.01, 0.02, 0.03]$ using the stored converged weights of Chamoli earthquake directly. Similarly the training with damping for time range 0 to 9.98 s (500 data points) is done and is tested with different hidden nodes. It was found that the response result is almost the same and good for 16 hidden layer nodes. The comparison between the desired and FNN response data for 120 % of Chamoli earthquake acceleration at Barkot (NE) with $\omega = [0.58981, 0.68981, 0.78981]$ and damping $\tilde{C} = [1.48033, 1.58033, 1.68033]$ using the converged weights of Uttarkashi earthquake are shown in Fig. 7a–c.

A comparison between desired and FNN peak acceleration values (testing) with various intensities of Uttarkashi (without damping) and Chamoli earthquake acceleration at Barkot (NE) (with damping) is presented in Table 1. The error % between desired and FNN Peak values of predicted data is given in Table 2.

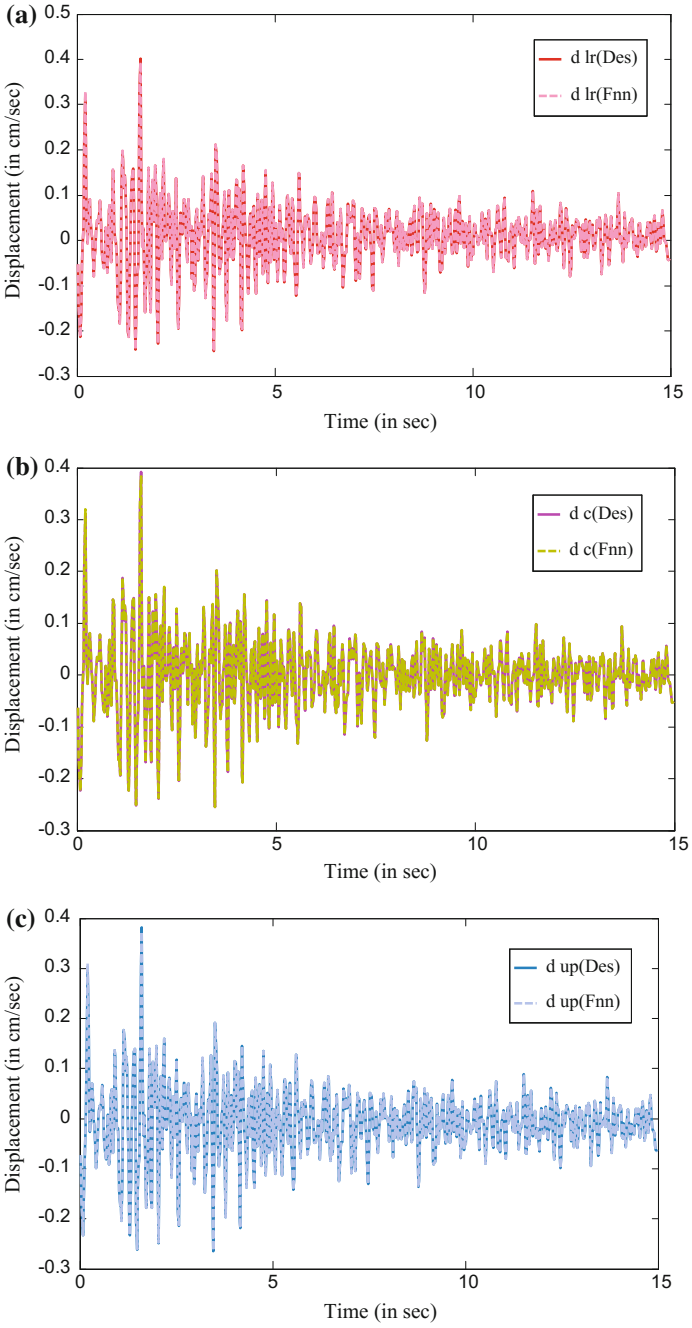

Fig. 3 **a** Comparison between the desired and FNN displacement for lower values (without damping) **b** Comparison between the desired and FNN displacement for centre values (without damping) **c** Comparison between the desired and FNN displacement for upper values (without damping)

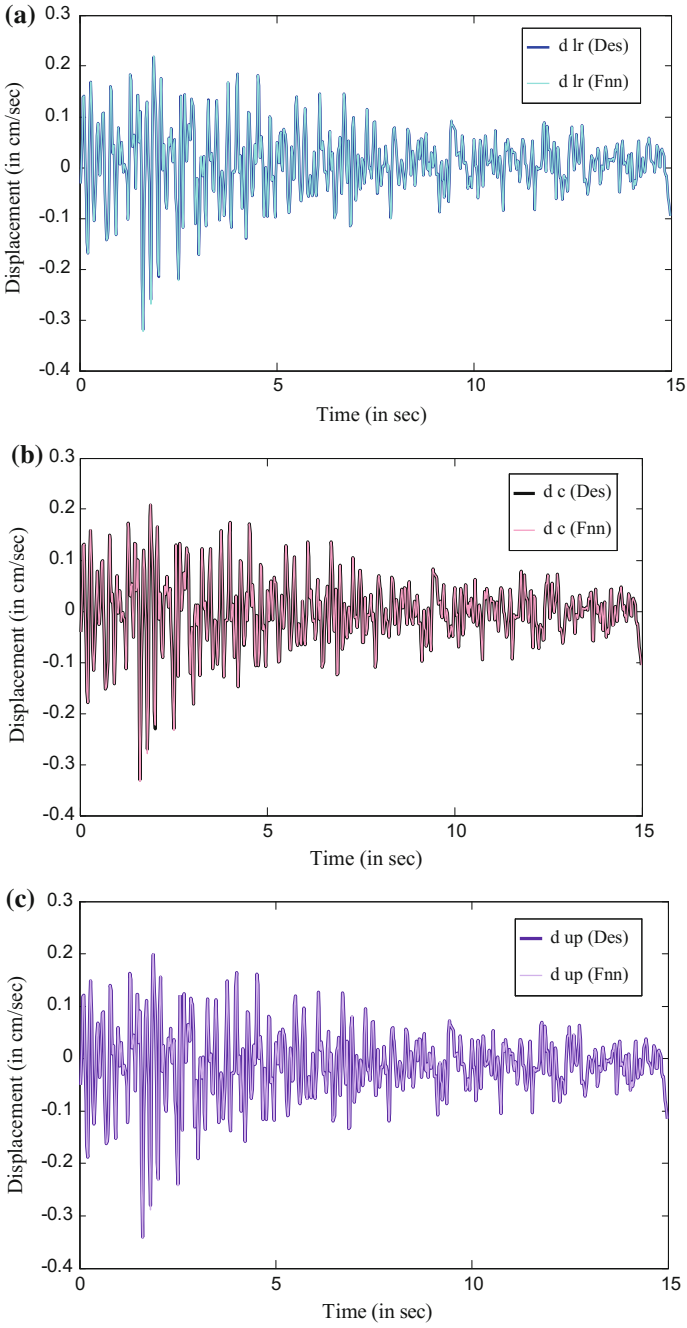

Fig. 4 **a** Comparison between the desired and FNN displacement for lower values (with damping) **b** Comparison between the desired and FNN displacement for centre values (with damping) **c** Comparison between the desired and FNN displacement for upper values (with damping)

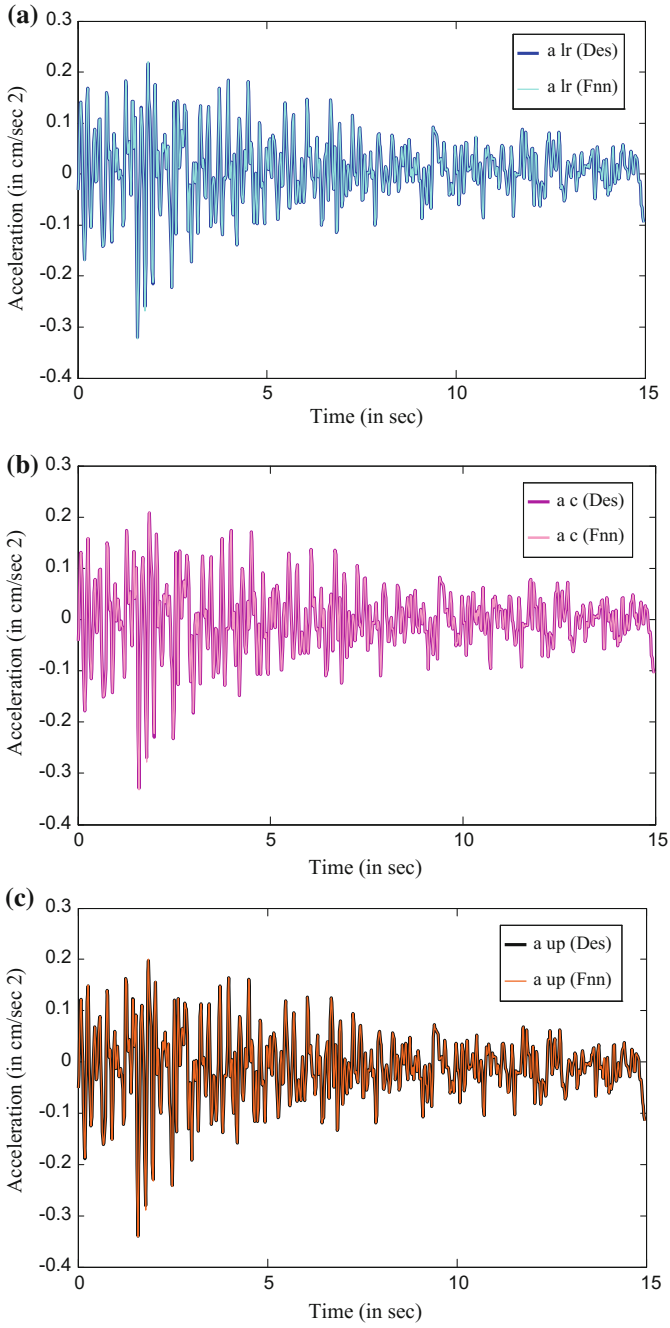

Fig. 5 **a** Comparison between the desired and FNN acceleration for lower values (with damping) **b** Comparison between the desired and FNN acceleration for centre values (with damping) **c** Comparison between the desired and FNN acceleration for upper values (with damping)

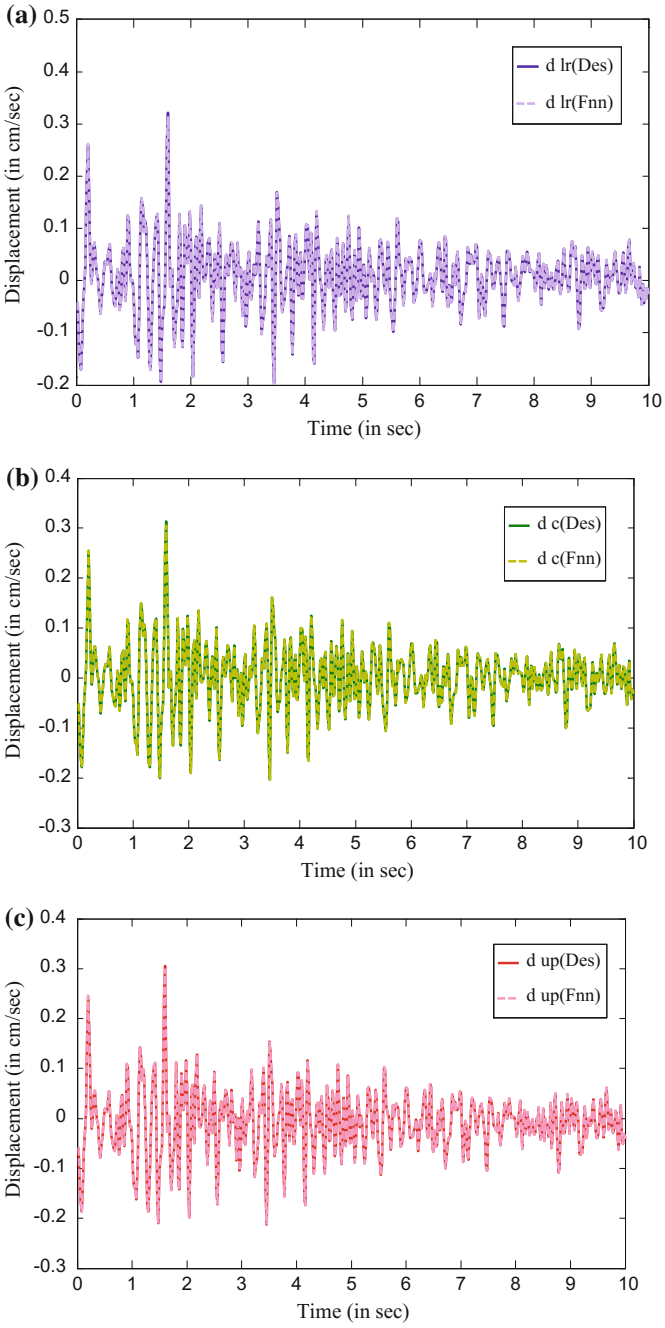

Fig. 6 **a** Comparison between the desired and FNN (Testing) displacement of 80 % for lower values (without damping) **b** Comparison between the desired and FNN (Testing) displacement of 80 % for centre values (without damping) **c** Comparison between the desired and FNN (Testing) displacement of 80 % for upper values (without damping)

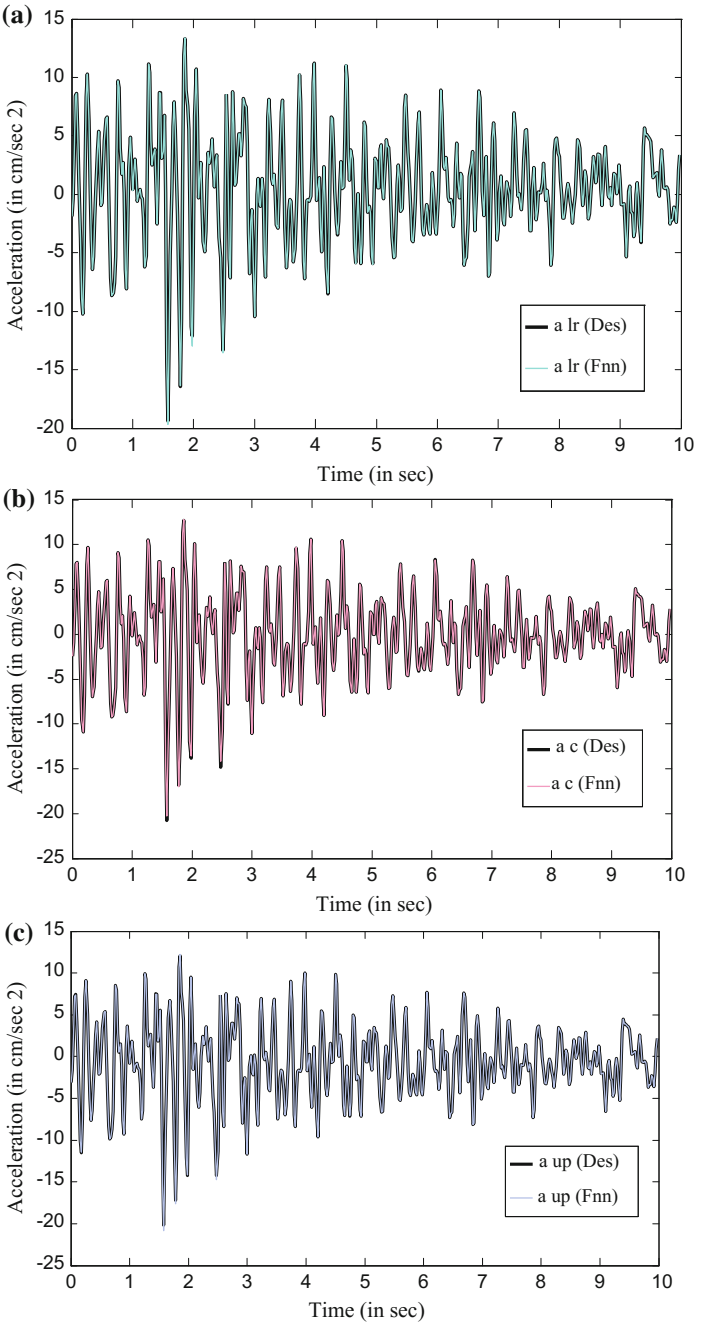

Fig. 7 **a** Comparison between the desired and FNN (Testing) acceleration of 120 % for lower values (with damping) **b** Comparison between the desired and FNN (Testing) acceleration of 120 % for centre values (with damping) **c** Comparison between the desired and FNN (Testing) acceleration of 120 % for upper values (with damping)

Table 1 Comparison between the desired and FNN peak acceleration values (Testing values)

Case	Intensities (%)	Desired			FNN		
		Lower	Centre	Upper	Lower	Centre	Upper
Without damping (Uttarkashi at Barkot NE)	80	15.27	15.67	16.07	14.95	15.34	15.71
	120	22.90	23.50	24.10	22.46	23.08	23.64
With damping (Chamoli at Barkot NE)	80	13.10	13.50	13.90	12.72	13.12	13.51
	120	19.66	20.26	20.86	19.42	20.81	20.21

Table 2 Error % between desired and FNN (Peak values)

Case	Response	Error %		
		Lower	Centre	Upper
Without damping (Chamoli at Barkot NE)	Acceleration $\omega = 0.02$	2	2	2
	Displacement $\omega = [0.4,\ \ 0.5,\ \ 0.6]$	2	2	2
With damping (Uttarkashi at Barkot NE)	Displacement $\omega = 0.68981$	0.08	0. 06	0. 04
	Acceleration $\omega = [0.589,\ \ 0.689,\ \ 0.6789]$	0.8	0.00	0.00

6 Conclusion

This chapter uses the powerful soft computing technique, Fuzzy Neural Network (FNN) to compute fuzzified structural response of structural system subject to Indian Earthquakes at Chamoli and Uttarkashi ground motion data. The difficulty faced in the present problem is when the data are in bipolar form. The fuzzy model cannot handle the negative data easily due to it computational complexities. So as to avoid these complexities first the fuzzified data are converted to α-cut form, then a transformation is used which changes these bipolar data to unipolar form. Once the training is done with these unipolar data then it is transferred back to its bipolar form by an inverse transformation. Different intensity earthquake data which are numerically generated are used as input to predict the direct response of the structure without using any mathematical analysis of the response prediction.

It is shown here that once the training is done then the trained architecture may be used to simulate for various intensity earthquakes, thereby showing the responses of the system which depend upon the structural properties (mass, stiffness and damping) of the structure. If the FNN is trained for various time periods of one earthquake with its corresponding maximum responses then the model can predict the fuzzified form of maximum response directly (to the corresponding time period) for another earthquake that had not been used during the training. In this way the safety of the structural systems may be predicted in term of fuzzy bound in case of future earthquakes.

Acknowledgments The authors would like to acknowledge funding from the Ministry of Earth Sciences, New Delhi to carry out this investigation and the department of Earthquake Engineering, IIT Roorkee for the data.

References

1. Masri SF, Bekey GA, Sassi H, Caughey TK (1982) Non parametric identification of a class of nonlinear multidegree dynamic systems. J Earthquake Eng Struct Dyn 10(1):1–30
2. Natke HG (1982) Identification of vibrating structures. Springer, Berlin, pp 1–510
3. Perry MJ, Koh CG (2007) Output-only structural identification in time domain: numerical and experimental studies. Earthquake Eng Struct Dyn 37(4):517–533
4. Nandakumar P, Shankar K (2013) Identification of structural parameters using consistent mass transfer matrix. Inverse Problems Sci Eng 22(3):436–457
5. Billmaier M, Bucher C (2013) System identification based on selective sensitivity analysis: a case-study. J Sound Vib 332(11):2627–2642
6. Chakraverty S (2007) Identification of structural parameters of two-storey shear buildings by the iterative training of neural networks. J Architectural Sci Rev 50(4):380–384
7. Khanmirza E, Khaji N, Majd VJ (2011) Model updating of multistory shear buildings for simultaneous identification of mass, stiffness and damping matrices using two different soft-computing methods. Expert Syst Appl 38(5):5320–5329
8. Angeles JM, Alvarez-Icaza L (2011) Identification of seismically excited buildings with two orthogonal horizontal components. J Vib Control 17(6):881–901
9. Niu L (2012) Monitoring of a frame structure model for damage identification using artificial neural networks. In: 2nd International conference on electronic and mechanical engineering and information technology (EMEIT-2012), pp 0438–0441
10. Derras B, Bekkouche A (2011) Use of the artificial neural network for peak ground acceleration estimation. Lebanese Sci J 12(2):101–114
11. Lagaros ND, Papadrakakis M (2012) Neural network based prediction schemes of the non-linear seismic response of 3D buildings. Adv Eng Softw 44(1):92–115
12. Zamani AS, Al-Arifi NS, Khan S (2012) response prediction of earthquake motion using artificial neural networks. IJAR-CSIT Research Paper 1(2):50–57
13. Robles GCMA, Hernandez-Bercerril RA (2012) Seismic alert system based on artificial neural networks. Int J Environ Earth Sci Technol 6(6):1–11
14. Liu HHT, Lee CS (2012) Observations on the application of artificial neural network to predicting ground motion measures. Earthquake Sci 25(2):161–175
15. Ramhormozian S, Omenzetter P, Orense R (2013) Artificial neural networks approach to predict principal ground motion parameters for quick post-earthquake damage assessment of bridges. In: NZSEE Conference, pp 1–9
16. Hegde G, Sinha R (2008) Parameter identification of torsionally coupled shear buildings from earthquake response records. Earthquake Eng Struct Dyn 37(11):1313–1331
17. Hong AL, Betti R, Lin CC (2009) Identification of dynamic models of a building structure using multiple earthquake records. Struct Control Health Monit 16(2):178–199
18. Masri SF, Smyth AW, Chassiakos AG, Caughey TK, Hunter NF (2000) Application of neural networks for detection of changes in nonlinear systems. J Eng Mech 126(7):666–676
19. Kao CY, Hung SL (2003) Detection of structural damage via free vibration responses generated by approximating artificial neural networks. Comput Struct 81(28–29):2631–2644
20. Pillai P, Krishnapillai S (2007) A hybrid neural network strategy for identification of structural parameters. Struct Infrastruct Eng 6(3):379–391
21. Bakhary N, Hao H, Deeks AJ (2010) structure damage detection using neural with multi-stage substructuring. Adv Struct Eng 13(1):1–16

22. Zhang S, Wang H, Wang W (2010) damage detection in structures using artificial neural networks. In: International conference on artificial intelligence and computational intelligence, vol 1, pp 207–210
23. Zhang K, Li H, Duan Z, Law SS (2011) A probabilistic damage identification approach for structures with uncertainties under unknown input. Mech Syst Signal Process 25(4):1126–1145
24. Shi A, Yu XH (2012) structural damage detection using artificial neural networks and wavelet transform. In: IEEE International conference on computational intelligence for measurement systems and applications (CIMSA) proceedings, pp 7–11
25. Lei Y, Su Y, Shen W (2013) A probabilistic damage identification approach for structure under unknown excitation and with measurement uncertainties. J Appl Math 2013:1–7
26. Hakim SJS, Razak HA (2013) Adaptive neuro fuzzy inference system (ANFIS) and artificial neural networks (ANNs) for structural damage identification. Struct Eng Mech 45(6):779–802
27. Oliva CSH, Pichardo FAN (2010) Seismic hazard assessment: an artificial neural network estimation. American Geophysical Union, Fall Meeting
28. Kerh T, Huang C, Gunaratnam D (2011) Neural network approach for analyzing seismic data to identify potentially hazardous bridges. Math Probl Eng 2011:1–15
29. Xu B, Song G, Masri SF (2012) Damage detection for a frame structure model using vibration displacement measurement. Struct Health Monit 11(3):281–292
30. Aghamohammadi H, Mesgari MS, Mansourian A, Molaei D (2013) Seismic human loss estimation for an earthquake disaster using neural network. Int J Environ Sci Technol 10 (5):931–939
31. Suryanita R, Adnan A (2013) Application of neural networks in bridge health prediction based on acceleration and displacement data domain. In: Proceedings of the international multi conference of engineers and computer scientists, vol 1. Kowloon, Hong Kong, 13–15 March, pp 42–47
32. Chakraverty S, Marwala T, Gupta P (2006) Response prediction of structural system subject to earthquake motions using artificial neural network. Asian J Civil Eng 7(3):301–308
33. Chakraverty S, Gupta P, Sharma S (2010) Neural network-based simulation for response identification of two-storey shear building subject to earthquake motion. Neural Comput Appl 19(3):367–375
34. Ishibuchi H, Fujioka R, Tanaka H (1992) An architecture of neural networks for input vectors of fuzzy numbers. In: IEEE International conference on fuzzy systems, pp 1293–1300
35. Ishibuchi H, Tanaka H, Okada H (1993) Fuzzy neural networks with fuzzy weights and fuzzy biases. In: IEEE International conference on neural networks, vol 3, pp 1650–1655
36. Ishibuchi H, Morioka K, Tanaka H (1994) A fuzzy neural network with trapezoid fuzzy weights, fuzzy systems. In: IEEE World congress on computational intelligence proceedings of the third IEEE conference, vol 1, pp 228–233
37. Ishibuchi H, Kwon K, Tanaka H (1995) A learning algorithm of fuzzy neural networks with triangular fuzzy weights. Fuzzy Sets Syst 71(3):277–293
38. Ishibuchi H, Morioka K, Turksen IB (1995) Learning by fuzzified neural networks. Int J Approximate Reasoning 13(4):327–358
39. Sahoo DM, Chakraverty S (2013) Fuzzified data based neural network modeling for health assessment of multistorey shear buildings. Adv Artif Neural Syst 2013:1–12
40. Pankaj DS, Wilscy M (2011) Face recognition using fuzzy neural network classifier advances in parallel distributed computing. Commun Comput Inf Sci 203:53–62
41. Umoh UA, Nwachukwu EO, Obot OU, Umoh AA (2011) Fuzzy-neural network model for effective control of profitability in a paper recycling plant. Am J Sci Ind Res 2(4):552–558
42. Vijaykumar A, Aruna Reddy MV (2011) A fuzzy neural network for speech recognition. ARPN J Syst Softw 1(9):284–290
43. Sharma R, Sinha AK (2012) A production planning model using fuzzy neural network: a case study of an automobile industry. Int J Comput Appl 40(4):19–22

44. Swaroop R (2012) Load forecasting for power system planning using fuzzy-neural networks. In: Proceedings of the world congress on engineering and computer science, San Francisco, USA, 24–26 Oct, 1:1–5
45. Zhang H, Dai X (2012) The application of fuzzy neural network in medicine-a survey. In: International conference on biology and biomedical sciences, vol 9, pp 111–116
46. Leu VQ, Mwasilu F, Choi HH, Lee J, Jung JW (2013) Robust fuzzy neural network sliding mode control scheme for IPMSM drives. Int J Electron 101(7):1–20
47. Zahedi G, Saba S, Elkamel A, Bahadori A (2013) Ozone pollution prediction around industrial areas using fuzzy neural network approach. Clean Soil, Air Water 41(9999):1–9
48. Wang CH, Hung KN (2013) Intelligent adaptive law for missile guidance using fuzzy neural networks. Int J Fuzzy Syst 15(2):182–191
49. Lee KH (2009) First course on fuzzy theory and applications. Springer International Edition, pp 1–333
50. Newmark NM, Rosenblueth E (1971) Fundamentals of earthquake engineering. Prentice-Hall, Inc., Englewood Cliffs, pp 1–640

Smart Control of Seismically Excited Highway Bridges

Yeesock Kim and Aniket Anil Mahajan

Abstract This chapter proposes a novel smart fuzzy control algorithm for mitigation of dynamic responses of seismically excited bridge structures equipped with control devices. The smart fuzzy controller is developed through the combination of discrete wavelet transform, backpropagation neural networks, and Takagi-Sugeno fuzzy model. To demonstrate the effectiveness of the proposed smart fuzzy controller, it is tested on a highway bridge equipped with magneto rheological (MR) dampers. It controls the smart dampers installed on the abutments of the highway bridge structure. The 1940 El-Centro and Kobe earthquakes are used as disturbance signals. It is demonstrated that the smart fuzzy controller is effective in reducing the structural responses of the highway bridge under a variety of seismic excitations.

1 Introduction

In recent years, smart control strategies have attracted a great deal of attention from the structural engineering community [39, 3, 4, 5, 6, 10, 28, 29, 31]. However, a difficult problem in dealing with smart structures is creating an effective control model for a nonlinear dynamic structure under a variety of environmental forces [21, 23–26, 37, 6, 15]. Nonlinear systems occur when highly nonlinear hysteretic dampers, such as the magnetorheological (MR) dampers, are implemented into a structure to aid in the structure's ability to withstand the destructive environmental forces such as strong winds and earthquake loads [36]. Being able to mathematically model the structure-nonlinear damping system and its corresponding con-

Y. Kim (✉)
Civil Engineering, California Baptist University, Riverside, CA, USA
e-mail: yekim@calbaptist.edu; controlga@gmail.com

A.A. Mahajan
Civil and Environmental Engineering, Worcester Polytechnic Institute, Worcester, MA, USA

M. Papadrakakis et al. (eds.), *Computational Methods in Earthquake Engineering*,
Computational Methods in Applied Sciences 44,
DOI 10.1007/978-3-319-47798-5_14

troller is a challenging task in smart control. Therefore, the challenge is to create a mathematical model to develop a relationship between the input and output of a smart structure that uses a nonlinear damping device. This chapter proposes a new smart control system for reducing nonlinear behavior of a seismically excited highway bridge structure with smart dampers.

The development of an effective smart control algorithm is essential in smart structures to operate the smart dampers within large civil structures. The goals of an effective smart controller is to reliably control how a system will behave under a variety of dynamic loading scenarios such as far- and near-field earthquakes, considering interactions between the structure and the smart dampers. Smart control algorithms can be separated into two categories: model-based and model-free algorithms [25]. The model-based control methods use the structural properties of the system, including stiffness and damping systems that are intrinsically imbedded in the structure and its materials [7, 8]. The model-free control approaches are implemented through training data to the input-output map of the structure employing the smart dampers [37, 38]. This model-free approach is useful to bridge the gap between the linear and nonlinear parts of the smart system. This has successfully been done with neural networks as well as fuzzy logic systems. In particular, the incorporation of the two systems provides a better learning model to use for training the model-free control models.

In this chapter, a new smart control model is developed through the integration of best features of discrete wavelet transform (WT), and fuzzy logic theory and neural network (NN). The first model used as a part of the proposed system in this chapter is a rule-based fuzzy logic. The fuzzy logic model has the main advantage of being used as a nonparametric method for system identification and control system design, and has been researched previously [44, 40, 21, 22, 27–33, 35], as well as general studies into the uncertainties and complexities of the dynamic system [34, 23]. Using a Takagi-Sugeno (TS) model for fuzzy logic theory allows for a representation of nonlinear systems using fuzzy rules and local linear models [40, 19, 41, 12, 20, 9, 11, 23, 42]. A disadvantage of using fuzzy inference systems as a control model is that it needs a time consuming optimization process of the parameters. The optimization process can be very complex, leading itself to the inclusion of NNs. The use of a NN is to develop a learning mechanism that emulates that of the human brain, such that it creates a network of interlinked nodes. These nodes, being connected, compute an output from the input to the node, and create a series of links between all nodes. As mentioned previously, the use of a fuzzy inference system can be complex and difficult in computations. Using a NN in combination with a fuzzy inference system can create a model that is more efficient. The NN adjusts parameters throughout the entirety of computation. The regulated parameters improve performance and decreases errors of the system. It is able to learn patterns and make adjustments as needed to further create a more improved model because it emulates the human brain and its cognitive mechanism. It has been studied previously to create a full model structure [16].

However, due to the complexities of training the using NNs, computation time can become excessive. Therefore, wavelet transform (WT) is used in conjunction with the combined fuzzy inference system, and NNs to compress input data and decrease computation time. WTs, combined with the neuro-fuzzy (NF) model, leads to a wavelet-based NF model (WNF). The WT can be used to filter out high or low frequency components from a time series. The WT improves upon previous methods due to its ability to incorporate an adjustable window function. It allows a user to analyze particular data points in a time series, rather than the entire time window, which is the case in Fourier transforms. Fast Fourier transforms (FFT) have been used previously for damage detection, system identification, and control systems, but require a fixed time-window for the entire data set [14]. This limitation of the FFT can induce difficulty when analyzing data for long periods of time, as in the case of real-time structural control, and can lead to missing key components, such as a particular control frequency. The WT allows for an adjustable window, and therefore is able to look into any portion of a time series. WTs can also be used as a means of filtering, which is critical in the use of the WNF control model. As previously mentioned, the NF system requires high computation time due to the stochastic learning mechanism of the NNs. Being able to decrease the amount of data points while still maintaining the important components allows for a reduced computational cost. The proposed model uses two levels of discrete WTs for compressing input data. Note that fuzzy logic controllers [2] and neuro-fuzzy controllers [13] have been widely researched previously. However, these controllers need extensive computation time to achieve adequate performance. Therefore, the creation of the new WNF system provides for decreased computation times while maintaining the performance. Thus, the creation of the WNF system for means of smart control algorithm is innovative in its application to smart damping systems for mitigation of responses of highway bridge structures.

2 Smart Highway Bridge Systems

2.1 Highway Bridge

To facilitate research in structural control, a benchmark bridge was developed based on an existing structure located at the crossing of the 91 and 5 highways in Orange County of California, USA [1]. A prestressed concrete box-girder is used with the span of 58.5 m. The deck has a width of 12.95 and 15 m for the east and west spans, respectively. The bridge carries four lanes of traffic atop columns of 6.9 m in height. The location of the bridge is within 20 km of two faults, the Whittier-Ellsinore and Newport-Inglewood fault zones, showing a great need for structural control due to its susceptibility to seismic events. Figure 1 shows the bridge schematic.

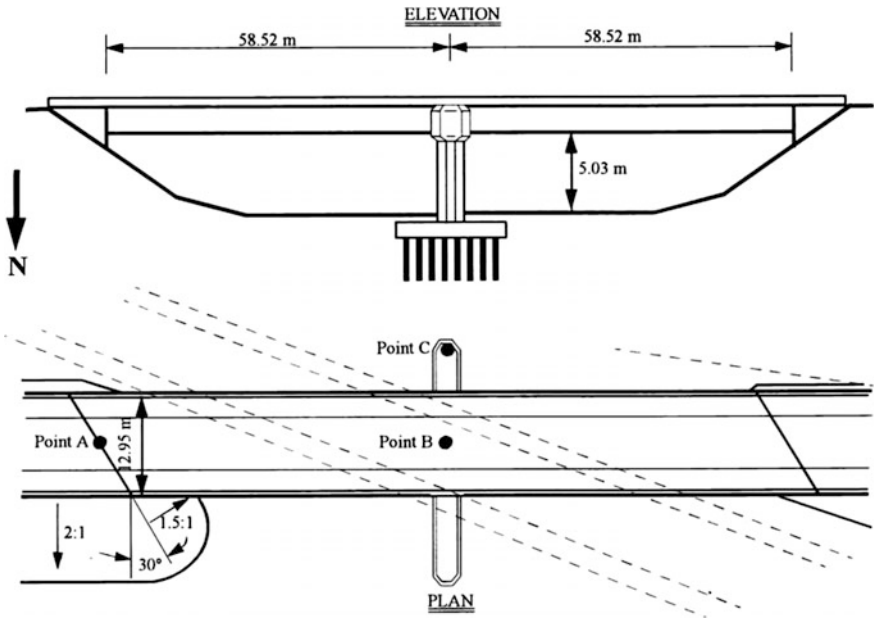

Fig. 1 Highway bridge structure

2.2 Magnetorheological (MR) Dampers

In recent years, smart structures have emerged from many engineering fields because the performance of structural systems can be improved without either significantly increasing the structure mass or requiring high cost of control power. They may be called intelligent structures, adaptive structures, active structures, and the related technologies adaptronics, structronics, etc. The reason to use these terminologies is that a smart structure is an integration of actuators, sensors, control units, and signal processing units with a structural system. The materials that are commonly used to implement the smart structure: piezoelectrics, shape memory alloys, electrostrictive, magnetostrictive materials, polymer gels, magnetorheological fluid, etc., researched in detail by Hurlebaus and Gaul [17].

Semiactive control systems have been applied to large structures because the semiactive control strategies combine favorable features of both active and passive control systems. Semiactive control devices include variable-orifice dampers, variable-stiffness devices, variable-friction dampers, controllable-fluid dampers, shape memory alloy actuators, piezoelectrics, etc., as described by Hurlebaus and Gaul [17]. In particular, one of the controllable-fluid dampers, magnetorheological (MR) damper has attracted attention in recent years because it has many attractive characteristics.

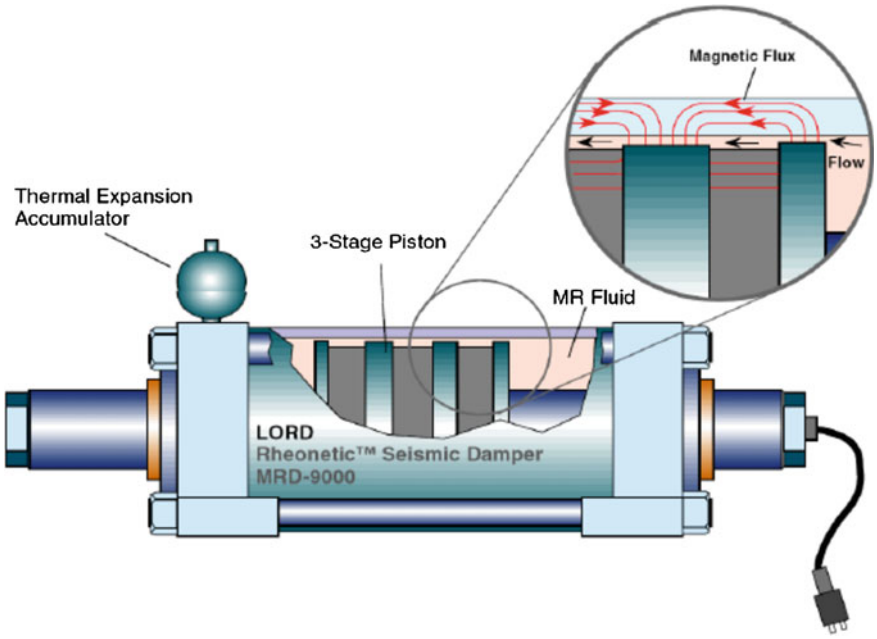

Fig. 2 Schematic of the prototype 20-ton large-scale MR damper

In general, a MR damper consists of a hydraulic cylinder, magnetic coils, and MR fluids that consist of micron-sized magnetically polarizable particles floating within oil-type fluids as shown in Fig. 2.

The MR damper is operated as a passive damper; however, when a magnetic field is applied to the MR fluids, the MR fluids are changed into a semi-solid state in a few milliseconds. This is one of the most unique aspects of the MR damper compared to active systems: the active control system malfunction might occur if some control feedback components, e.g., wires and sensors, are broken for some reasons during a severe earthquake event; while a semiactive system is still operational as at least a passive damping system even when the control feedback components are not functioning properly. Its characteristics are summarized by Kim et al. [23].

2.3 Smart Controller

In 1985, Takagi and Sugeno suggested an effective way for modeling complex nonlinear systems by introducing linear equations in consequent parts of a fuzzy model. It has led to reduction of computational cost because it does not need any defuzzification procedure. The fuzzy system used in the WNF model is of the form [22].

$$R_j : \text{If } u_{FZ}^1 \text{is } P_{1,j} \text{ and } u_{FZ}^2 \text{ is } P_{2,j} \ldots \text{and } u_{FZ}^i \text{ is } P_{i,j} \\ \text{Then } z = f_j\left(u_{FZ}^1, \ldots, u_{FZ}^i\right), \quad j = 1, 2, \ldots, N_r \tag{1}$$

where R_j is the jth fuzzy rule, N_j is the number of fuzzy rules, P_{ij} are fuzzy sets centered at the jth operating point, and u_{FZ}^i are premise variables that can be either input or output values. The equation of the consequent part $z = f(u_{FZ}^1, \ldots, u_{FZ}^i)$ can be any linear equation. Using fuzzy interpolation methods, all of the local subsystems are integrated

$$y = \sum_{j=1}^{N_r} W_j\left(u_{FZ}^i\right)\left[f_j\left(u_{FZ}^1, \ldots, u_{FZ}^i\right)\right] / \sum_{j=1}^{N_r} W_j\left(u_{FZ}^i\right) \tag{2}$$

where $W_j(u_{FZ}^i) = \prod_{i=1}^{n} \mu_{p_{i,j}}(u_{FZ}^i)$, n is the number of input variables and $\mu_{p_{i,j}}(u_{FZ}^i)$ is the membership grade of u_{FZ}^i in $P_{i,j}$. However, the main challenge in using a fuzzy model is the optimization of its parameters. Therefore, incorporating NNs to create a neuro-fuzzy system allows for these parameters to be optimized during computation.

The architecture of a NF model is shown in Fig. 3. This figure represents a two inputs, one output, and three membership functions (MFs). Each layer has particular tasks to complete before the data moves to the next layer.

In layer 1, the function of the node is represented by

$$F_{FZ}^{1,j} = \mu_{P_{i,j}}\left(u_{FZ}^i\right) \tag{3}$$

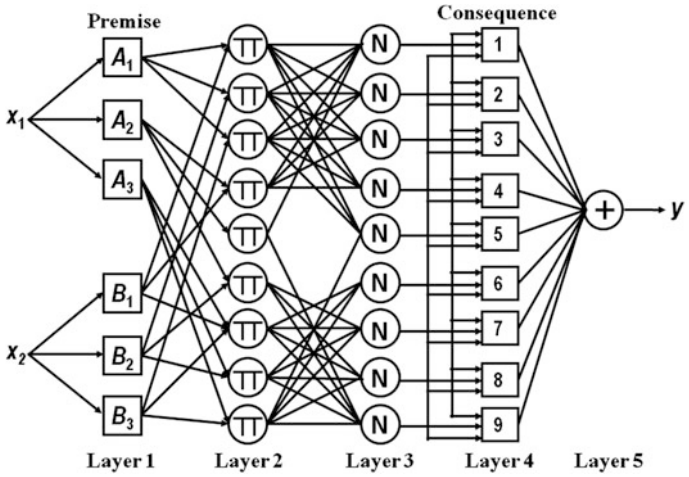

Fig. 3 Neuro-fuzzy model architecture

For a Gaussian MF used in this simulation,

$$\mu_{P_{i,j}}\left(u_{FZ}^{i}\right) = \exp\left[-(u-a_1)^2/2a_2^2\right] \tag{4}$$

where a_1 and a_2 are adjustable parameters of the Gaussian function. This MF is applied to each input in layer 1. Layer 2 then outputs the product of all inputs into layer 2, known as the firing strength

$$F_{FZ}^{2,j} = \mu_{P_{i,j}}\left(u_{FZ}^{1}\right) \times \mu_{P_{i,j}}\left(u_{FZ}^{2}\right) \times \cdots \times \mu_{P_{i,j}}\left(u_{FZ}^{i}\right) \tag{5}$$

Layer 3 takes a ratio of these layer 2 firing strengths in order to normalize the layer 2 outputs, such that

$$F_{FZ}^{3,j} = F_{FZ}^{2,j} / \sum_{j} \prod_{i=1}^{n} \mu_{P_{i,j}}\left(u_{FZ}^{i}\right) \tag{6}$$

Layer 4 then applies a node function to the normalized firing strengths

$$F_{FZ}^{4,j} = F_{FZ}^{3,j} \cdot f_j = F_{FZ}^{3,j}\left[f_j\left(u_{FZ}^{1}, \ldots, u_{FZ}^{i}\right)\right] \tag{7}$$

The last layer summates the layer inputs

$$F_{FZ}^{5,j} = \sum_{j} \prod_{i=1}^{n} \mu_{P_{i,j}}\left(u_{FZ}^{i}\right)\left[f_j\left(u_{FZ}^{1}, \ldots, u_{FZ}^{i}\right)\right] / \sum_{j} \prod_{i=1}^{n} \mu_{P_{i,j}}\left(u_{FZ}^{i}\right) \tag{8}$$

The output of this NF system is then used in a hybrid learning algorithm to create a linear combination of the consequent parameters. The key parameters for this simulation include the number of iterations, or epochs, the number of MFs and the type of MF, as well as the step size of the function. In this study, the premise part is determined by backpropagation algorithm while the consequent parameters are optimized using the least square estimator. Four Gaussian membership functions are adopted, the number of iterations is 300, the iteration step size is 0.9 and the increase rate of the step size is 1.2. Types of MFs can vary from a generalized bell function, Gaussian functions, sigmoidal functions, trapezoidal function, as well as other forms. Each change of variables will yield different output results [18, 43]. The fuzzy inference system sets up rules based on the number of MFs used in simulation. Fuzzy rules are set up for a five MF system. Each number represents one of the twenty-five fuzzy regions that are created through the use of five MFs in the neuro-fuzzy model. The fuzzy region is defined by the premise, and the output is generated through the consequent.

The inclusion of discrete wavelet transforms allows for an effective method to rid the control system of extraneous data, or noise. This methodology uses Daubechie wavelets filters in order to de-noise response data that are then used as

inputs to the smart fuzzy control model. As mentioned earlier, the use of discrete wavelet transforms allows for a fixed time-frequency resolution. It means that the window function is chosen, and then the resolution is fixed through processing. A reduction in the number of data points required for accurate representation of the system is possible due to representation of the function with several discretization steps. The proposed algorithm for the smart fuzzy control is shown in Fig. 4.

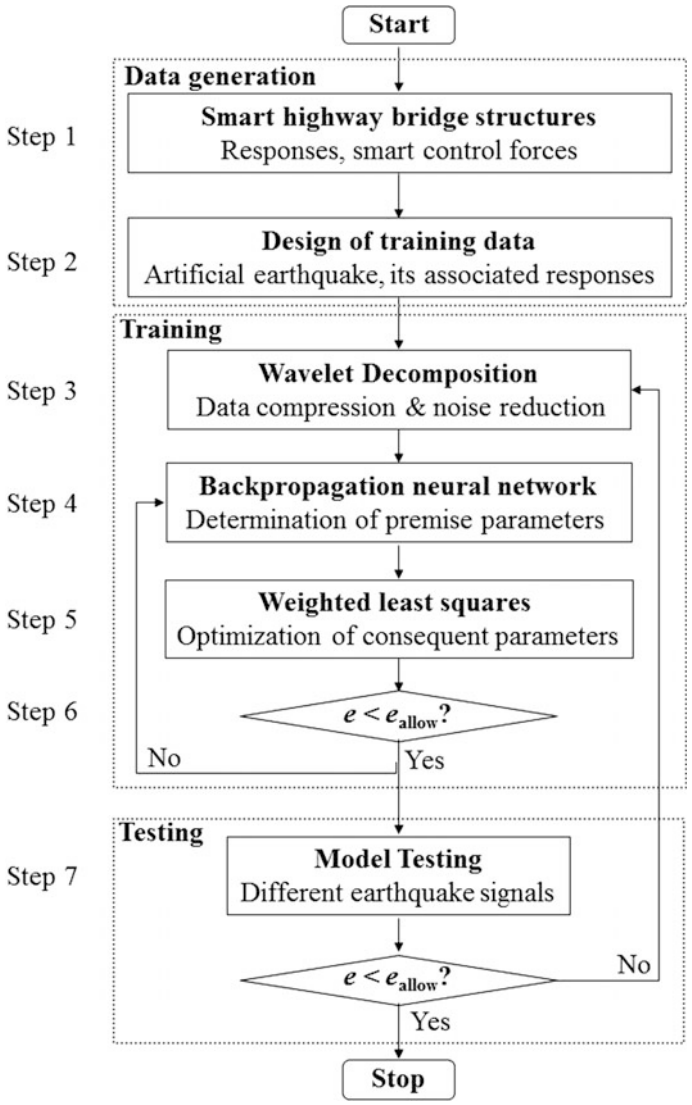

Fig. 4 Flowchart of the proposed algorithm

This control model proposes the use of two levels of discrete wavelet transform as a means of filtering as well as training the optimal control force. The architecture of this proposed smart fuzzy control system is depicted in Fig. 5. The smart fuzzy control algorithm is a two-input, one-output system to determine the control force of an MR damper. For this study, the inputs to the smart fuzzy control system are displacement and acceleration measurements. These were determined through an iterative process to maximize the results from training of the smart fuzzy control system, where velocity and drift responses were also studied to find the combination with the most favorable results. Next, simulations were performed on a highway bridge under a variety of earthquake loads to successfully reduce the seismic responses.

2.4 Simulation

Many simulations were performed to determine the best arrangement of control forces. It was found that the computation of only two control forces would need to be calculated for optimal voltage signals: x-direction and y-direction. This bridge is equipped with sixteen MR dampers in each *x*- and *y*-directions; all the MR dampers in each direction are commanded by a single control signal. To train the input-output mapping function of the smart fuzzy control model, an artificial earthquake signal that includes characteristics of the 1940 El-Centro and Kobe earthquake, as shown in Figs. 6 and 7.

Figures 8, 9, 10, 11, 12 and 13 show the simulation results. Figures 8 and 9 are the relative displacement responses to the 1940 El-Centro and Kobe earthquakes, respectively. Figures 10 and 11 are the absolute acceleration responses to the 1940 El-Centro and Kobe earthquakes, respectively. Figures 12 and 13 are the base shear

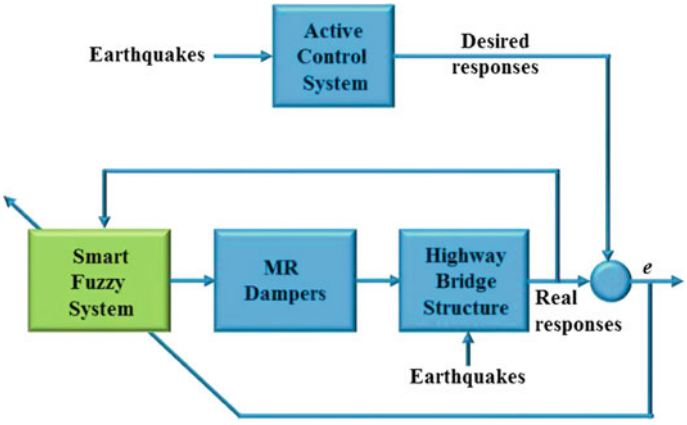

Fig. 5 Configuration of the proposed smart control

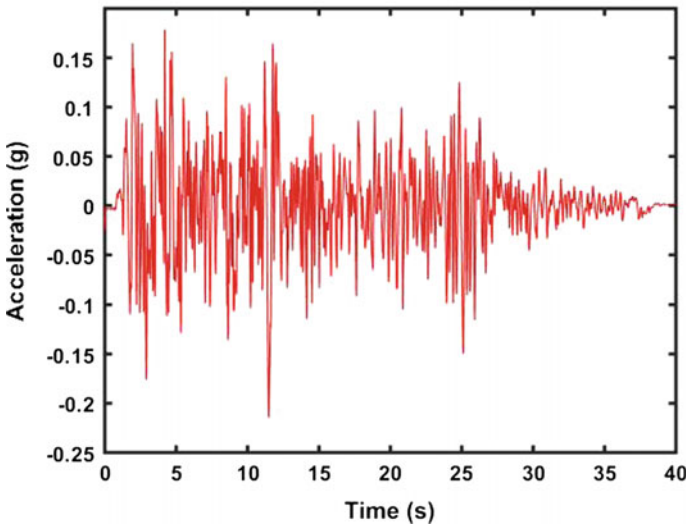

Fig. 6 1940 El-Centro earthquake

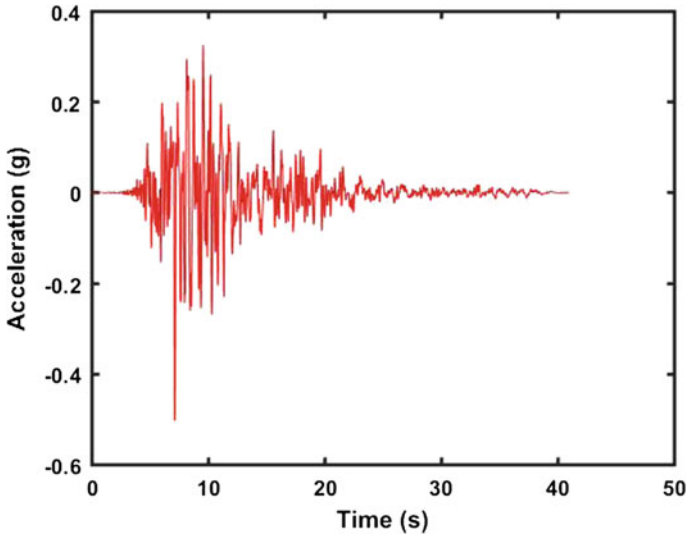

Fig. 7 Kobe earthquake

forces at the column to the 1940 El-Centro and Kobe earthquakes, respectively. The dotted lines represent the uncontrolled responses; while the solid red lines are the responses of the smart fuzzy control systems. As shown in figures, the proposed smart fuzzy control system is effective in mitigating the dynamic responses of highway bridge structures for most cases.

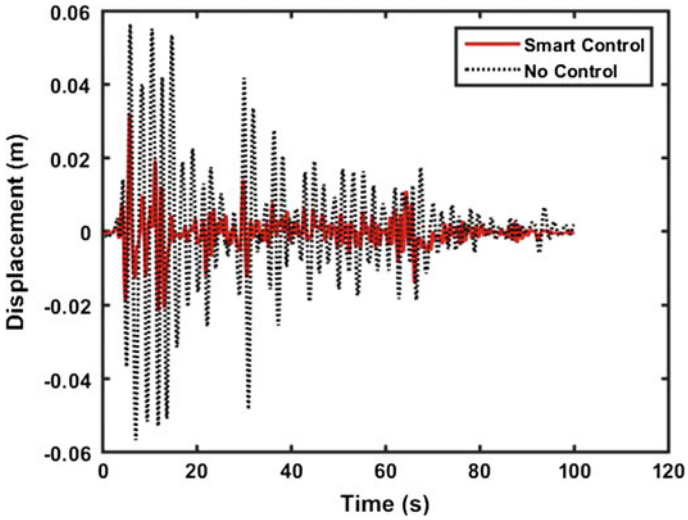

Fig. 8 Displacement: 1940 El-Centro earthquake

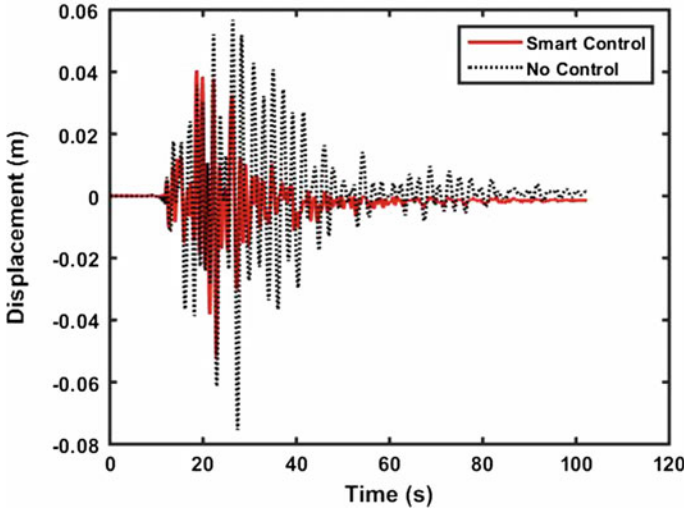

Fig. 9 Displacement: Kobe earthquake

As a means of validation and comparison, several evaluation indices are used. These indices compare structural responses and control outputs of the proposed smart control system to that of the uncontrolled structure, showing how much each index is reduced [1].

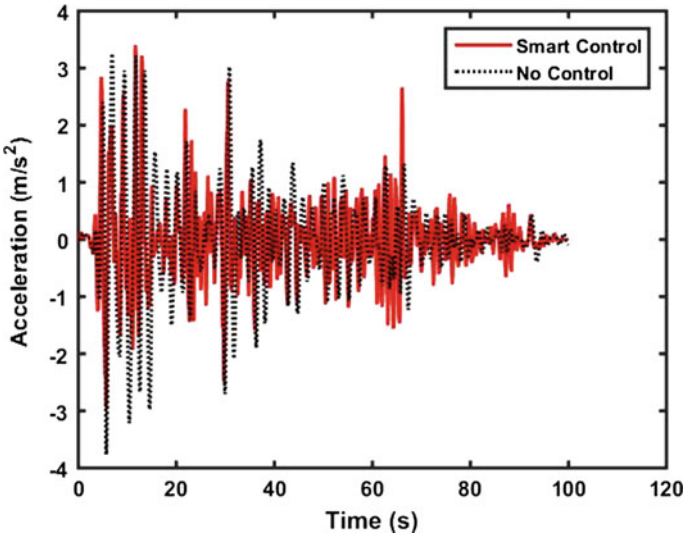

Fig. 10 Acceleration: 1940 El-Centro earthquake

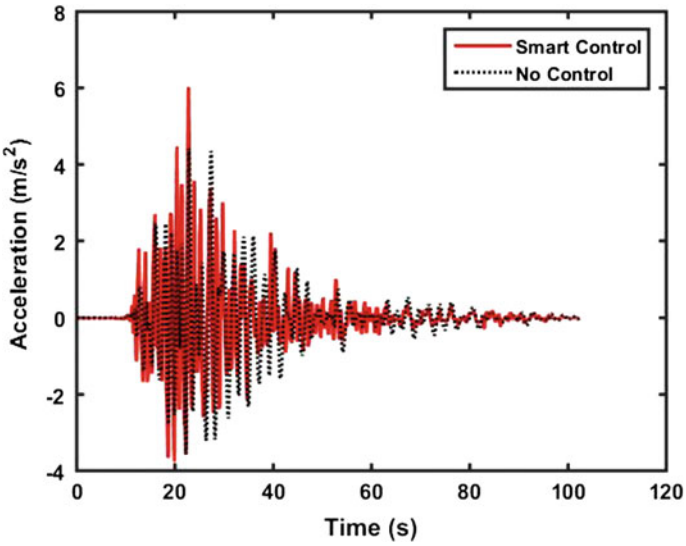

Fig. 11 Acceleration: Kobe earthquake

here $\hat{F}_{bi}(t)$ is the time history of shear force of the ith degree of freedom of the control system, $\hat{F}_{0b,\max}$ is the maximum shear force of the uncontrolled structure, $M_{bi}(t)$ is the time history of overturning moment, $M_{0b,\max}$ is the maximum overturning moment of the uncontrolled structure, $\hat{y}_{mi}(t)$ is the time history of the

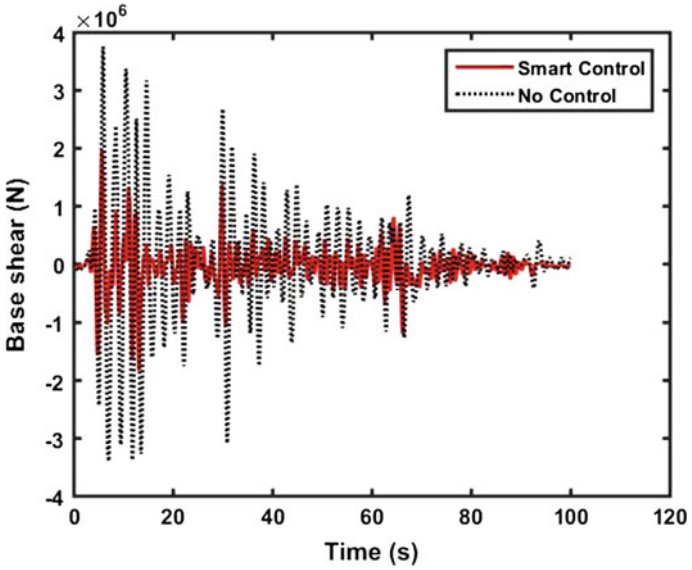

Fig. 12 Base shear: 1940 El-Centro earthquake

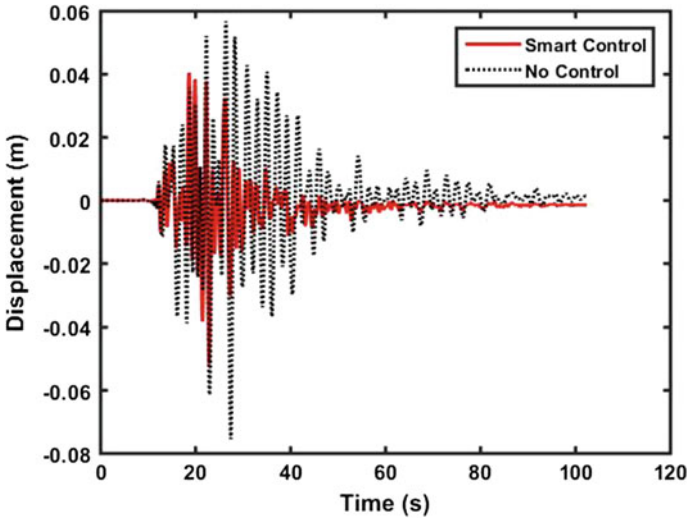

Fig. 13 Base shear: Kobe earthquake

midspan displacement, $\hat{y}_{0m,\max}(t)$ is the maximum midspan displacement of the uncontrolled structure, $|\ddot{\hat{y}}_{mi}(t)|$ is the time history of the midspan acceleration, $\ddot{\hat{y}}_{0m,\max}(t)$ is the maximum acceleration of the uncontrolled structure, $\hat{y}_{bi}(t)$ is the time history of the abutment displacement, $\hat{y}_{0b,\max}$ is the maximum abutment

Table 1 Control performance evaluation

	ElCentro	Kobe
$J_1 = \max\left\{\frac{\max\lvert\hat{F}_{bi}(t)\rvert}{\hat{F}_{0b,\max}}\right\}$	0.6967	0.8696
$J_2 = \max\left\{\frac{\max\lvert\hat{M}_{bi}(t)\rvert}{\hat{M}_{0b,\max}}\right\}$	0.5268	0.5901
$J_3 = \max\left\{\frac{\max\lvert\hat{y}_{mi}(t)\rvert}{\hat{y}_{0m,\max}}\right\}$	0.5627	0.6856
$J_4 = \max\left\{\frac{\max\lvert\ddot{\hat{y}}_{mi}(t)\rvert}{\ddot{\hat{y}}_{0m,\max}}\right\}$	0.9211	1.2205
$J_5 = \max\left\{\frac{\max\lvert\hat{y}_{bi}(t)\rvert}{\hat{y}_{0b,\max}}\right\}$	0.2942	0.5292
$J_6 = \max\left\{\frac{\max\lvert\hat{\Phi}_i(t)\rvert}{\hat{\Phi}_{\max}}\right\}$	0.5268	0.5901
$J_7 = \max\left\{\frac{\max\int d\hat{E}_i}{\hat{E}_{\max}}\right\}$	0	0
$J_8 = \max\left\{\frac{\hat{N}_{c,d}}{\hat{N}_d}\right\}$	0	0
$J_9 = \max\left\{\frac{\max\lVert\hat{F}_{bi}(t)\rVert}{\lVert\hat{F}_{0b,\max}\rVert}\right\}$	0.5679	0.7387
$J_{10} = \max\left\{\frac{\max\lVert\hat{M}_{bi}(t)\rVert}{\lVert\hat{M}_{bi,\max}\rVert}\right\}$	0.2954	0.5178
$J_{11} = \max\left\{\frac{\max\lVert\hat{y}_{mi}(t)\rVert}{\lVert\hat{y}_{0m,\max}\rVert}\right\}$	0.3052	0.5396
$J_{12} = \max\left\{\frac{\max\lVert\ddot{\hat{y}}_{mi}(t)\rVert}{\lVert\ddot{\hat{y}}_{0m,\max}\rVert}\right\}$	0.8069	1.0767
$J_{13} = \max\left\{\frac{\max\lVert\hat{y}_{bi}(t)\rVert}{\lVert\hat{y}_{0b,\max}\rVert}\right\}$	0.2330	0.4155
$J_{14} = \max\left\{\frac{\max\lVert\hat{\Phi}_i(t)\rVert}{\lVert\hat{\Phi}_{\max}\rVert}\right\}$	0.2954	0.5178
$J_{15} = \max\left\{\max\left(\frac{\hat{f}_i(t)}{\hat{W}}\right)\right\}$	0.0244	0.0248
$J_{16} = \max\left\{\max\left(\frac{\dot{d}_i(t)}{\dot{x}_{0m,\max}}\right)\right\}$	0.2705	0.5218
$J_{17} = \#$ of control devices	16	16
$J_{18} = \#$ of required sensors	12	12
$J_{19} = \dim(\hat{\mathrm{x}}_{\mathrm{c,k}})$	28	28

displacement of the uncontrolled structure, $\hat{\Phi}_i(t)$ is the time history of the ductility, $\hat{\Phi}_{\max}$ is the maximum ductility of the uncontrolled structure, $d\hat{E}_i$ is the dissipated energy of curvature at the column, $\hat{E}_{\max}$ is the maximum dissipated energy of the curvature at the column of the uncontrolled structure, $\hat{N}_{c,d}$ is the number of plastic connections of the control system, $\hat{N}_d$ is the number of plastic connections of the uncontrolled system, $|.|$ denotes the absolute value, $\|.\|$ denotes the normalized value, $\hat{f}_i(t)$ is the time history of the control force from the control device, $\hat{W}$ is the

seismic weight of the system, $\hat{d}_l(t)$ is the stroke of the control device, $x_{0m,\max}$ is the maximum bearing deformation of the uncontrolled system, $\hat{P}_l(t)$ is the time history of the instantaneous power required for the control device, $\dot{\hat{x}}_{0m,\max}$ is the maximum velocity of bearing of the uncontrolled system, and $\hat{x}_{c,k}$ is the discrete state vector for the control algorithm. Table 1 shows the evaluation results of the proposed smart control systems. It is observed from Table 1 that the "Max" peak response quantities using the smart controller are quite effective in reducing structural vibration to both the El-Centro and Kobe earthquakes. In particular, peak evaluation criteria J_2, J_3, $J_5 \sim J_{11}$, and J_{13}, J_{14}, J_{16} and J_{18} are significantly reduced during both ground motions. It should be noted that structural displacement responses are directly related to safety of the bridge structures.

3 Conclusion

In this chapter, a novel smart control system is proposed for seismic response controls of seismically-excited bridge structures employing magnetorheological (MR) dampers. The smart control system is an integrated model of Takagi-Sugeno fuzzy model, wavelet transforms, and artificial neural networks. Using the smart fuzzy control system combines the positive attributes of the three described methodologies to create a system that is believed to yield more efficient results for system control of smart structures and shorter training times. To train the input–output mapping function of the smart fuzzy control model, an artificial earthquake signal and an MR damper force signal are used as a disturbance input signal and a control input, respectively, while acceleration response is used as output data. It is demonstrated from the simulation that the proposed smart fuzzy control model is effective in reducing the behavior of the seismically excited bridge-MR damper system.

References

1. Agrawal A, Tan P, Nagarajaiah S, Zhang J (2009) Benchmark structural control problem for a seismically excited highway bridge—Part I: Phase I problem definition. Struct Control Health Monit 16:509–529
2. Ahlawat AS, Ramaswamy A (2002) Multi objective optimal design of FLC driven hybrid mass damper for seismically excited structures. Earthquake Eng Struct Dynam 31:1459–1479
3. Arsava SK, Kim Y, El-Korchi T, Park HS (2013) Nonlinear system identification of smart structures under high impact loads. J Smart Mater Struc 22. doi:10.1088/0964-1726/22/5/055008
4. Arsava SK, Chong JW, Kim Y (2014) A novel health monitoring scheme for smart structures. J Vib Control. doi:10.1177/1077546314533716
5. Arsava SK, Nam Y, Kim Y (2015) Nonlinear system identification of smart reinforced concrete structures under high impact loads. J Vib Control. doi:10.1177/1077546314563966

6. Arsava SK, Kim Y, Kim KH, Shin BS (2015) Smart fuzzy control of reinforced concrete structures excited by collision-type forces. Expert Syst Appl 42(21):7929–7941
7. Cha YJ, Agrawal AK, Kim Y, Raich A (2012) Multi-objective genetic algorithms for cost-effective distributions of actuators and sensors in large structures. Expert Syst Appl 39:7822–7833
8. Cha YJ, Kim Y, Raich A, Agrawal AK (2013) Multi-objective optimization for actuator and sensor layouts of actively controlled 3D buildings. J Vib Control 19:942–960
9. Chen Y, Yang B, Abraham A, Peng L (2007) Automatic design of hierarchical Takagi-Sugeno Type fuzzy systems using evolutionary algorithms. IEEE Trans Fuzzy Syst 15:385–397
10. Chong JW, Kim Y, Chon K (2014) Nonlinear multiclass support vector machine-based health monitoring system for buildings employing magnetorheological dampers. J Intell Mater Syst Struct 25:1456–1468
11. Du H, Zhang N (2008) Application of evolving Takagi-Sugeno Fuzzy Model to nonlinear system identification. Appl Soft Comput 8:676–686
12. Faravelli L, Yao T (1996) Use of adaptive networks in fuzzy control of civil structures. Microcomput Civil Eng 12:67–76
13. Gu Z, Oyadiji S (2008) Application of MR damper in structural control using ANFIS Method. Comput Struct 86:427–436
14. Gurley K, Kareem A (1999) Applications of wavelet transforms in earthquake, wind and ocean engineering. Eng Struct 21:149–167
15. Hughes JE, Kim Y, El-Korchi T (2015) Radar technology for structural hazard mitigation. J Vib Control
16. Hung SL, Huang CS, Wen CM, Hsu YC (2003) Nonparametric identification of a building structure from experimental data using wavelet neural network. Computer-Aided Civil Infrastruct Eng 18:356–368
17. Hurlebaus S, Gaul L (2006) Smart structure dynamics. Mech Syst Signal Process 20:255–286
18. Jang JSR (1993) ANFIS: adaptive-network-based fuzzy inference system. IEEE Trans Syst Man Cybern 23:665–685
19. Johansen TA (1994) Fuzzy model based control: stability, robustness, and performance issues. IEEE Trans Fuzzy Syst 2:221–234
20. Johansen TA, Babuška R (2003) Multiobjective identification of Takagi-Sugeno fuzzy models. IEEE Trans Fuzzy Syst 11:847–860
21. Kim Y, Langari R (2007) Nonlinear identification and control of a building structure with a magnetorheological damper system. *American control conference*, New York
22. Kim Y, Hurlebaus S, Sharifi R, Langari R (2009a) Nonlinear identification of MIMO smart structures. ASME dynamic systems and control conference, Hollywood, California
23. Kim Y, Langari R, Hurlebaus S (2009) Semiactive nonlinear control of a building using a magnetorheological damper system. Mech Syst Signal Process 23:300–315
24. Kim Y, Hurlebaus S, Langari R (2010) Control of a seismically excited benchmark building using linear matrix inequality-based semiactive nonlinear fuzzy control. ASCE J Struct Eng 136(8):1023–1026
25. Kim Y, Langari R, Hurlebaus S (2010) Model-based multi-input, multi-output supervisory semiactive nonlinear fuzzy controller. Computer-Aided Civil Infrastruct Eng 25:387–393
26. Kim Y, Kim C, Langari R (2010) Novel bio-inspired smart control for hazard mitigation of civil structures. J Smart Mater Struct 19:115009. doi:10.1088/0964-1726/19/11/115009
27. Kim Y, Hurlebaus S, Langari R (2011) Fuzzy identification of building-MR damper system. Int J Intell Fuzzy Syst 22(4):185–205
28. Kim Y, Chong JW, Chon K, Kim JM (2013) Wavelet-based AR-SVM for health monitoring of smart structures. J Smart Mater Struct 22(1):015003. doi:10.1088/0964-1726/22/1/015003
29. Kim Y, Mallick R, Bhowmick S, Chen B (2013) Nonlinear system identification of large-scale smart pavement systems. Expert Syst Appl 40:3551–3560
30. Kim Y, Kim KH, Shin BS (2014) Fuzzy model forecasting of offshore bar-shape profiles under high waves. Expert Syst Appl 41:5771–5779

31. Kim Y, Bai JW, Albano LD (2014) Fragility estimates of smart structures with sensor faults. J Smart Mater Struct 22:125012. doi:10.1088/0964-1726/22/12/125012
32. Kim Y, Shin SS, Plummer JD (2014) A wavelet-based autoregressive fuzzy model for forecasting algal blooms. Environ Model Softw 62:1–10
33. Kim Y, Kim YH, Lee S (2015) Multivariable nonlinear identification of smart buildings. Mech Syst Signal Process 62–63:254–271
34. Langari R (1999) Past, present and future of fuzzy control: a case for application of fuzzy logic in hierarchical control. In: Proceedings, 18th international conference of the north american fuzzy information processing society-NAFIPS, New York City, New York, USA, pp 760–765
35. Mohammadzadeh S, Kim Y, Ahn J (2015) PCA-based neuro-fuzzy model for system identification of smart structures. J Smart Struct Syst 15(4):1139–1158
36. Mitchell R, Kim Y, El-Korchi T (2012) System identification of smart structures using a wavelet neuro-fuzzy model. J Smart Mater Struct 21. doi:10.1088/0964-1726/21/11/115009
37. Mitchell R, Kim Y, El-Korchi T, Cha YJ (2013) Wavelet-neuro-fuzzy control of hybrid building-active tuned mass damper system under seismic excitations. J Vib Control 19 (12):1881–1894
38. Mitchell R, Cha YJ, Kim Y, Mahajan A (2015) Active control of highway bridges subject to a variety of earthquake loads. Earthq Eng Eng Vib 14(2):253–263
39. Sharifi R, Kim Y, Langari R (2010) Sensor fault isolation and detection of smart structures J Smart Mater Struct 19. doi:10.1088/0964-1726/19/10/105001
40. Takagi T, Sugeno M (1985) Fuzzy identification of systems and its applications to modeling and control. IEEE Trans Syst Man Cybern 15:116–132
41. Yager RR, Filev DP (1993) Unified Structure and parameter identification of fuzzy models. IEEE Trans Syst Man Cybern 23:1198–1205
42. Yan G, Zhou LL (2006) Integrated fuzzy logic and genetic algorithms for multi-objective control of structures using MR dampers. J Sound Vib 296:368–382
43. Yang YN, Lin S (2005) Identification of parametric variations of structures based on least squares estimation and adaptive tracking technique. ASCE J Eng Mech 131:290–298
44. Zadeh LA (1965) Fuzzy sets. Inf Control 8:338–353

A Real-Time Emergency Inspection Scheduling Tool Following a Seismic Event

Nikos Ath. Kallioras and Nikos D. Lagaros

Abstract Emergency infrastructure inspections are of the essence after a seismic event as a carefully planned inspection in the first and most critical hours can reduce the effects of such an event. Metaheuristics and more specifically nature inspired algorithms have been used in many hard combinatorial engineering problems with significant success. The success of such algorithms has attracted the interest of many researchers leading to an increased interest regarding metaheuristics. In the present literature many new and sophisticated algorithms have been proposed with interesting performance characteristics. On the other hand, up to date developments in the field of computer hardware have also had a significant influence on algorithm design. The increased computational abilities that are available to researchers through parallel programming have opened new horizons in architecture of algorithms. In this work, a methodology for real-time planning of emergency inspections of urban areas is presented. This methodology is based on two nature inspired algorithms, Harmony Search Algorithm (HS) and Ant Colony Optimization (ACO). HS is used for dividing the area into smaller blocks while ACO is used for defining optimal routes inside each created block. The proposed approach is evaluated in an actual city in Greece, Thessaloniki.

1 Introduction

Following a catastrophic seismic event, the first hours are critical as far as rescue operations, evacuation procedures and infrastructure repair procedures are considered. As such events can lead to severe short and long-term economic losses, the

N.Ath.Kallioras · N.D. Lagaros (✉)
Institute of Structural Analysis and Seismic Research,
National Technical University of Athens, 9, Iroon Polytechniou Str,
Zografou Campus, 15780 Athens, GR, Greece
e-mail: nlagaros@central.ntua.gr

N.Ath.Kallioras
e-mail: nkallioras@yahoo.com

M. Papadrakakis et al. (eds.), *Computational Methods in Earthquake Engineering*,
Computational Methods in Applied Sciences 44,
DOI 10.1007/978-3-319-47798-5_15

efficiency of the civil services has to be of a great level. In case of a hazardous seismic events civil services are challenged by damaged infrastructure networks, communities in a panicking state-of-mind and system vulnerabilities. Post-disaster management is a multi-level procedure which includes a thorough planning of system response, as well as tactical and operational management. Designing of an optimized inspection plan is definitely a very complex NP-hard combinatorial problem. Metaheuristics present a very successful behavior when dealing with such problems as the one previously described.

Latest advances in metaheuristic algorithms and specifically nature inspired algorithms present automated trial-and-error techniques mostly based on the survival-of-the-fittest principal as species evolution does. It is also important to point-out that the advances in the available hardware and parallel programming have also offered a significant assist in the implementation of metaheuristics. As performance features of single cores of Central Processing Units (CPUs) have not improved significantly in the last years, CPU manufacturers turned to producing multi-core CPUs to increase performance through parallel processing. Graphic processing units (GPUs) also consist of processing cores which in the recent past have been used for mathematical programming. Modern hi-end CPUs consist of 18 cores with clock rates up to 3.6 GHz. On the other hand, high-end GPUs have more than 2.500 cores with clock rates up to 875 MHz. These two different types of processors, each with advantages and disadvantages, offer the ability to efficiently handle problems that in the past were too demanding to be solved.

In this work, two algorithms are used for designing the emergency inspection plan of urban areas. The first algorithm, Improved Harmony Search (IHS), was presented by Kallioras et al. [1] in 2014 while the original version of the algorithm was introduced by Geem et al. [2] in 2001. The second algorithm used in this work is Ant Colony Optimization (ACO) which was presented by Dorigo and Stützle [3] in 2004. The problem of finding the optimal inspection plan of urban structures following a seismic event can be divided into two sub-problems. Firstly, the urban area must be divided into smaller areas, one for each available inspection crew (districting sub-problem), while for each defined area, an optimal route is designed inside its premises (routing sub-problem). The districting sub-problem is dealt with the use of IHS as presented later on in this work while the routing sub-problem is solved with the use of ACO. The biggest challenge in designing this formulation apart from the quality of proposed results, is the necessary computational work-time for the algorithms to locate the solution. In order for this implementation to be able to act as a real-time solution, executional time is rather critical. With the use of GPU programming, computational times are reduced to minimum as can be seen in this work.

2 Post-earthquake Response Mechanism

Inspection time required for assessment of possible damages in structure and infrastructure systems is critical for minimizing cost of effects of a possible hazardous event. Every scheduled event such as support, recovery and rehabilitation can only be properly scheduled after the inspection of infrastructures is completed. This proves the importance of a carefully designed inspection plan towards dealing with a seismic event in an urban area. Generally speaking, we can divide the disaster response procedure [4] into four basic steps:

- Mitigation [5], which includes assessment of seismic hazards, probabilistic damage projection [6, 7], and integration of emergency processes through decision support systems [8, 9].
- Preparedness, which includes preparation for dealing with seismic events and evacuation procedures [10–15].
- Response, which basically deals with creating a plan for response-relief operations [16–19] and post-disaster infrastructure performance evaluation [20–23].
- Recovery which deals with relief performance assessment [24], protection of infrastructure element [25], and repair-fund allocation [26, 27].

Emergency response has attracted the interest of many researchers and significant work has been done in this field in the past years. Despite that, after reviewing up-to-date literature, it can be seen that very little work is done considering the proper planning of inspection crews following a seismic event though it is a very important procedure. This can be explained due to the fact that necessary data is difficult to be collected, solving the associated mathematical problem is very demanding and also, formulating an algorithm that can handle such data and calculations in real-time procedure is exceptionally difficult. In this work, we present the mathematical formulation and solution of such a problem while we also present the parallel formulation of a software that solves such problems in real-time.

3 IHS and ACO Metaheuristic Algorithms

In this work, two metaheuristic algorithms are used for real-time inspection scheduling. As discussed previously, IHS is applied on the districting problem while ACO is used for solving the routing problem. IHS algorithm consists of four basic actions similar to HS. These actions are [1]:

- *Parameter Initialization*
  In this step, the parameters of the algorithm and the problem are defined: n is the number of decision variables, $s_i^L \leq s_i \leq s_i^U, i = 1, 2, \ldots, n$ are the lower and upper bounds of each ith decision variable, *HMS* is the size of the harmony

memory (*HM*) of solution vectors and *HMCR* is the rate for considering the harmony memory.

- *Harmony Memory Initialization*
  In this step, the initialization of the algorithm's memory is executed

$$HM = \begin{bmatrix} s_1^1 & s_2^1 & s_3^1 \ldots & s_n^1 \\ s_1^2 & s_2^2 & s_3^2 \ldots & s_n^2 \\ \ldots & \ldots & \ldots & \ldots \\ s_1^{HMS} & s_2^{HMS} & s_3^{HMS} \ldots & s_n^{HMS} \end{bmatrix} \tag{1}$$

  where s_i^j is the ith element of the jth solution vector s
- *New Harmony Improvisation*
  In this step, a new harmony-solution vector is generated with the use of the random selection procedure or memory consideration procedure. In random selection, each member of the solution vector is randomly generated with probability 1-HMCR ($0 \leq \text{HMCR} \leq 1$). In memory consideration, each variable of the solution vector is randomly chosen from HM with probability HMCR

$$s_i^{New} = \begin{cases} s_i \in [s_i^L, s_i^U] \text{ with probability } 1 - \text{HMCR} \\ s_i \in HM = \{s_i^1, s_i^2, \ldots, s_i^{HMS}\} \text{with probability HMCR} \end{cases} \tag{2}$$

  where $\boldsymbol{s}^{New}$ is the new generated solution vector
- *Harmony Memory Update*
  In this step, the generated solution vector is compared to the worst one stored in HM according to the objective function of each problem. If it is better, it replaces it. If not, it is dropped.

This procedure is repeated as many times as the population of the maximum function evaluations set by the user. Once the maximum function evaluations are completed, the best solution stored in HM is the solution of the problem.

ACO algorithm [3] was inspired by the food searching pattern of ants in nature. As ants search inside an area for possible food resources and the shortest route between the nest and the food position, artificial ants search inside a weighted graph for the optimal path. The search space consists of nodes which represent the places that need to be visited by the ants. At first, a colony of m ants are positioned randomly inside the search space. At each repetitive step of the algorithm, ant k decides which of the nodes it will visit next with the use of a random proportional rule. In order to avoid visiting nodes which are already visited by the same ant, ant k currently positioned at node i, maintains a memory M^k containing all nodes previously visited. This memory defines the feasible neighbourhood N_i^k which contains the nodes that have not been visited by ant k. Ant k, positioned at node i, chooses to move to node j with a probability defined as follows:

$$p_{i,j}^{k} = \frac{(\tau_{i,j})^{\alpha} \cdot (\eta_{i,j})^{\beta}}{\sum_{\ell \in \mathrm{N}_i^k} \left((\tau_{i,\ell})^{\alpha} \cdot (\eta_{i,\ell})^{\beta} \right)}, \quad \text{if } j \in \mathrm{N}_i^k \tag{3}$$

where $\tau_{i,j}$ is the amount of pheromone between nodes i and j, α is a parameter controlling the pheromone's influence, $\eta_{i,j}$ is a heuristic information denoting the desirability of the path between nodes i and j where:

$$\eta_{i,j} = \frac{1}{d_{i,j}} \tag{4}$$

while β is a parameter controlling the influence of the path's desirability $\eta_{i,j}$. The probability of choosing a particular connection i,j increases with the value of the pheromone trail $\tau_{i,j}$ and the heuristic information value $\eta_{i,j}$. When all ants have completed their routes, the pheromone concentration for each connection between i and j nodes, is updated for the next iteration $t + 1$ as follows:

$$\tau_{i,j}(t+1) = (1-\rho) \cdot \tau_{i,j}(t) + \sum_{k=1}^{m} \Delta\tau_{i,j}^{k}(t), \quad \forall (i,j) \in \mathrm{A} \tag{5}$$

where ρ is the rate of pheromone evaporation, A is the set of paths (edges or connections) that fully connects the set of nodes and $\Delta\tau_{i,j}^{k}(t)$ is the amount of pheromone ant k has deposited on connections it has visited during its tour T^k and it is given by:

$$\Delta\tau_{i,j}^{k} = \begin{cases} \frac{Q}{L(\mathrm{T}^k)} & \text{if connection}(i,j) \text{belongs to } \mathrm{T}^k \\ 0 & \text{otherwise} \end{cases} \tag{6}$$

The main concept behind the ACO algorithm is that connections chosen by many ants and have a shorter length, receive bigger amounts of pheromone due to more deposition and less evaporation. This ensures that these paths are more likely to be chosen by other ants in future iterations of the algorithm resulting to the path with the minimum distance.

4 Optimal Inspection Problem Formulation

As described previously, the optimal inspection problem is divided into the districting and the routing sub-problem. In the first sub-problem, the urban domain is divided into a number of areas of responsibility equal to the population of the available inspection crews. In the second sub problem, for each area of responsibility, the optimal route is designed. Urban areas consist of building blocks and

road structures. Each building block is defined by the coordinates of its edges, its area, use of land, building factor and maximum allowed height of constructions. These characteristics provide us with the demand evaluation of each building block. Neighbouring city blocks with similar characteristics regarding use of land, building factor and allowed height can be joined and considered as one in order to reduce the dimensionality of the problem without degrading the quality of the solution. The problem is formulated as a nonlinear optimization problem and the objective function is:

$$\min \sum_{i=1}^{N_{IC}} \sum_{k=1}^{n_{SB}^{(i)}} \left[\frac{D(k)}{U_{in}} + \frac{d(SB_k, C_i)}{U_{tr}} \right] \cdot \sigma_{IC} \tag{7}$$

where N_{IC} is the number of the available inspection crews, $n_{SB}^{(i)}$ is the number of structural (or building) blocks assigned to the ith inspection crew, $d(SB_k,C_i)$ is the distance between the SB_k building block and C_i is the starting block of the crew responsible for the ith group of structural blocks, U_{in} is the inspection speed of the inspection crews, and U_{tr} is the travelling speed of the inspection crews. $D(k)$ is inspection "demand" for the kth building block defined as the product of the building block total area $A(k)$ times the building factor $f_B(k)$ (i.e. the structured percentage of the area) and σ_{IC} is the value of the standard deviation of the working hours of all inspection crews. Thus, the districting problem is formulated as a discrete unconstrained nonlinear optimization problem where the objective is to define which inspection crew is responsible for which building block. The node of each building block is placed in its geometrical centre while all Euclidean distances are calculated with respect to the centre of weight of the building block.

According to the described formulation, every available inspection crew is assigned to a specific district. In the general form of the districting problem, the population of the design variables is equal to the number of building blocks. This leads to a problem with increased complexity. In order to avoid this complexity, the authors suggest a modification to the problem formulation by setting the starting point of the inspection crews as the design variables. This reduces the complexity from n_{SB} *to* N_{IC}. This is accomplished with the use of a four-step procedure where at first

- The starting positions of the inspection crews are defined
- Areas of responsibility are defined by assigning each building block to the closest inspection crew
- The centre of gravity of each area of responsibility is found and this becomes the starting point of each inspection crew and finally,
- New areas of responsibility are created around the new starting positions.

The optimal routing (also called scheduling) problem of the inspection crews is formulated as a travelling salesman problem (TSP). TSP is represented by a weighted graph G = (N, A), where N is the set of nodes and A is the set of connections/paths that connect all N nodes. A cost function is assigned to paths

between two nodes (i and j), represented by the distance between the two nodes $d_{i,j}$ $(i \neq j)$. A solution of the TSP is a permutation $\boldsymbol{p} = [p(1), \ldots, p(N)]^T$ of the node indices $[1, \ldots, N]$, as every node must not appear more than once in a solution. The solution that minimizes the total length $L(\boldsymbol{p})$ given by:

$$\mathrm{L}(\boldsymbol{p}) = \sum_{i=1}^{N-1} \left(d_{p(i),p(i+1)}\right) + d_{p(N),p(1)} \tag{4}$$

is noted as the optimal one. The corresponding scheduling problem is defined as follows:

$$\min \left[\sum_{k=1}^{n_{SB}^{(i)}-1} d(SB_k, SB_{k+1}) + d(SB_{n_{SB}^{(i)}}, SB_1) \right], i = 1, \ldots, N_{\mathrm{IG}} \tag{5}$$

where $d(SB_k, SB_{k+1})$ is the distance between the kth and kth + 1 building blocks. The desired result is to locate the shortest route between all structural blocks assigned to each inspection crew.

5 Numerical Tests

The development and testing of the proposed real-time application is executed on pragmatic data of a city. The chosen city Thessaloniki is the second biggest city in Greece and has in the past suffered from a seismic event. On the 20th of June of 1978 an earthquake with a magnitude of 6.5 R took place in Thessaloniki and caused the death of 45 people while 9.480 buildings suffered non-repairable damages. The city's area is equal to 154,205,128 m^2 while it consists of 471 joint structural blocks as it can be seen in Fig. 1. A hypothetical seismic event is applied in the urban structure of Thessaloniki and an inspection scenario is examined.

According to the scenario, there are 40 inspection crews available for the required task. These crews work in 8-hours shifts per day resulting to having 20 crews working in the city at any moment for 16 h per day. As we were expecting small differences in the necessary working hours of each crew, we set the time needed for the whole inspection to be completed equal to the maximum inspection time of the various crews. The parameter values for IHS and ACO algorithms are chosen with respect to a previous work of the authors which included a thorough sensitivity analysis [28]. In detail, HMS is chosen equal to 12 and HMCR is equal to 0.105693 regarding IHS. Regarding ACO, $\alpha = 1.0$, $\beta = 2.0$, $\rho = 0.10$, $m = 65$ and $Q = 0.306$. The average inspection speed of the crews, U_{in} is set equal to 50 square meters per minute while the average traveling speed of the crews, U_{tr} is set equal to 10 km/hour. For IHS the maximum iterations for are equal to 200,000 while for ACO they are equal to 200.

Fig. 1 The city-plan of Thessaloniki and the 471 joint city blocks

The hours needed for the inspection crews to complete the task can be seen in Table 1. In particular, the maximum time which also corresponds to the end of the inspection is equal to 5683.006 h. The average working hour of the ten crews is equal to 5142.285 h while the maximum variation from the average time needed for the crews to finish the inspection crew is equal to 11.11 %. The value of the objective function is equal to 18650882.911. The best and worst value of the objective function stored in IHS memory per each of the 200,000 iterations can be seen in Fig. 2.

Table 1 Inspection time and travel time per crew

Inspection crew	Inspection time (hours)	Travel time (hours)	Total time (hours)
Inspection crew 1	5556.778	3.150	5559.928
Inspection crew 2	5574.094	1.722	5575.816
Inspection crew 3	5679.853	3.152	5683.006
Inspection crew 4	4569.000	1.707	4570.708
Inspection crew 5	5154.745	1.764	5156.509
Inspection crew 6	4918.512	1.595	4920.107
Inspection crew 7	4826.740	1.676	4828.417
Inspection crew 8	5087.935	1.800	5089.735
Inspection crew 9	5097.223	1.554	5098.777
Inspection crew 10	4936.829	3.022	4939.851

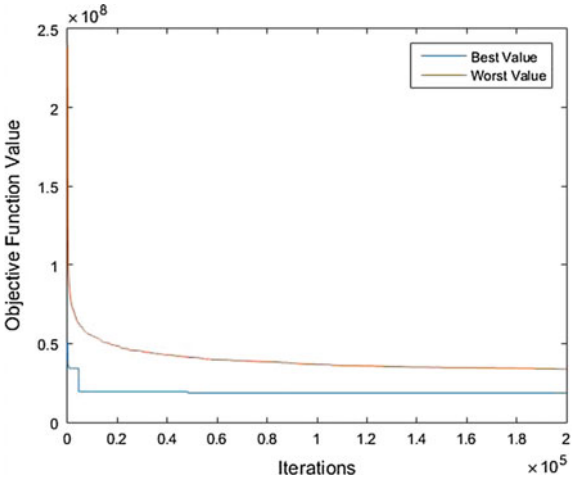

Fig. 2 Best and worst objective function value per IHS iteration

In Fig. 3, the results of IHS applied on the districting problem can be seen. Each colour represents an inspection crew and an area of responsibility. In Fig. 4 the routing results of ACO are presented while in Fig. 5, a closer look on 5 of the designed routes are visible.

The minimization of the computational effort and time needed to solve this problem is accomplished with the use of GPU programming applied on the ACO algorithm and parallelization of the IHS algorithm. In order to evaluate the gain of such an implementation, the same problem is solved twice, first with the suggested techniques and then without them. Both implementations are solved ten times and the average execution times are presented. The GPU version is completed after $T_1 = 225.65$ s while the unmodified version demands $T_2 = 1242.87$ s. The acceleration factor is equal to T2/T1 = 5.508 which is rather significant. The acceleration

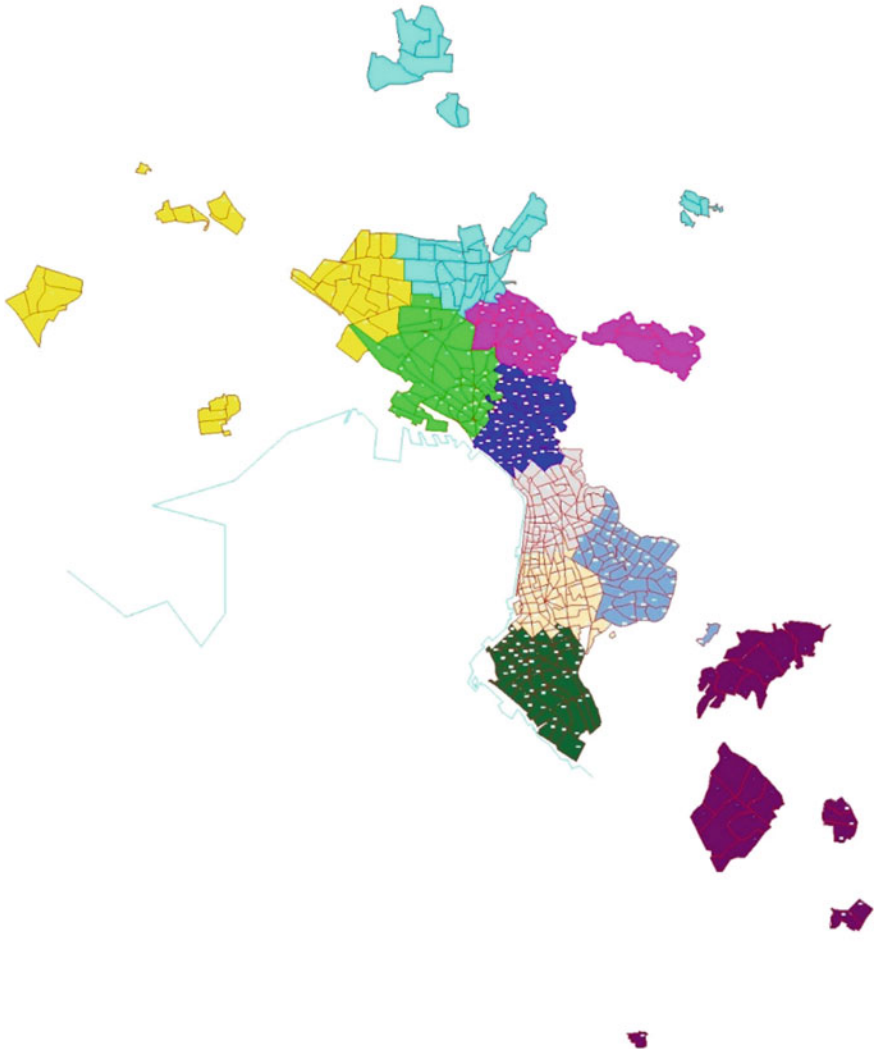

Fig. 3 Districting results for the city of Thessaloniki. Each color represents an area of responsibility for each of the 10 inspection crews

factor increases as the dimensionality of the problem increases as presented by Kallioras et al. [28] in a previous work. It is also important to point out that a more up to date GPU processing unit than the one used here would have given even better acceleration results. None the less, solving such a problem in less than 4 min does satisfy the criterion as a real-time solver. The experiments of the current study

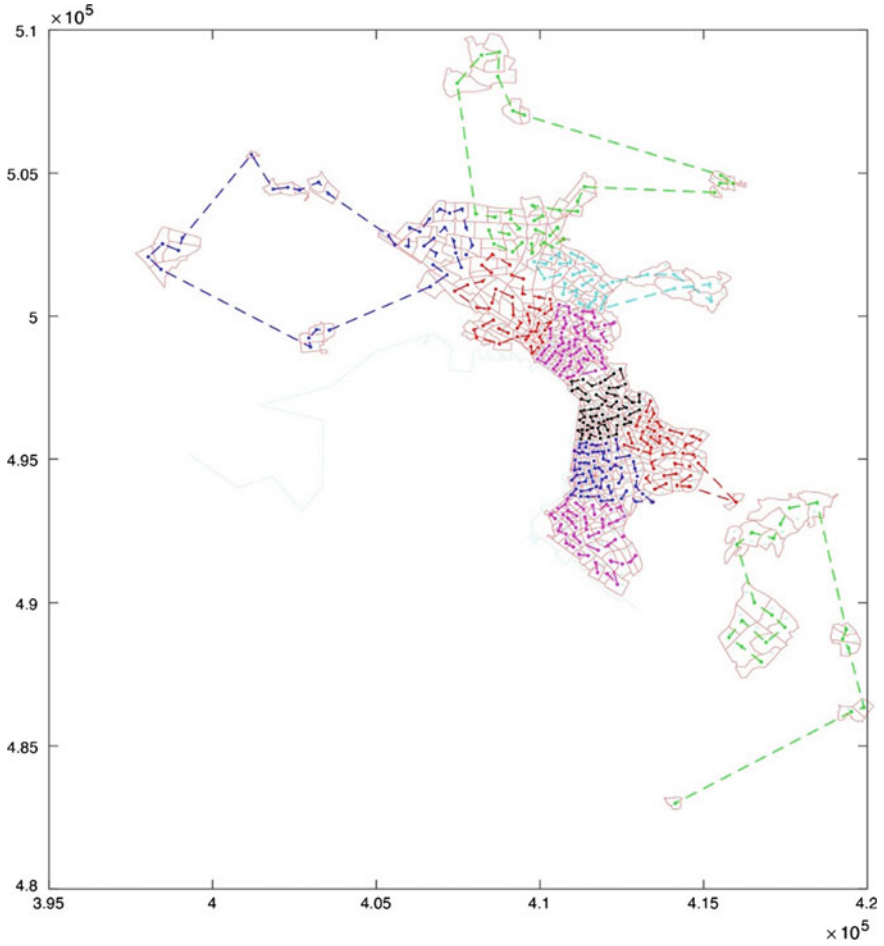

Fig. 4 Routing results for the city of Thessaloniki. The route of each of the 10 inspection crews is marked with a different color

were performed using the Intel i7 3610QM 2.30 Ghz processor with 4 cores paired with 12 GB memory and the NVIDIA GeForce GTX 660 M with 384 stream processors (CUDA cores) with 2 GB of memory and supports CUDA compute capability 3.0.

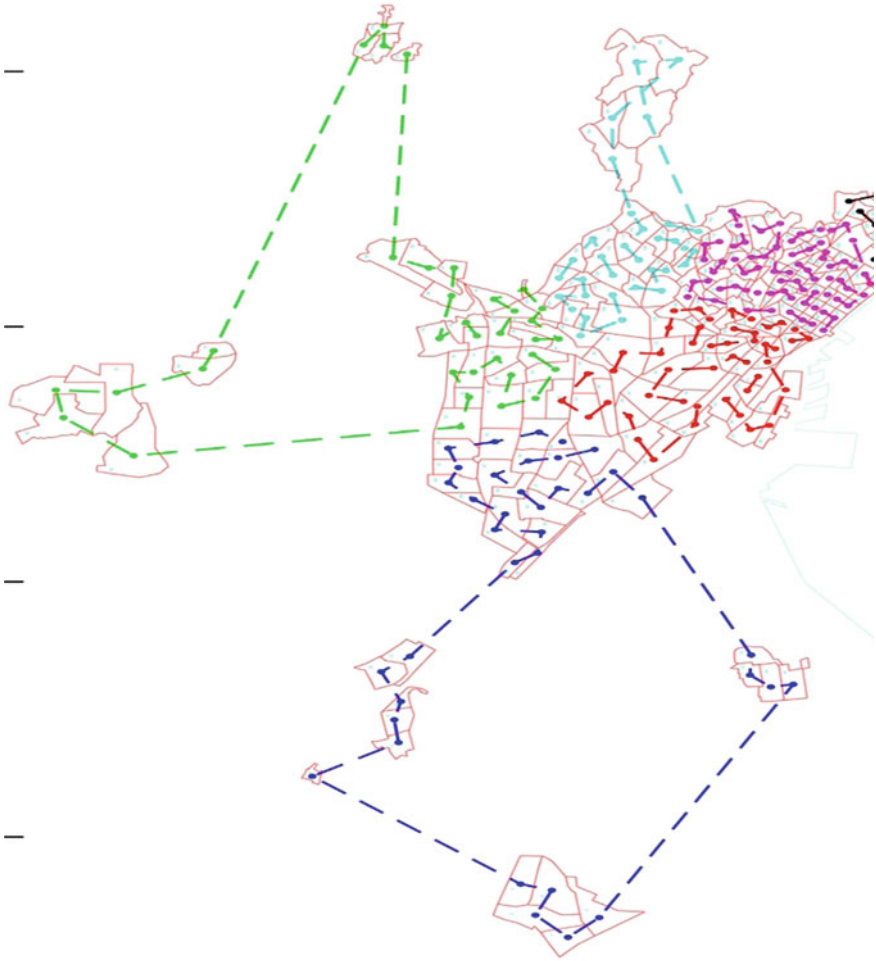

Fig. 5 Closer look on the routes for 5 of the inspection crews inside their area of responsibility

6 Conclusions

In this work, a real-time emergency inspection scheduling application following a seismic event is presented. This application is based on two nature-inspired metaheuristic algorithms, IHS and ACO. The first is a variation of the well-known and established Harmony Search algorithm while the second one is the also established Ant Colony Optimization algorithm. Both algorithms have proven their ability to handle hard combinatorial problems in literature. Both algorithms have also proven their robustness when applied on such problems. Through this work, a parallel GPU implementation of the algorithm is presented in order to minimize the computational time needed to solve such problems. Computational time is very

important when we are dealing with situations where solutions need to be presented in real-time. Dealing with a seismic event is such a situation as a delay in scheduling support and relief efforts can cost dramatically.

Our approach is implemented on the urban environment of the second largest city in Greece, Thessaloniki, who has suffered from a seismic event in the recent past. With the assumption that 20 inspection crews will be available and working on 8-hour shifts, we have 10 crews inspecting the urban structures for 16 h per day. Based on these estimations, along with the inspection and traveling speed of crews, the necessary time for the inspection of the whole area was equal to 5683.006 h while the variation between crews is also very small.

By implementing the algorithms with the use of GPU programming, a significant acceleration factor equal to 5.508 is achieved which is very important in real-time applications. It is also important to point out that the acceleration factor increases with the increase of the dimensionality of the problem. The proposed formulation has the ability to robustly solve the described problem in less than four minutes. In the future, it might be useful to apply modifications on the algorithm which will offer the end-user the ability to choose before executing the algorithm a series of joint city blocks that need to be inspected first. It can also be modified to resolve the problem while city blocks with increased level of damage are set by the user according to emergency calls. Another modification that is worth investigating is giving the algorithm the ability to un-assign city blocks from crews with large inspection areas and assigning them to those who finish first.

Acknowledgments The research study in the current chapter has been conducted in the frame of the Research Funding Program: Marie Sklodowska-Curie Research and Innovation Staff Exchanges (RISE) "OPTARCH—Optimization Driven Architectural Design of Structures", H2020-MSCA-RISE-2015.

References

1. Kallioras NA, Lagaros ND, Karlaftis MG (2014) An improved harmony search algorithm for emergency inspection scheduling. Eng Optimization 46:1570–1592
2. Geem ZW, Kim JH, Loganathan GV (2001) A new heuristic optimization algorithm: harmony search. Simulation 76:60–68
3. Dorigo M, Stützle T (2004) Ant Colony Optimization. The MIT Press, Cambridge
4. Altay N, Greene WG (2006) OR/MS research in disaster operations management. Eur J Oper Res 175:475–493
5. Dong WM, Chiang WL, Shah HC (1987) Fuzzy information processing in seismic hazard analysis and decision making. Soil Dyn Earthquake Eng 6(4):2202–2226
6. Peizhuangm W, Xihui L, Sanchez E (1986) Set-valued statistics and its application to earthquake engineering. Fuzzy Sets Syst 18(3):347–356
7. Tamura H, Yamamoto K, Tomiyama S, Hatono I (2000) Modelling and analysis of decision making problem for mitigating natural disaster risks. Eur J Oper Res 122(2):461–468
8. Mendonca D, Beroggi GEG, Wallace WA (2001) Decision support for improvisation during emergency response operations. Int J Emergency Manage 1(1):30–38

9. Mendonca D, Beroggi GEG, Van Gent D (2006) Designing gaming simulations for the assessment of group decision support systems in emergency response. Saf Sci 44:523–535
10. Viswanath K, Peeta S (2003) Multicommodity maximal covering network design problem for planning critical routes for earthquake response. Transp Res Rec 1857:1–10
11. Nicholson A, Du Z-P (1997) Degradable transportation networks systems: An integrated equilibrium model. Transp Res Part B 31(3):209–223
12. Sakakibara H, Kajitani Y, Okada N (2004) Road network robustness for avoiding functional isolation in disasters. J Transp Eng 130(5):560–567
13. Sohn J (2006) Evaluating the significance of highway network links under the flood damage: an accessibility approach. Transp Res Part A 40(6):491–506
14. Song J, Kim TJ, Hewings GJD, Lee JS, Jang S-G (2003) Retrofit priority of transport network links under an earthquake. J Urban Plann Develop 129(4):195–210
15. Verter V, Lapierre S (2002) Location of preventive healthcare facilities. Ann Oper Res 110:123–132
16. Barbarosoglou G, Arda Y (2004) A two-stage stochastic programming framework for transportation planning in disaster response. J Oper Res Soc 55(1):43–53
17. Barbarosoglou G, Ozdamar L, Cevik A (2002) An Interactive approach for hierarchical analysis of helicopter logistics in disaster relief operations. Eur J Oper Res Soc 140(1):118–133
18. Fiedrich F, Gehbauer F, Rickers U (2000) Optimized resource allocation for emergency response after earthquake disasters. Saf Sci 35(1–3):41–57
19. Ozdamar L, Ekinci E, Kucukyazici B (2004) Emergency logistics planning in natural disasters. Ann Oper Res 129(1–4):217–245
20. Bell MGH (2000) A game theory approach to measuring the performance reliability of transportation networks. Transp Res Part B 34(6):533–545
21. Chang SE, Nojima N (2001) Measuring post-disaster transportation system performance: the 1995 Kobe earthquake in comparative perspective. Transp Res Part A 35(6):475–494
22. Karaouchi F, Lida Y, Shimada H (2001). Evaluation of road network reliability considering traffic regulation after a disaster. In: Bell MGH, Lida Y (eds)The network reliability of transport: proceedings of the 1st international symposium on transportation network reliability (INSTR). Elsevier, Oxford, United Kingdom
23. Li Y, Tsukaguchi H (2001) Improving the reliability of street networks in highly densely populated urban areas. In: Bell MGH, Lida, Y (eds) The network reliability of transport: proceedings of the 1st international symposium on transportation network reliability (INSTR). Elsevier, Oxford, United Kingdom
24. Song B, Hao S, Murakami S, Sadohara S (1996) Comprehensive evaluation method on earthquake damage using fuzzy theory. J Urban Plann Dev 122(1):1–17
25. Cret L, Yamakazi F, Nagata S, Katayama T (1993) Earthquake damage estimation and decision-analysis for emergency shutoff of city gas networks using fuzzy set theory. Struct Saf 12(1):1–19
26. Karlaftis MG, Kepaptsoglou KL, Lampropoulos S (2007) Fund allocation for transportation network recovery following natural disasters. J Urban Plann Dev 133(1):82–89
27. Lagaros ND, Karlaftis MG (2011) A critical assessment of metaheuristics for scheduling emergency infrastructure inspections. Swarm Evol Comput 1(3):147–163
28. Kallioras N, Kepaptsoglou K, Lagaros ND (2015) Transit stop maintenance scheduling: a metaheuristic approach. Transportation Res Part C 55:246–260